THE UNIVERSITY of ADELAIDE

Luminescence dating and geochemistry constraints on late Pleistocene hydrological and ecological change for north-eastern Australia

Richard J. Lewis

Department of Earth Sciences
School of Physical Sciences
The University of Adelaide

This thesis is submitted in fulfilment of the requirements
for the degree of Doctor of Philosophy

Contents

Thesis Abstract

Extensive debate surrounds the timing and cause of late Pleistocene megafauna extinction across the continent of Sahul (Australia and New Guinea). Central to these debates is uncertainty in the timing and impact of key events during the last glacial cycle (125 – 12 thousand years ago; ka) including the arrival of humans on the continent, the effect climate change had on environments, and the geographical and temporal patterns of megafauna extinction. This uncertainty can be attributed to the lack of well-constrained palaeoenvironmental records, limited spatial coverage and dating reliability. To address these knowledge gaps, this thesis applies geochronological and geochemical techniques to a series of new palaeoenvironmental archives to investigate megafauna extinction in the context of climate-induced environmental change.

Chapters 2 and Chapter 3 of the thesis present optically stimulated luminescence (OSL) and radiocarbon (^{14}C) dating results on palaeoenvironmental archives (sediment cores) from two subtropical wetlands (Welsby Lagoon, Chapter 2; Brown Lake, Chapter 3). Analysis of twenty-one OSL ages and seven ^{14}C ages from Welsby Lagoon (Chapter 2) highlights the importance of carefully considering the material being dated, especially where contamination is likely. In general, ^{14}C ages derived from identifiable terrestrial plant macrofossils agree with OSL ages, while ^{14}C results derived from unidentifiable plant remains and charcoal are scattered and produce stratigraphic inversions. The need to consider different sediment accumulation histories on a site-by-site basis is also demonstrated in Chapter 2 and Chapter 3 using Bayesian modelling.

Further geochronological results are reported in Chapters 4 and Chapter 5, which combine OSL, ESR and U-series dating to establish megafauna last appearance at the new tropical megafauna fossil locality of South Walker Creek, Queensland (Chapter 4 & Chapter 5). Hierarchical Bayesian modelling – which incorporates 66 new ages from eight sites – is used to provide new evidence for megafauna disappearance in the Fitzroy River catchment between 41.7 and 35.8 ka (95 % C.I.; Chapter 5). Additionally, hierarchical Bayesian modelling of fluvial and fossil deposits at the South Walker Creek fossil locality indicates a decrease in hydrological activity in the area during mid- to late- Marine Isotope Stage 3 (MIS3) (Chapter 5).

The comprehensive dating approach presented in each study (Chapters 2 – 5) enables improved examination of the spatiotemporal pattern of climate-induced environmental change taking place across eastern Australia immediately prior to, during, and after, megafauna disappearance (Chapter 5). Alignment of XRF and age data from Welsby Lagoon shows two phases of increased dust deposition at 71 – 67 ka and 58 – 48 ka (Chapter 2) – the latter coinciding with the wetland transitioning from a lake to swamp. Brown Lake also experienced an increase in dust deposition through late MIS3, in addition to entering a phase of shoreline regression lasting until the Holocene (Chapter 3). Notably, when these sites are included in a regional spatiotemporal synthesis of hydrological activity (compiling data from other wetlands and regional catchments) and are considered in the context of local megafauna records (Chapter 4), there is evidence to suggest megafauna disappearance in the Fitzroy River Basin catchment was coincident with broader environmental change during mid- to late-MIS3 (Chapter 5).

This thesis employs a robust, geochronologically driven approach to examine ecological and environmental change during significant and understudied periods of Australian prehistory (e.g., pre-LGM). The overarching conclusion is that there is little support for rapid or synchronous human-mediated, continent-wide megafauna extinction during the late Pleistocene. Rather, the data suggest extinction coincided with a period of prolonged hydroclimate deterioration initiated during the mid- to late-MIS3.

Thesis Declaration

I certify that this work contains no material which has been accepted for the award of any other degree or diploma in my name in any university or other tertiary institution and, to the best of my knowledge and belief, contains no material previously published or written by another person, except where due reference has been made in the text. In addition, I certify that no part of this work will, in the future, be used in a submission in my name for any other degree or diploma in any university or other tertiary institution without the prior approval of the University of Adelaide and where applicable, any partner institution responsible for the joint award of this degree.

The author acknowledges that copyright of published works contained within this thesis resides with the copyright holder(s) of those works.

I give permission for the digital version of my thesis to be made available on the web, via the University's digital research repository, the Library Search and also through web search engines, unless permission has been granted by the University to restrict access for a period of time.

I acknowledge the support I have received for my research through the provision of an Australian Government Research Training Program Scholarship.

Date: 10 / 10 / 2021

Richard J. Lewis

Acknowledgement of Country

I wish to acknowledge and pay respects to the Aboriginal people past and present as the traditional owners of the land on which this research was conducted namely the Kaurna people, the traditional custodians whose ancestral lands on which the University of Adelaide's campuses at North Terrace, Waite and Roseworthy are built. I acknowledge the deep feelings of attachment and relationship of the Kaurna people to country, and I respect and value their past, present, and ongoing connection to the land and cultural beliefs. I also wish to acknowledge the Aboriginal people and traditional custodians of the land on which I conduced my fieldwork. I wish to acknowledge Minjerribah (North Stradbroke Island) and the surrounding waters as Quandamooka Country and thank the Quandamooka Yoolooburrabee Aboriginal Corporation for permission to undertake the work. I respect and value their past, present and ongoing connection to the land and cultural beliefs. I also thank them for their guidance and contributions for work undertaken in Minjerribah. I also wish to acknowledge and pay respect to the Barada Barna people, the traditional custodians of the land in central Queensland where South Walker Creek is located. I acknowledge the deep feelings of attachment and relationship of the Barada Barna people with country. I respect and value their past, present, and ongoing connection to the land and cultural beliefs. I also thank them for their guidance and contributions for work undertaken in South Walker Creek.

Acknowledgements

The completion of this PhD would not have been possible without the invaluable support and contribution of many people and organisations. There are too many to list individually, but without you all it would not have been possible to get to where I am today.

An enormous thank you goes to my supervisors without who none of this would be possible. My deepest gratitude goes out to Associate Professor Lee Arnold, whose professional demeanour has helped me grow not only as a researcher, but as a person, and who persists as a beacon of support, guidance and encouragement. Thank you to Associate Professor John Tibby who welcomed me into his research group and helped shape the direction of the thesis. Thank you to Professor David Chittleborough who would always find a way to get me to reflect on achievements to date making the journey ahead less daunting.

Thank you to my interstate colleges, particularly those from the Queensland Museum and State Government, for providing logistical support and expertise. My gratitude to Dr. Scott Hocknull, who became an unofficial supervisor and Rochelle Lawrence, who provided me with many opportunities to grow as a researcher. Thank you to Dr. Jonathan Marshall and Dr. Glenn McGregor without whom it would not have been possible to undertake research on the wetland sediments.

A special acknowledgement to everyone who helped me with data collection in the field and laboratory: Cameron Barr, Jo Blessing, Jie Chang, Jacinta Greer, Matthew Jones, Christopher Kemp, Rochelle Lawrence, Professor Patrick Moss, Peter Negus, Gilian Ross, Noel Sands, Cameron Shultz and the extended Queensland Museum Team.

This project would not have been possible without support from Australian Research Training Program and CRC LEME regolith science research scholarships (awarded to Richard Lewis), the Australian Research Council Future Fellowship (FT130100195 – awarded to Lee Arnold) and, Discovery Projects (DP150103875 awarded to John Tibby; Patrick Moss; Melanie Leng; Jeremy Shakun and Nigel Spooner), the Queensland Museum Foundation and BHP. In addition, I would like to recognise the support of ANSTO and staff Patricia Gadd and Dr. Geraldine Jacobsen in assisting with delivering core scanning XRF and radiocarbon dating capabilities, respectively (via portal projects AP11411, AP11643, AP12402).

I would also like to acknowledge the people who were there since the start of this journey, providing motivation and inspiration to push me through when things got tough: my family for supporting me through the moody, grumpy and emotional times; close university friends Dr. Briony Chamberlayne and Dr. Kamini Bhowany who always supported me through the hard times; the University of Adelaide Judo Club members – especially Michael Headland Sensei and Meera Verma Sensei – who were instrumental in keeping balance between my work and personal life, all the while enlightening me on how the principles of Judo can be a *Way of Life*; the entire Naracoorte Caves team for sharing their enthusiasm and interest of science while providing me with the opportunity to practice communicating science to the public.

Dissemination of research

Publications as primary author

Lewis, R. J., Tibby, J., Arnold, L. J., Gadd, P., Jacobsen, G., Barr, C., Negus, P. M., Mariani, M., Penny, D., Chittleborough, D. & Moss, E. 2021. Patterns of aeolian deposition in subtropical Australia through the last glacial and deglacial periods. Quaternary Research, 1-23.

Lewis, R.J., Tibby, J., Arnold, L.J., Barr, C., Marshall, J., McGregor, G., Gadd, P. and Yokoyama, Y., 2020. Insights into subtropical Australian aridity from Welsby Lagoon, North Stradbroke Island, over the past 80,000 years. Quaternary Science Reviews, 234, p.106262.

Publications as collaborator

Cadd, H., Sherborne-Higgins, B., Becerra-Valdivia, L., Tibby, J., Barr, C., Forbes, M., Cohen, T. J., Tyler, J., Vandergoes, M., Francke, A., Lewis, R., Arnold, L. J., Jacobsen, G., Marjo, C. & Turney, C. 2022. The application of pollen radiocarbon dating and Bayesian age-depth modeling for developing robust geochronological frameworks of wetland archives. Radiocarbon, 64, 213-235.

Hocknull, S. A., Lewis, R., Arnold, L. J., Pietsch, T., Joannes-Boyau, R., Price, G. J., Moss, P., Wood, R., Dosseto, A., Louys, J., Olley, J. & Lawrence, R. A. 2020. Extinction of eastern Sahul megafauna coincides with sustained environmental deterioration. Nature Communications, 11, 1-14.

Lisé-Pronovost, A., Fletcher, M.-S., Mallett, T., Mariani, M., Lewis, R., Gadd, P., Herries, A., Blaauw, M., Heijnis, H. & Hodgson, D. 2019. Scientific Drilling of Lake Sediments at Darwin Crater, Tasmania. Scientific Drilling, 25, 1-14.

Cadd, H. R., Tibby, J., Barr, C., Tyler, J., Unger, L., Leng, M. J., Marshall, J. C., McGregor, G., Lewis, R. & Arnold, L. J. 2018. Development of a Southern Hemisphere subtropical wetland (Welsby Lagoon, south-east Queensland, Australia) through the last glacial cycle. Quaternary Science Reviews, 202, 53-65.

Conference abstracts and research presentations

Lewis, R. J., Arnold, L. J., Hocknull, S., Tibby, J., Demuro, M. & Lawrence, R. 2021. The hydroclimatic and chronological context of late Pleistocene megafauna extinction in north-eastern Australia, Geological Society of Australia, Earth Sciences Student Symposium, South Australia, Adelaide, Australia.

Lewis, R. J., Arnold, L. J., Hocknull, S., Demuro, M., Lawrence, R. & Augusten, A. 2021. Single-grain OSL and extended-range luminescence dating of late to middle Pleistocene faunal assemblages from tropical eastern Australia, 16th International Luminescence and Electron Spin Resonance Dating conference (LED2021), South Australia, Adelaide, Australia.

Lewis, R. J. 2021. Glowing Sand: Illuminating ancient Australian waterflow, 3 Minute Thesis (3MT), School of Physical Sciences, University of Adelaide, Adelaide, Australia.

Lewis, R. J. 2021. Earth Science applications of OxCal. Department of Earth Sciences Seminar Series, University of Adelaide, Adelaide, Australia.

Lewis, R. J. 2021. Applying luminescence in sedimentary deposits to shine light on Australia's Late Pleistocene ecology. Institute for Photonics and Advance Sensing (IPAS): Awardee seminar series – best student led publication award, Adelaide, Australia.

Lewis, R. J. 2019. Wetland sediment geochemistry: what can it tell us about the past? Field Geology Club of SA, Adelaide, Australia.

Lewis, R. J., Tibby, J., Arnold, L. J., Barr, C., Marshall, J., McGregor, G.& Gadd, P. 2018. Independent Bayesian age modelling in subtropical wetlands to assess the influence of global climate drivers across Australia. Australian Quaternary Association: Biennial Conference, Canberra, Australia.

Lewis, R. J., Tibby, J., Arnold, L. J., Barr, C., Marshall, J. & McGregor, G. 2019. High-resolution, chronological study of a 120 ka continuous sedimentary record in subtropical Australia. SheMAX workshop, North Stradbroke Island, Australia.

List of Figures

List of Tables

Chapter 1 Introduction and thesis outline

Introduction

More than 150 genera of megafauna (animals of >45 kg in body mass) suffered global extinction during the past 60 ka (Lorenzen et al., 2011; Sandom et al., 2014; Stuart, 2015; Willerslev et al., 2014; Wroe & Field, 2006). Vertebrate fossil data from the late Pleistocene show that the extent of megafaunal extinction varied geographically (i.e., 18% of known mammalian genera disappeared from Africa, 36% from Eurasia, 72% – 83% across North and South America, and 88% in Australia; Fattorini, 2021). The disappearance of megafauna arguably had a distinct impact on local ecosystems including marked vegetation change, reduced seed dispersal, pollination (Pires et al., 2018) and disruption of food webs. Accompanying changes in habitat and local vegetation regimes are also argued to have impacted geography and climate, via changed albedo, nutrient recycling and feedback system processes (e.g., Malhi et al., 2016; Rule et al., 2012; Staal et al., 2020).

In Australia, there is significant uncertainty regarding the nature of events leading up to megafaunal extinction and substantial debate surrounds the timing of key events, including the arrival of humans, climate change, and the dynamics of megafauna demise across different regions. Explanations for widespread and relatively rapid megafaunal extinction vary geographically and, are often debated. Though many extinction scenarios have been proposed, all can be placed somewhere on a spectrum between two end-member causes (Horton, 1980): human-linked drivers, which attribute megafaunal extinction directly or indirectly to pressures arising from human practices (e.g., hunting, fire, environment modification; Bird et al., 2013; Brook & Johnson, 2006; Flannery, 1994), and climatic drivers, which attribute extinction to pressures arising from shifting oceanic and atmospheric conditions (including habitat change, reduced water availability and altered vegetation regimes; Field et al., 2008; Fillios et al., 2010; Wroe et al., 2013). Despite major disagreements between the proponents of these competing extinction hypotheses, most researchers are in agreement that there are too few well-dated palaeontological and palaeoenvironmental records to resolve the Australian megafaunal extinction debate.

This thesis contributes to ongoing megafaunal extinction discussions with the overarching aim of evaluating whether the extinction of Australian megafauna coincided with widespread climate-induced environmental change. The studies herein focus on the establishment of new, and the improvement of existing, palaeoenvironmental records in important, geographically underrepresented regions. Comprehensive geochronological studies involving multiple dating techniques and the latest Bayesian modelling approaches are used to provide deeper insights into the timing of key events associated with Australian megafaunal extinction.

Research context

Much of the debate surrounding the relationship between megafaunal extinction and environmental change in Australia is centred on the interpretation of available palaeoenvironmental proxy data spanning the last glacial cycle (David et al., 2021; Field et al., 2008; Grün et al., 2010). Multidisciplinary and multi-proxy analysis is increasingly commonplace in palaeoenvironmental research (Price et al., 2021). However, even when such an approach is undertaken, it can be difficult to differentiate whether past variations were influenced by anthropogenic or natural change (Price et al., 2021; Saltré et al., 2016; van der Kaars et al., 2017). Moreover, it can be a challenge to establish whether a change in a given site record is attributable to a widespread climate event or is a product of local variability (e.g., vegetation regime change due to increased frequency of localised bushfires and

burning, or changes in regional precipitation; Spessa et al., 2005). The establishment of reliable chronologies can help to disentangle some of these cause-and-effect relationships by enabling independent comparisons of palaeoenvironmental records on unified timescales and the identification of temporally linked change in proxy characteristics across different sites (David et al., 2021; Price et al., 2021).

Terrestrial palaeoenvironmental archives are useful for identifying palaeoenvironmental change as they tend to have higher rates of material accumulation (~0.3 m/ka; Chapter 3) relative to deep-marine sediments (~0.15 m/ka; Kissel et al., 1999), thus preserving higher resolution information (Birks & Birks, 2006). Targeting new terrestrial archives is particularly important in an Australian context as there are currently few long-term records that extend back to the period of megafaunal extinction (i.e., marine isotope stage (MIS) 3; Kemp et al., 2019). Numerous methods that analyse both biogenic and minerogenic materials as proxies for palaeoenvironmental conditions have been utilised to examine conditions over the last glacial cycle. In Australia common approaches for reconstructing temporal palaeoclimate and environmental change include: palynology (including pollen (Cadd et al., 2018; Moss, 2013b); charcoal (Kershaw et al., 2002; Mooney et al., 2011); and fungal spore (Dodson & Field, 2018; Rule et al., 2012) analysis) as an indicator for the presence of megafauna, temperature and fire impact; palaeontology (including vertebrates (Hocknull et al., 2020; Prideaux et al., 2007); diatoms (Barr et al., 2013; Tibby & Haberle, 2007); ostracods (De Deckker et al., 2011); foraminifera (Haller et al., 2018; Lisiecki & Raymo, 2005)) as an indicator for ecological, hydrological and sea level changes; geochemistry (e.g., dust (McGowan et al., 2008; Petherick et al., 2009); isotopes and lipid biomarkers (Diefendorf & Freimuth, 2017)) as an indicator for wind patterns, diagenesis and nutrient cycling; and geomorphology (e.g., shorelines (Cohen et al., 2018); dunefields (Patton et al., 2019); palaeochannels (Kemp et al., 2017; Kemp & Rhodes, 2010)), as an indicator for change in local and regional hydrological conditions. Caution is typically applied when inferences are made on the response of individual palaeoenvironmental proxies, as observations may equally be attributed to changes in local catchment conditions or those occurring further afield (Farebrother et al., 2017).

The research in this thesis focuses on improving both the chronological framework and range of terrestrial palaeoenvironmental archives available for examining Australian megafaunal extinction. The following sections outline the current state of research in three key areas of relevance to the Australian megafaunal extinction debate and the work conducted in this thesis: namely, climate change through time, late Pleistocene archaeological and palaeontological evidence in the geological record, and dating techniques in palaeoenvironmental research.

Climate change though time

Over tens to hundreds of thousand year timescales, the Earth has cycled between cooler (glacial) and warmer (interglacial) periods, as is evident from polar ice-core and marine records from the Northern and Southern Hemisphere. Examination of these records identified glacial-interglacial cyclic patterns with periodicity of 23,000, 41,000 and 100,000 years from the middle Pleistocene onwards (Imbrie et al., 1992; Lisiecki & Raymo, 2005). Notably, this periodicity is in tune with variation in the orbital parameters (i.e., precession, obliquity and eccentricity) of the Earth around the Sun (Berger, 1988; Milankovitch et al., 1941). Although there is broad temporal agreement between orbital forcing variables and global temperature responses, which supports the relationship between long-term climate cycles and changes in solar insolation (Berger, 1988; Imbrie et al., 1984), climate conditions

and responses also vary significantly across regions due to factors such as internal feedbacks (Helman & Tomlinson, 2018).

The expression, timing and interactions of the various climate system components are complex and not fully understood. For example, Dansgaard-Oeschger events (Dansgaard et al., 1982; Rasmussen et al., 2014; Rousseau et al., 2020), periods when oceanic and atmospheric conditions fluctuated dramatically between stadial (cold) and interstadial phases (warm), have been linked to mechanisms such as change in the coverage of Greenland sea ice and alterations of the Atlantic Meridional Overturning Circulation (Boers et al., 2018; Petersen et al., 2013; Rousseau et al., 2020). Dangaard-Oeschger events are additionally linked with Heinrich events (Bond et al., 1992; Heinrich, 1988; Hemming, 2004). Heinrich events are characterised by large iceberg discharge events, originating predominantly from the Laurentide icesheet, with eroded detritus from subsequent melting found in North Atlantic marine sediment cores (Hodell & Channell, 2016; Hodell et al., 2008). These and other regional drivers are responsible for localised internal feedbacks on the climate system, with the capacity to influence extreme climatic shifts on annual to millennial timescales (King et al., 2020). Despite the importance of understanding how these complex climate system components interact through time (Cooper et al., 2021; De Deckker, 2020), particularly in the context of long-term climate-induced environmental change, they are not well understood over the course of the Pleistocene.

The last glacial cycle (129 ka – Holocene) is a particularly important when reconstructing the evolution of the Australian landscape as it encompasses significant environmental change. Moreover, examination of marine sediment isotopic data has shown that the last glacial cycle hosts several major alternations between warm and cool phases, referred to as Marine Isotope Stages (MIS) (Lisiecki & Raymo, 2005). Similar isotopic signatures of these cooler and warmer phases have been found in other types of geological archives from around the world, including in equatorial speleothems (Wang et al., 2001) and polar region ice cores (Reeves et al 2013; Jouzel et al., 2007; Parrenin et al 2007), which collectively suggest a global climate response.

In Australia, the lack of palaeoclimate archives across the continent and offshore has been noted as a limitation in developing a deeper understanding of climate-induced environmental change (De Deckker, 2020, 2019; Moss, 2013b; Petherick et al., 2013; Reeves et al., 2013; Tibby et al., 2017). A synthesis study of all Australian MIS3 palaeoenvironmental records (n = 40; Kemp et al., 2019) found a strong spatial bias in the distribution of records. In particular, the tropical and subtropical regions are underrepresented, comprising only ~20% of the database despite ~60% of the continent positioned north of 30°S. Kemp et al. (2019) also identified a bias towards southern and coastal localities (Figure 1.1), while numerous records have missing information between 57 ka and 35 ka.

The scarce number, and coastal bias, of extended Australian palaeoenvironmental sites (Kemp et al., 2019) may be partly explained by regional changes in hydrological activity through time, which may have inhibited sediment deposition in some areas (Lowe & Walker, 2014). The occurrence of fewer MIS3 archives in the Australian interior likely reflects a combination of inaccessibility and less favourable preservation conditions for some proxies due to erosion and changes in soil alkalinity – the latter being driven by alternating wetter and drier conditions (Ascough et al., 2011; Braadbaart et al., 2009) associated with changes in the Indo-Australian monsoon and positioning of the Intertropical Convergence Zone (Cohen et al., 2018; Fu et al., 2017). Regardless, the lack of data hinders

deconvolution of palaeoecological responses to complex climate variation, particularly through the important MIS3 period (Reeves et al., 2013). As a result, multi-site comparative approaches, particularly over the last glacial cycle, often require strategic interpolation and modelling over large areas that are devoid of any palaeoenvironmental records (Fitzsimmons et al., 2013; Kemp et al., 2019; Tibby et al., 2017).

Discussions about MIS3 in Australian are broadly focused on evaluating the timing, magnitude and extent of millennial-scale climate variability across the Southern Hemisphere (Cohen et al., 2018; Fitzsimmons et al., 2013; Kershaw et al., 2007b; Petherick et al., 2011; Reeves et al., 2013). Records of lake filling events and fluvial activity suggest that central Australia became more arid from ~48 ka (Cohen et al., 2015; Cohen et al., 2018; Nanson et al., 2008). A broader synthesis of records from the Australian arid and semi-arid zones reinforces arguments for increased aridity and climatic instability across the continent (Fitzsimmons et al., 2013), but also highlight that more data is required to confirm such hypotheses. Moreover, geochemical analysis of subtropical records of aeolian (dust) activity spanning parts of late MIS3 suggest a decrease in moisture, coupled with increased atmospheric variability responsible for changes in prevailing wind direction (McGowan et al., 2008; Petherick et al., 2009), and greater mobilisation of dust around the MIS3 to MIS2 transition (Petherick et al., 2008). Notably, there are some discrepancies in the extent of aridification reported for the Australian continent. For example, the southern Murray-Darling Basin indicates increased fluvial activity during late MIS3 (Kemp & Rhodes, 2010; Page et al., 1996), which contrasts with the drying trend observed for the interior and more northerly sites (e.g., Cohen et al., 2015; Kershaw et al., 2007a; Petherick et al., 2011). Moreover, sedimentary ridges and terraces surrounding plunge pools in the Northern Territory support wetter conditions during the early to mid-Holocene and last glacial maximum, suggesting rainfall variations over many thousands of years (Nott & Price, 1994).

Subtropical palaeoclimate archives have an important role in developing deeper understanding of spatiotemporal change across the Australian landscape. Terrestrial deposits from the subtropical zone are needed to bridge the gap between the well-established records from the tropical (e.g., Lynch's Crater; Kershaw, 1976; Kershaw et al., 2007a; Turney et al., 2004) and temperate (e.g., Caledonia Fen; Kershaw et al., 2010) regions. Filling this gap is particularly important as diametrically opposed conclusions have previously been drawn from the available information at sites such as Lynch's Crater, which has been variously interpreted as reflecting both wetter (Muller et al., 2008) and drier (Turney et al., 2004) conditions during Heinrich Event 3 (e.g., Barr et al., 2017; Cadd et al., 2018). Records in coastal subtropical sedimentary locations have the potential to address such underlying questions, as this climatic zone is highly sensitive to changes in atmospheric and oceanic circulations, reflecting changes in Hadley Cell circulation (Chiang & Friedman, 2012), the Intertropical Convergence Zone (ITCZ) (Chiang et al., 2014), and ENSO (Barr et al., 2019; Bayon et al., 2017). To take full advantage of records from the subtropics it is of paramount importance to improve the chronological certainty of existing archives so that temporal change can be better assessed in the context of broader regional and global palaeoclimate change (i.e., Colhoun et al., 1999; Fitzsimmons et al., 2013; Longmore & Heijnis, 1999).

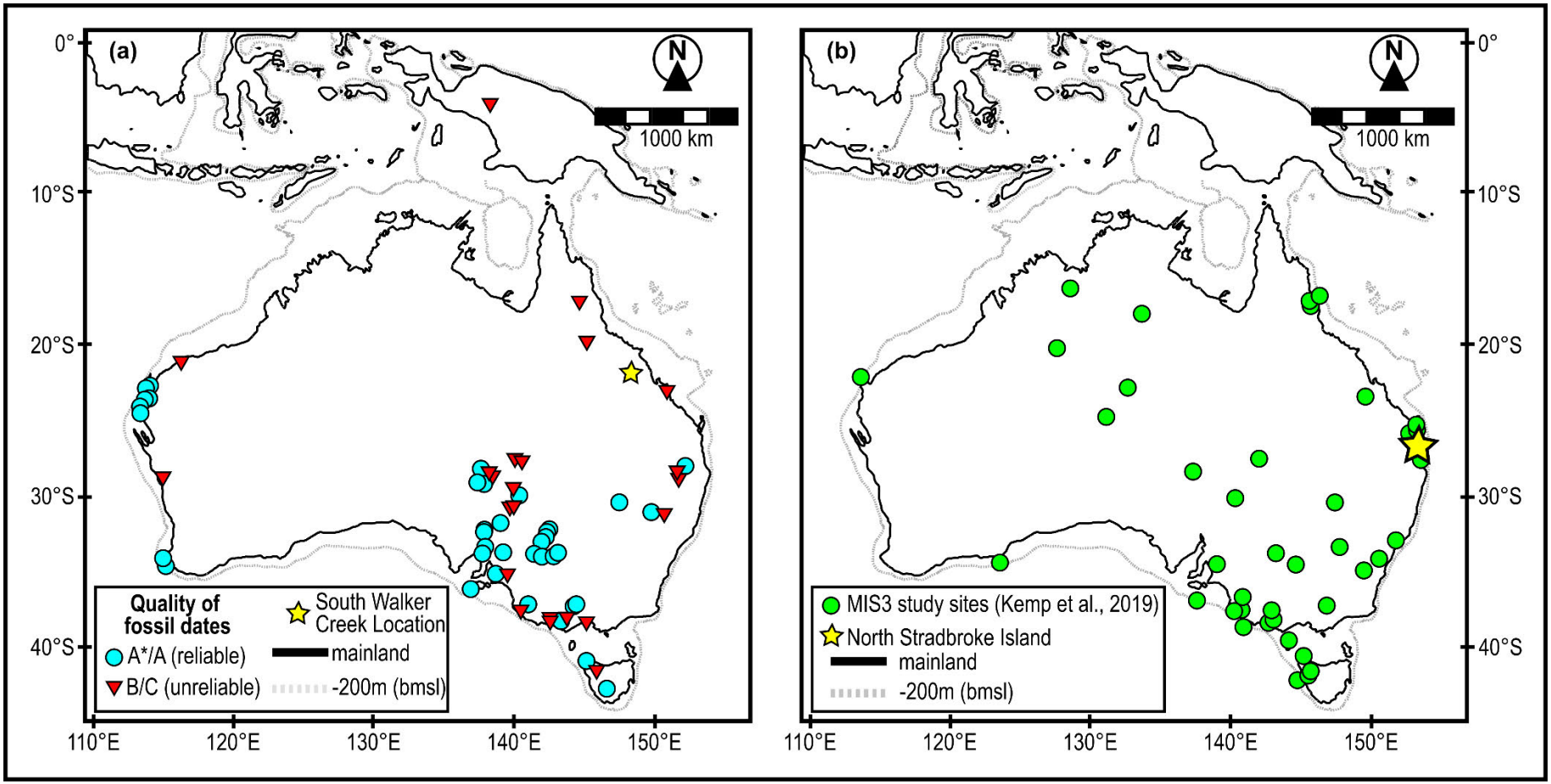

Figure 1.1 (a) Distribution of dated non-human vertebrate fossil records in the Sahul region for the period 40,000 – 80,000 years rated as reliable and unreliable (Rodríguez-Rey et al., 2015) with the map (Peters et al., 2019) modified to show the Sahul continental boundary and position of South Walker Creek. (b) Distribution of the 40 Australian lake, river and offshore sediment records used to reconstruct regional hydroclimate of MIS3 in Kemp et al. (2019).

Humans and the megafaunal extinction debate

The capacity to directly modify the environment (Laland & O'Brien, 2010) and exploit a range of different food sources (Crabtree et al., 2019; Crabtree et al., 2017; Dunne et al., 2016) are traits that have enabled anatomically modern humans (AMH) to efficiently and rapidly adapt to conditions over a large geographical range (Grothmann & Patt, 2005; Potts, 1998; Romanowska et al., 2017). The African continent hosts some of the oldest evidence of AMH habitation in the world (McDougall et al., 2005; Richter et al., 2017) with conceptual models placing Africa at the heart of the human evolution and migration story (Braje et al., 2017; Hershkovitz et al., 2018; Skoglund et al., 2016), which included colonisation of Oceania and Australia during the late Pleistocene (Tobler et al., 2017). However, the exact timing and rationale behind migration patterns of early *Homo sapiens* is not clear - including uncertainty surrounding interactions between *H. sapiens*, Denisovans and Neanderthals (Herrera et al., 2009; Zaidner et al., 2021; Demeter et al., 2022) – due to limited palaeoenvironmental data in key geographical locations (Breeze et al., 2016; Timmermann & Friedrich, 2016). Research does suggest a correlation between late Pleistocene human dispersion and orbitally linked episodes of climate change (Breeze et al., 2016; Jennings et al., 2015; Larrasoaña et al., 2013; Parton et al., 2015). This possible scenario may explain the rapid dispersal into south-east Asia and across to Australia sometime before MIS3 (Groucutt et al., 2015; Petraglia et al., 2010; Timmermann & Friedrich, 2016).

The first arrival of people to Sahul occurred in the late Pleistocene (Borreggine et al., 2019), with the seafaring journey from Sunda (Crabtree et al., 2021; O'Connell & Allen, 2004) made possible by island hopping between the exposed islands on the continental shelves during periods of lower sea level (Bird et al., 2018; Tobler et al., 2017). Several different ideas have been presented for the timing of human arrival to Sahul (i.e., 48 – 50 ka (O'Connell & Allen, 2004); 59.3 – 72.7 ka (Clarkson et al., 2017); 50 – 75 ka (Bradshaw et al., 2021)), however it is generally agreed that this occurred sometime before 50 ka given the Signor-Lipps effect (Saltré et al., 2016). Studies suggest that the strategies of the first humans reaching Sahul included preferential movement towards areas with established water sources (Figure 1.2) (Bird et al., 2016) and use of prominent landforms for orientation (Lock & Pouncett, 2010). Regardless of the strategies adopted, it is generally noted that these people had the ability to efficiently adapt to the new environmental challenges of the continent (Crabtree et al., 2021).

Interaction with, and adaptation to, the unique, endemic flora and fauna is likely to have been a particularly significant challenge facing the first people arriving to Sahul (Figure 1.3). One strategy likely adopted was landscape modification practices, particularly using fire to alter burning regimes (Bird et al., 2005) and establish more favourable environments for habitation (Bowman et al., 2011; Conedera et al., 2009). Evidence for increased charcoal accumulation and fire tolerant vegetation species has been observed in Australian palaeoenvironmental archives over the last 50,000 years and has been used to support arguments for increased anthropogenic burning (Moss et al., 2017; Thevenon et al., 2004). Conversely, a synthesis study of charcoal records has also been presented to argue that there was no distinct increase in charcoal across the likely arrival window (Mooney et al., 2011). Moreover, the contribution of human related burning events versus non-human induced burning across Australia varies both geographically and temporally (Kershaw et al., 2002; Mariani & Fletcher, 2017), suggesting the relationship between fire, humans and climate is complex (Mooney et al., 2012).

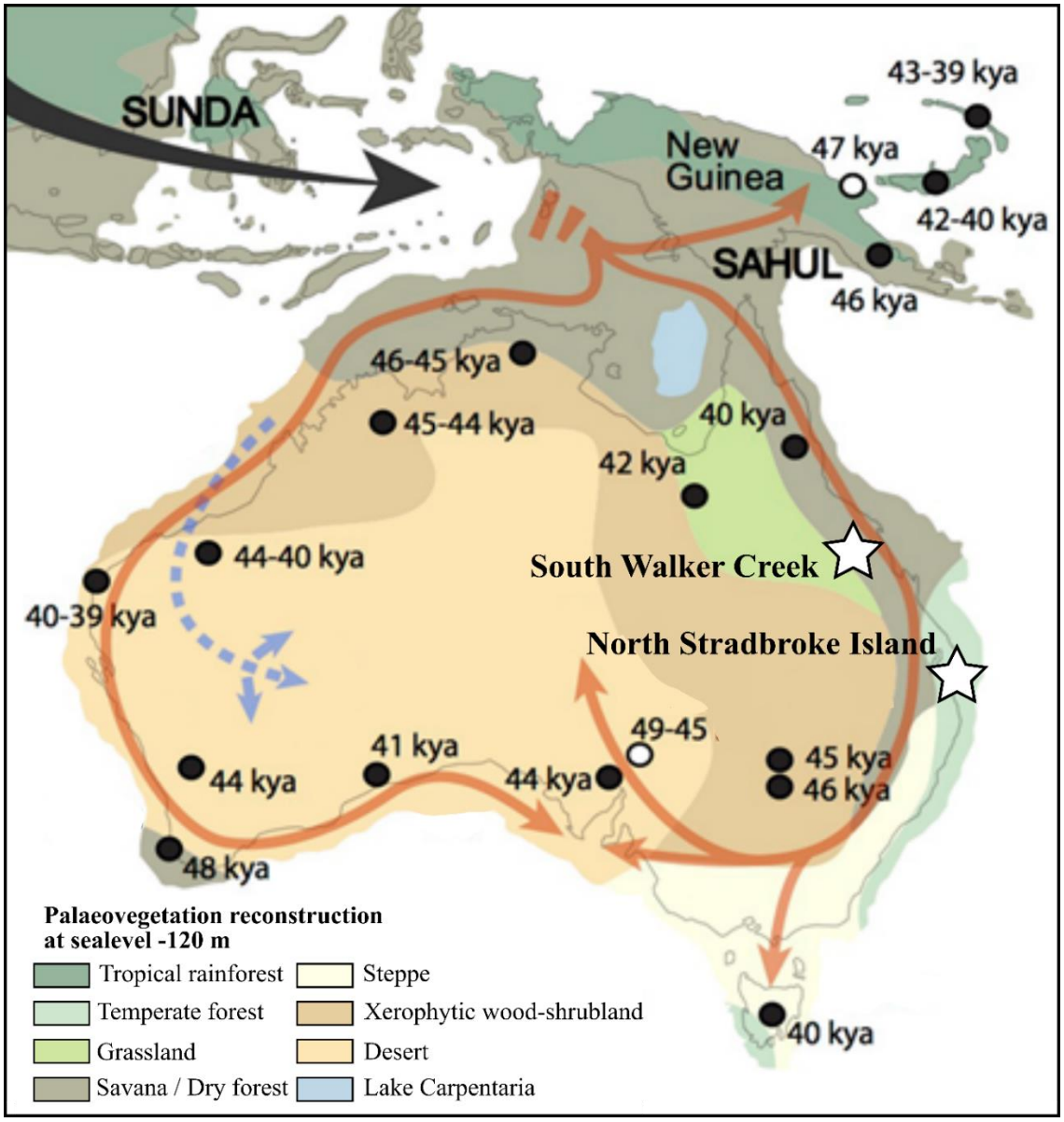

Figure 1.2 Model of the peopling of Australia combining genetic and archaeological data (Tobler et al., 2017), showing approximate, and stylised, coastal movements. Locations researched in this thesis (white stars) are shown alongside mean ages for earliest occupation used to model movements (black dots) and the occupation data that was not (white dots). Approximate late Pleistocene vegetation reconstructions are also shown with diagram modified from Tobler et al. (2017).

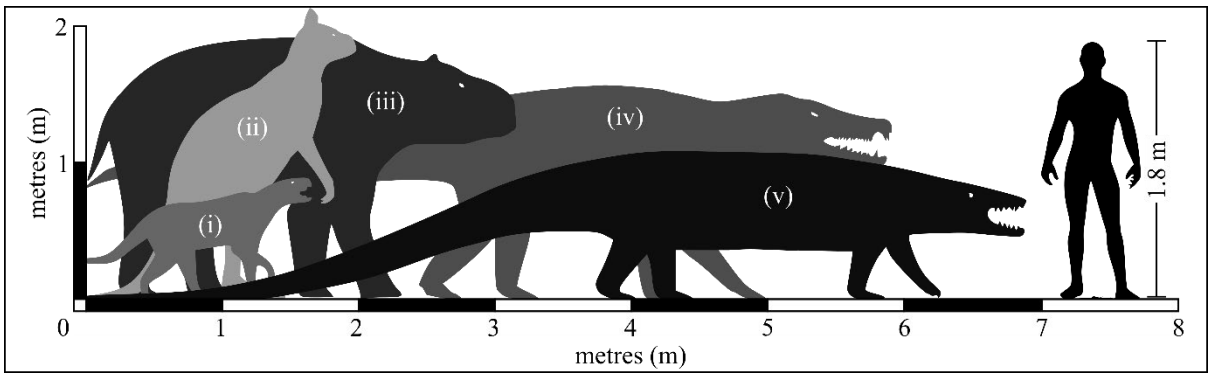

Figure 1.3 Adult size estimates for a selection of extinct Australian megafauna shown relative to a human (i) *Thylacoleo carnifex*; (ii) *Procoptodon goliah*; (iii) *Diprotodon optatum*; (iv) *Quinkana*; (v) *Varanus priscus*. (Adapted from Prehistoric Wildlife).

Co-existence of humans and extinct megafauna in Australia is supported by the results of chronometric studies at palaeontological and archaeological sites, which establish an overlapping chronological link between human artefacts and megafauna fossils (Grellet-Tinner et al., 2016; Hamm et al., 2016; Roberts et al., 2001). However, as limited chronological data exist for human (Saltré et al., 2016) and megafauna sites (Peters et al., 2019; Rodríguez-Rey et al., 2015), debate continues to surround the duration of the co-existence period. This problem is due to difficulties in acquiring suitable material for dating (Anderson et al., 1951; Ascough et al., 2011; David et al., 2021) and the practical limitations of some techniques (e.g., the relatively limited upper age limit of radiocarbon dating; Roberts et al., 1994). Therefore, there remains a spectrum of ideas regarding the nature and degrees of human involvement in native megafaunal extinction (Field et al., 2008).

One end of the Australian megafaunal extinction spectrum advocates an extinction age range of 39.8 – 51.2 ka (often referred to by its mean age of 46.4 ka), which is based on the 95% probability range of numerous genera (i.e. *Diprotodon*, *Phascolonus*, *Thylacoleo*, *Procoptodon*, *Protemnodon* and *Simosthenurus*) (Gillespie & Brook, 2006; Grellet-Tinner et al., 2016; Hocknull et al., 2020; Roberts & Brook, 2010; Turney et al., 2008). Notably, this extinction age range post-dates the generally agreed time of human arrival (i.e., before 50 ka; Bradshaw et al., 2021; Clarkson et al., 2017; O'Connell & Allen, 2004; Saltré et al., 2016) and implies a relatively short co-existence period between humans and megafauna (Figure 1.4a). It is therefore commonly used to support scenarios of fauna population decline resulting from human actions - both direct (Brook & Johnson, 2006; Flannery, 1994) and indirect (Bird et al., 2013).

The other end of Australia megafaunal extinction spectrum presents an argument for a prolonged co-existence between extinct species and humans. Specifically, the works emphasise there is no clear empirical evidence to support the hypothesis that megafaunal extinction was directly linked with humans overkilling populations (Field et al., 2008; Field et al., 2013; Fillios et al., 2010; Wroe & Field, 2006; Wroe et al., 2013), particularly as co-existence extended for up to 56,700 years when considered against the earliest arrival chronologies for humans (72.7 ka; Clarkson et al., 2017) (Figure 1.4b). Therefore, this prolonged coexistence of megafauna and people, combined with peak late Pleistocene climate change, would suggest that people were not the primary cause of megafaunal extinctions (David et al., 2021). For example, the fact that megafaunal extinction aligns with the harsh environment conditions experienced through the Last Glacial Maximum (LGM), is commonly used to argue that climate change, rather than humans, was the primary cause of megafaunal extinction (Saltré et al., 2016).

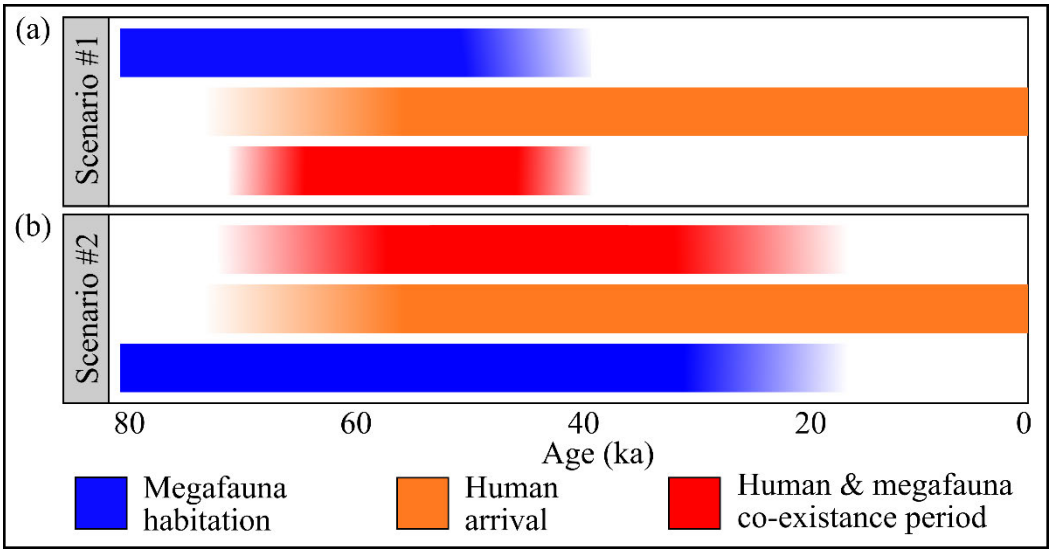

Figure 1.4 Conceptual graphical portrayal of the hypotheses related to the length of co-existence (red) between humans (orange) and megafauna (blue) considering (a) Scenario #1 - an early megafaunal extinction, and (b) Scenario #2 - late megafaunal extinction. Earliest human arrival times based on Clarkson et al. (2017), with gradational colouration used to indicate periods of chronological uncertainty or contention.

An intermediary stance commonly adopted by researchers is that both humans and climate played a near equal role in the ultimate demise of Australian megafauna. Palaeoenvironmental evidence suggests that hydroclimatic conditions began to abruptly deteriorate from 48 ka in parts of Australia (Cohen et al., 2015; Hesse et al., 2018; Kemp et al., 2019), with major fluctuations in effective rainfall inhibiting sufficient replenishment of large watersheds. This had a knock-on effect across Australian ecosystems (Cohen et al., 2011; Kershaw et al., 2003; Nanson et al., 1993; Wroe et al., 2013) with drier conditions promoting an expansion of more drought tolerant flora (Moss, 2013a; Moss, 2013b; Moss & Kershaw, 2007), intensified burning (Moss et al., 2017; Thevenon et al., 2004) and a marked change in megafauna diet (Miller et al., 2005; Murphy et al., 2012; Prideaux et al., 2009). As favourable habitation areas began to change in response to widespread hydroclimate breakdown, people and megafauna were placed under increasing ecological strain, and their interactions may have intensified in a bid for survival over ever shrinking water and food resources (Saltré et al., 2019).

Despite the extent of research already conducted, it is necessary to further explore competing Australian megafaunal extinction hypotheses by establishing new, robust palaeoenvironmental records that bridge the spatial and temporal gaps of those currently in existence.

Dating of palaeoenvironmental records

Geochronology underpins most palaeo-research as defining the age of rocks, sediment, artefacts and fossils is essential for making better informed interpretations and correlations across both time and space (Hajdas, 2009; Peters et al., 2019; Price et al., 2021; Price & Sobbe, 2011). Establishing the timing of a particular change in stratigraphic sequences is important when investigating regional signals through multi-site comparisons, as this enables a deeper understanding of cause-effect processes, feedback systems and spatio-temporal relationships (Bradshaw et al., 2021; Saltré et al., 2016). In Australia, the lack of robust dating is particularly problematic for late Pleistocene reconstructions and has fuelled several debates in palaeontological and archaeological science disciplines (Saltré et al., 2016; Wroe et al., 2013). For example, a synthesis of 11,871 ages (3,205 of these relating to megafauna) from 605 Australian fossil deposits (Peters et al., 2019) showed that there

were no reliable records (i.e., records classified as higher than a B rating; Rodríguez-Rey et al., 2015) for the central and northern regions of Australia. Moreover, it was found that many sites included in this synthesis had imprecise chronologies and few sedimentary records extended continuously beyond 40 ka (Kemp et al., 2019; Tibby et al., 2017). The deficit of older records (i.e., archives >40 ka) may be explained by a combination of preservation issues and a historical reliance on radiocarbon dating (Kemp et al., 2019) – a technique that has an upper calibration limit of ~55 ka (see "Radiocarbon (^{14}C) dating" section). However, new analytical and dating techniques emerging over the last 20 years have provided a means to enhance chronologies and help address existing temporal gaps.

Table 1.1 Examples of dating techniques utilised in palaeoenvironmental research.

	Dating technique	How it works	Examples of material
Chronometric dating	Archaeomagnetism	Measures the magnetic orientation of ferromagnetic minerals, the characteristic of which are imparted by the polarity of Earth during crystallisation.	Ferric minerals (e.g., magnetite and hematite)
	Dendrochronology	Counting of successive annual or seasonal growth rings of wood to establish the tree's age	Trees, wood
	Electron spin resonance *	Dating is based on the detection and quantification of electrons accumulated in defects of crystal lattices as a result of exposure to natural radioactivity; similar to luminescence.	Human or animal remains (teeth), pottery or ceramics, some minerals (e.g., aragonite, calcite, quartz)
	Fission-track	Determines age of various minerals and glasses based on damage tracks left in minerals due to the spontaneous fission of uranium-238.	uranium-rich minerals (e.g., apatite, zircon, titanite)
	Potassium-argon (K-Ar)	Measures the parent-daughter nuclide ratio of radioactive potassium (^{40}K) to argon (Ar) gas.	Igneous volcanic rocks and ejecta to estimate how much time has elapsed since the material cooled and solidified.
	Luminescence * - Thermoluminescence - Optically stimulated luminescence	Determines when mineral grains were last exposed to sunlight or significant heat by quantifying accumulated charge populations in crystal lattices as a result of exposure to natural radioactivity.	Minerals (commonly quartz and feldspar), pottery or ceramics
	Radiocarbon Dating *	Measures the decay of the radioactive isotope carbon-14 (^{14}C) in any organic material.	Wood, plants, textiles, and human or animal remains
	Uranium-series dating*	Measures the accumulation of Th or Pb daughter isotopes in U-bearing minerals according to known decay rates of radioactive isotopes in the ^{238}U, ^{235}U and ^{232}Th decay series.	Calcium carbonates (e.g. speleothem, coral), human and animal remains
Relative dating	Amino acid racemisation	Measures the ratio of amino acid configurations (i.e., ratio of left "L" and right "D" isomers) to rank organic fossil materials in relative order of age.	Human and animal remains (e.g., mollusc, eggshells, bone, teeth).
	Seriation	References the appearance or disappearance of assemblages or artefacts at a given site with a chronology developed on the assumption that one style (or typology) will slowly replace an earlier style over time.	Artefacts (e.g., pottery)
	Stratigraphy *	Adopts the principles of geology (i.e., uniformitarianism, original horizontality, superposition, cross-cutting relationships) to determine a relative chronological sequence. Also includes biostratigraphy and bicorrelation.	Geological features (e.g., bedding, volcanic intrusions, faults), human and animal remains, artifacts

* techniques that have been applied in studies presented in this thesis.

Technological advancements and improved instrumentation have led to the emergence of numerous chronometric dating approaches (e.g., electron spin resonance and luminescence dating). However, despite the availability of these techniques (Table 1.1), the practical and methodological suitability of applying a particular approach needs to be considered on a site-by-site basis (Wintle, 2008; Wood, 2015). Key considerations may include the applicability of the dating technique itself (e.g., whether the technique is applicable over the timescale of interest; Roberts et al., 1994), or the availability of material required for dating (i.e., whether there is readily available material or if the material has been altered; Wood, 2015). As various dating approaches have become more accessible, it is not uncommon for studies to implement more than one dating technique to increase the overall reliability of the resultant chronology (e.g., David et al., 2021). The studies carried out as part of this thesis focus on combining different chronological techniques to strengthen overall dating results. Two specific techniques are utilised in several chapters: luminescence dating and radiocarbon dating. An overview of these dating methods is provided in the following sections.

Luminescence dating

Thermoluminescence (TL) and optically stimulated luminescence (OSL) are the two main types of luminescence dating approaches applied in Quaternary research (Duller, 2004); though infrared stimulated luminescence (IRSL) (a variant of OSL dating that is applicable to K-feldspars) is gaining increasing popularity for middle Pleistocene deposits (Li et al., 2014; Rahimzadeh et al., 2019). The main difference between these approaches is the type of external stimulus applied to a sample to generate a luminescence response, with TL using heat stimulation and OSL using light stimulation (Huntley et al., 1985; Wintle & Murray, 1997). The application of either TL or OSL for dating purposes depends on the research being conducted, yet both require strict light control from sample extraction up until measurement, as the luminescence signal can be reduced when exposed to sunlight (Figure 1.5) (Wintle, 2008; Wintle & Huntley, 1982).

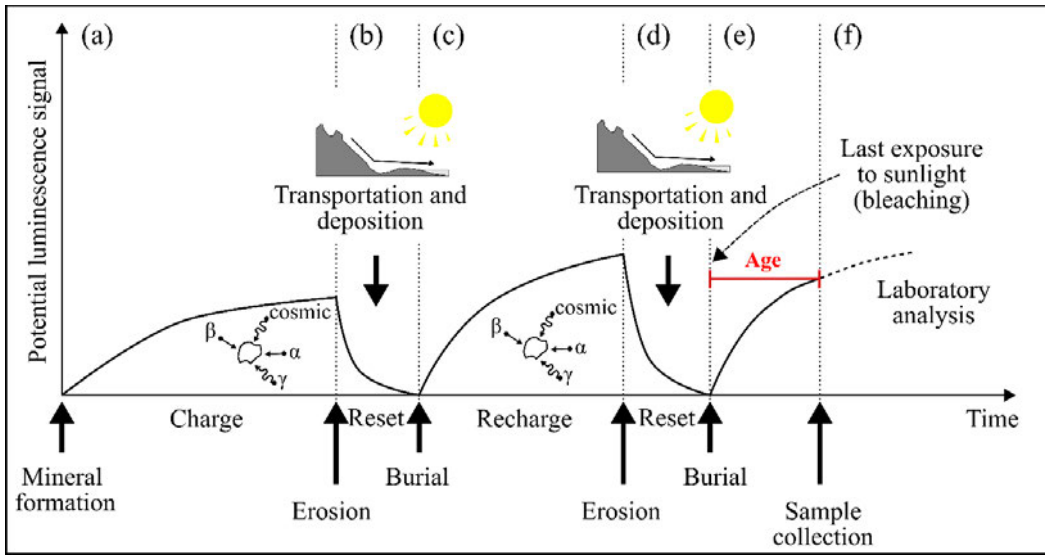

Figure 1.5 Conceptual model of processes associated with OSL dating. (a) Luminescence is acquired in mineral grains with exposure to ionizing radiation and trapping of electrons at metastable defect sites. (b) The luminescence signal for grains is zeroed by exposure to sunlight with erosion and transport. (c) With burial and exposure to ionizing radiation, free electrons are stored in defects within the grain's crystal lattice. (d) Further light exposure of grains with erosion and transport 'zeros' the luminescence. (e) The grains are buried again and the luminescence signal is acquired with exposure to ionizing radiation. (f) Careful sampling without light exposure and measuring of the natural luminescence, followed by a normalizing test dose (L_n/T_n) and comparison to regenerative doses obtained using a calibrated radiation source, is used to yield an equivalent dose (D_e). Adapted from Mellett (2013).

The application of luminescence dating in archaeology and palaeoenvironmental research has provided a way to date human artefacts, such as pottery and stone tools (Roberts et al., 1997), as well as the host sediment (Prescott & Robertson, 1997; Wintle & Huntley, 1979) and proxies therein – with a dateable age range spanning less than a few decades (Ollerhead et al., 1994) to almost a million years under ideal conditions (Huntley et al., 1994; Huntley et al., 1993). The broad applicability of these techniques is advantageous in an Australian context as it has allowed chronologies to be established in a range of environments, such as playa lakes (Barrows et al., 2020; Cohen et al., 2018; Fitzsimmons et al., 2007; Fu et al., 2017; Jankowski et al., 2016), wetlands (Cadd et al., 2018; Kemp et al., 2020; Lisé-Pronovost et al., 2019; Lisé-Pronovost et al., 2021; Tibby et al., 2017) and caves (Clarkson et al., 2017; David et al., 2021; Roberts et al., 1999). It has also enabled the establishment of finite ages for deposits that lie beyond the 'radiocarbon barrier' (i.e., beyond the upper limits achievable with ^{14}C dating of ~55 cal kyr; Bronk Ramsey, 2008b) and those without datable carbon present, thereby allowing new insights into Pleistocene age sediments.

The theory and models explaining luminescence production in silicate materials are complex, and focus on processes at subatomic and quantum levels (Aitken, 1985, 1998; Bailey, 2001; Bøtter-Jensen et al., 2003; McKeever & Chen, 1997). Essentially, some minerals (e.g., quartz and feldspars) contain defects and chemical impurities within their crystal lattice (Prescott & Robertson, 1997). When a mineral grain is exposed to ionising radiation, such as from radioactive decay in natural environments (i.e., alpha and beta particles, gamma rays from the surrounding soil and cosmic rays), free electrons are redistributed within the crystal lattice and can become "trapped" at localised defect sites (Huntley et al., 1985; Huntley et al., 1996). These trapped charge populations continue to accumulate at a rate proportional to the level of natural background radioactivity. The longer the mineral is irradiated, the greater the number of accumulated electrons, until the traps are filled and no more free electrons can be held. At this point the sample is considered "saturated" with respect to accumulated dose (Heydari & Guérin, 2018). When the mineral is exposed to an external stimulant (i.e., light or heat), the trapped electrons can be evicted from the metastable defect sites and diffuse around the crystal lattice (Huntley et al., 1996). Some of these electrons will become trapped again or return to the ground state. Other electrons recombine with different charge defect sites known as a recombination centres, where excess energy is given off instantaneously as either heat or light (i.e., the luminescence signal).

The underlying concept of luminescence dating techniques is depicted by Equation 1.

Equation 1.1. The luminescence dating equation.

$$age\ [ka] = \frac{equivalent\ dose\ D_e\ [Gy]}{environmental\ dose\ rate\ \left[\frac{Gy}{ka}\right]}$$

To calculate an OSL age it is necessary to estimate the total radiation dose that has been deposited in a mineral grain since burial (the equivalent dose (D_e); which is a laboratory derivation of the naturally accumulated 'burial dose' or 'palaeodose') and the rate at which the accumulated radiation dose was delivered to the mineral grain in the natural environment (the dose rate). The first part of acquiring a D_e value in OSL dating involves measuring the intensity of the natural luminescence signal as a

function of stimulation time, generating what is referred to as a decay curve (or "shine-down"). In the regenerative dose approach (Wintle, 1997), after resetting the luminescence signal to zero, different known doses are applied to the sample with a calibrated radioactive source, and the luminescence measurements conducted once again. A fixed known dose (test dose) is also commonly administered directly after measuring the natural and regenerative dose signals to correct for progressive sensitivity change through the measurement sequence. This sensitivity-corrected measurement process, known as the single aliquot regenerate dose (SAR; Wintle & Murray, 2006) protocol, enables a dose response curve to be constructed, which is used to evaluate the required laboratory dose needed to generate the natural luminescence signal (Figure 1.6). As laboratory radiation sources generally produce only beta or gamma radiation and do not subject the sample to other types of radiation produced in nature (i.e., alpha, beta or gamma, and cosmic radiation) the dose estimate is referred to as the "equivalent dose". To ensure a representative D_e is obtained for a sample, numerous measurements are conducted on replicate aliquots, with inter-sample D_e variation then taken into consideration using appropriate statistical models (i.e., central age model, three- and four-parameter minimum age models, and the finite mixture model (Galbraith et al., 1999; Roberts et al., 2000)).

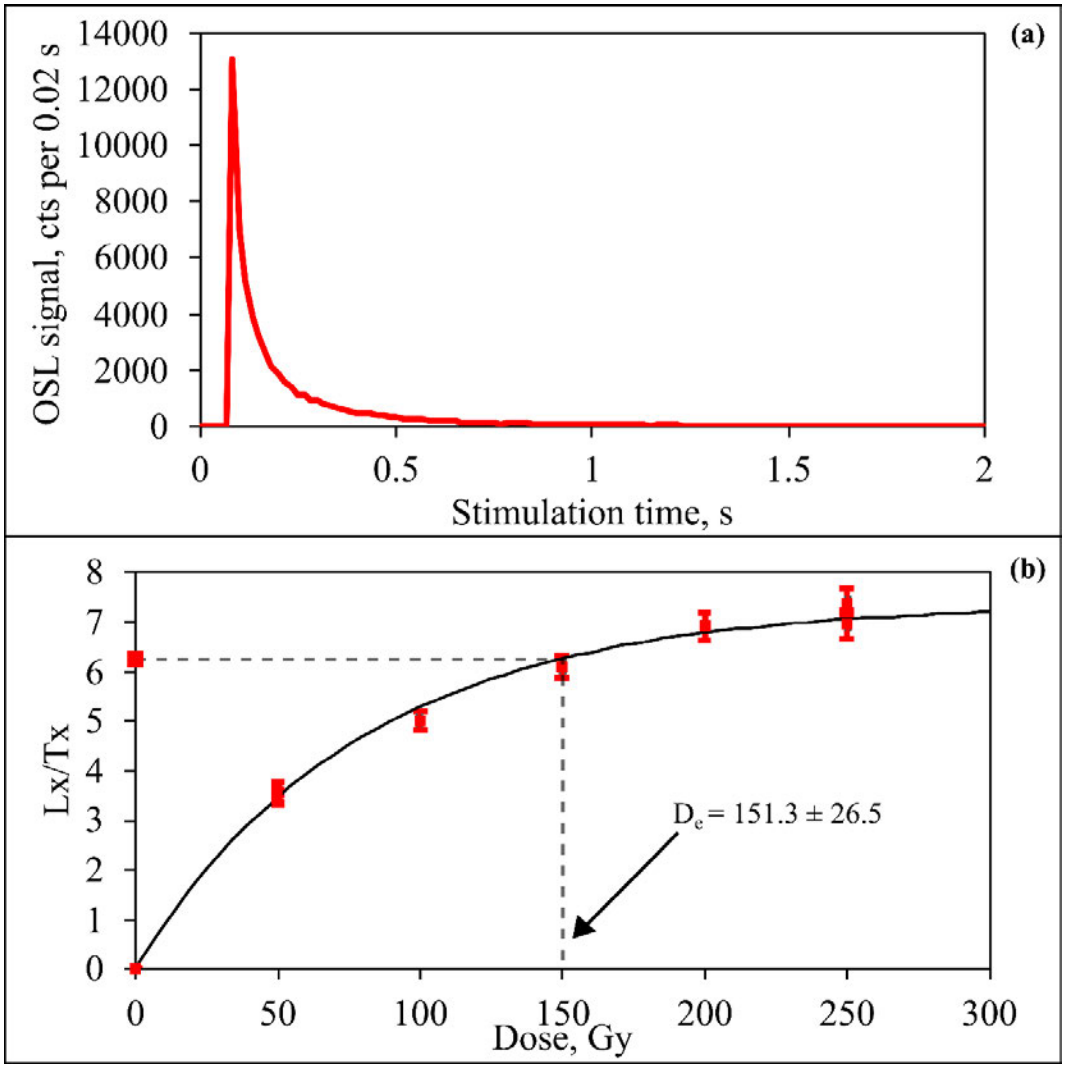

Figure 1.6 An example of (a) typical OSL decay curve and (b) dose response curve for a single grain of quartz. The dose response curve is fitted to the regenerative dose measurements (red squares) using a single saturating exponential function. D_e is obtained by projecting the sensitivity corrected (L_x/T_x) natural OSL signal (the upper of the two squares shown on the y-axis) onto the fitted curve and interpolating the dose on the x-axis (dashed line).

It is possible to undertake OSL D_e determination by measuring responses from single grains of quartz (Arnold et al., 2007; Duller, 2008; Jacobs et al., 2006). This is advantageous as it has enabled a deeper understanding of quartz OSL signal characteristics (Duller, 2008), including dose saturation properties and insights into the fast, medium, and slow components that make up composite quartz OSL signals (Arnold et al., 2016; Bailey, 2001; Bailey & Arnold, 2006). Moreover, D_e measurement at the single-grain level enable greater understanding of differences in the intrinsic luminescence characteristics within a sample, and the presence of mixed or heterogeneously bleached grains that would otherwise be masked in multi-grain approaches (e.g., Arnold & Roberts, 2009; Arnold et al., 2008). These findings have, in turn, led to advancements in the statistical approaches undertaken for determining the most appropriate sample-averaged D_e from a dataset (Arnold & Roberts, 2009; Arnold et al., 2009; Galbraith & Roberts, 2012).

The second part of the luminescence age equation requires calculation of the rate at which the mineral grains of interest were subjected to irradiation in nature, referred to as the "environmental dose rate". The environmental dose rate calculation considers four types of radiation: alpha particles, beta particles, gamma rays and cosmic rays; each of which is corrected for environmental attenuation effects (Jacobs et al., 2006; Mejdahl, 1987; Prescott & Hutton, 1994). Within the sediment matrix, alpha particles, beta particles and gamma rays are predominantly generated from the radioactive decay chains of potassium (^{40}K), uranium (^{238}U and ^{235}U) and thorium (^{232}Th) (Figure 1.7).

When OSL dating is applied to hydrofluoric acid etched silt-sized quartz grains, the alpha component of the environmental dose rate is effectively derived from radioactive decay of impurities within the mineral grain itself. This is also known as the internal dose rate (which also accounts for some of the beta dose rate component), and it is normally calculated using published values of ^{238}U and ^{232}Th measured from purified quartz fractions (Bowler et al., 2003; Jacobs et al., 2006; Mejdahl, 1987; Pawley et al., 2008). Notably, it is also possible to calculate the internal dose rate for an individual sample by measuring the concentration of radionuclides present in the quartz fraction being used for OSL dating (after having been etched) – as demonstrated in the OSL study of Welsby Lagoon (Chapter 2). The external beta component of the environmental dose rate can be measured directly using the sediment from which the mineral was extracted via laboratory techniques such as low-level beta counting, ICP-MS and high-resolution gamma spectrometry (Bøtter-Jensen et al., 2000).

The gamma component of the environmental dose rate can be calculated from measurements taken in either the laboratory or field, depending on the homogeneity of the host deposits. Laboratory based measurements are conducted on bulk sediment collected from the surrounding of the dating sample using high-resolution gamma spectrometry or ICP-MS. Field based measurements are possible with the use of a portable field gamma spectrometer, with *in situ* readings taken directly at the sample position after extraction of the sampling tube (Arnold et al., 2012; Duval & Arnold, 2013). The radionuclide concentration and specific activities that result from these laboratory and field approaches can then be converted to dose rates using published conversion factors (e.g., Guérin et al., 2011; Stokes et al., 2003) and assuming infinite matrix conditions. An advantage of *in situ* field-based gamma measurements is that this approach enables spatial variations in the gamma ionisation sphere (the surrounding ~30 cm of each sample) to be captured in the dose rate calculation (e.g., that arising from a nearby buried clast or proximity to a neighbouring stratigraphic unit). In contrast, laboratory-

based approaches make use of much smaller sample sizes and assume that the surrounding gamma radioactivity in the sediment is homogeneous, which may not always be the case.

The cosmic ray component of the environmental dose rate is calculated using the approach of Prescott & Hutton (1994). This approach takes into consideration geo-positioning variables that have an influence on the amount of cosmic radiation reaching the sample, such as the site altitude, geomagnetic latitude, density, thickness and geometry of sediment overburden.

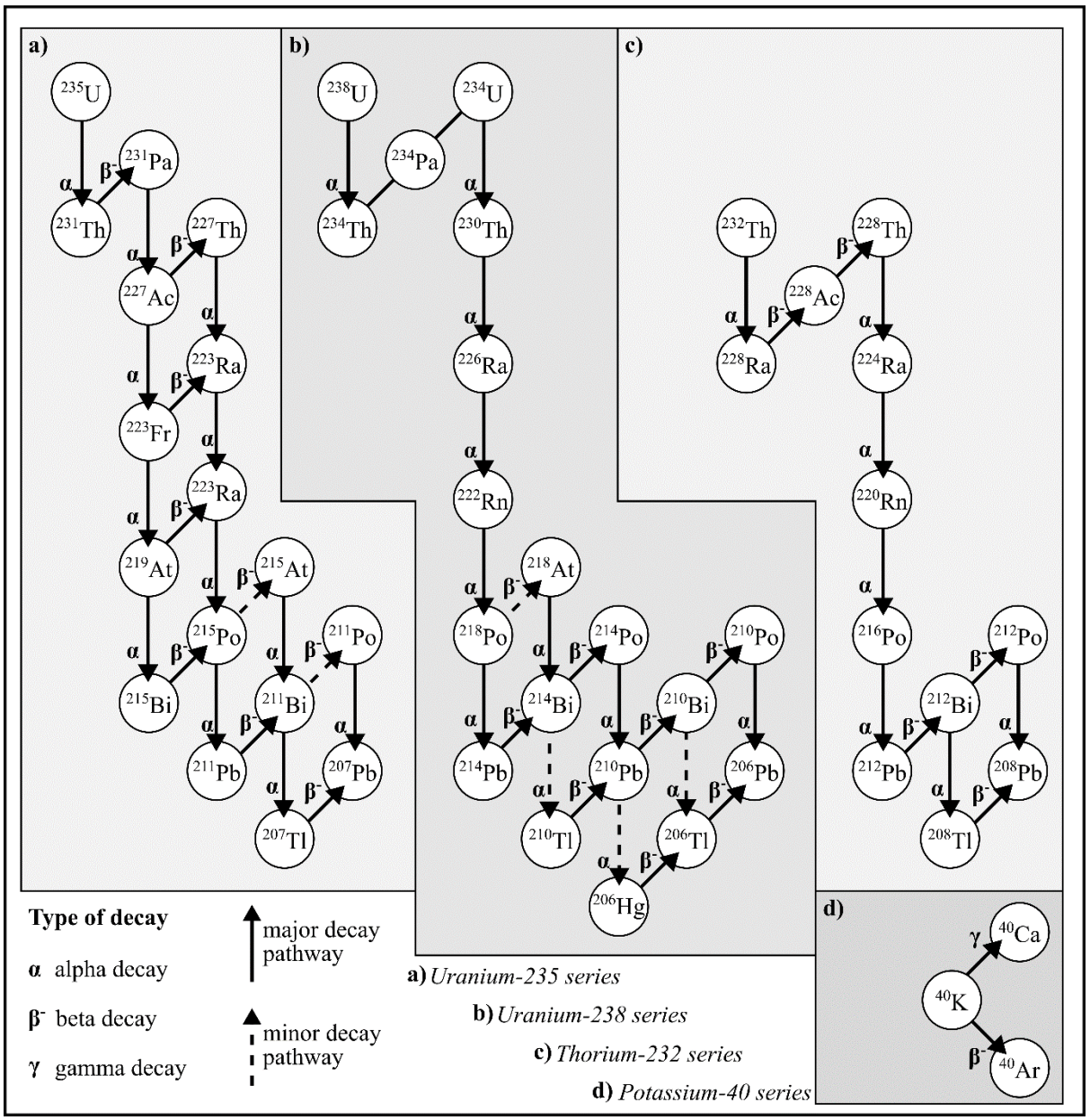

Figure 1.7 Simplified decay series diagram of (a) uranium-235 (^{235}U), (b) uranium-238 (^{238}U), (c) thorium-232 (^{232}Th), and (d) potassium-40 (^{40}K). Images are modified from the decay chain diagrams of Tan (2016) and Fiorentini et al. (2007).

Once the various components of the environmental dose rate have been summed, it is necessary to take into consideration any potential causes of time-dependent variation in the dose rate during the sample burial period. Several factors can create such complications, including mobilisation of radionuclides in the ^{238}U and ^{232}Th decay series, and past variations in the water content (as pore water can attenuate radiation); hence corrections for dose attenuation and dose rate evolution may have to be made (Aitken, 1985; Brennan, 2003; Mejdahl, 1979). Once these corrections are made and a final environmental dose rate is calculated, it is possible to use Equation 1.1 to derive an age.

Luminescence dating continues to evolve, with new techniques expanding the versatility and accuracy of the technique. Recent advancements have included analysis of different luminescence signals, building upon the concepts and measurement protocols that have now become standard in OSL dating (e.g., Murray & Wintle, 2000). For example, measurement of the single-grain thermally transferred OSL (TT-OSL) signal (Adamiec et al., 2010; Tsukamoto et al., 2008; Wang et al., 2006) has been demonstrated as being useful in extending the age range of quartz luminescence dating over middle Pleistocene timescales in some contexts (Arnold & Demuro, 2015; Arnold et al., 2016). As these new luminescence dating techniques become increasingly available, there is a great opportunity to improve our understanding of Australian palaeoenvironmental change through the Pleistocene.

Radiocarbon (^{14}C) dating

Radiocarbon dating has been widely applied in Quaternary science to determine the age of biological material since the mid-1900s (Wood, 2015). Accelerator mass spectrometry (AMS) radiocarbon dating is the most common approach as it enables analysis of small samples sizes to measure radioactive (^{14}C; half-life of ~5,730 years; Godwin, 1962) and stable (^{12}C) carbon isotopes (Nelson et al., 1977) (Equation 1.2). The theory of the technique is that ^{14}C is constantly generated in the upper atmosphere due to bombardment of ^{14}N atoms with neutrons, which are produced from cosmic rays (Libby, 1961). While an organism is alive, it maintains a steady state ratio of ^{14}C:^{12}C by continually replenishing the heavier, unstable isotope through food sources. Once the organism dies, it ceases to absorb ^{14}C and the concentration of this radioactive isotope continues to decrease due to radioactive decay (Arnold & Libby, 1949), becoming immeasurable around 55,000 years later. Therefore, by measuring the ^{14}C:^{12}C ratio in a geological sample and comparing it with that of a modern standard, it is possible to calculate the age of death for many different types of organic samples (Hajdas, 2009).

Equation 1.2 The radiocarbon dating equation.

$$age = \frac{ln\left(\frac{N_t}{N_0}\right) \times t^{\frac{1}{2}}}{(-0.693)}$$

where:

N_0 is the amount of ^{14}C present in the sample immediately at time of death.
N_t is the number of ^{14}C atoms in the sample at time of measurement.
$t^{1/2}$ is the half-life of ^{14}C (5,700 years).

Deriving a calendar age using ^{14}C is not as straightforward as just measuring the abundance of carbon isotopes in a sample and standard (Wood, 2015), not least because the amount of ^{14}C generated in the atmosphere has been variable through time, due to fluctuations in cosmic radiation and Earth's magnetic field. Corrections are therefore required via the use of calibration curves to convert ^{14}C ages into calendar years (Bronk Ramsey, 2008a; Bronk Ramsey et al., 2006). Mixing between carbon reservoirs can also complicate the derivation of reliable ^{14}C ages (Stuiver & Braziunas, 1993), particularly in freshwater systems where multiple carbon sources may be present (e.g., due to lithology or changing water conditions such as temperature; Ascough et al., 2010; Keaveney & Reimer, 2012). Moreover, alkaline sediments across many regions of Australia result in poor preservation of material such as charcoal (Ascough et al., 2011; Braadbaart et al., 2009), which ultimately restricts the applicability of ^{14}C dating. This barrier has had profound implications on refining understanding of Australian prehistory compared to other continents, but advancements in approaches have helped to extend viable ^{14}C chronologies back to the first arrival of people to the continent (Allen & O'Connell, 2014; Turney et al., 2001). Given contamination has the potential to influence the reliability of ^{14}C ages, it is important to not only carefully select appropriate samples (Waterbolk, 1971), but also to employ appropriate pre-treatment processes (Bronk Ramsey, 2008b; Hedges et al., 1989; Higham et al., 2011; Pettitt et al., 2003). This has become especially important as the ^{14}C technique has continued to develop because the required sample size can be small (0.03 mg carbon; Ruff et al., 2007; Santos et al., 2007) and thus a small percentage of contaminant present in the sample can have a large impact, particularly for samples that are close to the ^{14}C dating limit.

Bayesian age modelling

Statistical modelling approaches, particularly Bayesian age modelling, are increasingly being used to refine interpretations made from palaeoenvironmental records via the combination of stratigraphic and geochronological data (Becerra-Valdivia & Higham, 2020; Bronk Ramsey, 2008). In essence, Bayesian age models combine likelihoods (i.e., chronometric data obtained through techniques such as luminescence dating and radiocarbon dating) and priors (i.e., relative or numerical age information from stratigraphic groupings and ordering of layers, correlations using stratigraphic marker horizons, and associations with known-age historical events) (Harris, 2014). Once the likelihoods and priors are defined, the model produces posterior probability distributions of defined chronological events or sequences by running numerous iterations of a random sampling technique known as Markov chain Monte Carlo sampling (Gilks et al., 1995). In the context of modelling palaeoenvironmental records, it is important to consider stratigraphic constraints and changes in depositional processes at each site, particularly the occurrences of stratigraphic breaks, periods of non-deposition and variations in sedimentation rates over time (Bronk Ramsey, 2008). Introducing sufficient flexibility into the modelling framework to account for such complex sedimentation histories is required to produce accurate modelling outcomes (Blockley et al., 2007; Bronk Ramsey, 2008).

Study regions

This thesis focuses on two complementary study regions in the Australian sub-tropical and tropical zone: the wetland and fluvial sedimentary deposits of North Stradbroke Island, which have been shown to host a wealth of climate proxy information spanning millennia (Cadd et al., 2018; Kemp et al., 2020; Moss, 2013b; Petherick et al., 2017; Tibby et al., 2017), and South Walker Creek, which is located in a particularly underrepresented region of palaeoenvironmental research (Kemp et al., 2019;

Peters et al., 2019; Rodríguez-Rey et al., 2015); indeed, there are currently no robust dating studies of late Pleistocene megafauna in this tropical region (Peters et al., 2019). Before discussing the geology of these sites, it is important to outline the climatic context of the region and detail its importance with respect to understanding the current climate systems of Australia and the world.

Regional weather systems and climate

The landmass of Australia is large (~7.692 million km^2) and spans a wide range of latitudes (10°41'21" S – 43°38'40" S). Therefore, the continent experiences a number of contrasting climate regimes (Figure 1.8), which include: the wet summer and dry winter dominated conditions of the equatorial tropical zone; the relatively dry, mild summer conditions of the subtropical zone; the distinct, relatively uniform and winter dominant conditions experienced across the southerly temperate zone. However, it is important to note that these climate classes are based on generalised observations and temporal variations in conditions can and do occur.

Temporal variations in climate zones are largely influenced by systems of oceanic-atmospheric interaction including the El Nino-Southern Oscillation, the Inter-decadal Pacific Oscillation, the Indian Ocean Dipole and, the Southern Annular Mode, with changes in relative strength ultimately intertwined with other systems like the Inter Tropical Convergence Zone and South Pacific Convergence Zone (King et al., 2020; Marshall, 2003; McGee et al., 2014; Risbey et al., 2009; Ummenhofer et al., 2011), and movement in Hadley Cells (Chiang et al., 2014). These climate systems cause feedback with each other and result in the amplification (or suppression) of Australian weather, influencing seasonality, precipitation, and temperature over inter-annual, annual, decadal and millennial time scales (Gallant et al., 2013; Kiem & Franks, 2004; King et al., 2020).

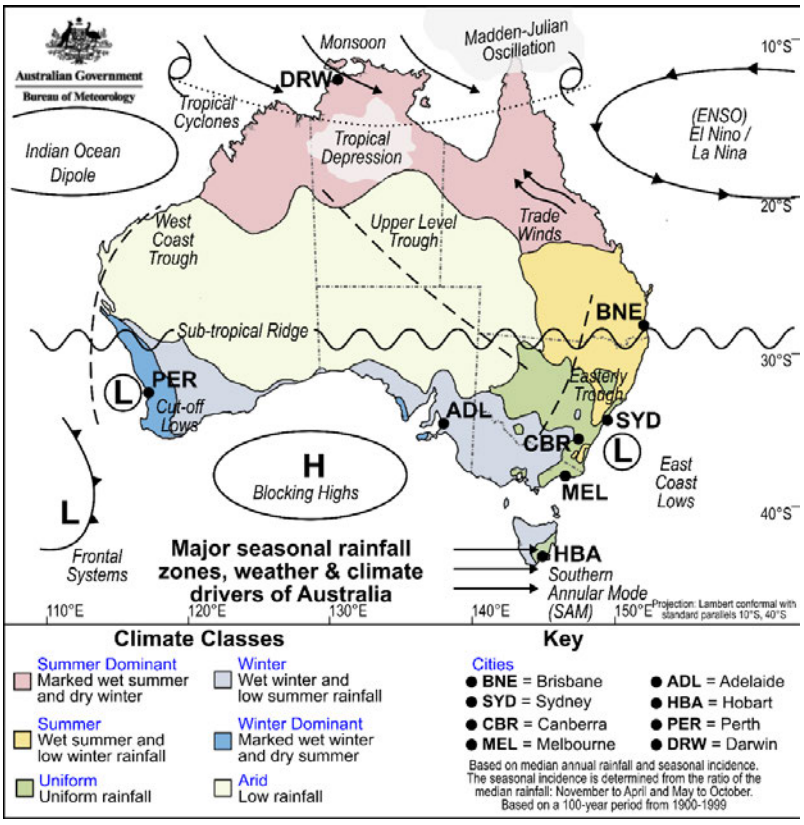

Figure 1.8 The six climate classes that describe the seasonal pattern of rainfall across Australia (BOM, 2019), overlain by the major climate drivers from Guthrie (2021).

Subtropics (North Stradbroke Island)

North Stradbroke Island is located ~30 km south-east of Brisbane, Queensland, and is the world's second largest sand island, occupying an area of ~275 km^2 (approximately 38 km long, 11 km wide). The traditional custodians of the island are Quandamooka people, a collective of three clans known as the Nughi of Moorgumpin (Moreton Island) and the Nunukul and Gorenpul of Minjerribah (North Stradbroke Island). Part of the Great Sandy Region, the island is composed of carbonaceous and siliceous sands (Patton et al., 2019; Pye, 1993), which form large northwest orientated parabolic dunes of Pleistocene and Holocene age (Patton et al., 2019; Walker et al., 2018; Ward, 2006). Sand mining has occurred across sections of the island since the late 1940s (Laycock, 1978) with mineral targets including rutile, monazite and zircon. North Stradbroke Island experiences warm, humid summers (annual mean 26°C) and mild, dry winters (annual mean 19°C), receiving approximately 1450 mm of rainfall per annum (BOM, 2019). Annual precipitation is large enough to support a high density of extended wetland records (Tibby et al., 2017), with contemporary climate conditions linked to the position and strength of the Inter-Tropical Convergence Zone and the El Niño–Southern Oscillation (Barr et al., 2017; Moss, 2013b).

The existence of many freshwater wetlands across North Stradbroke Island can be attributed to the unique hydrology and sediment properties across the island. Precipitation across catchment areas of the island can rapidly percolate through the coarse sand and mix into subterraneous aquifers (Leach, 2011). These freshwater aquifers can be one of the many perched aquifers found on North Stradbroke Island (confined by an impermeable sedimentary layer above the regional water table) or the regional water table itself (Figure 1.9). Given both types of aquifers exist on the island, wetlands are classified depending on their water source setting. For example, Welsby Lagoon and Brown Lake feed from perched aquifers – hence are designated as perched wetlands – while Blue Lake sources from the regional water table – hence is referred to as a window lake (Laycock, 1978). Irrespective of the water source, the sediment of North Stradbroke Island wetlands has been described as highly organic with varying amounts of inorganic material. The palaeoenvironmental histories archived in the sediment of perched wetlands, specifically Welsby Lagoon and Brown Lake, are the focus of this thesis as they are considered more sensitive to hydrological change than wetlands connected to the regional water table.

Welsby Lagoon (27°26'12" S, 153°26'55" E; 28 m A.H.D.) and Brown Lake (27°29'25" S, 153°25'56" E; 49 m A.H.D.) are both located on the north-western side of North Stradbroke Island in the MIS5 aged Yankee Jack dune unit (Pickett et al., 1989; Tejan-Kella et al., 1990; Ward, 2006). The waterbodies are categorised as a fluctuating freshwater wetland (Welsby Lagoon) and a perched lake (Brown Lake), have areas of ~19 Ha and ~25 Ha, respectively (Leach, 2011), and have been shown to preserve sedimentary archives extending beyond 50 ka (based on early OSL ages from Tibby et al., 2017). Both Welsby Lagoon and Brown Lake are endorheic (closed) basins with variable water levels that are linked to the net moisture balance of the respective perched aquifers. The lack of inflowing rivers or streams eliminates temporal variations brought about by downstream transportation of material, making these wetlands ideal candidates for examining long-term ecosystem change and dust transportation.

The complementary datasets and research outcomes from Welsby Lagoon and Brown Lake presented in this thesis (i.e., Chapter 2 and Chapter 3) bridge a critical spatial gap between the extensively

studied environmental archives of the last glacial cycle from central Australia (Cohen et al., 2015; Miller et al., 2016), the northern tropical zone (Kershaw et al., 2007a; Turney et al., 2006) and the southern temperate zone (Kershaw et al., 2010; Kershaw et al., 2007b). Moreover, the extensive dating and age modelling approach used to reconstruct basin evolution of these North Stradbroke Island wetlands provides unprecedented insights into eastern Australia hydrologic variation over the last glacial period (Chapter 5).

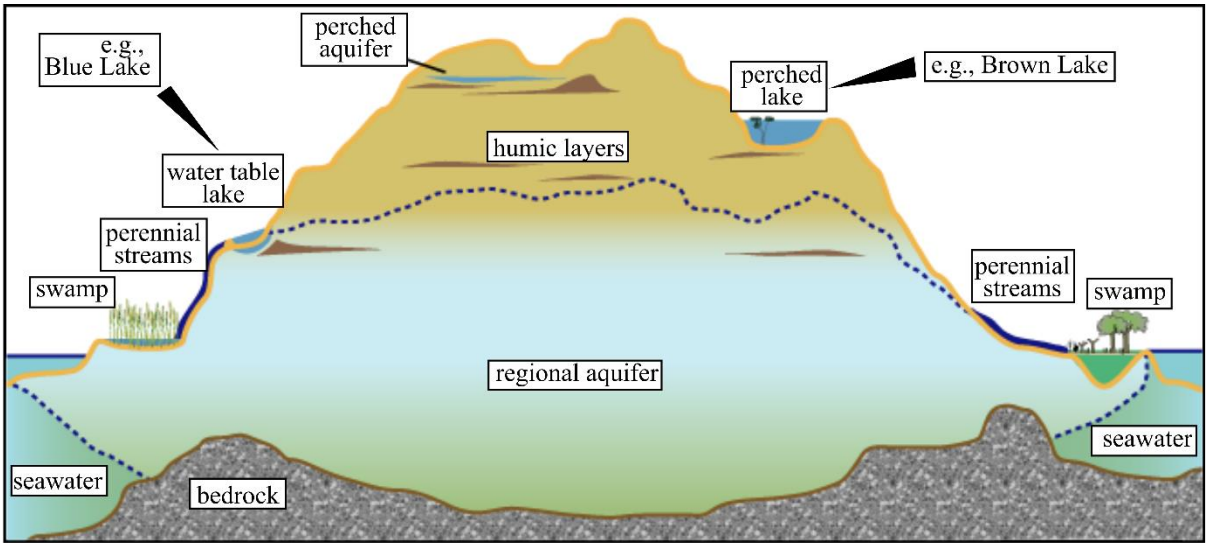

Figure 1.9 Diagram of features and wetland types found on North Stradbroke Island. Adapted from Department of Environment and Science Queensland (2013).

Tropics (South Walker Creek)

The South Walker Creek fossil deposits are located near the township of Nebo in north-eastern Australia. The fossil locality is situated in the tropical climate zone of Australia and in the northern-most portion of the Fitzroy River Basin catchment, an area underrepresented palaeoecologically and palaeontologically (Figure 1.1a; Peters et al., 2019; Price et al., 2021; Rodríguez-Rey et al., 2015). This open-air megafauna locality is unique in that it hosts well-preserved vertebrate fossil material (including articulated and associated remains), alongside crustaceans, insects, fish and seed remains. Moreover, the diverse fauna and preservation of multiple climate proxies provide unparalleled insights into the long-term ecological evolution of the basin both before and after human arrival (Hocknull et al., 2020).

Fossil material has been recovered from seven excavated sites (i.e., SW3, SW9, SWC-CC, SWJ, SWC-JS, SWC-S, SWC-P), with an eighth site (SWC-US) containing a succession of sedimentary units with well-defined bedding, and providing insights into the fluvial history of the catchment (Figure 1.10). The sedimentology of the sites ranges from singular matrix-supported muddy cobble beds (~50 cm thick) through fine-grained sandy muds (~1 – 1.5m thick) to confined coarse-grained gravel beds (~20 – 40 cm thick). Coarser grained material and a reduction in the preservation of fossil material within sedimentary units are generally found closer to the palaeo-river channel. There is currently fluvial activity near to the South Walker Creek fossil locality, although present-day and previous river flow patterns show the river has meandered through time. This is largely due to the river being constrained by the underlying basement of downward dipping Permo-Triassic Rangal and Fort Cooper Coal Measures and the Triassic Rewan Group. A unique combination of fauna and flora

(including three crocodilians, *Varanus priscus*, *Palorchestes*, *Sedophascolomys*, and at least two macropodids) are preserved across the various South Walker Creek sites; a rare finding for Australian open-air settings and offering an ideal opportunity to conduct new palaeoecological investigations in the understudied tropical northern Australian and eastern Sahul regions.

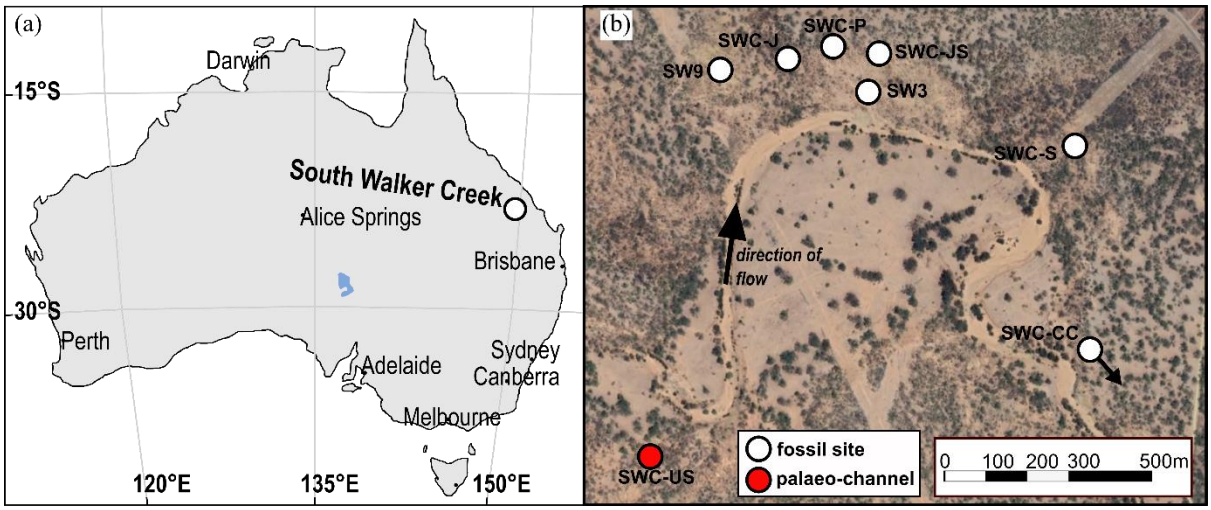

Figure 1.10 Location of South Walker Creek and site locations in relation to (a) major cities and (b) the South Walker Creek River.

Thesis outline and contextual statement

The environmental and climatic history of Australia through the Pleistocene is not well resolved, despite the cultural and ecological significance of this period. Ongoing debates into Australian palaeoenvironmental, palaeontological and archaeological histories, specifically those associated with the interconnection of climate, human and megafauna, highlight two common themes: (1) there is a severe lack in the number and spatial coverage of available archives, necessitating interpolation of information over wide geographic ranges when undertaking regional syntheses, (2) the information currently available often lacks robust chronological control as a result of methodological limitations and inappropriate application or interpretation.

Thesis structure and aims

This thesis aims to evaluate changes in Australian tropical and sub-tropical ecosystems over the last glacial cycle, and to strengthen understanding about the causes and context of megafaunal extinction (Figure 1.11). The research applies comprehensive chronometric and geochemical techniques (including robust age model approaches) across a number of terrestrial sites and demonstrates the importance of conducting multi-site and multi-disciplinary comparisons. Establishing unified chronological frameworks across different sites using a combination of dating techniques is also shown as important when distinguishing between local versus regional change and lead versus lag events.

Welsby Lagoon and 80,000 years of dust deposition (Chapter 2)

This chapter was published in *Quaternary Science Reviews* and establishes a comprehensive geochemical record and numerical dating framework for a 12.7 m subtropical wetland core from Welsby Lagoon, North Stradbroke Island. The purpose of this chapter is to improve the spatial and temporal coverage of existing late Quaternary palaeoenvironmental records and extend the island's

terrestrial dust record by more than 40,000 years. An XRF core scanner is used to evaluate a high-resolution geochemical profile for the sediment, the results of which are verified and calibrated with discrete XRF-WD assays. The continuous geochemical data is combined with an independent Bayesian age-depth model, which incorporates seven ^{14}C and twenty-one OSL ages, making this record one of the most comprehensively dated terrestrial palaeoenvironmental records in Australia. The results show that climate was a major variable in the flux of wind-transported sediment over the last 80,000 years and suggests increased dust mobilisation is linked with changing conditions in continental dust sources.

Synthesis of long-term coastal subtropical wetland evolution (Chapter 3)

This chapter was published in *Quaternary Research* and presents a geochemical and geochronological approach to reconstructing more than 60,000 years of wetland evolution from sediment extracted from Brown Lake, North Stradbroke Island. The study aims to evaluate the extent of regional moisture changes over the Last Glacial Maximum through the first inter-site comparison of extended palaeoenvironment archives from North Stradbroke Island. Stratigraphic logs and high-resolution XRF core scanning are used to guide the core correlating process between two cores, so the relationship between the local hydrology, morphology and vegetation could be evaluated. A robust chronological model is produced for the Brown Lake sediment sequence (incorporating ^{14}C and OSL ages) using Bayesian modelling software. The multi-wetland synthesis highlights the importance of developing an independent chronological framework for records, even when they are in relatively close proximity, particularly when comparing the response of sites to changing climates. This study reveals that Brown Lake persisted as a lake since its formation until water level dropped – in response to increased moisture stress - in late MIS3. Brown Lake then returned to conditions similar to those of the pre-existing lake. Notably, the timing of moisture stress is found to be coeval with other wetlands from North Stradbroke Island (e.g., Welsby Lagoon - Chapter 2) suggesting this was a result of a regional climate event.

Australian megafauna and the Australian hydroclimate (Chapter 4)

The chapter was published in *Nature Communications* and establishes an unprecedented archive of well-preserved, extensively dated Pleistocene aged fossil material at South Walker Creek, from the tropical zone of Queensland. Despite the site being an open-air deposit, the palaeo-floodplain sediments contain megafauna fossils alongside leaves, seeds, pollen and insects. The study incorporates a multi-technique dating approach, combining OSL, ESR and U-series dating, with the results making this site one of the best dated archives of its type in Australia. The chapter reports that megafaunal extinction occurred sometime after 40.1 ± 17 ka, based on a large number (n = 46) of chronometric ages from fossiliferous deposits. The results of this research challenge the hypothesis of rapid, human-mediated, continental-wide megafaunal extinction; rather, it argues for regionally staggered spatiotemporal climate deterioration.

Bayesian approach to modelling 60,000 years of Australian hydrology (Chapter 5)

This chapter provides new ages for additional megafauna fossil sites discovered at South Walker Creek, in addition to evaluating the relationship between local megafauna disappearance and hydrological change through a Bayesian approach. The timing of fluvial deposition utilises geochronological data and palaeoenvironmental interpretation outcomes presented in the preceding chapters (Chapters 2 – 4), as well as results published elsewhere in the literature. This multi-faceted

investigation into fluvial deposition across major catchments provides new insights into the geographic extent of hydrological change across eastern Australia, and examines whether any such environmental change was coeval with megafauna disappearance at South Walker Creek.

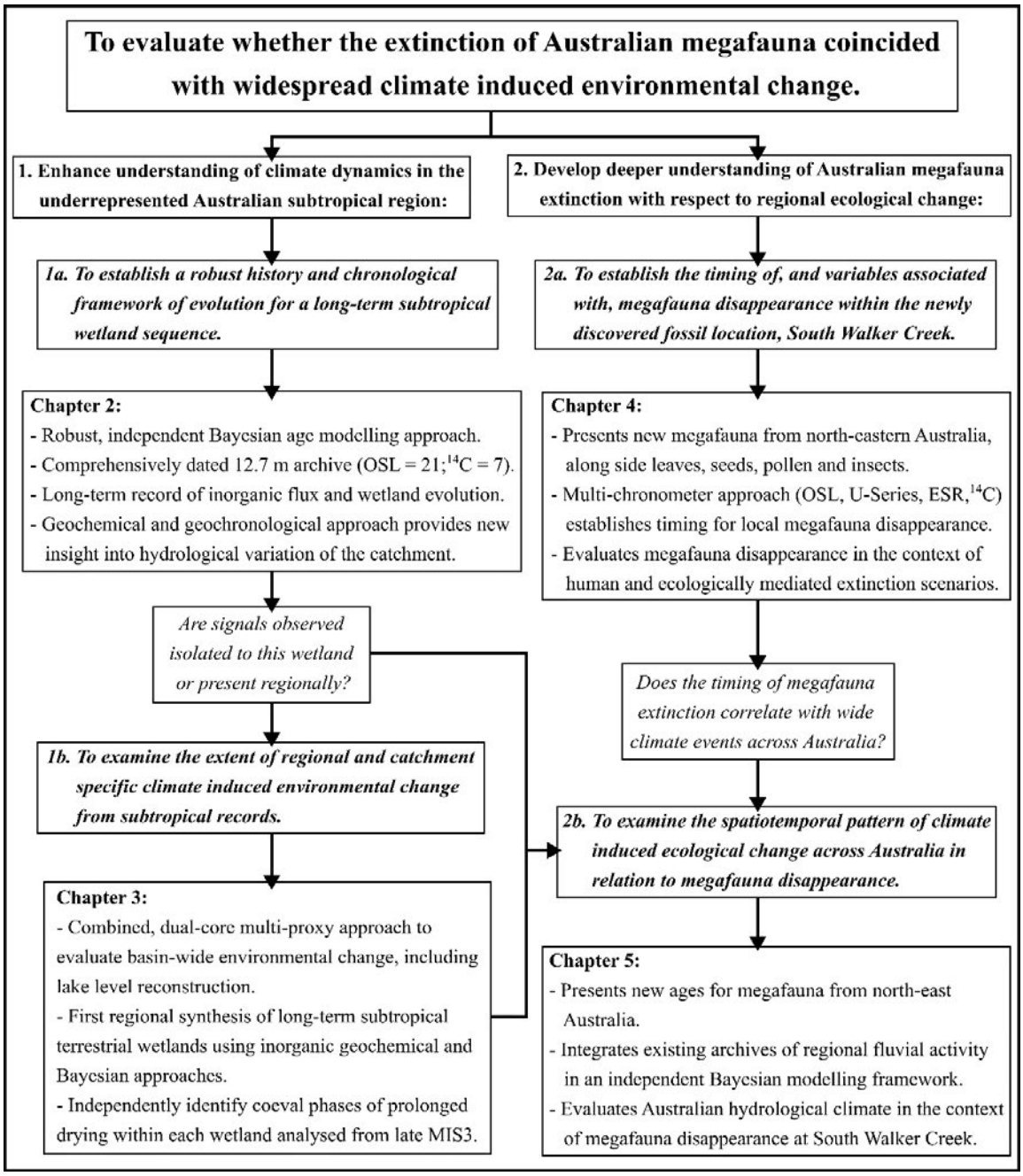

Figure 1.11 Conceptual model of the thesis research framework.

Conclusion and suggestions for further research (Chapter 6)

This chapter provides a summary of the thesis findings, in addition to a short discussion elaborating on the research outcomes of Chapter 5 and linking together the outcomes of Chapter 2, Chapter 3, and Chapter 4. It highlights the necessity to continue improving current approaches to dating palaeoecological archives, particularly in the context of the Australian megafaunal extinction debate and discussions about long-term climate change. This chapter also includes some final comments, in addition to suggestions for future research.

References

Adamiec, G., Duller, G., Roberts, H. & Wintle, A. 2010. Improving the TT-OSL SAR protocol through source trap characterisation. Radiation Measurements, 45, 768-777.

Aitken, M. J. 1985. Thermoluminescence dating: Past progress and future trends. Nuclear Tracks and Radiation Measurements (1982), 10, 3-6.

Aitken, M. J. 1998. Introduction to optical dating: the dating of Quaternary sediments by the use of photon-stimulated luminescence, Oxford, Oxford University Press.

Allen, J. & O'connell, J. 2014. Both half right: updating the evidence for dating first human arrivals in Sahul. Australian Archaeology, 79, 86-108.

Anderson, E., Arnold, J. & Libby, W. 1951. Measurement of low level radiocarbon. Review of Scientific Instruments, 22, 225-230.

Arnold, J. R. & Libby, W. F. 1949. Age determinations by radiocarbon content: checks with samples of known age. Science, 110, 678-680.

Arnold, L. J., Bailey, R. M. & Tucker, G. E. 2007. Statistical treatment of fluvial dose distributions from southern Colorado arroyo deposits. Quaternary Geochronology, 2, 162-167.

Arnold, L. J. & Demuro, M. 2015. Insights into TT-OSL signal stability from single-grain analyses of known-age deposits at Atapuerca, Spain. Quaternary Geochronology, 30, 472-478.

Arnold, L. J., Duval, M., Demuro, M., Spooner, N. A., Santonja, M. & Pérez-González, A. 2016. OSL dating of individual quartz 'supergrains' from the Ancient Middle Palaeolithic site of Cuesta de la Bajada, Spain. Quaternary Geochronology, 36, 78-101.

Arnold, L. J., Duval, M., Falguères, C., Bahain, J.-J. & Demuro, M. 2012. Portable gamma spectrometry with cerium-doped lanthanum bromide scintillators: Suitability assessments for luminescence and electron spin resonance dating applications. Radiation Measurements, 47, 6-18.

Arnold, L. J. & Roberts, R. G. 2009. Stochastic modelling of multi-grain equivalent dose (De) distributions: Implications for OSL dating of sediment mixtures. Quaternary Geochronology, 4, 204-230.

Arnold, L. J., Roberts, R. G., Galbraith, R. F. & Delong, S. B. 2009. A revised burial dose estimation procedure for optical dating of young and modern-age sediments. Quaternary Geochronology, 4, 306-325.

Arnold, L. J., Roberts, R. G., Macphee, R. D. E., Willerslev, E., Tikhonov, A. N. & Brock, F. 2008. Optical dating of perennially frozen deposits associated with preserved ancient plant and animal DNA in north-central Siberia. Quaternary Geochronology, 3, 114-136.

Ascough, P., Cook, G., Church, M., Dunbar, E., Einarsson, Á., Mcgovern, T., Dugmore, A., Perdikaris, S., Hastie, H. & Friðriksson, A. 2010. Temporal and spatial variations in freshwater 14C reservoir effects: Lake Mývatn, northern Iceland. Radiocarbon, 52, 1098-1112.

Ascough, P. L., Bird, M. I., Francis, S. & Lebl, T. 2011. Alkali extraction of archaeological and geological charcoal: evidence for diagenetic degradation and formation of humic acids. Journal of Archaeological Science, 38, 69-78.

Bailey, R. 2001. Towards a general kinetic model for optically and thermally stimulated luminescence of quartz. Radiation Measurements, 33, 17-45.

Bailey, R. M. & Arnold, L. J. 2006. Statistical modelling of single grain quartz De distributions and an assessment of procedures for estimating burial dose. Quaternary Science Reviews, 25, 2475-2502.

Barr, C., Tibby, J., Leng, M. J., Tyler, J. J., Henderson, A. C. G., Overpeck, J. T., Simpson, G. L., Cole, J. E., Phipps, S. J. & Marshall, J. C. 2019. Holocene el Niño–southern Oscillation variability reflected in subtropical Australian precipitation. Scientific reports, 9, 1-9.

Barr, C., Tibby, J., Marshall, J. C., Mcgregor, G. B., Moss, P. T., Halverson, G. P. & Fluin, J. 2013. Combining monitoring, models and palaeolimnology to assess ecosystem response to environmental change at monthly to millennial timescales: the stability of Blue Lake, North Stradbroke Island, Australia. Freshwater Biology, 58, 1614-1630.

Barr, C., Tibby, J., Moss, P. T., Halverson, G. P., Marshall, J. C., Mcgregor, G. B. & Stirling, E. 2017. A 25,000-year record of environmental change from Welsby Lagoon, North Stradbroke Island, in the Australian subtropics. Quaternary International, 449, 106-118.

Barrows, T. T., Fitzsimmons, K. E., Mills, S. C., Tumney, J., Pappin, D. & Stern, N. 2020. Late Pleistocene lake level history of Lake Mungo, Australia. Quaternary Science Reviews, 238, 106338.
Bayon, G., De Deckker, P., Magee, J. W., Germain, Y., Bermell, S., Tachikawa, K. & Norman, M. D. 2017. Extensive wet episodes in Late Glacial Australia resulting from high-latitude forcings. Scientific reports, 7, 1-7.
Becerra-Valdivia, L. & Higham, T. 2020. The timing and effect of the earliest human arrivals in North America. Nature, 584, 93-97.
Berger, A. 1988. Milankovitch theory and climate. Reviews of geophysics, 26, 624-657.
Bird, D. W., Bird, R. B. & Parker, C. H. 2005. Aboriginal Burning Regimes and Hunting Strategies in Australia's Western Desert. Human Ecology, 33, 443-464.
Bird, M. I., Beaman, R. J., Condie, S. A., Cooper, A., Ulm, S. & Veth, P. 2018. Palaeogeography and voyage modelling indicates early human colonization of Australia was likely from Timor-Roti. Quaternary Science Reviews, 191, 431-439.
Bird, M. I., Hutley, L. B., Lawes, M. J., Lloyd, J., Luly, J. G., Ridd, P. V., Roberts, R. G., Ulm, S. & Wurster, C. M. 2013. Humans, megafauna and environmental change in tropical Australia. Journal of Quaternary Science, 28, 439-452.
Bird, M. I., O'grady, D. & Ulm, S. 2016. Humans, water, and the colonization of Australia. Proceedings of the National Academy of Sciences, 113, 11477-11482.
Birks, H. H. & Birks, H. J. B. 2006. Multi-proxy studies in palaeolimnology. Vegetation history and Archaeobotany, 15, 235-251.
Blockley, S. P. E., Blaauw, M., Bronk Ramsey, C. & Van Der Plicht, J. 2007. Building and testing age models for radiocarbon dates in Lateglacial and Early Holocene sediments. Quaternary Science Reviews, 26, 1915-1926.
Boers, N., Ghil, M. & Rousseau, D.-D. 2018. Ocean circulation, ice shelf, and sea ice interactions explain Dansgaard–Oeschger cycles. Proceedings of the National Academy of Sciences, 115, E11005-E11014.
Bom. 2019. Climate Data Online [Online]. Australian Government, Bureau of Meteorology. Available: http://www.bom.gov.au/climate/data/ [Accessed 2021].
Bond, G., Heinrich, H., Broecker, W., Labeyrie, L., Mcmanus, J., Andrews, J., Huon, S., Jantschik, R., Clasen, S. & Simet, C. 1992. Evidence for massive discharges of icebergs into the North Atlantic ocean during the last glacial period. Nature, 360, 245-249.
Borreggine, M. J., Powell, E. M., Meadow, R. H., Mitrovica, J. X. & Tryon, C. A. Paleocurrents in a Least-Cost Pathway Model of Human Dispersal from Sunda to Sahul, 65-45,000 Years Ago. AGU Fall Meeting Abstracts, 2019. GC11A-06.
Bøtter-Jensen, L., Bulur, E., Duller, G. & Murray, A. 2000. Advances in luminescence instrument systems. Radiation Measurements, 32, 523-528.
Bøtter-Jensen, L., Mckeever, S. W. & Wintle, A. G. 2003. Optically stimulated luminescence dosimetry, Elsevier.
Bowler, J. M., Johnston, H., Olley, J. M., Prescott, J. R., Roberts, R. G., Shawcross, W. & Spooner, N. A. 2003. New ages for human occupation and climatic change at Lake Mungo, Australia. Nature, 421, 837-840.
Bowman, D. M., Balch, J., Artaxo, P., Bond, W. J., Cochrane, M. A., D'antonio, C. M., Defries, R., Johnston, F. H., Keeley, J. E. & Krawchuk, M. A. 2011. The human dimension of fire regimes on Earth. Journal of biogeography, 38, 2223-2236.
Braadbaart, F., Poole, I. & Van Brussel, A. 2009. Preservation potential of charcoal in alkaline environments: an experimental approach and implications for the archaeological record. Journal of archaeological science, 36, 1672-1679.
Bradshaw, C. J. A., Norman, K., Ulm, S., Williams, A. N., Clarkson, C., Chadœuf, J., Lin, S. C., Jacobs, Z., Roberts, R. G., Bird, M. I., Weyrich, L. S., Haberle, S. G., O'connor, S., Llamas, B., Cohen, T. J., Friedrich, T., Veth, P., Leavesley, M. & Saltré, F. 2021. Stochastic models support rapid peopling of Late Pleistocene Sahul. Nature Communications, 12, 2440.
Braje, T. J., Dillehay, T. D., Erlandson, J. M., Klein, R. G. & Rick, T. C. 2017. Finding the first Americans. Science, 358, 592-594.

Breeze, P. S., Groucutt, H. S., Drake, N. A., White, T. S., Jennings, R. P. & Petraglia, M. D. 2016. Palaeohydrological corridors for hominin dispersals in the Middle East∼ 250–70,000 years ago. Quaternary Science Reviews, 144, 155-185.
Brennan, B. J. 2003. Beta doses to spherical grains. Radiation Measurements, 37, 299-303.
Bronk Ramsey, C. 2008a. Deposition models for chronological records. Quaternary Science Reviews, 27, 42-60.
Bronk Ramsey, C. 2008b. Radiocarbon dating: revolutions in understanding. Archaeometry, 50, 249-275.
Bronk Ramsey, C., Buck, C. E., Manning, S. W., Reimer, P. & Plicht, H. V. D. 2006. Developments in radiocarbon calibration for archaeology. Antiquity, 80, 783-798.
Brook, B. W. & Johnson, C. N. 2006. Selective hunting of juveniles as a cause of the imperceptible overkill of the Australian Pleistocene megafauna. Alcheringa: an Australasian journal of palaeontology, 30, 39-48.
Cadd, H. R., Tibby, J., Barr, C., Tyler, J., Unger, L., Leng, M. J., Marshall, J. C., Mcgregor, G., Lewis, R. & Arnold, L. J. 2018. Development of a Southern Hemisphere subtropical wetland (Welsby Lagoon, south-east Queensland, Australia) through the last glacial cycle. Quaternary Science Reviews, 202, 53-65.
Chiang, J. C. & Friedman, A. R. 2012. Extratropical cooling, interhemispheric thermal gradients, and tropical climate change. Annual Review of Earth and Planetary Sciences, 40, 383-412.
Chiang, J. C. H., Lee, S.-Y., Putnam, A. E. & Wang, X. 2014. South Pacific Split Jet, ITCZ shifts, and atmospheric North–South linkages during abrupt climate changes of the last glacial period. Earth and Planetary Science Letters, 406, 233-246.
Clarkson, C., Jacobs, Z., Marwick, B., Fullagar, R., Wallis, L., Smith, M., Roberts, R. G., Hayes, E., Lowe, K. & Carah, X. 2017. Human occupation of northern Australia by 65,000 years ago. Nature, 547, 306-310.
Cohen, T. J., Jansen, J. D., Gliganic, L. A., Larsen, J. R., Nanson, G. C., May, J.-H., Jones, B. G. & Price, D. M. 2015. Hydrological transformation coincided with megafaunal extinction in central Australia. Geology, 43, 195-198.
Cohen, T. J., Meyer, M. C. & May, J.-H. 2018. Identifying extreme pluvials in the last millennia using optical dating of single grains of quartz from shorelines on Australia's largest lake. The Holocene, 28, 150-165.
Cohen, T. J., Nanson, G. C., Jansen, J. D., Jones, B. G., Jacobs, Z., Treble, P., Price, D. M., May, J.-H., Smith, A. M. & Ayliffe, L. K. 2011. Continental aridification and the vanishing of Australia's megalakes. Geology, 39, 167-170.
Colhoun, E. A., Pola, J. S., Barton, C. E. & Heijnis, H. 1999. Late Pleistocene vegetation and climate history of Lake Selina, western Tasmania. Quaternary International, 57, 5-23.
Conedera, M., Tinner, W., Neff, C., Meurer, M., Dickens, A. F. & Krebs, P. 2009. Reconstructing past fire regimes: methods, applications, and relevance to fire management and conservation. Quaternary Science Reviews, 28, 555-576.
Cooper, A., Turney, C. S., Palmer, J., Hogg, A., Mcglone, M., Wilmshurst, J., Lorrey, A. M., Heaton, T. J., Russell, J. M. & Mccracken, K. 2021. A global environmental crisis 42,000 years ago. Science, 371, 811-818.
Crabtree, S. A., Bird, D. W. & Bird, R. B. 2019. Subsistence transitions and the simplification of ecological networks in the Western Desert of Australia. Human Ecology, 47, 165-177.
Crabtree, S. A., Vaughn, L. J. & Crabtree, N. T. 2017. Reconstructing Ancestral Pueblo food webs in the southwestern United States. Journal of Archaeological Science, 81, 116-127.
Crabtree, S. A., White, D. A., Bradshaw, C. J. A., Saltré, F., Williams, A. N., Beaman, R. J., Bird, M. I. & Ulm, S. 2021. Landscape rules predict optimal superhighways for the first peopling of Sahul. Nature Human Behaviour.
Daly, C., Conklin, D. R. & Unsworth, M. H. 2010. Local atmospheric decoupling in complex topography alters climate change impacts. International Journal of Climatology, 30, 1857-1864.
Dansgaard, W., Clausen, H., Gundestrup, N., Hammer, C., Johnsen, S., Kristinsdottir, P. & Reeh, N. 1982. A new Greenland deep ice core. Science, 218, 1273-1277.

David, B., Arnold, L. J., Delannoy, J.-J., Fresløv, J., Urwin, C., Petchey, F., Mcdowell, M. C., Mullett, R., Land, G. & Mialanes, J. 2021. Late survival of megafauna refuted for Cloggs Cave, SE Australia: Implications for the Australian Late Pleistocene megafauna extinction debate. Quaternary Science Reviews, 253, 106781.
De Deckker, P. 2020. Airborne dust traffic from Australia in modern and Late Quaternary times. Global and Planetary Change, 184, 103056.
De Deckker, P., Arnold, L. J., Van Der Kaars, S., Bayon, G., Stuut, J.-B. W., Perner, K., Dos Santos, R. L., Uemura, R. & Demuro, M. 2019. Marine Isotope Stage 4 in Australasia: a full glacial culminating 65,000 years ago–global connections and implications for human dispersal. Quaternary Science Reviews, 204, 187-207.
De Deckker, P., Magee, J. & Shelley, J. 2011. Late Quaternary palaeohydrological changes in the large playa Lake Frome in central Australia, recorded from the Mg/Ca and Sr/Ca in ostracod valves and biotic remains. Journal of Arid Environments, 75, 38-50.
Department of Environment and Science Queensland. 2013. Wallum Freshwater Biogeographic Province [Online]. Available: https://wetlandinfo.des.qld.gov.au/wetlands/ecology/aquatic-ecosystems-natural/riverine/wallum/hydrology.html [Accessed 18 July 2021].
Diefendorf, A. F. & Freimuth, E. J. 2017. Extracting the most from terrestrial plant-derived n-alkyl lipids and their carbon isotopes from the sedimentary record: A review. Organic Geochemistry, 103, 1-21.
Demeter, F., Zanolli, C., Westaway, K. E., Joannes-Boyau, R., Duringer, P., Morley, M. W., Welker, F., Rüther, P. L., Skinner, M. M., Mccoll, H., Gaunitz, C., Vinner, L., Dunn, T. E., Olsen, J. V., Sikora, M., Ponche, J.-L., Suzzoni, E., Frangeul, S., Boesch, Q., Antoine, P.-O., Pan, L., Xing, S., Zhao, J.-X., Bailey, R. M., Boualaphane, S., Sichanthongtip, P., Sihanam, D., Patole-Edoumba, E., Aubaile, F., Crozier, F., Bourgon, N., Zachwieja, A., Luangkhoth, T., Souksavatdy, V., Sayavongkhamdy, T., Cappellini, E., Bacon, A.-M., Hublin, J.-J., Willerslev, E. & Shackelford, L. 2022. A Middle Pleistocene Denisovan molar from the Annamite Chain of northern Laos. Nature Communications, 13, 2557.
Dodson, J. & Field, J. H. 2018. What does the occurrence of Sporormiella (Preussia) spores mean in Australian fossil sequences? Journal of Quaternary Science, 33, 380-392.
Duller, G. A. 2004. Luminescence dating of Quaternary sediments: recent advances. Journal of Quaternary Science, 19, 183-192.
Duller, G. a. T. 2008. Single-grain optical dating of Quaternary sediments: why aliquot size matters in luminescence dating. Boreas, 37, 589-612.
Dunne, J. A., Maschner, H., Betts, M. W., Huntly, N., Russell, R., Williams, R. J. & Wood, S. A. 2016. The roles and impacts of human hunter-gatherers in North Pacific marine food webs. Scientific reports, 6, 1-9.
Duval, M. & Arnold, L. J. 2013. Field gamma dose-rate assessment in natural sedimentary contexts using LaBr3 (Ce) and NaI (Tl) probes: A comparison between the “threshold” and “windows” techniques. Applied Radiation and Isotopes, 74, 36-45.
Farebrother, W., Hesse, P. P., Chang, H.-C. & Jones, C. 2017. Dry lake beds as sources of dust in Australia during the Late Quaternary: A volumetric approach based on lake bed and deflated dune volumes. Quaternary Science Reviews, 161, 81-98.
Fattorini, S. 2021. Climate Change and Extinction Events. In: Alderton, D. & Elias, S. A. (eds.) Encyclopedia of Geology (Second Edition). Oxford: Academic Press.
Field, J., Fillios, M. & Wroe, S. 2008. Chronological overlap between humans and megafauna in Sahul (Pleistocene Australia–New Guinea): a review of the evidence. Earth-Science Reviews, 89, 97-115.
Field, J., Wroe, S., Trueman, C. N., Garvey, J. & Wyatt-Spratt, S. 2013. Looking for the archaeological signature in Australian megafaunal extinctions. Quaternary International, 285, 76-88.
Fillios, M., Field, J. & Charles, B. 2010. Investigating human and megafauna co-occurrence in Australian prehistory: mode and causality in fossil accumulations at Cuddie Springs. Quaternary International, 211, 123-143.
Fiorentini, G., Lissia, M. & Mantovani, F. 2007. Geo-neutrinos and Earth's interior. Phys. Rep., 453.

Fitzsimmons, K. E., Bowler, J. M., Rhodes, E. J. & Magee, J. M. 2007. Relationships between desert dunes during the late Quaternary in the Lake Frome region, Strzelecki Desert, Australia. Journal of Quaternary Science: Published for the Quaternary Research Association, 22, 549-558.
Fitzsimmons, K. E., Cohen, T. J., Hesse, P. P., Jansen, J., Nanson, G. C., May, J.-H., Barrows, T. T., Haberlah, D., Hilgers, A., Kelly, T., Larsen, J., Lomax, J. & Treble, P. 2013. Late Quaternary palaeoenvironmental change in the Australian drylands. Quaternary Science Reviews, 74, 78-96.
Flannery, T. 1994. The future eaters: an ecological history of the Australasian lands and people, Port Melbourne, Port Melbourne: Reed Books.
Fu, X., Cohen, T. J. & Arnold, L. J. 2017. Extending the record of lacustrine phases beyond the last interglacial for Lake Eyre in central Australia using luminescence dating. Quaternary Science Reviews, 162, 88-110.
Galbraith, R. F. & Roberts, R. G. 2012. Statistical aspects of equivalent dose and error calculation and display in OSL dating: an overview and some recommendations. Quaternary Geochronology, 11, 1-27.
Galbraith, R. F., Roberts, R. G., Laslett, G. M., Yoshida, H. & Olley, J. M. 1999. Optical dating of single and multiple grains of quartz from Jinmium rock shelter, northern Australia: Part I, experimental design and statistical models. Archaeometry, 41, 339-364.
Gallant, A. J., Phipps, S. J., Karoly, D. J., Mullan, A. B. & Lorrey, A. M. 2013. Nonstationary Australasian teleconnections and implications for paleoclimate reconstructions. Journal of Climate, 26, 8827-8849.
Gillespie, R. & Brook, B. W. 2006. Is there a Pleistocene archaeological site at Cuddie Springs? Archaeology in Oceania, 41, 1-11.
Gilks, W. R., Richardson, S. & Spiegelhalter, D. 1995. Markov chain Monte Carlo in practice, CRC press.
Godwin, H. 1962. Half-life of radiocarbon. Nature, 195, 984-984.
Grellet-Tinner, G., Spooner, N. A. & Worthy, T. H. 2016. Is the "Genyornis" egg of a mihirung or another extinct bird from the Australian dreamtime? Quaternary Science Reviews, 133, 147-164.
Grothmann, T. & Patt, A. 2005. Adaptive capacity and human cognition: the process of individual adaptation to climate change. Global environmental change, 15, 199-213.
Groucutt, H. S., Petraglia, M. D., Bailey, G., Scerri, E. M., Parton, A., Clark-Balzan, L., Jennings, R. P., Lewis, L., Blinkhorn, J. & Drake, N. A. 2015. Rethinking the dispersal of Homo sapiens out of Africa. Evolutionary Anthropology: Issues, News, and Reviews, 24, 149-164.
Grün, R., Eggins, S., Aubert, M., Spooner, N., Pike, A. W. G. & Müller, W. 2010. ESR and U-series analyses of faunal material from Cuddie Springs, NSW, Australia: implications for the timing of the extinction of the Australian megafauna. Quaternary Science Reviews, 29, 596-610.
Guérin, G., Mercier, N. & Adamiec, G. 2011. Dose-rate conversion factors: update. Ancient TL, 29, 5-8.
Guthrie, M. 2021. Climate drivers of the South West Land Division [Online]. Western Australia: Department of Primary Industries and Regional Development. Available: https://www.agric.wa.gov.au/climate-weather/climate-drivers-south-west-land-division [Accessed 9th August 2021 2021].
Hajdas, I. 2009. Applications of radiocarbon dating method. Radiocarbon, 51, 79-90.
Haller, C., Hallock, P., Hine, A. C. & Smith, C. G. 2018. Benthic foraminifera from the Carnarvon Ramp reveal variability in Leeuwin Current activity (Western Australia) since the Pliocene. Marine Micropaleontology, 142, 25-39.
Hamm, G., Mitchell, P., Arnold, L. J., Prideaux, G. J., Questiaux, D., Spooner, N. A., Levchenko, V. A., Foley, E. C., Worthy, T. H. & Stephenson, B. 2016. Cultural innovation and megafauna interaction in the early settlement of arid Australia. Nature, 539, 280-283.
Harris, E. C. 2014. Principles of archaeological stratigraphy, Elsevier.
Hedges, R., Law, I., Bronk, C. & Housley, R. 1989. The Oxford accelerator mass spectrometry facility: technical developments in routine dating. Archaeometry, 31, 99-113.
Heinrich, H. 1988. Origin and consequences of cyclic ice rafting in the northeast Atlantic Ocean during the past 130,000 years. Quaternary research, 29, 142-152.
Helman, P. & Tomlinson, R. 2018. Two Centuries of Climate Change and Climate Variability, East Coast Australia. Journal of Marine Science and Engineering, 6, 3.

Hemming, S. R. 2004. Heinrich events: Massive late Pleistocene detritus layers of the North Atlantic and their global climate imprint. Reviews of Geophysics, 42.
Herrera, K. J., Somarelli, J. A., Lowery, R. K. & Herrera, R. J. 2009. To what extent did Neanderthals and modern humans interact? Biological Reviews, 84, 245-257.
Hershkovitz, I., Weber, G. W., Quam, R., Duval, M., Grün, R., Kinsley, L., Ayalon, A., Bar-Matthews, M., Valladas, H. & Mercier, N. 2018. The earliest modern humans outside Africa. Science, 359, 456-459.
Hesse, P. P., Williams, R., Ralph, T. J., Fryirs, K. A., Larkin, Z. T., Westaway, K. E. & Farebrother, W. 2018. Palaeohydrology of lowland rivers in the Murray-Darling Basin, Australia. Quaternary Science Reviews, 200, 85-105.
Heydari, M. & Guérin, G. 2018. OSL signal saturation and dose rate variability: Investigating the behaviour of different statistical models. Radiation Measurements, 120, 96-103.
Higham, T. F. G., Bronk Ramsey, C., Brock, F., Baker, D. & Ditchfield, P. 2011. Radiocarbon dates from the Oxford AMS system: Archaeometry date list 34. Archaeometry, 53, 1067-1084.
Hocknull, S. A., Lewis, R., Arnold, L. J., Pietsch, T., Joannes-Boyau, R., Price, G. J., Moss, P., Wood, R., Dosseto, A., Louys, J., Olley, J. & Lawrence, R. A. 2020. Extinction of eastern Sahul megafauna coincides with sustained environmental deterioration. Nature communications, 11, 1-14.
Hodell, D. A. & Channell, J. E. 2016. Mode transitions in Northern Hemisphere glaciation: co-evolution of millennial and orbital variability in Quaternary climate. Climate of the Past, 12, 1805-1828.
Hodell, D. A., Channell, J. E., Curtis, J. H., Romero, O. E. & Röhl, U. 2008. Onset of "Hudson Strait" Heinrich events in the eastern North Atlantic at the end of the middle Pleistocene transition (~ 640 ka)? Paleoceanography, 23.
Horton, D. 1980. A review of the extinction question: man, climate and megafauna. Archaeology & Physical Anthropology in Oceania, 15, 86-97.
Huntley, D., Hutton, J. & Prescott, J. 1994. Further thermoluminescence dates from the dune sequence in the southeast of South Australia. Quaternary Science Reviews, 13, 201-207.
Huntley, D. J., Godfrey-Smith, D. I. & Thewalt, M. L. 1985. Optical dating of sediments. Nature, 313, 105-107.
Huntley, D. J., Hutton, J. T. & Prescott, J. R. 1993. Optical dating using inclusions within quartz grains. Geology, 21, 1087-1090.
Huntley, D. J., Short, M. A. & Dunphy, K. 1996. Deep traps in quartz and their use for optical dating. Canadian Journal of Physics, 74, 81-91.
Imbrie, J., Boyle, E. A., Clemens, S. C., Duffy, A., Howard, W. R., Kukla, G., Kutzbach, J., Martinson, D. G., Mcintyre, A., Mix, A. C., Molfino, B., Morley, J. J., Peterson, L. C., Pisias, N. G., Prell, W. L., Raymo, M. E., Shackleton, N. J. & Toggweiler, J. R. 1992. On the Structure and Origin of Major Glaciation Cycles 1. Linear Responses to Milankovitch Forcing. Paleoceanography, 7, 701-738.
Imbrie, J., Hays, J. D., Martinson, D. G., Mcintyre, A., Mix, A. C., Morley, J. J., Pisias, N. G., Prell, W. L. & Shackleton, N. J. 1984. The orbital theory of Pleistocene climate: support from a revised chronology of the marine d18O record.
Jacobs, Z., Duller, G. A., Wintle, A. G. & Henshilwood, C. S. 2006. Extending the chronology of deposits at Blombos Cave, South Africa, back to 140 ka using optical dating of single and multiple grains of quartz. Journal of Human Evolution, 51, 255-273.
Jankowski, N. R., Gully, G. A., Jacobs, Z., Roberts, R. G. & Prideaux, G. J. 2016. A late Quaternary vertebrate deposit in Kudjal Yolgah Cave, south-western Australia: refining regional late Pleistocene extinctions. Journal of Quaternary Science, 31, 538-550.
Jennings, R. P., Singarayer, J., Stone, E. J., Krebs-Kanzow, U., Khon, V., Nisancioglu, K. H., Pfeiffer, M., Zhang, X., Parker, A. & Parton, A. 2015. The greening of Arabia: Multiple opportunities for human occupation of the Arabian Peninsula during the Late Pleistocene inferred from an ensemble of climate model simulations. Quaternary International, 382, 181-199.
Jouzel, J., Masson-Delmotte, V., Cattani, O., Dreyfus, G., Falourd, S., Hoffmann, G., Minster, B., Nouet, J., Barnola, J.-M. & Chappellaz, J. 2007. Orbital and millennial Antarctic climate variability over the past 800,000 years. science, 317, 793-796.

Keaveney, E. M. & Reimer, P. J. 2012. Understanding the variability in freshwater radiocarbon reservoir offsets: a cautionary tale. Journal of Archaeological Science, 39, 1306-1316.
Kemp, C., Tibby, J., Arnold, L. J. & Barr, C. 2019. Australian hydroclimate during Marine Isotope Stage 3: a synthesis and review. Quaternary Science Reviews, 204, 94-104.
Kemp, C. W., Tibby, J., Arnold, L. J., Barr, C., Gadd, P. S., Marshall, J. C., Mcgregor, G. B. & Jacobsen, G. E. 2020. Climates of the last three interglacials in subtropical eastern Australia inferred from wetland sediment geochemistry. Palaeogeography, Palaeoclimatology, Palaeoecology, 538, 109463.
Kemp, J., Pietsch, T., Gontz, A. & Olley, J. 2017. Lacustrine-fluvial interactions in Australia's Riverine Plains. Quaternary Science Reviews, 166, 352-362.
Kemp, J. & Rhodes, E. 2010. Episodic fluvial activity of inland rivers in southeastern Australia: Palaeochannel systems and terraces of the Lachlan River. Quaternary Science Reviews, 29, 732-752.
Kershaw, A. P. 1976. A late Pleistocene and Holocene pollen diagram from Lynch's Crater, northeastern Queensland, Australia. New Phytologist, 77, 469-498.
Kershaw, A. P., Bretherton, S. C. & Van Der Kaars, S. 2007a. A complete pollen record of the last 230 ka from Lynch's Crater, north-eastern Australia. Palaeogeography, Palaeoclimatology, Palaeoecology, 251, 23-45.
Kershaw, A. P., Clark, J. S., Gill, A. M. & D'costa, D. M. 2002. A history of fire in Australia.
Kershaw, A. P., Mckenzie, G. M., Brown, J., Roberts, R. G. & Van Der Kaars, S. 2010. Beneath the peat: A refined pollen record from an interstadial at Caledonia Fen, highland eastern Victoria, Australia. Altered ecologies: fire, climate and human influence on terrestrial landscapes. Terra Australis, 32, 33-48.
Kershaw, A. P., Mckenzie, G. M., Porch, N., Roberts, R. G., Brown, J., Heijnis, H., Orr, M. L., Jacobsen, G. & Newall, P. R. 2007b. A high-resolution record of vegetation and climate through the last glacial cycle from Caledonia Fen, southeastern highlands of Australia. Journal of Quaternary Science: Published for the Quaternary Research Association, 22, 481-500.
Kershaw, A. P., Van Der Kaars, S. & Moss, P. T. 2003. Late Quaternary Milankovitch-scale climatic change and variability and its impact on monsoonal Australasia. Marine Geology, 201, 81-95.
Kiem, A. S. & Franks, S. W. 2004. Multi-decadal variability of drought risk, eastern Australia. Hydrological Processes, 18, 2039-2050.
King, A. D., Pitman, A. J., Henley, B. J., Ukkola, A. M. & Brown, J. R. 2020. The role of climate variability in Australian drought. Nature Climate Change, 10, 177-179.
Kissel, C., Laj, C., Labeyrie, L., Dokken, T., Voelker, A. & Blamart, D. 1999. Rapid climatic variations during marine isotopic stage 3: magnetic analysis of sediments from Nordic Seas and North Atlantic. Earth and Planetary Science Letters, 171, 489-502.
Kottek, M., Grieser, J., Beck, C., Rudolf, B. & Rubel, F. 2006. World map of the Köppen-Geiger climate classification updated.
Laland, K. N. & O'brien, M. J. 2010. Niche construction theory and archaeology. Journal of Archaeological Method and Theory, 17, 303-322.
Larrasoaña, J. C., Roberts, A. P. & Rohling, E. J. 2013. Dynamics of green Sahara periods and their role in hominin evolution. PloS one, 8, e76514.
Laycock, J. 1978. North Stradbroke Island.
Leach, L. Hydrology and physical setting of North Stradbroke Island. Proceedings of the Royal Society of Queensland, 2011.
Li, G., Jin, M., Wen, L., Zhao, H., Madsen, D., Liu, X., Wu, D. & Chen, F. 2014. Quartz and K-feldspar optical dating chronology of eolian sand and lacustrine sequence from the southern Ulan Buh Desert, NW China: Implications for reconstructing late Pleistocene environmental evolution. Palaeogeography, Palaeoclimatology, Palaeoecology, 393, 111-121.
Libby, W. F. 1961. Radiocarbon dating. Science, 133, 621-629.
Lisé-Pronovost, A., Fletcher, M.-S., Mallett, T., Mariani, M., Lewis, R., Gadd, P. S., Herries, A. I., Blaauw, M., Heijnis, H. & Hodgson, D. A. 2019. Scientific drilling of sediments at Darwin Crater, Tasmania. Scientific Drilling, 25, 1-14.

Lisé-Pronovost, A., Fletcher, M.-S., Simon, Q., Jacobs, Z., Gadd, P. S., Heslop, D., Herries, A. I. & Yokoyama, Y. 2021. Chronostratigraphy of a 270-ka sediment record from Lake Selina, Tasmania: Combining radiometric, geomagnetic and climatic dating. Quaternary Geochronology, 62, 101152.
Lisiecki, L. E. & Raymo, M. E. 2005. A Pliocene-Pleistocene stack of 57 globally distributed benthic δ18O records. Paleoceanography, 20.
Lock, G. & Pouncett, J. Walking the Ridgeway Revisited: The Methodological and Theoretical Implications of Scale Dependency for the Derivation of Slope and the Calculation of Least-Cost Pathways. Making History Interactive. CAA 2009–Proceedings of the 37th Conference, 2010. 192-203.
Longmore, M. E. & Heijnis, H. 1999. Aridity in Australia: Pleistocene records of palaeohydrological and palaeoecological change from the perched lake sediments of Fraser Island, Queensland, Australia. Quaternary International, 57, 35-47.
Lorenzen, E. D., Nogués-Bravo, D., Orlando, L., Weinstock, J., Binladen, J., Marske, K. A., Ugan, A., Borregaard, M. K., Gilbert, M. T. P., Nielsen, R., Ho, S. Y. W., Goebel, T., Graf, K. E., Byers, D., Stenderup, J. T., Rasmussen, M., Campos, P. F., Leonard, J. A., Koepfli, K.-P., Froese, D., Zazula, G., Stafford, T. W., Aaris-Sørensen, K., Batra, P., Haywood, A. M., Singarayer, J. S., Valdes, P. J., Boeskorov, G., Burns, J. A., Davydov, S. P., Haile, J., Jenkins, D. L., Kosintsev, P., Kuznetsova, T., Lai, X., Martin, L. D., Mcdonald, H. G., Mol, D., Meldgaard, M., Munch, K., Stephan, E., Sablin, M., Sommer, R. S., Sipko, T., Scott, E., Suchard, M. A., Tikhonov, A., Willerslev, R., Wayne, R. K., Cooper, A., Hofreiter, M., Sher, A., Shapiro, B., Rahbek, C. & Willerslev, E. 2011. Species-specific responses of Late Quaternary megafauna to climate and humans. Nature, 479, 359-364.
Lowe, J. J. & Walker, M. 2014. Reconstructing quaternary environments, Routledge.
Malhi, Y., Doughty, C. E., Galetti, M., Smith, F. A., Svenning, J.-C. & Terborgh, J. W. 2016. Megafauna and ecosystem function from the Pleistocene to the Anthropocene. Proceedings of the National Academy of Sciences, 113, 838-846.
Mariani, M. & Fletcher, M.-S. 2017. Long-term climate dynamics in the extra-tropics of the South Pacific revealed from sedimentary charcoal analysis. Quaternary Science Reviews, 173, 181-192.
Marshall, G. J. 2003. Trends in the Southern Annular Mode from observations and reanalyses. Journal of climate, 16, 4134-4143.
Mcdougall, I., Brown, F. H. & Fleagle, J. G. 2005. Stratigraphic placement and age of modern humans from Kibish, Ethiopia. Nature, 433, 733-736.
Mcgee, D., Donohoe, A., Marshall, J. & Ferreira, D. 2014. Changes in ITCZ location and cross-equatorial heat transport at the Last Glacial Maximum, Heinrich Stadial 1, and the mid-Holocene. Earth and Planetary Science Letters, 390, 69-79.
Mcgowan, H. A., Petherick, L. M. & Kamber, B. S. 2008. Aeolian sedimentation and climate variability during the late Quaternary in southeast Queensland, Australia. Palaeogeography, Palaeoclimatology, Palaeoecology, 265, 171-181.
Mckeever, S. W. S. & Chen, R. 1997. Luminescence models. Radiation Measurements, 27, 625-661.
Mejdahl, V. 1979. Thermoluminescence dating: beta-dose attenuation in quartz grains. Archaeometry, 21, 61-72.
Mejdahl, V. 1987. Internal radioactivity in quartz and feldspar grains. Ancient TL, 5, 10-17.
Mellett, C. L. 2013. Luminescence dating. Geomorphological Techniques. British Society for Geomorphology.
Milankovitch, M., Porter, S., An, Z. & Zheng, H. 1941. “Kanon der Erdestrahlung.” Beogard, Koninglich Serbische Akademie. (English translation: “Canon of Insolation and the Ice Age Problem,” by the Israel Program for Scientific Translation and published for the US Department of Commerce and the National Science Foundation.), 157-169.
Miller, G., Magee, J., Smith, M., Spooner, N., Baynes, A., Lehman, S., Fogel, M., Johnston, H., Williams, D. & Clark, P. 2016. Human predation contributed to the extinction of the Australian megafaunal bird Genyornis newtoni~ 47 ka. Nature Communications, 7, 1-7.
Miller, G. H., Fogel, M. L., Magee, J. W., Gagan, M. K., Clarke, S. J. & Johnson, B. J. 2005. Ecosystem collapse in Pleistocene Australia and a human role in megafaunal extinction. science, 309, 287-290.

Mooney, S., Harrison, S. P., Bartlein, P. J. & Stevenson, J. 2012. The prehistory of fire in Australasia. In: Bradstock, R. A., Gill, A. M. & Williams, R. J. (eds.) Flammable Australia: Fire Regimes, Biodiversity and Ecosystems in a Changing World. Collingwood, Victoria, Australia: CSIRO Publishing.
Mooney, S. D., Harrison, S. P., Bartlein, P. J., Daniau, A.-L., Stevenson, J., Brownlie, K. C., Buckman, S., Cupper, M., Luly, J. & Black, M. 2011. Late Quaternary fire regimes of Australasia. Quaternary Science Reviews, 30, 28-46.
Moss, E. 2013a. A Dust Record from Lacustrine Sediments on North Stradbroke Island, Queensland: Evidence for Climate Variability in Central and Southeastern Australia During the Late Quaternary. [Bachelor's Thesis], The University of Sydney.
Moss, P. T. 2013b. Palynology and its Application to Geomorphology. In: Shroder, J. F. (ed.) Treatise on Geomorphology. San Diego: Academic Press.
Moss, P. T., Dunbar, G. B., Thomas, Z., Turney, C., Kershaw, A. P. & Jacobsen, G. E. 2017. A 60 000-year record of environmental change for the Wet Tropics of north-eastern Australia based on the ODP 820 marine core. Journal of Quaternary Science, 32, 704-716.
Moss, P. T. & Kershaw, A. P. 2007. A late Quaternary marine palynological record (oxygen isotope stages 1 to 7) for the humid tropics of northeastern Australia based on ODP Site 820. Palaeogeography, Palaeoclimatology, Palaeoecology, 251, 4-22.
Muller, J., Kylander, M., Wüst, R. A., Weiss, D., Martinez-Cortizas, A., Legrande, A. N., Jennerjahn, T., Behling, H., Anderson, W. T. & Jacobson, G. 2008. Possible evidence for wet Heinrich phases in tropical NE Australia: the Lynch's Crater deposit. Quaternary Science Reviews, 27, 468-475.
Murphy, B. P., Williamson, G. J. & Bowman, D. M. 2012. Did central Australian megafaunal extinction coincide with abrupt ecosystem collapse or gradual climate change? Global Ecology and Biogeography, 21, 142-151.
Murray, A. S. & Wintle, A. G. 2000. Luminescence dating of quartz using an improved single-aliquot regenerative-dose protocol. Radiation measurements, 32, 57-73.
Nanson, G. C., East, T. J. & Roberts, R. G. 1993. Quaternary stratigraphy, geochronology and evolution of the Magela Creek catchment in the monsoon tropics of northern Australia. Sedimentary Geology, 83, 277-302.
Nanson, G. C., Price, D. M., Jones, B. G., Maroulis, J. C., Coleman, M., Bowman, H., Cohen, T. J., Pietsch, T. J. & Larsen, J. R. 2008. Alluvial evidence for major climate and flow regime changes during the middle and late Quaternary in eastern central Australia. Geomorphology, 101, 109-129.
Nelson, D. E., Korteling, R. G. & Stott, W. R. 1977. Carbon-14: direct detection at natural concentrations. Science, 198, 507-508.
Nott, J. & Price, D. 1994. Plunge pools and paleoprecipitation. Geology, 22, 1047-1050.
O'connell, J. F. & Allen, J. 2004. Dating the colonization of Sahul (Pleistocene Australia–New Guinea): a review of recent research. Journal of Archaeological Science, 31, 835-853.
Ollerhead, J., Huntley, D. & Berger, G. W. 1994. Luminescence dating of sediments from Buctouche Spit, New Brunswick. Canadian Journal of Earth Sciences, 31, 523-531.
Page, K., Nanson, G. & Price, D. 1996. Chronology of Murrumbidgee river palaeochannels on the Riverine Plain, southeastern Australia. Journal of Quaternary Science: Published for the Quaternary Research Association, 11, 311-326.
Parrenin, F., Barnola, J.-M., Beer, J., Blunier, T., Castellano, E., Chappellaz, J., Dreyfus, G., Fischer, H., Fujita, S. & Jouzel, J. 2007. The EDC3 chronology for the EPICA Dome C ice core. Climate of the Past, 3, 485-497.
Parton, A., White, T. S., Parker, A. G., Breeze, P. S., Jennings, R., Groucutt, H. S. & Petraglia, M. D. 2015. Orbital-scale climate variability in Arabia as a potential motor for human dispersals. Quaternary International, 382, 82-97.
Patton, N. R., Ellerton, D. & Shulmeister, J. 2019. High-resolution remapping of the coastal dune fields of south east Queensland, Australia: a morphometric approach. Journal of Maps, 15, 578-589.
Pawley, S. M., Bailey, R. M., Rose, J., Moorlock, B. S., Hamblin, R. J., Booth, S. J. & Lee, J. R. 2008. Age limits on Middle Pleistocene glacial sediments from OSL dating, north Norfolk, UK. Quaternary Science Reviews, 27, 1363-1377.

Peters, K. J., Saltré, F., Friedrich, T., Jacobs, Z., Wood, R., Mcdowell, M., Ulm, S. & Bradshaw, C. J. A. 2019. FosSahul 2.0, an updated database for the Late Quaternary fossil records of Sahul. Scientific data, 6, 1-7.
Petersen, S. V., Schrag, D. P. & Clark, P. U. 2013. A new mechanism for Dansgaard-Oeschger cycles. Paleoceanography, 28, 24-30.
Petherick, L., Bostock, H., Cohen, T. J., Fitzsimmons, K., Tibby, J., Fletcher, M.-S., Moss, P., Reeves, J., Mooney, S. & Barrows, T. 2013. Climatic records over the past 30 ka from temperate Australia–a synthesis from the Oz-INTIMATE workgroup. Quaternary Science Reviews, 74, 58-77.
Petherick, L., Mcgowan, H. & Moss, P. 2008. Climate variability during the Last Glacial Maximum in eastern Australia: evidence of two stadials? Journal of Quaternary Science: Published for the Quaternary Research Association, 23, 787-802.
Petherick, L. M., Mcgowan, H. A. & Kamber, B. S. 2009. Reconstructing transport pathways for late Quaternary dust from eastern Australia using the composition of trace elements of long travelled dusts. Geomorphology, 105, 67-79.
Petherick, L. M., Moss, P. T. & Mcgowan, H. A. 2011. Climatic and environmental variability during the termination of the Last Glacial Stage in coastal eastern Australia: a review. Australian Journal of Earth Sciences, 58, 563-577.
Petherick, L. M., Moss, P. T. & Mcgowan, H. A. 2017. An extended last glacial maximum in Subtropical Australia. Quaternary International, 432, 1-12.
Petraglia, M. D., Haslam, M., Fuller, D. Q., Boivin, N. & Clarkson, C. 2010. Out of Africa: new hypotheses and evidence for the dispersal of Homo sapiens along the Indian Ocean rim. Annals of human biology, 37, 288-311.
Pettitt, P. B., Davies, W., Gamble, C. S. & Richards, M. B. 2003. Palaeolithic radiocarbon chronology: quantifying our confidence beyond two half-lives. Journal of Archaeological science, 30, 1685-1693.
Pickett, J. W., Ku, T. L., Thompson, C. H., Roman, D., Kelley, R. A. & Huang, Y. P. 1989. A review of age determinations on Pleistocene corals in eastern Australia. Quaternary Research, 31, 392-395.
Pires, M. M., Guimarães, P. R., Galetti, M. & Jordano, P. 2018. Pleistocene megafaunal extinctions and the functional loss of long-distance seed-dispersal services. Ecography, 41, 153-163.
Potts, R. 1998. Variability selection in hominid evolution. Evolutionary Anthropology: Issues, News, and Reviews: Issues, News, and Reviews, 7, 81-96.
Prescott, J. R. & Hutton, J. T. 1994. Cosmic ray contributions to dose rates for luminescence and ESR dating: large depths and long-term time variations. Radiation measurements, 23, 497-500.
Prescott, J. R. & Robertson, G. B. 1997. Sediment dating by luminescence: a review. Radiation Measurements, 27, 893-922.
Price, G. J., Fitzsimmons, K. E., Nguyen, A. D., Zhao, J.-X., Feng, Y.-X., Sobbe, I. H., Godthelp, H., Archer, M. & Hand, S. J. 2021. New ages of the world's largest-ever marsupial: Diprotodon optatum from Pleistocene Australia. Quaternary International.
Price, G. J. & Sobbe, I. H. 2011. Morphological variation within an individual Pleistocene Diprotodon optatum Owen, 1838 (Diprotodontinae; Marsupialia): implications for taxonomy within diprotodontoids. Alcheringa, 35, 21-29.
Prideaux, G. J., Ayliffe, L. K., Desantis, L. R., Schubert, B. W., Murray, P. F., Gagan, M. K. & Cerling, T. E. 2009. Extinction implications of a chenopod browse diet for a giant Pleistocene kangaroo. Proceedings of the National Academy of Sciences, 106, 11646-11650.
Prideaux, G. J., Long, J. A., Ayliffe, L. K., Hellstrom, J. C., Pillans, B., Boles, W. E., Hutchinson, M. N., Roberts, R. G., Cupper, M. L. & Arnold, L. J. 2007. An arid-adapted middle Pleistocene vertebrate fauna from south-central Australia. Nature, 445, 422-425.
Pye, K. 1993. Late Quaternary development of coastal parabolic megadune complexes in northeastern Australia. Aeolian Sediments. Ancient and Modern. Blackwell Scientific Publications.
Rahimzadeh, N., Khormali, F., Gribenski, N., Tsukamoto, S., Kehl, M., Pint, A., Kiani, F. & Frechen, M. 2019. Timing and development of sand dunes in the Golestan Province, northern Iran—Implications for the Late-Pleistocene history of the Caspian Sea. Aeolian Research, 41, 100538.

Rasmussen, S. O., Bigler, M., Blockley, S. P., Blunier, T., Buchardt, S. L., Clausen, H. B., Cvijanovic, I., Dahl-Jensen, D., Johnsen, S. J., Fischer, H., Gkinis, V., Guillevic, M., Hoek, W. Z., Lowe, J. J., Pedro, J. B., Popp, T., Seierstad, I. K., Steffensen, J. P., Svensson, A. M., Vallelonga, P., Vinther, B. M., Walker, M. J. C., Wheatley, J. J. & Winstrup, M. 2014. A stratigraphic framework for abrupt climatic changes during the Last Glacial period based on three synchronized Greenland ice-core records: refining and extending the INTIMATE event stratigraphy. Quaternary Science Reviews, 106, 14-28.

Reeves, J. M., Barrows, T. T., Cohen, T. J., Kiem, A. S., Bostock, H. C., Fitzsimmons, K. E., Jansen, J. D., Kemp, J., Krause, C. & Petherick, L. 2013. Climate variability over the last 35,000 years recorded in marine and terrestrial archives in the Australian region: an OZ-INTIMATE compilation. Quaternary Science Reviews, 74, 21-34.

Richter, D., Grün, R., Joannes-Boyau, R., Steele, T. E., Amani, F., Rué, M., Fernandes, P., Raynal, J.-P., Geraads, D., Ben-Ncer, A., Hublin, J.-J. & Mcpherron, S. P. 2017. The age of the hominin fossils from Jebel Irhoud, Morocco, and the origins of the Middle Stone Age. Nature, 546, 293-296.

Risbey, J. S., Pook, M. J., Mcintosh, P. C., Wheeler, M. C. & Hendon, H. H. 2009. On the remote drivers of rainfall variability in Australia. Monthly Weather Review, 137, 3233-3253.

Roberts, R., Walsh, G., Murray, A., Olley, J., Jones, R., Morwood, M., Tuniz, C., Lawson, E., Macphail, M., Bowdery, D. & Naumann, I. 1997. Luminescence dating of rock art and past environments using mud-wasp nests in northern Australia. Nature, 387, 696-699.

Roberts, R. G. & Brook, B. W. 2010. Turning back the clock on the extinction of megafauna in Australia. Quaternary Science Reviews: International Multidisciplinary Review and Research Journal, 29, 593-595.

Roberts, R. G., Flannery, T. F., Ayliffe, L. K., Yoshida, H., Olley, J. M., Prideaux, G. J., Laslett, G. M., Baynes, A., Smith, M. A. & Jones, R. 2001. New ages for the last Australian megafauna: continent-wide extinction about 46,000 years ago. Science, 292, 1888-1892.

Roberts, R. G., Galbraith, R., Yoshida, H., Laslett, G. & Olley, J. M. 2000. Distinguishing dose populations in sediment mixtures: a test of single-grain optical dating procedures using mixtures of laboratory-dosed quartz. Radiation Measurements, 32, 459-465.

Roberts, R. G., Galbraith, R. F., Olley, J. M., Yoshida, H. & Laslett, G. M. 1999. Optical dating of single and multiple grains of quartz from Jinmium rock shelter, northern Australia: part II, results and implications. Archaeometry, 41, 365-395.

Roberts, R. G., Jones, R. & Smith, M. A. 1994. Beyond the radiocarbon barrier in Australian prehistory: a critique of Allen's commentary. Antiquity, 68, 611.

Rodríguez-Rey, M., Herrando-Pérez, S., Gillespie, R., Jacobs, Z., Saltré, F., Brook, B. W., Prideaux, G. J., Roberts, R. G., Cooper, A. & Alroy, J. 2015. Criteria for assessing the quality of Middle Pleistocene to Holocene vertebrate fossil ages. Quaternary Geochronology, 30, 69-79.

Romanowska, I., Gamble, C., Bullock, S. & Sturt, F. 2017. Dispersal and the Movius line: testing the effect of dispersal on population density through simulation. Quaternary International, 431, 53-63.

Rousseau, D.-D., Antoine, P., Boers, N., Lagroix, F., Ghil, M., Lomax, J., Fuchs, M., Debret, M., Hatté, C. & Moine, O. 2020. Dansgaard–Oeschger-like events of the penultimate climate cycle: the loess point of view. Climate of the Past, 16, 713-727.

Ruff, M., Wacker, L., Gäggeler, H., Suter, M., Synal, H.-A. & Szidat, S. 2007. A gas ion source for radiocarbon measurements at 200 kV. Radiocarbon, 49, 307-314.

Rule, S., Brook, B. W., Haberle, S. G., Turney, C. S., Kershaw, A. P. & Johnson, C. N. 2012. The aftermath of megafaunal extinction: ecosystem transformation in Pleistocene Australia. Science, 335, 1483-1486.

Saltré, F., Chadoeuf, J., Peters, K. J., Mcdowell, M. C., Friedrich, T., Timmermann, A., Ulm, S. & Bradshaw, C. J. 2019. Climate-human interaction associated with southeast Australian megafauna extinction patterns. Nature communications, 10, 1-9.

Saltré, F., Rodríguez-Rey, M., Brook, B. W., Johnson, C. N., Turney, C. S. M., Alroy, J., Cooper, A., Beeton, N., Bird, M. I. & Fordham, D. A. 2016. Climate change not to blame for late Quaternary megafauna extinctions in Australia. Nature communications, 7, 1-7.

Sandom, C., Faurby, S., Sandel, B. & Svenning, J.-C. 2014. Global late Quaternary megafauna extinctions linked to humans, not climate change. Proceedings of the Royal Society B: Biological Sciences, 281, 20133254.

Santos, G., Moore, R., Southon, J., Griffin, S., Hinger, E. & Zhang, D. 2007. AMS 14C sample preparation at the KCCAMS/UCI Facility: status report and performance of small samples. Radiocarbon, 49, 255-269.
Skoglund, P., Posth, C., Sirak, K., Spriggs, M., Valentin, F., Bedford, S., Clark, G. R., Reepmeyer, C., Petchey, F. & Fernandes, D. 2016. Genomic insights into the peopling of the Southwest Pacific. Nature, 538, 510-513.
Spessa, A., Mcbeth, B. & Prentice, C. 2005. Relationships among fire frequency, rainfall and vegetation patterns in the wet–dry tropics of northern Australia: an analysis based on NOAA-AVHRR data. Global Ecology and Biogeography, 14, 439-454.
Staal, A., Fetzer, I., Wang-Erlandsson, L., Bosmans, J. H. C., Dekker, S. C., Van Nes, E. H., Rockström, J. & Tuinenburg, O. A. 2020. Hysteresis of tropical forests in the 21st century. Nature Communications, 11, 4978.
Stokes, S., Ingram, S., Aitken, M., Sirocko, F., Anderson, R. & Leuschner, D. 2003. Alternative chronologies for Late Quaternary (Last Interglacial–Holocene) deep sea sediments via optical dating of silt-sized quartz. Quaternary Science Reviews, 22, 925-941.
Stuart, A. J. 2015. Late Quaternary megafaunal extinctions on the continents: a short review. Geological Journal, 50, 338-363.
Stuiver, M. & Braziunas, T. F. 1993. Modeling atmospheric 14C influences and 14C ages of marine samples to 10,000 BC. Radiocarbon, 35, 137-189.
Tan, C. 2016. Big Gaps and Short Bridges: A Model for Solving the Discontinuity Problem. Answers Research Journal, 9, 149–162.
Tejan-Kella, M. S., Chittleborough, D. J., Fitzpatrick, R. W., Thompson, C. H., Prescott, J. R. & Hutton, J. T. 1990. Thermoluminescence dating of coastal sand dunes at Cooloola and North Stradbroke Island, Australia. Soil Research, 28, 465-481.
Thevenon, F., Bard, E., Williamson, D. & Beaufort, L. 2004. A biomass burning record from the West Equatorial Pacific over the last 360 ky: methodological, climatic and anthropic implications. Palaeogeography, Palaeoclimatology, Palaeoecology, 213, 83-99.
Tibby, J., Barr, C., Marshall, J. C., Mcgregor, G. B., Moss, P. T., Arnold, L. J., Page, T. J., Questiaux, D., Olley, J. & Kemp, J. 2017. Persistence of wetlands on North Stradbroke Island (south-east Queensland, Australia) during the last glacial cycle: implications for Quaternary science and biogeography. Journal of Quaternary Science, 32, 770-781.
Tibby, J. & Haberle, S. 2007. A late glacial to present diatom record from Lake Euramoo, wet tropics of Queensland, Australia. Palaeogeography, Palaeoclimatology, Palaeoecology, 251, 46-56.
Timmermann, A. & Friedrich, T. 2016. Late Pleistocene climate drivers of early human migration. Nature, 538, 92-95.
Tobler, R., Rohrlach, A., Soubrier, J., Bover, P., Llamas, B., Tuke, J., Bean, N., Abdullah-Highfold, A., Agius, S. & O'donoghue, A. 2017. Aboriginal mitogenomes reveal 50,000 years of regionalism in Australia. Nature, 544, 180-184.
Tsukamoto, S., Duller, G. A. & Wintle, A. G. 2008. Characteristics of thermally transferred optically stimulated luminescence (TT-OSL) in quartz and its potential for dating sediments. Radiation Measurements, 43, 1204-1218.
Turney, C. S., Kershaw, A. P., Moss, P., Bird, M. I., Fifield, L. K., Cresswell, R., Santos, G., Di Tada, M., Hausladen, P. & Zhou, Y. 2001. Redating the onset of burning at Lynch's Crater (North Queensland): implications for human settlement in Australia. Journal of Quaternary Science: Published for the Quaternary Research Association, 16, 767-771.
Turney, C. S. M., Flannery, T. F., Roberts, R. G., Reid, C., Fifield, L. K., Higham, T. F. G., Jacobs, Z., Kemp, N., Colhoun, E. A., Kalin, R. M. & Ogle, N. 2008. Late-surviving megafauna in Tasmania, Australia, implicate human involvement in their extinction. Proceedings of the National Academy of Sciences, 105, 12150-12153.
Turney, C. S. M., Kershaw, A. P., Clemens, S. C., Branch, N., Moss, P. T. & Keith Fifield, L. 2004. Millennial and orbital variations of El Niño/Southern Oscillation and high-latitude climate in the last glacial period. Nature, 428, 306-310.
Turney, C. S. M., Kershaw, A. P., James, S., Branch, N., Cowley, J., Fifield, L. K., Jacobsen, G. & Moss, P. 2006. Geochemical changes recorded in Lynch's Crater, Northeastern Australia, over the past 50 ka. Palaeogeography, Palaeoclimatology, Palaeoecology, 233, 187-203.

Ummenhofer, C. C., Gupta, A. S., Li, Y., Taschetto, A. S. & England, M. H. 2011. Multi-decadal modulation of the El Nino–Indian monsoon relationship by Indian Ocean variability. Environmental Research Letters, 6, 034006.
Van Der Kaars, S., Miller, G. H., Turney, C. S., Cook, E. J., Nürnberg, D., Schönfeld, J., Kershaw, A. P. & Lehman, S. J. 2017. Humans rather than climate the primary cause of Pleistocene megafaunal extinction in Australia. Nature Communications, 8, 1-7.
Walker, J., Lees, B., Olley, J. & Thompson, C. 2018. Dating the Cooloola coastal dunes of south-eastern Queensland, Australia. Marine Geology, 398, 73-85.
Wang, Y.-J., Cheng, H., Edwards, R. L., An, Z., Wu, J., Shen, C.-C. & Dorale, J. A. 2001. A high-resolution absolute-dated late Pleistocene monsoon record from Hulu Cave, China. Science, 294, 2345-2348.
Wang, X., Wintle, A. & Lu, Y. 2006. Thermally transferred luminescence in fine-grained quartz from Chinese loess: basic observations. Radiation Measurements, 41, 649-658.
Ward, W. 2006. Coastal dunes and strandplains in southeast Queensland: sequence and chronology. Australian Journal of Earth Sciences, 53, 363-373.
Waterbolk, H. T. Working with radiocarbon dates. Proceedings of the prehistoric society, 1971. Cambridge University Press, 15-33.
Willerslev, E., Davison, J., Moora, M., Zobel, M., Coissac, E., Edwards, M. E., Lorenzen, E. D., Vestergård, M., Gussarova, G., Haile, J., Craine, J., Gielly, L., Boessenkool, S., Epp, L. S., Pearman, P. B., Cheddadi, R., Murray, D., Bråthen, K. A., Yoccoz, N., Binney, H., Cruaud, C., Wincker, P., Goslar, T., Alsos, I. G., Bellemain, E., Brysting, A. K., Elven, R., Sønstebø, J. H., Murton, J., Sher, A., Rasmussen, M., Rønn, R., Mourier, T., Cooper, A., Austin, J., Möller, P., Froese, D., Zazula, G., Pompanon, F., Rioux, D., Niderkorn, V., Tikhonov, A., Savvinov, G., Roberts, R. G., Macphee, R. D. E., Gilbert, M. T. P., Kjær, K. H., Orlando, L., Brochmann, C. & Taberlet, P. 2014. Fifty thousand years of Arctic vegetation and megafaunal diet. Nature, 506, 47-51.
Wintle, A. & Huntley, D. 1979. Thermoluminescence dating of a deep-sea sediment core. Nature, 279, 710-712.
Wintle, A. & Murray, A. 1997. The relationship between quartz thermoluminescence, photo-transferred thermoluminescence, and optically stimulated luminescence. Radiation Measurements, 27, 611-624.
Wintle, A. G. 1997. Luminescence dating: laboratory procedures and protocols. Radiation measurements, 27, 769-817.
Wintle, A. G. 2008. Fifty years of luminescence dating. Archaeometry, 50, 276-312.
Wintle, A. G. & Huntley, D. J. 1982. Thermoluminescence dating of sediments. Quaternary Science Reviews, 1, 31-53.
Wintle, A. G. & Murray, A. S. 2006. A review of quartz optically stimulated luminescence characteristics and their relevance in single-aliquot regeneration dating protocols. Radiation measurements, 41, 369-391.
Wood, R. 2015. From revolution to convention: the past, present and future of radiocarbon dating. Journal of Archaeological Science, 56, 61-72.
Wroe, S. & Field, J. 2006. A review of the evidence for a human role in the extinction of Australian megafauna and an alternative interpretation. Quaternary Science Reviews, 25, 2692-2703.
Wroe, S., Field, J. H., Archer, M., Grayson, D. K., Price, G. J., Louys, J., Faith, J. T., Webb, G. E., Davidson, I. & Mooney, S. D. 2013. Climate change frames debate over the extinction of megafauna in Sahul (Pleistocene Australia-New Guinea). Proceedings of the National Academy of Sciences, 110, 8777-8781.
Zaidner, Y., Centi, L., Prévost, M., Mercier, N., Falguères, C., Guérin, G., Valladas, H., Richard, M., Galy, A. & Pécheyran, C. 2021. Middle Pleistocene Homo behavior and culture at 140,000 to 120,000 years ago and interactions with Homo sapiens. Science, 372, 1429-1433.

Chapter 2 Insights into subtropical Australian aridity from Welsby Lagoon, North Stradbroke Island, over the past 80,000 years

---

This chapter has been published in *Quaternary Science Reviews* as:

Lewis, R. J., Tibby, J., Arnold, L. J., Barr, C., Marshall, J., McGregor, G., Gadd, P. & Yokoyama, Y., 2020, Insights into subtropical Australian aridity from Welsby Lagoon, North Stradbroke Island, over the past 80,000 years. Quaternary Science Reviews, 234, 106262.

Statement of Authorship

Title of Paper	Insights into subtropical Australian aridity from Welsby Lagoon, north Stradbroke Island, over the past 80,000 years
Publication Status	[X] Published [ ] Accepted for Publication [ ] Submitted for Publication [ ] Unpublished and Unsubmitted work written in manuscript style
Publication Details	Lewis, R. J., Tibby, J., Arnold, L. J., Barr, C., Marshall, J., Mcgregor, G., Gadd, P. & Yokoyama, Y. 2020. Insights into subtropical Australian aridity from Welsby Lagoon, north Stradbroke Island, over the past 80,000 years. *Quaternary Science Reviews*, 234, 106262.

Principal Author

Name of Principal Author (Candidate)	Richard J. Lewis	
Contribution to the Paper	Conceptualization; Data curation; Formal analysis; Funding acquisition; Investigation; Methodology; Project administration; Resources; Software; Data Validation; Visualization; Writing – original draft; Writing – review & editing	
Overall percentage (%)	80	
Certification:	This paper reports on original research I conducted during the period of my Higher Degree by Research candidature and is not subject to any obligations or contractual agreements with a third party that would constrain its inclusion in this thesis. I am the primary author of this paper.	
Signature		Date 19th July 2021

Co-Author Contributions

By signing the Statement of Authorship, each author certifies that:

i. the candidate's stated contribution to the publication is accurate (as detailed above);
ii. permission is granted for the candidate in include the publication in the thesis; and
iii. the sum of all co-author contributions is equal to 100% less the candidate's stated contribution.

Name of Co-Author	John Tibby	
Contribution to the Paper	Conceptualization; Funding acquisition; Methodology; Project administration; Resources; Supervision; Writing – review & editing	
Signature		Date 19th July 2021

Name of Co-Author	Lee J. Arnold	
Contribution to the Paper	Conceptualization; Formal analysis; Funding acquisition; Methodology; Project administration; Resources; Software; Supervision; Data validation; Visualization; Writing – review & editing	
Signature		Date 22nd July

Name of Co-Author	Cameron Barr	
Contribution to the Paper	Conceptualization; Supervision; Writing – review & editing	
Signature		Date 13th September 2021

Name of Co-Author	Jonathan Marshall	
Contribution to the Paper	Resources; Data validation; Writing – review & editing	
Signature		Date 19th July 2021

Name of Co-Author	Glenn McGregor	
Contribution to the Paper	Resources; Data validation; Writing – review & editing	
Signature		Date 21st July 2021

Name of Co-Author	Patricia Gadd	
Contribution to the Paper	Resources; Data validation; Writing – review & editing	
Signature		Date 19th July 2021

Name of Co-Author	Yusuke Yokoyama	
Contribution to the Paper	Resources; Writing – review & editing	
Signature		Date 3rd November July 2021

Abstract

Terrestrial sedimentary archives that record environmental responses to climate over the last glacial cycle are underrepresented in subtropical Australia. Limited spatial and temporal palaeo-environmental record coverage across large parts of eastern Australia contribute to uncertainty regarding the relationship between long-term climate change and palaeoecological turnover, including the extinction of Australian megafauna during the late Pleistocene. This study presents a new, high-resolution, calibrated geochemical record and numerical dating framework from Welsby Lagoon, a wetland from North Stradbroke Island that records key periods of late Pleistocene environmental change. Single-grain optically stimulated luminescence and radiocarbon dating are integrated into a Bayesian age-depth model for the sedimentary sequence spanning Marine Isotope Stage (MIS) 5 to the present. Scanning micro-X-ray fluorescence (XRF) and bulk sediment XRF assays are used to infer past dust dynamics, with changes in the abundance of silica and potassium interpreted as proxies for aridity across local and regional sources. Variations in dust flux were contemporaneous with hydrological change, concordant with changes in vegetation cover on the island and, relate to deflation events at major dust source regions on the Australian continent. The Welsby Lagoon record supports the notion of a variable MIS4 within which an increased dust flux (71–67 ka) may be indicative of drier climate. Additionally, the record shows a lower dust flux through the Last Glacial Maximum (LGM) than is evident in other Australian aeolian records. However, this low LGM flux is attributed to the wetland's evolution, rather than a reduction in total dust flux.

Introduction

The last glacial cycle was a period of marked cultural and environmental importance in Australia, associated with the arrival of humans (ca. 65 thousand years ago (ka) (Clarkson et al., 2017)), widespread megafaunal extinctions (Saltré et al., 2016) and regional environmental change (Kershaw & Nanson, 1993). Despite extensive research, the causal links between human activities, fire regime modifications, natural climate change and Australian megafaunal extinction remain unclear (Saltré et al., 2016; Wroe et al., 2013). This is primarily due to a combination of low temporal and spatial resolution of mainland Australian palaeoenvironmental archives (Reeves et al., 2013) and limited coverage of numerical age control over pre-Last Glacial Maximum (LGM) timescales (Kemp et al., 2019). Reliable testing of anthropogenic- and climate-driven megafaunal extinction hypotheses requires higher resolution palaeoenvironmental records with improved chronological constraints against which local, regional, and continental palaeoecological changes can be scrutinised (Hesse et al., 2004).

In addition to improving the resolution of the Australian late Quaternary palaeoenvironmental record, there is a need to address important geographic imbalances across the continent, particularly in the subtropics. The limited number of sedimentary sequences that capture parts of the last glacial cycle are primarily situated in the continental interior (e.g., Cohen et al., 2015; Fu et al., 2017; Miller et al., 1999), on the east coast (e.g., McGowan et al., 2005; Moss & Kershaw, 2000) and offshore (e.g., De Deckker et al., 2019; Moss et al., 2005). Direct comparisons between these regions is difficult owing to varying resolution and continuity of sediment accumulation. Meanwhile, detailed intra-regional comparisons are further complicated by the significant geographical ranges that separate individual sites (e.g., >2000 km in the case of Lynch's Crater (Kershaw, 1976) and Caledonia Fen (Kershaw et al., 2007b). The unavoidable dependence on such a temporally and spatially restricted dataset, from

which regional palaeoenvironmental reconstructive syntheses are drawn, often means interpolations occur across expansive geographical ranges – particularly problematic as highlighted by Saltré et al. (2019), who stressed the importance of understanding regional climate history when explaining megafaunal extinctions in south-east Australia.

The generation of reliable age-depth models in combination with high-resolution geochemical profiling is of critical importance for reliable palaeoenvironmental reconstructions over glacial-interglacial timescales. Improvements in the resolution of geochemical data acquisition, via techniques such as micro-XRF scanning, now allow near-continuous evaluation of temporal geochemical variations within sediment profiles (McLauchlan et al., 2019; Ott et al., 2018). Micro-XRF scanning is additionally valuable for identifying dust accumulation in deposits where it may not otherwise be apparent from standard sedimentological evaluation (De Deckker et al., 2008).

Reliable dating of Australian palaeoenvironmental sequences that span multiple past interglacial periods has traditionally proved difficult, and the limited coverage of numerical dating frameworks continues to hinder late Pleistocene climate reconstructions across large parts of Australia. Radiocarbon (^{14}C) dating has been widely used to develop age models for wetland and fluvial records (e.g., Dortch et al., 2016; Mohapatra et al., 2019; Tully et al., 2019), although its usefulness is limited to ca. 50 ka and complications may arise in organic-rich wetlands that are prone to humic acid contamination, reservoir effects, or post-depositional organic mixing processes (Brock et al., 2011; Nilsson et al., 2001; Turetsky et al., 2004). One approach that has been used to overcome the 'radiocarbon barrier' involves chronostratigraphic correlations to a peripheral location where the chronology has been constrained by orbitally tuned isotopic age modelling. Generally, this approach has employed non-quantitative comparisons of proxy data to marine core records (e.g., Gasse & Van Campo, 2001; Imbrie et al., 1984; Kershaw et al., 2007a; Moss & Kershaw, 2000). A drawback of this approach is that correlative interpretations are dependent on the accuracy of both the correlations between sites and the chronology to which records are tuned, subsequently producing tentative age models (Chase, 2010; Gasse & Van Campo, 2001). Orbitally tuned isotopic proxy data from terrestrial records, particularly wetland records, may also partly reflect local climate, and therefore may not directly parallel the Milankovitch cycle signatures typically observed in marine records (Tzedakis et al., 1997). Misidentification of isotopic peaks also remains a possibility in non-continuous terrestrial sedimentary sequences and may introduce errors in the timing of proxy changes or incorrect attribution of purely localised isotopic signals to astronomical cycles (Malinverno et al., 2010).

Optically stimulated luminescence (OSL) dating provides a potentially useful means of filling existing chronological gaps across many Australian palaeoenvironmental contexts, as it is applicable to readily preserved sedimentary materials (containing quartz grains) and permits finite age evaluation over the last several hundred thousand years (kyr) under ideal circumstances (e.g., Arnold & Demuro, 2015; Arnold et al., 2016). The advent of single-grain OSL dating, which involves measuring burial dose values for individual sand-sized grains rather than aliquots containing hundreds or thousands of grains, has opened up the possibility for detailed evaluations of complex sediment depositional histories otherwise unachievable with the application of traditional multiple-grain aliquot OSL age method (e.g., Arnold et al., 2013; Demuro et al., 2013). Single-grain OSL dating of quartz has proved useful for establishing reliable late-Pleistocene chronologies across a range of Australian lacustrine, fluvial and marine palaeoenvironmental sequences (e.g., Cohen et al., 2015; De Deckker et al., 2019;

Fitzsimmons et al., 2014; Fu et al., 2017), including several wetland sites preserved on North Stradbroke Island (Cadd et al., 2018; Kemp et al., 2020; Tibby et al., 2017).

Here we present a geochemical record and numerical dating framework for a 12.7 m palaeoenvironmental sequence from Welsby Lagoon (Cadd et al., 2018), North Stradbroke Island, with the aim of improving the spatial and temporal coverage of existing late Quaternary palaeoenvironmental records across subtropical south-east Queensland. Geochemical analysis is combined with an independent Bayesian age-depth model – incorporating ^{14}C and OSL dating – to ascertain climatic links with wind-transported inorganic sediment over the last 80 kyr. In this study, the term dust is used to refer to any inorganic particle characterised smaller than the upper sand size limit as defined in Bagnold (1973) and transported via suspension or saltation. This study aims to provide a robust, independently dated dust deposition history for Welsby Lagoon. Through our combined dating and geochemical approach, we attempt to improve uncertainties and chronological gaps in the regional record, particularly those that currently hamper reliable interpretation of ecological responses to key climate change events (e.g., as shown to be important for palaeoecological correlations across South Africa (Chase, 2010).

Regional Setting

North Stradbroke Island

North Stradbroke Island (NSI; Minjerribah) is located off the Queensland coast, 30 km south-east of Brisbane (Figure 2.1a). It is the second largest sand island in the world (285 km^2) (Barr et al., 2013), and is situated within the subtropical climate zone (Coll & Whitaker, 1990). The island has an annual average rainfall of 1500 mm and mean annual temperature range between 18.5 °C and 25.6 °C (Bom, 2019). NSI was connected to the mainland during glacial sea level low stands, but was isolated following the Holocene inundation of Moreton Bay (Beaton, 1995).

North-west orientated parabolic dunes dominate the NSI topography (Thompson, 1992), indicating dune building by onshore winds from the south-east. The dunes are dominated by silica quartz sand with lower abundances (<2 %; Thompson, 1992) of ilmenite, rutile, zircon and monazite – trace amounts of other minerals are also found within the sands (Pickett et al., 1985). In-between these dunes, within the older degraded shoreline sands (Ward, 1978) (Figure 2.1b), more than 50 wetlands source water from either the regional water table or one of many perched aquifers (Tibby et al., 2017). Wetland sediments from Native Companion Lagoon and Tortoise Lagoon on NSI have accumulated far-travelled dust over the last 40 kyr (McGowan et al., 2008; Petherick et al., 2011). Despite offshore easterlies being the primary wind direction across NSI (Figure 2.1c), geochemical analysis of dust material in wetlands has traced the source back to the mainland (Petherick et al., 2009); the likely provenance of which derives from a combination of alluvial sources and lakebed deflation (Farebrother et al., 2017). A modern analogue for dust migration across the continent may be drawn from the 2009 drought that triggered major dust storms which propagated towards the east from the continental interior (Figure 2.1a). However, discrepancies exist between the two dust records on NSI (Tortoise Lagoon and Native Companion Lagoon), which may be attributed to surrounding morphology, age model differences and, a likely contribution of fluvial and alluvial components to the sediment flux at Tortoise Lagoon (Petherick et al., 2017) which is fed by a creek during high rainfall events (Lee-Manwar et al., 1980).

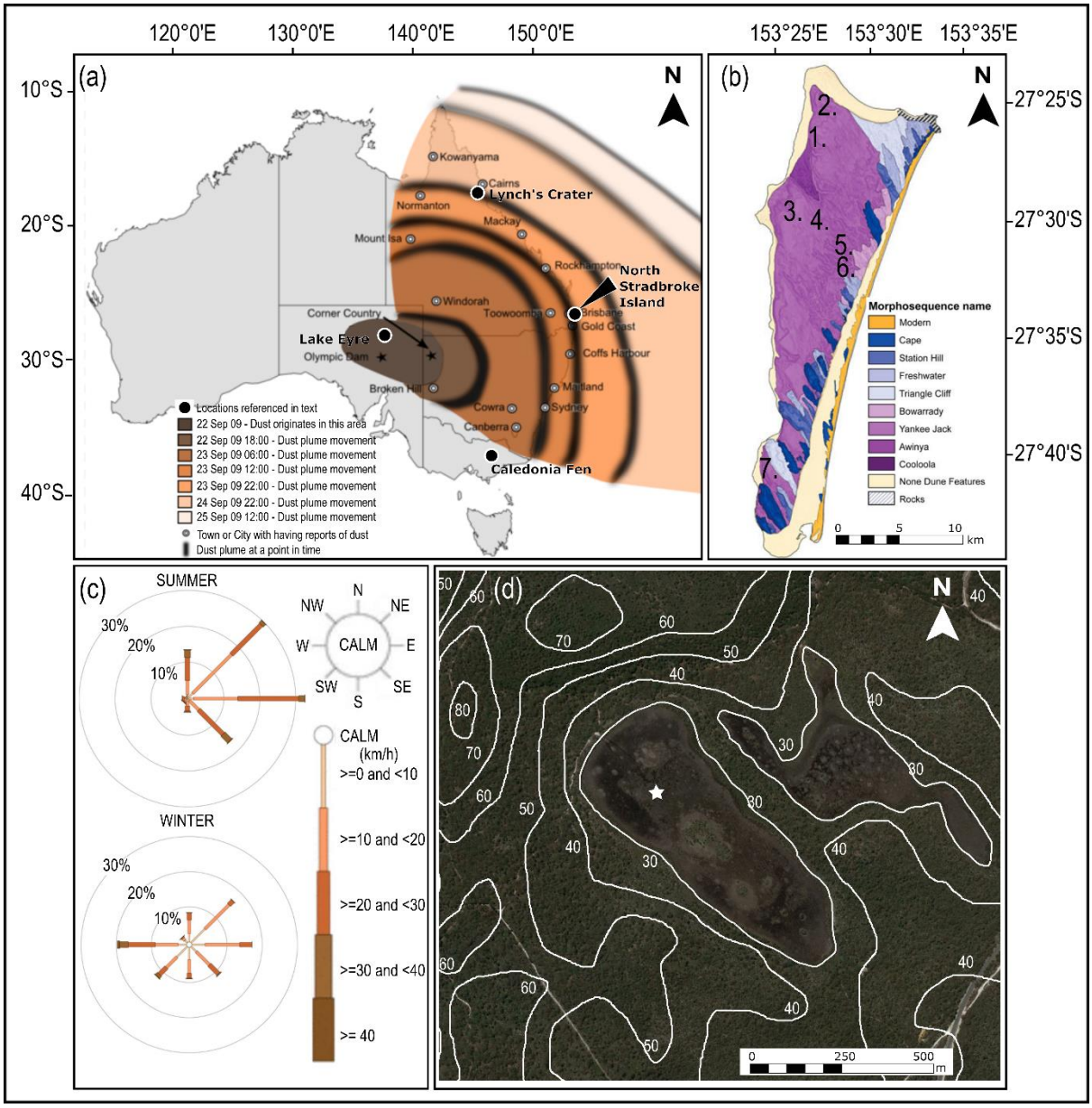

Figure 2.1 The location of Welsby Lagoon in relation to North Stradbroke Island, the Australian continent and other studies referred to in the main text. (a) The extent of the September 2009 Australian dust storm (adapted from Hallegraeff et al., 2014. (b) Distribution of wetlands referenced in the main text: 1. Welsby Lagoon; 2. Fern Gully Lagoon; 3. Brown Lake; 4. Swallow Lagoon; 5. Tortoise Lagoon; 6. Blue Lake; 7 Native Companion Lagoon; overlaying sand dune fields (adapted from Patton et al., 2019 coordinates approximate). (c) Mean afternoon summer and winter wind speed and direction rose diagrams from 1950 to 2000 from Brisbane Aero weather tower (source: Bom, 2019). (d) Satellite image of Welsby Lagoon (source: Google Earth). Contour lines show height, in metres, above modern sea-level, while the star represents the position of the cores obtained for this study.

Welsby Lagoon

Welsby Lagoon is a perched wetland situated in the north-west of NSI, within the Yankee Jack Dune Unit (Patton et al., 2019; Ward, 1978). The lagoon has no inflowing streams (Figure 2.1d) with recharge dependent on effective precipitation. The wetland is acidic, oligotrophic (Cadd et al., 2018) and assumed to have started developing around MIS5 (Tibby et al., 2017), consistent with proximal coral assemblages unearthed during dune excavations (Pickett et al., 1989). Plant macrofossil, pollen and stable isotope data from Welsby Lagoon suggest a transition to a swamp environment around 30 kyr BP (Cadd et al., 2018). However, the sedimentary record to date has had limited age control.

Materials and methods

Coring

Two parallel and 0.5 m offset cores (WEL15-1 and WEL15-2) were recovered from a Kawhaw floating platform at the depocentre of Welsby Lagoon (Cadd et al., 2018), penetrating to depths of 12.78 m and 12.72 m respectively. The coring approach was optimised to eliminate light contamination and ensure the sedimentary sequence would be suitable for OSL dating, by using black PVC tubes in a Bolivia corer. As an additional precautionary measure, each 1 m drive was immediately sealed in opaque black plastic upon surface extraction. All core sections were opened under subdued red LED lighting conditions at The University of Adelaide's Prescott Environmental Luminescence Laboratory.

There are three sedimentological facies present in the Welsby Lagoon core. The majority of the sediment is dark brown to black organic-rich peat, which forms a matrix that supports fine – medium sand material. At the bottom of the core, below 12.66 m, a layer of sand was intersected, which is separated from the overlying homogenous, elastic, fine-grained, dark organic sediments by a visible contact (Cadd et al., 2018). A change in sedimentology is also observed above 5.0 m, with a lower abundance of sand grains being supported by a matrix of poorly decomposed, sub-fibrous, organic sediments.

Geochemical and physical characterisation of sediments

Micro-XRF scanning spectroscopy analysis

The elemental composition of the WEL15-1 (Figure A10) and WEL15-2 (Figure 2.2) sediment sequences was analysed using a micro-XRF core scanner (Itrax) (Croudace et al., 2006) at the Australian Nuclear Science and Technology Organisation. Photon emissions were measured every 1 mm for a suite of 33 elements following stimulation with x-rays produced from a chromium (Cr) tube (50 kV, 30 mA and dwell time of 10 s). Silicon, potassium, titanium and iron were selected as elements of interest because their emission counts were coherent, measured high above background and, accurately measured by comparison to XRF (Figure 2.2). Furthermore the elements were also found to be accurately predicted by Itrax at nearby Fern Fully Lagoon (Kemp et al., 2020).

Bulk sediment analyses (LOI) (XRF)

Moisture content, bulk density and inorganic content of the WEL15-2 core were calculated from 1 cm^3 sediment samples extracted every 10 cm (n = 101). A standard loss on ignition approach was followed, which included weighing the samples before and after heating at 100 °C and 550 °C (Heiri et al., 2001). Fifteen fused disc samples were prepared for wavelength dispersive XRF (WD-XRF) (Appendix A2) to generate quantified elemental concentrations throughout the core sequence and to enable calibration of Itrax elemental intensities from raw counts to concentration. WD-XRF elemental concentrations were compared to the corresponding sample range of the Itrax data (i.e., average counts over ~5 cm) (Figure 2.2). A linear calibration was considered acceptable to explain the relationship between WD-XRF elemental concentrations and corresponding Itrax intensities, with statistically significant correlations observed for the four main elements of interest ($R2 > 0.82$, $p < 0.05$) (Figure 2.2, Figure A6).

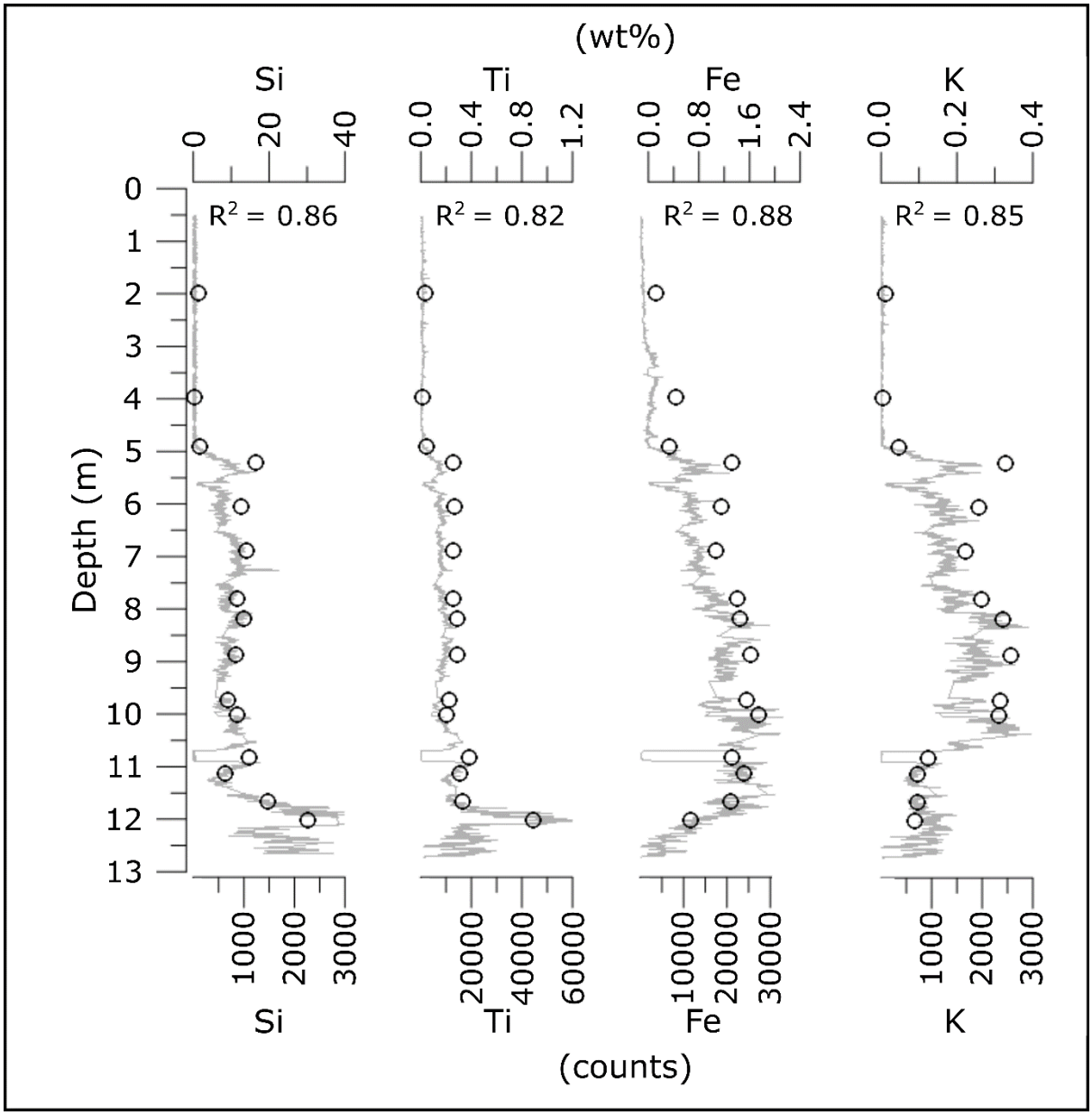

Figure 2.2 Bulk sediment geochemical profile of WEL15-2 showing elemental data measured as counts from Itrax core scanning (grey) and elemental concentration (wt%) calculated from XRF-WD (open circles).

Sequence slotting and cluster analysis

Sequence slotting was used as an objective method to numerically align the two offset cores (WEL15-1 and WEL15-2) (Thompson & Clark, 1990). The program CPLslot v2.4b (Hounslow & Clark, 2016) was used as part of the sequence slotting procedure, and the abundances of silicon, potassium, iron, and titanium were selected as input variables to produce a continuous composite stratigraphic sequence. Only three constraints were included in the slotting algorithm, to minimise overfitting, and these were based on clear sedimentological changes (see Figure A8 caption). The quality of fit was evaluated using the delta value of Gordon (1982) prior to conducting a depth-constrained hierarchical cluster analysis in PAST v3.19 (Hammer et al., 2001). The latter incorporated several chemical and physical properties of the sediment, as shown in Figure A7, to determine the groupings of sedimentological units.

Core chronology

Cadd et al. (2018) recently inferred the history of Welsby Lagoon based on three OSL ages from the site. In this paper, we present nineteen new OSL and twenty new radiocarbon ages and, develop a comprehensive Bayesian age model for the composite sediment sequence that takes into consideration sedimentary unit boundaries related to the wetland evolution from a lake to a swamp.

Radiocarbon (^{14}C) dating

A total of twenty samples were extracted from WEL15-2 for radiocarbon dating at Tokyo University. The samples included plant macrofossils, plant remains and charcoal, which were prepared using standard ABA preparation techniques (Brock et al., 2010) (Table A5). AMS ^{14}C ages were calibrated against the SHCal13 calibration curve (Hogg et al., 2013) in OxCal v4.3.2 (Bronk Ramsey, 2008, 2009) during the development of the final age model.

Optically stimulated luminescence (OSL) dating

Thirty samples were extracted from WEL15-1 and WEL15-2 for single-grain OSL dating, of which twenty-one yielded sufficient quartz grains for dating following laboratory preparation. Samples were extracted from the inner surface of core sections that had been split down their longitudinal axis under safe light conditions (dim red, filtered). Care was taken to exclude grains that might have been disturbed or exposed to light during the coring and splitting process by cleaning the exposed sediment face down to a depth of ~1 cm and avoiding sampling sediment that was in contact with the coring tube surface. Purified quartz grains (Ø180–250 μm) were prepared for burial dose measurements using standard procedures, as described in Arnold & Roberts (2011) (Appendix A1.1). Single-grain OSL measurements were undertaken using equipment and machine parameters outlined in Appendix A, section A1.2. Equivalent dose (D_e) values were determined using the single aliquot regenerative dose (SAR) procedure (Murray & Wintle, 2000), as detailed in Appendix A1.3 and Table A1. D_e values were only considered in the final age calculations if they passed a series of standard and well-documented acceptance criteria (Table A2).

For each OSL dating sample, 30 g (dry weight) of bulk sediment material was retained for dosimetric analysis, which was undertaken using a combination of inductively coupled plasma mass spectrometry (ICP-MS) and inductively coupled plasma optical emission spectrometry (ICP-OES) (Table A4). Beta and gamma radiation dose rates for individual samples were then calculated from the elemental concentrations using conversion factors published by Guérin et al. (2011). Corrections for beta-dose attenuation and long-term moisture content were incorporated into total environmental dose rate calculations (Aitken, 1998; Brennan, 2003; Mejdahl, 1979) (Appendix A1.4), which additionally included evaluations of internal dose rate and cosmic ray dose rate contributions (Prescott & Hutton, 1994). Long-term average water content for each OSL sample was considered equivalent to the 'as measured' values (Figure A7) and determined separately for the beta, gamma, and cosmic dose rates (Appendix A1.4).

Age-depth modelling

Bayesian age-depth models were produced for the composite Welsby Lagoon sequence using OxCal (Bronk Ramsey, 2009, 2017). Initially, all age constraints were included as likelihoods in the modelling process, allowing for randomly variable deposition rates through the sequence by utilising a Poisson depositional model (*P_Sequence*) (Bronk Ramsey, 2008, 2009; Bronk Ramsey & Lee,

2013). However, the number of likelihood estimates included in the model was subsequently revised down to 28 following suitability evaluation of the ^{14}C dating results (see 4.2.2). The base rigidity perimeter (k_0) of the *P_Sequence* model was set to a single event per 1 cm of sedimentation and was allowed to vary between 0.01 and 100 events per centimetre to accommodate any major fluctuations in the rate of sediment deposition. The model was run using the SHCal13 (Hogg et al., 2013) calibration curve and included a general outlier function (assigned with a prior outlier probability of 5%) (Bronk Ramsey, 2009; Bronk Ramsey & Lee, 2013; Christen, 1994). Samples with outlier probabilities >5 % were not excluded from the model but were proportionally down-weighted during the Monte Carlo iterations (Bronk Ramsey, 2009).

Three separate depositional units have been included in the OxCal modelling framework (Unit 1 – basal sands, Unit 2 – lacustrine muds, and Unit 3 – organic-rich swamp deposits) on the basis of the sedimentological changes identified using cluster analysis (Figure A7), and the lithological interpretations presented in Cadd et al. (2018). For modelling purposes, it has been assumed that continuous sediment deposition took place within this wetland system through time, without any major hiatuses or erosional events once the wetland basin became established. Boundaries have been inserted between the three identified sedimentary units in the *P_Sequence* model at depths of 12.5 and 5.0 m, to delineate sedimentological changes between the basal dune, lake, and swamp phases of the sequence. Posterior dated events have been interpolated at 1 cm intervals throughout the sequence.

As part of our broader assessment of modelling priors, several additional depositional scenarios and boundary schemes were modelled to examine alternative sedimentary dynamics between subsequent wetland phases (Figure A5). These modelling sensitivity tests included a scenario whereby a single, uninterrupted lacustrine sedimentation phase occurred following establishment of the wetland basin (i.e., no boundary was included at a depth of 500 cm; Figure A5a) and a scenario that did not presume continuous wetland deposition, and was able to accommodate potential hiatuses or erosional discontinuities or both, between the various sedimentary units (i.e., the three depositional phases are represented by separate *P_Sequences*, each with delineating start and end boundaries, nested within a master Sequence (Figure A5b)). In all cases, however, the modelling results are relatively insensitive to our choice of stratigraphic priors (compare Figure 2.4 and Figure A5); hence, we have opted for the modelling representation that is most consistent with the current sedimentological interpretations for Welsby Lagoon (Cadd et al., 2018).

Results

Lithology, physical and chemical properties

The Welsby Lagoon sedimentary sequence is comprised of highly organic (>70 % average) black-brown lake mud and peat with no clear laminations, except for the base of WEL15-2 where lake mud is juxtaposed with the underlying white sand unit (Figure A7). Below 12 m, the basal sands and overlying sandy mud has the lowest organic matter (OM) content, <15 %. Between 12 and 5 m, the OM content increases to an average of 60 %, and at depths <5 m the sediment contains the highest OM, with an average > 95 %. Sediment moisture content (% wet weight) shows non-monotonic variations over the 0 – 5 m range of the sediment sequence, and decreases slightly towards the base between the 12 – 5 m range, to a mean value of approximately 85 % (Figure A7). Below 12 m, sediment water content drops significantly and ranges between 20 and 55%; a trend that is likely

explained by the high porosity of the basal sand deposits which allowed water to drain following field extraction (see discussions in Appendix A1.4).

The four main elements of interest for geochemical analysis (silicon, potassium, iron, titanium) were selected to provide insights into the transportation of inorganic material into the wetland and because their concentrations, as quantitatively determined using WD-XRF, showed strong correlation with the Itrax core scanning data (Figure 2.2). In WEL15-2, several elements declined to almost background before returning to higher values between 10.5 m and 9.5 m. The WD-XRF data within this section of the core did not co-vary with the Itrax data, nor was this feature observed in the WEL15-1 core scans. Therefore, the WEL15-2 features at these depths were considered artefacts of the scanning process and removed from subsequent analysis (open diamonds in Figure A6). Sequence slotting of WEL15-1 to WEL15-2 returned an acceptable quality match statistic of Delta = 0.652 (Figure A8); a value which is within the range expected for chemo-physical variations in lake sediments (Thompson & Clark, 1990).

Principal component analysis

Principal component analysis (PCA) was used to describe the geochemical variance, originating from biogenic (e.g., diatoms) and aeolian deposition, for the scanning XRF data obtained from the Welsby Lagoon cores. A subset of elemental concentrations and elemental ratios were utilised in the PCA, which were chosen to represent local and regional siliciclastic sediment (Al, Fe, K, Rb, Si, Ti), and biogenic sediment (Si/Ti, Ca/Ti, Sr/Ti), following Hendy et al. (2015). The PCA data is presented in Table A7, with the variables plotted against the first two principal components in Figure A9. The first principal component (PC1) explains the 76.2 % of variability in the data. The elements with the highest loadings associated with PC1 are those that represent the siliciclastic sediment, namely Al, Si, K, Ti, Fe and Rb. The second principal component (PC2) explains 23.0 % of the variance and has high loadings for Si and Ti, both of which are abundant in dunes proximal to the wetland.

The first two principal components for the Welsby Lagoon sediment explain >99 % of the variance within the scanning XRF data. The loadings for the selected elements and element ratios that represent biogenic sediment are low in comparison to the terrigenous component across both PC1 and PC2. This is likely caused by the low numbers of preserved diatoms and other biogenic silica in the wetland sediment due to dissolution (Barr and Tibby unpublished data), as observed in other wetlands on Stradbroke Island, such as Eighteen Mile Swamp (Mettam et al., 2011). Therefore, PC1 has been interpreted as an indicator of the abundance of terrigenous material.

Chronology

OSL dating

The single-grain OSL D_e analysis and dating results are presented in Table 2.1, with representative D_e distributions presented as radial plots in Figure 2.3. Following application of SAR quality assurance criteria, grain acceptance rates ranged between 12 % and 28 % per sample (Table A2). The majority of samples (19 out of 21) exhibited intermediate D_e scatter with overdispersion values between 26 % and 40 %. Although this range of overdispersion is above the average value reported for ideal, well-bleached, undisturbed samples in the literature (e.g., global average of 20 ± 1% reported by Arnold & Roberts (2009)), the D_e distributions are generally well-represented by their weighted mean dose estimate (grey shaded area on radial plot) and they do not generally exhibit asymmetric tails of high

values. These D_e distribution characteristics suggest the OSL signals were adequately reset prior to deposition, with addition scatter related to beta dose heterogeneity in the organic-rich matrices or minor near-surface bioturbation (e.g., root penetration) immediately following deposition. The final D_e values for these samples have therefore been calculated using the central age model (CAM) reported in Galbraith et al., 1999.

The remaining two samples, WEL15-2(3) and WEL15-2(9) exhibit statistically significant asymmetric D_e distributions and overdispersion values (Figure 2.3a & 2.3d) in excess of the site-specific baseline estimate of underlying dose dispersion, calculated as being 34 ± 1 % at 2σ from the mean overdispersion of the nineteen well-bleached samples fitted with CAM. These D_e distributions are more consistent with those commonly reported for heterogeneously bleached samples (e.g., Arnold & Roberts, 2011; Arnold et al., 2008; Bailey & Arnold, 2006). We have therefore used the minimum age model (MAM) of Galbraith et al. (1999) for calculating the final D_e values. The decision of whether to use the three- or four-parameter version of the MAM (MAM-3 or MAM-4) for these two samples was made according to the maximum log likelihood (L_{max}) criterion of Arnold et al. (2009). WEL15-2(3) additionally contains near-zero and negative D_e values (overlapping with 0 Gy at 2σ) so it was necessary to calculate the burial dose estimate using the unlogged version of the minimum age model (MAM-4_{UL}) (Arnold et al., 2009). The final OSL ages have been calculated using the individual dose rate measured for each sample and are presented in Table 2.1.

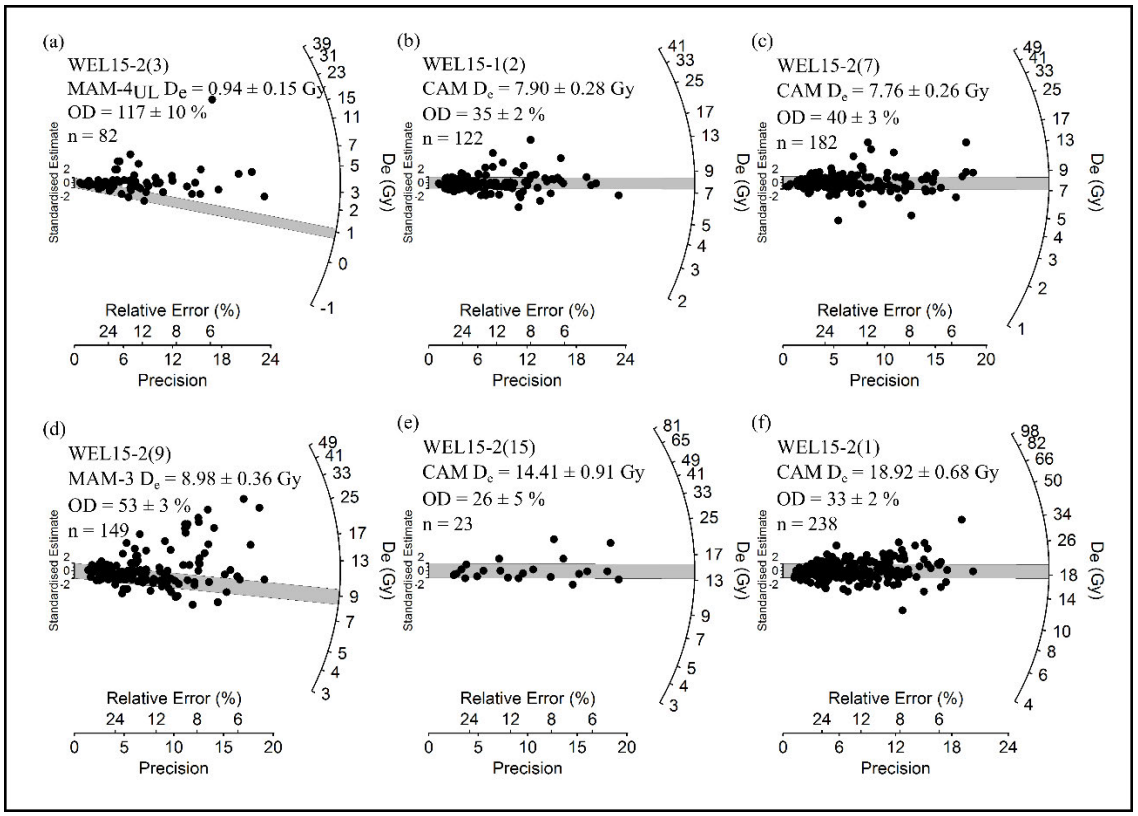

Figure 2.3 A representative subset of radial plots showing the single-grain D_e distributions obtained for OSL samples from core WEL15-1 and WEL15-2. The plots have been ordered from highest to lowest core position (A – F) relative to WEL15-2. The grey shaded band on each plot is centred on the D_e value (in Gy) used for the final age calculation. For all samples, except WEL15-2(3) and WEL15-2(9), the D_e value was calculated using the central age model (CAM) of Galbraith et al. (1999). For samples WEL15-2(3) and WEL15-2(9), the final D_e value was calculated using the unlogged, four-parameter minimum age model (MAM-4_{UL}) of Arnold and Roberts (2009) and the three-parameter minimum age model (MAM-3) (Galbraith et al., 1999), respectively. The D_e distributions of the remaining OSL samples from Welsby Lagoon can be found in the Appendix A (Figure A4).

Table 2.1 Dose rate data, equivalent doses (D_e), overdispersion values, and OSL ages for lacustrine samples from Welsby Lagoon, North Stradbroke Island. The final OSL age of each sample has been calculated by dividing the D_e value by the total dose rate.

			Environmental dose rate data [b, c, d, e, f]				*Equivalent dose (D_e) data*				
Lab code	***Depth (cm)***	***Grain size (μm)***	***Water content ($\%_{Dry}$)*** [a]			***Total dose rate (Gy/kyr)***	***n/N*** [h]	***OD (%)*** [i]	***Age model*** [g]	***D_e (Gy)*** [f, k]	***Final age (kyr)*** [f, j]
WEL15-2(3) [k]	*380*	180 – 250	505	630	923	0.05 ± 0.01	82 / 500	117 ± 10	MAM-4_{UL}	0.94 ± 0.15	18.6 ± 4.1
WEL15-2(6) [k]	*510*	180 – 250	575	620	945	0.12 ± 0.01	113 / 500	34 ± 3	CAM	5.46 ± 0.22	43.7 ± 5.4
WEL15-1(2)	543	180 – 250	484	573	918	0.21 ± 0.02	122 / 700	35 ± 2	CAM	7.90 ± 0.28	37.6 ± 4.3
WEL15-2(7)	580	180 – 250	586	611	902	0.17 ± 0.02	182 / 1200	40 ± 3	CAM	7.76 ± 0.26	44.7 ± 5.4
WEL15-2(8)	610	180 – 250	500	555	881	0.19 ± 0.02	154 / 700	29 ± 2	CAM	8.76 ± 0.25	46.4 ± 5.2
WEL15-2(9)	680	180 – 250	468	474	841	0.19 ± 0.02	149 / 800	53 ± 3	MAM-3	8.98 ± 0.36	46.2 ± 5.1
WEL15-2(10)	710	180 – 250	505	489	824	0.20 ± 0.02	227 / 900	35 ± 2	CAM	9.94 ± 0.27	50.5 ± 5.5
WEL15-2(11)	775	180 – 250	489	476	800	0.22 ± 0.02	239 / 900	36 ± 2	CAM	13.10 ± 0.35	59.9 ± 6.5
WEL15-2(12)	815	180 – 250	450	442	785	0.25 ± 0.03	197 / 800	33 ± 2	CAM	13.78 ± 0.37	55.8 ± 5.9
WEL15-2(13)	880	180 – 250	463	465	761	0.22 ± 0.02	27 / 200	34 ± 6	CAM	13.74 ± 1.01	62.4 ± 7.9
WEL15-1(5)	892	180 – 250	442	457	774	0.24 ± 0.02	141 / 600	39 ± 3	CAM	13.34 ± 0.48	55.7 ± 6.0
WEL15-2(15)	980	180 – 250	454	473	731	0.18 ± 0.02	23 / 200	26 ± 5	CAM	14.41 ± 0.91	79.1 ± 9.6
WEL15-1(21)	1047	180 – 250	435	469	741	0.21 ± 0.02	56 / 400	35 ± 4	CAM	14.65 ± 0.76	70.7 ± 8.0
WEL15-1(22)	1119	180 – 250	403	412	715	0.27 ± 0.03	73 / 400	31 ± 3	CAM	19.96 ± 0.82	73.8 ± 7.7
WEL15-2(19)	1180	180 – 250	274	276	679	0.36 ± 0.03	87 / 500	33 ± 3	CAM	29.01 ± 1.16	79.6 ± 6.8
WEL15-2(20)	1210	212 – 250	231	258	664	0.30 ± 0.02	93 / 600	31 ± 3	CAM	24.08 ± 0.86	79.5 ± 6.5
WEL15-1(23)	1213	180 – 250	450	432	690	0.24 ± 0.02	55 / 400	38 ± 4	CAM	18.63 ± 1.05	78.5 ± 8.6
WEL15-2(2)	1259	212 – 250	209	191	655	0.22 ± 0.02	241 / 900	33 ± 2	CAM	22.56 ± 0.60	102.5 ± 7.9
WEL15-1(6)	1261	212 – 250	195	244	655	0.18 ± 0.01	172 / 700	31 ± 2	CAM	22.52 ± 0.54	125.1 ± 9.5
WEL15-1(7)	1263	212 – 250	89	78	643	0.19 ± 0.01	247 / 800	31 ± 2	CAM	24.32 ± 0.74	130.0 ± 8.2
WEL15-2(1)	1270	212 – 250	78	73	643	0.13 ± 0.01	238 / 900	33 ± 2	CAM	18.92 ± 0.68	142.9 ± 11.3

[a] Long-term water contents used for beta/gamma/cosmic-ray dose rate attenuation, respectively, expressed as % of dry mass of mineral fraction, with an assigned relative uncertainty of ±5%. The final beta dose rates have been adjusted for moisture attenuation using the measured water contents determined from the midpoint of each OSL sample depth. The final gamma dose rates have been adjusted using the average water content measured from each OSL sample midpoint, as well as from 1 cm^3 bulk sediment samples collected for the overlying and underlying 10 cm depth. The final cosmic-ray dose rates have been adjusted using the average water content measured from 1 cm^3 bulk sediment samples collected at 10 cm intervals throughout the overlying core sequence.

[b] Beta, gamma and internal dose rates have been calculated on dried and powdered sediment samples using ICP-MS and ICP-OES.

[c] Radionuclide concentrations have been converted to alpha, beta and gamma dose rates using the published conversion factors of Guérin et al. (2011), allowing for beta dose attenuation (Mejdahl, 1979; Brennan, 2003) and long-term water content (Aitken, 1985).

[d] An internal dose rate of 0.02 ± 0.01 Gy / ka has been included in the final dose rate calculations, based on ICP-MS U and Th measurements made on etched quartz grains from sample WEL15-2(1) and an alpha efficiency factor (a-value) of 0.04 ± 0.01 (Rees-Jones, 1995; Rees-Jones and Tite, 1997).

[e] Cosmic-ray dose rates were calculated using the approach of Prescott and Hutton (1994) and assigned a relative uncertainty of ±10%.

[f] Mean ± total uncertainty (68% confidence interval), calculated as the quadratic sum of the random and systematic uncertainties.

[g] MAM-4_{UL} = unlogged four-parameter minimum age model (Arnold et al., 2009); CAM = central age model (Galbraith et al., 1999); MAM-3 = Minimum age model (Galbraith et al., 1999).

[h] Number of D_e measurements that passed the SAR quality assurance criteria and were used for D_e determination/total number of grains analysed.

[i] OD = overdispersion; the relative spread in the D_e dataset beyond that associated with the measurement uncertainties for individual D_e values, calculated using the CAM (19 of 21 samples) or CAM_{UL} (WL15-2(3)).

[j] Total uncertainty includes a systematic component of ±2% associated with laboratory beta-source calibration.

[k] WEL15-2(3) and WEL15-2(6) were previously presented and discussed in Cadd et al. (2018).

^{14}C dating

The AMS ^{14}C ages obtained in this study are presented in Table A5 and show a moderate amount of scatter. There is broad stratigraphic agreement between the ^{14}C results derived from the measurement of identifiable, terrestrial plant macrofossil material. However, the ^{14}C ages derived from the analysis of unidentifiable plant remains, charcoal and plant residuals exhibit a large amount of scatter and consistently produce stratigraphic inversions. These trends are in agreement with those recently reported for different ^{14}C sample materials at Fern Gully Lagoon, a nearby wetland on NSI (Kemp et al., 2020), and suggest that ^{14}C age inaccuracies may be a common occurrence for certain sample materials in these complex, organic-rich depositional environments; especially when using standard ABA pre-treatments procedures that may not completely remove organic contaminants and residues (Bird et al., 2014; Brock et al., 2011). To further examine the biasing effects of different ^{14}C sample materials in this setting, we analysed a series of replicate samples from a depth of 480 cm, including a charcoal sample (YAUT-023334), plant residuals (YAUT-022712) and a terrestrial macro (wood) sample (YAUT-023333) (Table A5). Notably, the charcoal sample (YAUT-023334) yielded a significantly younger age compared to the other two replicate samples (Table A5). In addition, the plant residual sample (YAUT-022712) was found to be younger than three overlying samples derived from macrofossils (YAUT-023523, YAUT-022711, YAUT-023327) at depths of 430 cm and 460 cm (Table A5). Based on these results, as well as the similar trends reported at nearby Fern Gully Lagoon, and recommendations published elsewhere for highly organic sediments (Martin et al., 2019), we have opted to include only the plant macrofossil ^{14}C ages in the final age model (Table 2.2).

Table 2.2 Radiocarbon (^{14}C) ages included in the final age model. Measured ages have been calibrated using SHCal13 within the OxCal program (Bronk Ramsey, 2009; Bronk Ramsey and Lee, 2013; Hogg et al., 2013). All samples were treated using acid-base-acid (ABA) pre-treatments. The calibrated age range shown is the 95 % probability range (combining two or more potential calibration ranges, where they exist). For further sample information see Table A5.

Lab Code	Depth (cm)	Material	Conventional ^{14}C age (yrs BP)	Calibrated age range (cal yrs BP)
YAUT-023321	80	Leaf	1260 ± 64	1324-1196
YAUT-022709	360	Bark	9602 ± 54	9656-9548
YAUT-023326	360	Seeds	9553 ± 64	9617-9489
YAUT-023523	430	Seeds	16887 ± 78	16965-16809
YAUT-022711	440	Bark	17646 ± 91	17737-17555
YAUT-023327	460	Bark	17538 ± 55	17593-17483
YAUT-023333	480	Wood	17453 ± 67	17520-17386

Bayesian age-depth modelling results

The Bayesian-age depth model developed for the Welsby Lagoon sedimentary sequence using the twenty one single-grain OSL dating and seven ^{14}C plant macrofossil likelihoods is presented in Figure 2.4. This model has an agreement index (A_{model}) of 94.9 % and an overall agreement index ($A_{overall}$) of 104.4 %, showing the model is statistically supported by the input parameters. The outlier analysis identified two ages, YAUT-022709/YAUT-023326 and WL15-2(6) as having relatively high posterior outlier probabilities (21 % and 14 %), with all other likelihood estimates yielding posterior outlier values of 0 – 5%. The posterior (modelled) age for the basal sand unit in the sequence, presented at the 68 % confidence interval, is 126 ± 2 ka (mean ± 1σ uncertainty; assuming normal distribution). Meanwhile, the overlying organic rich muds started accumulating from 83 ± 5 ka and the transition from lake to swamp which occurred at 5 m and has a mean modelled age of 28 ± 6 ka. Utilising the mean modelled age from the OxCal output, a rate of sediment accumulation per annum was calculated and utilised in the calculation of elemental and inorganic material flux per given year (Figure 2.5).

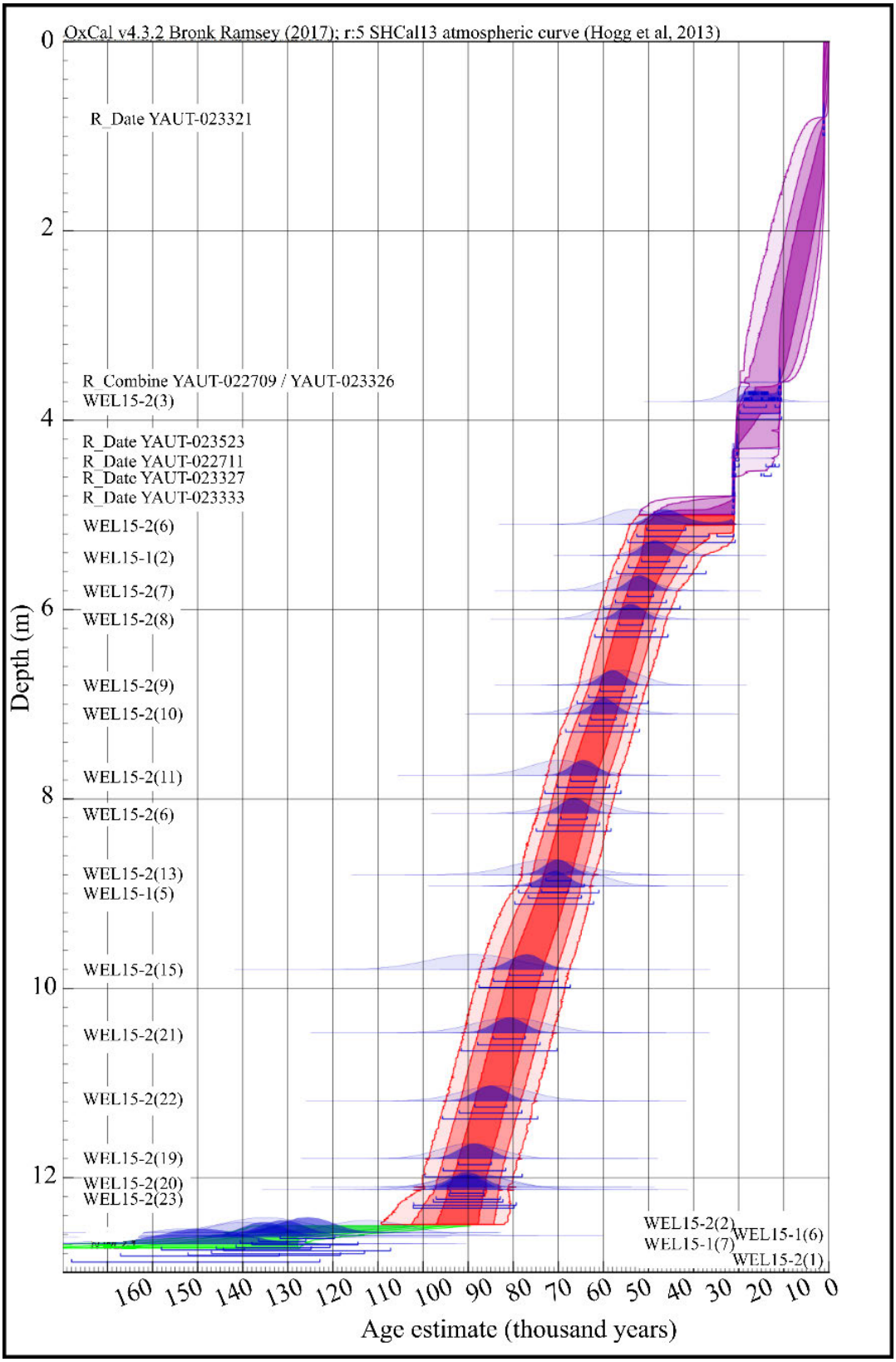

Figure 2.4 Bayesian age-depth model constructed using the single-grain OSL and macrofossil ^{14}C ages obtained for Welsby Lagoon. Ages were modelled in OxCal version 4.3.2. The original probability distributions for the OSL and ^{14}C age estimates (the likelihoods) are shown in light blue and the posterior modelling distributions are represented by dark blue shading. The age-depth model envelopes show the 99 %, 95 % and 68 % highest probability density ranges for each of the three wetland phases/sedimentary units (green, red, and purple), as identified by the cluster analysis and reported in Cadd et al. (2018).

Sedimentological Units

The Welsby Lagoon sediment sequence can be sub-divided into three sedimentary units according to cluster analysis performed on the suite of chemo-physical properties shown in Figure A7. The results of the Bayesian age model show that these sedimentary units broadly align with transitions between Marine Isotope Stages (MIS) spanning late MIS5 to present (Figure 2.5).

Unit 1

The lowermost unit, Unit 1, exists between depths 12.72 – 12.50 m and includes the basal sand dune unit and intermixed sandy organic muds (Figure 2.5). The sedimentology is complex in this part of the core and the presence of sand lenses suggests intermixing of sands and muds occurred during the initial formation of the wetland (Cadd et al., 2018; Tibby et al., 2017). Geochemically, Unit 1 hosts higher concentrations of silicon with generally lower potassium, similar to the composition of the surrounding dunes. While it was possible to model an age for this lower most unit (Figure 2.4), which provided a posterior mean age of 126 ± 2 ka (±1σ uncertainty; assuming normal distribution), it is difficult to interpret the palaeoenvironmental history for this unit using geochemistry alone as hydrological variation during deposition and sediment mixing may have diluted the aeolian signal. However, according to the age model, Unit 1 sediment accumulation can be constrained to MIS5 or the MIS6/5 transition.

Unit 2

Unit 2, (12.5 – 5.0 m; 83 ± 5 – 28 ± 6 ka) directly overlies the basal sands and is classified as organic rich muds (Figure 2.5). It has lower silicon values in contrast to Unit 1 and increased range of silicon and potassium concentrations. WEL15-1 and WEL15-2 both contain what is assumed to be a highly organic band, of approximately 20 cm thick sediment at 11.5 m and 10.8 m respectively, reflected in the element intensity data by a drop in the number of counts for elements measured with Itrax. Moreover, the ratio of incoherent to coherent scatter, an indicator for organic content (Croudace & Rothwell, 2015), showed higher values. Therefore, the WD-XRF sample extracted from 10.8 m did not provide a strong correlation to the Itrax data is a result of signal dilution from increased organic abundance (Löwemark et al., 2011). The upper section of Unit 2 (9.0 – 5.0 m depth) is distinguished by an early spike in the concentration of potassium, which then follows a similar decreasing trend as observed in silicon. At the top of the section, the concentrations of silicon and potassium reduce to near detection limit, which is attributed to the transition from lake to a swamp. The mean model age for the top of this unit is 28 ± 6 ka, therefore sediment accumulation had persisted from MIS5 to at least MIS3.

Unit 3

Silicon and potassium concentrations in Unit 3, which starts at 5.0 m, are lower in contrast to underlying units. The lowest silicon and potassium concentration is between 5.0 m and 3.6 m with increased values returning above 3.6 m. The basal age of the unit is constrained by ^{14}C sample YAUT-023333 (^{14}C age of 17.4 – 17.5 cal kyr BP), while YAUT-023321 (^{14}C age of 1.2 – 1.3 cal kyr BP) defines the top. The Bayesian age model places the accumulation of this unit to MIS2, with continued sedimentation up to the present.

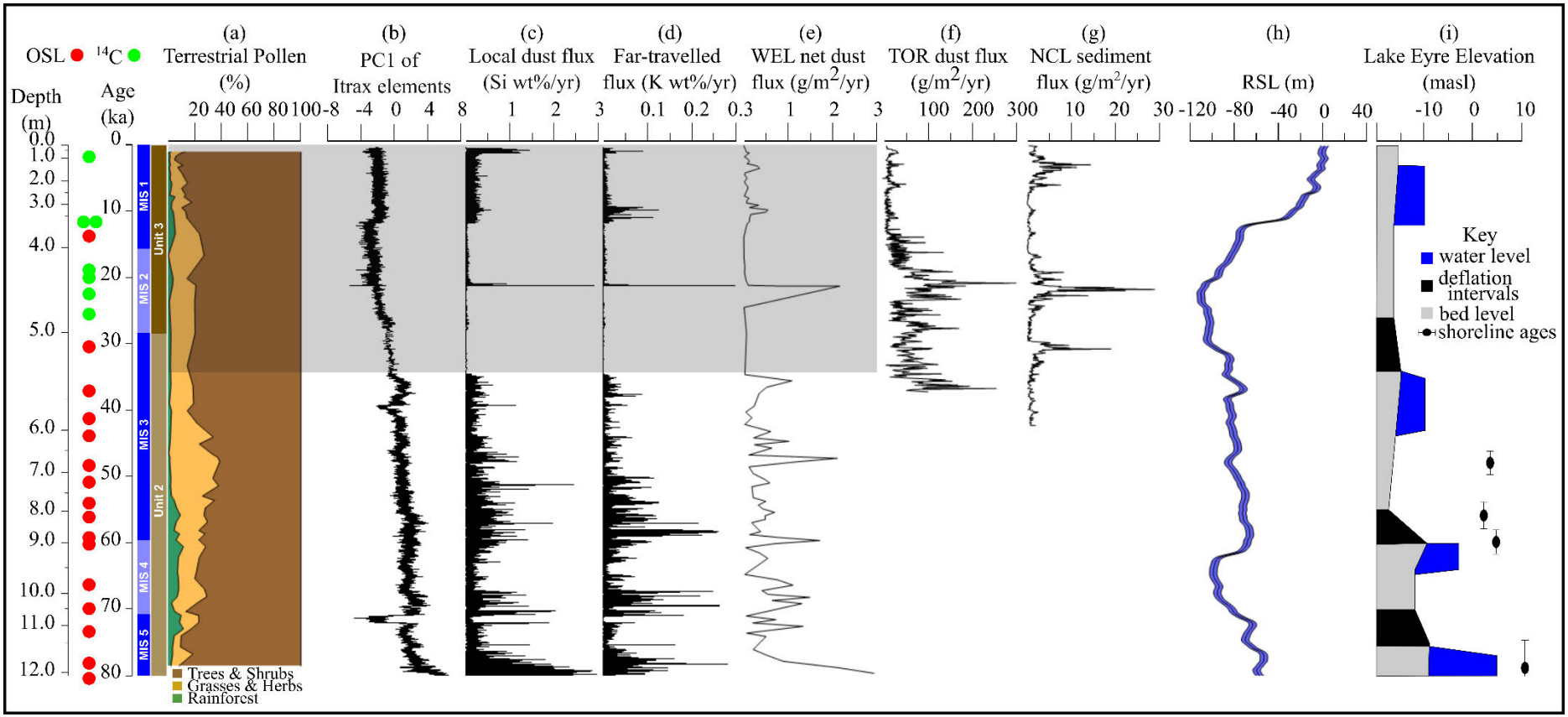

Figure 2.5 Welsby Lagoon sedimentological record aligned by time to other regionally important records of dust and hydrological change. Sedimentological units identified using hierarchical cluster analysis are shown alongside the Marine Isotope Stages within which they were deposited. (a) the terrestrial pollen record for the Welsby Lagoon sequence is as presented in Cadd et al. (2018) with the transition to swamp designated by a transparent grey overlay; (b) the first principal component from the Itrax scanning XRF count data; (c, d) local and far-travelled dust flux in Welsby Lagoon sediment calculated from calibrated scanning XRF data respectively; (e) empirically measured dust flux for Welsby Lagoon; (f, g) North Stradbroke Island dust records from Tortoise Lagoon (TOR) (Petherick et al., 2017) and Native Companion Lagoon (NCL) (Mcgowan et al., 2008); (h) radiometrically dated relative sea-level (RSL) from the Red Sea (Grant et al., 2014); (i) Lake Eyre water level and deflationary events as reported in Farebrother et al. (2017).

Discussion

Interpretive framework

As Welsby Lagoon is a closed wetland (Cadd et al., 2018), with highly organic sediment and no sediment influx from flowing streams, changes in the inorganic geochemistry are primarily driven by the accumulation of dust. As a first principle, we assume increased dust deposition is indicative of hydrological change in the source area(s). PC1 is used to infer the accumulation of dust into Welsby Lagoon while silicon and potassium are used to distinguish between sediment sourced locally and distally, respectively. This interpretation is based on the composition of the surrounding dunes, which are dominated by silica minerals (McGowan et al., 2008) but deficient in elements associated with the weathering of feldspars, micas and clays (i.e. potassium and iron) (Pickett et al., 1985). The three sedimentological units established for Welsby Lagoon are attributed to changes in dust accumulation through time. However, it is important to consider sediment accumulation in the context of the three broad phases of wetland evolution identified in Cadd et al. (2018) which were: (1) wetland formation; (2) persistent lake and; (3) a shallow swamp.

Defining a direct link between increased dust flux at Welsby Lagoon and aridification of the Australian interior is difficult given the few available records from which to draw information. For example, many dust sources experienced episodic wetting, driven by transient periods of effective precipitation (Cohen et al., 2015; Fu et al., 2017). These oscillations of wetting and drying may have increased the supply of fine-grain dust into sources. However, factors that would also need to be considered that may limit the transportation of this dust to NSI may include increased vegetation cover proximal to the source (Hesse et al., 2004; Magee et al., 2004), or a deficit of sediment being produced due to fluvial mobilisation of dust from the floodplain (Farebrother et al., 2017). In addition, periods of extensive prolonged aridification may have impeded entrainment of dust, with the surface of the catchments desiccating and becoming more aerodynamic (Marx et al., 2018).

Perched aquifer formation and lake establishment (MIS5)

The basal sand bands were dated to MIS5 and overlap with the timing of the Amity dune emplacement at 120 ± 11 ka (Tejan-Kella et al., 1990). However, the intermixing of organic muds and sands, in addition to sand lenses, within the Welsby Lagoon sediment makes interpretation of this section of core difficult, particularly as minor unconformities related to variable lake conditions may be present. The overlying organic muds, however, were constrained to ca. 80 ka and reflect sediment accumulated after Welsby Lagoon had established as a lake (Cadd et al., 2018). The higher flux of silicon in relation to potassium indicates increased inorganic sediment sourced locally from 80 to 75 ka. Notably, this period coincides with a decrease in local woody vegetation cover, which may have destabilised the surrounding dunes (Cadd et al., 2018). Although the exact cause of the variability in the far-travelled dust is unknown due to a lack of mainland records from this period, it is likely linked to the climatic fluctuations experienced during the end of MIS5 and beginning of MIS4 (Bayon et al., 2017).

MIS4 climate and environmental change

Welsby Lagoon existed as a lake during MIS4 when the organic-rich deposits of Unit 2 were accumulating. This was a time when significant global ice cap growth (Grant et al., 2014) coincided with substantially cooler climate (De Deckker et al., 2012). The major feature of MIS4 at Welsby Lagoon is the increased influx of both local and regional dust between 71 ka and 67 ka. This increased

dust deposition overlaps with drier conditions as indicated by an expansion of grasses over rainforest, trees and shrubs (Cadd et al., 2018). The vegetation change and reduction in plant cover would have allowed increased mobilisation of proximal dune sand into Welsby Lagoon.

The increased far-travelled dust flux between 71 ka and 67 ka may be attributed to drying across central Australia, potentially linked to decreased precipitation across Australia and the deflation of major dust sources such as the Lake Eyre Basin (Figure 2.5) (Farebrother et al., 2017; Magee et al., 2004). Notably, Lake Eyre would not have been the only source of dust – as indicated by the reconstruction of transportation pathways via geochemical fingerprinting (e.g., Marx et al., 2018; Petherick et al., 2009) – however, it is one of the few continental interior records that captures the extent of MIS4, and with which a comparison can be made. The lack of records to which the Welsby Lagoon dust record can be compared limits regional dust reconstructions, particularly when playa lake dust sources only contribute 13 – 22 % to total dust emissions, with a larger proportion likely originating from other mainland alluvial sources (Farebrother et al., 2017).

Geochemical response to catchment morphology change during MIS3

The MIS3 dust record shows an initial increase in contrast to MIS4, during a time when the surrounding vegetation of Welsby Lagoon experienced a shift towards further expansion of grass and herbs at the expense of rainforest, trees, and shrub taxa (Cadd et al., 2018). The concordant shift in vegetation regimes and dust flux may be indicative of increased availability of inorganic material due to more arid conditions or highlights the decreased influence of proximal vegetation to act as a sediment trap for entrained dust.

There was an initial increase in both the regional and local dust influx at the start MIS3; in particular, the far-travelled dust record has several short-lived periods of increased influx, notably between 58 ka and 48 ka. The onset of this enhanced dust influx corresponds with the variations in the tree pollen record of Caledonia Fen (Kershaw et al., 2010; Kershaw et al., 2007b), and an increase in Poaceae at Lynch's Crater (Kershaw et al., 2007a), suggesting potentially more arid conditions at this time. Additionally, there is evidence that aridification was synchronous throughout the Australian interior in early MIS3, as recorded in eggshell isotope records (Miller et al., 1999) and deflation associated with low lake levels (Cohen et al., 2015; Magee & Miller, 1998; Magee et al., 2004). Consequently, the variations in the far-travelled dust flux record of Welsby Lagoon are contemporaneous with central Australian lake deflation, particularly during the MIS3/4 transition, inferring a variable hydroclimate throughout the continent interior (Figure 2.5). The climate variability recorded in MIS3, in addition to the arrival of people, elsewhere across Australia may have contributed to the decline and subsequent extinction of the Australian megafauna during this time.

The late MIS3 dust record at Welsby Lagoon, from ca. 35 ka onwards, is characterised by a return to the low dust flux levels seen during late MIS4. While this may suggest reduced aridity, it is not the only possible scenario as continual erosion of material from dust sources is limited by the supply of sediment. Moreover, morphological changes at Welsby Lagoon, as it evolved from a lake to a swamp (Cadd et al., 2018), likely inhibited the wetland's ability to entrap and retain dust. The difference in basin morphology between Welsby Lagoon and the other two NSI dust records would explain why the Welsby Lagoon dust record exhibits a substantial increase in MIS3 accumulation rate (Figure 2.5) (Petherick et al., 2008; Petherick et al., 2017).

Dust mobilisation during MIS2 and the LGM

The MIS2 dust record accumulated when Welsby Lagoon was a swamp, similar to today. Welsby Lagoon currently has fluctuating water levels and from 2015 to 2019 has fallen from 1.5 m to below the sediment surface. Unit 3 has the lowest net dust flux, accompanied by an increase in the local tree and shrub taxa (Cadd et al., 2018). As observed in the underlying units, increased vegetation cover may have inhibited the transportation of local dust by inhibiting particle entrainment and, subsequent deposition into Welsby Lagoon. Additionally, Cadd et al. (2018) reported the emergence of aquatic plants across the surface of Welsby Lagoon, another factor which may inhibit the transportation of windswept material to the central coring position.

There is similarity between the Welsby Lagoon and the only two other dust records on NSI - Tortoise Lagoon and Native Companion Lagoon – which both show a flux that is greater during the LGM than the Holocene (Petherick et al., 2017), an observation supported by South Pacific sediment deposition studies (Hesse, 1994; Lamy et al., 2014). The Welsby Lagoon record indicates a short period of increased dust deposition around 21 ka, which is shorter in duration than that observed elsewhere. The truncation of the dust record at Welsby Lagoon may be due the site having been a swamp at this same time and the limited information available to constrain the chronological model through this period. Additionally, fluctuating water depths may have induced the periodic deflation of the sediment surface, thereby eroding part of the record of enhanced dust flux through the LGM. However, the extent to which this pattern was attributed to basin infill, increased aridity or a combination of both remains unclear.

Conclusion

The Welsby Lagoon record offers a unique insight into climate variability across subtropical Australia from MIS5 to present. This study has produced the best-dated terrestrial sediment record for an Australian wetland through MIS3 and MIS4 via the integration of an independent Bayesian age model incorporating a total of 28 radiocarbon and OSL ages across the 12.7 m core. The robust age modelling has allowed an unprecedented insight into the timing of environmental change recorded in the sediment and, by extension, provided a record of aridity that fills an important geographical and temporal gap for Australia.

The dating conducted in this study has allowed a more precise estimate of when changes occurred through the evolution of Welsby Lagoon, constraining the timing of transition from lake to swamp to late MIS3. Moreover, the approach to age modelling has identified the timing of changes in the far-travelled dust flux record that may be linked to deflation events in central Australian lakes during periods of hydrological variability. This is particular evident for the Welsby Lagoon dust record across the 71 – 67 ka and 58 – 48 ka time intervals, when sea-level and regional water tables were lower than today. The study has highlighted links between hydrology and environmental factors that were likely responsible for dust accumulation on NSI; although the lack of continental records with which to compare the Welsby Lagoon dust record currently hinders more spatially precise interpretations.

The Welsby Lagoon sediment contains an extended dust record for coastal south-east Queensland and with the detailed age model presented, allows direct comparison between key palaeoclimate archives that span the late Quaternary. This provides important context for the timing of local and regional

palaeoecological change and in particular, enhancing the understanding of key events in Australia through the late Pleistocene including the arrival of humans and the extinction of megafauna.

Acknowledgements

We acknowledge Minjerribah (NSI) and the surrounding waters as Quandamooka Country. We thank Jie Chang, Jacinta Greer, Matthew Jones and Patrick Moss for their help in the field and Haidee Cadd for discussions.

The work was supported by the Australian Research Council DP150103875. R.L. was supported by an Australian Government Research Training Program Scholarship and a CRC LEME Regolith Science Scholarship. The OSL dating research undertaken was supported by Australian Research Council Future Fellowship grant FT130100195.

References

Aitken, M. J. 1985. Thermoluminescence dating: Past progress and future trends. Nuclear Tracks and Radiation Measurements (1982), 10, 3-6.

Aitken, M. J. 1998. Introduction to optical dating: the dating of Quaternary sediments by the use of photon-stimulated luminescence, Oxford, Oxford University Press.

Arnold, L. J. & Demuro, M. 2015. Insights into TT-OSL signal stability from single-grain analyses of known-age deposits at Atapuerca, Spain. Quaternary Geochronology, 30, 472-478.

Arnold, L. J., Demuro, M., Navazo, M., Benito-Calvo, A. & Pérez-González, A. 2013. OSL dating of the Middle Palaeolithic Hotel California site, Sierra de Atapuerca, north-central Spain. Boreas, 42, 285-305.

Arnold, L. J., Duval, M., Demuro, M., Spooner, N. A., Santonja, M. & Pérez-González, A. 2016. OSL dating of individual quartz 'supergrains' from the Ancient Middle Palaeolithic site of Cuesta de la Bajada, Spain. Quaternary Geochronology, 36, 78-101.

Arnold, L. J. & Roberts, R. G. 2009. Stochastic modelling of multi-grain equivalent dose (De) distributions: Implications for OSL dating of sediment mixtures. Quaternary Geochronology, 4, 204-230.

Arnold, L. J. & Roberts, R. G. 2011. Paper I–Optically stimulated luminescence (OSL) dating of perennially frozen deposits in north-central Siberia: OSL characteristics of quartz grains and methodological considerations regarding their suitability for dating. Boreas, 40, 389-416.

Arnold, L. J., Roberts, R. G., Galbraith, R. F. & Delong, S. B. 2009. A revised burial dose estimation procedure for optical dating of youngand modern-age sediments. Quaternary Geochronology, 4, 306-325.

Arnold, L. J., Roberts, R. G., Macphee, R. D. E., Willerslev, E., Tikhonov, A. N. & Brock, F. 2008. Optical dating of perennially frozen deposits associated with preserved ancient plant and animal DNA in north-central Siberia. Quaternary Geochronology, 3, 114-136.

Bagnold, R. A. 1973. The Physics of Blown Sand and Desert Dunes, Chapman & Hall.

Bailey, R. M. & Arnold, L. J. 2006. Statistical modelling of single grain quartz De distributions and an assessment of procedures for estimating burial dose. Quaternary Science Reviews, 25, 2475-2502.

Barr, C., Tibby, J., Marshall, J. C., Mcgregor, G. B., Moss, P. T., Halverson, G. P. & Fluin, J. 2013. Combining monitoring, models and palaeolimnology to assess ecosystem response to environmental change at monthly to millennial timescales: the stability of Blue Lake, North Stradbroke Island, Australia. Freshwater Biology, 58, 1614-1630.

Bayon, G., De Deckker, P., Magee, J. W., Germain, Y., Bermell, S., Tachikawa, K. & Norman, M. D. 2017. Extensive wet episodes in Late Glacial Australia resulting from high-latitude forcings. Scientific reports, 7, 1-7.

Beaton, J. M. 1995. The transition on the coastal fringe of Greater Australia. Antiquity, 69, 798.

Bird, M. I., Levchenko, V., Ascough, P. L., Meredith, W., Wurster, C. M., Williams, A., Tilston, E. L., Snape, C. E. & Apperley, D. C. 2014. The efficiency of charcoal decontamination for radiocarbon dating by three pre-treatments–ABOX, ABA and hypy. Quaternary Geochronology, 22, 25-32.
Brennan, B. J. 2003. Beta doses to spherical grains. Radiation Measurements, 37, 299-303.
Brock, F., Higham, T., Ditchfield, P. & Ramsey, C. B. 2010. Current pretreatment methods for AMS radiocarbon dating at the Oxford Radiocarbon Accelerator Unit (ORAU). Radiocarbon, 52, 103-112.
Brock, F., Lee, S., Housley, R. A. & Bronk Ramsey, C. 2011. Variation in the radiocarbon age of different fractions of peat: A case study from Ahrenshöft, northern Germany, Quat. Geochronol., 6, 550–555.
Bronk Ramsey, C. 2008. Deposition models for chronological records. Quaternary Science Reviews, 27, 42-60.
Bronk Ramsey, C. 2009. Dealing with outliers and offsets in radiocarbon dating. Radiocarbon, 51, 1023-1045.
Bronk Ramsey, C. 2017. Methods for summarizing radiocarbon datasets. Radiocarbon, 59, 1809-1833.
Bronk Ramsey, C. & Lee, S. 2013. Recent and planned developments of the program OxCal. Radiocarbon, 55, 720-730.
Cadd, H. R., Tibby, J., Barr, C., Tyler, J., Unger, L., Leng, M. J., Marshall, J. C., Mcgregor, G., Lewis, R. & Arnold, L. J. 2018. Development of a Southern Hemisphere subtropical wetland (Welsby Lagoon, south-east Queensland, Australia) through the last glacial cycle. Quaternary Science Reviews, 202, 53-65.
Chase, B. M. 2010. South African palaeoenvironments during marine oxygen isotope stage 4: a context for the Howiesons Poort and Still Bay industries. Journal of Archaeological Science, 37, 1359-1366.
Christen, J. A. 1994. Bayesian interpretation of radiocarbon results. University of Nottingham.
Clarkson, C., Jacobs, Z., Marwick, B., Fullagar, R., Wallis, L., Smith, M., Roberts, R. G., Hayes, E., Lowe, K. & Carah, X. 2017. Human occupation of northern Australia by 65,000 years ago. Nature, 547, 306-310.
Cohen, T. J., Jansen, J. D., Gliganic, L. A., Larsen, J. R., Nanson, G. C., May, J.-H., Jones, B. G. & Price, D. M. 2015. Hydrological transformation coincided with megafaunal extinction in central Australia. Geology, 43, 195-198.
Coll, K. & Whitaker, R. 1990. The Australian Weather Book: Understanding our climate and how it affect us, Syndey, Australia, Associates Publishing Pty Ltd.
Croudace, I. W., Rindby, A. & Rothwell, R. G. 2006. ITRAX: description and evaluation of a new multi-function X-ray core scanner. Geological Society, London, Special Publications, 267, 51-63.
Croudace, I. W. & Rothwell, R. G. 2015. Micro-XRF Studies of Sediment Cores: Applications of a non-destructive tool for the environmental sciences, Springer.
De Deckker, P., Abed, R. M., De Beer, D., Hinrichs, K. U., O'loingsigh, T., Schefuß, E., Stuut, J. B. W., Tapper, N. J. & Van Der Kaars, S. 2008. Geochemical and microbiological fingerprinting of airborne dust that fell in Canberra, Australia, in October 2002. Geochemistry, Geophysics, Geosystems, 9.
De Deckker, P., Arnold, L. J., Van Der Kaars, S., Bayon, G., Stuut, J.-B. W., Perner, K., Dos Santos, R. L., Uemura, R. & Demuro, M. 2019. Marine Isotope Stage 4 in Australasia: a full glacial culminating 65,000 years ago–global connections and implications for human dispersal. Quaternary Science Reviews, 204, 187-207.
De Deckker, P., Moros, M., Perner, K. & Jansen, E. 2012. Influence of the tropics and southern westerlies on glacial interhemispheric asymmetry. Nature Geoscience, 5, 266-269.
Demuro, M., Arnold, L. J., Froese, D. G. & Roberts, R. G. 2013. OSL dating of loess deposits bracketing Sheep Creek tephra beds, northwest Canada: dim and problematic single-grain OSL characteristics and their effect on multi-grain age estimates. Quaternary Geochronology, 15, 67-87.
Dortch, J., Cupper, M., Grün, R., Harpley, B., Lee, K. & Field, J. 2016. The timing and cause of megafauna mass deaths at Lancefield Swamp, south-eastern Australia. Quaternary Science Reviews, 145, 161-182.

Farebrother, W., Hesse, P. P., Chang, H.-C. & Jones, C. 2017. Dry lake beds as sources of dust in Australia during the Late Quaternary: A volumetric approach based on lake bed and deflated dune volumes. Quaternary Science Reviews, 161, 81-98.
Fitzsimmons, K. E., Stern, N. & Murray-Wallace, C. V. 2014. Depositional history and archaeology of the central Lake Mungo lunette, Willandra Lakes, southeast Australia. Journal of Archaeological Science, 41, 349-364.
Fu, X., Cohen, T. J. & Arnold, L. J. 2017. Extending the record of lacustrine phases beyond the last interglacial for Lake Eyre in central Australia using luminescence dating. Quaternary Science Reviews, 162, 88-110.
Galbraith, R. F., Roberts, R. G., Laslett, G. M., Yoshida, H. & Olley, J. M. 1999. Optical dating of single and multiple grains of quartz from Jinmium rock shelter, northern Australia: Part I, experimental design and statistical models. Archaeometry, 41, 339-364.
Gasse, F. & Van Campo, E. 2001. Late Quaternary environmental changes from a pollen and diatom record in the southern tropics (Lake Tritrivakely, Madagascar). Palaeogeography, Palaeoclimatology, Palaeoecology, 167, 287-308.
Gordon, A. 1982. An Investigation of two Sequence-Comparison Statistics. Australian Journal of Statistics, 24, 332-342.
Grant, K. M., Rohling, E. J., Ramsey, C. B., Cheng, H., Edwards, R. L., Florindo, F., Heslop, D., Marra, F., Roberts, A. P. & Tamisiea, M. E. 2014. Sea-level variability over five glacial cycles. Nature communications, 5, 1-9.
Guérin, G., Mercier, N. & Adamiec, G. 2011. Dose-rate conversion factors: update. Ancient TL, 29, 5-8.
Hallegraeff, G., Coman, F., Davies, C., Hayashi, A., Mcleod, D., Slotwinski, A., Whittock, L. & Richardson, A. J. 2014. Australian dust storm associated with extensive Aspergillus sydowii fungal "bloom" in coastal waters. Applied and environmental microbiology, 80, 3315-3320.
Hammer, Ø., Harper, D. a. T. & Ryan, P. D. 2001. PAST: Paleontological statistics software package for education and data analysis. Palaeontologia electronica, 4, 9.
Heiri, O., Lotter, A. F. & Lemcke, G. 2001. Loss on ignition as a method for estimating organic and carbonate content in sediments: reproducibility and comparability of results. Journal of paleolimnology, 25, 101-110.
Hendy, I. L., Napier, T. J. & Schimmelmann, A. 2015. From extreme rainfall to drought: 250 years of annually resolved sediment deposition in Santa Barbara Basin, California. Quaternary International, 387, 3-12.
Hesse, P. P. 1994. The record of continental dust from Australia in Tasman Sea sediments. Quaternary Science Reviews, 13, 257-272.
Hesse, P. P., Magee, J. W. & Van Der Kaars, S. 2004. Late Quaternary climates of the Australian arid zone: a review. Quaternary International, 118, 87-102.
Hogg, A. G., Hua, Q., Blackwell, P. G., Niu, M., Buck, C. E., Guilderson, T. P., Heaton, T. J., Palmer, J. G., Reimer, P. J. & Reimer, R. W. 2013. SHCal13 Southern Hemisphere calibration, 0–50,000 years cal BP. Radiocarbon, 55, 1889-1903.
Hounslow, M. W. & Clark, R. M. 2016. CPLSlot a program for objective correlation between successions using sequence slotting.
Imbrie, J., Hays, J. D., Martinson, D. G., Mcintyre, A., Mix, A. C., Morley, J. J., Pisias, N. G., Prell, W. L. & Shackleton, N. J. 1984. The orbital theory of Pleistocene climate: support from a revised chronology of the marine d18O record.
Kemp, C., Tibby, J., Arnold, L. J. & Barr, C. 2019. Australian hydroclimate during Marine Isotope Stage 3: a synthesis and review. Quaternary Science Reviews, 204, 94-104.
Kemp, C. W., Tibby, J., Arnold, L. J., Barr, C., Gadd, P. S., Marshall, J. C., Mcgregor, G. B. & Jacobsen, G. E. 2020. Climates of the last three interglacials in subtropical eastern Australia inferred from wetland sediment geochemistry. Palaeogeography, Palaeoclimatology, Palaeoecology, 538, 109463.
Kershaw, A. P. 1976. A late Pleistocene and Holocene pollen diagram from Lynch's Crater, northeastern Queensland, Australia. New Phytologist, 77, 469-498.

Kershaw, A. P., Bretherton, S. C. & Van Der Kaars, S. 2007a. A complete pollen record of the last 230 ka from Lynch's Crater, north-eastern Australia. Palaeogeography, Palaeoclimatology, Palaeoecology, 251, 23-45.
Kershaw, A. P., Mckenzie, G. M., Brown, J., Roberts, R. G. & Van Der Kaars, S. 2010. Beneath the peat: A refined pollen record from an interstadial at Caledonia Fen, highland eastern Victoria, Australia. Altered ecologies: fire, climate and human influence on terrestrial landscapes. Terra Australis, 32, 33-48.
Kershaw, A. P., Mckenzie, G. M., Porch, N., Roberts, R. G., Brown, J., Heijnis, H., Orr, M. L., Jacobsen, G. & Newall, P. R. 2007b. A high-resolution record of vegetation and climate through the last glacial cycle from Caledonia Fen, southeastern highlands of Australia. Journal of Quaternary Science: Published for the Quaternary Research Association, 22, 481-500.
Kershaw, A. P. & Nanson, G. C. 1993. The last full glacial cycle in the Australian region. Global and Planetary Change, 7, 1-9.
Lamy, F., Gersonde, R., Winckler, G., Esper, O., Jaeschke, A., Kuhn, G., Ullermann, J., Martínez-Garcia, A., Lambert, F. & Kilian, R. 2014. Increased dust deposition in the Pacific Southern Ocean during glacial periods. Science, 343, 403-407.
Lee-Manwar, G., Arthington, A. & Timms, B. Comparative studies of brown lake, tortoise lagoon and blue lake, North stradbroke Island, Queensland. I. Morphometry and origin of the lakes. Proceedings of the Royal Society of Queensland, 1980. 53-60.
Löwemark, L., Chen, H.-F., Yang, T.-N., Kylander, M., Yu, E.-F., Hsu, Y.-W., Lee, T.-Q., Song, S.-R. & Jarvis, S. 2011. Normalizing XRF-scanner data: a cautionary note on the interpretation of high-resolution records from organic-rich lakes. Journal of Asian Earth Sciences, 40, 1250-1256.
Magee, J. W. & Miller, G. H. 1998. Lake Eyre palaeohydrology from 60 ka to the present: beach ridges and glacial maximum aridity. Palaeogeography, Palaeoclimatology, Palaeoecology, 144, 307-329.
Magee, J. W., Miller, G. H., Spooner, N. A. & Questiaux, D. 2004. Continuous 150 ky monsoon record from Lake Eyre, Australia: insolation-forcing implications and unexpected Holocene failure. Geology, 32, 885-888.
Malinverno, A., Erba, E. & Herbert, T. D. 2010. Orbital tuning as an inverse problem: Chronology of the early Aptian oceanic anoxic event 1a (Selli Level) in the Cismon APTICORE. Paleoceanography, 25.
Martin, L., Goff, J., Jacobsen, G. & Mooney, S. 2019. The radiocarbon ages of different organic components in the Mires of Eastern Australia. Radiocarbon, 61, 173-184.
Marx, S. K., Kamber, B. S., Mcgowan, H. A., Petherick, L. M., Mctainsh, G. H., Stromsoe, N., Hooper, J. N. & May, J.-H. 2018. Palaeo-dust records: A window to understanding past environments. Global and Planetary Change, 165, 13-43.
Mcgowan, H. A., Kamber, B., Mctainsh, G. H. & Marx, S. K. 2005. High resolution provenancing of long travelled dust deposited on the Southern Alps, New Zealand. Geomorphology, 69, 208-221.
Mcgowan, H. A., Petherick, L. M. & Kamber, B. S. 2008. Aeolian sedimentation and climate variability during the late Quaternary in southeast Queensland, Australia. Palaeogeography, Palaeoclimatology, Palaeoecology, 265, 171-181.
Mclauchlan, K. K., Lascu, I., Mellicant, E., Scharping, R. J. & Williams, J. J. 2019. Influences of forested and grassland vegetation on late Quaternary ecosystem development as recorded in lacustrine sediments. Quaternary Research, 92.
Mejdahl, V. 1979. Thermoluminescence dating: beta-dose attenuation in quartz grains. Archaeometry, 21, 61-72.
Mettam, P., Tibby, J., Barr, C. & Marshall, J. C. 2011. Development of eighteen mile swamp, North Stradbroke Island: a palaeolimnological study. Proceedings of the Royal Society of Queensland, The, 117, 119-131.
Miller, G. H., Magee, J. W., Johnson, B. J., Fogel, M. L., Spooner, N. A., Mcculloch, M. T. & Ayliffe, L. K. 1999. Pleistocene Extinction of Genyornis newtoni: Human Impact on Australian Megafauna. Science, 283, 205.
Mohapatra, P. P., Stephen, A., Prasad, S., Singh, P. & Anupama, K. 2019. Late Pleistocene and Holocene vegetation changes and anthropogenic impacts in the Cauvery delta plains, southern India. Quaternary International, 507, 249-261.

Moss, P. T., Kershaw, A. P. & Grindrod, J. 2005. Pollen transport and deposition in riverine and marine environments within the humid tropics of northeastern Australia. Review of Palaeobotany and Palynology, 134, 55-69.
Moss, P. T. & Kershaw, P. A. 2000. The last glacial cycle from the humid tropics of northeastern Australia: comparison of a terrestrial and a marine record. Palaeogeography, Palaeoclimatology, Palaeoecology, 155, 155-176.
Murray, A. S. & Wintle, A. G. 2000. Luminescence dating of quartz using an improved single-aliquot regenerative-dose protocol. Radiation measurements, 32, 57-73.
Nilsson, M., Klarqvist, M., Bohlin, E. & Possnert, G. 2001. Variation in 14C age of macrofossils and different fractions of minute peat samples dated by AMS. The Holocene, 11, 579-586.
Ott, F., Kramkowski, M., Wulf, S., Plessen, B., Serb, J., Tjallingii, R., Schwab, M., Słowiński, M., Brykała, D. & Tyszkowski, S. 2018. Site-specific sediment responses to climate change during the last 140 years in three varved lakes in Northern Poland. The Holocene, 28, 464-477.
Patton, N. R., Ellerton, D. & Shulmeister, J. 2019. High-resolution remapping of the coastal dune fields of south east Queensland, Australia: a morphometric approach. Journal of Maps, 15, 578-589.
Petherick, L., Mcgowan, H. & Moss, P. 2008. Climate variability during the Last Glacial Maximum in eastern Australia: evidence of two stadials? Journal of Quaternary Science: Published for the Quaternary Research Association, 23, 787-802.
Petherick, L. M., Mcgowan, H. A. & Kamber, B. S. 2009. Reconstructing transport pathways for late Quaternary dust from eastern Australia using the composition of trace elements of long traveled dusts. Geomorphology, 105, 67-79.
Petherick, L. M., Moss, P. T. & Mcgowan, H. A. 2011. Climatic and environmental variability during the termination of the Last Glacial Stage in coastal eastern Australia: a review. Australian Journal of Earth Sciences, 58, 563-577.
Petherick, L. M., Moss, P. T. & Mcgowan, H. A. 2017. An extended last glacial maximum in Subtropical Australia. Quaternary International, 432, 1-12.
Pickett, J. W., Ku, T. L., Thompson, C. H., Roman, D., Kelley, R. A. & Huang, Y. P. 1989. A review of age determinations on Pleistocene corals in eastern Australia. Quaternary Research, 31, 392-395.
Pickett, J. W., Thompson, C. H., Kelley, R. A. & Roman, D. 1985. Evidence of high sea level during isotope stage 5c in Queensland, Australia. Quaternary Research, 24, 103-114.
Prescott, J. R. & Hutton, J. T. 1994. Cosmic ray contributions to dose rates for luminescence and ESR dating: large depths and long-term time variations. Radiation measurements, 23, 497-500.
Rees-Jones, J. 1995. Optical dating of young sediments using fine-grain quartz. Ancient TL, 13, 9-14.
Rees-Jones, J. & Tite, M. S. 1997. Optical dating results for British archaeological sediments. Archaeometry, 39, 177-187.
Reeves, J. M., Barrows, T. T., Cohen, T. J., Kiem, A. S., Bostock, H. C., Fitzsimmons, K. E., Jansen, J. D., Kemp, J., Krause, C. & Petherick, L. 2013. Climate variability over the last 35,000 years recorded in marine and terrestrial archives in the Australian region: an OZ-INTIMATE compilation. Quaternary Science Reviews, 74, 21-34.
Saltré, F., Chadoeuf, J., Peters, K. J., Mcdowell, M. C., Friedrich, T., Timmermann, A., Ulm, S. & Bradshaw, C. J. 2019. Climate-human interaction associated with southeast Australian megafauna extinction patterns. Nature communications, 10, 1-9.
Saltré, F., Rodríguez-Rey, M., Brook, B. W., Johnson, C. N., Turney, C. S. M., Alroy, J., Cooper, A., Beeton, N., Bird, M. I. & Fordham, D. A. 2016. Climate change not to blame for late Quaternary megafauna extinctions in Australia. Nature communications, 7, 1-7.
Tejan-Kella, M. S., Chittleborough, D. J., Fitzpatrick, R. W., Thompson, C. H., Prescott, J. R. & Hutton, J. T. 1990. Thermoluminescence dating of coastal sand dunes at Cooloola and North Stradbroke Island, Australia. Soil Research, 28, 465-481.
Thompson, C. H. 1992. Genesis of podzols on coastal dunes in southern Queensland. I. Field relationships and profile morphology. Soil Research, 30, 593-613.
Thompson, R. & Clark, R. M. 1990. Sequence slotting for stratigraphic correlation between cores: theory and practice. Paleolimnology and the Reconstruction of Ancient Environments. Springer.

Tibby, J., Barr, C., Marshall, J. C., Mcgregor, G. B., Moss, P. T., Arnold, L. J., Page, T. J., Questiaux, D., Olley, J. & Kemp, J. 2017. Persistence of wetlands on North Stradbroke Island (south-east Queensland, Australia) during the last glacial cycle: implications for Quaternary science and biogeography. Journal of Quaternary Science, 32, 770-781.

Tully, C. D., Rech, J. A., Workman, T. R., Santoro, C. M., Capriles, J. M., Gayo, E. M. & Latorre, C. 2019. In-stream wetland deposits, megadroughts, and cultural change in the northern Atacama Desert, Chile. Quaternary Research, 91, 63-80.

Turetsky, M. R., Manning, S. W. & Wieder, R. K. 2004. Dating recent peat deposits. Wetlands, 24, 324-356.

Tzedakis, P. C., Andrieu, V., De Beaulieu, J.-L., Crowhurst, S. J., Follieri, M., Hooghiemstra, H., Magri, D., Reille, M., Sadori, L. & Shackleton, N. J. 1997. Comparison of terrestrial and marine records of changing climate of the last 500,000 years. Earth and Planetary Science Letters, 150, 171-176.

Ward, W. T. 1978. Notes on the origin of Stradbroke Island.

Wroe, S., Field, J. H., Archer, M., Grayson, D. K., Price, G. J., Louys, J., Faith, J. T., Webb, G. E., Davidson, I. & Mooney, S. D. 2013. Climate change frames debate over the extinction of megafauna in Sahul (Pleistocene Australia-New Guinea). Proceedings of the National Academy of Sciences, 110, 8777-8781.

Chapter 3 Patterns of aeolian deposition in subtropical Australia through the last glacial and deglacial periods

---

This chapter has been published in *Quaternary Research* as:

Lewis, R. J., Tibby, J., Arnold, L. J., Gadd, P., Jacobsen, G., Barr, C., Negus, P. M., Mariani, M., Penny, D., Chittleborough, D. & Moss, E. 2021. Patterns of aeolian deposition in subtropical Australia through the last glacial and deglacial periods. Quaternary Research, 1-23.

Statement of Authorship

Title of Paper	Patterns of aeolian deposition in subtropical Australia through the last glacial and deglacial periods.
Publication Status	[X] Published [ ] Accepted for Publication [ ] Submitted for Publication [ ] Unpublished and Unsubmitted work written in manuscript style
Publication Details	Lewis, R. J., Tibby, J., Arnold, L. J., Gadd, P., Jacobsen, G., Barr, C., Negus, P. M., Mariani, M., Penny, D., Chittleborough, D. & Moss, E. 2021. Patterns of aeolian deposition in subtropical Australia through the last glacial and deglacial periods. *Quaternary Research*, 1-23.

Principal Author

Name of Principal Author (Candidate)	Richard J. Lewis	
Contribution to the Paper	Conceptualization; Data curation; Formal analysis; Funding acquisition; Investigation; Methodology; Project administration; Resources; Software; Data Validation; Visualization; Writing – original draft; Writing – review & editing	
Overall percentage (%)	80	
Certification:	This paper reports on original research I conducted during the period of my Higher Degree by Research candidature and is not subject to any obligations or contractual agreements with a third party that would constrain its inclusion in this thesis. I am the primary author of this paper.	
Signature		Date 19th July 2021

Co-Author Contributions

By signing the Statement of Authorship, each author certifies that:

iv. the candidate's stated contribution to the publication is accurate (as detailed above);
v. permission is granted for the candidate in include the publication in the thesis; and
vi. the sum of all co-author contributions is equal to 100% less the candidate's stated contribution.

Name of Co-Author	John Tibby	
Contribution to the Paper	Conceptualization; Data curation; Funding acquisition; Investigation; Project administration; Resources; Software; Data Validation; Visualization; Writing – original draft; Writing – review & editing	
Signature		Date 19th July 2021

Name of Co-Author	Lee J. Arnold	
Contribution to the Paper	Conceptualization; Data curation; Formal analysis; Funding acquisition; Investigation; Methodology; Project administration; Resources; Software; Data Validation; Visualization; Writing – original draft; Writing – review & editing	
Signature		Date 22nd July 2021

Name of Co-Author	Patricia Gadd	
Contribution to the Paper	Data curation; Formal analysis; Methodology; Resources; Software; Writing – review & editing	
Signature		Date 19th July 2021

Name of Co-Author	Geraldine Jacobsen	
Contribution to the Paper	Data curation; Formal analysis; Methodology; Resources; Software; Writing – review & editing	
Signature		Date 29th July 2021

Name of Co-Author	Cameron Barr	
Contribution to the Paper	Data curation; Formal analysis; Methodology; Resources; Software; Writing – review & editing	
Signature		Date 13th September 2021

Name of Co-Author	Peter M. Negus	
Contribution to the Paper	Data curation; Formal analysis; Methodology; Resources; Software; Writing – review & editing	
Signature		Date 19th July 2021

Name of Co-Author	Michela Mariani	
Contribution to the Paper	Data curation; Formal analysis; Methodology; Resources; Software; Writing – review & editing	
Signature		Date 19th July 2021

Name of Co-Author	Daniel Penny	
Contribution to the Paper	Data curation; Formal analysis; Methodology; Resources; Software; Writing – review & editing	
Signature		Date 19th July 2021

Name of Co-Author	David Chittleborough	
Contribution to the Paper	Data curation; Formal analysis; Methodology; Resources; Software; Writing – review & editing	
Signature		Date 19th July 2021

Name of Co-Author	Edward Moss	
Contribution to the Paper	Data curation; Formal analysis; Methodology; Resources; Software; Writing – review & editing	
Signature		Date 3rd November 2021

Abstract

Debate about the nature of climate and the magnitude of ecological change across Australia during the last glacial maximum (LGM; 26.5 – 19 ka) persists despite considerable research into the late Pleistocene. This is partly due to a lack of detailed palaeoenvironmental records and reliable chronological frameworks. Geochemical and geochronological analyses of a 60 ka sedimentary record from Brown Lake, subtropical Queensland, are presented and considered in the context of climate-controlled environmental change. Optically stimulated luminescence dating of dune crests adjacent to prominent wetlands across North Stradbroke Island (Minjerribah) returned a mean age of 119.9 ± 10.6 ka; indicating relative dune stability soon after formation in Marine Isotope Stage 5. Synthesis of wetland sediment geochemistry across the island was used to identify dust accumulation and applied as an aridification proxy over the last glacial-interglacial cycle. A positive trend of dust deposition from ca. 50 ka was found with highest influx occurring leading into the LGM. Complexities of comparing sedimentary records and the need for robust age models are highlighted with local variation influencing the accumulation of exogenic material. An inter-site comparison suggests enhanced moisture stress regionally during the last glaciation and throughout the LGM, returning to a more positive moisture balance ca. 8 ka.

Introduction

The last glacial maximum (LGM), which occurred ca. 26.5 – 19 ka (Clark et al., 2009), remains somewhat poorly understood in Australian late Quaternary palaeoenvironmental records (Reeves et al., 2013), despite being an example of a prominent, extreme climate event (Barrows & Juggins, 2005). In the context of the Southern Hemisphere, it has been suggested that the onset of cold and dry climates was earlier (ca. 35–30 ka; Petherick et al., 2011) than the equivalent Northern Hemisphere conditions. The timing of the climatic shift in the Southern Hemisphere is based on proxy records indicating increased aridity along the eastern margin of Australia (e.g., Colhoun et al., 1999; Kershaw et al., 2007; Petherick et al., 2008) and internationally (e.g., Denton et al., 1999; Vandergoes et al., 2005). The ensuing LGM was characterized by lowering of sea-level (Grant et al., 2014; Lambeck et al., 2014), reduced precipitation (Hesse et al., 2004), expansion of the continental landmass, and cooler climates across much of the Australian continent (Bowler, 1976; Galloway, 1965; Kemp & Spooner, 2007). However, recent comparative studies of palaeoenvironmental records have highlighted the need for robust chronological frameworks because site-specific proxy responses can be complex and hinder deeper understanding of how the LGM influenced the magnitude of environmental change in different regions (Harrison, 1993; Reeves et al., 2013; Turney et al., 2006a; Williams et al., 2009).

In order to unravel the complex history of Australian environmental change, it is essential to distinguish between locally driven proxy responses (e.g., change in vegetation cover, fire regimes, topographical influences) and those induced by large-scale shifts in the climate system (Svitok et al., 2011). The challenge is that environmental change may be explained by both local and regional forces; for example, vegetation change may result from local fire regime changes or moisture balance shifts forced by regional climate. Deconvolution between local and regional drivers is important when investigating dust flux as the net mobilization of lithogenic material can be a result of processes at the source (e.g., Washington et al., 2006) and depositional locus (Farebrother et al., 2017). Two ways to separate local and regional signals are to: (1) increase the current multi-proxy palaeoenvironmental

dataset for the LGM in Australia (Turney et al., 2006a), with particular emphasis on capturing records of sufficient antiquity in underrepresented and climatically sensitive locations; and (2) establish robust chronologies, in combination with multi-proxy datasets, which can be used to infer changes in local variables (e.g., effective precipitation, temperature, catchment conditions, and available moisture) and how they have influenced the palaeoenvironmental record.

Lake sediments are important archives of palaeoenvironmental information, capable of preserving a multitude of proxies from which, regional, local, and global climate dynamics can be inferred (Reeves et al., 2013). The benefit of lake archives is that they have the capacity to accumulate temporally high-resolution changes through time (Schnurrenberger et al., 2003). However, it is not uncommon for lake sediment records to preserve unconformities due to depositional hiatuses, erosional episodes, or both (Kershaw et al., 2006; Mandl et al., 2016; Moss & Kershaw, 2007). To effectively interrogate palaeoenvironmental records from lakes, it is critical to establish an understanding of how lake catchments evolve and how these changes may influence deposition through time (Birks & Birks, 2006). In instances where there is a hiatus in the lake sediment record, the missing information can sometimes be inferred from other associated deposits (e.g., marginal dunes; Fitzsimmons et al., 2007). However, for this approach to be effective, robust age controls are needed for the complementary sedimentary archives (Hesse, 2016).

Many unique biological and geochemical proxies are available within lacustrine sediments, from which physical and chemical analyses can provide insights into environmental change through time. Specific examples of biological proxies often investigated include pollen and charcoal (Ellerton et al., 2017; Kershaw et al., 2010; Lisé-Pronovost et al., 2019; Xiao et al., 2020), diatoms (Gasse & Van Campo, 2001; Song et al., 2020), and stable isotopes of sediments and preserved organisms (Long et al., 2018; Zhang et al., 2011). Analysis of terrigenous particles (e.g., dust) and sedimentary depositional features can be used to evaluate exogenous and in-lake condition changes. Advances in analytical techniques now allow the identification of complex, fine-scale change in sedimentary sequences, including features associated with dust deposition. Moreover, dust characterization from lake records provides a means to trace source locations, thereby providing an important understanding of wind regimes and environmental change in at the source location through time (e.g., McGowan et al., 2008; Petherick et al., 2011).

Identifying changes in lake sediments, particularly those predominantly composed of organic matter, can be challenging because changes in sedimentology may be inconspicuous. In instances when sedimentology is unclear or complex, the application of micro-XRF core scanning (μXRF) can provide high-resolution (sub-millimetre) sediment geochemistry without the need for destructive sampling (Croudace & Rothwell, 2015). The success of applying μXRF to analyse finely laminated sediment archives has been demonstrated in a range of key palaeoenvironmental studies, including climate change (e.g., Kylander et al., 2011; Lauterbach et al., 2011), anthropogenic disturbance (e.g., Guyard et al., 2007; Niemann et al., 2013), identification of pyroclastic material (e.g., McCanta et al., 2015; Vogel et al., 2010), and changes in lake oxygenation conditions (e.g., Davies et al., 2015).

Interpretation of geochemical data obtained using μXRF requires careful consideration, particularly in sediments where composition is highly variable (Boyle, 2002). Lighter elements in particular can be influenced by changes in water and organic content (Tjallingii et al., 2007; Weltje & Tjallingii, 2008), the effects of which can be minimized by normalizing to the total sum of Compton and Rayleigh

scatter (incoherent and coherent scatter: inc/coh) (e.g., Jouve et al., 2013; Kylander et al., 2012). Moreover, the setting of the catchment (e.g., local geology and lake-water properties) must be considered when inferring changes in any element quantified using μXRF, particularly because post-depositional changes in lake and catchment conditions can influence geochemistry (Kylander et al., 2011).

Geochemical studies from wetlands on North Stradbroke Island show that variations in sediment chemistry are strongly influenced by aeolian influx (e.g., Kemp et al., 2020; Lewis et al., 2020; McGowan et al., 2008; Petherick et al., 2009). Trace element geochemistry of the inorganic sediment fraction from Native Companion Lagoon found the origin of the material was both from the Australian continent, important for providing context during the LGM, and local dunes (McGowan et al., 2008). Subsequent models of aeolian transportation pathways to North Stradbroke Island (Petherick et al., 2009) support this finding, with dust records now improving the understanding of regional climate during the LGM in coastal subtropical Australia (Kemp et al., 2020; Lewis et al., 2020; McGowan et al., 2008; Petherick et al., 2011).

This study examines environmental changes associated with climate variability since MIS5 from Brown Lake, North Stradbroke Island, using a combination of geochemistry (μXRF core scanning) and geochronology (optically stimulated luminescence [OSL] and radiocarbon [^{14}C] dating). The potential of Brown Lake for improved regional reconstructions of LGM conditions was highlighted by an initial OSL age of 47 ka for the base of the sediment sequence (Tibby et al., 2017). Moreover, there is limited information regarding the timing of dune emplacement proximal to Brown Lake and other wetlands on North Stradbroke Island. The aims of this study are three-fold: (1) to develop the first Bayesian age-depth model for the Brown Lake sediment; (2) to compare dust deposition in Brown Lake with nearby wetlands, to infer the history of late Pleistocene local dust deposition on North Stradbroke Island; and (3) to undertake direct OSL dating of dune fields, which host wetland sediment archives, in order to improve the spatial and temporal coverage of existing palaeoenvironmental records for North Stradbroke Island. This will be achieved by examining high-resolution geochemical measurements from cores extracted at two different locations along the longitudinal axis of the water body. The separation between the cores will enable spatial changes attributed to basin evolution to be considered when investigating changes in moisture balance at both local and regional scales.

Study Sites

North Stradbroke Island is situated ~30 km east of the city of Brisbane, Queensland and is the second largest sand island in the world (Figure 3.1a). North Stradbroke Island is positioned in the subtropics with mean annual summer and winter temperatures between 22 – 30 °C and 12 – 20 °C, respectively (BOM, 2019). The dominant wind direction is the south-east, driven by onshore trade winds (Coll & Whitaker, 1990). Winter months on North Stradbroke Island are mild and dry with a large proportion of annual precipitation (1545 mm; BOM, 2019) occurring during the warm, humid summer and autumn seasons.

North Stradbroke Island is part of the extensive south-east Queensland dune system that includes Fraser Island, Moreton Island (Figure 3.1a), and the Cooloola Sand Mass (Patton et al., 2019; Ward, 1978). The topography of North Stradbroke Island is, in part, determined by the overprinting of older dunes by more recent dune units, becoming younger towards the east coast; as inferred from morphological analysis (Ward, 2006) and remote sensing (Patton et al., 2019) data (Figure 3.1b).

What remains less clear, however, is what mechanisms are responsible for dune development on North Stradbroke Island, within which numerous wetlands lie (Figure 3.1c). This study presents ages for dunes adjacent to prominent wetlands and evaluates the timing of advancement in the context of key climate events, including climate and sea-level change (Grant et al., 2014).

Brown Lake (27°29′10″S, 153°26′01″E; 56 m a.s.l.) is a naturally acidic (pH = 4.85 ± 0.02; Mosisch & Arthington, 2001) perched, endorheic lake that lies within the Yankee Jack dune formation (Patton et al., 2019; Ward, 2006,). It is the largest lake on North Stradbroke Island and has a 1743 ha drainage basin (Leach, 2011). Brown Lake has a maximum water depth of 8.3 m, which varies in concert with effective precipitation (Figure 3.2). The present-day vegetation consists of open sclerophyll woodland, with a canopy dominated by *Eucalyptus* and *Allocasuarina* (Clifford & Specht, 1979).

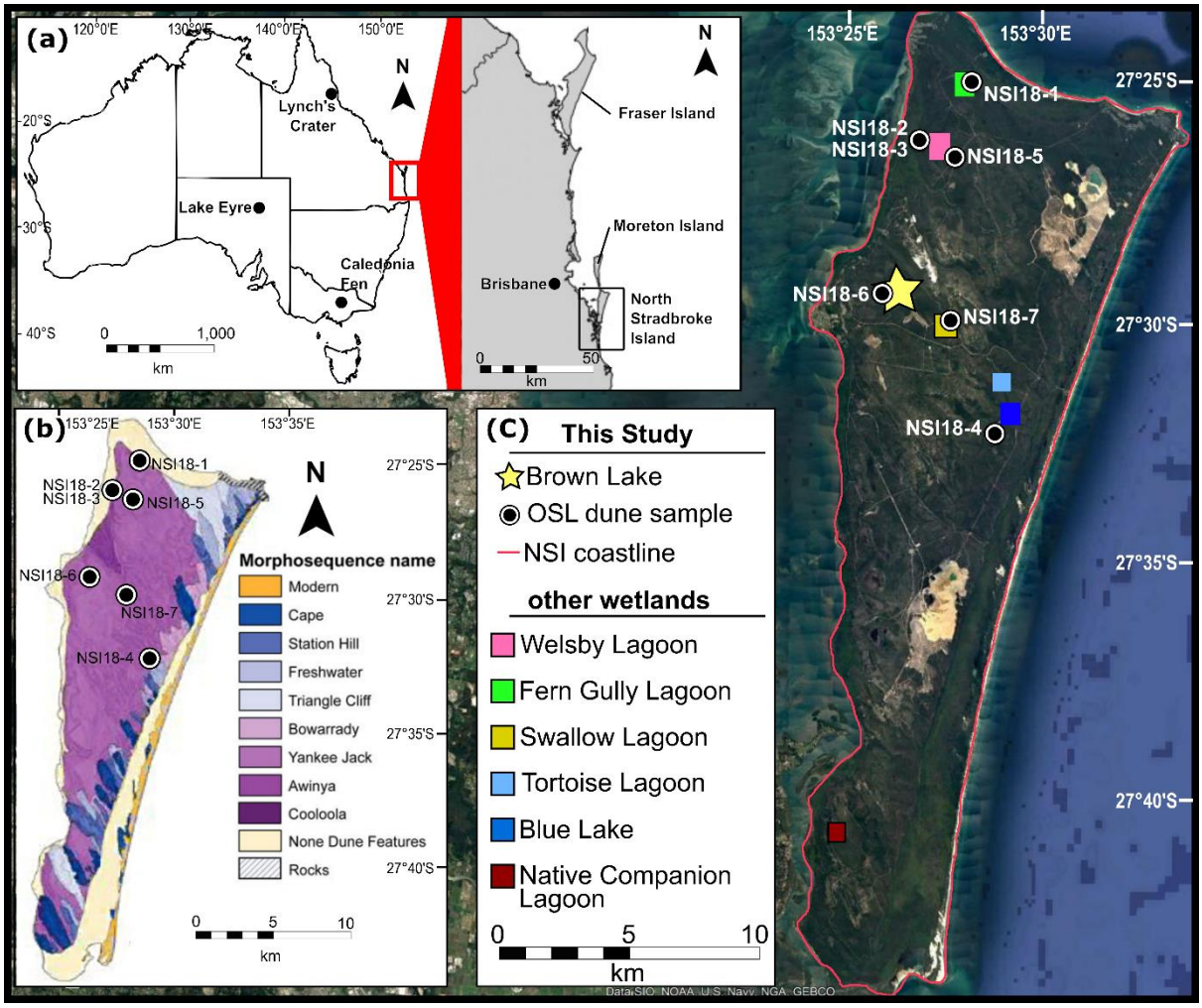

Figure 3.1 Location of North Stradbroke Island, dune sample sites, and locations referenced in text. (a) Position of the island in relation to Australia, outlined by a red square. (**b**) Dune field map adapted from Patton et al. (2019), overlain by the OSL sample sites in this study. (**c**) Satellite image of North Stradbroke Island (source: Google Earth) and the position of wetlands referenced in text.

Methods

Coring and bathymetry

Lake sediment cores were extracted from Brown Lake in two expeditions taking place in 2009 and 2018 (Figure 3.2). A single, 3.95 m core was extracted from the central point of the lake in 2009 (BL09) using a Livingstone Corer, capturing 1.0 m of sediment with each successive drive. Sediment from BL09 was extruded into PVC trays, wrapped in cling film, and transported to the University of Adelaide. In 2011, a bathymetric survey was undertaken using a boat-mounted sonar system (Altimeter: Tritech Int Ltd, Model PA500/6-S) attached to a data recorder (Rugged Brookhouse NMEA 0813) and a GPS (Garmin GPSMAP 60Cx), allowing bottom lake topography to be linked with the core locations. A follow-up coring expedition occurred in 2018, with the aim of acquiring sediment from the northern end of the basin along the 2011 bathymetric transect line (Figure 3.2). The two cores were then used to generate a sedimentological profile of Brown Lake and evaluate subsurface heterogeneity. In order to increase the reliability of interpretations from the sediment collected in 2018, two parallel and vertically offset sediment cores (BL18-3 and BL18-4) were collected 2 m apart using a modified Bolivia piston corer aboard a Kawhaw floating platform. The sediment was extracted in one-metre drives, with BL18-3 and BL18-4 reaching depths of 3.57 m and 2.73 m, respectively. To minimize sediment compaction and exposure to light, each drive was sealed in the core tube rather than being extruded in the field. The cores were split along their longitudinal axis under subdued red LED lighting to prevent daylight contamination and preserve sample integrity for subsequent OSL dating. One half of each core remained under strict lighting conditions (sealed in opaque black plastic) to prevent bleaching of the luminescence signal, while the other was used to conduct further, non-light-sensitive sampling.

Loss on ignition

Sediment descriptions were defined using standardized sedimentological terminology and characteristics based on analysing the sediment both in the core and as a smear, where possible. Sediment properties (i.e., water content, bulk density, and the organic:inorganic ratio) were measured using loss on ignition (LOI) and evaluated at centimetre scale down the length of BL18-3 (n = 347). BL09 LOI samples were taken every two centimetres (n = 217). Samples were extracted as 1 cm^3 of bulk sediment and measured following Heiri et al. (2001). This included weighing sediment before and after oven drying at 100°C and ashing at 550°C.

µXRF core scanning

Geochemical analysis was undertaken using a µXRF core scanner, measuring at millimetre resolution, at the Australian Nuclear Science and Technology Organisation (ANSTO) facility (see Appendix B for details). Elements of interest for this study were selected using the following criteria: (1) element ratios and element count data from µXRF scanning that represented chemical variation resulting from biogenic productivity (Ca/Ti, Br, Ca, inc/coh, Si/Ti) and siliciclastic influx (Rb, Al, Si, K, Ze, Fe, Ti) from within the sediment matrix were targeted (Hendy et al., 2015); (2) elements with large systematic uncertainties (e.g., influenced by the air gap between the sensor and the sediment) were removed from the dataset; and (3) elements and elemental ratios were categorized as intrinsic organic production indicators and extrinsically aeolian-derived lithic indicators—given that Brown Lake is a perched lake with no inflowing streams, sediment accumulation is a function of both. A principal component analysis (PCA) was undertaken on the selected suite of elements, which identified the

inorganic component, represented by Axis 1 (PC1), as the major factor of sediment chemical composition (Figure B1). The statistical link between siliciclastic accumulations and element variation enabled direct comparisons with the nearby Fern Gully Lagoon and Welsby Lagoon (Figure 3.1c) sediment records where aeolian-derived material is a primary influence on sediment chemistry (Kemp et al., 2020; Lewis et al., 2020).

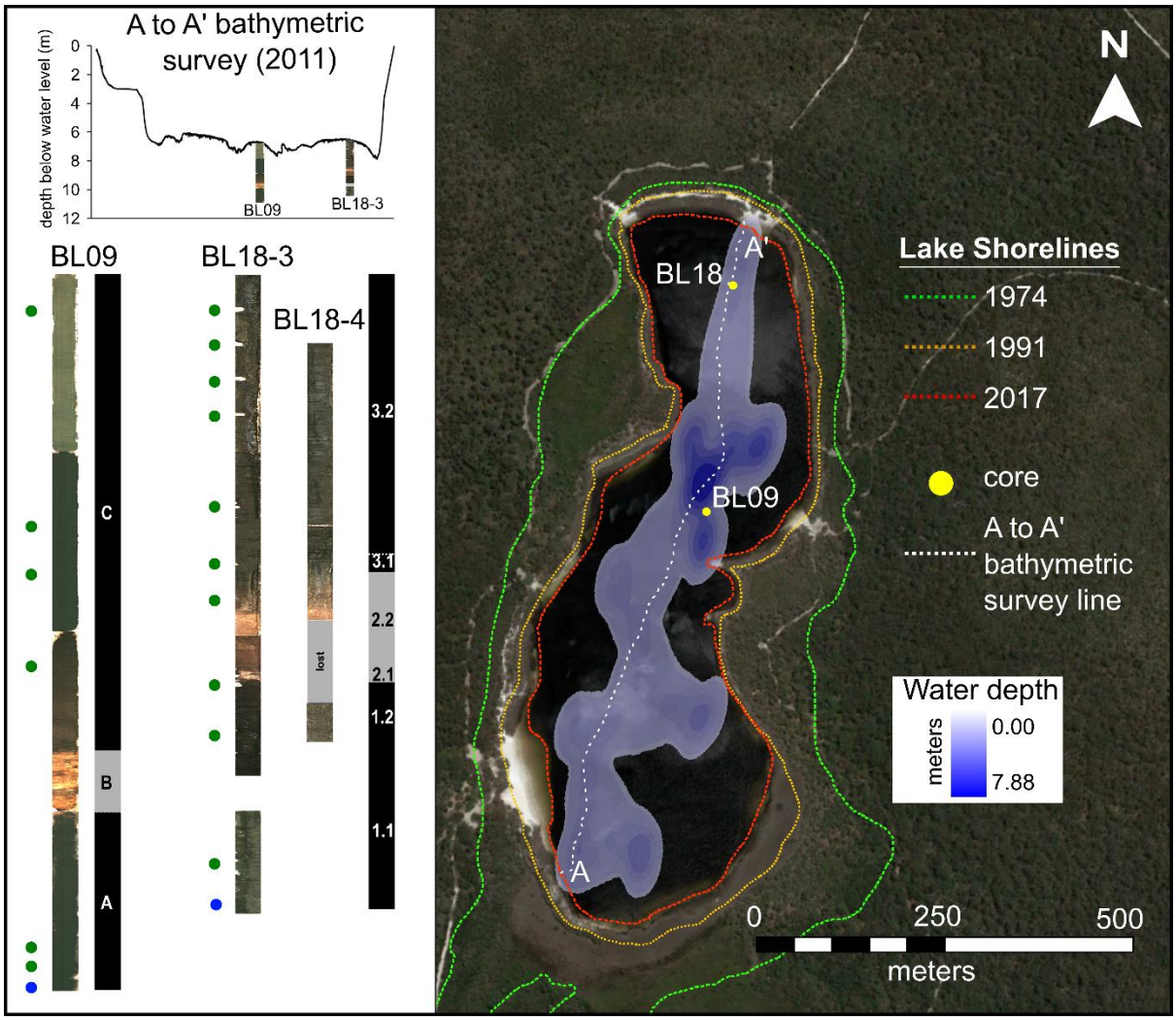

Figure 3.2 Position of sediment cores BL18 and BL09 recovered from Brown Lake. BL18 and BL09 cores placed on a 2011 bathymetric transect of Brown Lake. Optical images of BL18 and BL09 are shown next to position of radiocarbon samples (green circles), OSL samples (blue circles), and stratigraphic units (black and grey rectangles). Lake shorelines shown on the Google Earth satellite image were identified using historic aerial photos presented in Figure B9.

Core correlation

To overcome artificial breaks resulting from the coring process itself, the parallel and vertically offset cores BL18-3 and BL18-4 were combined using sequence slotting, hereafter denoted BL18. Sequence slotting was undertaken in CPLslot v2.4 (Hounslow & Clark, 2016) using the µXRF values for Al, Si, Ca, and Br as input variables. These elements provided accurate estimates of detrital and biochemical input based on their positions and grouping on the PC1 axis for Brown Lake (Figure B1) and other sites on North Stradbroke Island (e.g., Kemp et al., 2020; Lewis et al., 2020). Element count data were normalized by inc/coh because this was found to correlate with measured LOI values (r2 = 0.90; p-

value <0.05) (Figure B2), thus reducing the influence of water content and, or, organic matter on geochemistry.

The sequence slotting procedure included the following constraints: (1) the combined sequence started with the top of BL18-3; (2) the combined sequence ended with the bottom of BL18-3; and (3) BL18-4 was vertically offset from the surface by at least 0.5 m, and therefore did not overlap with BL18-3 above this depth. Additionally, a series of minor user choices were included in the sequence-slotting algorithm to accommodate the physical characteristics of the sediment in each core (i.e., sediment was lost between 2.02 – 2.50 m during retrieval of BL18-4 drive 2 - likely a result of increased porosity at the base of the drive relative to BL18-3).

The BL09 and the BL18 cores were not correlated using sequence-slotting because of lithological differences in the sediment profiles (i.e., the presence of a large sand band in the BL18 cores, which was absent in BL09) and the distance between the two coring locations (Figure 3.2). Therefore, comparisons between the BL18 and BL09 cores were based on stratigraphic similarities and were used primarily to interpret lake history and the extent of heterogeneous sedimentation along a basin transect.

Dating and age modelling

Radiocarbon dating was undertaken on the BL18-3 and BL09 profiles (Figure 3.2) with measurements made on bulk sediment (2 cm^3) due to a lack of macrofossils. Eleven bulk sediment samples from BL18-3 were analysed at the ANSTO Accelerator Mass Spectrometry (AMS) facility, and six samples from BL09 were analysed at Beta Analytic and the Waikato Radiocarbon Dating Laboratories. The samples were prepared using conventional approaches (see Appendix B for details), including standard ABA treatments (Brock et al., 2010). The ^{14}C ages were calibrated to calendar years using OxCal v4.3.2 and the SHCal13 calibration curve (Bronk Ramsey, 2009; Hogg et al., 2013).

Single-grain OSL dating was undertaken on quartz grains from a sample extracted from the base of BL18-3.3 and compared with the single-grain OSL age reported previously for BL09 (Tibby et al., 2017). An additional seven OSL samples were collected from the crest of dunes found adjacent to five prominent North Stradbroke Island wetlands (Figure 4.1c). These dune samples were taken from areas with surface exposures classified as the Yankee Jack Formation (Ward, 2006). Three OSL samples were collected from two different dune crests surrounding Welsby Lagoon in order to better constrain variability in dune emplacement and preservation dynamics.

The Brown Lake core sample was extracted under subdued red-light conditions, with care taken to ensure contaminant grains from coring were not included in the final analysis, ~1 cm of sediment was removed from the exposed sediment core face, with sediment within 1 cm of the coring tube also excluded (this material was retained for dosimetric analysis). The dune samples were collected from freshly dug pits to enable three-dimensional assessments of stratigraphy and ensure that zones affected by extensive root systems and bioturbation were avoided. Dune crests were targeted to maximize the likelihood of sampling primary (non-reworked) aeolian deposits. Individual OSL samples were collected by hammering opaque PVC tubes into cleaned exposures of A2 and B Horizons at depths of 70–180 cm beneath the surface, taking care to avoid the modern root layer and active bioturbation zones (Figure B3). Approximately 500 g of additional bulk sediment was collected

from the walls of each OSL sample hole (i.e., the surrounding ~2–3 cm of material in all directions) for evaluation of beta dose rate, secular equilibrium, and water content.

The environmental dose rates of the dune samples have been calculated using a combination of in situ field gamma-ray spectrometry and low-level beta counting. Gamma dose rates were determined from in situ measurements made using a Canberra NaI:Tl detector to account for any spatial heterogeneity in the surrounding (~30 cm diameter) gamma radiation field of each sample. The 'energy windows' approach described in Arnold et al. (2012) was used to derive individual estimates of U, Th, and K concentrations from the field gamma-ray spectra. External beta dose rates were determined from measurements made using a Risø GM-25-5 beta counter (Bøtter-Jensen & Mejdahl, 1988) on dried and homogenized, bulk sediments collected directly from the OSL sampling positions. High-resolution gamma spectrometry was additionally performed on the dune samples to examine the state of secular equilibrium in the ^{238}U and ^{232}Th decay series.

Elemental concentrations and specific activities were converted to dose rates using accepted conversion factors (Guérin et al., 2011). A small, assumed internal (alpha plus beta) dose rate component of 0.02 ± 0.01 Gy/ka has been included in the final dose rate calculation based on ICP-MS U and Th measurements made on etched quartz grains from nearby Welsby Lagoon (Lewis et al., 2020) and an alpha efficiency factor of 0.04 ± 0.01 (Rees-Jones, 1995; Rees-Jones & Tite, 1997). Cosmic-ray dose rates were calculated (Prescott & Hutton, 1994), after taking into consideration lake water level, site altitude, geomagnetic latitude, and density and thickness of sediment overburden.

The final dose rates for the lake core and dune OSL samples have been corrected for beta-dose attenuation and long-term water content (Aitken, 1998; Brennan, 2003; Mejdahl, 1979). The long-term water content for the Brown Lake OSL sample was considered to be equivalent to the empirical values determined as part of the LOI procedures, with separate corrections applied to the beta, gamma, and cosmic dose rate terms (see Table B1 for details). An assumed long-term water content of 7 ± 3 % was applied to the NSI18 dune samples, following approaches used in comparable OSL dating studies of dune deposits from the region (e.g., Ellerton et al., 2020).

Purified quartz grains (Ø 180–212 μm or 212–250 μm) were prepared using procedures described in Lewis et al. (2020), with single-grain equivalent dose (D_e) measurements undertaken using apparatus and conditions detailed in the Supplementary Information. Single-grain D_e values were determined using the single aliquot regenerative dose (SAR) procedure (Murray & Wintle, 2000), shown in Table B2. Individual D_e values were only included in the final age calculation if they satisfied a series of widely accepted quality assurance criteria (Table B3).

Bayesian age-depth models were produced for BL18 and BL09 cores in OxCal (Bronk Ramsey, 2009; Bronk Ramsey & Lee, 2013), following the procedures outlined in Lewis et al. (2020) and discussed in Appendix B. Separate depositional units have been included in the OxCal models for BL18 and BL09 on the basis of independent sedimentological and lithological interpretations (as detailed in the Results).

Brown Lake's sedimentological history, and the climate implications influencing deposition with respect to other North Stradbroke Island and Australian records, is discussed in relation to a subset of the eight phases identified through the OZ-INTIMATE climate synthesis (Reeves et al., 2013). We

have combined the early and late deglacial phases and considered the Holocene as a whole (Reeves et al., 2013).

Results

Sedimentology

The sediment units present in the BL18 (based on descriptions of BL18-3) and BL09 cores (Figure 3.3) are broadly similar and are dominated by very dark-brown to black lake mud with fine- to coarse-grained sands incorporated within the sedimentary matrix. BL18 contains three distinct units, Unit 1 (3.57–2.29 m), Unit 2 (2.29–1.65 m), and Unit 3 (1.65–0 m), each of which contains two sub-units. BL09 also contains three units denoted Unit A (3.98–3.14 m), Unit B (3.14–2.67 m), and Unit C (2.67–0 m) (Moss, 2013a).

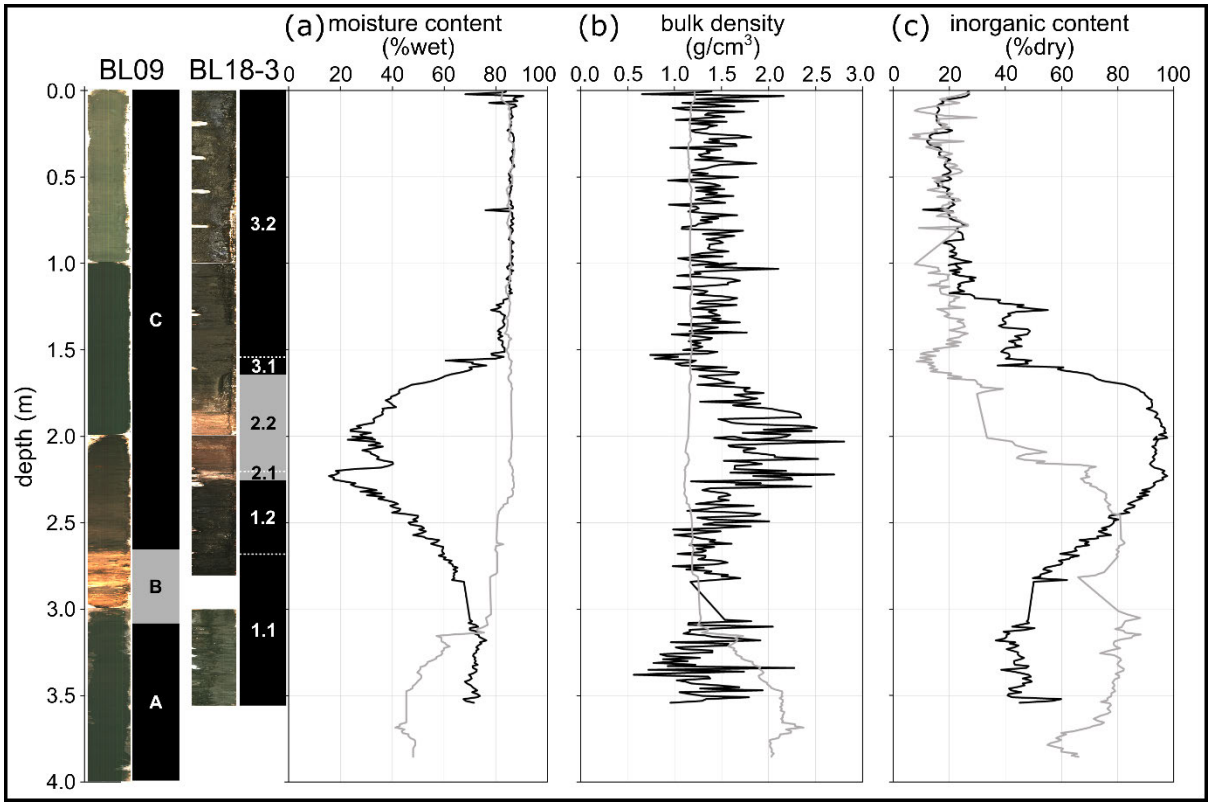

Figure 3.3 Optical images, sedimentary units, and properties of BL18 (black) and BL09 (grey) as measured using the loss on ignition approach. Graphs are aligned by depth and show sediment (**a**) moisture content, (**b**) bulk density, and (**c**) inorganic content.

The lowest units present in both cores (Unit 1 and Unit A; Figure 3.3) are very dark-brown to black mud (10YR 2/2, 10YR 2/1) with a blocky texture. In the BL18 core, sub-unit 1.1 (3.57–2.69 m) gradually becomes increasingly pliable towards the top of the unit. Sub-unit 1.2 (2.69–2.29 m) is distinguished by a transition from clay to more silty texture and an increased abundance of fine-grained sand. Additionally, this unit also hosts a thin (4 mm wide) coarse-grained sand vein that is perpendicular to the bedding for ~20 cm from the top of the unit.

In the BL18 core, Unit 2 is distinguished from Unit 1 by an overall increase in the proportion of sand. The base of the unit is identified by the presence of a distinctive thin (6 cm), coarse-grained sand layer that contains intermixed angular black clasts (<1 mm) and light brown grains (Figure 3.3) from 2.29 m. A distinctive contact with the underlying sub-unit 1.2 is identified by the juxtaposition of the grey-

white sand (10YR 7/1) overlying very dark brown mud (7.5YR 2.5/2). This sand layer is designated sub-unit 2.1 (2.29–2.23 m) and is only present in the BL18 record. The shared sedimentology between BL18 and BL09 is re-established from sub-unit 2.2 (2.23–1.65 m) and Unit B (3.14–2.67 m) upwards (Figure 3.3). The sedimentology of these units both increase in clay content up core with a decrease in the proportion of sand grains towards the surface more apparent in BL18. The sediment changes from the grey-white sand of sub-unit 2.1 into a dark brown (10YR 3/2) towards the middle, before grading into a black mud (10YR 2/1) towards the top. However, the colour gradient is not as obvious in BL09, due to the as the absence of the underlying sandy layer.

The youngest, and thickest unit in the BL18 and BL09 cores is Unit 3 (1.65–0 m) and Unit C (2.67–0 m), respectively (Figure 3.3). The base of this unit in BL18 is designated sub-unit 3.1 (1.65–1.55 m), which is characterized by the sediment having had transitioned from the mud of sub-unit 2.2 to a more organic-rich, silty clay-like texture. This subsequently transitions into the homogenous organic black (10YR 2/1) mud of sub-unit 3.2 (1.55–0 m). The change in texture between sub-unit 3.1 and 3.2 is concordant with the incorporation of very fine-grained sand material within the sediment matrix towards the top of Unit 3.

Moisture and organic content

The moisture and organic content of the BL18 and BL09 records reflect the sedimentary unit divisions (Figure 3.3). The sediment from BL18 has a wider range of moisture content (15.5 – 90.6 $\%_{wet}$), bulk density (0.5–2.8 g/cm^3), and inorganic content (10.5 – 97.7 $\%_{dry}$) than BL09 (41.1 – 87.2 $\%_{wet}$; 1.1 – 2.4 g/cm^3; 5.7 – 88.2 $\%_{dry}$). Our analysis of these properties focusses on BL18 because this core sequence would have experienced less physical alteration during the core extraction in comparison to BL09, which was extruded in the field.

Unit 3 of BL18 has the highest moisture content of the three units of the same core, with a mean value of ~84 % (Unit 2 and Unit 1 have mean values of 36 % and 61 %, respectively). Unit 2 has the highest inorganic content on average (91 $\%_{dry}$), which is more than double that of Unit 3 (26 $\%_{dry}$) and higher than Unit 1 (59 $\%_{dry}$). The sandy Unit 2 has a mean bulk density of 1.8 g/cm^3, which was considerably higher than that of Unit 3 and Unit 1 (both have an average of 1.4 g/cm^3). This difference in bulk density likely reflects the influence of increased inorganic material having been deposited within the soil matrix of Unit 2.

µXRF elemental scanning and principal component analysis

The elemental counts from the µXRF core scanning of BL18 and BL09 exhibit amplitude changes that correspond with transitions between sedimentary units (Figure 3.4, Figure B7). µXRF Rayleigh scattering (i.e., incoherent/coherent) had a strong correlation ($r^2 = 0.95$, p-value <0.05; Figure B2) with organic matter content as determined by LOI. Elements of interest (see Methods) were subsequently incorporated into a PCA to evaluate their variability down core. Elements associated with clastic terrestrial origins had high loadings on PC1 (Figure B1). Additionally, the correlation between these elements (Figure B1) suggests that the sediment chemistry is strongly influenced by the influx of aeolian transported inorganic material, as observed in neighbouring organic-rich wetland sediments (Kemp et al., 2020; Lewis et al., 2020). Geochemical variation driven by inorganic material deposition is further supported by the separate grouping of biogenic and lithogenic element proxies and ratios (Figure B1), particularly the low loading on PC1 for the organic indicator (i.e., inc/coh).

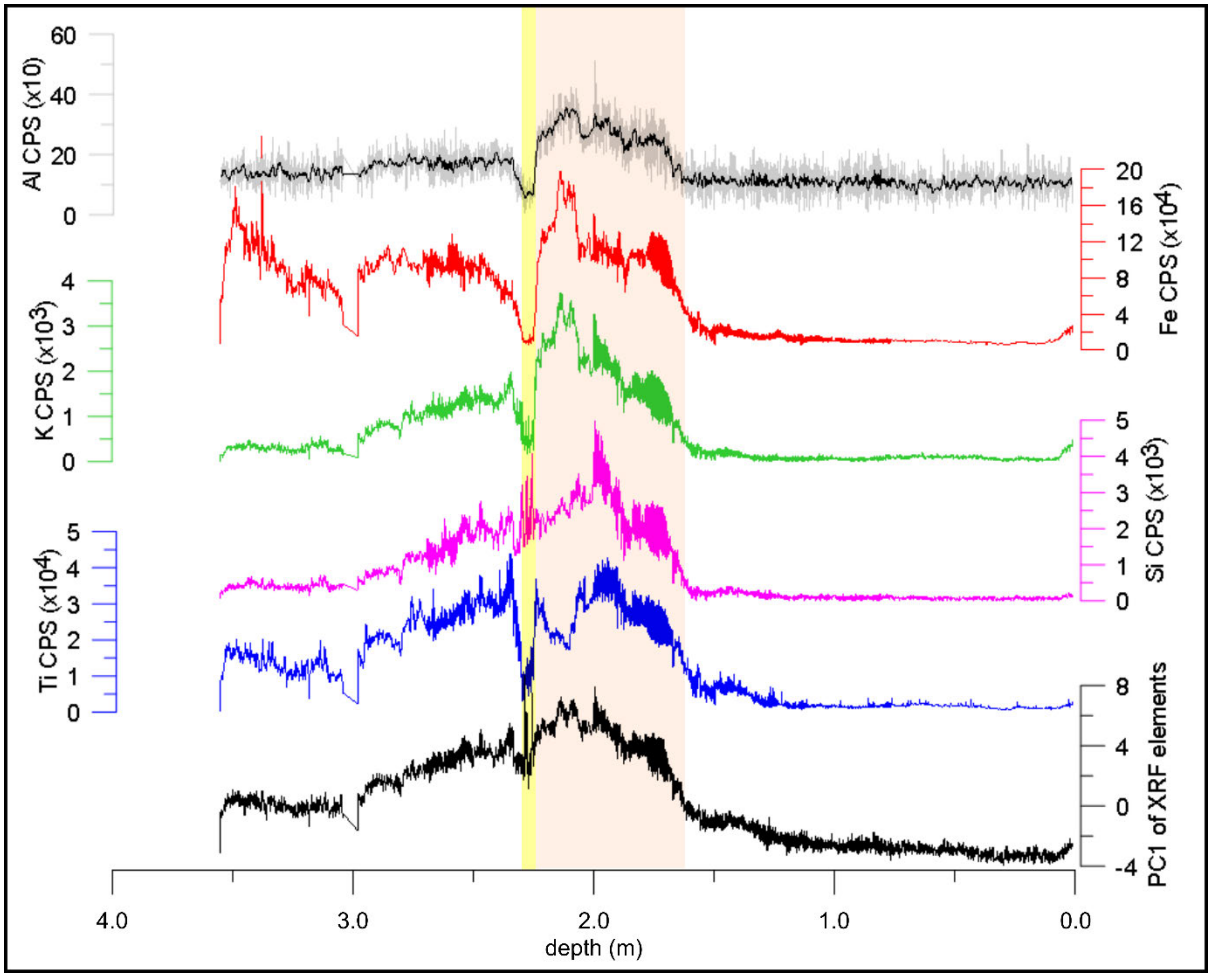

Figure 3.4 Scanning XRF elemental counts per second (CPS) of selected terrigenous elements (as identified using Principal Component Analysis). Aluminium elemental counts (grey line) overlain by a 10 point moving average (black line). Yellow and orange shading represent the sand (sub-unit 2.1) and transitional (sub-unit 2.2) layers observed in the BL18 sedimentary sequence, respectively. For biogenic element correlations the reader is directed to Figure B8.

Core correlation

Sequence-slotting successfully matched the element concentrations from BL18-4 to those in BL18-3, as shown in Figure B10. The potential range of sequence-slotting configurations is demonstrated in the H-matrix (Figure B10) (Gordon, 1982) and represents all possible depths at which slotting could occur. For this study, the central correlative depth is taken from the H-matrix to represent the best fit of the two cores thus used to project the depths of BL18-4 onto those of BL18-3. The suitability of using this approach is also supported by the high delta value (0.828), indicating that the sequences were well matched.

Chronology

^{14}C dating

The AMS ^{14}C ages obtained for BL18 and BL09 are presented in Table 3.1. Overall, there is stratigraphic agreement between the ^{14}C results from core BL18 and BL09. Moreover, the ages of replicate samples collected from the same depth in the BL18 core (OZX792/OZX793) overlap at 1σ. The ^{14}C sample extracted from the bottom of the BL18 core (OZX794a) produced a 95.4 % C.I. calibrated age range of 40,120 – 38,790 cal yr BP, which was confirmed with a replicate measurement (OZX794b = 40,400 – 39,070 cal yr BP). The ^{14}C ages for this sample are systematically younger than the overlying replicate samples (OZX792, OZX793), which yielded replicate 95.4 % C.I. calibrated age range of 48,790 – 45,620 cal yr BP and 49,830 – 46,710 cal yr BP, respectively. The cause of the inversion is currently uncertain and is possibly linked to sediment mixing from turbulence, humification, or both (Shore et al., 1995).

Table 3.1 Radiocarbon (^{14}C) ages for the samples extracted from BL18 and BL09 Brown Lake sediment cores, respectively. Ages have been calibrated against SHCal13 using the OxCal software (Bronk Ramsey, 2009; Bronk Ramsey & Lee, 2013; Hogg et al., 2013). All samples were treated using acid-base-acid (ABA) pre-treatments. The calibrated age range shown is the 95.4 % probability range (combining two or more potential calibration ranges, where they exist).

Lab Code	Depth (cm)	Material	δ13C	Conventional ^{14}C age (^{14}C yr BP)	Uncertainty (1σ)	Calibrated age range (cal yr BP) [c]
OZX784	20	Lake Sediment	-29.1	640	20	640 – 550
OZX785	43	Lake Sediment	-28.3	1430	25	1350 – 1270
OZX786	62	Lake Sediment	-33.8	2130	25	2150 – 2000
OZX787	80	Lake Sediment	-29.6	3100	25	3360 – 3180
OZX788	130	Lake Sediment	-29.6	5570	30	6400 – 6280
OZX789	163	Lake Sediment	-27.6	7120	30	7980 – 7840
OZX790	183	Lake Sediment	-27.3	16,660	70	20,310 – 19,790
OZX791	230	Lake Sediment	-27.9	36,570	290	41,790 – 40,430
OZX792[a]	258	Lake Sediment	-28.0	43,770	490	48,790 – 45,620
OZX793[a]	258	Lake Sediment	-26.6	44,870	410	49,830 – 46,710
OZX794a[b]	330	Lake Sediment	-28.0	34,970	220	40,110 – 38,790
OZX794b[b]	330	Lake Sediment	-28.2	35,230	190	40,400 – 39,070
Beta-361743	21	Organic Sediment	-29.7	540	30	550 – 500
Beta-361744	142	Organic Sediment	-29.9	2420	30	2680 – 2340
Beta-361745	167	Organic Sediment	-30.1	3310	40	3590 – 3390
Beta-361746	219	Organic Sediment	-25.3	6530	110	7580 – 7170
Beta-361748	376	Organic Sediment	-27.6	31,980	230	36,330 – 35,300
Wk-33179	386	Organic Sediment	-33.1	36,970	740	42,610 – 40,130

[a, b] replicate samples, which were combined in the Bayesian age-depth modelling using the OxCal 'combine' function.
[c] rounded to nearest ten years.

OSL dating

The results of the single-grain OSL D_e analysis and age determination are reported in Table 3.2 and Figure 3.5. The acceptance rate of grains for each OSL sample, following application of the SAR quality assurance criteria, ranged between 2 – 8 % (Table B3). Most samples (5 out of 8) exhibit relatively homogeneous single-grain D_e distributions with low overdispersion values of 18 – 20 %. These overdispersion values are consistent with those typically reported for well-bleached and undisturbed single-grain D_e datasets at 2σ (e.g., the average overdispersion of 20 ± 1 %; Arnold &

Roberts, 2009; Olley et al., 2004), as well as those reported for 'ideal' lacustrine samples from related North Stradbroke Island wetland localities (e.g., Kemp et al., 2020; Lewis et al., 2020). The final D_e values of these five samples (BL18-A, NSI18-1, NSI18-2, NSI18-3, and NSI18-6) have therefore been calculated using the central age model (CAM) (Galbraith et al., 1999).

Interestingly, the limited D_e scatter and low overdispersion obtained for Brown Lake sample BL18-A contrast with the D_e characteristics reported for sample GU5.3 from core BL09 (Tibby et al., 2017), despite being extracted from the same sediment body. Sample GU5.3 has an overdispersion of 40 % (approximately twice that of BL18-A; 19 ± 3 %), which was originally attributed to a combination of sediment disturbance (e.g., Arnold & Roberts, 2011) and insufficient resetting of residual signals prior to burial (e.g., Arnold et al., 2007; Arnold & Roberts, 2009). Given the homogenous D_e distribution we report for sample BL18-A, an alternative explanation for the GU5.3 D_e scatter might relate to the coring approach utilized (Tibby et al., 2017). Unlike the BL18 sediment, which was retained within the core tubes, the BL09 core was extruded in the field with limited protection from light exposure. Considering these contrasting sampling approaches, the BL09 sediment may have additionally experienced some vertical grain transfer or light contamination prior to OSL sampling, which could have given rise to a seemingly mixed or heterogeneously bleached D_e signature (incorporating both low and high D_e scatter). For the purpose of this study, we have included the originally published age for sample GU5.3 in our site assessment (45 ± 8.9 ka; Tibby et al., 2017) because it has been derived using a statistical age model designed to account for additional D_e scatter related to potential sampling contamination (finite mixture model; Galbraith & Green, 1990); although we note potential caveats regarding the original interpretation of this D_e dataset.

Three of the dune samples (NSI18-4, NSI18-5, NSI18-7) exhibit complex D_e distributions characterized by broad D_e scatter and high overdispersion values (43 ± 6 % to 74 ± 8 %) that do not overlap at 2σ with the site-specific 'baseline' estimates of underlying dose overdispersion determined from dune samples NSI18-1, NSI18-2, NSI18-3, and NSI18-6. Application of the FMM to these three D_e datasets also confirms the presence of multiple discrete dose components (Tables B4 – B6). Similar multimodal and scattered single-grain OSL D_e datasets have been reported elsewhere for the Cooloola Sand Mass (Walker et al., 2018), and have been interpreted as reflecting aeolian reactivation and localized reworking of original dune emplacements. This type of post-depositional mixing, whereby pre-existing aeolian deposits are incorporated into more recent dune building events, could be considered a possible explanation for some of the discrete dose components observed in samples NSI18-4, NSI18-5, and NSI18-7. However, given the low dose rates of these quartz-rich dune sands (Table 3.2), and the known presence of heavy minerals (zircons, monazites) and K-feldspar grains that could have acted as radioactivity hotspots in the Yankee Jack Formation (Tejan-Kella et al., 1990; Thompson, 1981), it is feasible that this enhanced dose dispersion could have arisen from spatial variations in beta dose rates experienced by individual grains (e.g., Nathan et al., 2003). Intrinsic sources of D_e scatter (e.g., Demuro et al., 2013) or bioturbation could have further contributed to the observed scatter in these three samples; though it is notable that such complications were not similarly observed in the other samples from these sites that displayed ideal D_e distributions (NSI18-1, NSI18-2, NSI18-3, and NSI18-6).

Table 3.2 Dose rate data, equivalent doses (D_e), overdispersion values, and OSL ages for lacustrine samples from Brown Lake and dune samples from North Stradbroke Island. The final age for each sample is shown in bold, which has been derived using the age model considered to be most appropriate on statistical and interpretative grounds (see main text and Tables B3–B6 for details).

ID	Wetland Catchment	Depth (cm)	Grain Size (μm)	Water Content (%Dry) [a]			Total Dose Rate (Gy/kyr) [b, c]	n/N [d]	OD (%)[e]	Age Model [f]	D_e (Gy) [c]	Final Age (ka) [c]
				Gamma	Beta	Cosmic						
BL18-A (BL18)	Brown Lake	353	180 – 212	253 ± 13	242 ± 12	340 ± 17	0.67 ± 0.04[e]	46 / 600	19 ± 3	**CAM**	**37.1 ± 1.3**	**55.6 ± 4.4**
GU5.3 [g] (BL09)	Brown Lake	397	180 – 212	24 ± 2	24 ± 2	68 ± 7	0.73 ± 0 14	66	40	**FMM**	**32.8 ± 2.0 (94%)**	**45.0 ± 8.9**
											16.3 ± 2.0 (6%)	22.4 ± 5.0
NSI18-1	Fern Gully Lagoon	160	212 – 250	7 ± 3	7 ± 3	7 ± 3	0.33 ± 0.02	31 / 900	19 ± 3	**CAM**	**34.5 ± 1.4**	**104.8 ± 8.7**
NSI18-2	Welsby Lagoon	183	212 – 250	7 ± 3	7 ± 3	7 ± 3	0.41 ± 0.03	32 / 900	18 ± 3	**CAM**	**63.5 ± 2.6**	**155.4 ± 11.7**
NSI18-3	Welsby Lagoon	150	212 – 250	7 ± 3	7 ± 3	7 ± 3	0.58 ± 0.03	37 / 900	20 ± 3	**CAM**	**59.1 ± 2.2**	**102.2 ± 7.6**
NSI18-4	Blue Lake	170	212 – 250	7 ± 3	7 ± 3	7 ± 3	0.30 ± 0.02	32 / 1100	46 ± 7	**CAM**	**50.9 ± 4.4**	**167.8 ± 19.1**
										FMM	37.0 ± 9.3 (51%)	122.0 ± 32.0
											70.54 ± 19.0 (49%)	232.6 ± 65.0
NSI18-5	Welsby Lagoon	70	212 – 250	7 ± 3	7 ± 3	7 ± 3	1.26 ± 0.07	32 / 1600	43 ± 6	**CAM**	**115.1 ± 9.5**	**91.0 ± 9.1**
										FMM	77.4 ± 7.7 (49%)	61.2 ± 7.0
											166.6 ± 14.5 (51%)	131.7 ± 13.6
NSI18-6	Brown Lake	170	212 – 250	7 ± 3	7 ± 3	7 ± 3	0.35 ± 0.02	37 / 600	19 ± 3	**CAM**	**42.1 ± 1.6**	**119.4 ± 9.4**
NSI18-7	Swallow Lagoon	130	212 – 250	7 ± 3	7 ± 3	7 ± 3	0.40 ± 0.03	55 / 1100	74 ± 8	**CAM**	**10.4 ± 1.1**	**25.8 ± 3.2**
										FMM	4.5 ± 0.3 (36%)	11.2 ± 1.1
											10.8 ± 1.0 (29%)	26.8 ± 3.1
											24.2 ± 1.8 (35%)	60.1 ± 6.0

[a] Long-term water contents used for beta / gamma / cosmic-ray dose rate attenuation, respectively, expressed as % of dry mass of mineral fraction, with an assigned relative uncertainty of ±5%. For sample BL18-A, the final beta dose rate has been adjusted for moisture attenuation using the measured water contents determined from the midpoint of the OSL sample depth. The final gamma dose rate has been adjusted using the average water content measured from the OSL sample midpoint, as well as from 1 cm^3 bulk sediment samples collected for the overlying and underlying 10 cm depth. The final cosmic-ray dose rate has been adjusted using the average water content measured from 1 cm^3 bulk sediment samples collected at 1 cm intervals throughout the overlying core sequence (refer to Figure 3.3). For the NSI18 samples, beta, gamma and cosmic dose rates have been corrected using a fixed long-term water content of 7 ± 3%, following approaches used in comparable OSL dating studies of dune deposits in the region (e.g., Ellerton et al., 2020).

[b] Individual dose rate components (i.e., gamma, beta, internal and cosmic dose rate contributions) are outlined in Table B1.

[c] Mean ± total uncertainty (68% confidence interval), calculated as the quadratic sum of the random and systematic uncertainties.

[d] Number of D_e measurements that passed the SAR quality assurance criteria and were used for D_e determination (n) / total number of grains analysed (N).

[e] OD = overdispersion; the relative spread in the D_e dataset beyond that associated with the measurement uncertainties for individual D_e values.

[f] CAM = central age model; FMM = finite mixture model. See Tables B4 – B6 for details of the FMM fitting results. The FMM parameter values shown here were obtained from the optimum FMM fit (i.e., the fit with the lowest BIC score; Arnold & Roberts, 2009). Percentage values shown in parentheses refer to the proportion of measured grains falling within each identified FMM dose component. The FMM dose component containing the highest proportion of accepted grains has been nominally selected for the final FMM D_e calculation, see main text for further discussions and sample-specific interpretations.

[g] Sample GU5.3 is taken from core BL09 and was originally presented in Tibby et al. (2017). This sample is included for comparative purposes is presented according to the information provided in the original publication.

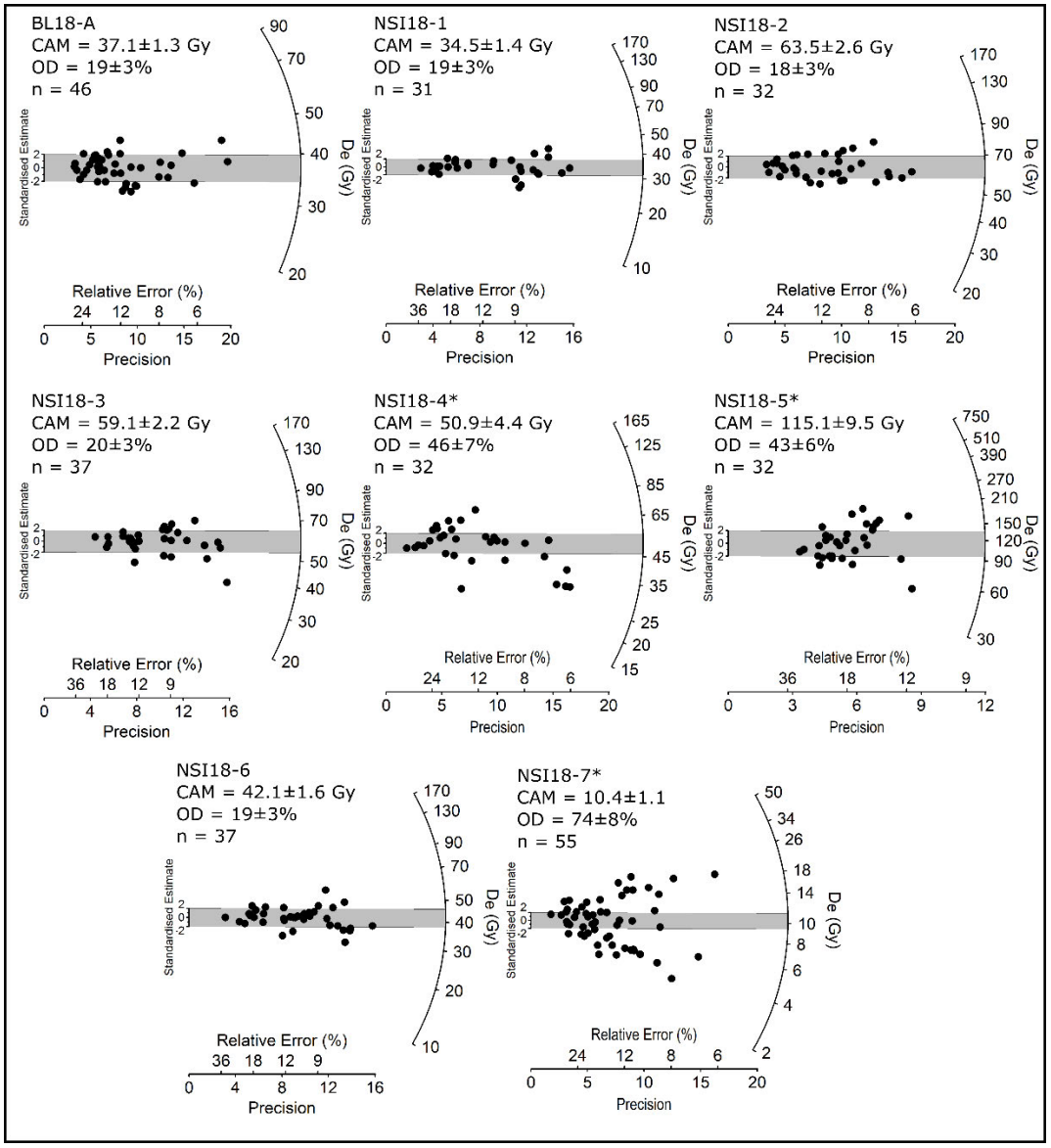

Figure 3.5 Radial plots showing the single-grain D_e distributions obtained for OSL samples from the BL18-3 core and NSI18 dunes. The grey shaded band on each plot is centred on the D_e value (in Gy) used for the final age calculation. For all samples, the D_e value has been calculated using the central age model (CAM) of Galbraith et al. (1999). For comparative purposes, the finite mixture model (FMM) dose components identified for samples marked with an asterisk (*) are shown in Figure B5b.

The difficulties of ascertaining the true underlying sources of D_e scatter for NSI18-4, NSI18-5, and NSI18-7, and the impracticalities of retrospectively calculating suitable dose rates for the identified multiple dose components, mean that use of the FMM for OSL age evaluation is not necessarily straightforward in this study. These interpretive complications are compounded by the fact that the identified components of each sample contain very similar proportions of grains (i.e., there are no clear dominant dose components). As a pragmatic solution, we have therefore used the CAM D_e and bulk (sample-averaged) dose rate to derive the final age estimates for NSI18-4, NSI18-5, and NSI18-7 (Table 3.2). For comparative purposes, Table 3.2 also shows the ages derived for these samples using the FMM components, assuming that the sample-averaged dose rates are broadly representative of those experienced by individual dose components during burial. This assumption may be reasonable given the shared local source of accumulated sediment in a given dune field, but further research would be required to demonstrate its suitability for the individual deposits under consideration here.

The CAM ages for samples NSI18-4 and NSI18-5 are broadly consistent (at 2σ) with those obtained for the well-bleached and unmixed samples from the Yankee Jack Formation (Table 3.2). However, the CAM age for NSI18-7 is significantly younger than those obtained at our other dune study sites, as well as those published previously by Walker et al. (2018) and Ellerton et al. (2020). Reliable interpretation of NSI18-7 is complicated by the identification of three discrete FMM dose components, and we cannot discount the possibility that this sample has been compromised by significant post-depositional sediment mixing or disturbances related to recent human activity (e.g., forestry operations; Walker et al., 2018).

Lake sequence age modelling

The Bayesian age-depth models for the Brown Lake sedimentary sequences, as produced using OxCal v4.3.2 (Bronk Ramsey, 2017), are shown in Figure 3.6. The likelihood estimates of the BL18 and BL09 sediment cores are constrained by two single-grain OSL ages (BL18-A and GU5.3, respectively) and a combined total of sixteen ^{14}C ages. A preliminary version of the BL18 age-depth model included the replicate OZX94a and OZX94b ^{14}C ages. However, the modelled likelihood estimates failed to converge, with these two samples identified as statistical outliers (79 %) owing to their incompatibility with the surrounding OSL (BL18-A) and ^{14}C ages (OZX793 and OXZ792). As such, these two major outliers were not included in the final Bayesian age-depth model for BL18.

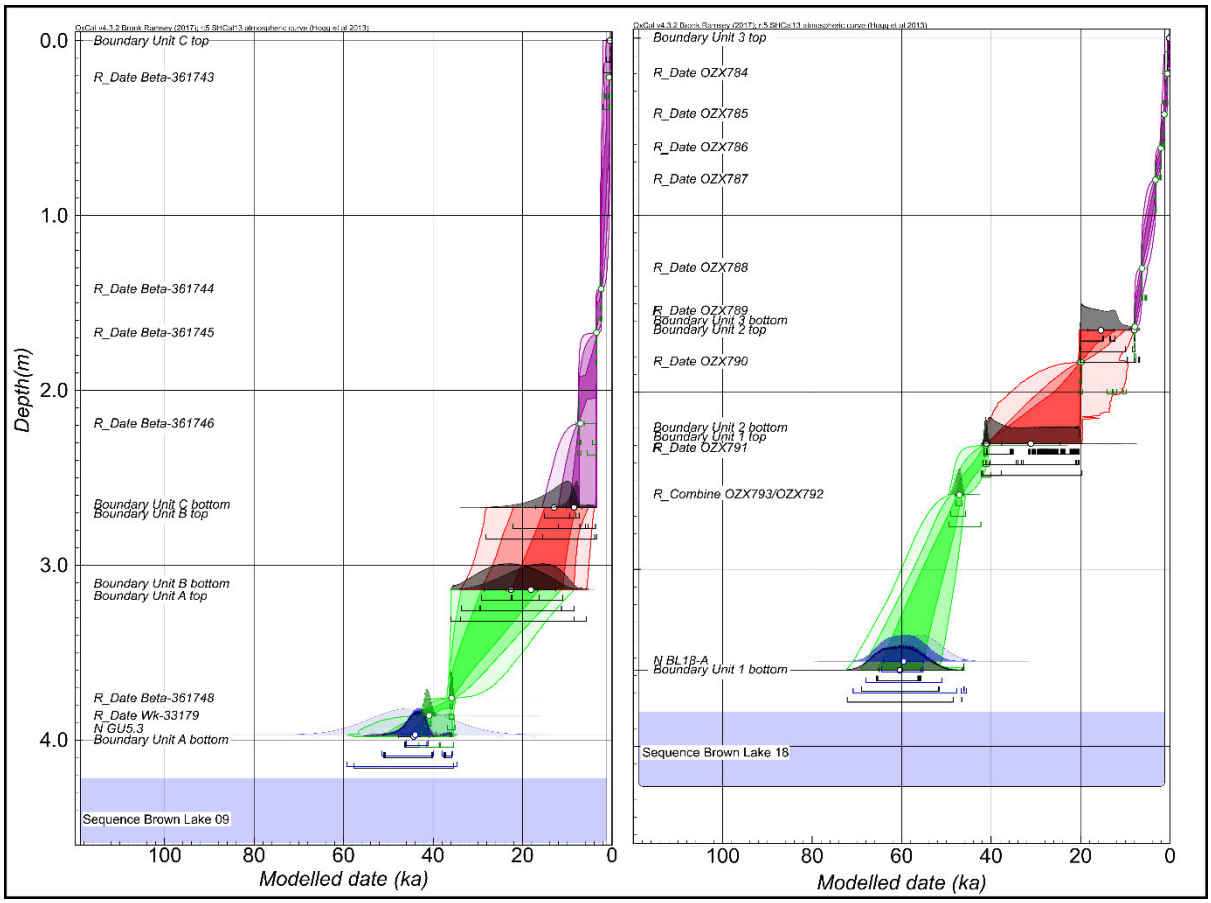

Figure 3.6 Bayesian age-depth model constructed in OxCal version 4.3.2 using the single-grain OSL and ^{14}C ages obtained for the BL09 (left) and BL18 (right) cores. The original probability distributions for the OSL (blue) and ^{14}C (green) age estimates (the likelihoods) and the posterior modelling distributions are represented as light and dark shading of the respective colours. The age-depth model envelopes show the 99 %, 95 %, and 68 % highest probability density ranges for each of the main depositional units (green, red, and magenta), as identified by sedimentological analysis. The modelled posterior distributions for the unit boundaries are shown in grey.

The BL18 and BL09 Bayesian models have agreement index (A_{model}) values of 100.4 % and 101.2 %, respectively, and overall agreement index ($A_{overall}$) values of 99.9 % and 100.6 %, respectively—all above the minimum threshold of 60 % (Bronk Ramsey, 2009). The outlier analysis of BL09 identified Beta-361743 as having a relatively high posterior probability of 22 %. In core BL18, there were no samples that had exceptionally high posterior outlier probabilities (Figure 3.6), with combined ^{14}C samples OZX793/OZX792 identified as having low outlier probability of 8 %. The modelled boundary ages and use of the OxCal Difference query (see Appendix B) show for the lowermost BL09 unit (Unit A) and equivalent BL18 unit (Unit 1) that deposition occurred between 44.3 ± 3.4 – 22.5 ± 6.0 ka and 60.4 ± 4.7 – 41.1 ± 0.6 ka, respectively. Deposition of the overlying units (BL09, Unit B; BL18, Unit 2) initiated ca. 18.1 ± 5.6 ka and 31.2 ± 6.5 ka, and ceased at 12.9 ± 4.2 ka and 15.5 ± 3.0 ka, respectively.

Discussion

North Stradbroke Island OSL dune ages

The majority of dune crest ages in this study—excluding NSI18-7, for which the timing is uncertain due to the complex distribution of the grain populations (Figure 3.5)—corroborate previously inferred dune activation during MIS5 on North Stradbroke Island (Pickett et al., 1989; Tejan-Kella et al., 1990). Additionally, none of the final dune ages shown in Table 3.2 overlaps with the timing of the LGM (with the exception of the potentially compromised sample NSI18-7), suggesting limited mobilization of dune material at this time, despite increased aridity inferred from low lake levels (Figures 3.7 & 3.8).

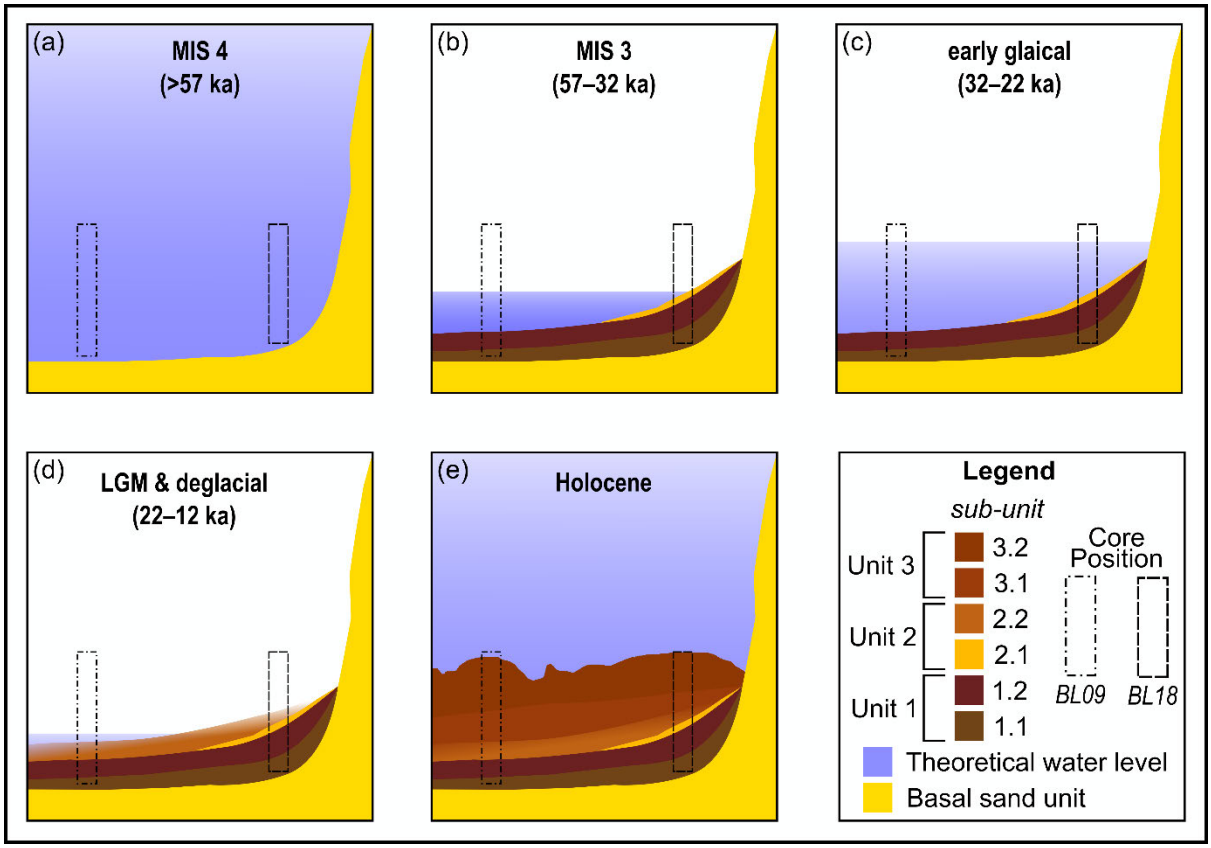

Figure 3.7 Conceptual model of sediment deposition and water level at Brown Lake during major climate phases referred to in text. The BL18 stratigraphic log was selected to represent the sedimentary units for the basin.

The mean OSL age for the samples in this study excluding NSI17-7 is 119.9 ± 10.6 ka. Notably, this overlaps with the timing of the Yankee Jack unit emplacement reported (e.g., Ellerton et al., 2020) (Figure 3.8) and supports the local distribution of the morphosequence as remapped using remote sensing (Patton et al., 2019) (Figure 3.1b). The OSL results from this study show limited dune building during the LGM on North Stradbroke Island despite increased aridity, a similar finding to Fraser Island (Miot da Silva & Shulmeister, 2016) and across the Cooloola Sand Mass (Ellerton et al., 2020). There appears to be a link between dune emplacement and higher sea-levels during MIS5 (Figure 3.8). This finding is in agreement with dune activation mechanisms proposed in the south-east Australian dune fields (Ellerton et al., 2020; Lees, 2006, 2006). Moreover, the absence of substantial evidence indicating Holocene activation suggests the sand dunes had stabilized soon after deposition. However, an increase in the spatial resolution of dune samples across North Stradbroke Island is required to fully assess this hypothesis.

Lacustrine sediment accumulation in wetlands within the Yankee Jack dune sequence did not initiate synchronously, based on our regional dating comparison (i.e., Fern Gully Lagoon = ca. 209 ka, Kemp et al., 2020; Welsby Lagoon = ca. 83 ka, Lewis et al., 2020; and Brown Lake = ca. 60 ka, Figure 3.8). This supports the notion that the formation of the respective perching layers is not dictated purely by the mineralogical composition of the Yankee Jack dune sequence. Rather, it was likely a combination of local catchment morphology and hydroclimate (*cf.*, Brooke et al., 2008).

Brown Lake BL09 and BL18 age models

The difference in sediment accumulation rate between the two Brown Lake records (Figure 3.6) suggests that sedimentation was influenced by their position relative to water level (Figure 3.7). The bathymetry of the modern lake-floor has a downwards slope trending in a north-east direction with an undulating surface (Figure 3.2). During times of lower lake level, water turbulence in combination with the uneven surface may have changed the position of the fine-sediment accumulation zone (Blais & Kalff, 1995). This change in the sediment-focusing position would likely not affect the deposition of the sand band because this feature is likely accumulation of local material near the edge of the lake (Figure 3.7); thus, explaining why the distinctive sand band is observed in BL18 and not BL09.

The difference between the ages for the BL18 and BL09 records may also be grounded in the resolution of input parameters in the age model. The BL18 age-depth model has a resolution of more than three dating samples per metre (ten ^{14}C samples, including one replicate from 258 cm, and one OSL sample), whereas BL09 has notably fewer (six ^{14}C samples and one OSL sample) (Tables 3.1 & 3.2). The proximity of the individual age estimates to the unit boundaries in each core also likely influences the age model outcomes. For example, the transition between Unit 2 and Unit 3 in BL18 is bracketed by ^{14}C samples OZX790 and OZX789 (Table 3.1; Figure 3.2), thereby increasing confidence that the depositional interval has been modelled accurately. In contrast, the same boundary transition in the BL09 core (i.e., Unit B and Unit C transition) is not as well constrained, and the modelled age for Unit B relies on interpolation between ages from underlying and overlying units (Table 3.1, Figure 3.6). The disparity in ages observed between parts of the BL18 and BL09 cores highlights the need to understand basin morphology, and the importance of developing robust age models before drawing inferences from palaeoenvironmental proxies.

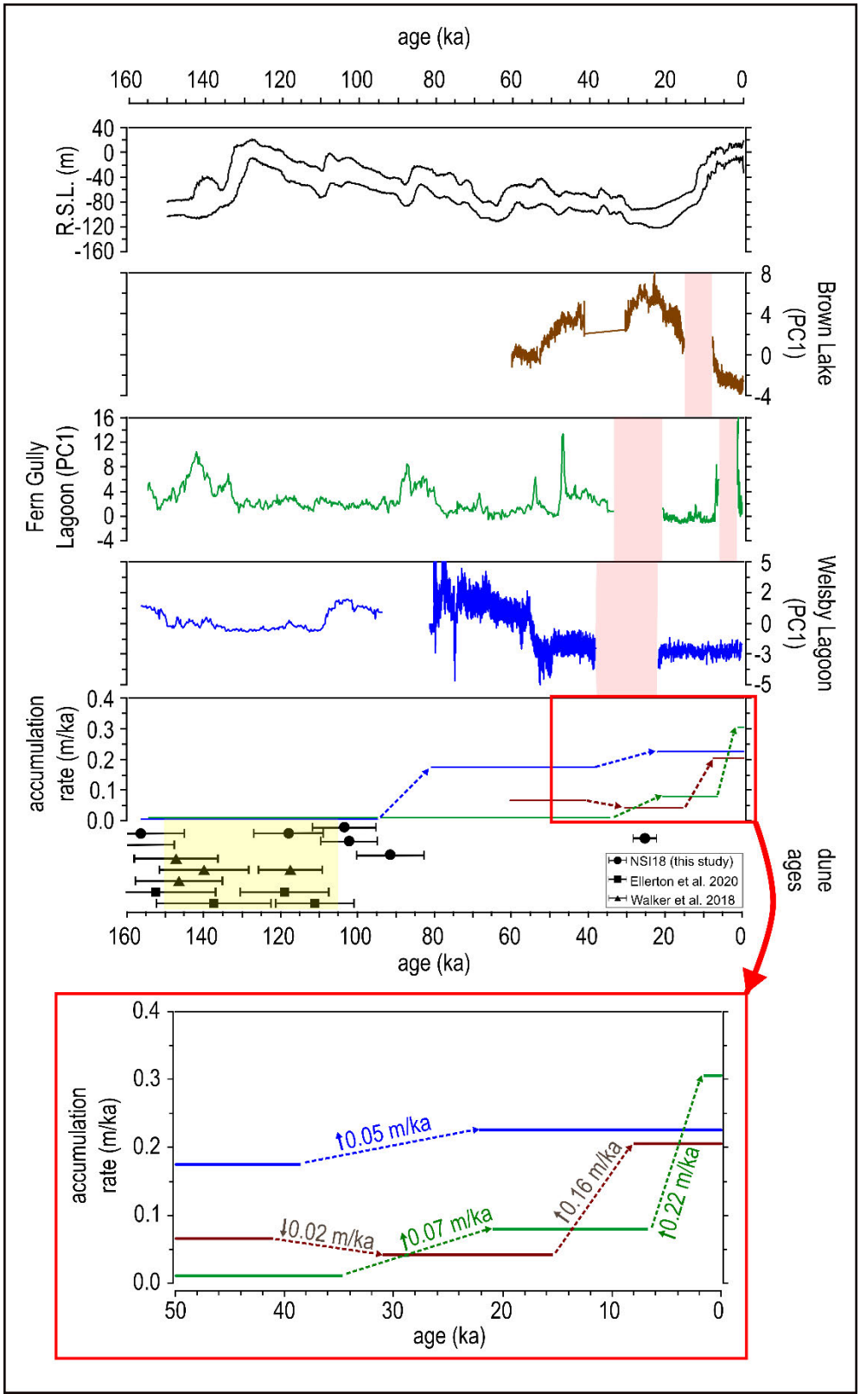

Figure 3.8 North Stradbroke Island wetland records with an extended range of inorganic sediment accumulation, and North Stradbroke Island dune crest ages over the last 160 ka. A global sea level curve is shown (Grant et al., 2014) (R.S.L. = relative sea level) along with the Brown Lake, Fern Gully Lagoon (Kemp et al., 2020), and Welsby Lagoon (Lewis et al., 2020) inorganic sediment accumulation records. The pink areas represent hiatus periods experienced at these wetlands. The red rectangle and arrow show the portion of the graph expanded in the bottom inset and identifies the change in mean accumulation rate between the wetland records. Dune OSL ages from this study (circles) are compared with those of Ellerton et al. (2020) (squares) and Walker et al. (2018) (triangles) from the Cooloola Sand Mass, with the timing of Yankee Jack dune building highlighted in yellow (Ellerton et al., 2020).

History of aeolian sediment deposition in Brown Lake

The change and variability inferred from Brown Lake are based on the BL18 record, which has the better age-depth model. Reconstructing the broader evolution of the wetland, however, considers both BL18 and BL09 (Figure 3.7) and draws on comparisons to other North Stradbroke Island records where variation in inorganic sediment geochemistry has been used to infer aeolian deposition (e.g., Kemp et al., 2020; Lewis et al., 2020; Moss et al., 2013; Petherick et al., 2008). In this study, comparisons to Welsby Lagoon have utilized the alternate age-depth model presented in Lewis et al. (2020) (Figure A5b). The use of this alternate age model was preferred given the co-occurrence of hydrological change inferred in the Brown Lake and Fern Gully Lagoon records, the expression of which appears dampened in Welsby Lagoon due to its transition from a lake to a swamp (Cadd et al., 2018). Use of this alternative age model is acceptable because it was shown to be relatively insensitive to the choice of stratigraphic priors (Lewis et al., 2020). Moreover, interpretations of dust flux were considered with respect to increased atmospheric dust loads (Harrison et al., 2001), which in Australia resulted from reduced vegetation due to drier climate (Hesse & McTainsh, 2003; McGowan et al., 2008), changing wind direction or strength (Kohfeld et al., 2013), sediment recharge in dust-source areas (Farebrother et al., 2017), or a complex mix of all these variables in response to hydrological variation (Marx et al., 2018).

MIS4 (>57 ka)

The mean modelled age for the base of Brown Lake (BL18) is 60.4 ± 4.7 ka (Figure 3.6), though the perched indurated layer must have formed before this time. Prior to this study, the oldest date from Brown Lake (BL09) was 47.2 ka (Tibby et al., 2017). The early portion of the Brown Lake MIS4 sedimentary record (Figure 3.7a) likely accumulated during a phase of positive moisture balance with a lowered influx of aeolian material (Figure 3.9) and lake-full conditions promoting substantial organic matter production and preservation (Figure 3.7). The Fern Gully Lagoon record also has a low inorganic flux through MIS4 (Kemp et al., 2020; Figure 3.9), which may be related to increased vegetation cover. Because dust on North Stradbroke Island is sourced from the central Australian basins (Cohen et al., 2015; Magee et al., 2004; Miller et al., 2016) during MIS4, it is likely that the coeval decline in dust flux is linked to wetter conditions regionally—an inference that would support the increase in rainforest taxa in ODP820 offshore from north-east Queensland (Kershaw et al., 2003). However, inferring climate from changes in dust flux sourced far afield should be made with caution because moisture and vegetation are not the only variables influencing dust mobilization. Dust flux can be influenced by source area surface aerodynamics (Webb & Strong, 2011) and sediment recharge (Marx et al., 2018). The inorganic flux to Brown Lake and North Stradbroke Island is likely influenced by widespread fluctuations in moisture across Australia (Farebrother et al., 2017), with an additional factor being changed vegetation regimes from deep-rooted trees and shrubs to grasses and herbs.

MIS3 (57 – 32 ka)

The Brown Lake MIS3 record shows increasing variation in PC1, attributed to progressively increasing influx of inorganic windswept material into the basin relative to MIS4 (Figure 3.9) rather than a proportional decrease in organic production (Figure 3.7a, b). This is particularly notable between ca. 54 ka and 41 ka (Figure 3.9), with concurrent trends observed in the Welsby Lagoon and the Fern Gully Lagoon records. However, unlike Fern Gully Lagoon, where two peaks of inorganic deposition occur at ca. 54 ka and ca. 47 ka (Kemp et al., 2020), the Brown Lake record shows a

gradual increase in aeolian deposition through MIS3, suggesting the difference may be attributed to local factors such as variation in lake water surface area, current flow, or vegetation regime changes influencing dust transport into the wetlands (Cadd et al., 2018). The history of marginal dune vegetation is not as well established for Brown Lake, in contrast to some other North Stradbroke Island sites (e.g., Moss et al., 2013).

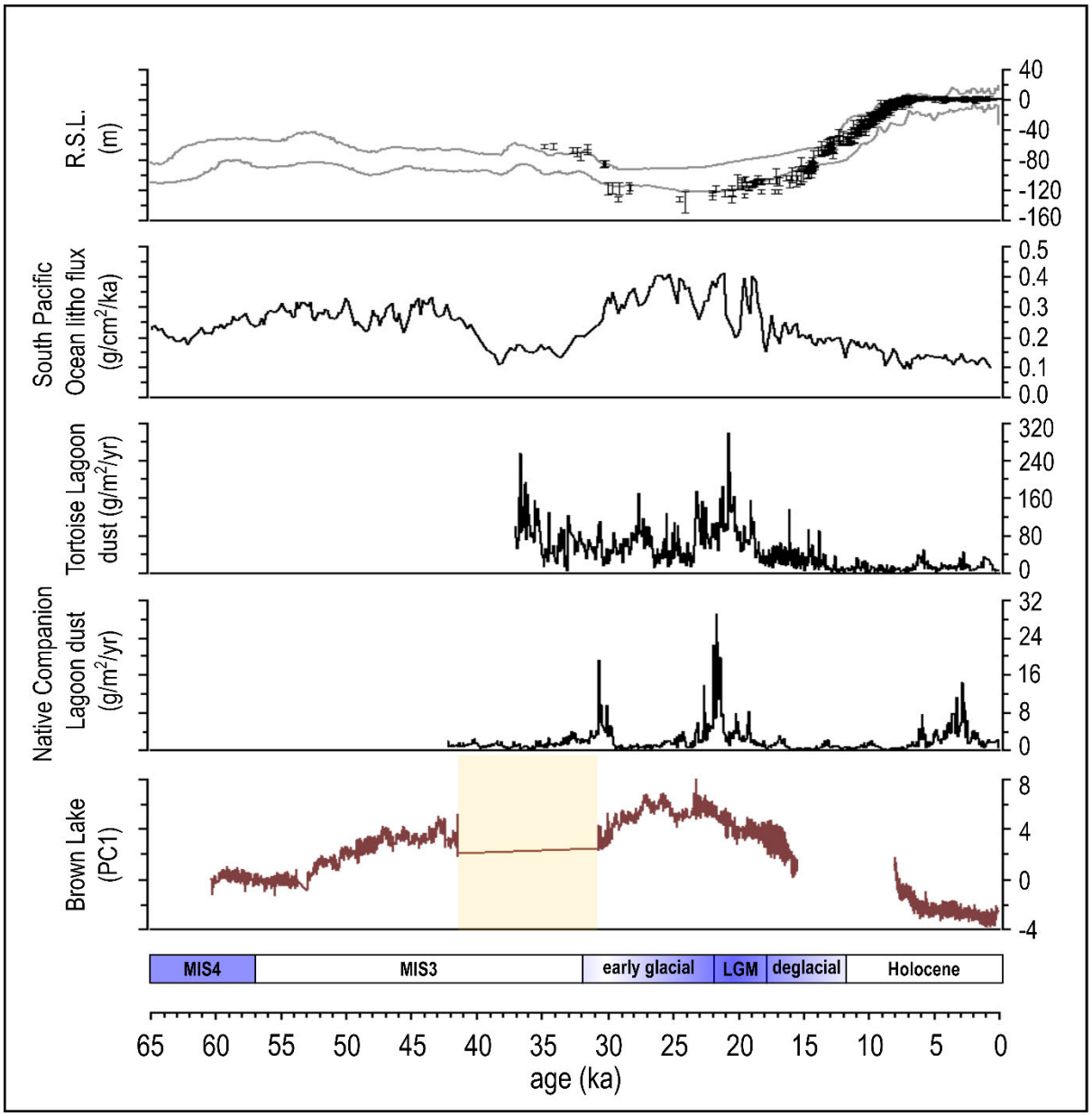

Figure 3.9 Compilation of dust and inorganic flux records from North Stradbroke Island and the ocean for the past 65 ka. Periods shown are modified from those identified in the OZ-INTIMATE climate synthesis (Reeves et al., 2013). The dust records shown include dust flux from Tortoise Lagoon, Native Companion Lagoon (Petherick et al., 2011, 2017), the South Pacific Ocean (Lamy et al., 2014), and Brown Lake. Relative sea level data from the Red Sea (Grant et al., 2014) are displayed in grey and overlain by composite sea-level record data (Lambeck et al., 2014). The yellow shaded box represents a potentially eroded section containing mixture of non-lacustrine and aeolian material, as discussed in the text.

MIS3 and early glacial period

Through MIS3, Brown Lake experienced a phase of sustained negative moisture balance, subsequently leading to shoreline transgression and deposition of the sandy sub-unit 2.1 ca. 30.9 ka (Figure 3.7). The extent to which fire was a factor in enhancing local sand transportation remains unclear because charcoal records from nearby Welsby Lagoon show limited evidence for increased activity between MIS4 and MIS3 (Cadd et al., 2018; 2020). Moreover, owing to the lack of structure in the black muds (Unit 1) of Brown Lake, it is difficult to determine whether disruption occurred during the emplacement of the sandy sub-unit 2.1. Additionally, when considering the spatial variability factors such as fires and surface roughness have on sediment erosion (Sankey et al., 2011), it is unreasonable to exclude deposition of the sand layer as occurring as part of a rapid event (e.g., storm activity). Nevertheless, there is a relationship between the increase in dust flux to Brown Lake (Figure 3.9) and lower lake water levels, indicating negative moisture balance locally.

Wetlands nearby Brown Lake, (i.e., Fern Gully Lagoon and Welsby Lagoon records) also show a hiatus in late MIS3 (Figure 3.8 & Figure 3.9) and support lower precipitation. This is contrary to the Tortoise Lagoon and Native Companion Lagoon records, which continue to accumulate dust through this phase, although at a decreased rate (McGowan et al., 2008; Petherick et al., 2008; Petherick et al., 2017), and generally support a regional shift towards warm and wet conditions; as suggested by pollen records (Moss, 2013b). The disparity between these sites may be attributed to contrasting local catchment conditions and morphologies, which may have altered sediment infilling dynamics (e.g., Fern Gully Lagoon and Welsby Lagoon), shoreline migrations (e.g., Brown Lake), establishment of denser vegetation communities in close proximity (e.g., Tortoise Lagoon and Native Companion Lagoon), or a combination of these factors. Given age models show breaks in the Brown Lake, Fern Gully, and Welsby Lagoon cores are coeval, the cause of which is considered to be a result of more arid conditions attributed to changes in the relative positioning and strength of ENSO (Merkel et al., 2010) and key rainfall bands across the Pacific Ocean—as shown in modern interannual climate models (Brown et al., 2020). Therefore, the suppression of rainfall across the Brown Lake catchment during glacial times would cause water level to fall and shorelines to regress. Moreover, reduced evaporation from lowered temperatures may have prevented the lake drying completely as reported in nearby wetlands (Cadd et al., 2018). However, as presented in the age model results and supporting information, the choice of age model may affect the interpretation of lake evolution. As glacial conditions began to weaken North Atlantic meridional overturning circulation, thus modifying ENSO once more, changing local precipitation patterns and the strength of winds carrying continentally sourced dust to North Stradbroke Island (e.g., Harrison, 1993; Petherick et al., 2008). This ultimately drove the changes in lake water levels for wetlands, particularly Brown Lake, and allowed them to persist through MIS2 (Figure 3.7c, d).

Last glacial maximum (21 – 18 ka)

The Brown Lake, Fern Gully Lagoon, and Welsby Lagoon sediment records show that there has been a pause in, or erosion of, lacustrine deposition leading into the LGM (Figure 3.9). The difference between these records, despite their relatively close proximity (<8 km; Figure 3.1), may reflect local variations in conditions favouring expansion of the indurating layer (Brooke et al., 2008), subsequently leaving wetlands with smaller perched aquifer catchments more susceptible to water level decline and shoreline regression during periods of moisture stress. Additionally, differences between the wetlands at this time (e.g., Welsby Lagoon transitioning into a swamp; Cadd et al., 2018)

may have limited their ability to accumulate aeolian material. The various morphological changes that these wetlands can experience have profound influences on how records may be interpreted, highlighting the need establish thoroughly dated records in order reliably compare to regional archives of an early glacial change.

The Brown Lake record shows that dust deposition was highest through the early glacial and LGM phases, peaking at ca. 23 ka (Figure 3.9), a timing comparable to peaks observed in the Native Companion Lagoon (Petherick et al., 2008) and Tortoise Lagoon (Petherick et al., 2017). Considered together, the agreement between these North Stradbroke Island wetlands could indicate a localized signal attributed to dune destabilization from vegetation burning and enhanced dust mobilization, although there is limited change in the charcoal record (Cadd et al., 2020). A similar dust record is reflected in South Pacific Ocean marine cores (De Deckker, 2001; Lamy et al., 2014), where it is suggested dust generation was a result of regional climatic change. Thus, it can be inferred that the Brown Lake record hosts information related to the increased supply, entrainment, and transport of material from regional dust sources (Marx et al., 2018), the deflation of which was enhanced by drier conditions associated with the early glacial period and into the LGM. Moreover, the dust transportation pathways (Petherick et al., 2009) show the source of the inorganic material was far-travelled, originating from the Australian mainland, where dust generation was linked to changes in moisture balance (Hesse & McTainsh, 2003). Movement of the South Pacific Convergence Zone and the on-flowing effect to how ENSO is expressed have the capacity to influence generally drier conditions, including enhancement of the SW winds, through displacement and suppression of other synoptic fronts on the east coast (Brown et al., 2020; Rudeva et al., 2019).

The modelled mean accumulation rate for Brown Lake through the LGM (0.04 m/ka) was surprisingly lower than MIS3 (0.06 m/ka) (Figure 3.8), although this may reflect limited age-model precision between Unit 2 and Unit 1. Therefore, the Brown Lake data should be expected to be in agreement with Fern Gully Lagoon and Welsby Lagoon, which show accumulation rates increasing from 0.01 m/ka to 0.08 m/ka (Kemp et al., 2020) and 0.17 m/ka to 0.23 m/ka (Lewis et al., 2020), respectively (Figure 3.8). Furthermore, an increase in lithogenic material accumulation would correlate with increased atmospheric dust loads (Harrison et al., 2001), which likely resulted from drier climate, albeit modulated by other factors.

The variation in chemical composition in the Brown Lake record for the early glacial phase and LGM (i.e., the clays of Unit 2) supports the hypothesis that dust was being sourced outside of North Stradbroke Island (Petherick et al., 2009). Moreover, the sedimentological properties of sub-unit 2.2 suggest that the Brown Lake water level fluctuated soon after the LGM, falling below the sediment surface between 15.4 ± 3.1 ka (top of Unit 2) and 8.0 ± 0.2 ka (bottom of Unit 3) (Figure 3.7c, d). The timing of this break in sedimentation is different from other North Stradbroke Island wetlands (Figure 3.9) and may be a product of different conditions between each catchment, or their respective age models. Nevertheless, the mechanism influencing precipitation across the catchments is likely regional, possibly linked to the Antarctic Cold Reversal (Barr et al., 2017), or ENSO because geographically separate climate records across the Australian continent also indicate a change towards more positive moisture balance during the deglacial phase (Petherick et al., 2013; Turney et al., 2006b; Williams et al., 2009).

The Holocene (11.7 – 0 ka)

Following the depositional hiatus at Brown Lake during the deglacial period, a return to higher lake levels, according to our model, occurred ca. 8 ka and allowed aeolian inorganic material to accumulate once again. Notably, the timing of the hiatus is in agreement with drier conditions observed in Lake Allom from the nearby Fraser Island (Donders et al., 2006). Because the increase in lake water level is coeval between two separate lakes, it is more likely this reflects a regional increase in moisture across eastern Australia, the timing of which aligns with enhancement of Southern Hemisphere circulation (Woodward et al., 2014). The Brown Lake, Welsby Lagoon, and Fern Gully Lagoon records have contrasting Holocene dust flux, with Brown Lake showing a declining PC1 signal, Welsby Lagoon relatively stable (Lewis et al., 2020), and Fern Gully Lagoon showing an increasing flux (Kemp et al., 2020) (Figure 3.9). The variance between the records may be linked to differing hydrological sensitivities, chronological model frameworks, or other site-specific factors (Cadd et al., 2018) Conversely, following the hiatus at Brown Lake, the basin returned to a deeper lacustrine system similar to its expression today (Figure 3.7e). Elsewhere, the smaller catchment size of Fern Gully Lagoon relative to other North Stradbroke Island wetlands (Kemp et al., 2020) appears to have increased the wetland's susceptibility to drying out during periods of lower rainfall on the island (Barr et al., 2019).

Differing human land-use practices may also be a factor in the different signals observed in the wetland records. Increased burning may have induced changes in vegetation cover (Barr et al., 2017; Mariani et al., 2019), thereby altering the erosivity of the soil. However, information pertaining to human occupation on North Stradbroke Island is limited, with late Pleistocene archaeological evidence from Wallen Creek providing the earliest known activity (ca. 20,560 ± 250 ^{14}C yr BP; SUA-2341, Neal & Stock, 1986).

Conclusion

Single-grain OSL ages obtained on dune crests in this study indicate activation of the Yankee Jack dune sequence on North Stradbroke Island through MIS5, the earliest initiation being 167.8 ± 19.1 ka. Subsequent to this prominent phase of dune building, there was long-term stabilization of the local dune landscape with no indication of subsequent large-scale dune mobilization. This may be attributed to vegetation stabilizing the MIS5 age dunes of North Stradbroke Island shortly after emplacement by 91.0 ± 9.1ka.

The new palaeoenvironmental record from Brown Lake, which includes a Bayesian age depth model derived from 10 (ten) ^{14}C ages and an OSL date, has enabled inference of climate variability over the past 60 ka. Geochemical and sedimentological changes, driven by changes in dust deposition, highlight the sensitivity of this perched wetland to climate change. The age model suggests the sedimentary sequence is continuous from lake initiation to the LGM. However, the sedimentology at the base of Unit 2 may indicate dry lake conditions or rapid sand deposition; further chronological control through this part of the record is required to differentiate between these scenarios. Nevertheless, from late MIS3 and MIS2 the dust flux signal intensifies across North Stradbroke Island, the result of which aligns with continental aridification and ecological change across Australia.

The increase in dust deposition across Brown Lake, Tortoise Lagoon, and Native Companion Lagoon during the early glacial phase and LGM, and the coeval hiatuses between Brown Lake and nearby

wetlands, support a climate-driven local expression of negative moisture balance. This contrasts with interferences of a largely positive moisture balance at this time (e.g., Moss et al., 2013; Tibby et al., 2017), however it should be noted these have relatively fewer dates incorporated into the respective age models. Hence there is a need for better chronological controls so that local and regional changes can be evaluated. The inferred negative hydrological period in this study is in agreement with other terrestrial records across mainland Australia and New Zealand, potentially linked to changes in the positioning of the South Pacific Convergence Zone (Brown et al., 2020), ENSO (Merkel et al., 2010), South Westerly Winds (Rudeva et al., 2019), or a combination thereof. Comparisons of Brown Lake to proximal wetlands through MIS2 in particular (i.e., Welsby Lagoon and Fern Gully Lagoon) have highlighted the importance of understanding variations in local catchment ecology and morphology, particularly when considering the impact of basin infilling on palaeoenvironmental records.

The return to a more positive moisture balance at Brown Lake in the early Holocene, and the recommencement of sediment accumulation, suggests a local shift from dry to wet. However, interrogating the dust record alone for regional changes in climate following recommencement is less reliable because landscape alteration from human practices both locally and in source locations had likely initiated. In order to better understand the effects of climate variation on the environment, particularly in association with the LGM and climate extremes, multi-proxy analytical approaches should also consider the surrounding landscape (e.g., associated dune deposits), which may hold missing or complementary information about local variations in environmental conditions.

Acknowledgements

We acknowledge Minjerribah (North Stradbroke Island) and the surrounding waters as Quandamooka Country and thank the Quandamooka Yoolooburrabee Aboriginal Corporation for permission to undertake the work. We thank Haidee Cadd and Jo Blessing for assistance in the field and Chris Kemp for discussions pertaining to Fern Gully Lagoon. Many thanks are also extended to Jonathan Marshall and Glenn McGregor for assistance in data acquisition. The work was supported by the Australian Research Council Discovery Project (DP150103875). R.L. was supported by an Australian Government Research Training Program Scholarship and a CRC LEME Regolith Science Scholarship. The OSL dating was supported by Australian Research Council Future Fellowship (FT130100195). Radiocarbon dating and XRF core scanning was made possible through the ANSTO facility access program (AP11643; AP12402). We acknowledge the financial support from the Australian Government for the Centre for Accelerator Science at ANSTO through the National Collaborative Research Infrastructure Strategy (NCRIS).

References

Aitken, M. J. 1998. Introduction to optical dating: the dating of Quaternary sediments by the use of photon-stimulated luminescence, Oxford, Oxford University Press.

Arnold, L. J., Bailey, R. M. & Tucker, G. E. 2007. Statistical treatment of fluvial dose distributions from southern Colorado arroyo deposits. Quaternary Geochronology, 2, 162-167.

Arnold, L. J., Duval, M., Falguères, C., Bahain, J.-J. & Demuro, M. 2012. Portable gamma spectrometry with cerium-doped lanthanum bromide scintillators: Suitability assessments for luminescence and electron spin resonance dating applications. Radiation Measurements, 47, 6-18.

Arnold, L. J. & Roberts, R. G. 2009. Stochastic modelling of multi-grain equivalent dose (De) distributions: Implications for OSL dating of sediment mixtures. Quaternary Geochronology, 4, 204-230.

Arnold, L. J. & Roberts, R. G. 2011. Paper I–Optically stimulated luminescence (OSL) dating of perennially frozen deposits in north-central Siberia: OSL characteristics of quartz grains and methodological considerations regarding their suitability for dating. Boreas, 40, 389-416.

Barr, C., Tibby, J., Leng, M. J., Tyler, J. J., Henderson, A. C. G., Overpeck, J. T., Simpson, G. L., Cole, J. E., Phipps, S. J. & Marshall, J. C. 2019. Holocene el Niño–southern Oscillation variability reflected in subtropical Australian precipitation. Scientific reports, 9, 1-9.

Barr, C., Tibby, J., Moss, P. T., Halverson, G. P., Marshall, J. C., Mcgregor, G. B. & Stirling, E. 2017. A 25,000-year record of environmental change from Welsby Lagoon, North Stradbroke Island, in the Australian subtropics. Quaternary International, 449, 106-118.

Barrows, T. T. & Juggins, S. 2005. Sea-surface temperatures around the Australian margin and Indian Ocean during the Last Glacial Maximum. Quaternary Science Reviews, 24, 1017-1047.

Birks, H. H. & Birks, H. J. B. 2006. Multi-proxy studies in palaeolimnology. Vegetation history and Archaeobotany, 15, 235-251.

Blais, J. M. & Kalff, J. 1995. The influence of lake morphometry on sediment focusing. Limnology and Oceanography, 40, 582-588.

Bøtter-Jensen, L. & Mejdahl, V. 1988. Assessment of beta dose-rate using a GM multicounter system. International Journal of Radiation Applications and Instrumentation. Part D. Nuclear Tracks and Radiation Measurements, 14, 187-191.

Bowler, J. M. 1976. Aridity in Australia: age, origins and expression in aeolian landforms and sediments. Earth-science reviews, 12, 279-310.

Boyle, J. F. 2002. Inorganic geochemical methods in palaeolimnology. Tracking environmental change using lake sediments. Springer.

Brennan, B. J. 2003. Beta doses to spherical grains. Radiation Measurements, 37, 299-303.

Brock, F., Higham, T., Ditchfield, P. & Ramsey, C. B. 2010. Current pretreatment methods for AMS radiocarbon dating at the Oxford Radiocarbon Accelerator Unit (ORAU). Radiocarbon, 52, 103-112.

Bronk Ramsey, C. 2009. Dealing with outliers and offsets in radiocarbon dating. Radiocarbon, 51, 1023-1045.

Bronk Ramsey, C. 2017. Methods for summarizing radiocarbon datasets. Radiocarbon, 59, 1809-1833.

Bronk Ramsey, C. & Lee, S. 2013. Recent and planned developments of the program OxCal. Radiocarbon, 55, 720-730.

Brooke, B., Preda, M., Lee, R., Cox, M., Olley, J., Pietsch, T. & Price, D. 2008. Development, composition and age of indurated sand layers in the Late Quaternary coastal deposits of northern Moreton Bay, Queensland. Australian Journal of Earth Sciences, 55, 141-157.

Brown, J. R., Lengaigne, M., Lintner, B. R., Widlansky, M. J., Van Der Wiel, K., Dutheil, C., Linsley, B. K., Matthews, A. J. & Renwick, J. 2020. South Pacific Convergence Zone dynamics, variability and impacts in a changing climate. Nature Reviews Earth & Environment, 1, 530-543.

Cadd, H. R., Tibby, J., Barr, C., Tyler, J., Unger, L., Leng, M. J., Marshall, J. C., Mcgregor, G., Lewis, R. & Arnold, L. J. 2018. Development of a Southern Hemisphere subtropical wetland (Welsby Lagoon, south-east Queensland, Australia) through the last glacial cycle. Quaternary Science Reviews, 202, 53-65.

Cadd, H. R., Tyler, J., Tibby, J., Baldock, J., Hawke, B., Barr, C. & Leng, M. J. 2020. The potential for rapid determination of charcoal from wetland sediments using infrared spectroscopy. Palaeogeography, Palaeoclimatology, Palaeoecology, 542, 109562.
Clark, P. U., Dyke, A. S., Shakun, J. D., Carlson, A. E., Clark, J., Wohlfarth, B., Mitrovica, J. X., Hostetler, S. W. & Mccabe, A. M. 2009. The last glacial maximum. science, 325, 710-714.
Clifford, H. T. & Specht, R. L. 1979. The vegetation of North Stradbroke Island, Queensland, University of Queensland Press.
Cohen, T. J., Jansen, J. D., Gliganic, L. A., Larsen, J. R., Nanson, G. C., May, J.-H., Jones, B. G. & Price, D. M. 2015. Hydrological transformation coincided with megafaunal extinction in central Australia. Geology, 43, 195-198.
Colhoun, E. A., Pola, J. S., Barton, C. E. & Heijnis, H. 1999. Late Pleistocene vegetation and climate history of Lake Selina, western Tasmania. Quaternary International, 57, 5-23.
Coll, K. & Whitaker, R. 1990. The Australian Weather Book: Understanding our climate and how it affect us, Syndey, Australia, Associates Publishing Pty Ltd.
Croudace, I. W. & Rothwell, R. G. 2015. Micro-XRF Studies of Sediment Cores: Applications of a non-destructive tool for the environmental sciences, Springer.
Davies, S. J., Lamb, H. F. & Roberts, S. J. 2015. Micro-XRF core scanning in palaeolimnology: recent developments. Micro-XRF studies of sediment cores, 189-226.
De Deckker, P. 2001. Late Quaternary cyclic aridity in tropical Australia. Palaeogeography, Palaeoclimatology, Palaeoecology, 170, 1-9.
Demuro, M., Arnold, L. J., Froese, D. G. & Roberts, R. G. 2013. OSL dating of loess deposits bracketing Sheep Creek tephra beds, northwest Canada: dim and problematic single-grain OSL characteristics and their effect on multi-grain age estimates. Quaternary Geochronology, 15, 67-87.
Denton, G. H., Heusser, C. J., Lowel, T. V., Moreno, P. I., Andersen, B. G., Heusser, L. E., Schlühter, C. & Marchant, D. R. 1999. Interhemispheric linkage of paleoclimate during the last glaciation. Geografiska Annaler: Series A, Physical Geography, 81, 107-153.
Donders, T. H., Wagner, F. & Visscher, H. 2006. Late Pleistocene and Holocene subtropical vegetation dynamics recorded in perched lake deposits on Fraser Island, Queensland, Australia. Palaeogeography, Palaeoclimatology, Palaeoecology, 241, 417-439.
Ellerton, D., Rittenour, T., Shulmeister, J., Gontz, A., Welsh, K. J. & Patton, N. 2020. An 800 kyr record of dune emplacement in relationship to high sea level forcing, Cooloola Sand Mass, Queensland, Australia. Geomorphology, 354, 106999.
Ellerton, D., Shulmeister, J., Woodward, C. & Moss, P. 2017. Last Glacial Maximum and Last Glacial–Interglacial Transition pollen record from northern NSW, Australia: evidence for a humid late Last Glacial Maximum and dry deglaciation in parts of eastern Australia. Journal of Quaternary Science, 32, 717-728.
Farebrother, W., Hesse, P. P., Chang, H.-C. & Jones, C. 2017. Dry lake beds as sources of dust in Australia during the Late Quaternary: A volumetric approach based on lake bed and deflated dune volumes. Quaternary Science Reviews, 161, 81-98.
Fitzsimmons, K. E., Bowler, J. M., Rhodes, E. J. & Magee, J. M. 2007. Relationships between desert dunes during the late Quaternary in the Lake Frome region, Strzelecki Desert, Australia. Journal of Quaternary Science: Published for the Quaternary Research Association, 22, 549-558.
Galbraith, R. F. & Green, P. F. 1990. Estimating the component ages in a finite mixture. International Journal of Radiation Applications and Instrumentation. Part D. Nuclear Tracks and Radiation Measurements, 17, 197-206.
Galbraith, R. F., Roberts, R. G., Laslett, G. M., Yoshida, H. & Olley, J. M. 1999. Optical dating of single and multiple grains of quartz from Jinmium rock shelter, northern Australia: Part I, experimental design and statistical models. Archaeometry, 41, 339-364.
Galloway, R. 1965. Late quaternary climates in Australia. The Journal of Geology, 73, 603-618.
Gasse, F. & Van Campo, E. 2001. Late Quaternary environmental changes from a pollen and diatom record in the southern tropics (Lake Tritrivakely, Madagascar). Palaeogeography, Palaeoclimatology, Palaeoecology, 167, 287-308.
Gordon, A. 1982. An Investigation of two Sequence-Comparison Statistics. Australian Journal of Statistics, 24, 332-342.

Grant, K. M., Rohling, E. J., Ramsey, C. B., Cheng, H., Edwards, R. L., Florindo, F., Heslop, D., Marra, F., Roberts, A. P. & Tamisiea, M. E. 2014. Sea-level variability over five glacial cycles. Nature communications, 5, 1-9.
Guérin, G., Mercier, N. & Adamiec, G. 2011. Dose-rate conversion factors: update. Ancient TL, 29, 5-8.
Guyard, H., Chapron, E., St-Onge, G., Anselmetti, F. S., Arnaud, F., Magand, O., Francus, P. & Mélières, M.-A. 2007. High-altitude varve records of abrupt environmental changes and mining activity over the last 4000 years in the Western French Alps (Lake Bramant, Grandes Rousses Massif). quaternary science reviews, 26, 2644-2660.
Harrison, S. P. 1993. Late Quaternary lake-level changes and climates of Australia. Quaternary Science Reviews, 12, 211-231.
Harrison, S. P., Kohfeld, K. E., Roelandt, C. & Claquin, T. 2001. The role of dust in climate changes today, at the last glacial maximum and in the future. Earth-Science Reviews, 54, 43-80.
Heiri, O., Lotter, A. F. & Lemcke, G. 2001. Loss on ignition as a method for estimating organic and carbonate content in sediments: reproducibility and comparability of results. Journal of paleolimnology, 25, 101-110.
Hendy, I. L., Napier, T. J. & Schimmelmann, A. 2015. From extreme rainfall to drought: 250 years of annually resolved sediment deposition in Santa Barbara Basin, California. Quaternary International, 387, 3-12.
Hesse, P. P. 2016. How do longitudinal dunes respond to climate forcing? Insights from 25 years of luminescence dating of the Australian desert dunefields. Quaternary International, 410, 11-29.
Hesse, P. P., Magee, J. W. & Van Der Kaars, S. 2004. Late Quaternary climates of the Australian arid zone: a review. Quaternary International, 118, 87-102.
Hesse, P. P. & Mctainsh, G. H. 2003. Australian dust deposits: modern processes and the Quaternary record. Quaternary Science Reviews, 22, 2007-2035.
Hogg, A. G., Hua, Q., Blackwell, P. G., Niu, M., Buck, C. E., Guilderson, T. P., Heaton, T. J., Palmer, J. G., Reimer, P. J. & Reimer, R. W. 2013. SHCal13 Southern Hemisphere calibration, 0–50,000 years cal BP. Radiocarbon, 55, 1889-1903.
Hounslow, M. W. & Clark, R. M. 2016. CPLSlot a program for objective correlation between successions using sequence slotting.
Jouve, G., Francus, P., Lamoureux, S., Provencher-Nolet, L., Hahn, A., Haberzettl, T., Fortin, D., Nuttin, L. & Team, T. P. S. 2013. Microsedimentological characterization using image analysis and μ-XRF as indicators of sedimentary processes and climate changes during Lateglacial at Laguna Potrok Aike, Santa Cruz, Argentina. Quaternary Science Reviews, 71, 191-204.
Kemp, C. W., Tibby, J., Arnold, L. J., Barr, C., Gadd, P. S., Marshall, J. C., Mcgregor, G. B. & Jacobsen, G. E. 2020. Climates of the last three interglacials in subtropical eastern Australia inferred from wetland sediment geochemistry. Palaeogeography, Palaeoclimatology, Palaeoecology, 538, 109463.
Kemp, J. & Spooner, N. A. 2007. Evidence for regionally wet conditions before the LGM in southeast Australia: OSL ages from a large palaeochannel in the Lachlan Valley. Journal of Quaternary Science: Published for the Quaternary Research Association, 22, 423-427.
Kershaw, A. P., Bretherton, S. C. & Van Der Kaars, S. 2007. A complete pollen record of the last 230 ka from Lynch's Crater, north-eastern Australia. Palaeogeography, Palaeoclimatology, Palaeoecology, 251, 23-45.
Kershaw, A. P., Mckenzie, G. M., Brown, J., Roberts, R. G. & Van Der Kaars, S. 2010. Beneath the peat: A refined pollen record from an interstadial at Caledonia Fen, highland eastern Victoria, Australia. Altered ecologies: fire, climate and human influence on terrestrial landscapes. Terra Australis, 32, 33-48.
Kershaw, A. P., Van Der Kaars, S. & Moss, P. T. 2003. Late Quaternary Milankovitch-scale climatic change and variability and its impact on monsoonal Australasia. Marine Geology, 201, 81-95.
Kershaw, P., Van Der Kaars, S., Moss, P., Opdyke, B., Guichard, F., Rule, S. & Turney, C. 2006. Environmental change and the arrival of people in the Australian region. Before Farming, 2006, 1-25.

Kohfeld, K., Graham, R., De Boer, A., Sime, L., Wolff, E., Le Quéré, C. & Bopp, L. 2013. Southern Hemisphere westerly wind changes during the Last Glacial Maximum: paleo-data synthesis. Quaternary Science Reviews, 68, 76-95.
Kylander, M. E., Ampel, L., Wohlfarth, B. & Veres, D. 2011. High-resolution X-ray fluorescence core scanning analysis of Les Echets (France) sedimentary sequence: new insights from chemical proxies. Journal of Quaternary Science, 26, 109-117.
Kylander, M. E., Lind, E. M., Wastegård, S. & Löwemark, L. 2012. Recommendations for using XRF core scanning as a tool in tephrochronology. The Holocene, 22, 371-375.
Lambeck, K., Rouby, H., Purcell, A., Sun, Y. & Sambridge, M. 2014. Sea level and global ice volumes from the Last Glacial Maximum to the Holocene. Proceedings of the National Academy of Sciences, 111, 15296-15303.
Lamy, F., Gersonde, R., Winckler, G., Esper, O., Jaeschke, A., Kuhn, G., Ullermann, J., Martínez-Garcia, A., Lambert, F. & Kilian, R. 2014. Increased dust deposition in the Pacific Southern Ocean during glacial periods. Science, 343, 403-407.
Lauterbach, S., Brauer, A., Andersen, N., Danielopol, D. L., Dulski, P., Hüls, M., Milecka, K., Namiotko, T., Obremska, M. & Von Grafenstein, U. 2011. Environmental responses to Lateglacial climatic fluctuations recorded in the sediments of pre-Alpine Lake Mondsee (northeastern Alps). Journal of Quaternary Science, 26, 253-267.
Leach, L. Hydrology and physical setting of North Stradbroke Island. Proceedings of the Royal Society of Queensland, 2011.
Lees, B. 2006. Timing and formation of coastal dunes in northern and eastern Australia. Journal of Coastal Research, 22, 78-89.
Lewis, R. J., Tibby, J., Arnold, L. J., Barr, C., Marshall, J., Mcgregor, G., Gadd, P. & Yokoyama, Y. 2020. Insights into subtropical Australian aridity from Welsby Lagoon, north Stradbroke Island, over the past 80,000 years. Quaternary Science Reviews, 234, 106262.
Lisé-Pronovost, A., Fletcher, M.-S., Mallett, T., Mariani, M., Lewis, R., Gadd, P. S., Herries, A. I., Blaauw, M., Heijnis, H. & Hodgson, D. A. 2019. Scientific drilling of sediments at Darwin Crater, Tasmania. Scientific Drilling, 25, 1-14.
Long, K., Wood, R., Williams, I. S., Kalish, J., Shawcross, W., Stern, N. & Grün, R. 2018. Fish otolith microchemistry: Snapshots of lake conditions during early human occupation of Lake Mungo, Australia. Quaternary International, 463, 29-43.
Magee, J. W., Miller, G. H., Spooner, N. A. & Questiaux, D. 2004. Continuous 150 ky monsoon record from Lake Eyre, Australia: insolation-forcing implications and unexpected Holocene failure. Geology, 32, 885-888.
Mandl, M. B., Shuman, B. N., Marsicek, J. & Grigg, L. 2016. Estimating the regional climate signal in a late Pleistocene and early Holocene lake-sediment δ18O record from Vermont, USA. Quaternary Research, 86, 67-78.
Mariani, M., Tibby, J., Barr, C., Moss, P., Marshall, J. C. & Mcgregor, G. B. 2019. Reduced rainfall drives biomass limitation of long-term fire activity in Australia's subtropical sclerophyll forests. Journal of Biogeography, 46, 1974-1987.
Marx, S. K., Kamber, B. S., Mcgowan, H. A., Petherick, L. M., Mctainsh, G. H., Stromsoe, N., Hooper, J. N. & May, J.-H. 2018. Palaeo-dust records: A window to understanding past environments. Global and Planetary Change, 165, 13-43.
Mccanta, M. C., Hatfield, R. G., Thomson, B. J., Hook, S. J. & Fisher, E. 2015. Identifying cryptotephra units using correlated rapid, nondestructive methods: VSWIR spectroscopy, X-ray fluorescence, and magnetic susceptibility. Geochemistry, Geophysics, Geosystems, 16, 4029-4056.
Mcgowan, H. A., Petherick, L. M. & Kamber, B. S. 2008. Aeolian sedimentation and climate variability during the late Quaternary in southeast Queensland, Australia. Palaeogeography, Palaeoclimatology, Palaeoecology, 265, 171-181.
Mejdahl, V. 1979. Thermoluminescence dating: beta-dose attenuation in quartz grains. Archaeometry, 21, 61-72.
Merkel, U., Prange, M. & Schulz, M. 2010. ENSO variability and teleconnections during glacial climates. Quaternary Science Reviews, 29, 86-100.

Miller, G. H., Fogel, M. L., Magee, J. W. & Gagan, M. K. 2016. Disentangling the impacts of climate and human colonization on the flora and fauna of the Australian arid zone over the past 100 ka using stable isotopes in avian eggshell. Quaternary Science Reviews, 151, 27-57.
Miot Da Silva, G. & Shulmeister, J. 2016. A review of coastal dunefield evolution in Southeastern Queensland. Journal of Coastal Research, 308-312.
Mosisch, T. D. & Arthington, A. H. 2001. Polycyclic aromatic hydrocarbon residues in the sediments of a dune lake as a result of power boating. Lakes & Reservoirs: Research & Management, 6, 21-32.
Moss, E. 2013a. A Dust Record from Lacustrine Sediments on North Stradbroke Island, Queensland: Evidence for Climate Variability in Central and Southeastern Australia During the Late Quaternary. [Bachelor's Thesis], The University of Sydney.
Moss, P. T. 2013b. Palynology and its Application to Geomorphology. In: Shroder, J. F. (ed.) Treatise on Geomorphology. San Diego: Academic Press.
Moss, P. T. & Kershaw, A. P. 2007. A late Quaternary marine palynological record (oxygen isotope stages 1 to 7) for the humid tropics of northeastern Australia based on ODP Site 820. Palaeogeography, Palaeoclimatology, Palaeoecology, 251, 4-22.
Moss, P. T., Tibby, J., Petherick, L., Mcgowan, H. & Barr, C. 2013. Late Quaternary vegetation history of North Stradbroke Island, Queensland, eastern Australia. Quaternary Science Reviews, 74, 257-272.
Murray, A. S. & Wintle, A. G. 2000. Luminescence dating of quartz using an improved single-aliquot regenerative-dose protocol. Radiation measurements, 32, 57-73.
Nathan, R. P., Thomas, P. J., Jain, M., Murray, A. S. & Rhodes, E. J. 2003. Environmental dose rate heterogeneity of beta radiation and its implications for luminescence dating: Monte Carlo modelling and experimental validation. Radiation Measurements, 37, 305-313.
Neal, R. & Stock, E. 1986. Pleistocene occupation in the south-east Queensland coastal region. Nature, 323, 618-621.
Niemann, H., Matthias, I., Michalzik, B. & Behling, H. 2013. Late Holocene human impact and environmental change inferred from a multi-proxy lake sediment record in the Loja region, southeastern Ecuador. Quaternary International, 308, 253-264.
Olley, J. M., Pietsch, T. & Roberts, R. G. 2004. Optical dating of Holocene sediments from a variety of geomorphic settings using single grains of quartz. Geomorphology, 60, 337-358.
Patton, N. R., Ellerton, D. & Shulmeister, J. 2019. High-resolution remapping of the coastal dune fields of south east Queensland, Australia: a morphometric approach. Journal of Maps, 15, 578-589.
Petherick, L., Bostock, H., Cohen, T. J., Fitzsimmons, K., Tibby, J., Fletcher, M.-S., Moss, P., Reeves, J., Mooney, S. & Barrows, T. 2013. Climatic records over the past 30 ka from temperate Australia–a synthesis from the Oz-INTIMATE workgroup. Quaternary Science Reviews, 74, 58-77.
Petherick, L., Mcgowan, H. & Moss, P. 2008. Climate variability during the Last Glacial Maximum in eastern Australia: evidence of two stadials? Journal of Quaternary Science: Published for the Quaternary Research Association, 23, 787-802.
Petherick, L. M., Mcgowan, H. A. & Kamber, B. S. 2009. Reconstructing transport pathways for late Quaternary dust from eastern Australia using the composition of trace elements of long traveled dusts. Geomorphology, 105, 67-79.
Petherick, L. M., Moss, P. T. & Mcgowan, H. A. 2011. Climatic and environmental variability during the termination of the Last Glacial Stage in coastal eastern Australia: a review. Australian Journal of Earth Sciences, 58, 563-577.
Petherick, L. M., Moss, P. T. & Mcgowan, H. A. 2017. An extended last glacial maximum in Subtropical Australia. Quaternary International, 432, 1-12.
Pickett, J. W., Ku, T. L., Thompson, C. H., Roman, D., Kelley, R. A. & Huang, Y. P. 1989. A review of age determinations on Pleistocene corals in eastern Australia. Quaternary Research, 31, 392-395.
Prescott, J. R. & Hutton, J. T. 1994. Cosmic ray contributions to dose rates for luminescence and ESR dating: large depths and long-term time variations. Radiation measurements, 23, 497-500.
Rees-Jones, J. 1995. Optical dating of young sediments using fine-grain quartz. Ancient TL, 13, 9-14.

Rees-Jones, J. & Tite, M. S. 1997. Optical dating results for British archaeological sediments. Archaeometry, 39, 177-187.
Reeves, J. M., Barrows, T. T., Cohen, T. J., Kiem, A. S., Bostock, H. C., Fitzsimmons, K. E., Jansen, J. D., Kemp, J., Krause, C. & Petherick, L. 2013. Climate variability over the last 35,000 years recorded in marine and terrestrial archives in the Australian region: an OZ-INTIMATE compilation. Quaternary Science Reviews, 74, 21-34.
Rudeva, I., Simmonds, I., Crock, D. & Boschat, G. 2019. Midlatitude fronts and variability in the Southern Hemisphere tropical width. Journal of Climate, 32, 8243-8260.
Sankey, J. B., Eitel, J. U. H., Glenn, N. F., Germino, M. J. & Vierling, L. A. 2011. Quantifying relationships of burning, roughness, and potential dust emission with laser altimetry of soil surfaces at submeter scales. Geomorphology, 135, 181-190.
Schnurrenberger, D., Russell, J. & Kelts, K. 2003. Classification of lacustrine sediments based on sedimentary components. Journal of Paleolimnology, 29, 141-154.
Shore, J. S., Bartley, D. D. & Harkness, D. D. 1995. Problems encountered with the 14C dating of peat. Quaternary Science Reviews, 14, 373-383.
Song, B., Kong, L., Hu, Z., Wang, Q. & Yang, X. 2020. Pollen and diatom record of climate and environmental change over the last 170 years in Tingming Lake, Yunnan Province, SW China. Quaternary International, 536, 85-91.
Svitok, M., Hrivnák, R., Oťaheľová, H., Dúbravková, D., Paľove-Balang, P. & Slobodník, V. 2011. The importance of local and regional factors on the vegetation of created wetlands in Central Europe. Wetlands, 31, 663-674.
Tejan-Kella, M. S., Chittleborough, D. J., Fitzpatrick, R. W., Thompson, C. H., Prescott, J. R. & Hutton, J. T. 1990. Thermoluminescence dating of coastal sand dunes at Cooloola and North Stradbroke Island, Australia. Soil Research, 28, 465-481.
Thompson, C. H. 1981. Podzol chronosequences on coastal dunes of eastern Australia. Nature, 291, 59-61.
Tibby, J., Barr, C., Marshall, J. C., Mcgregor, G. B., Moss, P. T., Arnold, L. J., Page, T. J., Questiaux, D., Olley, J. & Kemp, J. 2017. Persistence of wetlands on North Stradbroke Island (south-east Queensland, Australia) during the last glacial cycle: implications for Quaternary science and biogeography. Journal of Quaternary Science, 32, 770-781.
Tjallingii, R., Röhl, U., Kölling, M. & Bickert, T. 2007. Influence of the water content on X-ray fluorescence core-scanning measurements in soft marine sediments. Geochemistry, Geophysics, Geosystems, 8.
Turney, C. S. M., Haberle, S., Fink, D., Kershaw, A. P., Barbetti, M., Barrows, T. T., Black, M., Cohen, T. J., Correge, T. & Hesse, P. P. 2006a. Integration of ice-core, marine and terrestrial records for the Australian Last Glacial Maximum and Termination: a contribution from the OZ INTIMATE group. Journal of Quaternary Science: Published for the Quaternary Research Association, 21, 751-761.
Turney, C. S. M., Kershaw, A. P., James, S., Branch, N., Cowley, J., Fifield, L. K., Jacobsen, G. & Moss, P. 2006b. Geochemical changes recorded in Lynch's Crater, Northeastern Australia, over the past 50 ka. Palaeogeography, Palaeoclimatology, Palaeoecology, 233, 187-203.
Vandergoes, M. J., Newnham, R. M., Preusser, F., Hendy, C. H., Lowell, T. V., Fitzsimons, S. J., Hogg, A. G., Kasper, H. U. & Schlüchter, C. 2005. Regional insolation forcing of late Quaternary climate change in the Southern Hemisphere. Nature, 436, 242-245.
Vogel, H., Zanchetta, G., Sulpizio, R., Wagner, B. & Nowaczyk, N. 2010. A tephrostratigraphic record for the last glacial–interglacial cycle from Lake Ohrid, Albania and Macedonia. Journal of Quaternary Science: Published for the Quaternary Research Association, 25, 320-338.
Walker, J., Lees, B., Olley, J. & Thompson, C. 2018. Dating the Cooloola coastal dunes of south-eastern Queensland, Australia. Marine Geology, 398, 73-85.
Ward, W. 2006. Coastal dunes and strandplains in southeast Queensland: sequence and chronology. Australian Journal of Earth Sciences, 53, 363-373.
Ward, W. T. 1978. Notes on the origin of Stradbroke Island.
Washington, R., Todd, M. C., Lizcano, G., Tegen, I., Flamant, C., Koren, I., Ginoux, P., Engelstaedter, S., Bristow, C. S. & Zender, C. S. 2006. Links between topography, wind, deflation, lakes and dust: The case of the Bodélé Depression, Chad. Geophysical research letters, 33.

Webb, N. P. & Strong, C. L. 2011. Soil erodibility dynamics and its representation for wind erosion and dust emission models. Aeolian Research, 3, 165-179.
Weltje, G. J. & Tjallingii, R. 2008. Calibration of XRF core scanners for quantitative geochemical logging of sediment cores: Theory and application. Earth and Planetary Science Letters, 274, 423-438.
Williams, M., Cook, E., Van Der Kaars, S., Barrows, T., Shulmeister, J. & Kershaw, P. 2009. Glacial and deglacial climatic patterns in Australia and surrounding regions from 35 000 to 10 000 years ago reconstructed from terrestrial and near-shore proxy data. Quaternary Science Reviews, 28, 2398-2419.
Woodward, C., Shulmeister, J., Bell, D., Haworth, R., Jacobsen, G. & Zawadzki, A. 2014. A Holocene record of climate and hydrological changes from Little Llangothlin Lagoon, south eastern Australia. The Holocene, 24, 1665-1674.
Xiao, X., Yao, A., Hillman, A., Shen, J. & Haberle, S. G. 2020. Vegetation, climate and human impact since 20 ka in central Yunnan Province based on high-resolution pollen and charcoal records from Dianchi, southwestern China. Quaternary Science Reviews, 236, 106297.
Zhang, J., Chen, F., Holmes, J. A., Li, H., Guo, X., Wang, J., Li, S., Lü, Y., Zhao, Y. & Qiang, M. 2011. Holocene monsoon climate documented by oxygen and carbon isotopes from lake sediments and peat bogs in China: a review and synthesis. Quaternary Science Reviews, 30, 1973-1987.

Chapter 4 Extinction of eastern Sahul megafauna coincides with sustained environmental deterioration

---

This chapter has been published in *Nature Communications* as:

Hocknull, S. A., Lewis, R., Arnold, L. J., Pietsch, T., Joannes-Boyau, R., Price, G. J., Moss, P., Wood, R., Dosseto, A., Louys, J., Olley, J. & Lawrence, R. A. 2020. Extinction of eastern Sahul megafauna coincides with sustained environmental deterioration. Nature communications, 11, 1-14.

Statement of Authorship

Title of Paper	Extinction of eastern Sahul megafauna coincides with sustained environmental deterioration.
Publication Status	[X] Published [ ] Accepted for Publication [ ] Submitted for Publication [ ] Unpublished and Unsubmitted work written in manuscript style
Publication Details	Hocknull, S. A., Lewis, R., Arnold, L. J., Pietsch, T., Joannes-Boyau, R., Price, G. J., Moss, P., Wood, R., Dosseto, A., Louys, J., Olley, J. & Lawrence, R. A. 2020. Extinction of eastern Sahul megafauna coincides with sustained environmental deterioration. Nature Communications, 11, 1-14.

Principal Author

Name of Principal Author (Candidate)	Scott A. Hocknull | (Richard J. Lewis)	
Contribution to the Paper	Conceptualization; Data curation; Formal analysis; Funding acquisition; Investigation; Methodology; Project administration; Resources; Software; Data Validation; Visualization; Writing – original draft; Writing – review & editing	
Overall percentage (%)	70 | (20)	
Certification:	This paper reports on original research I conducted during the period of my Higher Degree by Research candidature and is not subject to any obligations or contractual agreements with a third party that would constrain its inclusion in this thesis. I am an author of this paper.	
Signature		Date 7th August 2021 19th July 2021

Co-Author Contributions

By signing the Statement of Authorship, each author certifies that:

vii. the candidate's stated contribution to the publication is accurate (as detailed above);
viii. permission is granted for the candidate in include the publication in the thesis; and
ix. the sum of all co-author contributions is equal to 100% less the candidate's stated contribution.

Name of Co-Author	Richard J. Lewis	
Contribution to the Paper	Data curation; Formal analysis; Investigation; Methodology; Project administration; Resources; Software; Data Validation; Visualization; Writing – original draft; Writing – review & editing	
Signature		Date 19th July 2021

Name of Co-Author	Lee J. Arnold	
Contribution to the Paper	Data curation; Formal analysis; Funding acquisition; Investigation; Methodology; Resources; Software; Data Validation; Visualization; Writing – original draft; Writing – review & editing	
Signature		Date 13th August 2021

Name of Co-Author	Tim Pietsch	
Contribution to the Paper	Data curation; Formal analysis; Investigation; Methodology; Resources; Data Validation; Writing – original draft; writing – review & editing	
Signature		Date 13th August 2021

Name of Co-Author	Renaud Joannes-Boyau	
Contribution to the Paper	Data curation; Formal analysis; Investigation; Methodology; Resources; Data Validation; Writing – original draft; writing – review & editing	
Signature		Date 13th August 2021

Name of Co-Author	Gilbert J. Price	
Contribution to the Paper	Data curation; Formal analysis; Investigation; Methodology; Resources; Data Validation; Writing – original draft; writing – review & editing	
Signature		Date 13th August 2021

Name of Co-Author	Patrick Moss	
Contribution to the Paper	Data curation; Formal analysis; Investigation; Methodology; Resources; Data Validation; Writing – original draft; writing – review & editing	
Signature		Date 13th August 2021

Name of Co-Author	Rachel Wood	
Contribution to the Paper	Data curation; Formal analysis; Investigation; Methodology; Resources; Data Validation; Writing – original draft; writing – review & editing	
Signature		Date 3rd November 2021

Name of Co-Author	Anthony Dosseto	
Contribution to the Paper	Data curation; Formal analysis; Investigation; Methodology; Resources; Data Validation; Writing – original draft; writing – review & editing	
Signature		Date 16th August 2021

Name of Co-Author	Julien Louys	
Contribution to the Paper	Data curation; Formal analysis; Investigation; Methodology; Resources; Data Validation; Writing – original draft; writing – review & editing	
Signature		Date 13th August 2021

Name of Co-Author	Jon Olley	
Contribution to the Paper	Data curation; Formal analysis; Investigation; Methodology; Resources; Data Validation; Writing – original draft; writing – review & editing	
Signature		Date 18th August 2021

Name of Co-Author	Rochelle A. Lawrence	
Contribution to the Paper	Conceptualization; Data curation; Formal analysis; Investigation; Methodology; Resources; Data Validation; Writing – original draft; writing – review & editing	
Signature		Date 13th August 2021

Abstract

Explanations for the Upper Pleistocene extinction of megafauna from Sahul (Australia and New Guinea) remain unresolved. Extinction hypotheses have advanced climate or human-driven scenarios, in spite of over three quarters of Sahul lacking reliable biogeographic or chronologic data. Here we present new megafauna from north-eastern Australia that suffered extinction sometime after 40,100 (±1700) years ago. Megafauna fossils preserved alongside leaves, seeds, pollen and insects, indicate a sclerophyllous forest with heathy understorey that was home to aquatic and terrestrial carnivorous reptiles and megaherbivores, including the world's largest kangaroo. Megafauna species diversity is greater compared to southern sites of similar age, which is contrary to expectations if extinctions followed proposed migration routes for people across Sahul. Our results do not support rapid or synchronous human-mediated continental-wide extinction, or the proposed timing of peak extinction events. Instead, megafaunal extinctions coincide with regionally staggered spatio-temporal deterioration in hydroclimate coupled with sustained environmental change.

Introduction

The Pleistocene megafauna of Sahul are defined here as non-marine vertebrates that exceed a mass of ~40 – 44 kg (Martin & Klein, 1984), comprising giant species of birds, reptiles and marsupials. They have vastly different phylogenetic histories (Long et al., 2002), occupying a diverse range of habitats (Hocknull et al., 2007; Price & Webb, 2006; Prideaux et al., 2007a) and reaching maximal body size by the Upper Pleistocene (Hocknull et al., 2009; Price, 2008; Prideaux, 2004) (126,000–11,700 years ago (ka)). In the context of this work we do not consider unusually large-bodied taxa with a mass <40 kg as megafauna, but acknowledge that many species <40 kg also suffered extinction during the Pleistocene (Price et al., 2018; Wroe et al., 2013). Some megafauna species were widely distributed across Sahul during the Quaternary, such as the giant wombat-like *Diprotodon optatum* (Price, 2008); however, data on the biochronology and palaeobiogeography of most species remains poor and patchy (Price et al., 2018; Wroe et al., 2013).

The megafauna fossil record of Sahul worsens when only those vertebrate fossil sites considered to be reliably-dated are considered (Rodríguez-Rey et al., 2015). Thus assessing extinction chronologies using the presently available vertebrate fossil record is hampered by few reliably-dated Upper Pleistocene sites within Marine Isotope Stage 3 (MIS3) (57–29 ka). This period of time is particularly important because it occurs at a time controversially proposed to encompass the complete continental-wide extinction of megafauna (Roberts et al., 2001; Wroe & Field, 2006) with the peak of extinction events occurring around 42.1 ka (Price et al., 2018; Saltré et al., 2016).

To augment this poor record, dung fungal spores (*Sporormiella*) recovered from lake and marine sediments have been used as a proxy of megafauna presence and abundance with reduced spore counts interpreted as indicating megafauna decline and extinction (Rule et al., 2012; van der Kaars et al., 2017). However the validity of fungal spores as useful proxies for megafauna requires cautious interpretation due to the numerous factors impacting their dispersal and survival into the fossil record, including taphonomic, sedimentological and biological considerations (Baker et al., 2013; Perrotti & van Asperen, 2019). Without a clear link between Sahul megafauna and these dung fungi its utility as a robust proxy is equivocal (Dodson & Field, 2018; Price et al., 2018).

Current explanations for megafaunal extinction are therefore based on a significant spatio-temporal gap in the vertebrate fossil record, which approximates three quarters of the area of the Sahul continent (Figure 4.1e). This problem is most evident for central and northern Australia, and New Guinea, where no reliably-dated megafauna occur within MIS3. This conspicuous gap has not restricted the development of generalised and polarised interpretations to explain the continental-wide extinction of the megafauna, with the prevailing extinction scenarios advancing climate change

(Cohen et al., 2015; Wroe et al., 2013) or anthropogenic (Brook et al., 2013; Johnson et al., 2016; Roberts et al., 2001; Saltré et al., 2016) factors.

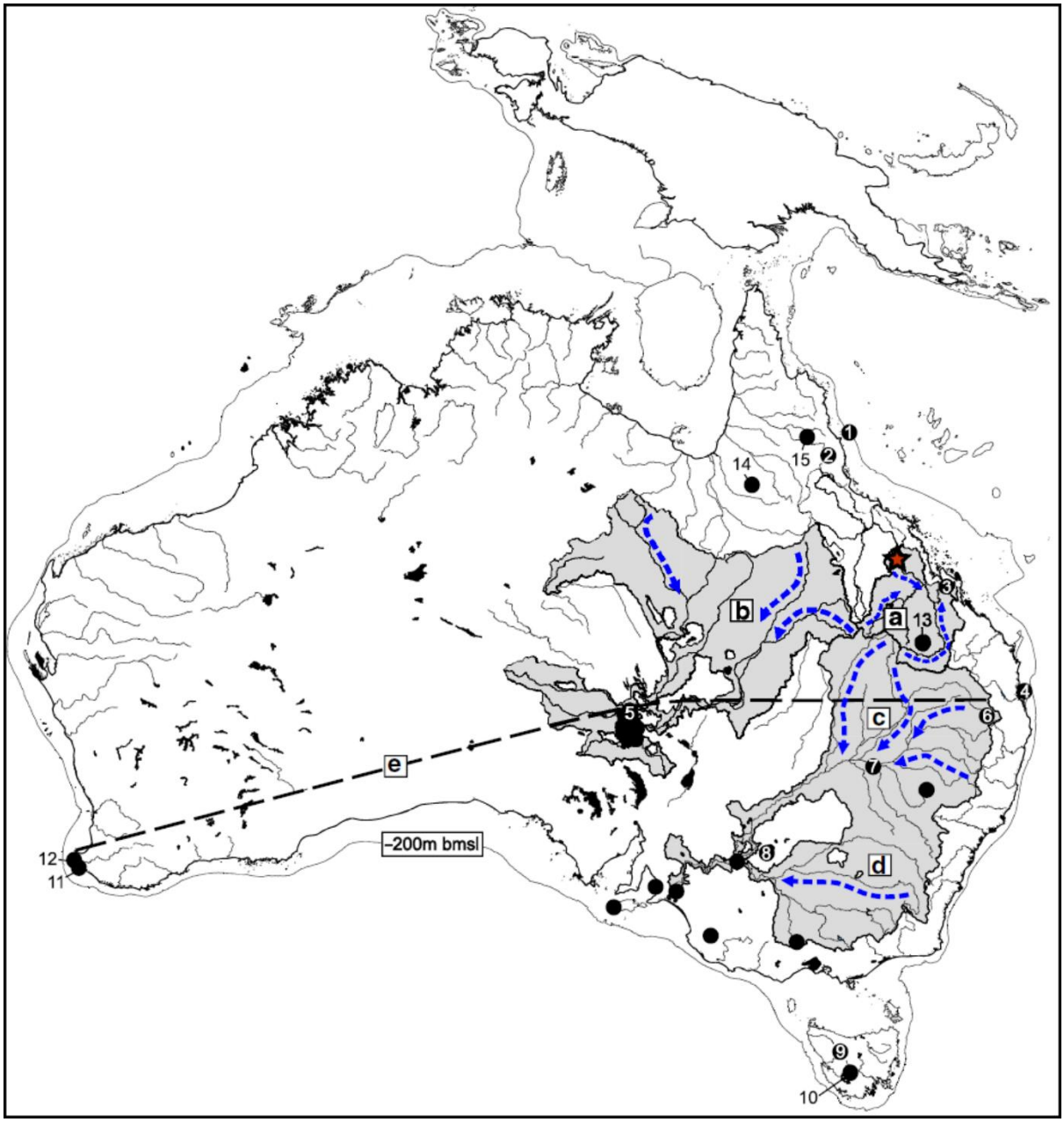

Figure 4.1 Map of Sahul (Australia and New Guinea) showing the distribution of reliably-dated megafauna sites within MIS3 (57 – 29 ka) and locations mentioned in the text. Red star indicates South Walker Creek. a The Fitzroy River Basin (FRB). b The Lake Eyre Basin (LEB). c The northern Darling and d southern Murray River catchments of the Murray-Darling Basin (MDB). e Over three quarters of the continental area of Sahul is missing reliably-dated sites from MIS3, here indicated north of the dashed line. Other localities mentioned in text, 1. ODP 820, 2. Lynch's Crater, 3. Capricorn Caves, 4. North Stradbroke Island, 5. Kati Thanda–Lake Eyre, 6. Ned's Gully, 7. Cuddie Springs, 8. Lake Mungo, 9. Mt. Cripps, 10. Titan's Shelter, 11. Tight Entrance Cave, 12. Kudjal Yolgah Cave, 13. Kenniff Cave, 14. Gledswood Shelter and 15. Ngarrabullgan. Blue arrows indicate catchment flow direction. bmsl = below mean present day sea level indicating outline of the Sahul continent. The baseline map was generated in QGIS using shoreline data from https://www ngdc.noaa.gov/mgg/shorelines/ under GNU Lesser General Public License v3 or later; and drainage basin data (Geoscience Australia, 2013) from https://data.gov.au/data/dataset/f55ec9b3-ab74-4056-93a2-b4b8aa65ead1 under Creative Commons Attribution 4.0 International; and bathymetry data (Whiteway, 2009) from https://data.gov.au/data/dataset/australian-bathymetry-and-topography-grid-june-2009 under Creative Commons Attribution 4.0 International. The base map was composited using Corel Draw and altered to delineate 'Lake Carpentaria'.

The discovery of fossil bones by Barada Barna Traditional Owners at South Walker Creek (SWC), Queensland Museum Locality (QML) 1470, near the township of Nebo, north-eastern Australia, resulted in systematic excavation of new fossil deposits that recovered Pleistocene megafauna. These sites are located in tropical Australia at the northern-most portion of the Fitzroy River Basin (FRB), an east-draining catchment that exits south onto the southern Great Barrier Reef, near Rockhampton, central-eastern Queensland (Figure 4.1). Importantly, the FRB is located within the 'data gap' for megafauna and adjoins Australia's two largest basins to the west. Both of these basins, the inland-draining Lake Eyre Basin (LEB) and the south-draining Murray-Darling Basin (MDB), have reliably-dated megafauna sites and possess established palaeoenvironmental proxies (Bowler et al., 2012; Cohen et al., 2015; Croke et al., 2011; Hesse et al., 2018; Kemp et al., 2019; Moss et al., 2017; Moss & Kershaw, 2007).

Here we present a new and diverse Pleistocene megafaunal assemblage unique to eastern Sahul. We then provide a chronology for these megafauna that combine observations of site geology and taphonomy with a chronometric dating assessment. Reliable numerical ages are reported for four megafauna sites using multiple dating techniques and applied quality rating criteria (Rodríguez-Rey et al., 2015). These results are then integrated into the established regional and local palaeoenvironmental and archaeological records that provide important context for testing the prevailing megafaunal extinction hypotheses for Sahul. Our results do not support rapid or synchronous human-mediated continental-wide extinction or the proposed timing of peak extinctions around 42.1 ka. Instead, megafaunal extinctions coincide with regionally staggered spatio-temporal deterioration in hydroclimate coupled with locally sustained environmental changes that were arguably detrimental to megafauna survival.

Results

New and diverse tropical megafauna

Four sites along a stretch of Walker Creek represent the South Walker Creek fossil deposits reported here that contain the remains of a new and diverse megafauna assemblage (Figure 4.2). Fossil fauna and flora are taxonomically identified along with descriptions of these remains (Appendix C1–C3), their taphonomic, depositional and stratigraphic context (Appendix C2 & C4). The deposits preserve body and trace fossils from small to megafauna-sized vertebrates, aquatic and terrestrial invertebrates (e.g., bivalves and insects) and floral remains (e.g. seeds, leaves and pollen) (Figure 4.2a, f–x, Figures C1–C7 & C10).

The combination of fauna and flora preserved within an open fossil site in Australia is rare. Recently, modelled suitability ratings for preservation and discoverability of megafauna fossils rates the SWC area at, or close to, zero (Block et al., 2016). This suggests that either these fossil deposits are truly exceptional or the models require further refinement before being considered useful. The SWC sites thus offer a rare opportunity to develop a holistic account of megafauna within a tropical northern palaeoenvironment from northern Australia and eastern Sahul.

At least sixteen megafauna species are present, including thirteen extinct and three extant species. Carnivorous megafauna are represented by the marsupial 'lion', *Thylacoleo*, at least three crocodilians (*Crocodylus* sp. cf. C. *porosus*, *Pallimnarchus* sp. and '*Quinkana'* sp.) and two giant monitor lizards (*Varanus priscus* ("Megalania") and a Komodo Dragon-sized species). Mega- and Macroherbivores are diverse with five species of kangaroo, two wombats, one palorchestid, two diprotodontids and the emu, *Dromaius* sp. cf. *D. novaehollandiae* (Table 4.1, Appendix C1).

The macropodids are morphologically distinct taxa but remain largely enigmatic due to low numbers of preserved dental remains and uncertain species-level taxonomies (Appendix C1 and Figure C5). Five species of macropodine, including a species each of *Macropus*, *Notamacropus*, *Osphranter* and *Protemnodon*, as well as a species of small-sized sthenurine, define a kangaroo fauna that bears little

resemblance to the 'typical' Upper Pleistocene sthenurine-dominated kangaroo faunas of southern Australia (Jankowski et al., 2016; Prideaux, 2004). Also, macropodines that are commonly documented from Pleistocene open sites in the bordering MDB catchment to the south of the FRB; such as *Macropus giganteus titan*, *Macropus ferragus*, *Notamacropus agilis siva* and *Protemnodon anak* (Molnar & Kurz, 1997), are notably absent from the SWC macropodid fauna. These taxa are of similar body size to those found at SWC; therefore, it is unlikely that these faunal absences are due to taphonomic sampling bias.

The SWC macropodines are all high crowned forms, including the species of *Protemnodon*, which is either a new species or a northern variant of the similar-sized *Protemnodon brehus* (Appendix C1; Figure C5ab–an). The largest and most common macropodine is possibly a new species of *Macropus* that possesses a combination of characteristics found in Pliocene-aged *Macropus pan* and Pleistocene-aged *Macropus pearsoni*. Comparison of limb dimensions of this giant species to those of other giant macropodid skeletons indicates that this taxon is the largest species of kangaroo. Maximum tibial length is at least 250 mm longer than that of the largest known specimens of *Procoptodon goliah*, *Macropus giganteus titan*, and *Macropus ferragus* (Janis et al., 2014) (Appendix C1; Figures C4 & C5, l-aa). Based on femoral circumference, mass is estimated at around 274 kg, ~43 kg heavier than the second largest species, the sthenurine *Procoptodon goliah* (Helgen et al., 2006) (Appendix C3). A species of *Notamacropus* is distinguishable from *N. agilis siva*, thus likely a new species or another northern variant (Appendix C1; Figure C5a–i). A species of *Osphranter* is morphologically indistinguishable from very large individuals of the extant Red Kangaroo (*Osphranter rufus*) (Appendix C1; Figure C5j). Together, the dominance of new macropodid forms along with the absence of common and widely distributed species indicates that the Pleistocene palaeoenvironment at SWC is presently unique in Sahul.

A species of *Palorchestes* is morphologically similar to *P. azael* but much smaller and is distinguishable from species similar in size (e.g. *P. parvus*) (Appendix C1; Figure C6a–c). This species may represent either a new species or another northern variant. The remaining megafauna are referrable to known taxa, including *Diprotodon optatum*, *Zygomaturus trilobus*, *Phascolonus gigas* and *Sedophascolomys* sp. cf. *S. medius* (Appendix C1; Figures C6 & C7). The specimens of SWC *Diprotodon optatum* are within the smallest size range when compared with those of Pleistocene sites from the MDB and LEB (Price, 2008; Price & Piper, 2009) (Table C2).

Reliable megafauna ages for eastern Sahul

The four SWC sites presented here were assessed geologically, taphonomically and chronometrically so that the new fauna could be placed within a reliable chronology. The detailed results of these assessments are provided in Appendix C3–C8. All of the sites occur within Quaternary alluvial deposits accumulated atop shallow-dipping Permo-Triassic bedrock. Each deposit represents a different sedimentary accumulation ranging from small-scale rapid burial events to larger-scale accretionary deposits (Figure 4.2a–e; Appendix C4; Figures C11–C14 and Tables C4–C7). Although common, large channel-fill deposits are consistently unfossiliferous.

Taphonomic and sedimentological evidence indicates a primary depositional context for the fossils with no evidence of secondary reworking other than present day exposure and erosion. Taphonomic characteristics of the vertebrate remains range from direct bone modification made by predators (e.g. crocodiles (Figures 4.2v) and *Thylacoleo* sp. bite marks (Figure C10d)) to dry and wet bone fractures dominated by weathering stage 0, indicating short-term exposure (Lyman & Fox, 1989) (Appendix C4; Figure C9). Voorhies Groups I, II and III are observed in combination at most sites and each site preserves different degrees of skeletal association ranging from articulated to isolated elements indicating varying levels of transport (Lyman & Lyman, 1994) (Figure 4.2w; Appendix C2 & C4; Figures C5, C6, C9, C10 and Table C3). We acknowledge the complex taphonomic processes at play within fluvial systems (Evans, 2015); however, the presence of articulated and associated remains

with limited pre-depositional weathering at two sites in particular (QML1470 (SW9) and QML1470 (SW3)) demonstrates low levels of transport prior to burial (Figure 4.2w; Appendix C2 & C4). The preservation of delicate remains, such as insect and seed parts, further supports rapid deposition at SW9 (Figure 4.2f–I; Figure C1). Post-depositional alterations of the fossils (e.g. bones, teeth, leaves, seeds, molluscs and insects) are localised at each site and include iron-oxide and carbonate precipitation, cortical bone and tooth enamel splitting, microscopic surface bone striations and bone deformation (Figure C10). Taphonomic characteristics developed for vertebrates (Fernandez-Jalvo & Andrews, 2016) form the basis for our interpretation, including subsurface alterations via long-term drying and compaction of the mud-dominated host matrix (Appendix C4). Post-depositional introduction of younger sediment is only observed within the north-east portion at one site (SW9) as sediment-filled cracks. This indicates post-depositional drying of the deposit and introduction of younger sediment into these cracks, which were avoided or sampled separately during sampling for optically stimulated luminescence (OSL) (Figures C11 & C15). Sediment-filled cracks were not observed anywhere else within SW9, or at any other site.

No evidence has been found to indicate reworking of older faunal remains into deposits at SW9, which is independently supported by uranium-series (U-series) assessments of fossilised teeth from SW9 (Appendix C7). Six megafauna species from SW9 were directly dated using U-series laser ablation and micro-profiling, all returning consistent and younger ages than other techniques, therefore, supporting the primary context of the deposit through the absence of reworked older fossils (Table 4.2, Appendix C7). Together, this gives us confidence that the chronometric assessment of the fossils and sediments entraining them accurately reflect the depositional age of the fossils.

To chronometrically constrain the age of the megafauna sites we used multiple dating techniques to age the fossils or the sediment they were buried in. Direct dating of fossils is considered the most reliable approach for establishing extinction chronologies with a quality rating of A* or A (Rodríguez-Rey et al., 2015), therefore, we applied radiocarbon, U-series, and U-series combined with electron spin resonance (ESR) techniques to fossilised megafauna teeth and bones from the best preserved and most fossiliferous site, SW9. U-series and U-series-ESR techniques provided viable results (Table 4.2, Appendix C7 & C8); however, radiocarbon assessment of megafauna bones was unsuccessful due to a lack of collagen (Appendix C6).

Dating of sediments derived from above, within, and below the fossil-bearing layer using single-grain OSL is considered an A-rated method for indirectly dating fossils and is readily applicable to undisturbed sediment (Rodríguez-Rey et al., 2015). We applied the OSL dating technique to all of our fossil sites and these returned viable results (Table 4.2, Appendix C5). The combined geological, taphonomic, faunal, floral and chronometric studies support an undisturbed primary context for the fossil deposits and their remains, thus by combining A* or A-rated dating techniques and using multiple independent laboratories to do so we are confident that the chronometric ages obtained for each site are of high quality and thus reliable (Rodríguez-Rey et al., 2015) (Table 4.2, Methods and Appendix C1–C9).

The chronometric ages for the four sites are summarised in Table 4.2 with detailed methodology and datasets provided in the Methods section and Appendix C1–C9. Together, the four sites span ~20,000 years from ~60 to ~40 ka. The oldest fossil-bearing layer occurs at SWJ, which has a maximum weighted mean OSL age of 65.6 ± 2.2 ka (n = 6). The next youngest fossil layers occur at SWCC, which has a weighted mean OSL age of 58.2 ± 6.1 ka (n = 2), and SW3 which has a weighted mean OSL age of 47.7 ± 3.2 ka (n = 5). The youngest fossil deposit which occurs at SW9 has a weighted mean age of 40.1 ± 1.7 ka (n = 24), which has been calculated from 19 OSL ages and 5 US-ESR ages (Tables 4.1 & 4.2, Appendix C5–C8).

Figure 4.2 Summary of field sites and diversity of fossil remains from South Walker Creek (QML1420). **a** Aerial map of main South Walker Creek fossil sites SW9, SWJ and SW3 with downstream site SWCC indicated by arrow. Megafauna taxa recovered from each site indicated by numbered silhouette: 1. *Pallimnarchus* sp. 2. '*Quinkana*' sp., 3. *Crocodylus* sp. cf. *C. porosus*, 4. *Varanus priscus*, 5. *Varanus* sp. (large), 6. *Dromaius* sp., 7. *Diprotodon optatum*, 8. *Phascolonus* gigas, 9. *Sedophascolomys* sp. cf. *S. medius*, 10. *Thylacoleo* sp., 11. *Palorchestes* sp., 12. *Macropus* sp. (giant), 13. *Protemnodon* sp., 14. *Notamacropus* sp. (giant), 15. *Osphranter* sp. cf. *O. rufus*, 16. sthenurine. **b** Stratigraphic section A–A′ crossing through SW9, SWJ and SW3 (indicated by dashed line in (**a**)). Quaternary (Qa) alluvial sediment overlies dipping basement Permo-Triassic Rewan Group (Rw) bedrock (vertical exaggeration 5×). Fossil deposit surface expression at SW9 (**c**), SW3 (**d**) and SWCC (**e**). Summary of the diverse fossil remains recovered from SWC sites (see Appendix C1 for detailed descriptions): **f** leaves and bivalves in situ at SW9; **g** Goodeniaceae seed; **h** *Velesunio wilsoni* bivalve; **i** insect elytron (?Curculionidae); **j** *Pallimnarchus* sp. osteoderm; **k** *Crocodylus* sp. cf. *C. porosus* osteoderm; isolated crocodile teeth from **l** *Pallimnarchus*, **m** *Crocodylus* sp. and **n** '*Quinkana*'; **o** *Varanus priscus* tooth; **p** *Macropus* sp. (giant) tibia in situ at SW9; **q** *Varanus priscus* dorsal vertebra; associated appendicular elements from *Thylacoleo* sp., **r** metacarpal, **s** phalange and **t** fibula; **u** *Diprotodon optatum* right dentary; **v** *Macropus* sp. (giant) humerus with crocodile puncture marks (indicated by arrows); **w** Articulated pelvis and caudal vertebrae of *Phascolonus gigas* from SW9; **x** associated hind limb of juvenile *Protemnodon* sp. from SW9. Scale bars equal 1 mm in (**g**, **i**); 5 mm in (**h**, **j – t**, **v**, **x**); 10 mm in (**u**); and 50 mm in (**w**).

Extinctions coincide with environmental deterioration

The known limitations of the fossil record, such as those described by the Signor-Lipps effect (Signor & Lipps, 1982), can bias the estimated timing of extinction for a fossil taxon (Wang & Marshall, 2016). Therefore, the youngest fossil record for a particular taxon should only be considered as indicative of the last appearance of an extinct taxon, not its true time of extinction. With this in mind, we can conclude that the extinct megafauna taxa at SWC suffered local extinction sometime after their youngest last appearance age at SW9, which is 40.1 ± 1.7 ka.

With our new fauna and chronology in mind, we investigated available palaeoenvironmental proxies, in particular those recording regional and local changes that are likely to have impacted the survival of megafauna (e.g. water, vegetation, fire and climate). Hydroclimatic proxies that include palaeomonsoon activity, catchment flow and lake levels are available for northern Australia and the three basins associated with our fauna, the FRB, LEB and MDB. Chronologically staggered and abrupt hydroclimatic deterioration starts around 48 ka in the LEB (Cohen et al., 2015; Kemp et al., 2019) (Figures 4.3a), then from 45 ka in the MDB (Bowler et al., 2012; Hesse et al., 2018; Kemp et al., 2019) (Figures 4.3b and c), and then from 40 ka in the FRB (Croke et al., 2011; Kemp et al., 2019) (Figures 4.3d). Hydroclimate in northern Australia falls below present day levels after 40 ka (Kemp et al., 2019; Krause et al., 2019) indicating a significant drying trend (Figures 4.3e). Together, these records show abrupt and major fluctuations with a sustained reduction in effective rainfall reaching the watersheds of the LEB, MDB and FRB from 48 ka and lasting until at least 30 ka. Within each basin, the youngest reliably-dated megafauna occur during, or just prior to, the onset of abrupt hydroclimatic deterioration (Figures 4.3a–e). Given that the extinction of these megafauna occurred after their last appearances, we infer that local extinctions in these basins occurred during abrupt deterioration in hydroclimate.

The correspondence between the staggered chronologies of both the youngest megafauna and the onset of sustained hydroclimatic deterioration for each basin suggests hydroclimatic change as a possible driver of catchment-based extinctions, occurring first in the LEB, then in the MDB and then in the FRB. The sustained loss of effective catchment flow within the FRB would not favour survival of aquatically-dependent megafauna, such as the three crocodilians. *Crocodylus* likely survived this inland deterioration by occupying viable coastal environments whilst *Pallimnarchus* and '*Quinkana'* did not. At some point since 30 ka the hydroclimate of the FRB returned to levels similar to that experienced prior to 40 ka, presumably after the Last Glacial Maximum; however, the aquatic environments that were once conducive for crocodilians at SWC did not return indicating that the hydrological system was irrevocably altered.

We acknowledge that for open sites there may be reduced preservation potential of vertebrate remains due to the deterioration of the hydroclimate; therefore, a taphonomic bias against the preservation of younger sites may have occurred as the hydroclimate deteriorated. This potential bias of preservation can be reconciled with the discovery of reliably-dated sites within these basins that preserve only extant megafauna.

In addition to hydroclimate, we investigated Quaternary proxy records of vegetation (Moss et al., 2017; Moss & Kershaw, 2007; Moss et al., 2013), fire (Moss et al., 2017; Moss et al., 2013; Rule et al., 2012; Thevenon et al., 2004) and climate change (Cadd et al., 2018; Croke et al., 2011) from east of the Great Dividing Range in Queensland. These records represent palaeoenvironmental proxies closest to our sites and likely better reflect more direct environmental changes influencing megafaunal survival. Palynological data from the offshore ODP82027 drill record is the most appropriate for indicating changes in vegetation and fire frequency relevant to our locality because it preserves a signal that is not constrained by local terrestrial site depositional biases (Moss et al., 2005). This record indicates an overall drying with sustained reduction of complex rainforest beginning ~50 ka. Importantly, there is a regional reduction in grasslands (sclerophyll herbs), which is a key dietary

component of herbivorous megafauna. This reduction begins around 50 ka and reaches its lowest levels for the entire record at ~35 ka (Figure 4.3f). Arboreal sclerophyll taxa (e.g. *Eucalyptus*, *Melaleuca*, *Acacia* and Casuarinaceae) generally follow the same trends seen in sclerophyll herbs over the last 250 kyr (Moss & Kershaw, 2007); however, they approximately double their proportional representation after ~36–35 ka (Moss et al., 2017; Moss & Kershaw, 2007; Moss et al., 2013) indicating a sustained change in the sclerophyllous vegetation structure along the eastern seaboard.

Our palynological assessment of SW9 shows similarities to the regional pollen record of ODP820 and the local record at Lynch's Crater (Kershaw et al., 2007) during MIS3. The overall taxonomic composition of pollen taxa at SW9 is also similar to that of the present day SWC area (Appendix C9, Figure C32 and Table C23), therefore, this indicates limited change in floral composition since the deposition of SW9 ~40 ka. A greater proportional representation of arboreal sclerophyllous taxa compared with low counts of sclerophyllous herbs (e.g., Poaceae) is surprising but may be indicative of the observed regional reduction of grasslands from 50 to 35 ka and suggests suboptimal forage for the grazing megafauna. The dominance of arboreal sclerophyllous taxa may also be indicative of the transition to a more dominant arboreal sclerophyll vegetation structure recorded later in MIS3 further to the north (Croke et al., 2011; Kershaw et al., 2007; Moss et al., 2017).

The ODP820 charcoal record illustrates an increased fire frequency starting ~44 ka, intensifies from ~40 ka, and peaking ~28 ka (Moss et al., 2017; Moss & Kershaw, 2007; Thevenon et al., 2004) (Figure 4.3g). While anthropogenic landscape burning has been attributed to these increases over the last 50,000 years (Moss et al., 2017; Thevenon et al., 2004), this has been challenged and a more likely explanation involves the complex relationship between climate and vegetation with fire frequency (Mooney et al., 2012). Importantly, the increased and sustained burning from ~44 ka indicates a fundamental shift toward environmental deterioration and instability that would have impacted the survival of megafauna. The extinction of grazing megafauna sometime after ~40 ka would have reduced grazing pressure on grasslands and potentially created the conditions favouring intensified burning (Archibald et al., 2005; Archibald et al., 2019), and possibly contributing to the peak in burning seen regionally around 28 ka. Our assessment of charcoal particles at SW9 (Appendix C9) demonstrates preservable indicators of fire within the environment; however, these results will be uninformative until a longer sequence is available to assess and compare relative charcoal frequencies through time as well as any taphonomic bias within this alluvial system.

Together, the multiple proxies investigated here show regionally sustained vegetation change with reduction of grasslands and a sustained higher representation of arboreal sclerophyll taxa, which is also reflected locally at SWC. These vegetation changes occurred alongside sustained and intensified fire along with reduced catchment flow and thus available free water. Such deterioration of the environment is set within a backdrop of intensifying aridity (Kemp et al., 2019). The culmination of these changes would have impacted terrestrial megafauna survival, especially the herbivores and more specifically the grazers. These negative impacts from a deteriorating environment on herbivorous megafauna survival would likewise have affected the hypercarnivorous megafauna.

The SWC megafauna were a diverse aquatic and terrestrial megafauna community, occurring locally from at least 60 ka until 40.1 ± 1.7 ka, with their local extinction occurring sometime after this. The regional environmental changes that began ~48–50 ka did not have an obvious or immediate impact. However, we propose that the intensification of environmental deterioration and instability starting ~40–41 ka played a key role in their local extinction (Figure 4.3).

Table 4.1 Megafauna species within MIS3 from South Walker Creek and other Fitzroy River basin sites compared with species lists from other similarly-aged regions of Australia.

Region		TAS	SW-WA	Lake Eyre Basin	Murray-Darling Basin			Fitzroy River Basin				
Sites					Willandra Lakes	Ned's Gully	Cuddie Springs SU6A + B	SW9	SW3	SWCC	SWJ	Other sites
Chronometric ages		48- ~41	50-41 ± 2	47.5 ± 2.5	>33- <36	47 ± 4	~35 ka- >45-~50	40.1 ± 1.7	47.0 ± 3.2	58.2 ± 6.1	<65.6 ± 2.2 a	<50
A or A* age in bold		n = 12	n = 12	n = 11	n = 3	n = 2	n = 5	n = 24	n = 5	n = 2	n = 6	
Dating Criteria Rating		A-A*	A	A + A*	A + B	A	A* + B	A + A*	A	A	A	N/A
†*Progura* (egg shell)	MeH			–								
Megafauna												
†*Genyornis*	McH						–					
Dromaius sp.	*McH*	–	–	–			–	Y	–			
†*Pallimnarchus* sp.	MC							Y	–	–	–	b
Crocodylus sp. cf. C *porosus*	*MC*							Y	–	–		
† *Quinkana'* sp.	MC								–	–	–	
†*Varanus* sp. (large)	LC							Y	–			C
†*Varanus priscus*	MC							Y	–	–	–	
Macropus fuliginosus	MeH		–									
Macropus giganteus	MeH		–				–					
†*Macropus titan*	McH	Y	–			Y	–					
†*Macropus* sp. (giant)	McH							Y	–	–	–	
†*Notamacropus* sp. (giant)	McH							Y	–	–		b
Osphranter rufus	McH						–		–			
†*Protemnodon* sp.	McH	Y	Y			d	–	Y	–	–		
†*Sthenurus* sp.	McH						–					
†*Procoptodon* sp.	McH		Y			d				–		
†*Simosthenurus* sp.	MeH	–	2spp									
†*Phascolonus gigas*	McH					d	–	Y				
†*Sedophascolomys* sp. Cf. S. medius	MeH							Y	–			b
†*Diprotodon optatum.*	MH					Y	–	Y	–			
†*Zygomaturus trilobus*	MH		–		?Y							? b
†*Palorchestes* sp.	McH							Y				
†*Thylacoleo* sp.	MC		–			d		Y				
Extinct Megafauna		3	7	0		7 (+2 uncertain)				13 (+1 uncertain)		
Extant Megafauna		2	3	1		3				3		
Total Megafauna Species		5	10	1		10 +2 uncertain				16 +1 uncertain		

Megafauna listed are from sites within the last 50 ka that have been reliably-dated with an A or A* rating using defined rating criteria (Rodríguez-Rey et al., 2015) (see Methods). Those with equivocal B-ratings are discussed in the Methods. Y denotes the youngest reliably-dated megafauna from each region. Megacarnivore (MC) (>100 kg) (Malhi et al., 2016); Large carnivore (LC) (21.5–99 kg) (Malhi et al., 2016); Megaherbivore (MH) (>1000 kg) (Owen-Smith, 2013); Macroherbivore (McH) (100–1000 kg) (Owen-Smith, 2013); Mesoherbivore (MeH) (10–100 kg) (Owen-Smith, 2013). TAS Tasmania, SW-WA Southwest Western Australia, spp species, ka thousands of years.

†Extinct.

[a] Oldest site at SWC (SWJ) included for completeness.

[b] Undated Upper Pleistocene fauna from Quaternary sites (Kemmis and Homevale) close to SWC included for completeness.

[c] Dated occurrence (30–<50 ka) of a large-bodied varanid from Capricorn Caves, FRB (Price et al., 2015), B-rated (Peters et al., 2019).

[d] Taxa from Ned's Gully locality without direct association with dated fossil layer (Price, 2012), B-rated.

Reduction of the *Sporormiella* dung fungus occurring around 41 ka at Lynch's Crater, ~560 km north of SWC, has been used as a proxy for both the presence of megaherbivores and their rapid population decline to extinction (Rule et al., 2012; van der Kaars et al., 2017). However, the use of *Sporormiella* as a megaherbivore proxy has been challenged on taphonomic and biological grounds (Baker et al., 2013; Dodson & Field, 2018; Feranec et al., 2011; Price et al., 2018; Wood & Wilmshurst, 2012). Variable concentrations of *Sporormiella* spores are present in the sediment samples taken at SW9 for palynological assessment (Appendix C9, Table C23). Some samples indicate high concentrations similar to those recovered from Lynch's Crater (Rule et al., 2012) and off-shore Western Australia (van der Kaars et al., 2017); however, it is unclear whether there are other depositional or taphonomic biases at play in the fluvial system that can explain such variation in concentrations. Therefore, the presence of some high concentrations of *Sporormiella* potentially supports the presence of megaherbivores within the environment at the time of SW9 deposition; however, this will remain equivocal until a detailed assessment of depositional and taphonomic biases is undertaken.

A role for people in the extinction of Sahul megafauna through their direct extirpation has been previously proposed. However, with no evidence of butchery or kill sites, it has been proposed that extinction occurred rapidly across Sahul shortly after human arrival (Brook & Johnson, 2006; Field et al., 2008; Field et al., 2013; Hamm et al., 2016; Johnson et al., 2016; Roberts et al., 2001; Saltré et al., 2016; Wroe & Field, 2006). In the absence of evidence for direct extirpation, indirect human-mediated factors such as landscape burning have been proposed but are difficult to differentiate from non-human factors (Bird et al., 2013; Brook & Bowman, 2002; Brook et al., 2013; Rule et al., 2012; van der Kaars et al., 2017).

The occupation of Sahul most-likely occurred in northwest Sahul, at least 50 ka (O'Connell & Allen, 2004; O'Connell et al., 2018) or as early as 65 ka (Clarkson et al., 2017), with much of mainland Australia inhabited by 45 ka (Allen & O'Connell, 2014; David et al., 2019; David et al., 2007). People most-likely dispersed across the continent via migratory routes either reflecting connectivity to available freshwater (Bird et al., 2016) or first along coastal routes and then dispersing inland (Tobler et al., 2017). Therefore, under a human-driven extinction scenario where megafauna suffer extinction shortly after human arrival it would be expected that megafauna would suffer extinction first in the north and then along the continental periphery of Sahul before extinction occurred in southern and interior regions.

SWC represents the most northerly and the only diverse megafauna site from the easterly-draining seaboard to be reliably-dated within the period of human occupation of Sahul. Therefore, it is well situated to test these scenarios. If the youngest megafauna ages in an area are considered to be the closest age approximation for their extinction, then the most reliable records indicate that extinctions occurred first within the interior (e.g. LEB) after 48 ka, then within the southern MDB after 45 ka; and then around the continental periphery (e.g. southwest Western Australia, Tasmania and SWC) after 41–40 ka (Table 4.1). This result is contrary to what would be expected and so our assessment does not support rapid or synchronous continental-wide extinction of megafauna by people.

Based on what archaeological evidence is available, we cannot firmly place people at SWC, or within the FRB, at the time the fossil deposits formed. The oldest archaeological record closest to SWC has an occupation age of ~19 ka at Kenniff Cave (Reid & Ulm, 2000), Carnarvon Gorge, ~380 km south of SWC. The earliest evidence for human occupation, that is closest to the FRB, comes from two sites over 660 km to the north and northwest of SWC. The two locations, Gledswood Shelter (Lowe et al., 2018) and Ngarrabullgan (David et al., 2019), record human occupation at or younger than 40 ka and occur within the north and westerly-draining Flinders and Mitchell River Basins of Gulf of Carpentaria. Neither basin shares topographic or hydrological connection with the FRB to the southeast.

With no evidence for a human presence within the FRB before ~19 ka, or even more regionally before 40 ka, we cannot implicate people in the extinction of the SWC megafauna. Acknowledging the limited number of archaeological sites older than ~30 ka from eastern Sahul (Bird et al., 2013; Williams et al., 2018) we cannot rule out that this absence is a result of significant under sampling, therefore, future concentrated field effort in eastern Sahul may establish an archaeological record older than 40 ka.

Table 4.2 Chronometric ages for South Walker Creek sites and their reliability score.

QML1470	Dating method		Association	Score	N	Age interpretation	Age (ka)
SW9	US-ESR (SCU)	Direct (m*)	Yes – w	A*	5	Age of megafauna fossils within Unit C.	32.5 ± 2.5 (2σ)a
	US (UQ)	Direct (m)	Yes – w	A	4	Minimum age of megafauna fossils within Unit C.	24.5 ± 0.1 (2σ)b
	US (UOW)	Direct (m)	Yes – w	A	2	Minimum age of megafauna fossils within Unit C.	25.5 ± 0.1 (2σ)b
	OSL (AU + GU)	Direct (m)	Yes – a, w + b	A	19	Age of Unit C, including fossiliferous layer.	41.3 ± 1.9 (1σ)a
	OSL + US-ESR (ALL)	Both	Yes – a, w + b	A* + A	24	Combined age of megafauna and deposit.	40.1 ± 1.7 (1σ)a
	^{14}C (charcoal) (ANU)	Indirect (B)	Yes – w + b	B	3	Minimum maximum age of deposit.	> 40–50 kac
SW3	OSL (AU)	Indirect (m)	Yes – a + w	A	5	Age of entire deposit including fossiliferous layer.	47.7 ± 3.2 (1σ)a
SWCC	OSL (AU)	Indirect (m)	Yes – b	A	2	Age of entire deposit (Units B, C & D), including fossiliferous layers.	58.2 ± 6.1 (1σ)a
SWJ	OSL (AU)	Indirect (m)		A	6	Age of Unit B, maximum age of fossiliferous Unit C.	65.6 ± 2.2 (1σ)a

Ratings of dating methods uses established criteria (Rodríguez-Rey et al., 2015). All chronometric results, including detailed methods, are provided in the Methods and Appendix C5. m, m*, B, A and A* are categories and ratings defined here (Rodríguez-Rey et al., 2015).
a above, b below, w within the fossiliferous layer.
[a] Weighted mean age and uncertainty.
[b] Oldest age and uncertainty.
[c] Reworked macro-charcoal represents a maximum age for the deposit, however, this material only survived ABA treatment, therefore must be considered a minimum age range. Radiocarbon dates on sediment are not included here as the data is not acceptable according to Rodríguez-Rey et al. (2015).

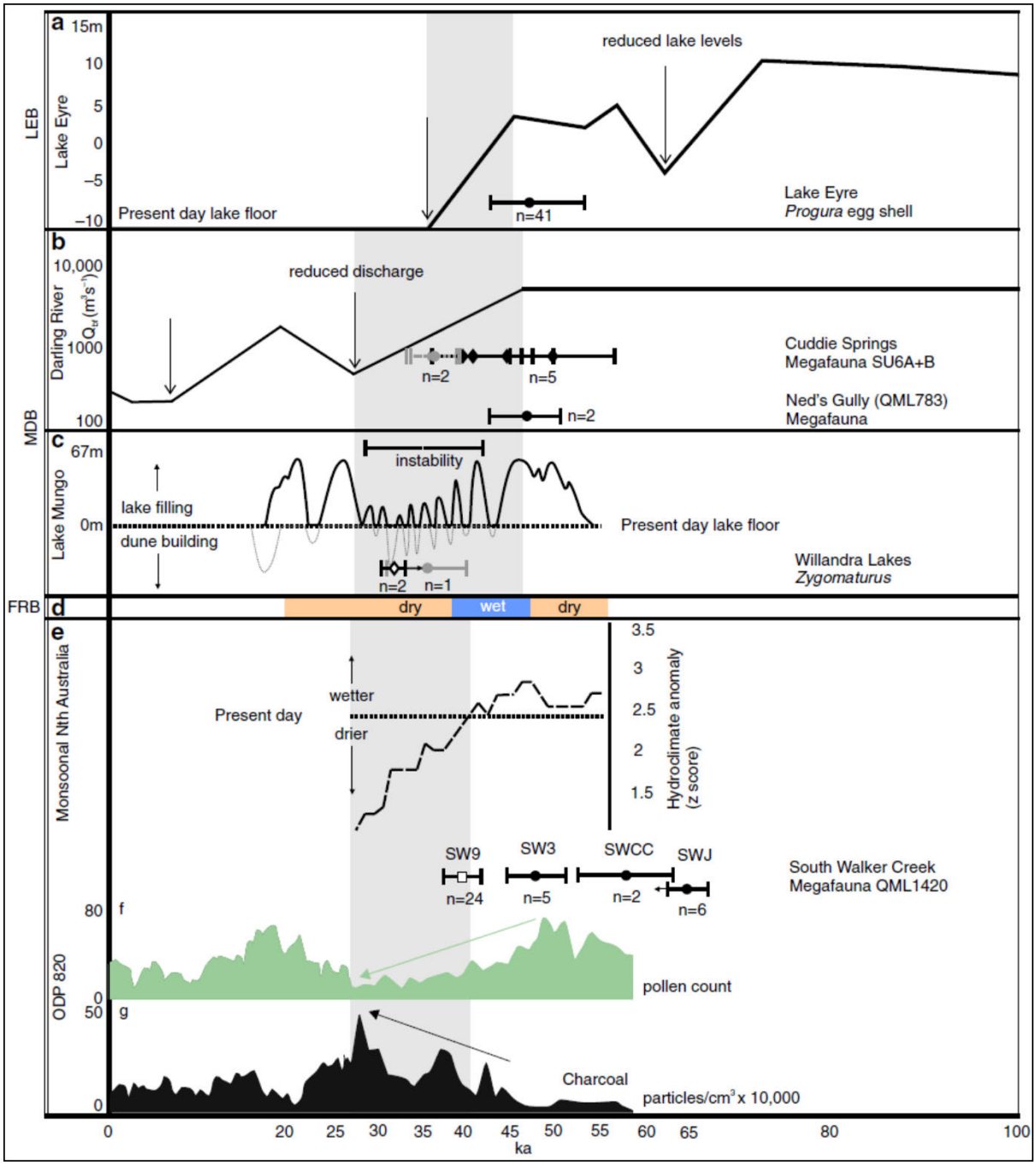

Figure 4.3 Regional hydroclimate and local palaeoenvironmental proxies since 100 ka compared with young megafauna sites from the Lake Eyre, Murray-Darling and Fitzroy River basins. **a** Hydroclimatic proxies include Kati Thanda–Lake Eyre levels (adapted from Cohen et al. (2015)). **b** Palaeodischarge of the Darling River (adapted from Hesse et al. (2018)). **c** Mungo Lake levels and dune development (adapted from Bowler et al. (2012)). **d** FRB catchment activity (adapted from Croke et al. (2011) and Kemp et al. (2019)). **e** Hydroclimate relative to present day of northern monsoonal Australia (adapted from Kemp et al. (2019)). **f** Local palaeoenvironmental proxies including counts of grass pollen (Poaceae) (**f**) and micro-charcoal (**g**) from ODP 820 (adapted from Moss et al. (2017)). Young megafauna sites within each basin are plotted using A or A* quality-rated ages (black plots) (Table 4.1). All SWC sites are plotted here for completeness. Published OSL ages for Cuddie Springs (Field et al., 2008) and the Willandra Lakes Zygomaturus (Westaway et al., 2017) are B-rated here but are equivocal so we have included them (plotted in grey). Extinctions are interpreted as occurring sometime after the youngest A or A* age. Note the timing of onset of trajectory of hydroclimatic deterioration (light grey bars) within each region and megafauna ages. Closed circles denote OSL ages (1σ); open diamonds denote U-series minimum ages (2σ); filled diamonds denote US-ESR ages (2σ); open circles denote combined radiocarbon and OSL ages (*Progura* egg shell) (1σ); and open square denotes combined OSL and US-ESR ages (1σ).

Discussion

Our discoveries provide the first reliably-dated occurrences for several megafauna taxa within the last 50 ka, including all three crocodilians, *Varanus priscus*, *Palorchestes*, *Sedophascolomys*, and at least two macropodids including the largest species known. This increases the total number of megafauna species present at the time of human arrival in Sahul to at least 24. Our new record refutes the claimed extinction timing of *Pallimnarchus* (Grün et al., 2010) and the modelled extinction timing for *Palorchestes*, *Thylacoleo*, and megafauna representatives of *Macropus* (Saltré et al., 2016). These new records also document biogeographic extension into north-eastern Australia of several taxa during MIS3, including *Thylacoleo*, *Phascolonus*, *Diprotodon* and *Protemnodon*. Furthermore, the number of megafauna species identified at our youngest site is greater than that of similar-aged megafauna sites elsewhere in Australia, increasing the number of taxa surviving the modelled (Saltré et al., 2016) peak of extinction to 13. This amounts to more than half the total number of species now confirmed to be present in Sahul during human occupation.

The age and north-eastern location of our megafauna assemblage is contrary to that which would be expected if continental-wide extinction was human-mediated through direct hunting, where extinctions shortly followed the currently proposed timing and route of human migration across Sahul. Instead, our results favour a scenario of local changes in catchment flow, vegetation structure and fire regime that was not conducive to the survival of aquatic and terrestrial megafauna. These changes should be considered within the context of a regional backdrop of spatio-temporally staggered hydroclimatic deterioration and instability from ~48 ka that occurred across major interior, southern and eastern drainage basins.

Our understanding of the local and regional impacts of environmental deterioration during MIS3 on megafauna in northern Sahul must also be considered within the context of much longer-term hydroclimate deterioration (Kawamura et al., 2006; Nanson et al., 1993; Nanson et al., 2008; Peerdeman et al., 1993; Webster & Davies, 2003) and vegetation change (Kawamura et al., 2006; Longmore & Heijnis, 1999; Moss & Kershaw, 2007) that was underway since the Middle Pleistocene, well before human occupation. These earlier changes have been implicated in major faunal (Hocknull et al., 2007) and floral (Moss & Kershaw, 2007) turnovers in northeast Australia, and yet similar turnovers are not recorded in southern Australian sites spanning similar timeframes (Prideaux et al., 2007a; Prideaux et al., 2007b). Therefore the timing of environmental deterioration and the subsequent responses of fauna and flora differ between regions of Sahul, and have done so across much of the Quaternary. Therefore, more complex scenarios are needed to explain extinctions that take into account these spatio-temporal differences.

Methods

Fossil collection and taxonomic identifications

We employed standard palaeontological and geological procedures during the excavation, including the mapping and recording of positions and associations of fossil remains within the stratigraphic and sedimentological context for each site. Taxonomic identifications were undertaken through indirect comparative assessment via available literature or through direct comparisons with collections held at the Queensland Museum, Museums Victoria, Australian Museum and South Australian Museum (Appendix C1–C4).

Geochronology

Dating samples were collected during field excavation and laboratory preparation from 2009 to 2017, with focus on collecting adequate material to undertake multidisciplinary age assessments using four independent dating techniques, specifically optically stimulated luminescence (OSL); radiocarbon (^{14}C), uranium series (US), and combined US and Electron Spin Resonance (US-ESR) dating. All sites were sampled; however, due to the poor quality of some samples, not every technique could be

applied successfully across all sites. OSL dating has been applied across all sites and via two independent laboratories (Griffith University (GU) and The University of Adelaide (UA)). ^{14}C and U-series assessments were undertaken by two independent laboratories (^{14}C by Beta Analytic (Beta) and Australian National University (ANU)) and U-series by The University of Queensland (UQ) and University of Wollongong (UOW). ESR assessment was undertaken by a single laboratory at Southern Cross University (SCU).

The matrix depositional age was assessed using OSL, whilst the age of the organic inclusions (teeth/bones/charcoal/organic sediment) was assessed using ^{14}C, US and ESR. OSL measurements were undertaken independently at GU and UA, and the various burial dose datasets were then analysed using a combined data approach. Associated fossilised teeth were assessed using US, ESR, and combined US-ESR to determine the uptake history of the fossils and allow modelling of finite numerical ages. Attempts were made to radiocarbon date bones, teeth, charcoal and sediment using a variety of pre-treatment methods. Unfortunately, no megafauna could be directly dated due to a lack of collagen. The radiocarbon methods which could be applied to macro-charcoal produced minimum age estimates only. Detailed methodologies are provided in Appendix C5–C8 for all dating techniques used.

Optically stimulated luminescence

OSL core samples were collected by QM in 2009, 2011, 2015 and 2016 using extraction techniques and methodologies provided by GU laboratory and through best practice literature (see Appendix C5). This included choosing sampling localities that (1) were freshly exposed through excavation into cohesive sedimentary matrix; (2) avoided areas showing sediment introduction via recent or old sediment cracking; (3) entirely avoided unconformities, major lithological boundaries and complex sedimentary matrices; (4) were positioned at least 20–30 cm below the exposed ground surface to avoid inaccuracies in gamma dose rates determined using ex situ (laboratory-based) dosimetry techniques. Sediment samples were taken from above and below each core at a radius of between 15 and 20 cm for sedimentological, high-resolution gamma spectrometry (HRGS) and water content assessments. Where possible, OSL core samples were collected in vertical and horizontal sequences to provide both stratigraphic and duplicate samples for any particular layer, including samples taken specifically above, within and below the fossiliferous horizons.

Additional OSL samples were collected by UA in 2017, and included the use of in situ gamma-ray spectrometry (NaI:Tl crystal) to measure external gamma dose rates via the energy windows method (Arnold et al., 2012). Low-level beta counting was conducted on homogenised sediment collected from the OSL sampling holes to determine external beta dose rates. Conversion and attenuation factors (Brennan, 2003; Guérin et al., 2011; Mejdahl, 1979) were applied to determine the gamma and beta components of the total dose rate. The dose rate contributions from cosmic-rays have been calculated using previous approaches (Prescott & Hutton, 1994). The beta, gamma and cosmic-ray dose rates have been corrected for long-term sediment moisture contents (Aitken, 1985), which were taken to be 40 % of the saturated water content following assessments made on samples from freshly-dug pits across various sites.

Quartz grains (212–250-μm diameter) from the 2015 and 2017 samples were purified at UA following standard laboratory procedures (Demuro et al., 2019), including the removal of the alpha-irradiated grain margins through treatment with 48 % hydrofluoric acid (40 min) (Aitken, 1998). Equivalent dose (D_e) values were determined for single quartz grains using the single aliquot regenerative dose (SAR) procedure (Murray & Wintle, 2000) and only accepted for dating purposes if they satisfied a series of quality assurance criteria (Arnold et al., 2016). Single-grain D_e measurements were made using the experimental apparatus described by Demuro et al. (2015) and Méndez-Quintas et al. (2018) after manually loading quartz grains into standard single-grain aluminium discs drilled with an array of 300 × 300-μm holes.

The single-grain quartz D_e measurement procedures employed by GU for the 2009, 2011 and 2016 samples are as described above, with the exception that the 180–212 μm diameter quartz fractions which were isolated for dating using the single-grain quality assurance criteria (Pietsch, 2009) (see Appendix C5).

We have considered a range of statistical age models to characterise each single-grain D_e distribution and to derive representative burial dose estimates for the AU and GU OSL samples (central age model (CAM), the three-parameter minimum age model (MAM-3), the four-parameter minimum age model (MAM-4) and the finite mixture model (FMM) (Galbraith & Green, 1990; Galbraith et al., 1999). The rationale behind the age model choice for each sample is provided in Appendix C5, and is based on consideration of D_e overdispersion, the presence of discrete dose populations, and the statistical suitability of the various age model fits (maximum log likelihood criterion) (Arnold et al., 2009). The same age model selection criteria have been applied to both the AU and GU D_e datasets to ensure consistency with the final OSL age evaluations. The software, R (luminescent package), was used for the evaluation of the equivalent dose and modelling distributions for CAM and MAM (see Code availability).

Uranium-series dating

Several fossil teeth were directly dated using U-series methods (see Appendix C7 & C8). This included both micro-drilling and laser ablation of dentine with subsequent measurement using multi-collector inductively coupled plasma mass spectrometers (MC-ICP-MS). For micro-drilling, multiple powdered dentine samples were collected with a 1 mm diameter stainless steel hand drill bit through the respective teeth following standard techniques (Price et al., 2013). This allowed for the construction of both U-concentration and ^{230}Th-age profiles though the teeth, thus, allowing investigation of the mode of U-uptake/loss in the teeth, and essentially, the reliability of the resulting ages. The micro-drilled dentine samples were measured at Radiogenic Isotope Facility, The University of Queensland. using a Nu Plasma MC-ICP-MS following the laboratory's standard protocols (Zhou et al., 2011).

Open-system U-series dating of the teeth via laser ablation MC-ICP-MS was undertaken at the Wollongong Isotope Geochronology Laboratory, University of Wollongong. Laser ablation was performed on a NWR 193 excimer laser coupled to a MC-ICPMS Thermos Plus, at parameters of fluence of 0.9 J/cm^2, pulse rate of 10 Hz, spot size of 150 μm and scan speed of 5 μm/s. Helium was used as a carrier gas at a flow rate of 0.9 L/min. Before and after each sample, three rasters were done on NIST612, MK10 (a MIS7 coral used as primary standard (Woodroffe et al., 1991)) and MK16 (a MIS5 coral used as secondary standard). Measured ^{234}U/^{238}U and ^{230}Th/^{238}U isotopic ratios were corrected for elemental fractionation and Faraday cup/SEM yield by comparison with MK10 coral (see above) for which ratios were previously characterised internally by solution analysis. Background subtraction, concentration quantification and ratio corrections were performed using Iolite™ software. Open-system U-Th ages were modelled following the Diffusion-Adsorption-Decay model (Sambridge et al., 2012) and using the UThwigl R package (Dosseto & Marwick, 2019) (see Code availability).

Combined U-series and electron spin resonance dating

ESR dating was performed on a Freiberg MS5000 X-band, coupled to a X-ray Varian irradiator. ESR measurements were performed at 1G modulation amplitude, 2 mW power, 100G sweep, 100 kHz modulation frequency, while sequence of 90 s, 380 s, 900 s, 1800s, 3600, 7200, 14,400 s was undertaken at 40 kV voltage and 0.5 mA current. For each irradiation step the fragment was measured over 180° in x, y and z-configurations with a 20° step. Dose response curve (DRC) and equivalent dose (D_e) were calculated using the MCDoseE 2.0 program (Joannes-Boyau et al., 2018). The external dose was calculated using the values obtained by the gamma spectrometer measurements in the field.

Radiocarbon dating

Attempts to date bones, teeth and macro-charcoal at Beta-Analytic using their standard collagen and carbon pre-treatment techniques (Appendix C6) were unsuccessful as no collagen was preserved and macro-charcoal did not survive the processing. Instead bulk organics were extracted and dated from the sediments instead. Radiocarbon dates on sediments are notoriously unreliable given the multiple sources of carbon present, each of which may have a different age. Charcoal found within the fossiliferous layer was dated at the Australian National University using techniques outlined in Appendix C6. Unfortunately, samples were too small and/or too poorly preserved for acid base oxidation-stepped combustion techniques (ABOx-SC), and were cleaned with an acid-base-acid (ABA) protocol. This protocol does not effectively remove contaminants, and the radiocarbon dates on charcoal must be regarded as minimum age estimates. This complicates interpretation as charcoal in fluvial deposits can be considerably older than the deposition of the sediment. We suspect that the macro-charcoal pieces assessed in the fossiliferous layer are reworked within clay-rich rip-up clasts that are observed within the fossiliferous layer but likely derive from older scoured alluvial sediments (Appendix C4 & C6).

Palynological assessment

Clay-rich matrix was sampled from QML1470 SW9 that preserved macroplant fossil remains. These samples were then subsampled for palynological assessment (Appendix C9). Ten subsamples were processed to assess the palynological concentrate to determine the floral diversity of the site (Figure C33 and Table C23). Each subsample (~10 g of sediment) was analysed using a method developed for pollen extraction from marine sediments, i.e. low organic content (van der Kaars, 1991) and successfully applied to a range of depositional settings (Moss, 2013). Samples are deflocculated in sodium pyrophosphate (10 %) and then using sodium polytungstate heavy liquid (specific gravity of 1.9) to separate the palynomorph rich organic layer from the mineral clay fraction of the sediment. The pollen concentrate then underwent acetolysis using a 9 to 1 mixture of acetic anhydride and concentrated sulphuric acid. Samples were then placed in glycerol for pollen and micro-charcoal (particles < 125 μm) counting using a ×400 compound light microscope.

Quality assessment and choice of fossil ages

Applying selective criteria when choosing or rating the quality of dates for Quaternary-aged fossil fauna is an area of evolving study and refinement (Becerra-Valdivia et al., 2020; Meltzer & Mead, 1985; Roberts et al., 2001; Rodríguez-Rey et al., 2015). We follow established criteria for assessing the quality of dating techniques used to choose the most reliable ages for megafauna fossils in Sahul (Rodríguez-Rey et al., 2015) dating from MIS3 (Figure 4.1 and Table 4.1). We apply these same criteria to our own results (Table 4.2). Those considered to be reliable (e.g. rating of A or A*) were preferred over those that were considered unreliable (e.g. rating of B or C). We then used these same ages to place the youngest records of megafauna within their respective catchments and relate these to available palaeoenvironmental proxies recorded for each catchment and region, thus relating these patterns to our location within the Fitzroy River Basin (Figure 4.3).

Youngest high quality-rated megafauna fossil ages are provided in Table 4.1. Megafauna fossils from Tasmania were directly dated using radiocarbon (Gillespie et al., 2012) and were A*-rated (Rodríguez-Rey et al., 2015). Sediment containing megafauna fossils from southwest Western Australia were dated using associated speleothem (U-series) and sediments (OSL) and were A-rated (Jankowski et al., 2016; Prideaux et al., 2010). Egg shell from the LEB has been dated using radiocarbon, OSL and amino acid racemisation, including remains previously identified as the extinct giant flightless bird *Genyornis* and the extant Emu *Dromaius* (Miller et al., 2016). The egg shell identified as *Genyornis* has been challenged and is now identified as a species of megapode *Progura* (Grellet-Tinner et al., 2016). *Progura* does not meet our mass definition of megafauna; however, we will use it to represent faunal extinction in the LEB. Based on the direct and indirect dating methods

applied to these egg shells the ages are A* and A-rated. A specimen of *Zygomaturus* from Willandra Lakes (Westaway et al., 2017) within the MDB was dated using U-series laser ablation applied to bone, returning a minimum age estimate. Sediment found with the specimen was also dated using OSL; however, a lack of field data renders the sediment association uncertain. Therefore, a rating of A and B is applied here for the U-series and OSL dates, respectively, with the U-series minimum age preferred. Articulated megafauna remains from the upper Darling River system (Ned's Gully) have been dated using OSL from within the fossil-bearing layer (Roberts et al., 2001); however, many of the fauna listed from this site (Roberts et al., 2001) lack direct association with the fossil layer (Price, 2012). Therefore, we have A-rated the fauna known from the fossil layer and B-rated the fauna with unconfirmed association with the dated fossil layer. Megafauna recovered from Units 6A and 6B, from Cuddie Springs, northern New South Wales, have been dated using A*-rated US-ESR and A-rated OSL methods. The US-ESR ages (Grün et al., 2010) are consistently older than the OSL ages (Roberts et al., 2001) which may reflect fossil reworking, sediment mixing, or both at the site (Gillespie & Brook, 2006; Grün et al., 2010; Roberts & Brook, 2010). This conclusion has been questioned (Field et al., 2013); however, based on the uncertainty surrounding the OSL ages they are B-rated. We acknowledge the uncertainty surrounding the age of megafauna at Cuddie Springs and thus present an age range in Table 4.1, including A* and B-rated ages.

Acknowledgements

We acknowledge and pay respect to the traditional owners past and present of the lands of the Barada Barna people and thank them for their guidance and contributions. We thank all QM Geosciences staff and volunteers for assistance with this project and in particular thank C. Chiotakis, N. Sands, P. Bishop, E. Cannon, K. Spring, J. Wilkinson, P. Tierney, J. Cramb, N. Newman, I. Mitchell, D. Kennedy, A. Hodgkinson, A. Hollingsworth, T. Clifford, D. Lewis, A. Rozefelds, E. Hatte, C. O'Bryen, Andrey Atuchin, Vlad Konstantinov and Capricorn Caves for their contributions and support. We thank the local land holders of the South Walker and Kemmis Creek areas for their hospitality, in particular the Baulch family. We thank L. Reed, A. Camens, S. Bourne, T. Ziegler, H. Janetzki, P. Couper, A. Amey and C. Janis for their contribution of comparative specimens and imagery. We thank all BHP and BHP Mitsui Coal South Walker Creek Mine staff past and present who have been involved with this project, in particular we thank J. Simpson, B. Clarke, R. Hailstone, J. Schumacher, S. Batten, M. Jones, J. McGill, J. Yanes, A. Cooke, A. Bull, C. Lavey, P. Jeston and V. O'Brien for their support. This project has been supported by the Queensland Museum Foundation, Queensland Museum, BHP, BHP Mitsui Coal and BMA. We thank I. Galloway, S. Miller, J. Thompson, J. Palmer, E. Muller, E. Stolberg J. Hooper, M. Anderson, R. Rew, D. Bunting, M. Partridge, R. Adlard, A. Turley, and S. Baker for this. The OSL dating research undertaken by R.L. and L.J.A. was supported by Australian research Council Future Fellowship grant FT130100195. Useries dating at UQ was supported by Australian Research Council grants DP0881279 and DP120101752 to G.J.P. J.L. is supported by ARC Future Fellowship grant FT160100450. Queensland Xray, St. Vincents Hospital, Princess Alexandra Hospital, Mater Hospital and Museums Victoria are thanked for provision of CT scan data.

References

Aitken, M. J. 1985. Thermoluminescence dating: Past progress and future trends. Nuclear Tracks and Radiation Measurements (1982), 10, 3-6.

Aitken, M. J. 1998. Introduction to optical dating: the dating of Quaternary sediments by the use of photon-stimulated luminescence, Oxford, Oxford University Press.

Allen, J. & O'connell, J. 2014. Both half right: updating the evidence for dating first human arrivals in Sahul. Australian Archaeology, 79, 86-108.

Archibald, S., Bond, W. J., Stock, W. D. & Fairbanks, D. H. K. 2005. Shaping the landscape: fire–grazer interactions in an African savanna. Ecological applications, 15, 96-109.

Archibald, S., Hempson, G. P. & Lehmann, C. 2019. A unified framework for plant life-history strategies shaped by fire and herbivory. New Phytologist, 224, 1490-1503.

Arnold, L. J., Duval, M., Demuro, M., Spooner, N. A., Santonja, M. & Pérez-González, A. 2016. OSL dating of individual quartz 'supergrains' from the Ancient Middle Palaeolithic site of Cuesta de la Bajada, Spain. Quaternary Geochronology, 36, 78-101.

Arnold, L. J., Duval, M., Falguères, C., Bahain, J.-J. & Demuro, M. 2012. Portable gamma spectrometry with cerium-doped lanthanum bromide scintillators: Suitability assessments for luminescence and electron spin resonance dating applications. Radiation Measurements, 47, 6-18.

Arnold, L. J., Roberts, R. G., Galbraith, R. F. & Delong, S. B. 2009. A revised burial dose estimation procedure for optical dating of youngand modern-age sediments. Quaternary Geochronology, 4, 306-325.

Baker, A. G., Bhagwat, S. A. & Willis, K. J. 2013. Do dung fungal spores make a good proxy for past distribution of large herbivores? Quaternary Science Reviews, 62, 21-31.

Becerra-Valdivia, L., Leal-Cervantes, R., Wood, R. & Higham, T. 2020. Challenges in sample processing within radiocarbon dating and their impact in 14C-dates-as-data studies. Journal of Archaeological Science, 113, 105043.

Bird, M. I., Hutley, L. B., Lawes, M. J., Lloyd, J., Luly, J. G., Ridd, P. V., Roberts, R. G., Ulm, S. & Wurster, C. M. 2013. Humans, megafauna and environmental change in tropical Australia. Journal of Quaternary Science, 28, 439-452.

Bird, M. I., O'grady, D. & Ulm, S. 2016. Humans, water, and the colonization of Australia. Proceedings of the National Academy of Sciences, 113, 11477-11482.

Block, S., Saltré, F., Rodríguez-Rey, M., Fordham, D. A., Unkel, I. & Bradshaw, C. J. 2016. Where to dig for fossils: combining climate-envelope, taphonomy and discovery models. PloS one, 11, e0151090.

Bowler, J. M., Gillespie, R., Johnston, H. & Sporcic, K. 2012. Wind v water: Glacial maximum records from the Willandra Lakes. In: Haberle, S. & David, B. (eds.) Peopled Landscapes (Terra Australis 34): Archaeological and Biogeographic Approaches to Landscapes. Canberra: ANU Press.

Brennan, B. J. 2003. Beta doses to spherical grains. Radiation Measurements, 37, 299-303.

Brook, B. W. & Bowman, D. M. J. S. 2002. Explaining the Pleistocene megafaunal extinctions: models, chronologies, and assumptions. Proceedings of the National Academy of Sciences, 99, 14624-14627.

Brook, B. W., Bradshaw, C. J. A., Cooper, A., Johnson, C. N., Worthy, T. H., Bird, M., Gillespie, R. & Roberts, R. G. 2013. Lack of chronological support for stepwise prehuman extinctions of Australian megafauna. Proceedings of the National Academy of Sciences, 110, E3368-E3368.

Brook, B. W. & Johnson, C. N. 2006. Selective hunting of juveniles as a cause of the imperceptible overkill of the Australian Pleistocene megafauna. Alcheringa: an Australasian journal of palaeontology, 30, 39-48.

Cadd, H. R., Tibby, J., Barr, C., Tyler, J., Unger, L., Leng, M. J., Marshall, J. C., Mcgregor, G., Lewis, R. & Arnold, L. J. 2018. Development of a Southern Hemisphere subtropical wetland (Welsby Lagoon, south-east Queensland, Australia) through the last glacial cycle. Quaternary Science Reviews, 202, 53-65.

Clarkson, C., Jacobs, Z., Marwick, B., Fullagar, R., Wallis, L., Smith, M., Roberts, R. G., Hayes, E., Lowe, K. & Carah, X. 2017. Human occupation of northern Australia by 65,000 years ago. Nature, 547, 306-310.

Cohen, T. J., Jansen, J. D., Gliganic, L. A., Larsen, J. R., Nanson, G. C., May, J.-H., Jones, B. G. & Price, D. M. 2015. Hydrological transformation coincided with megafaunal extinction in central Australia. Geology, 43, 195-198.
Croke, J., Jansen, J. D., Amos, K. & Pietsch, T. J. 2011. A 100 ka record of fluvial activity in the Fitzroy River Basin, tropical northeastern Australia. Quaternary Science Reviews, 30, 1681-1695.
David, B., Delannoy, J.-J., Mialanes, J., Clarkson, C., Petchey, F., Geneste, J.-M., Manne, T., Bird, M. I., Barker, B. & Richards, T. 2019. 45,610–52,160 years of site and landscape occupation at Nawarla Gabarnmang, Arnhem Land plateau (northern Australia). Quaternary Science Reviews, 215, 64-85.
David, B., Roberts, R. G., Magee, J., Mialanes, J., Turney, C., Bird, M., White, C., Fifield, L. K. & Tibby, J. 2007. Sediment mixing at Nonda Rock: investigations of stratigraphic integrity at an early archaeological site in northern Australia and implications for the human colonisation of the continent. Journal of Quaternary Science, 22, 449-479.
Demuro, M., Arnold, L. J., Aranburu, A., Gomez-Olivencia, A. & Arsuaga, J.-L. 2019. Single-grain OSL dating of the Middle Palaeolithic site of Galería de las Estatuas, Atapuerca (Burgos, Spain). Quaternary Geochronology, 49, 254-261.
Demuro, M., Arnold, L. J., Parés, J. M. & Sala, R. 2015. Extended-range luminescence chronologies suggest potentially complex bone accumulation histories at the Early-to-Middle Pleistocene palaeontological site of Huéscar-1 (Guadix-Baza basin, Spain). Quaternary International, 389, 191-212.
Dodson, J. & Field, J. H. 2018. What does the occurrence of Sporormiella (Preussia) spores mean in Australian fossil sequences? Journal of Quaternary Science, 33, 380-392.
Dosseto, A. & Marwick, B. 2019. UThwigl—An R Package for Closed- and Opensystem Uranium-thorium Dating.
Evans, T. V. 2015. A critical evaluation of our understanding of bone transport and deposition in fluvial channels. Montana State University-Bozeman, College of Letters & Science.
Feranec, R. S., Miller, N. G., Lothrop, J. C. & Graham, R. W. 2011. The Sporormiella proxy and end-Pleistocene megafaunal extinction: a perspective. Quaternary International, 245, 333-338.
Fernandez-Jalvo, Y. & Andrews, P. 2016. Atlas of taphonomic identifications: 1001+ images of fossil and recent mammal bone modification, Springer.
Field, J., Fillios, M. & Wroe, S. 2008. Chronological overlap between humans and megafauna in Sahul (Pleistocene Australia–New Guinea): a review of the evidence. Earth-Science Reviews, 89, 97-115.
Field, J., Wroe, S., Trueman, C. N., Garvey, J. & Wyatt-Spratt, S. 2013. Looking for the archaeological signature in Australian megafaunal extinctions. Quaternary International, 285, 76-88.
Galbraith, R. F. & Green, P. F. 1990. Estimating the component ages in a finite mixture. International Journal of Radiation Applications and Instrumentation. Part D. Nuclear Tracks and Radiation Measurements, 17, 197-206.
Galbraith, R. F., Roberts, R. G., Laslett, G. M., Yoshida, H. & Olley, J. M. 1999. Optical dating of single and multiple grains of quartz from Jinmium rock shelter, northern Australia: Part I, experimental design and statistical models. Archaeometry, 41, 339-364.
Geoscience Australia 2013. In: Bioregional Assessment Source Dataset (ed.) Bioregional Assessment Programme. Geoscience Australia.
Gillespie, R. & Brook, B. W. 2006. Is there a Pleistocene archaeological site at Cuddie Springs? Archaeology in Oceania, 41, 1-11.
Gillespie, R., Camens, A. B., Worthy, T. H., Rawlence, N. J., Reid, C., Bertuch, F., Levchenko, V. & Cooper, A. 2012. Man and megafauna in Tasmania: closing the gap. Quaternary Science Reviews, 37, 38-47.
Grellet-Tinner, G., Spooner, N. A. & Worthy, T. H. 2016. Is the “Genyornis” egg of a mihirung or another extinct bird from the Australian dreamtime? Quaternary Science Reviews, 133, 147-164.
Grün, R., Eggins, S., Aubert, M., Spooner, N., Pike, A. W. G. & Müller, W. 2010. ESR and U-series analyses of faunal material from Cuddie Springs, NSW, Australia: implications for the timing of the extinction of the Australian megafauna. Quaternary Science Reviews, 29, 596-610.

Guérin, G., Mercier, N. & Adamiec, G. 2011. Dose-rate conversion factors: update. Ancient TL, 29, 5-8.
Hamm, G., Mitchell, P., Arnold, L. J., Prideaux, G. J., Questiaux, D., Spooner, N. A., Levchenko, V. A., Foley, E. C., Worthy, T. H. & Stephenson, B. 2016. Cultural innovation and megafauna interaction in the early settlement of arid Australia. Nature, 539, 280-283.
Helgen, K. M., Wells, R. T., Kear, B. P., Gerdtz, W. R. & Flannery, T. F. 2006. Ecological and evolutionary significance of sizes of giant extinct kangaroos. Australian Journal of Zoology, 54, 293-303.
Hesse, P. P., Williams, R., Ralph, T. J., Fryirs, K. A., Larkin, Z. T., Westaway, K. E. & Farebrother, W. 2018. Palaeohydrology of lowland rivers in the Murray-Darling Basin, Australia. Quaternary Science Reviews, 200, 85-105.
Hocknull, S. A., Piper, P. J., Van Den Bergh, G. D., Due, R. A., Morwood, M. J. & Kurniawan, I. 2009. Dragon's paradise lost: palaeobiogeography, evolution and extinction of the largest-ever terrestrial lizards (Varanidae). PloS one, 4, e7241.
Hocknull, S. A., Zhao, J.-X., Feng, Y.-X. & Webb, G. E. 2007. Responses of Quaternary rainforest vertebrates to climate change in Australia. Earth and Planetary Science Letters, 264, 317-331.
Janis, C. M., Buttrill, K. & Figueirido, B. 2014. Locomotion in extinct giant kangaroos: were sthenurines hop-less monsters? PloS one, 9, e109888.
Jankowski, N. R., Gully, G. A., Jacobs, Z., Roberts, R. G. & Prideaux, G. J. 2016. A late Quaternary vertebrate deposit in Kudjal Yolgah Cave, south-western Australia: refining regional late Pleistocene extinctions. Journal of Quaternary Science, 31, 538-550.
Joannes-Boyau, R., Duval, M. & Bodin, T. 2018. MCDoseE 2.0 A new Markov Chain Monte Carlo program for ESR dose response curve fitting and dose evaluation. Quaternary Geochronology, 44, 13-22.
Johnson, C. N., Alroy, J., Beeton, N. J., Bird, M. I., Brook, B. W., Cooper, A., Gillespie, R., Herrando-Pérez, S., Jacobs, Z. & Miller, G. H. 2016. What caused extinction of the Pleistocene megafauna of Sahul? Proceedings of the Royal Society B: Biological Sciences, 283, 20152399.
Kawamura, H., Holbourn, A. & Kuhnt, W. 2006. Climate variability and land–ocean interactions in the Indo Pacific Warm Pool: a 460-ka palynological and organic geochemical record from the Timor Sea. Marine Micropaleontology, 59, 1-14.
Kemp, C., Tibby, J., Arnold, L. J. & Barr, C. 2019. Australian hydroclimate during Marine Isotope Stage 3: a synthesis and review. Quaternary Science Reviews, 204, 94-104.
Kershaw, A. P., Bretherton, S. C. & Van Der Kaars, S. 2007. A complete pollen record of the last 230 ka from Lynch's Crater, north-eastern Australia. Palaeogeography, Palaeoclimatology, Palaeoecology, 251, 23-45.
Krause, C. E., Gagan, M. K., Dunbar, G. B., Hantoro, W. S., Hellstrom, J. C., Cheng, H., Edwards, R. L., Suwargadi, B. W., Abram, N. J. & Rifai, H. 2019. Spatio-temporal evolution of Australasian monsoon hydroclimate over the last 40,000 years. Earth and Planetary Science Letters, 513, 103-112.
Long, J. A., Archer, M., Flannery, T. & Hand, S. 2002. Prehistoric mammals of Australia and New Guinea: one hundred million years of evolution, JHU Press.
Longmore, M. E. & Heijnis, H. 1999. Aridity in Australia: Pleistocene records of palaeohydrological and palaeoecological change from the perched lake sediments of Fraser Island, Queensland, Australia. Quaternary International, 57, 35-47.
Lowe, K. M., Mentzer, S. M., Wallis, L. A. & Shulmeister, J. 2018. A multi-proxy study of anthropogenic sedimentation and human occupation of Gledswood Shelter 1: exploring an interior sandstone rockshelter in Northern Australia. Archaeological and Anthropological Sciences, 10, 279-304.
Lyman, R. L. & Fox, G. L. 1989. A critical evaluation of bone weathering as an indication of bone assemblage formation. Journal of Archaeological Science, 16, 293-317.
Lyman, R. L. & Lyman, C. 1994. Vertebrate taphonomy, Cambridge University Press.
Malhi, Y., Doughty, C. E., Galetti, M., Smith, F. A., Svenning, J.-C. & Terborgh, J. W. 2016. Megafauna and ecosystem function from the Pleistocene to the Anthropocene. Proceedings of the National Academy of Sciences, 113, 838-846.

Martin, P. S. & Klein, R. G. 1984. Quaternary Extinctions: A Prehistoric Revolution, Tucson, University of Arizona Press.
Mejdahl, V. 1979. Thermoluminescence dating: beta-dose attenuation in quartz grains. Archaeometry, 21, 61-72.
Meltzer, D. J. & Mead, J. I. 1985. Dating late Pleistocene extinctions: theoretical issues, analytical bias, and substantive results. Environments and Extinctions: Man in Late Glacial North America, 145-174.
Méndez-Quintas, E., Santonja, M., Pérez-González, A., Duval, M., Demuro, M. & Arnold, L. J. 2018. First evidence of an extensive Acheulean large cutting tool accumulation in Europe from Porto Maior (Galicia, Spain). Scientific reports, 8, 1-13.
Miller, G., Magee, J., Smith, M., Spooner, N., Baynes, A., Lehman, S., Fogel, M., Johnston, H., Williams, D. & Clark, P. 2016. Human predation contributed to the extinction of the Australian megafaunal bird Genyornis newtoni∼ 47 ka. Nature Communications, 7, 1-7.
Molnar, R. & Kurz, C. The distribution of Pleistocene vertebrates on the eastern Darling Downs, based on the Queensland Museum collections. Proceedings-Linnean Society of New South Wales, 1997. Linnean Society of New South Wales, 107-134.
Mooney, S., Harrison, S. P., Bartlein, P. J. & Stevenson, J. 2012. The prehistory of fire in Australasia. In: Bradstock, R. A., Gill, A. M. & Williams, R. J. (eds.) Flammable Australia: Fire Regimes, Biodiversity and Ecosystems in a Changing World. Collingwood, Victoria, Australia: CSIRO Publishing.
Moss, P. T. 2013. Palynology and its Application to Geomorphology. In: Shroder, J. F. (ed.) Treatise on Geomorphology. San Diego: Academic Press.
Moss, P. T., Dunbar, G. B., Thomas, Z., Turney, C., Kershaw, A. P. & Jacobsen, G. E. 2017. A 60 000-year record of environmental change for the Wet Tropics of north-eastern Australia based on the ODP 820 marine core. Journal of Quaternary Science, 32, 704-716.
Moss, P. T. & Kershaw, A. P. 2007. A late Quaternary marine palynological record (oxygen isotope stages 1 to 7) for the humid tropics of northeastern Australia based on ODP Site 820. Palaeogeography, Palaeoclimatology, Palaeoecology, 251, 4-22.
Moss, P. T., Kershaw, A. P. & Grindrod, J. 2005. Pollen transport and deposition in riverine and marine environments within the humid tropics of northeastern Australia. Review of Palaeobotany and Palynology, 134, 55-69.
Moss, P. T., Tibby, J., Petherick, L., Mcgowan, H. & Barr, C. 2013. Late Quaternary vegetation history of North Stradbroke Island, Queensland, eastern Australia. Quaternary Science Reviews, 74, 257-272.
Murray, A. S. & Wintle, A. G. 2000. Luminescence dating of quartz using an improved single-aliquot regenerative-dose protocol. Radiation measurements, 32, 57-73.
Nanson, G. C., East, T. J. & Roberts, R. G. 1993. Quaternary stratigraphy, geochronology and evolution of the Magela Creek catchment in the monsoon tropics of northern Australia. Sedimentary Geology, 83, 277-302.
Nanson, G. C., Price, D. M., Jones, B. G., Maroulis, J. C., Coleman, M., Bowman, H., Cohen, T. J., Pietsch, T. J. & Larsen, J. R. 2008. Alluvial evidence for major climate and flow regime changes during the middle and late Quaternary in eastern central Australia. Geomorphology, 101, 109-129.
O'connell, J. F. & Allen, J. 2004. Dating the colonization of Sahul (Pleistocene Australia–New Guinea): a review of recent research. Journal of Archaeological Science, 31, 835-853.
O'connell, J. F., Allen, J., Williams, M. A., Williams, A. N., Turney, C. S., Spooner, N. A., Kamminga, J., Brown, G. & Cooper, A. 2018. When did Homo sapiens first reach Southeast Asia and Sahul? Proceedings of the National Academy of Sciences, 115, 8482-8490.
Owen-Smith, N. 2013. Contrasts in the large herbivore faunas of the southern continents in the late Pleistocene and the ecological implications for human origins. Journal of Biogeography, 40, 1215-1224.
Peerdeman, F., Davies, P. & Chivas, A. The stable oxygen isotope signal in shallow-water, upper-slope sediments off the Great Barrier Reef (Hole 820A). Proceedings of the Ocean Drilling Program, Scientific Results, 1993 Texas. College Station, Texas, 163-173.
Perrotti, A. G. & Van Asperen, E. 2019. Dung fungi as a proxy for megaherbivores: opportunities and limitations for archaeological applications. Vegetation History and Archaeobotany, 28, 93-104.

Peters, K. J., Saltré, F., Friedrich, T., Jacobs, Z., Wood, R., Mcdowell, M., Ulm, S. & Bradshaw, C. J. A. 2019. FosSahul 2.0, an updated database for the Late Quaternary fossil records of Sahul. Scientific data, 6, 1-7.
Pietsch, T. J. 2009. Optically stimulated luminescence dating of young (< 500 years old) sediments: Testing estimates of burial dose. Quaternary Geochronology, 4, 406-422.
Prescott, J. R. & Hutton, J. T. 1994. Cosmic ray contributions to dose rates for luminescence and ESR dating: large depths and long-term time variations. Radiation measurements, 23, 497-500.
Price, G. J. 2008. Taxonomy and palaeobiology of the largest-ever marsupial, Diprotodon (Diprotodontidae, Marsupialia). Zoological Journal of the Linnean Society, 153, 369-397.
Price, G. J. 2012. Plio-Pleistocene climate and faunal change in central eastern Australia. Episodes, 35, 160-165.
Price, G. J., Feng, Y.-X., Zhao, J.-X. & Webb, G. E. 2013. Direct U–Th dating of vertebrate fossils with minimum sampling destruction and application to museum specimens. Quaternary Geochronology, 18, 1-8.
Price, G. J., Louys, J., Cramb, J., Feng, Y.-X., Zhao, J.-X., Hocknull, S. A., Webb, G. E., Nguyen, A. D. & Joannes-Boyau, R. 2015. Temporal overlap of humans and giant lizards (Varanidae; Squamata) in Pleistocene Australia. Quaternary Science Reviews, 125, 98-105.
Price, G. J., Louys, J., Faith, J. T., Lorenzen, E. & Westaway, M. C. 2018. Big data little help in megafauna mysteries. Nature Publishing Group.
Price, G. J. & Piper, K. J. 2009. Gigantism of the Australian Diprotodon Owen 1838 (Marsupialia, Diprotodontoidea) through the Pleistocene. Journal of Quaternary Science: Published for the Quaternary Research Association, 24, 1029-1038.
Price, G. J. & Webb, G. E. 2006. Late Pleistocene sedimentology, taphonomy and megafauna extinction on the Darling Downs, southeastern Queensland. Australian Journal of Earth Sciences, 53, 947-970.
Prideaux, G. 2004. Systematics and evolution of the sthenurine kangaroos, Univ of California Press.
Prideaux, G. J., Gully, G. A., Couzens, A. M., Ayliffe, L. K., Jankowski, N. R., Jacobs, Z., Roberts, R. G., Hellstrom, J. C., Gagan, M. K. & Hatcher, L. M. 2010. Timing and dynamics of Late Pleistocene mammal extinctions in southwestern Australia. Proceedings of the National Academy of Sciences, 107, 22157-22162.
Prideaux, G. J., Long, J. A., Ayliffe, L. K., Hellstrom, J. C., Pillans, B., Boles, W. E., Hutchinson, M. N., Roberts, R. G., Cupper, M. L. & Arnold, L. J. 2007a. An arid-adapted middle Pleistocene vertebrate fauna from south-central Australia. Nature, 445, 422-425.
Prideaux, G. J., Roberts, R. G., Megirian, D., Westaway, K. E., Hellstrom, J. C. & Olley, J. M. 2007b. Mammalian responses to Pleistocene climate change in southeastern Australia. Geology, 35, 33-36.
Reid, J. & Ulm, S. 2000. Index of dates from archaeological sites in Queensland. Queensland Archaeological Research, 12, 1.
Roberts, R. G. & Brook, B. W. 2010. Turning back the clock on the extinction of megafauna in Australia. Quaternary Science Reviews: International Multidisciplinary Review and Research Journal, 29, 593-595.
Roberts, R. G., Flannery, T. F., Ayliffe, L. K., Yoshida, H., Olley, J. M., Prideaux, G. J., Laslett, G. M., Baynes, A., Smith, M. A. & Jones, R. 2001. New ages for the last Australian megafauna: continent-wide extinction about 46,000 years ago. Science, 292, 1888-1892.
Rodríguez-Rey, M., Herrando-Pérez, S., Gillespie, R., Jacobs, Z., Saltré, F., Brook, B. W., Prideaux, G. J., Roberts, R. G., Cooper, A. & Alroy, J. 2015. Criteria for assessing the quality of Middle Pleistocene to Holocene vertebrate fossil ages. Quaternary Geochronology, 30, 69-79.
Rule, S., Brook, B. W., Haberle, S. G., Turney, C. S., Kershaw, A. P. & Johnson, C. N. 2012. The aftermath of megafaunal extinction: ecosystem transformation in Pleistocene Australia. Science, 335, 1483-1486.
Saltré, F., Rodríguez-Rey, M., Brook, B. W., Johnson, C. N., Turney, C. S. M., Alroy, J., Cooper, A., Beeton, N., Bird, M. I. & Fordham, D. A. 2016. Climate change not to blame for late Quaternary megafauna extinctions in Australia. Nature communications, 7, 1-7.
Sambridge, M., Grün, R. & Eggins, S. 2012. U-series dating of bone in an open system: the diffusion-adsorption-decay model. Quaternary Geochronology, 9, 42-53.

Signor, P. W. & Lipps, J. H. 1982. Sampling bias, gradual extinction patterns and catastrophes in the fossil record. In: Silver, L. T. & Schultz, P. H. (eds.) Geological Implications of Impacts of Large Asteroids and Comets on the Earth. Colorado: The Geological Society of America.
Thevenon, F., Bard, E., Williamson, D. & Beaufort, L. 2004. A biomass burning record from the West Equatorial Pacific over the last 360 ky: methodological, climatic and anthropic implications. Palaeogeography, Palaeoclimatology, Palaeoecology, 213, 83-99.
Tobler, R., Rohrlach, A., Soubrier, J., Bover, P., Llamas, B., Tuke, J., Bean, N., Abdullah-Highfold, A., Agius, S. & O'donoghue, A. 2017. Aboriginal mitogenomes reveal 50,000 years of regionalism in Australia. Nature, 544, 180-184.
Van Der Kaars, S., Miller, G. H., Turney, C. S., Cook, E. J., Nürnberg, D., Schönfeld, J., Kershaw, A. P. & Lehman, S. J. 2017. Humans rather than climate the primary cause of Pleistocene megafaunal extinction in Australia. Nature Communications, 8, 1-7.
Van Der Kaars, W. A. 1991. Palynology of eastern Indonesian marine piston-cores: a Late Quaternary vegetational and climatic record for Australasia. Palaeogeography, Palaeoclimatology, Palaeoecology, 85, 239-302.
Wang, S. C. & Marshall, C. R. 2016. Estimating times of extinction in the fossil record. Biology letters, 12, 20150989.
Webster, J. M. & Davies, P. J. 2003. Coral variation in two deep drill cores: significance for the Pleistocene development of the Great Barrier Reef. Sedimentary Geology, 159, 61-80.
Westaway, M. C., Olley, J. & Grün, R. 2017. At least 17,000 years of coexistence: Modern humans and megafauna at the Willandra Lakes, South-Eastern Australia. Quaternary Science Reviews, 157, 206-211.
Whiteway, T. 2009. In: Australia, G. (ed.) Geoscience Australia. Canberra: Geoscience Australia.
Williams, A. N., Ulm, S., Sapienza, T., Lewis, S. & Turney, C. S. 2018. Sea-level change and demography during the last glacial termination and early Holocene across the Australian continent. Quaternary Science Reviews, 182, 144-154.
Wood, J. R. & Wilmshurst, J. M. 2012. Wetland soil moisture complicates the use of Sporormiella to trace past herbivore populations. Journal of Quaternary Science, 27, 254-259.
Woodroffe, C. D., Short, S. A., Stoddart, D. R., Spencer, T. & Harmon, R. S. 1991. Stratigraphy and chronology of late Pleistocene reefs in the southern Cook Islands, south Pacific. Quaternary Research, 35, 246-263.
Wroe, S. & Field, J. 2006. A review of the evidence for a human role in the extinction of Australian megafauna and an alternative interpretation. Quaternary Science Reviews, 25, 2692-2703.
Wroe, S., Field, J. H., Archer, M., Grayson, D. K., Price, G. J., Louys, J., Faith, J. T., Webb, G. E., Davidson, I. & Mooney, S. D. 2013. Climate change frames debate over the extinction of megafauna in Sahul (Pleistocene Australia-New Guinea). Proceedings of the National Academy of Sciences, 110, 8777-8781.
Zhou, H., Zhao, J., Qing, W., Feng, Y. & Tang, J. 2011. Speleothem-derived Asian summer monsoon variations in Central China, 54–46 ka. Journal of Quaternary Science, 26, 781-790.

Chapter 5 The hydroclimatic and chronological context of late Pleistocene megafauna extinction in north-eastern Australia

---

This chapter has been written in the format of an article and intended for submission as:

Lewis, R. J., Arnold, L. J.; Hocknull, S. A.; Tibby, J.; Demuro, M.; Lawrence, R. A., The hydroclimatic and chronological context of late Pleistocene megafauna extinction in north-eastern Australia

---

Statement of Authorship

Title of Paper	
Publication Status	[ ] Published [ ] Accepted for Publication [ ] Submitted for Publication [X] Unpublished and Unsubmitted work written in manuscript style
Publication Details	Written in the format of an article and intended for submission.

Principal Author

Name of Principal Author (Candidate)	Richard J. Lewis	
Contribution to the Paper	Conceptualization; Data curation; Formal analysis; Funding acquisition; Investigation; Methodology; Project administration; Resources; Software; Data Validation; Visualization; Writing – original draft; Writing – review & editing	
Overall percentage (%)	80	
Certification:	This paper reports on original research I conducted during the period of my Higher Degree by Research candidature and is not subject to any obligations or contractual agreements with a third party that would constrain its inclusion in this thesis. I am a primary author of this paper.	
Signature		Date 19th July 2021

Co-Author Contributions

By signing the Statement of Authorship, each author certifies that:

x. the candidate's stated contribution to the publication is accurate (as detailed above);
xi. permission is granted for the candidate in include the publication in the thesis; and
xii. the sum of all co-author contributions is equal to 100% less the candidate's stated contribution.

Name of Co-Author	Lee J. Arnold	
Contribution to the Paper	Conceptualization; Formal analysis; Funding acquisition; Investigation; Methodology; Resources; Software; Data Validation; Writing – original draft; Writing – review & editing	
Signature		Date 22nd July 2021

Name of Co-Author	Scott Hocknull	
Contribution to the Paper	Conceptualization; Formal analysis; Funding acquisition; Investigation; Methodology; Resources; Software; Data Validation; Writing – original draft; Writing – review & editing	
Signature		Date 7th August 2021

Name of Co-Author	John Tibby	
Contribution to the Paper		
Signature		Date 19th July 2021

Name of Co-Author	Martina Demuro	
Contribution to the Paper	Formal analysis; Investigation; Resources; Software; Data Validation; Writing – review & editing	
Signature		Date 21st July 2021

Name of Co-Author	Rochelle A. Lawrence	
Contribution to the Paper	Conceptualization; Funding acquisition; Investigation; Project administration; Writing – review & editing	
Signature		Date 20th July 2021

Abstract

The scarcity of well-dated palaeoenvironmental archives continues to limit resolution of the late Pleistocene megafaunal extinction debate for Sahul (Australian and New Guinea). Conventionally, palaeoenvironmental reconstructions and inferences of human- verses climate-mediated causes of megafaunal extinction have relied on biological proxy data, particularly pollen records. However, a wealth of environmental information can also be inferred from abiotic data, including the type and mode of sediment deposition itself. Here we examine the timing and palaeoenvironmental significance of fossil-bearing sediment archives from South Walker Creek, eastern Australia, and use a Bayesian modelling approach to compare the resulting chronometric datasets with a range of other Australian catchment records. The improved regional chronological framework is used to consider spatiotemporal patterns of hydrological activity and megafauna disappearance in the context of changing environmental conditions during the late Pleistocene. Our results support a link between the last appearance date of megafauna at South Walker Creek around 37.9 thousand years ago (ka) and a regional trend towards a more negative moisture balance during late Marine Isotope Stage 3 (MIS3). Limited fluvial and lacustrine deposition persist across several northern and central Australian catchments through late MIS3 and early- to mid-MIS2, including the Last Glacial Maximum – coincident with an absence of preserved fluvial deposition at South Walker Creek between 43.6 and 15.8 ka – before renewed fluvial deposition is recorded across various basins from late MIS2 onwards (~16 ka). The outcome of this analysis provides important insights into regional Australian palaeoenvironmental reconstructions during the late Pleistocene; revealing differences in catchment responses related to synoptic climate conditions during MIS3–1, and adding new constraints on megafaunal extinction dynamics in the underrepresented tropical zone of Sahul.

Introduction

Debate continues to surround the timing and causes of late Pleistocene megafaunal extinction across the continent of Sahul (defined herein as species >44 kg body mass, after Martin & Klein (1984). The discussion is centred around a continuum between two hypothesised end-member extinction drivers. On the one end, climatically induced extinctions are hypothesised due to sustained alterations in vegetation and reduction in water availability, which resulted in the loss of viable species habitat (e.g., Cohen et al., 2015; Murphy et al., 2012; Price et al., 2011; Wroe et al., 2013). At the other end, human induced extinctions are inferred to have occurred due to overhunting of fauna and/or significant habitat modification through alterations, such as landscape burning. (e.g., Flannery, 1990; Johnson et al., 2016a; Martin & Klein, 1989; Roberts et al., 2001). The main issue with the human induced extinction hypothesis is the exceptionally poor archaeological record associated with megafauna, showing no clear relationship between humans and hunting of megafauna (Field et al., 2013). Equally, the precise timing and magnitude of key ecological and climatic events, the results of which would have increased survivability pressure for megafauna during the Pleistocene, are poorly understood (Koch & Barnosky, 2006). All hypotheses are confounded by a lack of well-dated records across the Australian continent (Hocknull et al., 2020; Peters et al., 2019; Rodríguez-Rey et al., 2016).

Geographically there is a strong spatial bias in megafauna fossil sites, the majority of which are situated along the southern Australian coastal margin, towards the east coast and within the mid-latitudes (Peters et al., 2019; Rodríguez-Rey et al., 2016). This bias is likely due to more favourable fossil preservation conditions in temperate regions (Noto, 2011), but is also likely due to historical

aspects of museum collections and fieldwork being initially focused on sites close to major city centres and caves. This is in stark contrast to the archaeological record, where focus on discovery of late Pleistocene human occupation sites has inevitably centred around the northern and north-western regions of Australia. In general, megafauna fossil sites and palaeoenvironmental records are significantly underrepresented in tropical Australia and New Guinea (Rodríguez-Rey et al., 2016; Reeves et al., 2013). Thus, continental-wide megafaunal extinction models that include tropical Sahul have relied on interpolation across vast areas of landmass with no, or limited, data (Hocknull et al., 2020; Price et al., 2018). Ultimately, this lack of data creates considerable uncertainty when testing the viability of continent-wide, human-mediated megafaunal extinction (e.g., Johnson et al., 2016b; Roberts et al., 2001; Saltré et al., 2016b) versus climate-mediated extinction hypotheses (e.g., Cohen et al., 2015; Wroe et al., 2013).

The limited temporal and spatial coverage of Sahul's megafauna record is exacerbated by the poor reliability of available age control. An attempt at determining a quality rating scheme for megafauna fossil ages was presented by Rodríguez-Rey et al. (2015), which revealed that only 26% of the 9,302 established chronological records in the FosSahul database were classified as high-quality (ages ranking A* or A) when considering their methodological veracity and association with the event of interest. This continent-wide synthesis study highlights the potentially significant influence that unsuitable chronological datasets may be exerting on spatio-temporal reconstructions of megafaunal extinction.

The types of depositional settings that have commonly yielded well-preserved megafauna fossil assemblages across Sahul include pitfall trap cave systems and rock shelters (e.g., Hamm et al., 2016; Hocknull et al., 2007; Prideaux et al., 2007; Reed & Bourne, 2000), as well as open-air floodplain and lake settings that are associated with relatively rapid sedimentation rates (e.g., Hocknull et al., 2020; Price et al., 2011). Fluvial and lacustrine localities often have the advantage of containing a diverse range of associated palaeoenvironmental proxies, which can provide independent, local-scale insights into how ecological dynamics were influenced by humans and climate during the Pleistocene (e.g., Kemp et al., 2020; Lewis et al., 2021; Rule et al., 2012; Saltré et al., 2019; Wroe et al., 2013).

Recent palaeontological research conducted in the Fitzroy River Basin, north-eastern Queensland, has demonstrated the significance of this fluvial catchment for understanding late Pleistocene extinctions in the tropical zone, with the preservation of at least thirteen extinct megafauna species recorded in association with indicators of past vegetation including leaves, fruit, seeds and pollen at four sites (Hocknull et al., 2020). By applying multiple dating methods in conjunction with quality rating assessments, Hocknull et al. (2020) were able to constrain the chronology of the South Walker Creek megafauna fossil sites to between 65.6 ± 2.2 and 40.1 ± 1.7 thousand years ago (ka), concluding that megafaunal extinction occurred sometime thereafter.

Hocknull et al. (2020) highlighted the correspondence between inferred extinction and hydroclimatic deterioration, particularly at regional scales, such as the Fitzroy River Basin. However, the available hydroclimatic datasets need to be critically evaluated and augmented with new records to better evaluate the broader relationships between megafaunal extinction at South Walker Creek and the regional hydrological changes reported for the Fitzroy River Basin (Croke et al., 2011). Most of the datasets available for the region are constrained to spatially disparate and temporally discontinuous palaeoenvironmental records, with fluvial activity reconstructions focused on the Fitzroy River Basin.

A useful means of addressing such a broad suite of data is to interrogate chronometric datasets from individual site records using Bayesian statistical methods (e.g., Bronk Ramsey, 2009b; Clarkson et al., 2017; Demuro et al., 2019; 2020; Hamm et al., 2016), and to subsequently combine the results via meta-analysis of pooled datasets in order to examine regional palaeoenvironmental and palaeoecological events (e.g. Becerra-Valdivia & Higham, 2020; Higham et al., 2014; Kennett et al., 2015). The results of such hierarchical modelling provide a means to statistically evaluate common trends between temporally associated but geographically separated locations, and to potentially differentiate between locally and regionally significant signals.

In this study, we present new and existing (Hocknull et al., 2020) chronometric data from multiple South Walker Creek sites, combined within a Bayesian framework to investigate the timing of hydrological change and local megafauna disappearance. We present new chronological datasets for palaeontological and fluvial archives from the underrepresented Australian tropical zone and, utilise a meta-analysis Bayesian modelling approach to compare spatially dispersed localities and examine regional megafaunal extinction trends. To do this we first present new optically stimulated luminescence (OSL) ages for fluvial activity at South Walker Creek and refine the timing of megafauna habitation in the area. We then evaluate whether there is a clear relationship between palaeohydrological changes and timing of megafauna disappearance in the Fitzroy River Basin, and surrounding regions of eastern Australia. Finally, we compare late Pleistocene to Holocene trends in fluvial activity with wetland dynamics across the region, providing interpretations of catchment-wide responses to climate change.

Regional Setting

South Walker Creek

The South Walker Creek fossil deposit area, resides in the lands of the Barada Barna people, situated west of Mackay in north-eastern Australia. The fossil locality is contained within the northern extent of the Fitzroy River Basin catchment area (Figure 5.1), which drains eastwards and outflows along the central-eastern Queensland coast near Rockhampton. South Walker Creek is positioned within the tropical zone (Colls & Whitaker, 1990) with summer and winter temperatures ranging between 21 – 34°C and 25 – 10°C respectively (BOM, 2019).

Palaeontological surveys and excavations undertaken between 2008 and 2019 have uncovered several sites preserving articulated and isolated fossil faunal and floral remains, including megafauna, along eroded gully and rill systems of South Walker Creek. Based on the current extent of surveys, the fossil sites are concentrated over short stretches of two meanders presently eroding Quaternary-aged alluvial deposits. The meanders are bedrock-controlled, with the basement of the creek system and alluvial deposits wedged upon the downward slope of locally dipping, Permo-Triassic Rangal and Fort Cooper Coal Measures and the Triassic Rewan Group (Hocknull et al., 2020; Lawrence & Hocknull, 2019). Sediments preserving the Quaternary fossils range from singular muddy cobble beds (~50 cm thick) through fine-grained sandy muds (~1-1.5 m thick) to confined coarse-grained gravel beds (~20 – 40 cm thick). These fossil deposits occur within broadly horizontally distributed, fine-grained, and internally unstructured, alluvial overbank fines. The deposits are laterally discontinuous over scales of tens to hundreds of metres with limited opportunity to directly correlate each site stratigraphically.

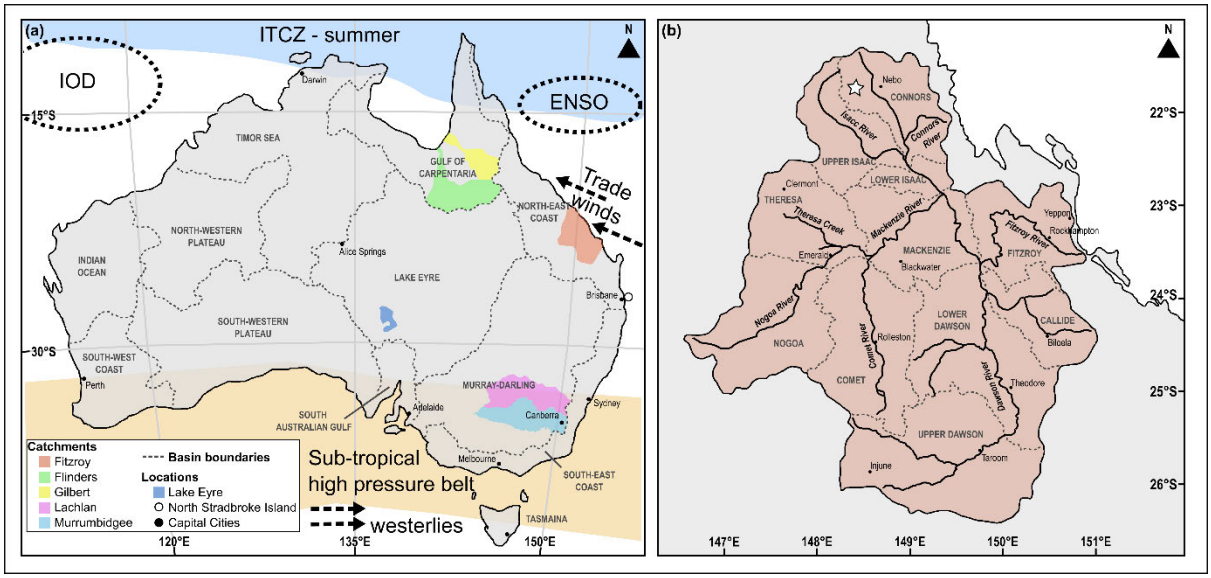

Figure 5.1 (a) Map of Australia showing the location of the Fitzroy River Basin (red) in relation to major drainage divisions, catchments and playa lakes. Present-day relative position of major weather and climate drivers discussed in text are shown in black: ITCZ – Inter-tropical Convergence Zone (austral summer position – blue); IOD – Indian Ocean Dipole; ENSO – El Nino Southern Oscillation; Sub-tropical high pressure belt (summer – yellow). Note, IOD and ENSO are modes of climatic variability operating in the Indian and Pacific oceans respectively (b) Fitzroy River Basin showing the position of sub-catchments and major tributaries that flow into the Fitzroy River. South Walker Creek is designated by a star. Adapted from Croke et al. (2011).

Hocknull et al. (2020) presented multi-technique (OSL, U-series, radiocarbon (^{14}C) and combined U-series/electron spin resonance (US-ESR)) age constraint for four of the South Walker Creek fossil sites (SW9, SW3, SWCC, SWJ) that preserve body and trace fossils of small to megafauna-sized vertebrates, as well as aquatic and terrestrial invertebrates (bivalves and insects) and floral remains (seeds, leaves and pollen). The ages obtained at site SWJ underly the fossil-bearing layer, producing a maximum weighted mean OSL age of 65.6 ± 2.2 ka (n = 6; 1σ). SWCC and SW3 have yielded weighted mean OSL ages of 58.2 ± 6.1 ka (n = 2; 1σ) and 47.7 ± 3.2 ka (n = 5; 1σ), respectively, while SW9 records the youngest megafauna fossil deposit, with a weighted mean OSL and US-ESR age of 40.1 ± 1.7 ka (n = 24; 1σ)[1]. Taphonomic and sedimentological evidence (articulated and associated remains, limited pre-depositional weathering, preservation of delicate insect and seed remains) indicates a primary depositional context for the fossils at these sites, with relatively rapid deposition and no evidence of secondary reworking (Hocknull et al., 2020).

[1] Note – the five US-ESR samples from SW9 yielded an average age of 35.2 ± 2.5 ka (2σ), which was incorrectly reported as 32.5 ± 2.5 ka in Table 2 of Hocknull et al. (2020). The weighted mean OSL and US-ESR age of 40.1 ± 1.7 ka (1σ) originally presented in Hocknull et al. (2020) is unaffected by this typographic error.

Study sites

Full details of the chronology, stratigraphy, fauna and taphonomy of sites SW9, SW3, SWCC, SWJ are presented in Hocknull et al. (2020). The current study presents results for new South Walker Creek sites of palaeontological and palaeoenvironmental significance: SWP, SWS, SWJS and SWC-US. Table 5.1 summarises the main palaeontological findings for each of the South Walker Creek sites. Of the four new sites presented in this study, SWP, SWS and SWJS preserve megafauna fossils within sediment primarily consisting of sandy silts and clays. Importantly, SWP preserves an associated macropodid mandible and SWS preserves associated macropodid post-cranial remains. SWC-US is unique in the sense that no fossil material has been recovered from this site; rather, the sedimentary deposit hosts successive units of cross-bedded, coarse-grain sands, sandy clays and clays, and therefore provides useful insights into the longer-term hydrological dynamics of the catchment.

Table 5.1 Faunal associations observed across the South Walker Creek fossil locality.

Sites	**SWP**	**SWS**	**SWJS**	**SW9**	**SW3**	**SWCC**	**SWJ**	**SWC-US**
Chelidae	X	X						
†*Genyornis*								
Dromaius sp.				X	X			
†*Pallimnarchus* sp.		X		X	X	X	X	
Crocodylus sp. cf. C *porosus*				X	X	X		
† *Quinkana'* sp.					X	X	X	
†*Varanus* sp. (large)				X	X			
†*Varanus priscus*				X	X	X	X	
Macropus fuliginosus								
Macropus giganteus								
†*Macropus titan*								
†*Macropus* sp. (giant)			X	X	X	X	X	
†*Notamacropus* sp. (giant)	X	X		X	X	X		
Osphranter rufus					X			
†*Protemnodon* sp.		X		X	X	X		
†*Sthenurus* sp.								
†*Procoptodon* sp.						X		
†*Simosthenurus* sp.								
†*Phascolonus gigas*				X				
†*Sedophascolomys* sp. Cf. S. medius				X	X			
†*Diprotodon optatum.*				X	X			
†*Zygomaturus trilobus*								
†*Palorchestes* sp.				X				
†*Thylacoleo* sp.				X				

SWC-US

The SWC-US site is located furthest upstream in the South Walker Creek fossil locality area (Figure 5.2). Seven distinct sedimentary units can be identified in the channel bank exposure, the lowest of which (Unit 1) unconformably overlies the Rewan Formation. Each unit is internally well sorted, upward fining and capped by a clay drape. Units 1 and 2 contain the thickest beds (up to 2 m), with successive unit bedding (Units 3 – 7) gradually thinning to <30 cm. There are relatively minor differences in sedimentology between the lower and topmost units. Unit 1 is relatively homogeneous, composed of clay, and shows early stages of diagenesis. Scour marks can be observed at the contact between Unit 1 and Unit 2 (Figure 5.2a), with the latter consisting of cross-bedded, sub-rounded to sub-angular coarse grain sand that grades into fine clay (Figure 5.2b). Sub-angular boulders can be observed eroding out of the deposit and can be traced back to Unit 2 (Figure 5.2c). The top five units (Units 3 – 7) share similar sedimentology, consisting primarily of sandy clay.

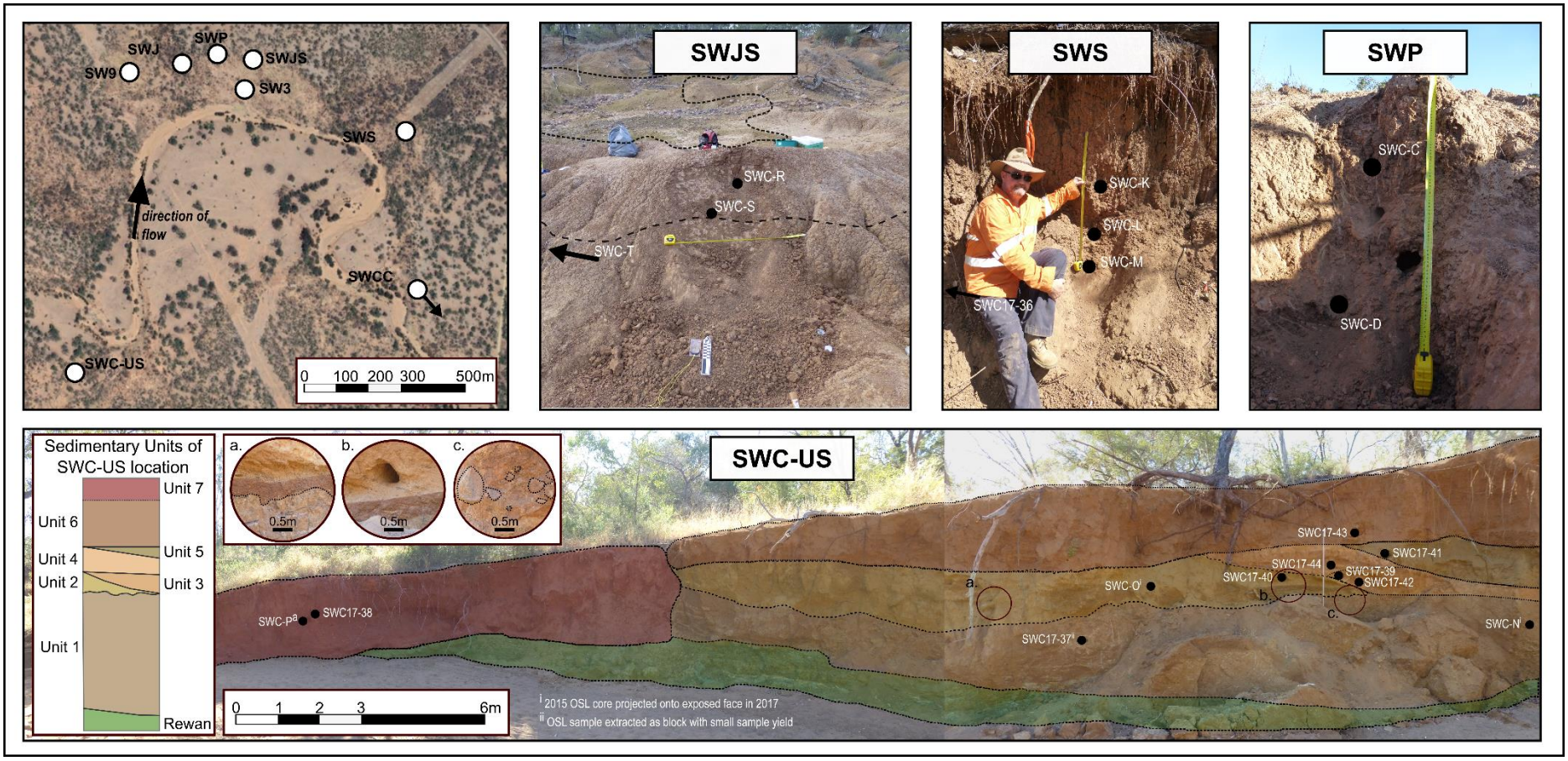

Figure 5.2 Aerial map of main South Walker Creek fossil sites and composite images of the new sites presented in this study. The top left image shows the relative position of all South Walker Creek excavation sites including those published in Hocknull et al. (2020). The succeeding images (left to right) show sediment deposits at SWJS, SWS and SWP, annotated to show sedimentology and positions of OSL core samples. The bottom figure shows SWC-US with inset images showing sedimentary features unique to the deposit: (a) scour unconformity made into Unit 1 by Unit 2; (b) cross bedding with red/brown zone at the base of the unit; (c) sub-angular to sub-rounded boulder inclusion eroding out of the unit. Photo credit: Scott Hocknull, Rochelle Lawrence and Richard Lewis.

SWC-S, SWC-P & SWC-JS

The sedimentology of site SWS, SWP and SWJS are similar and consist of poorly sorted, sandy mud matrices (Figure 5.2) overlying basement bedrock. The SWS, SWP and SWJS sedimentary sequences are laterally extensive with changes in the appearance of vertebrate fossil material (Table 5.1) used to define individual units. In this instance, SWS and SWP are defined as containing separate, single sedimentary units - due to the less defined distribution of fossil material throughout the excavated profiles - with respective thickness of approximately 3.5 m and 1.5 m. In the SWJS site however, there is a discernible bone bed within which bone material is concentrated and therefore this site has been defined by two units both of which are <1 m in thickness.

Methods

Optically stimulated luminescence

Sample acquisition and preparation

A total of 20 OSL samples were collected from the four new sites (SWP, SWS, SWJS and SWC-US) as part of the present study, expanding on the original OSL dataset (n = 34) published by Hocknull et al. (2020) for sites SW9, SW3, SWCC, SWJ. OSL core tube samples were taken from each sedimentary unit of hydrological or palaeontological significance at a given site (Table D1).

Sample extraction from the core tubes and all subsequent preparation was conducted under safe light conditions (subdued red lighting) at the Prescott Environmental Luminescence Laboratory, University of Adelaide. Purified coarse-grain quartz (Ø 212 – 250 μm) fractions were isolated from the unexposed central portion of each core tube using standard procedures (Aitken, 1998), including a 48% hydrofluoric acid etch for 40 min to remove the alpha-irradiated outer rinds, followed by 30% HCl treatment to remove any precipitated fluorides (see Appendix D for further details).

OSL measurement and D_e calculation

OSL measurements were performed using a Risø TL/OSL DA-20 reader equipped with an EMI9235QA photomultiplier tube and a mounted $^{90}Sr/^{90}Y$ β source. Optical stimulation was provided by a 10mW Nd:YVO_4 single-grain laser attachment emitting at 532 nm, and ultraviolet emissions were detected with a 7.5 mm-thick Hoya U-340 filter. Single-grain equivalent dose (D_e) values were determined using a modified SAR protocol (Murray & Wintle, 2000), which included a natural/regenerative dose preheat of 240°C for 10 s and a test dose preheat of 160°C for 10 s (Table D2). The appropriateness of the SAR measurement procedure was confirmed by undertaking dose recovery tests on representative samples from each of the four study sites (see Appendix D, Figure D2 and Table D3). Individual grains were only included in the final D_e calculations if they satisfied a series of routine quality assurance criteria (see Appendix D and Table D4).

The final burial dose estimates were calculated using either the central age model (CAM) or minimum age model (MAM) (Galbraith et al., 1999), depending on the single-grain D_e distribution characteristics of each sample and the results of applying the maximum log likelihood (llik) test of Arnold & Roberts (2009) (see Appendix D for details and Table D5).

Environmental dose rate calculation

The individual components used to calculate the environmental dose rates are presented in Table D6. External beta and gamma dose rates were determined using a combination of *in situ* field gamma

spectrometry (FGS) and low-level beta counting for samples collected in 2017 (SWC17-36 to SWC17-44), and high-resolution gamma spectrometry (HRGS) for the samples collected in 2015 (SWC-C to SWC-T) (see Appendix D and Hocknull et al. (2020)). HRGS measurements were additionally performed on the 2017 samples to evaluate the state of secular equilibrium in their ^{238}U, ^{235}U and ^{232}Th decay series (Table D7). FGS measurements were used to derive individual U, Th and K concentrations using the "energy windows" approach, following Arnold et al. (2012) and Duval & Arnold (2013). FGS radionuclide concentrations and HRGS specific activities were converted into dose rates using appropriate conversion factors (Guérin et al., 2011; Stokes et al., 2003). External beta dose rates were determined from measurements made using a Risø GM-25-5 beta counter (Bøtter-Jensen & Mejdahl, 1988) on dried and homogenised, bulk sediments collected directly from the 2017 OSL sampling positions.

An assumed internal dose rate of 0.03 ± 0.01 Gy/ka was included in the final dose rate calculation based on published values for etched quartz grains from a suite of locations (Bowler et al., 2003; Jacobs et al., 2006; Mejdahl, 1987; Pawley et al., 2008) and an alpha efficiency factor (a-value) of 0.04 ± 0.01 (Rees-Jones, 1995; Rees-Jones & Tite, 1997). The contribution of cosmic rays to the environmental dose rate was calculated following Prescott & Hutton (1994), taking into consideration the geomagnetic latitude, altitude and overburden thickness of each sample.

The final dose rates for the OSL samples were corrected for beta-dose attenuation and long-term water content (Aitken, 1985; Brennan, 2003; Mejdahl, 1979). The upper and lower bounds of the latter can reasonably be assumed to correspond to the measured present-day and saturated water content values of each sample, respectively (Figure D4). Representative long-term water contents for each sample were calculated from empirical proportional saturation assessments detailed in Hocknull et al. (2020) and include a 1σ relative uncertainty of 20% (40% at 2σ) to accommodate any variations in hydrological conditions during burial (see Appendix D).

Bayesian modelling of hydrological change and megafauna last appearance ages

A series of interrelated Bayesian models were used in this study to (i) derive combined ages for the various depositional units at each site, (ii) refine the timing of common layers or events recorded across multiple sites in the basin, and (iii) provide a stronger statistical foundation for examining chronostratigraphic relationships between different regions of Australia. Bayesian age modelling was performed in OxCal v4.4 (see Bronk Ramsey (1995, 2009b); Bronk Ramsey (2017) for mathematical descriptions and software algorithms), which enables the integration of reliable numerical dating results (likelihoods) with all known stratigraphic and relative dating information (priors) to derive unified chronostratigraphic frameworks. Our modelling approach was based on methods outlined for similar discontinuous terrestrial sediment sequences (e.g., Demuro et al., 2019; Demuro et al., 2020; Hamm et al., 2016; Macken et al., 2013), as well as those commonly employed when undertaking meta-analysis of pooled chronological datasets (e.g., Becerra-Valdivia & Higham, 2020; Bronk Ramsey, 2017; Higham et al., 2014; Kennett et al., 2015). Sequence models were used to represent individual stratigraphic units and sites where the relative ordering of events is sufficiently well-constrained (Bronk Ramsey, 2008). *Phase* models are used to represent groups of stratigraphically unordered events, including geographically disparate likelihoods pertaining to shared events. *Boundaries* were used to delineate the start and end of each *Sequence* or *Phase*, and to specify that all

likelihoods or events included in these groupings have a uniform prior likelihood of occurrence (Bronk Ramsey, 2008).

Where appropriate, *Phase* and *Sequence* models have been run using the general *Outlier Function* (Bronk Ramsey, 2009b), with prior outlier probabilities of 5% equally assigned to all likelihood samples to identify potentially significant statistical outliers. Likelihood estimates with posterior outlier probabilities >5% were not excluded from the final models; rather they were proportionally downweighted in the Monte Carlo iterations (Bronk Ramsey, 2009b).

Probability density functions were used to visualise the modelling outputs and to derive 68.2% and 95.4% credible intervals (C.I.) for the posterior likelihood and boundary distributions. Kernel density estimates (KDE) were also used to visualise underlying temporal data distributions (Becerra-Valdivia & Higham, 2020; Bronk Ramsey, 2017). The latter has been derived using the *KDE_Plot* function (with default kernel and bandwidth shaping parameters), and allow spatially disparate but stratigraphically unique chronometric data to be considered against one another when evaluating localised, basin-specific events (i.e., temporal range of megafauna) and broader regional events (i.e. changes in moisture balance).

Four groups of hierarchical Bayesian models have been constructed to examine the following spatio-temporal dynamics: (i) the combined temporal range of megafauna layers across the South Walker Creek area (Model 1); (ii) the timing of fluvial depositional events at each site in the South Walker Creek area (Model 2); (iii) the temporal distribution of fluvial activity across South Walker Creek as a whole (Model 3); (iv) the temporal distribution of hydrological activity across different regional catchments of Australia (Model 4). Together, these models allow us to infer changes in local and regional hydroclimatic conditions, and to better characterise the relationship between the last appearance of South Walker Creek megafauna and relate this to changing moisture balances regionally.

The South Walker Creek Bayesian models (Models 1 – 3) incorporate the ages published by Hocknull et al. (2020) and the numerical dating results presented in this study. The Bayesian models constructed for other regionally significant palaeoenvironmental archives (grouped under Model 4) utilise previously published chronological and stratigraphic constraints (see Model 4 description). The conceptual foundation and relationships between these different models are illustrated schematically in Figure 5.3, and described in further detail below:

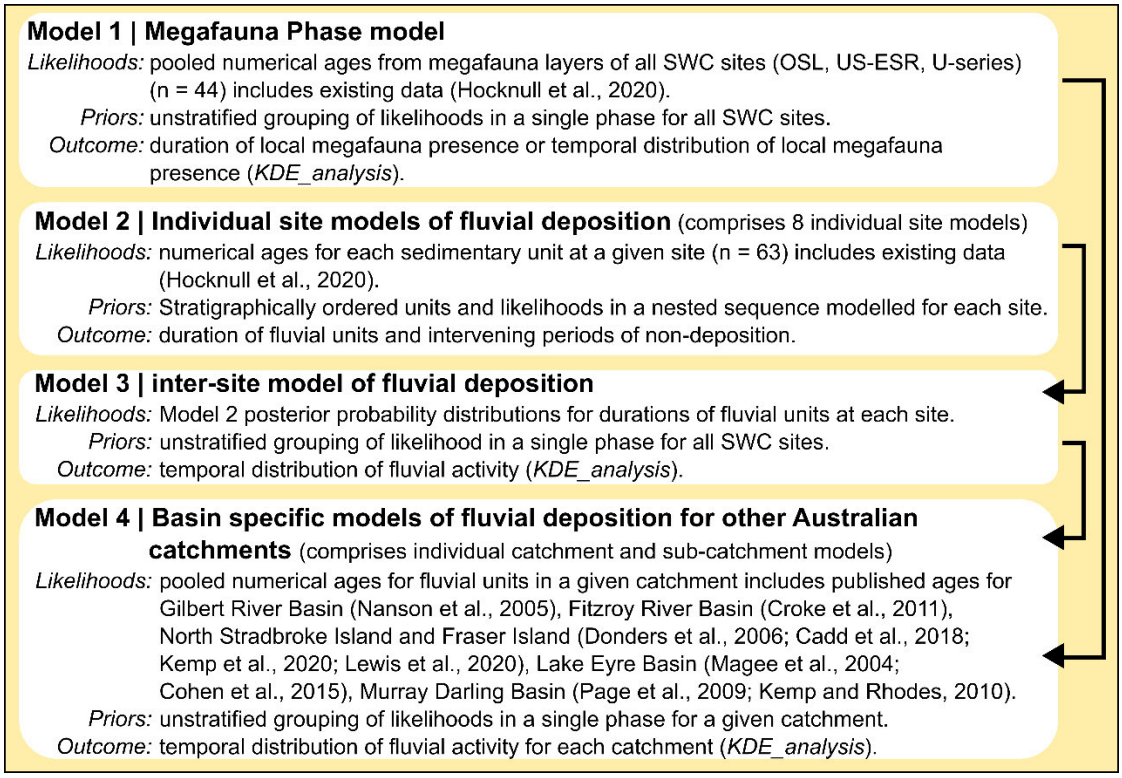

Figure 5.3 Schematic of the Bayesian modelling approach used in this study. The likelihoods, priors and outcomes of each model are indicated, as well as their hierarchical relationships for interrogating local and regional palaeoenvironmental signals. The black triangles indicate how input and output data of individual models are used in subsequent modelling processes.

Model 1: Temporal range of megafauna layers across all South Walker Creek sites

To calculate the combined age range of the megafauna layers preserved at South Walker Creek, we have pooled all chronometric likelihoods in direct association with megafauna units as a single, unordered *Phase* model. This model spans all seven SWC palaeontological sites and includes the new OSL ages obtained in the present study, together with all published A and A* rated ages from Hocknull et al. (2020) (n = 44) (Table D1). The open-system U-series results obtained on fossil remains are considered minimum age estimates, and have therefore been modelled using the *Before()* command. The OxCal *Date* function (Bronk Ramsey, 2009a) has been used to calculate the duration of the megafauna event from the posterior probabilities of the upper and lower *Boundaries* of the *Phase* model.

Model 2: Timing of fluvial deposition at individual South Walker Creek sites

Separate deposition models have been constructed for each site using stratigraphically ordered *Sequence* successions. Individual stratigraphic units have been represented as nested sub-*Sequences* within the broader depositional framework of each site since their overall stratigraphic ordering is sufficiently well-preserved. The relative ordering of dating samples from individual units is also sufficiently clear for the various sites, hence the likelihood groupings have been modelled as sub-*Sequences* instead of sub-*Phases*. Separate rather than shared *Boundaries* have been used to delineate the beginning and end of each stratigraphic unit, which ensures that the model is able to better accommodate any prolonged depositional hiatuses or erosional discontinuities between successive layers. The entire *Sequence* for each site has been constrained with a minimum age of 0 years for the uppermost boundary (using the *Before* command) and a maximum age of 100 ka for the lowermost

boundary (using the *After* command). The latter represents a relatively arbitrary maximum age constraint for the South Walker Creek stratigraphic sequences, but it has been chosen to sufficiently predate (by at least 3σ) the oldest likelihood estimate obtained on any of the individual sites (i.e., OSL sample SWC-J from site SWJ = 74.7 ± 6.3 ka; Hocknull et al. (2020)). The *Difference* and *Interval* functions (Bronk Ramsey, 2009b) have been used to evaluate the durations of potential hiatuses between units from the posterior probabilities of their associated upper and lower boundaries. The posterior *Boundary* probabilities for each sedimentary unit have also been used to derive the timing of each fluvial deposition event, as well as the timing of statistically significant depositional hiatuses between units, using the *Date* command.

Model 3: Temporal distribution of fluvial activity across all South Walker Creek sites

To investigate hydroclimatic changes at the basin scale, the posterior probability durations of individual fluvial depositional events obtained in Model 2 were subsequently pooled as a single, unordered *Phase* model. In Model 3, the *Sum* and *KDE_Plot* query functions (Bronk Ramsey, 2009b; Bronk Ramsey, 2017) have been used to visualise and characterise the resultant temporal distributions of fluvial activity, and to compare with the modelled temporal range of megafauna presence in the basin.

Model 4: Temporal distribution of hydrological activity across other regional catchments

Model 4 aims to explore whether the moisture balance changes inferred for South Walker Creek (Model 3) reflect localised basin responses (including possible non-preservation of preceding depositional events) or broader hydroclimatic responses expressed elsewhere at the regional scale. Basin-specific models of hydrological activity were constructed for a range of Australian catchments that have sufficiently reliable and high-resolution chronological datasets spanning comparable time ranges to the South Walker Creek record (i.e., spanning at least MIS3 – 2) (Figure 5.1a): namely, the Gilbert River from the Australian tropics (Nanson et al., 2005), the Fitzroy River Basin and its sub-catchments from the north-east coast (Croke et al., 2011), the North Stradbroke Island wetlands from sub-tropical Queensland (Cadd et al., 2018; Kemp et al., 2020; Lewis et al., 2020; Lewis et al., 2021), the Murray Darling Basin in south-eastern Australia (Kemp & Rhodes, 2010; Page et al., 2009) and the central lakes region (Lake Eyre; Cohen et al., 2015; Magee et al., 2004). For each of these catchments, previously published likelihoods have been grouped in single *Phase* models to ensure that chronometric information obtained from multiple sites and stratigraphic sections can be combined without making potentially inaccurate assumptions about relative ordering of past events. The basin-specific *Phase* models were then examined using the *Sum* and *KDE_Plot* query function (Bronk Ramsey, 2009b; Bronk Ramsey, 2017), and the resultant temporal distributions of hydrological activity compared with the South Walker Creek modelled temporal range for fluvial activity (Model 3) and megafauna presence/last appearance (Model 1). In the case of the North Stradbroke Island wetland records, lake accumulation episodes were used to derive the *Sum* and *KDE_Plot* outputs, as these were inferred to best reflect variation in moisture balance across the island and provide a means to collate possible depositional hiatuses (Lewis et al., 2021).

Results

OSL dating results

The single-grain OSL dating results for sites SWP, SWJ, SWJS and SWC-US are summarised in Table 5.2, Figure 5.4 and Figure D3. The single-grain classification statistics for each OSL sample, following vetting against the SAR quality assurance criteria, are presented in Table D4. Together, these quality assurance criteria resulted in grain acceptance rates of 2 – 9 % for burial dose determination.

The majority of samples (12 out of 20; SWC-C, -D, -L, -M, -Q, -R, -S, -T, -N, -O, 17-36, 17-40) exhibit relatively homogeneous D_e distributions with low to moderate D_e scatter (relative D_e ranges = 1.2 – 1.8) and with overdispersion values ranging between 21 ± 4% and 39 ± 5% (Table 5.2). These overdispersion values are broadly consistent with those typically reported for ideal well-bleached unmixed populations (e.g., the global average overdispersion of 20 ± 1% reported for ideal samples by Arnold & Roberts, 2009), and they overlap at 1σ or 2σ with the locality-specific baseline overdispersion value of 22 ± 4% determined by Hocknull et al. (2020) for well-bleached and unmixed sediments in the South Walker Creek area. None of the 12 D_e datasets are considered significantly positively skewed according to the weighted skewness test outlined by Bailey & Arnold (2006) and Arnold & Roberts (2011). Application of the maximum log likelihood (llik) test (Arnold et al., 2009) also indicates that the CAM is statistically favoured over the MAM-3 or MAM-4 for all these D_e datasets (Table D5).

Table 5.2 Dose rate data, equivalent doses (D_e), overdispersion values, and OSL ages from South Walker Creek.

		Dose rate data		Equivalent dose (D_e) data						
Site	**Sample ID**	**WC (%$_{Dry}$)[a]**	**Dose Rate (Gy/kyr)[b,c]**	**n/N[d]**	**OD (%)[e]**	**Age Model[f]**	**Skewness ± 2σ**	**Relative range[g]**	**D_e (Gy)[c]**	**Final Age (ka)[h]**
SWP	SWC-C^{MF}	25 ± 5	1 90 ± 0.1	64 / 800	30 ± 4.4	CAM	-0.74 ± 0.61	1.8	111.9 ± 5.6	58.9 ± 5.0
SWP	SWC-D^{MF}	25 ± 5	1.88 ± 0.1	56 / 800	21 ± 3.7	CAM	-0.69 ± 0.65	1.6	106.4 ± 4.4	56.5 ± 4.5
SWS	SWC-K^{MF}	31 ± 6	1 91 ± 0.1	39 / 500	48 ± 7.3	CAM	-0.80 ± 0.78	1.8	101.6 ± 9.2	53.1 ± 6.2
SWS	SWC-L^{MF}	10 ± 2	2 29 ± 0.1	47 /1000	30 ± 4.4	CAM	-0.64 ± 0.71	1 5	113.2 ± 6.1	49.5 ± 3.7
SWS	SWC-M^{MF}	19 ± 4	1.84 ± 0.1	51 / 800	22 ± 3.7	CAM	-0.10 ± 0.69	1 5	100.9 ± 4.2	54.7 ± 4.1
SWS	SWC17-36^{MF}	27 ± 5	2.01 ± 0.1	40 / 1400	25 ± 3.6	CAM	-0.05 ± 0.77	1 2	92.7 ± 4.2	46.0 ± 3.7
SWJS	SWC-Q^{MF}	7 ± 1	2.62 ± 0.1	44 / 1100	35 ± 4.5	CAM	-0.48 ± 0.74	1.7	101.4 ± 5.9	38.8 ± 3.0
SWJS	SWC-R	10 ± 2	1 95 ± 0.1	73 / 800	21 ± 2.8	CAM	-0.73 ± 0.57	1.6	88.2 ± 2.9	45.2 ± 2.8
SWJS	SWC-S	9 ± 2	2 22 ± 0.1	30 / 800	35 ± 6.1	CAM	-0.17 ± 0.89	1.6	94.8 ± 7.3	42.7 ± 4.0
SWJS	SWC-T^{MF}	5 ± 1	2 34 ± 0.1	37 / 1200	34 ± 5.2	CAM	-0.47 ± 0.89	1.4	98.9 ± 6.4	42.3 ± 3.5
SWC-US	SWC-N	7 ± 1	1.67 ± 0.1	47 / 800	39 ± 5.4	CAM	-0.12 ± 0.71	2 1	80.6 ± 5.4	48.4 ± 4.2
SWC-US	SWC-O	7 ± 1	1.83 ± 0.1	32 / 400	36 ± 5.8	CAM	0.13 ± 0.87	1.6	84.0 ± 6.1	45.8 ± 4.0
SWC-US	SWC-P	6 ± 1	1.61 ± 0.1	54 / 700	78 ± 8.3	MAM3	0.86 ± 0.67	8 5	5.0 ± 4.2	3.1 ± 2.6
SWC-US	SWC17-38	17 ± 3	1.73 ± 0.1	19 / 1200	112 ± 18.8	MAM3	-0.05 ± 1.12	4.4	7.0 ± 5.8	4.0 ± 3.3
SWC-US	SWC17-39	19 ± 4	1 50 ± 0.1	126 / 1400	51 ± 3.4	MAM3	1.57 ± 0.44	5 2	15.0 ± 2.0	10.0 ± 1.5
SWC-US	SWC17-40	17 ± 3	1 32 ± 0.1	69 / 1400	28 ± 3.0	CAM	-0.02 ± 0.59	1.6	60.4 ± 2.3	45.9 ± 3.1
SWC-US	SWC17-41	12 ± 2	1 57 ± 0.1	50 / 600	81 ± 8.3	MAM3	0.27 ± 0.69	3.4	20.0 ± 3.7	12.8 ± 2.5
SWC-US	SWC17-42	12 ± 2	1.40 ± 0.1	66 / 1100	84 ± 7.4	MAM3	0.23 ± 0.60	4 2	20.0 ± 3.7	14.3 ± 2.8
SWC-US	SWC17-43	12 ± 2	1.43 ± 0.1	58 / 800	72 ± 6.9	MAM3	0.67 ± 0.64	5.0	15.0 ± 3.0	10.5 ± 2.1
SWC-US	SWC17-44	11 ± 2	1 55 ± 0.1	80 / 1900	76 ± 6.2	MAM3	-0.21 ± 0.55	2.8	25.0 ± 3.5	16.1 ± 2.4

[a] Long-term water content, expressed as % of dry mass of mineral fraction, with an assigned relative uncertainty of ±20%.
[b] Total dose rate components (i.e., combined gamma, beta, internal and cosmic contributions); the breakdown of individual dose rate components is outlined in Table D6.
[c] Mean ± total uncertainty (68% confidence interval), calculated in quadrature as the sum of the random and systematic uncertainties.
[d] Number of grains that passed the SAR rejection criteria (n) / total number of grains measured (N) (Table D4).
[e] OD = overdispersion; the relative spread in the D_e dataset beyond that associated with the measurement uncertainties of individual D_e values, calculated using the central age model (CAM) of Galbraith et al. (1999).
[f] Age model used to calculate the sample averaged D_e value for each sample: Central Age Model (CAM); Three Parameter Minimum Age Model (MAM3) (Galbraith et al., 1999). MAM-3 D_e estimates were calculated after adding, in quadrature, a relative error of 20% to each individual D_e error to approximate the underlying dose overdispersion observed in 'ideal' (well-bleached and unmixed) sedimentary samples from SWC (e.g., samples SWC-D, SWC-M, SWC-R, plus samples SWC17-53 and SW9-2 from Hocknull et al., 2020); consistent with global overdispersion datasets (Arnold and Roberts, 2009). The choice of whether to use the CAM or MAM3 for each sample has been made on statistical grounds using the maximum log likelihood (llik) score criterion outlined by Arnold et al. (2009) (Table D5).
[g] Relative range = (maximum D_e - minimum D_e) / mean D_e; i.e., an estimate of the amount of dispersion independent of the magnitude of the D_e dataset under consideration.
[h] Total uncertainty includes a systematic component of ±2% associated with laboratory beta-source calibration.
MF Sample was extracted from a sedimentary layer that contains megafauna fossil material.

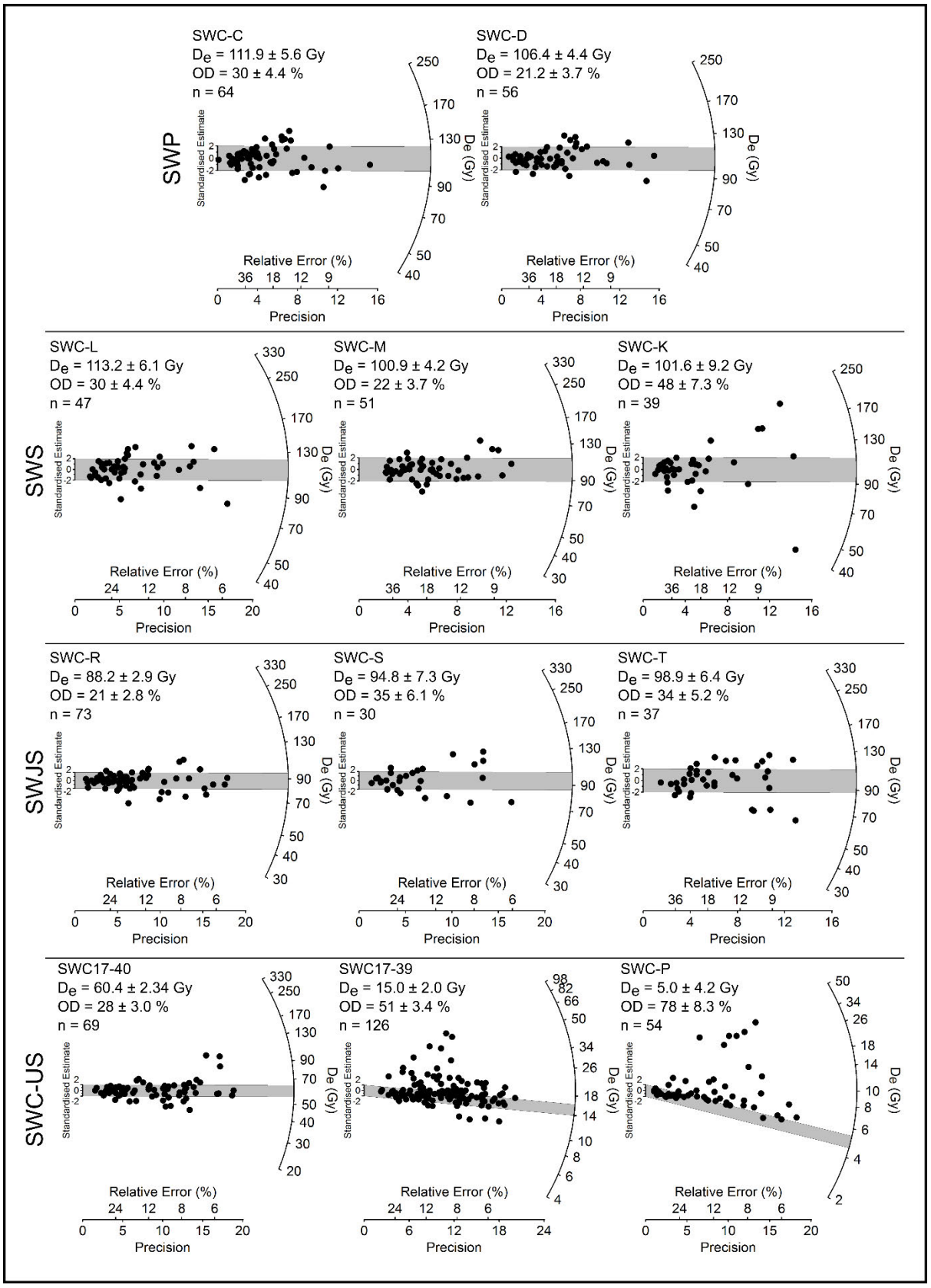

Figure 5.4 Representative subset of radial plots showing the single-grain OSL De distributions obtained for the South Walker Creek sites in this study (D_e errors are shown at 1σ). The dark grey bands identify the subpopulation of well-bleached grains, which are centred on either the CAM D_e value (SWC-C, -D, -L, -M, -K, R, -S, -T and SWC17-40) or MAM3 D_e value (SWC17-39 and SWC-P). Refer to Figure D3 for additional sample D_e distributions.

Seven of the remaining eight samples (SWC-P, -17-38, -17-39, -17-41, -17-42, -17-43, -17-44; all of which are from the SWC-US site) exhibit more complex D_e distributions characterised by moderate to high dose dispersion (relative D_e range = 2.8 – 8.5), high overdispersion values of 51 ± 3% to 112 ± 19% (Table 5.2), and larger proportions of individual D_e values lying outside of the weighted mean burial dose 2σ ranges, which do not overlap with the locality-specific baseline overdispersion value at 2σ (22 ± 4%; Hocknull et al., 2020). Three of these samples (SWC-P, -17-39, -17-43) exhibit distinct leading-edges of low D_e values or tails of higher D_e values (Figure 5.4 and Figure D3) and are considered to be positively skewed according to their weighted skewness test scores (Table 5.2). The other four samples show largely unstructured and broadly symmetric D_e scatter (SWC17-38, -17-44) or moderate asymmetry that is not considered statistically significant when compared against their critical skewness scores (SWC17-41, -17-42). Application of the llik test (Arnold et al., 2009) indicates that the MAM-3 is statistically favoured over the CAM for all seven D_e datasets (Table D5). These various D_e characteristics are consistent with those commonly reported for heterogeneously bleached single-grain OSL samples (e.g., Arnold et al., 2007; Arnold & Roberts, 2011; Arnold et al., 2008; Bailey & Arnold, 2006), which seems reasonable in this sedimentary context given the host deposits were deposited by fluvial and alluvial processes that could have involved limited transportation distances, UV-filtered (subaqueous) daylight exposures or localised erosion and entrainment of pre-existing deposits (syn-depositional mixing).

Sample SWC-K shares a similarly complex D_e distribution to these seven samples (i.e., a high overdispersion value of 48 ± 7% that is not consistent with the locality-specific baseline estimate; broad and unstructured D_e scatter; Table 5.2). However, unlike the aforementioned samples, SWC-K exhibits much lower dose dispersion (relative D_e range = 1.8), and the D_e distribution is considered significantly negatively skewed according to the weighted skewness test (compare Figure 5.4 and Figure D3). Application of the llik criterion also indicates that the CAM is statistically favoured over the MAM-3 or MAM-4. The limited number of accepted grains for SWC-K (n = 39) makes it difficult to fully resolve the underlying D_e characteristics. It is feasible that the enhanced overdispersion of this sample could have arisen from spatial variations in beta dose rates experienced by individual grains (e.g., Nathan et al., 2003) or intrinsic sources of D_e scatter (e.g., Demuro et al., 2013). The final burial dose of this sample has been calculated using the CAM, in accordance with its llik test result (Table D5). It is worth noting that the resultant age obtained for SWC-K (53.1 ± 6.2 ka) is statistically indistinguishable from that obtained for three other samples from Unit 2 at Site SWS (46.0 ± 3.7 ka to 54.7 ± 4.0 ka) (Table 5.2), providing further support for the choice of the CAM over the MAM in this instance.

The resultant age range obtained for each site after the application of the most statistically appropriate model describing the D_e distribution is as follows: SWP = 53.1 ± 6.2 – 58.9 ± 5.0 ka, SWS = 46.0 ± 3.7 – 54.7 ± 4.1 ka, SWJS = 38.8 ± 3.0 – 45.2 ± 2.8 ka, SWC-US = 48.4 ±4.2 – 3.1 ± 2.6 ka. Notably SWC-US has the greatest age range relative to the other sites, which may be a product of its more complex sedimentological history.

Bayesian modelling results

We follow the approach outlined in Becerra-Valdivia & Higham (2020) for synthesising the modelled age ranges of different events in Models 1–4: the *Date* function is used to provide a combined posterior age estimate for dated events included in *Phase* models (comprising unordered likelihoods,

unstratified sites, or pooled likelihoods drawn from multiple-site datasets). Additionally, the start and end *Boundary* posterior distributions are used to constrain the commencement or termination of events recorded in stratified *Sequence* models (namely the individual site models of fluvial deposition; Model 2). All except two of the models exhibit average convergence integrals >95% for individual posterior distributions thereby supporting the overall effectiveness of the Monte Carlo solutions (Table D9). The exceptions are Model 2 for SWJS and SW9 which returned lower convergence due to the limited numbers of likelihoods (Figure D9) and, the distribution of younger ages (Figure D7) in each model respectively.

Model 1: South Walker Creek megafaunal age range

The results of Model 1 are detailed in Figure D5 and Table D8, with the combined age ranges for the megafauna *Phase* model shown in Figure 5.5. The posterior age estimate for the depositional layers containing megafauna fossils is calculated as 57.7 – 37.9 ka (95% C.I.) using the *Date* command ("megafauna duration" in Figure 5.5). For comparison, the start and end *Boundary* ages for the local appearance and disappearance of preserved megafauna fossil remains in South Walker Creek are 62.5 – 50.4 ka ("megafauna bottom" in Figure 5.5) and 41.7 – 35.8 ka ("megafauna to non-megafauna transition" in Figure 5.5), respectively (95% C.I.). In this particular modelling context, the "megafauna to non-megafauna transition" *Boundary* age may be more representative of the megafauna last appearance age at South Walker Creek than the *Date* command age estimate of the *Phase* grouping, given that the actual timing of megafauna disappearance will have inevitably post-dated the sampled events included in the *Phase* model (owing to the Signor-Lipps effect; Signor & Lipps, 1982). However, the lowermost 95% C.I. for the "megafauna to non-megafauna transition" *Boundary* remains relatively imprecisely constrained in this model as it incorporates a limited number of *Phase* groupings. Bearing this in mind, we conservatively conclude that megafauna suffered local extinction at South Walker Creek sometime after the youngest last appearance age in the fossil record, which is modelled as being 37.9 ka using the lowermost 95% C.I. for the *Date* function posterior distribution.

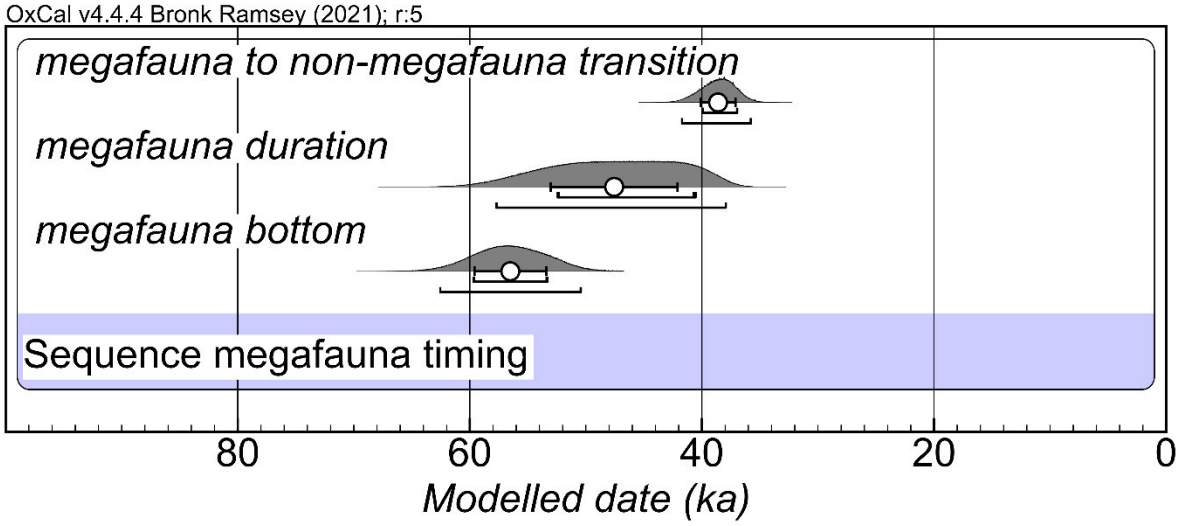

Figure 5.5 *Phase* model output for the megafauna fossil-bearing units within the South Walker Creek area (Model 1). The modelled distributions represent (from top to bottom) the local disappearance of preserved megafauna fossils, the combined age range of megafauna fossil deposits, and the local appearance of preserved megafauna fossils in the South Walker Creek area. See Figure D5 and Table D8 for detailed output of Model 1.

Model 2 and Model 3: The timing of fluvial activity at individual South Walker Creek sites and at the basin scale

The Bayesian modelling results for the timing of fluvial deposition at the eight South Walker Creek sites (Model 2) are presented in Table D9 and Figures D6 – D13. Figure 5.6 summarises the combined modelled age ranges for individual fluvial units preserved at each site (calculated in Model 2 by applying the *Date* query to the posterior age ranges of the unit start and end *Boundaries*), as well as the basin-wide temporal distributions of fluvial activity obtained by applying the *Sum* and *KDE_Plot* query functions to the pooled, unordered *Phase* model for South Walker Creek (Model 3). Only 9 of the 63 likelihood estimates included in the various site-specific models (Model 2) exhibit posterior outlier probabilities >5% (Table D9), which is marginally greater than modelling expectations of one in twenty individual age estimates being considered likely to be significantly offset from the event of interest when adopting a prior outlier threshold of 5% (Bronk Ramsey, 2009a).

Six of the South Walker Creek sites (SW9, SWCC, SWJ, SWP, SWS and SW3) preserve single fluvial episodes with posterior age estimates spanning 81.7 – 31.1 ka (all unit ages calculated using the *Date* command 95% C.I. and shown as "durations" in Figure 5.6). Of these sites, SW9, SWS and SW3 exhibit similar MIS3 fluvial histories, with modelled depositional age ranges of 41.3 – 37.6 ka, 57.3 – 42.8 ka and 52.8 – 44.3 ka, respectively; while SWP and SWCC preserve broader, albeit less precisely constrained, fluvial episodes spanning 68.3 – 46.3 ka and 81.7 – 31.1 ka, respectively; and SWJ records the second earliest fluvial deposition event in the basin, commencing 72.3 ka and lasting until 58.8 ka.

One of the South Walker Creek sites (SWJS) records two successive fluvial deposition events spanning 48.1 – 38.6 ka (Unit 1) and 45.3 – 37.2 ka (Unit 2). The modelled age ranges for the units at SWJS are indistinguishable from the fluvial episodes recorded at sites SW9, SWS and SW3 (41.3 – 37.6 ka, 57.3 – 42.8 ka and 52.8 – 44.3 ka, respectively), highlighting broad-scale similarities in hydroclimatic signatures across multiple sites. The timing of SWJS Unit 2 overlaps with the extended fluvial deposition event recorded at SWCC, however covers a shorter time range terminating at 37.2 ka rather than 31.1 ka. Application of the *Difference* and *Interval* functions reveals that the boundaries of the successive fluvial units at SWJS are not separated by any statistically significant temporal hiatuses.

The modelling results for SWC-US provide the most comprehensive temporal constraints on long-term hydrological change in the catchment, reflecting the more central position of this site within the former river channel (Figure 5.2). The two lowermost units at SWC-US, which are devoid of fossils owing to the higher energy depositional environment, overlap with the timing of fluvial sedimentation and megafauna fossil accumulation at several other sites in the basin. In particular, SWC-US Unit 1 (57.3 – 43.3 ka; Table 5.3) shares similar modelled upper or lower 95% C.I. age ranges to fluvial deposition events preserved at SWCP, SWCS, SW3, SW9, SWJS (Unit 1) and SWCC. SWC-US Unit 2 (50.3 – 36.1 ka) shares a similar lower 95% C.I. age range as SWJS (Unit 2), and SWCC, indicating renewed fluvial deposition at some of the proximal channel sites lasting until mid-to-late MIS3. SWC-US Units 3 – 7 reveal a series of significantly younger fluvial deposition episodes, which are not observed at any of the South Walker Creek sites located further downstream. SWC-US Units 3, 4 and 5 record fluvial deposition during the late glacial to early Holocene between 25.7 – 11.3 ka, 18.3 – 10.4 ka and 15.3 – 8.5 ka, respectively. Additional early-to-mid Holocene fluvial deposits are

recorded at SWC-US between 12.2 ka and 5.1 ka (Unit 6), with a final mid-to-late Holocene depositional event from 5.0 ka until the commencement of the historical erosion phase (Unit 7).

Table 5.3 OxCal model outputs for the SWC-US sedimentary units.

	Unmodelled (BP)				Modelled (BP)			
SWC-US	68%		95%		68%		95%	
	from	to	from	to	from	to	from	to
Boundary SWC-US Unit 7 top					2791	-2	5057	-2
SWC-US Unit 7 duration					5056	1463	6986	349
SWC-P	5778	422	8300	-2	4372	1278	5958	316
SWC17-38	7399	601	10600	-2	5620	2089	7303	769
Boundary SWC-US Unit 7 bottom					6877	2727	8958	1157
SWC-US Unit 6-7 Transition								
Boundary SWC-US Unit 6 top					9748	-2	11417	3579
SWC-US Unit 6 duration					10446	-2	12199	5045
SWC17-43	12663	8337	14700	6300	10498	7264	12052	5710
Boundary SWC-US Unit 6 bottom					11332	7977	13121	6337
SWC-US Unit 5-6 Transition								
Boundary SWC-US Unit 5 top					12698	-2	14567	7759
SWC-US Unit 5 duration					13315	-2	15276	8454
SWC17-41	15375	10225	17800	7800	13350	9975	15250	8550
Boundary SWC-US Unit 5 bottom					14037	-2	16078	9015
SWC-US Unit 4-5 Transition								
Boundary SWC-US Unit 4 top					15406	11351	17574	10040
SWC-US Unit 4 duration					15999	11727	18295	10428
SWC17-44	18572	13628	20900	11300	16048	11848	18256	10504
Boundary SWC-US Unit 4 bottom					16694	12082	19150	10777
SWC-US Unit 3-4 Transition								
Boundary SWC-US Unit 3 top					18058	12514	20814	11239
SWC-US Unit 3 duration					19387	12705	25689	11307
SWC17-42	17184	11416	19900	8700	18884	12612	21600	11492
SWC17-39	11545	8455	13000	7000	19945	12640	24340	11500
Boundary SWC-US Unit 3 bottom					20923	12864	31161	11575
SWC-US Unit 2-3 hiatus duration [a]					39288	22118	43595	15753
Boundary SWC-US Unit 2 top					46104	39172	48904	29717
SWC-US Unit 2 duration					47018	41174	50283	36112
SWC17-40	49093	42707	52100	39700	46122	41379	48509	38744
SWC-O	49920	41680	53800	37800	47200	42400	49600	40000
Boundary SWC-US Unit 2 bottom					48378	43114	51290	40636
SWC-US Unit 1-2 Transition								
Boundary SWC-US Unit 1 top					51163	45155	54610	42507
SWC-US Unit 1 duration					52815	46155	57265	43316
SWC-N	52726	44074	56800	40000	52624	46366	56194	43678
Boundary SWC-US Unit 1 bottom					54513	46964	60269	43941

[a] modelled age represents the duration of time missing between adjacent units (expressed as a temporal range in years, rather than a numerical age in years ago). This modelled duration has been calculated using the *Interval*() query function, and provides the temporal range between the posterior probability density distributions of successive stratigraphic boundaries.

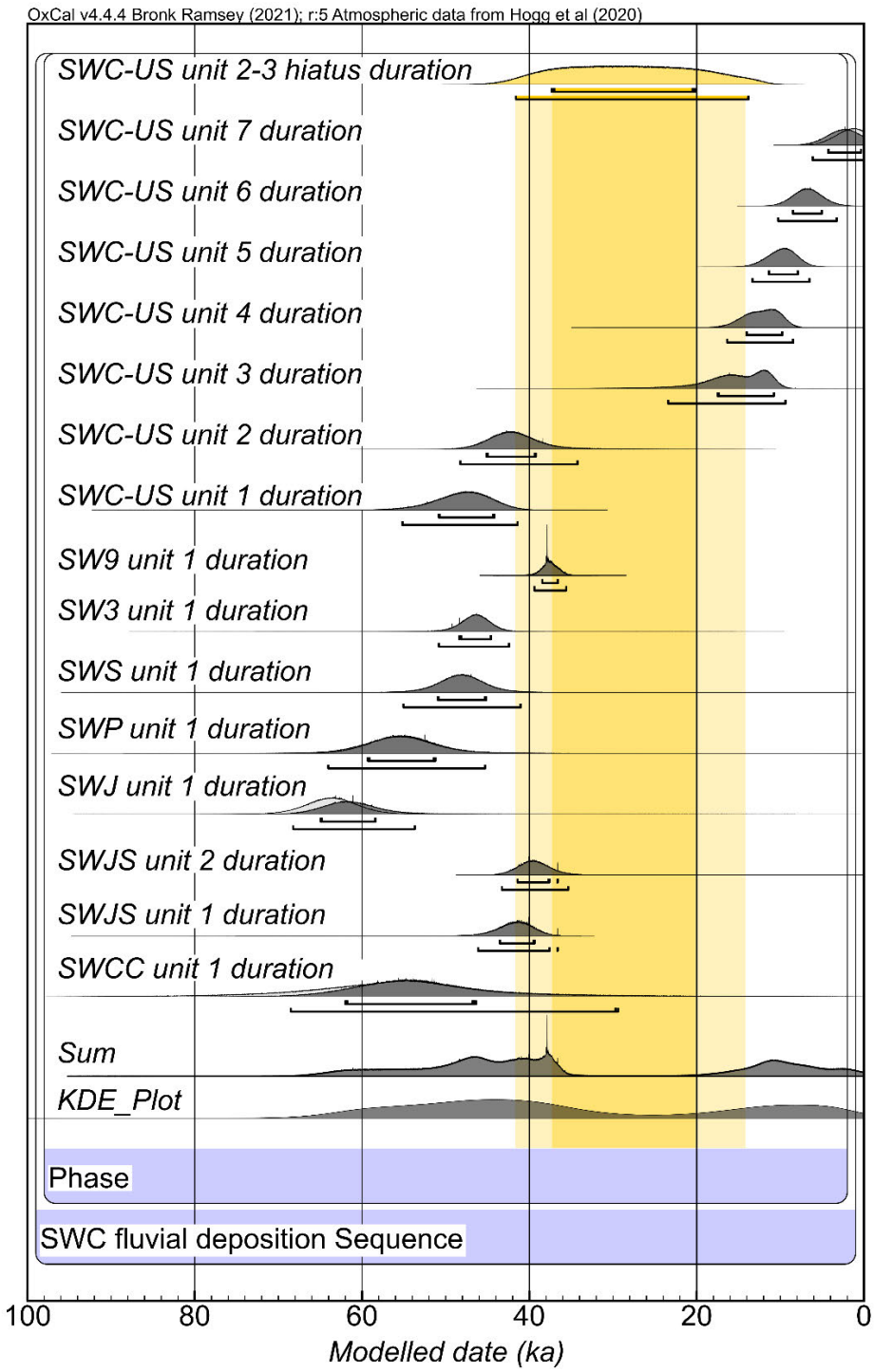

Figure 5.6 Bayesian modelling results used to constrain the temporal distribution of fluvial activity across all South Walker Creek sites (Model 3). The posterior probability distributions of individual fluvial depositional events obtained in Model 2 (shown in grey; see Figures D6 – D13 and Table D9 for derivation) have been recalled using the *Prior* function and combined in a single *Phase* model, delineated by start and end *Boundaries*. The 68.2% and 95.4% ranges of the highest posterior probabilities are indicated by the horizontal bars underneath the probability density functions. The *Sum* and *KDE_Plot* query functions (Bronk Ramsey, 2009a, 2017) have been used to visualise and characterise the resultant temporal distributions of fluvial activity. The SWC-US hiatus duration has been calculated in Model 2 by applying the *Date* command between the posterior probability density distributions of SWC-US Units 2 and 3 boundaries. The posterior probability distribution of this *Date* query has been recalled in Model 3 using the *Prior* function and used to determine the 68.2% and 95.4% C.I. age range of reduced fluvial activity in the South Walker Creek locality (delineated using the dark and light shaded vertical orange bands, respectively). This identified fluvial hiatus, which is inferred to represent a shift towards a more negative moisture balance, has been determined specifically from the SWC-US sequence because this site contains the most comprehensive fluvial succession in the South Walker Creek area, and therefore provides the most complete insights into the longer-term hydrological dynamics of the catchment.

The *Difference* query reveals a statistically significant temporal gap between SWC-US Units 2 and 3, with a calculated mean temporal duration of 22.0 ± 7.3 ka (1σ C.I. uncertainty; calculated using the Interval function;). This identified hiatus reflects a prolonged period of non-deposition spanning part of late MIS3 and MIS2 or a statistically significant amounts of undated (either non-sampled or missing) material in this part of the SWC-US profile. The fact that late MIS3 to MIS2 fluvial deposits are absent at all other South Walker Creek sites, with possible exception to SW9 and SWCC (where lower 95% C.I. boundary ages remains imprecisely resolved), may be indicative of a genuine shift towards a more negative moisture balance during this period, though improved insights into this possibility can be gleaned from the Model 4 results (see next section).

The posterior probability density distribution of the SWC-US fluvial hiatus (calculated in Model 2 by applying the *Date* command between the distributions of SWC-US Units 2 and 3 boundaries) is shown in Figure 5.6, alongside the basin-wide temporal distributions of fluvial deposition obtained using the *Sum* and *KDE_Plot* functions in Model 3. The *Sum* function generates a superposition of the modelled distributions for all the fluvial deposition events included within the Model 3 *Phase* grouping, and therefore exhibits some noise related to the limited number of likelihoods at some sites. The *Sum* function also exhibits some spread in the summed tail(s) related to uncertainty in the 99 – 95% C.I. constraints for some of the posterior distributions included in the *Phase* model (Bronk Ramsey, 2017). In contrast, the *KDE_Plot* produces a continuous distribution of fluvial deposition events in the modelled Phase using the sum of kernel weighting functions applied to discrete data points. The *KDE_Plot* temporal distribution is therefore less susceptible to uncertainty in the extreme tails of the marginal distributions in comparison to the *Sum* plot. The former however, produces an oversmoothed distribution, which seems to affect most of the sites. Therefore, we present both the *Sum* plot and *KDE_Plot* results for our characterisation of fluvial activity in Model 3 and 4. Irrespective, both comparative modelled distributions reveal consistent patterns of hydroclimatic change across Australian catchments spanning MIS5 to MIS1.

The *KDE_Plot* and *Sum* plot for Model 3 shows continuous fluvial deposition at the basin scale between 68 ka and 36 ka, with a broad peak in probability spanning 50 – 38 ka (Figure 5.6). The frequency distribution of preserved fluvial deposition at South Walker Creek is generally lower during MIS4 than MIS3, with a gradual increase in fluvial activity recorded during early- to mid-MIS3 (60 – 46 ka) and a distinctive decline after 38 ka (Figure 5.7). The probability of fluvial deposition becomes particularly limited at South Walker Creek from 35 ka onwards, with the onset of this hydrological shift closely coinciding with the modelled last appearance age for megafauna in the basin (i.e., 37.9 ka using the lowermost 95% C.I. of the megafauna *Phase* grouping in Model 1) (Figure 5.5 and Figure 5.7). The ensuing period of limited fluvial deposition persists through much of late MIS3 and early- to mid-MIS2, effectively spanning the modelled 68 and 95% C.I. of the fluvial hiatus identified at SWC-US (Figure 5.6; highlighted using an orange vertical band). Renewed fluvial deposition is recorded in the basin from the late glacial period onwards (~16 ka), with the probability of fluvial deposition gradually increasing during the early Holocene and reaching a peak 12 – 8 ka. Following this early- to mid-Holocene probability maximum, the distribution of fluvial deposition declines towards the present-day (Figure 5.6).

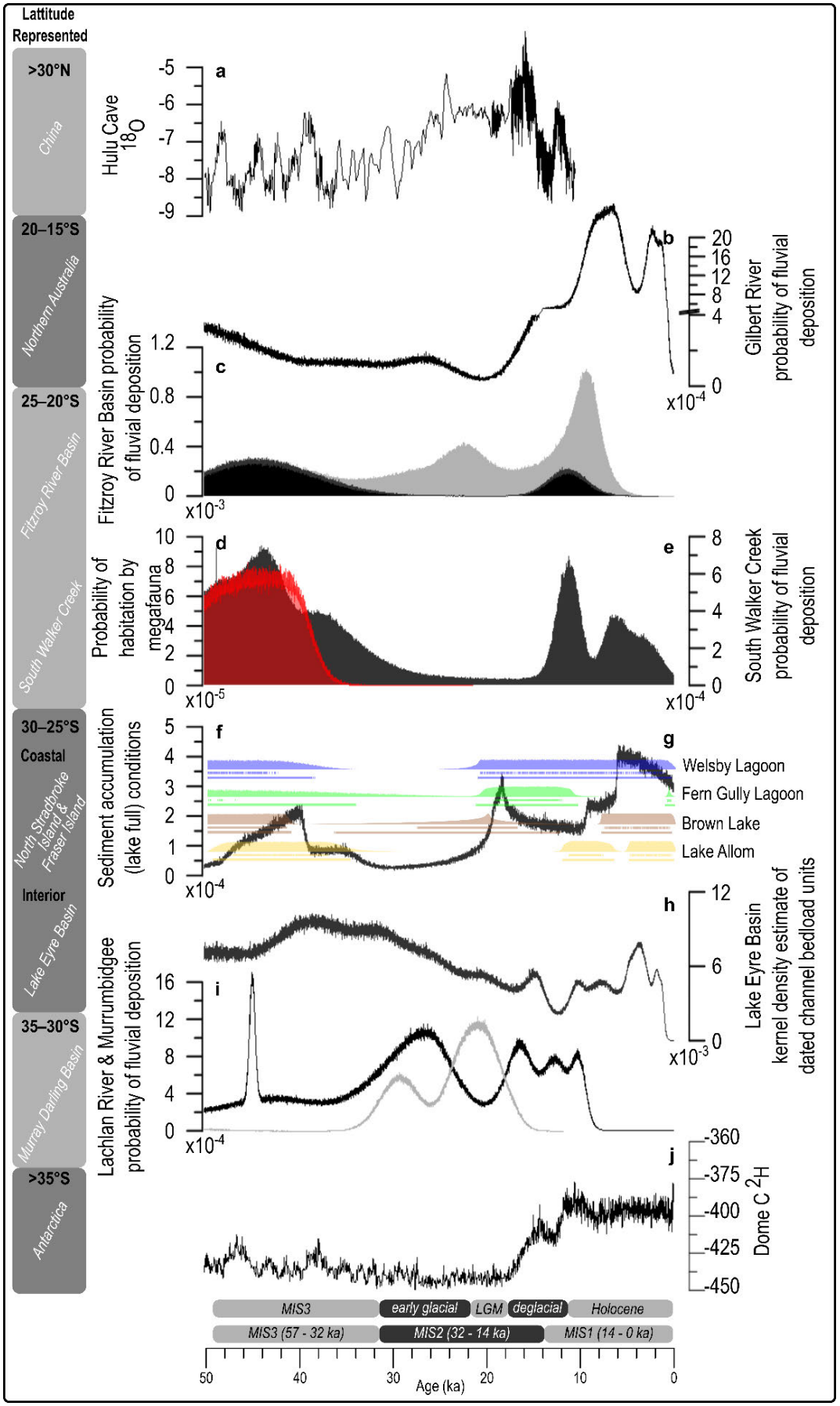
Lattitude Represented
>30°N
China
20–15°S
Northern Australia
25–20°S
Fitzroy River Basin
South Walker Creek
30–25°S
Coastal
North Stradbroke Island & Fraser Island
Interior
Lake Eyre Basin
35–30°S
Murray Darling Basin
>35°S
Antarctica
Hulu Cave δ18O
a
b
Gilbert River probability of fluvial deposition
c
Fitzroy River Basin probability of fluvial deposition
d
Probability of habitation by megafauna
e
South Walker Creek probability of fluvial deposition
f
Sediment accumulation (lake full) conditions
g
Welsby Lagoon
Fern Gully Lagoon
Brown Lake
Lake Allom
h
Lake Eyre Basin kernel density estimate of dated channel bedload units
i
Lachlan River & Murrumbidgee probability of fluvial deposition
j
Dome C δ2H
MIS3
early glacial
LGM
deglacial
Holocene
MIS3 (57 - 32 ka)
MIS2 (32 - 14 ka)
MIS1 (14 - 0 ka)
Age (ka)

Figure 5.7 (opposite page) Comparison of frequency distributions of fluvial activity and lake sediment accumulation phases determined for a range of Australian catchments using the results of Model 4. The temporal distributions of hydrological activity for individual basins are shown in plots (b – c) and (e – h), and compared with the frequency distribution of megafauna presence at South Walker Creek (Model 1) in plot (d), as well as selected long-term speleothem and icecore records hydrological change from China and Antarctica (a and i). The reference timings of glacial and interglacial periods shown below plot m are based on those defined by Reeves et al. (2013) (top row) and Lisiecki & Raymo (2005) (bottom row). (a) oxygen isotope records from Hulu Cave speleothems (black) (Wang et al., 2001); (b) modelled fluvial deposition events in the Gilbert River Basin, determined from the Model 4 *Phase* grouping of the Nanson et al. (2005) chronological dataset; (c) modelled fluvial deposition of Isaacs and Comet sub-catchments (black) and the total Fitzroy River Basin (grey) determined from the Model 4 *Phase* grouping of chronological dataset for the region (Croke et al., 2011); (d) modelled probability density distribution of known megafauna presence at South Walker Creek (red), determined using the 95% C.I. of the megafauna Phase grouping in Model 1; (e) modelled fluvial deposition events at South Walker Creek (black), determined from the Model 3 Phase grouping of site-specific chronological ranges produced in the current study (Model 2); (f) sediment accumulation (lake full) phases (95.4% C.I.) for the combined North Stradbroke Island and Fraser Island wetlands, determined from (g) the modelled probability density distributions of sediment accumulation (lake full) phases (95.4% C.I.) the Model 4 *Phase* groupings of the Lewis et al. (2021); Kemp et al. (2020); Lewis et al. (2020); Cadd et al. (2018); Donders et al. (2006) chronological datasets; (h) fluvial deposition for rivers feeding into the Lake Eyre Basin (Cohen et al., 2015); (i) modelled fluvial deposition for the Lachlan River (black) and Murrumbidgee (grey) sub-catchments of the Murray Darling Basin, determined from the Model 4 Phase grouping of the Kemp & Rhodes (2010) and Page et al. (2009) chronological datasets, respectively; (j) deuterium isotopic record from Antarctica Dome C (Jouzel et al., 2007).

Model 4: Temporal distribution of hydrological activity across other catchments

Figure 5.7 summarises the modelled temporal distributions of hydrological activity (fluvial or lacustrine deposition) for a range of Australian catchments, as determined from the *Sum* plot and *KDE_Plot* results of basin-specific *Phase* groupings in Model 4 (see Figures D14 – D23 and Tables D10 – D17 for details of the individual basin modelling results used to derive distributions). Our comparison focuses on the last 50 ka, as this is the most completely represented time period across the combined datasets.

Figure 5.7 shows that the distinct decrease in fluvial deposition observed at South Walker Creek from 38 ka onwards is similarly recorded across other northern Australia tropical basins. The Gilbert River shows a decline in fluvial deposition between 50 ka and 42 ka, followed by a sustained period of low probability fluvial deposition between 38 ka and 25 ka, and then a renewed decline to a depositional minimum spanning 23 – 19 ka (Figure 5.7). Similar trends are recorded in several headwater sub-catchments of the Fitzroy River Basin, including the Isaac River that neighbours South Walker Creek. Together, the Isaac and Comet Rivers record a steady decrease in fluvial deposition beginning 44 ka, with lower fluvial deposition present between 26 ka and 18 ka (Figure 5.7). The same decline in late-MIS3 fluvial deposition is recorded at the broader Fitzroy River Basin scale (Figure 5.7); though there is evidence of renewed fluvial deposition in some of the Fitzroy sub-catchments during early- to -mid MIS2, which likely partly reflects time-transgressive fluvial responses in different parts of these networks. The Gilbert, Isaac and Comet Rivers, and combined Fitzroy River Basin all show sustained increases in fluvial deposition from late-MIS2 or early-MIS1 onwards (Figure 5.7), mirroring the trends seen at South Walker Creek during these time periods (Figure 5.7).

The combined temporal distribution of sediment accumulation (lake full) phases at the sub-tropical North Stradbroke Island and Fraser Island wetland sites (Figure 5.7) shows a two-stage decline during late- MIS3 at 41 ka and 35 ka, followed by a sustained minimum in sediment accumulation at three of the four sites until 22 ka, again reflecting broader trends observed in the tropical river basin frequency distributions. The sub-tropical coastal wetlands exhibit several peaks of sediment accumulation during the late glacial (18 ka), early- to mid-Holocene (9 ka and 6 ka) and late Holocene (3 ka onwards), with many of these peaks coinciding with fluvial activity peaks identified in one or more of the South

Walker Creek, Fitzroy River and Gilbert River basins. Similarly, the Lake Eyre filling record (Figure 5.7) – which primarily reflects periods of sustained river flow from extensive northern catchments minus evaporative losses (Figure 5.7), and thus the influence of tropical and sub-tropical air masses – exhibits two episodic high stands and megalake phases during the last 50 ka. These took place prior to 30 ka and after 12 ka (Cohen et al., 2015) and are coincident with peaks in fluvial activity across the northern basins shown in Figure 5.7. The intervening and subsequent periods at Lake Eyre were characterised by protracted drying phases, playa-like conditions and minor episodic filling events, as seen today (Cohen et al., 2015).

Interestingly, the temporal distributions of fluvial deposition in the northern and central Australian basins seem to be distinctly different from those of the Murray Darling Basin in the southern latitudes – the latter characterised by relatively limited fluvial deposition in the Lachlan and Murrumbidgee Rivers during MIS3 (Figure 5.7), and an increase in fluvial deposition during MIS2, inclusive of the Last Glacial Maximum.

Discussion

The rich sedimentological, taxonomic and taphonomic information preserved in conjunction at South Walker Creek underscores the significance of this area for investigating relationships between climate variation and ecological change through the late Pleistocene (Hocknull et al., 2020). However, prior to the present study it has only been possible to undertake limited examination of the spatio-temporal accumulation dynamics across the South Walker Creek fossil locality, and to conduct relatively general comparisons with regional records of climate change. The new chronological constraints and Bayesian modelling analyses presented herein provide an improved quantitative framework for such evaluations. In the sections that follow, we discuss the timing and significance of the South Walker Creek fluvial and megafauna records, placing them in broader regional contexts of existing palaeoecological research across eastern and central Australia, and examining their implications for understanding climatic and anthropogenic links with megafaunal extinction.

Megafauna presence and last appearance at South Walker Creek

A diverse aquatic and terrestrial megafauna community is known to have thrived locally at South Walker Creek between at least 62.5 ka and 35.8 ka (95% modelled C.I. of age estimates on fossil-bearing units; n = 44), with local extinction occurring sometime after this period, and potentially within the modelled transitional (end *Boundary*) age range of 41.7 – 35.8 ka (Figure 5.5). The absence of megafauna fossils prior to the modelled first appearance date at 62.5 ka most likely reflects erosion and non-preservation of older fossil-bearing sediments, consistent with observations that the host deposits unconformably overlie bedrock at the various South Walker Creek sites (Hocknull et al., 2020). The likelihood of significant fluvial erosion prior to deposition of the earliest fossil layer at South Walker Creek (SWCC Unit 1 with 95% C.I. modelled age of 81.7 – 31.1 ka (Figure D8)); is also supported by regional evidence for relatively limited fluvial deposition within the Fitzroy River Basin during large parts of MIS5 and MIS4 (Croke et al., 2011; Figure D15).

The modelled duration age range of 57.7 – 37.9 ka for South Walker Creek is noteworthy as it represents one of the few reliable mid-late MIS3 constraints on megafauna presence across the poorly studied north-eastern region of Australia. Moreover, it constitutes one of the youngest multi-site evaluations of megafauna last appearance published so far for the Sahul continent. Several such multi-

site or regional chronological syntheses of megafauna demise have been published previously. The first of these focused on 19 fossil sites containing articulated megafauna remains from across the continent (Roberts et al., 2001), and derived a 95% C.I. maximum likelihood estimate of extinction spanning 51.2 ka to 39.8 ka (thereafter commonly referred to as the "extinction window"). Consistent last appearance age ranges were subsequently reported for two taxa-specific, regional chronological syntheses: 50 ± 5 ka for *Genyornis newtoni* eggshells from the Lake Eyre and Murray-Darling basins (Miller et al., 1999; Demarchi et al., 2022), which has recently been updated to 53.9 – 43.4 ka at 95% C.I. (Miller et al., 2016b), and ~40 – 50 ka for *Diprotodon optatum* teeth from a range of South Australian fossil sites (Grün et al., 2008).

Some of the original interpretations from these regional syntheses have been questioned following broader examinations of palaeoecological and palaeoenvironmental trends over extended timescales (e.g., Murphy et al., 2012; Wroe et al., 2013). Irrespective of this, these regional-scale chronological datasets remain the only multi-site constraints on late megafauna survival available.

As noted in the introduction, chronological reliability is increasingly being recognised as a key consideration in reconstructing reliable extinction timelines. Therefore, evaluations of robust chronologies are undoubtedly more important than merely examining published age distributions through time. Several regional syntheses have sought to incorporate quality control evaluations of chronological datasets published for Sahul megafauna fossil deposits (e.g., Gillespie & Brook, 2006; Rodríguez-Rey et al., 2015). The most comprehensive of these meta-analysis studies (Saltré et al., 2016b) – which employed ensemble hind cast frequentist modelling to account for incomplete sampling and taphonomic biases and incorporated quality-filtered time series data for 16 megafauna genera – estimated continent-wide extinction spanning 36.7 – 48.1 ka (75^{th} and 25^{th} percentiles of modelled extinction age distributions), with a median extinction peak at 42.1 ka.

The mean Bayesian modelled age of 38.6 ± 1.5 ka for last known megafauna occurrence at South Walker Creek is consistent with the modelled extinction range of Saltré et al. (2016b), though it lies towards the younger end of their proposed extinction timeframe and beyond their median extinction peak at 42.1 ka. This latter observation may be significant because, unlike the modelled extinction age of Saltré et al. (2016b), our primary datasets do not explicitly account for the Signor-Lipps effect and therefore likely yield a maximum age estimate on the actual regional extinction event. Our modelled age for last known megafauna occurrence at South Walker Creek is also systematically younger than that obtained for other Australian regions using similar, multi-site chronological assessments (e.g., Grün et al., 2008; Miller et al., 2016a; Miller et al., 1999; Roberts et al., 2001). These outcomes could imply regional differences in the timing of megafaunal extinction across Sahul (e.g., Hocknull et al., 2021; Saltré et al., 2016b) or, equally, may reveal that the existing geographic and temporal coverage of chronological datasets remains insufficient to fully resolve continental megafaunal extinction dynamics using meta-analyses approaches (Price, et al., 2018).

Perhaps most significantly, the local last appearance of megafauna in north-eastern Australia ~37 ka appears to have taken place in the context of potentially significant regional environmental deterioration and instability. As detailed below, these hydrological and ecological changes are recorded across multiple catchments, with possible implications for understanding the complex causes behind megafauna demise.

Regional comparisons of hydrological and ecological change

The preserved sedimentary record for South Walker Creek provides limited insights into environmental conditions during the last interglacial complex, with evidence of MIS5 fluvial activity absent from all sites, most likely reflecting the occurrence of preceding erosional phases. However, there is clear sedimentological and fossil evidence for sustained periods of catchment flow during MIS4 and early-MIS3. Evidence for sediment mobilisation and fluvial deposition during this period is recorded at all eight South Walker Creek sites (Figure 5.6), mirroring trends across various other tropical and sub-tropical catchments (Figure 5.7), and indicating seemingly favourable hydroclimatic conditions regionally. Aside from this sedimentological evidence, the fossil fauna indicate the presence of a diverse freshwater fauna (e.g., crustaceans, bivalves, fish and turtles) with at least three crocodilians (*Crocodylus* sp. cf. *C. porosus*, *Pallimnarchus* sp. and '*Quinkana'* sp.) during MIS4 to early-MIS3 at South Walker Creek (Hocknull et al., 2020). This suggests that the catchment received sufficient water flow from tributaries to support permanent aquatic environments proximal to the main channel, as well as sustaining favourable hunting habitats for large aquatic predators.

These various indicators of more positive moisture balances across South Walker Creek and neighbouring catchments during MIS4 to early-MIS3 are consistent with the findings of a recent compilation study of 40 Australian hydroclimatic records spanning MIS3 (Kemp et al., 2019). This synthesis revealed that a coeval trend of more positive moisture balances, increased fluvial activity and higher lake levels existed regionally across Australia through MIS4 and into MIS3, with catchments in the tropics, subtopics, temperate regions and central arid interior found to have experienced wetter climates relative to their modern baselines between 57 and 40 ka, with wettest conditions evident between ~49 and 40 ka.

Figure 5.7 reveals a progressive, regional-scale shift towards less favourable hydroclimatic conditions from mid- to late-MIS3 onwards across a range of northern and central Australian catchments. South Walker Creek records a variation in fluvial deposition between 43.0 and 37.0 ka, followed by a prolonged period of limited fluvial deposition spanning much of late MIS3 and early- to mid-MIS2. These deteriorating hydroclimatic conditions are most closely mirrored in the Gilbert River and several other Fitzroy Basin sub-catchments between 41 ka and 18 ka, but are also similarly recorded in southeast Queensland wetlands and the Lake Eyre Basin. The fact that the MIS3 and MIS2 temporal distributions of fluvial activity observed at South Walker Creek are largely replicated at the regional scale suggests that the hydrological changes inferred from Models 2 – 3 do not simply reflect site-specific preservation dynamics at individual South Walker Creek exposures (e.g., localised erosion of pre-existing deposits by subsequent flooding events). It is not possible to rule out the potential for complex spatial responses and time-transgressive preservation of fluvial material in different parts of the South Walker Creek catchment; indeed, there appears to be some evidence for transgressive preservation between some of the northern and southern sub-catchments of the Fitzroy River Basin (Figure 5.7). However, it seems unlikely that such consistent inter-basin responses would emerge if our modelling results were significantly affected by such complications.

The trends towards more negative moisture balances during mid- to late- MIS3 and into MIS2 shown in Figure 5.7 are consistent with a range of other palaeoclimate archives across Australia. The MIS3 hydroclimate synthesis of Kemp et al. (2019), for instance, reveals gradual continental drying after ~40 ka, with mean water availability conditions becoming 30% lower than modern baseline estimates

by the end of MIS3. At Lynch's Crater, tropical northeast Queensland, there is evidence for a major change in vegetation structure from ~41 ka onwards, with a progressive increase in sclerophyllous taxa and grasses relative to rainforest taxa during the second half of MIS3 and into MIS2. These vegetation turnovers are broadly consistent with palynological assessments undertaken at South Walker Creek (Hocknull et al., 2020), which reveal a dominance of sclerophyll vegetation at site SW9 during mid- to late-MIS3.

Evidence for increased dust flux across various regions of Australasia may also be consistent with progressively drier conditions during mid- to late- MIS4 and MIS 2 (i.e., De Deckker et al., 2019; McGowan et al., 2008; Petherick et al., 2009). However, some care needs to be taken when inferring aridity from such dust records, as the sedimentary material preserved can also be indicative of wetter conditions, or changes in other synoptic conditions (Farebrother et al., 2017; Marx et al., 2018).

The modelled hydroclimatic responses across different Australian regions during MIS3 are shown alongside the probability distributions of megafauna presence at South Walker Creek in Figure 5.7. These comparisons show that progressive, regional-scale hydroclimatic change during mid- to late-MIS3 (43 – 37 ka onwards) was broadly coincident with the modelled last appearance age of megafauna at South Walker Creek ~38 ka. Similar chronological comparisons of new and existing megafauna fossil localities across tropical Australia are now needed to examine the potential for shared biogeographic responses during late-MIS3. For South Walker Creek, at least, our data suggests that the disappearance of megafauna did not necessarily take place during a period of climate stability but rather during a period characterised by regional shifts towards reduced fluvial activity and lacustrine sedimentation.

An absence of evidence for significant climate change during the megafauna "extinction window" has traditionally been cited in favour of human-induced megafauna demise; with examination of climate dynamics often restricted to broad-scale comparisons using ice- or marine-core records (e.g., Johnson et al., 2016a; Saltré et al., 2016a; Wroe et al., 2013). It is worth keeping in mind that such remote climate records may provide relatively limited insights into the magnitude or even timing of localised palaeoenvironmental change across certain regions of Australia, as discussed below. Our synthesis of hydroclimate change for different Australian catchments reveals that equally important insights can be gained from consideration of multiple terrestrial proxy records in tandem, particularly those that are directly associated with megafaunal fossil localities.

It remains unclear whether the magnitude of hydroclimate change experienced in these catchments during mid-late MIS3 and MIS2 was significantly different than that experienced during previous glacial or stadial episodes, especially given the continent-wide paucity of reliably dated terrestrial palaeoenvironmental records beyond these time periods (see review by Kemp et al. (2019)). However, Hocknull et al. (2007) demonstrate major faunal turnover, including local extinction at Mt. Etna caves of closed-forest (rainforest) fauna, coincident with major changes in middle Pleistocene climate, and located within the same Fitzroy River Basin as South Walker Creek.

Interestingly, the onset of MIS3 environmental deterioration identified across multiple catchments in Figure 5.7 broadly coincides with the timing of the Lachamps geomagnetic excursion, which has been documented recently in ancient Kauri records and postulated to be the cause of globally synchronous climate upheavals, extinctions and behavioural changes across human populations (Cooper et al.,

2021). However, the hydroclimatic changes observed across central and northern Australia during this time period appear to be progressive rather than abrupt (even taking into consideration the resolution of available records), spanning multiple millennia in all cases, and preceding the 42 ka geomagnetic excursion event in several regional catchments (Figure 5.7). The modelled age range of 37.6 ± 1.1 ka for the last known megafauna occurrence at South Walker Creek also post-dates the Lachamps excursion by several millennia. The temporal dynamics of regional environmental and ecological change during mid-MIS3 therefore do not appear to provide particularly strong support for the short-lived, threshold-crossing and geographically synchronous upheavals postulated by Cooper et al. (2021); especially when considering that the Signor-Lipps effect is likely to further offset the true timing of regional megafaunal extinction and hydroclimatic change from the Lachamps event.

Finally, our modelling results reveal evidence for contrasting hydroclimatic responses between northern and southern geographic regions of Australia during MIS3 and MIS2. In the northern and central latitudes of the continent, most of the examined catchments exhibit more favourable hydrological conditions in MIS3 compared to MIS2. In contrast, the Murray Darling Basin in the southeast of the continent records relatively limited fluvial deposition during MIS3, and an increase in fluvial deposition during MIS2, which likely reflects the distinct geographic and topographic features of this catchment (including recharge by seasonal melting of snow and ice; Hesse et al., 2018). Kemp et al. (2019) similarly observed differences between the MIS3 hydroclimatic responses of monsoon-influenced regions and those in the southerly latitudes that are strongly influenced by south-westerly air masses and winter-dominated precipitation. In particular, monsoon-influenced northern and central region records exhibited stronger hydrological deterioration (relative to their modern baselines) during MIS3 compared to the south-westerly-influenced regions. While continental drying was occurring across large parts of the northern and central continent in late MIS3, comparatively wetter climates appear to have persisted in southern Australia and Tasmania (Deer, 2011; Kemp et al., 2019).

Insights into the likely synoptic causes of the contrasting latitudinal hydroclimatic histories shown in Figure 5.7 can be gained by comparing the individual basin records with palaeoclimate records from beyond the Australasia region; particularly the Northern Hemisphere isotopic records of Hulu Cave and Yangzi Cave, southwestern China (Wang et al., 2001; Wu et al., 2020), which provide insights into the relative influence of the East Asia summer monsoon and changes in the Intertropical Convergence Zone (ITCZ).

As Figures 5.7 shows, there appears to be a general relationship between the timing of major isotopic change in long-term speleothem and ice core records, and the nature / timing of hydrological change recorded in Australian basins positioned latitudinally north of 30°S, potentially supporting the hypotheses of wetter climates being driven by the position of the ITCZ (Figure 5.7). In contrast, the catchments located in more southerly latitudes exhibit more limited (or complex) frequency distribution correlations with the Northern Hemisphere records, and thus may have been largely insulated from any such shared synoptic drivers (Figure 5.7). From these comparisons it seems feasible that the hydroclimate deterioration seen across the northern and central catchments during late MIS3 and MIS2 reflects shifts in the strength of the Indo-Australian monsoon, which in turn reflected changes in the position of the ITCZ that influenced the East Asian summer monsoon (English et al., 2001; Godfred-Spenning & Reason, 2002; Magee et al., 2004) and ENSO (Clement et al., 1999; Russell et al., 2014). Thus, atmospheric and oceanic factors in the Pacific Ocean and Indian

Ocean would have been significantly different from modern conditions (e.g., wind regimes (England et al., 2014) and ENSO (Godfred-Spenning & Reason, 2002)).

Equatorial climatic change may have influenced conditions across more southerly latitudes causing changes in the timing, strength and positioning of the south-westerly air mass (and oceanic conditions); a variable likely exerting more dominant influences on moisture in these areas during late MIS3 and MIS2 (De Deckker, 2020; De Deckker et al., 2019; Kemp et al., 2019). Therefore, it is important to consider such changes in the mechanisms that drive regional climate conditions if we are to advance the geographic and temporal disparities between records (e.g., Kemp et al., 2019).

Ultimately, the contrasting latitudinal hydroclimate responses revealed by our modelling synthesis highlights the importance of considering region-specific late Pleistocene extinction dynamics rather than merely focusing on continent-wide explanations of megafauna demise. Such considerations, in turn, necessitate improved spatial and temporal constraints on megafauna deposits across understudied regions of Sahul, particularly the tropical zones.

Conclusion

The single-grain OSL dating results obtained in this study for four new South Walker Creek sites are consistent with those presented recently by Hocknull et al. (2020). Using this expanded chronological dataset, we have been able to constrain the occurrence of a diverse aquatic and terrestrial megafauna community at South Walker Creek between at least 57.7 – 37.9 ka, with local extinction occurring sometime after this period. This study represents one of the few reliable, multi-site evaluations of the last appearance of megafauna, especially for the poorly studied north-eastern, tropical region of Australia. Comparisons between our dating results and previously published regional syntheses highlight that further coverage of late Pleistocene fossil sites is needed to fully ascertain regional extinction dynamics across the whole of Sahul.

Hierarchical Bayesian modelling of megafauna sites and fluvial deposits at the South Walker Creek fossil locality, combined with syntheses of hydrological activity across a range of regional catchments, reveals evidence for significant environmental change during mid- to late-MIS3, coincident with the last appearance of megafauna at South Walker Creek. These results are broadly consistent with other recent hydroclimate synthesis studies (e.g., Kemp et al., 2019) that suggest regional trends towards more negative moisture balances during late MIS3 across large parts of northern and central Australia.

The implication of our modelling results is that the demise of megafauna at South Walker Creek did not take place during a period of climate stability, and that the causes of megafaunal extinction were therefore likely more complex than two competing end-member hypotheses (e.g., human vs climate). Instead, our study confirms and re-iterates the need to explore synergistic drivers in region-specific contexts that recount known responses of megafauna in the lead up to their ultimate extinction. The relatively limited MIS3 archaeological record for Australia, especially in proximity and context to megafauna fossil sites, makes disentangling the causes of megafaunal extinction a continuing elusive goal.

Finally, our study highlights the importance of contextualising the Sahulian megafaunal extinction debate using terrestrial palaeoenvironmental records from the Australian region (particularly those directly associated with megafauna fossil sites), rather than relying solely on comparisons with remote

global climate records from beyond the Australasian region. We find evidence for contrasting hydroclimate responses across the monsoon-influenced northern and central regions and the south-westerly-influenced southern regions of Australia during MIS3 and MIS2. These trends highlight the geographically variable roles played by shifting synoptic drivers during the late Pleistocene, and therefore the limited insights that some extra-regional climate records may offer for certain regions of Australia.

Acknowledgements

We acknowledge and pay respect to the traditional owners past and present of the lands of the Barada Barna people and thank them for their guidance and contributions. We thank all QM Geosciences staff and volunteers for assistance with this project and in particular thank N. Sands, C. Chiotakis, E. Cannon, P. Bishop, N. Dworniczek, P. Tierney, J. Cramb, K. Spring, J. Wilkinson, D. Kennedy, I. Mitchell, N. Newman, A. Hodgkinson, A. Hollingsworth, T. Clifford, D. Lewis, A. Rozefelds, E. Hatte, C. O'Bryen, A. Atuchin, V. Konstantinov. We thank the local landholders of the South Walker and Kemmis Creek areas for their hospitality, in particular the Baulch family. We thank all BHP and BHP Mitsui Coal South Walker Creek Mine staff for their support. This project has been supported by the Queensland Museum and BHP through Project DIG. R.L. was supported by an Australian Government Research Training Program Scholarship. The OSL dating research was supported by Australian Research Council Future Fellowship grant FT130100195 awarded to LA.

References

Aitken, M. J. 1985. Thermoluminescence dating: Past progress and future trends. Nuclear Tracks and Radiation Measurements (1982), 10, 3-6.

Aitken, M. J. 1998. An introduction to optical dating: the dating of Quaternary sediments by the use of photon-stimulated luminescence, Oxford, Oxford University Press.

Andersen, K. K., Azuma, N., Barnola, J. M., Bigler, M., Biscaye, P., Caillon, N., Chappellaz, J., Clausen, H. B., Dahl-Jensen, D., Fischer, H., Flückiger, J., Fritzsche, D., Fujii, Y., Goto-Azuma, K., Grønvold, K., Gundestrup, N. S., Hansson, M., Huber, C., Hvidberg, C. S., Johnsen, S. J., Jonsell, U., Jouzel, J., Kipfstuhl, S., Landais, A., Leuenberger, M., Lorrain, R., Masson-Delmotte, V., Miller, H., Motoyama, H., Narita, H., Popp, T., Rasmussen, S. O., Raynaud, D., Rothlisberger, R., Ruth, U., Samyn, D., Schwander, J., Shoji, H., Siggard-Andersen, M. L., Steffensen, J. P., Stocker, T., Sveinbjörnsdóttir, A. E., Svensson, A., Takata, M., Tison, J. L., Thorsteinsson, T., Watanabe, O., Wilhelms, F., White, J. W. C. & North Greenland Ice Core Project, M. 2004. High-resolution record of Northern Hemisphere climate extending into the last interglacial period. *Nature*, 431**,** 147-151.

Arnold, L. & Roberts, R. 2009. Stochastic modelling of multi-grain equivalent dose (De) distributions: Implications for OSL dating of sediment mixtures. *Quaternary Geochronology*, 4**,** 204-230.

Arnold, L. J., Bailey, R. M. & Tucker, G. E. 2007. Statistical treatment of fluvial dose distributions from southern Colorado arroyo deposits. *Quaternary Geochronology*, 2**,** 162-167.

Arnold, L. J., Duval, M., Falguères, C., Bahain, J. J. & Demuro, M. 2012. Portable gamma spectrometry with cerium-doped lanthanum bromide scintillators: Suitability assessments for luminescence and electron spin resonance dating applications. *Radiation Measurements*, 47**,** 6-18.

Arnold, L. J. & Roberts, R. G. 2011. Paper I–Optically stimulated luminescence (OSL) dating of perennially frozen deposits in north-central Siberia: OSL characteristics of quartz grains and methodological considerations regarding their suitability for dating. *Boreas*, 40**,** 389-416.

Arnold, L. J., Roberts, R. G., Galbraith, R. F. & Delong, S. B. 2009. A revised burial dose estimation procedure for optical dating of youngand modern-age sediments. *Quaternary Geochronology*, 4**,** 306-325.

Arnold, L. J., Roberts, R. G., Macphee, R. D. E., Willerslev, E., Tikhonov, A. N. & Brock, F. 2008. Optical dating of perennially frozen deposits associated with preserved ancient plant and animal DNA in north-central Siberia. *Quaternary Geochronology*, 3**,** 114-136.

Bailey, R. M. & Arnold, L. J. 2006. Statistical modelling of single grain quartz De distributions and an assessment of procedures for estimating burial dose. *Quaternary Science Reviews*, 25**,** 2475-2502.

Becerra-Valdivia, L. & Higham, T. 2020. The timing and effect of the earliest human arrivals in North America. *Nature*.

Bom. 2019. *Climate Data Online* [Online]. Available: http://www.bom.gov.au/climate/data/ [Accessed 2019].

Bøtter-Jensen, L. & Mejdahl, V. 1988. Assessment of beta dose-rate using a GM multicounter system. International Journal of Radiation Applications and Instrumentation. Part D. Nuclear Tracks and Radiation Measurements, 14**,** 187-191.

Bowler, J., Johnston, H., Olley, J., Prescott, J., Roberts, R., Shawcross, W. & Spooner, N. 2003. New ages for human occupation and climatic change at Lake Mungo, Australia. *Nature*, 421**,** 837.

Brennan, B. J. 2003. Beta doses to spherical grains. *Radiation Measurements*, 37**,** 299-303.

Bronk Ramsey, C. 1995. Radiocarbon Calibration and Analysis of Stratigraphy: The OxCal Program. *Radiocarbon.*

Bronk Ramsey, C. 2008. Deposition models for chronological records. *Quaternary Science Reviews*, 27**,** 42-60.

Bronk Ramsey, C. 2009a. Bayesian Analysis of Radiocarbon Dates. *Radiocarbon*, 51**,** 337-360.

Bronk Ramsey, C. 2009b. Dealing with outliers and offsets in radiocarbon dating. *Radiocarbon*, 51**,** 1023-1045.

Bronk Ramsey, C. 2017. Methods for summarizing radiocarbon datasets. *Radiocarbon*, 59**,** 1809-1833.

Cadd, H. R., Tibby, J., Barr, C., Tyler, J., Unger, L., Leng, M. J., Marshall, J. C., Mcgregor, G., Lewis, R. & Arnold, L. J. 2018. Development of a Southern Hemisphere subtropical wetland (Welsby Lagoon, south-east Queensland, Australia) through the last glacial cycle. *Quaternary Science Reviews,* 202**,** 53-65.

Clarkson, C., Jacobs, Z., Marwick, B., Fullagar, R., Wallis, L., Smith, M., Roberts, R. G., Hayes, E., Lowe, K. & Carah, X. 2017. Human occupation of northern Australia by 65,000 years ago. *Nature,* 547**,** 306-310.

Clement, A. C., Seager, R. & Cane, M. 1999. Orbital controls on the El Nino/Southern Oscillation and the tropical climate. *Paleoceanography,* 14**,** 441-456.

Cohen, T. J., Jansen, J. D., Gliganic, L. A., Larsen, J. R., Nanson, G. C., May, J. H., Jones, B. G. & Price, D. M. 2015. Hydrological transformation coincided with megafaunal extinction in central Australia. *Geology,* 43**,** 195-198.

Colls, K. & Whitaker, R. 1990. The Australian Weather Book. Associates Publishing Pty Ltd, Sydney, Australia.

Cooper, A., Turney, C. S., Palmer, J., Hogg, A., Mcglone, M., Wilmshurst, J., Lorrey, A. M., Heaton, T. J., Russell, J. M. & Mccracken, K. 2021. A global environmental crisis 42,000 years ago. *Science,* 371**,** 811-818.

Croke, J., Jansen, J. D., Amos, K. & Pietsch, T. J. 2011. A 100 ka record of fluvial activity in the Fitzroy River Basin, tropical northeastern Australia. *Quaternary Science Reviews,* 30**,** 1681-1695.

De Deckker, P. 2020. Airborne dust traffic from Australia in modern and Late Quaternary times. *Global and Planetary Change,* 184**,** 103056.

De Deckker, P., Arnold, L., Van Der Kaars, S., Bayon, G., Stuut, J.-B. W., Perner, K., Lopes Dos Santos, R. A., Uemura, R. & Demuro, M. 2019. Marine Isotope Stage 4 in Australasia: a full glacial culminating 65,000 years ago - global connections and implications for human dispersal. *Supplement to: De Deckker, P et al. (accepted): Marine Isotope Stage 4 in Australasia: a full glacial culminating 65,000 years ago - global connections and implications for human dispersal.*: PANGAEA.

Deer, L. N. 2011. Limestone and speleothem trace element geochemistry as tools for palaeoclimatic reconstruction, Mount Etna region, central-coastal Queensland. PhD, Queensland University of Technology.

Demarchi, B., Stiller, J., Grealy, A., Mackie, M., Deng, Y., Gilbert, T., Clarke, J., Legendre, L. J., Boano, R. & Sicheritz-Pontén, T. 2022. Ancient proteins resolve controversy over the identity of Genyornis eggshell. Proceedings of the National Academy of Sciences, e2109326119.

Demuro, M., Arnold, L. J., Aranburu, A., Gomez-Olivencia, A. & Arsuaga, J.-L. 2019. Single-grain OSL dating of the Middle Palaeolithic site of Galería de las Estatuas, Atapuerca (Burgos, Spain). *Quaternary Geochronology,* 49**,** 254-261.

Demuro, M., Arnold, L. J., Duval, M., Méndez-Quintas, E., Santonja, M. & Pérez-González, A. 2020. Refining the chronology of Acheulean deposits at Porto Maior in the River Miño basin (Galicia, Spain) using a comparative luminescence and ESR dating approach. *Quaternary International,* 556**,** 96-112.

Demuro, M., Arnold, L. J., Froese, D. G. & Roberts, R. G. 2013. OSL dating of loess deposits bracketing Sheep Creek tephra beds, northwest Canada: Dim and problematic single-grain OSL characteristics and their effect on multi-grain age estimates. *Quaternary Geochronology,* 15**,** 67-87.

Donders, T. H., Wagner, F. & Visscher, H. 2006. Late Pleistocene and Holocene subtropical vegetation dynamics recorded in perched lake deposits on Fraser Island, Queensland, Australia. *Palaeogeography, Palaeoclimatology, Palaeoecology,* 241**,** 417-439.

Duval, M. & Arnold, L. J. 2013. Field gamma dose-rate assessment in natural sedimentary contexts using LaBr3 (Ce) and NaI (Tl) probes: A comparison between the "threshold" and "windows" techniques. *Applied Radiation and Isotopes,* 74**,** 36-45.

England, M. H., Mcgregor, S., Spence, P., Meehl, G. A., Timmermann, A., Cai, W., Gupta, A. S., Mcphaden, M. J., Purich, A. & Santoso, A. 2014. Recent intensification of wind-driven circulation in the Pacific and the ongoing warming hiatus. *Nature Climate Change,* 4**,** 222-227.

English, P., Spooner, N. A., Chappell, J., Questiaux, D. G. & Hill, N. G. 2001. Lake Lewis basin, central Australia: environmental evolution and OSL chronology. *Quaternary International,* 83-85**,** 81-101.

Farebrother, W., Hesse, P. P., Chang, H.-C. & Jones, C. 2017. Dry lake beds as sources of dust in Australia during the Late Quaternary: A volumetric approach based on lake bed and deflated dune volumes. *Quaternary Science Reviews,* 161**,** 81-98.
Field, J., Wroe, S., Trueman, C. N., Garvey, J. & Wyatt-Spratt, S. 2013. Looking for the archaeological signature in Australian megafaunal extinctions. Quaternary International, 285, 76-88.
Flannery, T. F. 1990. Pleistocene faunal loss: implications of the aftershock for Australia's past and future. *Archaeology in Oceania,* 25**,** 45-55.
Galbraith, R. F., Roberts, R. G., Laslett, G. M., Yoshida, H. & Olley, J. M. 1999. Optical dating of single and multiple grains of quartz from Jinmium Rock Shelter, Northern Australia: part I, experimental design and statistical models. *Archaeometry,* 41**,** 339-364.
Gillespie, R. & Brook, B. W. 2006. Is there a Pleistocene archaeological site at Cuddie Springs? *Archaeology in Oceania,* 41**,** 1-11.
Godfred-Spenning, C. R. & Reason, C. J. C. 2002. Interannual variability of lower-tropospheric moisture transport during the Australian monsoon. *International Journal of Climatology,* 22**,** 509-532.
Grün, R., Wells, R., Eggins, S., Spooner, N., Aubert, M., Brown, L. & Rhodes, E. 2008. Electron spin resonance dating of South Australian megafauna sites. *Australian Journal of Earth Sciences,* 55**,** 917-935.
Guérin, G., Mercier, N. & Adamiec, G. 2011. Dose-rate conversion factors: update. *Ancient TL,* 29**,** 5-8.
Hamm, G., Mitchell, P., Arnold, L. J., Prideaux, G. J., Questiaux, D., Spooner, N. A., Levchenko, V. A., Foley, E. C., Worthy, T. H. & Stephenson, B. 2016. Cultural innovation and megafauna interaction in the early settlement of arid Australia. *Nature,* 539**,** 280-283.
Hesse, P. P., Williams, R., Ralph, T. J., Fryirs, K. A., Larkin, Z. T., Westaway, K. E. & Farebrother, W. 2018. Palaeohydrology of lowland rivers in the Murray-Darling Basin, Australia. *Quaternary Science Reviews,* 200**,** 85-105.
Higham, T., Douka, K., Wood, R., Ramsey, C. B., Brock, F., Basell, L., Camps, M., Arrizabalaga, A., Baena, J. & Barroso-Ruíz, C. 2014. The timing and spatiotemporal patterning of Neanderthal disappearance. *Nature,* 512**,** 306-309.
Hocknull, S. A., Lewis, R., Arnold, L. J., Pietsch, T., Joannes-Boyau, R., Price, G. J., Moss, P., Wood, R., Dosseto, A., Louys, J., Olley, J. & Lawrence, R. A. 2020. Extinction of eastern Sahul megafauna coincides with sustained environmental deterioration. *Nature Communications,* 11**,** 2250.
Hocknull, S. A., Zhao, J.-X., Feng, Y.-X. & Webb, G. E. 2007. Responses of Quaternary rainforest vertebrates to climate change in Australia. *Earth and Planetary Science Letters,* 264**,** 317-331.
Jacobs, Z., Duller, G. A., Wintle, A. G. & Henshilwood, C. S. 2006. Extending the chronology of deposits at Blombos Cave, South Africa, back to 140 ka using optical dating of single and multiple grains of quartz. *Journal of Human Evolution,* 51**,** 255-273.
Johnson, C. N., Alroy, J., Beeton, N. J., Bird, M. I., Brook, B. W., Cooper, A., Gillespie, R., Herrando-Pérez, S., Jacobs, Z. & Miller, G. H. 2016a. What caused extinction of the Pleistocene megafauna of Sahul? *Proceedings of the Royal Society B: Biological Sciences,* 283**,** 20152399.
Johnson, C. N., Alroy, J., Beeton, N. J., Bird, M. I., Brook, B. W., Cooper, A., Gillespie, R., Herrando-Pérez, S., Jacobs, Z., Miller, G. H., Prideaux, G. J., Roberts, R. G., Rodríguez-Rey, M., Saltré, F., Turney, C. S. M. & Bradshaw, C. J. A. 2016b. What caused extinction of the Pleistocene megafauna of Sahul? *Proceedings of the Royal Society B: Biological Sciences,* 283**,** 20152399.
Kemp, C., Tibby, J., Arnold, L. J. & Barr, C. 2019. Australian hydroclimate during Marine Isotope Stage 3: a synthesis and review. *Quaternary Science Reviews,* 204**,** 94-104.
Kemp, C. W., Tibby, J., Arnold, L. J., Barr, C., Gadd, P. S., Marshall, J. C., Mcgregor, G. B. & Jacobsen, G. E. 2020. Climates of the last three interglacials in subtropical eastern Australia inferred from wetland sediment geochemistry. *Palaeogeography, Palaeoclimatology, Palaeoecology,* 538**,** 109463.
Kemp, J. & Rhodes, E. 2010. Episodic fluvial activity of inland rivers in southeastern Australia: Palaeochannel systems and terraces of the Lachlan River. *Quaternary Science Reviews,* 29**,** 732-752.

Kennett, J. P., Kennett, D. J., Culleton, B. J., Tortosa, J. E. A., Bischoff, J. L., Bunch, T. E., Daniel, I. R., Erlandson, J. M., Ferraro, D. & Firestone, R. B. 2015. Bayesian chronological analyses consistent with synchronous age of 12,835–12,735 Cal BP for Younger Dryas boundary on four continents. *Proceedings of the National Academy of Sciences,* 112**,** E4344-E4353.

Koch, P. L. & Barnosky, A. D. 2006. Late Quaternary extinctions: state of the debate. *Annu. Rev. Ecol. Evol. Syst.,* 37**,** 215-250.

Lawrence, R. A. & Hocknull, S. A. 2019. Lost in space and time: New Quaternary small verterbrate records from the Fitzroy River Basin of tropical Queensland, Australia. *SVP 79th Annual meeting.* Brisbane, Queensland, Australia: Society of vertebrate paleontology.

Lewis, R. J., Tibby, J., Arnold, L. J., Barr, C., Marshall, J., Mcgregor, G., Gadd, P. & Yokoyama, Y. 2020. Insights into subtropical Australian aridity from Welsby Lagoon, north Stradbroke Island, over the past 80,000 years. *Quaternary Science Reviews,* 234**,** 106262.

Lewis, R. J., Tibby, J., Arnold, L. J., Gadd, P., Jacobsen, G., Barr, C., Negus, P. M., Mariani, M., Penny, D., Chittleborough, D. & Moss, E. 2021. Patterns of aeolian deposition in subtropical Australia through the last glacial and deglacial periods. *Quaternary Research***,** 1-23.

Lisiecki, L. E. & Raymo, M. E. 2005. A Pliocene-Pleistocene stack of 57 globally distributed benthic δ18O records. *Paleoceanography,* 20.

Macken, A. C., Staff, R. A. & Reed, E. H. 2013. Bayesian age-depth modelling of Late Quaternary deposits from Wet and Blanche Caves, Naracoorte, South Australia: A framework for comparative faunal analyses. *Quaternary Geochronology,* 17**,** 26-43.

Magee, J. W., Miller, G. H., Spooner, N. A. & Questiaux, D. 2004. Continuous 150 ky monsoon record from Lake Eyre, Australia: insolation-forcing implications and unexpected Holocene failure. *Geology,* 32**,** 885-888.

Martin, P. S. & Klein, R. G. 1984. *Quaternary Extinctions: A Prehistoric Revolution,* Tucson, University of Arizona Press.

Martin, P. S. & Klein, R. G. 1989. *Quaternary extinctions: a prehistoric revolution,* University of Arizona Press.

Marx, S. K., Kamber, B. S., Mcgowan, H. A., Petherick, L. M., Mctainsh, G. H., Stromsoe, N., Hooper, J. N. & May, J.-H. 2018. Palaeo-dust records: A window to understanding past environments. *Global and Planetary Change,* 165**,** 13-43.

Mcgowan, H. A., Petherick, L. M. & Kamber, B. S. 2008. Aeolian sedimentation and climate variability during the late Quaternary in southeast Queensland, Australia. *Palaeogeography, Palaeoclimatology, Palaeoecology,* 265**,** 171-181.

Mejdahl, V. 1979. Thermoluminescence dating: Beta-dose attenuation in quartz grains. *Archaeometry,* 21**,** 61-72.

Mejdahl, V. 1987. Internal radioactivity in quartz and feldspar grains. *Ancient TL,* 5**,** 10-17.

Miller, G., Magee, J., Smith, M., Spooner, N., Baynes, A., Lehman, S., Fogel, M., Johnston, H., Williams, D. & Clark, P. 2016a. Human predation contributed to the extinction of the Australian megafaunal bird Genyornis newtoni~ 47 ka. *Nature Communications,* 7**,** 1-7.

Miller, G. H., Fogel, M. L., Magee, J. W. & Gagan, M. K. 2016b. Disentangling the impacts of climate and human colonization on the flora and fauna of the Australian arid zone over the past 100 ka using stable isotopes in avian eggshell. *Quaternary Science Reviews,* 151**,** 27-57.

Miller, G. H., Magee, J. W., Johnson, B. J., Fogel, M. L., Spooner, N. A., Mcculloch, M. T. & Ayliffe, L. K. 1999. Pleistocene Extinction of Genyornis newtoni: Human Impact on Australian Megafauna. *Science,* 283**,** 205.

Murphy, B. P., Williamson, G. J. & Bowman, D. M. 2012. Did central Australian megafaunal extinction coincide with abrupt ecosystem collapse or gradual climate change? *Global Ecology and Biogeography,* 21**,** 142-151.

Murray, A. S. & Wintle, A. G. 2000. Luminescence dating of quartz using an improved single-aliquot regenerative-dose protocol. *Radiation measurements,* 32**,** 57-73.

Nanson, G. C., Jones, B. G., Price, D. M. & Pietsch, T. J. 2005. Rivers turned to rock: Late Quaternary alluvial induration influencing the behaviour and morphology of an anabranching river in the Australian monsoon tropics. *Geomorphology,* 70**,** 398-420.

Nathan, R. P., Thomas, P. J., Jain, M., Murray, A. S. & Rhodes, E. J. 2003. Environmental dose rate heterogeneity of beta radiation and its implications for luminescence dating: Monte Carlo modelling and experimental validation. *Radiation Measurements,* 37**,** 305-313.

Noto, C. R. 2011. Hierarchical Control of Terrestrial Vertebrate Taphonomy Over Space and Time: Discussion of Mechanisms and Implications for Vertebrate Paleobiology. *In:* Allison, P. A. & Bottjer, D. J. (eds.) *Taphonomy: Process and Bias Through Time.* Dordrecht: Springer Netherlands.

Page, K. J., Kemp, J. & Nanson, G. C. 2009. Late Quaternary evolution of Riverine Plain paleochannels, southeastern Australia. *Australian Journal of Earth Sciences,* 56**,** S19-S33.

Pawley, S. M., Bailey, R. M., Rose, J., Moorlock, B. S., Hamblin, R. J., Booth, S. J. & Lee, J. R. 2008. Age limits on Middle Pleistocene glacial sediments from OSL dating, north Norfolk, UK. *Quaternary Science Reviews,* 27**,** 1363-1377.

Peters, K. J., Saltré, F., Friedrich, T., Jacobs, Z., Wood, R., Mcdowell, M., Ulm, S. & Bradshaw, C. J. 2019. FosSahul 2.0, an updated database for the Late Quaternary fossil records of Sahul. *Scientific data,* 6**,** 1-7.

Petherick, L. M., Mcgowan, H. A. & Kamber, B. S. 2009. Reconstructing transport pathways for late Quaternary dust from eastern Australia using the composition of trace elements of long traveled dusts. *Geomorphology,* 105**,** 67-79.

Prescott, J. R. & Hutton, J. T. 1994. Cosmic ray contributions to dose rates for luminescence and ESR dating: large depths and long-term time variations. *Radiation measurements,* 23**,** 497-500.

Price, G. J., Louys, J., Faith, J. T., Lorenzen, E. & Westaway, M. C. 2018. Big data little help in megafauna mysteries. Nature Publishing Group.

Price, G. J., Webb, G. E., Zhao, J.-X., Feng, Y.-X., Murray, A. S., Cooke, B. N., Hocknull, S. A. & Sobbe, I. H. 2011. Dating megafaunal extinction on the Pleistocene Darling Downs, eastern Australia: the promise and pitfalls of dating as a test of extinction hypotheses. *Quaternary Science Reviews,* 30**,** 899-914.

Prideaux, G. J., Long, J. A., Ayliffe, L. K., Hellstrom, J. C., Pillans, B., Boles, W. E., Hutchinson, M. N., Roberts, R. G., Cupper, M. L. & Arnold, L. J. 2007. An arid-adapted middle Pleistocene vertebrate fauna from south-central Australia. *Nature,* 445**,** 422-425.

Reed, E. H. & Bourne, S. 2000. Pleistocene fossil vertebrate sites of the South East region of South Australia, Royal Society of South Australia.

Rees-Jones, J. 1995. Optical dating of young sediments using fine-grain quartz. *Ancient TL,* 13**,** 9-14.

Rees-Jones, J. & Tite, M. S. 1997. Optical dating results for British archaeological sediments. *Archaeometry,* 39**,** 177-187.

Reeves, J. M., Barrows, T. T., Cohen, T. J., Kiem, A. S., Bostock, H. C., Fitzsimmons, K. E., Jansen, J. D., Kemp, J., Krause, C. & Petherick, L. 2013. Climate variability over the last 35,000 years recorded in marine and terrestrial archives in the Australian region: an OZ-INTIMATE compilation. *Quaternary Science Reviews,* 74**,** 21-34.

Roberts, R. G., Flannery, T. F., Ayliffe, L. K., Yoshida, H., Olley, J. M., Prideaux, G. J., Laslett, G. M., Baynes, A., Smith, M. A. & Jones, R. 2001. New ages for the last Australian megafauna: continent-wide extinction about 46,000 years ago. *Science,* 292**,** 1888-1892.

Rodríguez-Rey, M., Herrando-Pérez, S., Brook, B. W., Saltré, F., Alroy, J., Beeton, N., Bird, M. I., Cooper, A., Gillespie, R. & Jacobs, Z. 2016. A comprehensive database of quality-rated fossil ages for Sahul's Quaternary vertebrates. *Scientific data,* 3**,** 1-7.

Rodríguez-Rey, M., Herrando-Pérez, S., Gillespie, R., Jacobs, Z., Saltré, F., Brook, B. W., Prideaux, G. J., Roberts, R. G., Cooper, A. & Alroy, J. 2015. Criteria for assessing the quality of Middle Pleistocene to Holocene vertebrate fossil ages. *Quaternary Geochronology,* 30**,** 69-79.

Rule, S., Brook, B. W., Haberle, S. G., Turney, C. S., Kershaw, A. P. & Johnson, C. N. 2012. The aftermath of megafaunal extinction: ecosystem transformation in Pleistocene Australia. *Science,* 335**,** 1483-6.

Russell, J. M., Vogel, H., Konecky, B. L., Bijaksana, S., Huang, Y., Melles, M., Wattrus, N., Costa, K. & King, J. W. 2014. Glacial forcing of central Indonesian hydroclimate since 60,000 y BP. *Proceedings of the National Academy of Sciences,* 111**,** 5100-5105.

Saltré, F., Chadoeuf, J., Peters, K. J., Mcdowell, M. C., Friedrich, T., Timmermann, A., Ulm, S. & Bradshaw, C. J. 2019. Climate-human interaction associated with southeast Australian megafauna extinction patterns. *Nature communications,* 10**,** 1-9.

Saltré, F., Rodríguez-Rey, M., Brook, B. W., Johnson, C. N., Turney, C. S. M., Alroy, J., Cooper, A., Beeton, N., Bird, M. I. & Fordham, D. A. 2016a. Climate change not to blame for late Quaternary megafauna extinctions in Australia. *Nature communications,* 7**,** 1-7.

Saltré, F., Rodríguez-Rey, M., Brook, B. W., Johnson, C. N., Turney, C. S. M., Alroy, J., Cooper, A., Beeton, N., Bird, M. I., Fordham, D. A., Gillespie, R., Herrando-Pérez, S., Jacobs, Z., Miller, G. H., Nogués-Bravo, D., Prideaux, G. J., Roberts, R. G. & Bradshaw, C. J. A. 2016b. Climate change not to blame for late Quaternary megafauna extinctions in Australia. *Nature Communications,* 7**,** 10511.

Signor, P. W. & Lipps, J. H. 1982. Sampling bias, gradual extinction patterns and catastrophes in the fossil record. *In:* Silver, L. T. & Schultz, P. H. (eds.) *Geological Implications of Impacts of Large Asteroids and Comets on the Earth.* Colorado: The Geological Society of America.

Stokes, S., Ingram, S., Aitken, M. J., Sirocko, F., Anderson, R. & Leuschner, D. 2003. Alternative chronologies for Late Quaternary (Last Interglacial–Holocene) deep sea sediments via optical dating of silt-sized quartz. *Quaternary Science Reviews,* 22**,** 925-941.

Wang, Y.-J., Cheng, H., Edwards, R. L., An, Z., Wu, J., Shen, C.-C. & Dorale, J. A. 2001. A high-resolution absolute-dated late Pleistocene monsoon record from Hulu Cave, China. *Science,* 294**,** 2345-2348.

Wroe, S., Field, J. H., Archer, M., Grayson, D. K., Price, G. J., Louys, J., Faith, J. T., Webb, G. E., Davidson, I. & Mooney, S. D. 2013. Climate change frames debate over the extinction of megafauna in Sahul (Pleistocene Australia-New Guinea). *Proceedings of the National Academy of Sciences,* 110**,** 8777-8781.

Wu, Y., Li, T.-Y., Yu, T.-L., Shen, C.-C., Chen, C.-J., Zhang, J., Li, J.-Y., Wang, T., Huang, R. & Xiao, S.-Y. 2020. Variation of the Asian summer monsoon since the last glacial-interglacial recorded in a stalagmite from southwest China. *Quaternary Science Reviews,* 234**,** 106261.

Chapter 6 Conclusion and suggestions for further research

Overview of research outcomes in preceding chapters

This thesis has contributed high-resolution, robustly dated, multi-proxy datasets that advance understanding of late Pleistocene megafaunal extinction and environmental dynamics for eastern Australia. Specifically, this research has provided new insights into long-term context and possible causes of megafaunal extinction across the underrepresented tropical and subtropical regions of eastern Australia (Chapters 2 – 5). Moreover, the first regional chronological synthesis of eastern and central Australia has been presented as an independent means to investigate spatiotemporal hydrological variability over the last glacial cycle (Chapter 5).

Chapter specific outcomes

Chapter 2: Welsby Lagoon and 80,000 years of dust deposition

The aim of Chapter 2 was to establish a robust history and chronological framework for the subtropical Welsby Lagoon wetland sediment sequence. The study involved a comprehensive Bayesian modelling approach to develop an age-depth profile for the 12.7 m core, together with high-resolution geochemical analysis. Three sedimentary units were identified in the study, namely the basal dune sands (>12.5 m; 126 ± 2 ka), overlying lake sediments (12.5 – 5.0 m; 83 ± 5 – 28 ± 6 ka), and peat deposits (<5.0 m; <28 ± 6 ka) (Chapter 2). Two phases of increased dust flux (71 – 67 ka and 58 – 48 ka) were identified from the sediment geochemistry and linked to drying events in central Australian lakes during periods of hydrological change.

Twenty-one single-grain OSL and seven ^{14}C ages were used in parallel to establish one of the highest resolution dated, pre-LGM sedimentary sequences for a single wetland core from Australia (>2 ages / m). Additionally, the suitability of applying OSL and ^{14}C dating methodologies in a lagoon environment was explored. The ^{14}C results showed that ages derived from charcoal and plant residues were systematically younger than those from macrofossils, likely attributed to contamination by younger carbon in the complex organic-rich environment. Moreover, single-grain OSL demonstrated the complexities of the depositional environment, particularly near to the surface, where samples showed asymmetric D_e distributions and scatter related to beta dose heterogeneity or minor near-surface bioturbation. The study cautioned that different Bayesian modelling configurations could be used to support either a continuous depositional sequence, with positive moisture balance at Welsby Lagoon through the LGM, or a discontinuous sequence and depositional hiatus associated with a drier LGM. Thus, this study highlighted the need to develop a deep understanding of individual sedimentary histories before the implementation of multi-site, multi-proxy syntheses for palaeoecological and climate reconstructions.

Chapter 3: Synthesis of palaeoenvironmental information from subtropical wetlands

Chapter 3 examined the extent of regional- and catchment-specific climate-induced environmental change. This included synthesis of palaeoenvironmental data from several long-term subtropical records from North Stradbroke Island, including an examination of the age of the Yankee Jack dune sequence and Brown Lake's history. Single-grain OSL ages obtained from Yankee Jack dune crests showed that following a phase of dune building (167.8 ± 19.1 ka – 91.0 ± 9.1 ka), the dunes did not undergo subsequent large-scale mobilization, likely due to increased dune stabilisation from vegetation cover.

For the newly established Brown Lake palaeoenvironmental record, OSL and ^{14}C dating results were combined within a Bayesian age depth model, which provided significant insight into local and regional environmental change. Specifically, the study included the first compilation of sediment accumulation histories from several long North Stradbroke Island wetland records, demonstrating coeval depositional hiatuses leading into the LGM at Brown Lake (Chapter 3), Fern Gully Lagoon (Kemp et al., 2020) and Welsby Lagoon (Chapter 2). The geochemical and geochronological analysis of Brown Lake sediment identified an increased dust flux from the early glacial – attributed to changes in regional wind regimes and suppressed precipitation – coincided with shallowing of nearby wetlands. These findings are contrary to a recent synthesis study, which suggested continuous sediment accumulation from MIS3 to the Holocene across sixteen North Stradbroke Island sites (Tibby et al., 2017) – including Brown Lake (Chapter 3) and Welsby Lagoon (Chapter 2) - highlighting the importance of founding interpretations on robust, high-resolution age-depth modelling approaches. Despite the differences between the chronometric data of this thesis and published datasets, there was agreement that the wetland-hosting dune fields remained relatively stable since their emplacement in MIS5. Moreover, the study supported previous interpretations of increased dust transportation to North Stradbroke Island in response to changing climate conditions, around the time of the LGM.

Chapter 4: Australian megafauna fauna disappearance and hydroclimate

Previously undated and undescribed fossiliferous deposits (including flora and fauna) were presented in Chapter 4. This dataset was used to establish the timing of, and variables associated with, megafauna disappearance at the newly discovered fossil locality of South Walker Creek. A comprehensive, multi-technique dating approach was presented and established South Walker Creek as the first open-air fossil site of its kind in the Australian tropical zone to be ranked as a reliably dated record (i.e., achieving an A* or A ranking according to the scheme of Rodríguez-Rey et al., 2015). Sedimentological and taxonomical data presented in this study not only fills an important spatial gap in the fossil record for tropical Queensland, but also yielded relatively young ages (40.1 ± 1.7 ka) for Australian megafauna remains (including all three crocodilians, *Varanus priscus*, *Palorchestes*, *Sedophascolomys*, and at least two macropodids). Additionally, the depositional setting of the fossil deposit (in an anabranching river system) provided unique insight into how megafauna interacted around important water sources, revealing a greater diversity of species than more southerly locations and predation of kangaroos by extinct crocodilians, as shown by teeth impressions on limbs of kangaroos (Hocknull et al., 2020).

Given the north-eastern location of the megafauna fossil locality, and the fact that the ages of the sites significantly post-date the proposed timing for human migration across Sahul, the results of this study do not strongly support human-mediated extinction via direct hunting. Rather, an initial synthesis of the youngest reliably dated megafauna and hydroclimate proxies across northern Australia, the Fitzroy River Basin, Lake Eyre Basin and Murray Darling Basin showed extinction occurred just prior to the onset of abrupt hydroclimatic deterioration. Specifically, the results suggested a chronologically staggered and abrupt hydroclimate change from ~48 ka, which supports the scenario that increased survival pressures were placed on aquatic and terrestrial megafauna due to changes in catchment flow, vegetation structure and fire regimes.

Chapter 5: A Bayesian approach to modelling 60,000 years of Australian hydrology

This Chapter presented an integrated chronometric approach that examined the spatiotemporal pattern of climate-induced environmental change taking place in Australia immediately prior to, during, and after, megafauna disappearance. Hierarchical Bayesian modelling incorporated a range of information from Australian palaeoenvironmental sites, including new ages from four additional South Walker Creek sites, existing megafauna disappearance ages from Chapter 4, the syntheses of subtropical wetland histories (Chapter 2 and Chapter 3), and published chronological records of hydrological activity across a range of regional catchments. This integrated study provided new evidence that megafauna disappearance in the Fitzroy River Basin catchment was coincident with broader environmental change during mid- to late-MIS3. The modelling results suggest that the demise of megafauna did not necessarily take place during a period of climate stability (*sensu* MIS3), rather, megafaunal extinction was likely more complex, involving synergistic hydrological drivers and region-specific ecological responses. It was also found that hydroclimate responses across the monsoon-influenced northern and central regions of Australia contrasted with south-westerly wind influenced southern regions during MIS3 and MIS2.

Contribution of research to the wider community

This thesis provides invaluable datasets of relevance to one of the longest standing and highest profile debates in prehistory: the causes and context of Sahulian megafauna demise. In Australia, considerable debate persists regarding the relationship between the first peopling of the mainland and the widespread disappearance of megafauna during the late Pleistocene (Bird et al., 2013; David et al., 2021; Field et al., 2013; Flannery, 1994). Contrasting interpretations of megafauna demise primarily result from the limited geographical coverage of MIS3 palaeoenvironmental records (Kemp et al., 2020; Petherick et al., 2013; Reeves et al., 2013) and the limited availability of reliably dated fossil archives (Peters et al., 2019; Rodríguez-Rey et al., 2015), particularly for the northern and western regions of the continent. These knowledge gaps remain despite significant recent advances across the fields of archaeology (Clarkson et al., 2017; David et al., 2021; O'Connell & Allen, 2004), palaeontology (Miller et al., 2005; Turney et al., 2008) and palaeoclimatology (De Deckker et al., 2019; Fu et al., 2017; Kershaw et al., 2003; Reeves et al., 2013). In particular, relatively limited uptake of comprehensive dating approaches continues to hinder detailed hypothesis testing of existing megafaunal extinction scenarios (e.g., Peters et al., 2019; Price et al., 2021; Saltré et al., 2016) and prevents deeper understanding of the spatiotemporal relationships between palaeoecological and palaeoclimate events (e.g., Cooper et al., 2021). This thesis fills important spatial and chronological gaps in the Australian megafaunal extinction debate by (i) establishing new palaeoenvironmental and palaeontological records from the severely underrepresented tropical and subtropical regions of Queensland, and (ii) utilising a combination of conventional and innovative methods to establish reliably dated records of past climate conditions and long-term ecological variation.

The research conducted in the subtropical zone of Queensland (Chapter 2 and Chapter 3) has provided robust archives of climate-induced environmental change spanning more than 80,000 years. As a result of this research, the Welsby Lagoon and Brown Lake sedimentary records now rank as two of the best dated wetland archives across the Australian subtropical region. More specifically, the combined chronometric datasets from Welsby Lagoon and Brown Lake make up >35% of all ages obtained across 16 different wetlands (Moss et al., 2013; Tibby et al., 2017; Table E1) from North

Stradbroke Island (Figure 6.1) and demonstrate how improved dating approaches can help to better understand regional environmental change. The robust chronological approaches employed in this thesis, made possible using Bayesian age modelling, has ultimately established an independent framework for exploring environmental change in response to relatively subtle climate events across different sites. Chapter 3 has demonstrated the feasibility of achieving such multi-site comparisons, leveraging chronometric alignment of records to reveal a coeval period of lower moisture availability from late MIS3 – MIS2, with conditions persisting until the early Holocene.

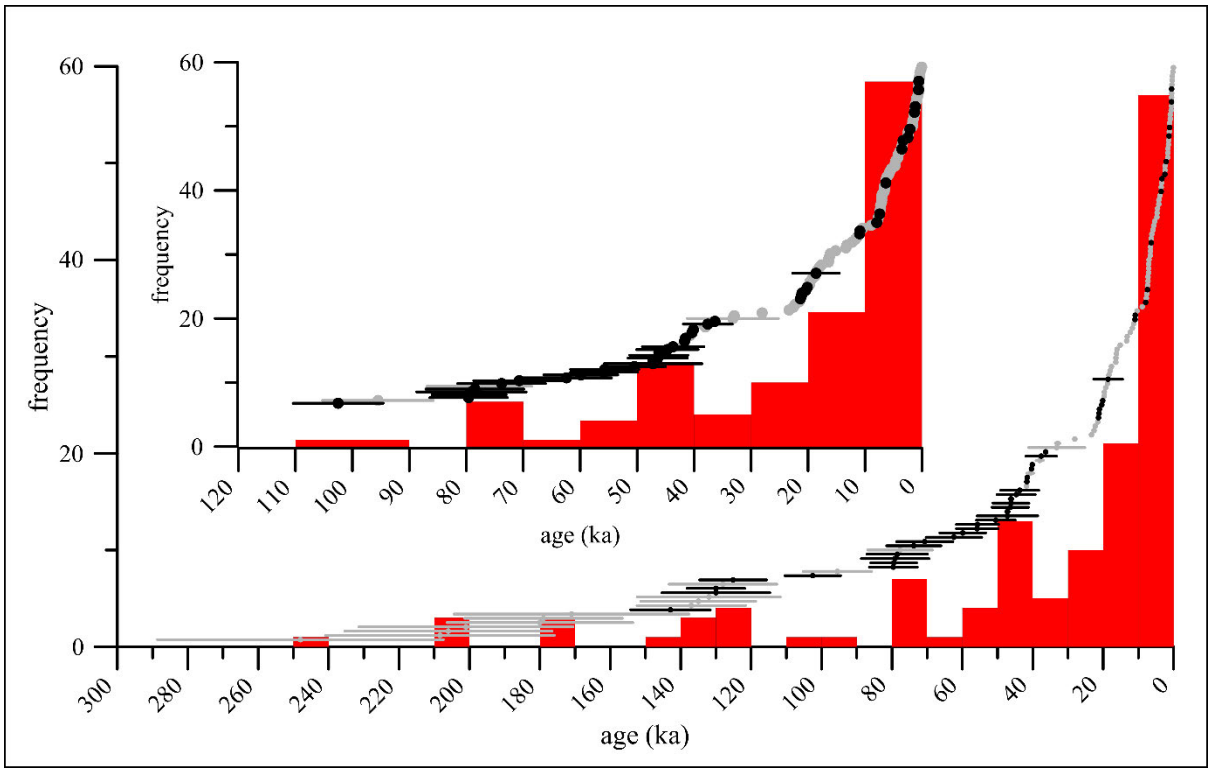

Figure 6.1 Synthesis of ages from North Stradbroke Island wetlands including new ages from this thesis (Chapter 2 and Chapter 3) (black circles), and those presented in Tibby et al. (2017) and references therein (Table E1) (grey circles). Ages are shown with 1 sigma errors and represented as ranked distributions across two ranges, namely (main graph) 300 ka to present and (inset graph) 120 ka to present. Frequency histograms are shown in red with bins set to 10,000 years.

Late Pleistocene fossil material described and dated from South Walker Creek (Chapter 4) has provided deeper understanding of the ecological transformations endured by tropical megafauna prior to extinction. The temporal range of radiometric ages associated with the diverse flora and fauna of this catchment are important as they span the time when the first people are estimated to have arrived on the mainland. Therefore, the palaeoecological and palaeoenvironmental datasets generated in this thesis for South Walker Creek contribute invaluable insights into local flora and fauna responses to climate change in the tropical region, including before and after the arrival of people in the area.

The advancement in knowledge of tropical megafauna resulting from the dating studies undertaken in Chapter 4 and Chapter 5 can be appreciated when considering existing megafauna chronological databases. By utilising a comprehensive dating approach that combined OSL, U-series and ESR techniques for the South Walker Creek area (n = 66 samples), this fossil locality alone has increased the total number of reliable fossil ages (i.e., those with an A* or A rating in Peters et al. (2019); Rodríguez-Rey et al. (2015)) in tropical mainland Australia by >5% (Figure 6.2). This represents a significant step towards better understanding the late Pleistocene ecology of the north-eastern region

of the continent, particularly because these new chronological datasets also enable reliable, independent comparisons with regional hydroclimate records, as demonstrated in Chapter 5. Hierarchical Bayesian modelling of hydrological change undertaken in Chapter 5 suggests that megafauna disappearance in South Walker Creek coincided with regionally staggered hydroclimate deterioration, thereby supporting the potential for complex extinction drivers in this catchment.

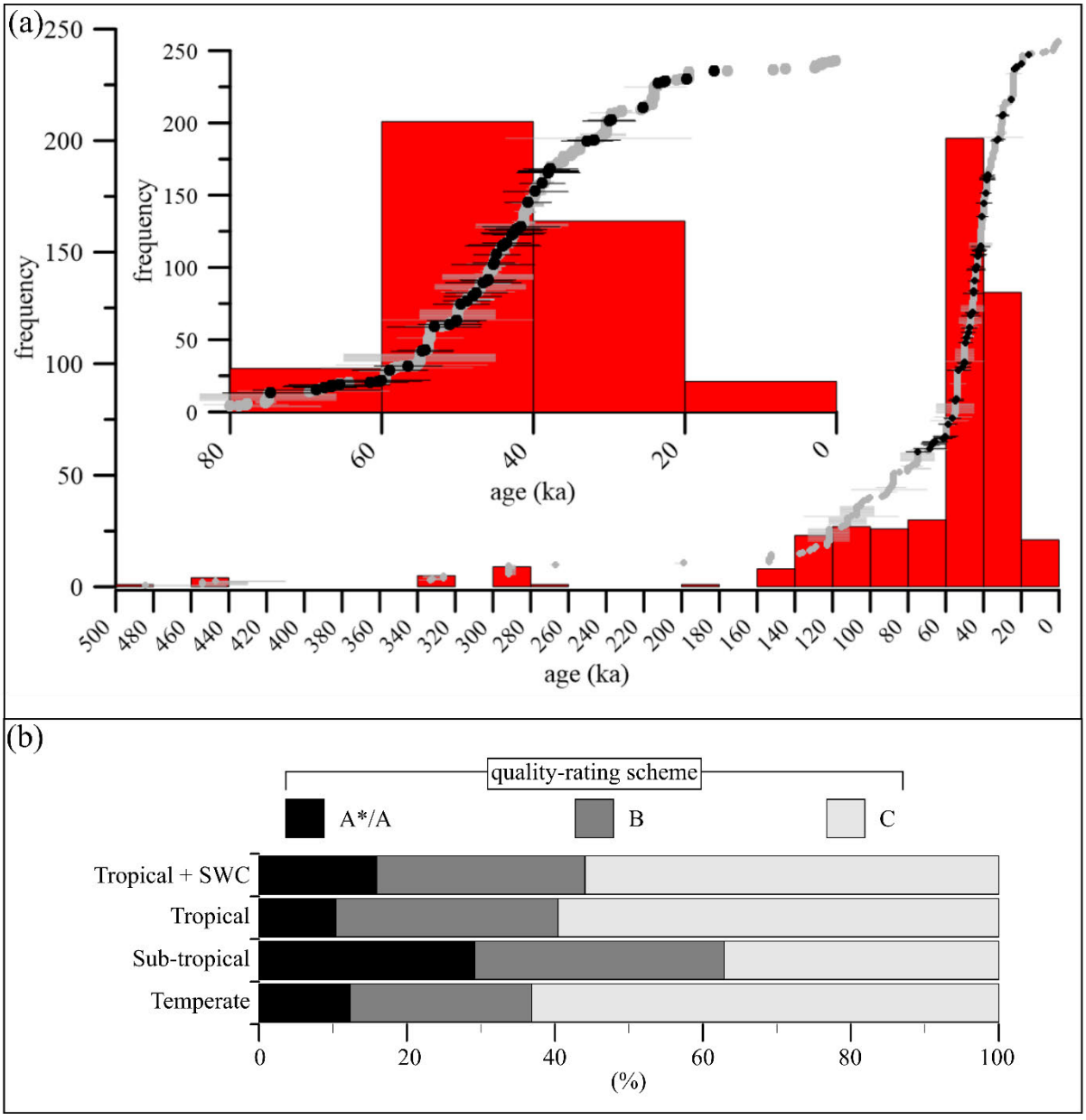

Figure 6.2 New megafauna fossil ages presented in this thesis locality (Chapter 4 and Chapter 5) considered alongside extinct megafauna ages from the FosSahul database (Peters et al., 2019; Rodríguez-Rey et al., 2015). (a) OSL, ESR and U-series ages associated with megafauna fossils from South Walker Creek (black circles), and ages of extinct megafauna from the Australian tropical zone in the FosSahul database (grey circles) where age type and precision was defined. Ages are shown at 1 sigma and represented as ranked distributions for two time ranges: 500 ka to present (main graph), and 80 ka to present (inset graph). Frequency histograms are shown in red with bins set to 20,000 years. (b) Change in the distribution of the quality-rating scheme for extinct megafauna ages across different mainland Australia climate zones according to the FosSahul database. Ages listed in the tropical zone are considered with and without the inclusion of the South Walker Creek megafauna ages ("Tropical + SWC" and "Tropical" respectively).

Future research directions

While the novel outcomes generated in this thesis represent significant advancements in understanding for the Australasian palaeoenvironmental and palaeontological communities, the datasets also highlight the need for further research to establish additional, reliable records of long-term Australian palaeoecological evolution. Given the multitude of proxies currently in use or being developed in palaeoenvironmental research, it is not possible to provide an exhaustive list of research directions that could build on the outcomes of this thesis. However, there are several interesting avenues of research that would capitalise on the platform of work conducted in this thesis, the results of which would provide a deeper understanding of MIS3 climate change and megafaunal extinction.

Further investigation of the inorganic and organic components of the wetland records would particularly enhance understanding of catchment evolution and dust transportation processes. Given that suitable sediment cores have already been extracted, with material remaining for further analysis, it would be relatively straightforward to conduct additional studies. One such novel research avenue would be to investigate the provenancing of inorganic material using three-dimensional thermal luminescence (3D-TL), a technique that examines luminescence intensity as a function of both stimulation wavelength and temperature (Figure 6.3). As the luminescence properties of silicate materials can vary according to microstructures and geochemistry (e.g., Chiavari et al., 2001), 3D-TL may provide a way to identify the source location of material (e.g., Demuro et al., 2020). Prescott & Fox (1993) showed that it was possible to discern the 3D-TL spectra from thirty different types of feldspars covering the whole composition range from high potassium (orthoclase) through high sodium (albite) to high calcium (anorthite). Therefore, by analysing the 3D spectra of silicates and using a fingerprinting method (Figure 6.3), it may be possible to provenance material to advance understanding of dust transportation pathways. The development of such a technique would additionally provide a means to trace dust back to the source using a smaller sample size relative to existing XRF and XRD geochemical methods (e.g., McGowan et al., 2008; Petherick et al., 2009).

Given the difficulty experienced in separating pure organic and inorganic components from the North Stradbroke wetland sediments, there is an opportunity to develop new processes of sample extraction, storage, and treatment. Specifically, such a study would aim to overcome the alteration of various organic and inorganic components after their extraction from highly organic hydromorphic sediments (Vodyanitskii & Minkina, 2020), to ensure palaeopedological analysis represents the natural physical and chemical composition of the record (Stout et al., 2021). This may be accompanied by investigations into groundwater using atomic trap trace analysis (ATTA) (Reichel et al., 2013). ATTA has enabled ultra-low concentrations of radioactive noble gases (e.g., 39Ar, 81Kr, 85Kr) to be measured (Lu & Mueller, 2010), providing new insights into the age, origin, and interconnectivity of groundwater systems – including the calculation of catchment recharge rates (Zappala, 2017) – by building on the existing investigations using stable isotope (i.e., δ2H, δ18O and δ13C) chemistry (Hoffmann et al., 2017).

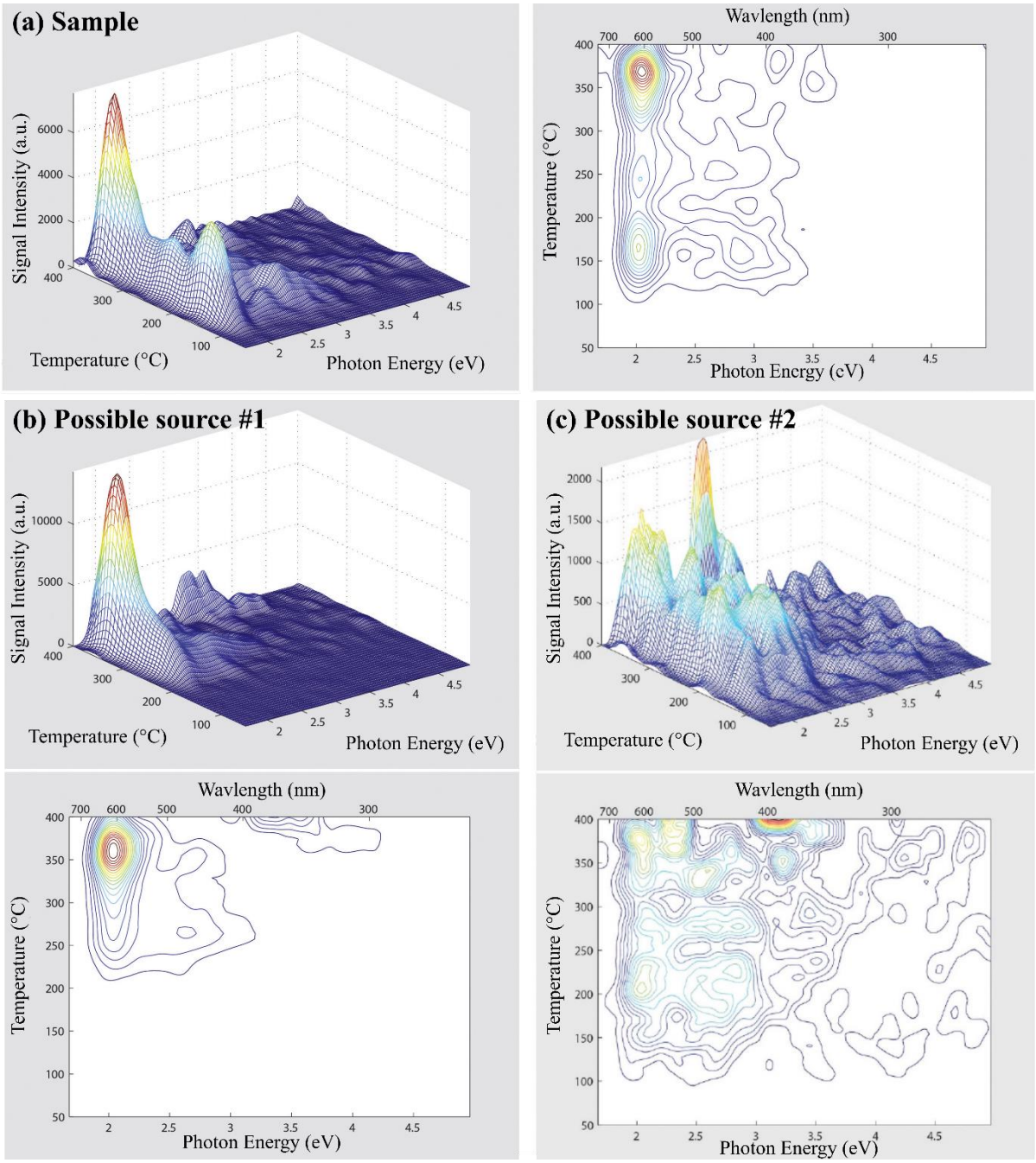

Figure 6.3 A conceptual model of how 3D thermoluminescence (3D-TL) spectral measurements could be used to identify the source of silicates. In this hypothetical example (a) the sample, shows better agreement with source location (b) in comparison with source location (c). Data was adapted from results presented in Demuro et al. (2020).

Additional research into the chronological framework set out in this thesis, such as the identification of correlative stratigraphic markers in lake core records, would also be advantageous. One approach could be to examine the sediments for cryptotephra, fine grain glass shards and ash that originate from volcanic eruptions. Wetland sediments are highly effective archives for the preservation of cryptotephra (Gehrels et al., 2008) and, if present, these pyroclastic fragments can be used to directly link and synchronize the palaeoenvironmental records against those already established (via tephrochronology) – enabling very precise evaluations of the timing of particular events (Lowe, 2011). Investigating additional chronological time markers (e.g., palaeomagnetic excursions such as Laschamp or Blake Events) from the sediment would also be advantageous as this would improve the

overall chronological precision of the record. These geochronological datasets could then be used to expand the hierarchical Bayesian modelling presented in Chapter 5 – which may also be complemented by the inclusion of other archaeological records, additional megafauna site chronologies and hydrological records. This would ultimately enable further scrutiny of the variables and timings central to the Australian megafaunal extinction debate.

In terms of further research into the organic component of the North Stradbroke Island lake sediments, the application of organic geochemistry techniques could be advantageous in refining existing palaeoenvironmental histories. Examination of lipid biomarkers (i.e., *n-alkanes* and *n-alkanoic* acids) from sediment has the potential to yield new insights into climate-induced change across these catchments (Diefendorf & Freimuth, 2017; Makou et al., 2007). Specifically, the outcomes of research into *n-alkanoic* acids could be used to infer changes in precipitation, as this has been used as a proxy for differentiating terrestrial (C_3 and C_4) plant types (Andrae et al., 2020).

Ultimately, any investigation involving one or more of these research directions would enable worthwhile refinements of catchment evolutionary histories, thereby providing more information to test competing megafaunal extinction hypotheses. Further experimentation on the organic component of the Brown Lake sediments, such as analysis of isotopes such as $\delta^{18}O$ or carbon in cellulose, would offer a particularly interesting opportunity to undertake any number of additional research approaches. As discussed in Chapter 3, the Brown Lake sedimentary record preserves unique features in contrast to other wetlands across North Stradbroke Island (Chapter 2 and Chapter 3). By establishing a deeper understanding of the depositional environment during emplacement of the defined sand layer, Brown Lake may become a keystone location for rationalising subtropical environmental evolution though time.

Expansion of the research conducted at South Walker Creek would provide a deeper understanding of tropical Australian palaeoecology. For example, investigating additional sediment deposits both up- and downstream of South Walker Creek would enhance existing knowledge of fluvial history in the Fitzroy River Basin, potentially leading to the discovery of new megafauna fossil deposits. A better understanding of upstream-downstream variation would enable improved understanding of extreme seasonal and spatial variation in rainfall, fluvial activity, erosion and sedimentation; i.e., how the broader catchment environment has changed through time (e.g., responding to flooding and drying events; Nepal et al., 2014). Moreover, as the South Walker Creek megafauna fossil site is located proximal to an active mine, there is likely an avenue to investigate human and megafauna relationships through the correlation of local archaeological information (generated during cultural heritage clearances prior to land disturbance) with excavated fossil sites.

A prospective downstream site for examining additional long-term hydrological conditions of the Fitzroy River Basin is Gracemere Lagoon (Figure 6.4), which remains largely unstudied. This wetland is located downstream of the Mackenzie River and Dawson River confluence, providing an archive of catchment-wide fluvial activity (see Figure of river systems in Chapter 4) that can be compared to river channel activation events reported by Croke et al. (2011) The lake margins also exhibit exposed shorelines on satellite imagery, suggesting significant fluctuations in past water levels. Moreover, semi-permanent Gracemere Lagoon exhibits conditions favourable for environmental proxy preservation such as a relatively neutral pH (Genade, 2020) and likely hosts environmentally indicative microfossils (ostracods, pollen, charcoal). Deeper understanding of pre-European

conditions would additionally help inform action on wetland management and regeneration. This is particularly important as the site may serve as a potential habitat for several fish species of conservation significance, none of which are protected under legislation (Gladstone Area Water Board, 2008).

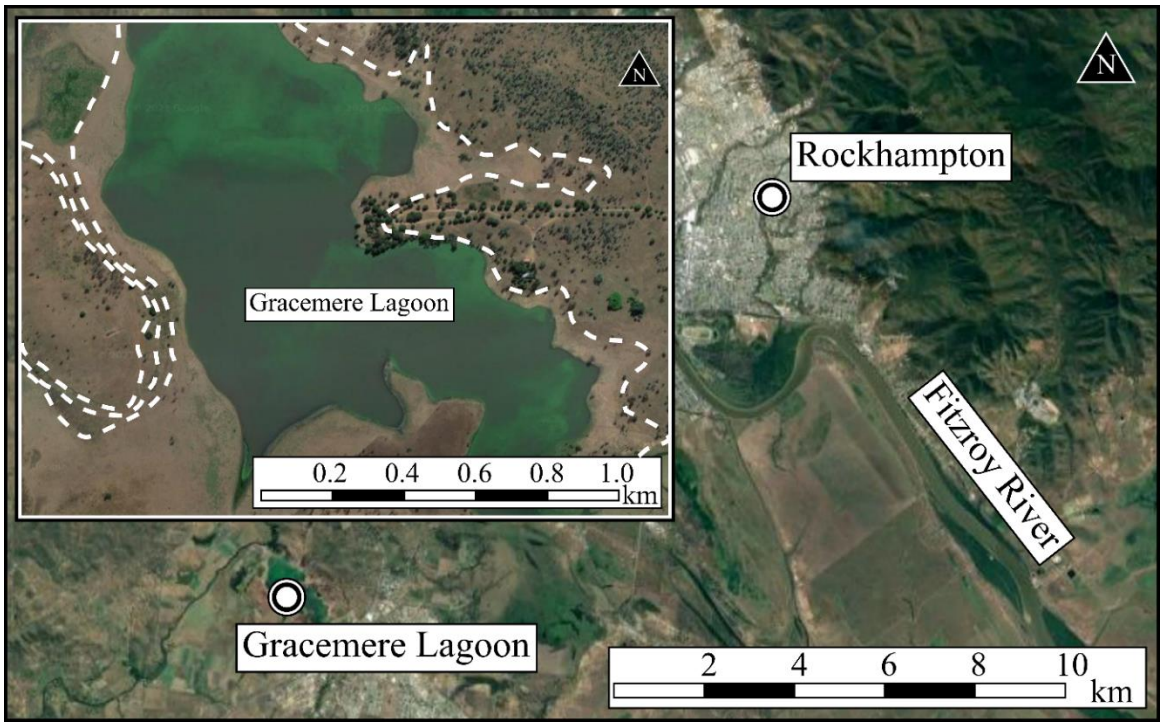

Figure 6.4 Location map of Gracemere Lagoon, a promising study location downstream of South Walker Creek along the Fitzroy River. The inset map shows an aerial image of Gracemere Lagoon, with potential shorelines identified using dashed white lines.

Concluding remarks

This thesis set out to explore the question, "Did the extinction of Australian megafauna coincide with widespread climate-induced environmental change?", by establishing reliable records of long-term ecological and climate variation in severely underrepresented geographic regions. It was found that palaeoenvironmental records from the subtropical region of Australia record a phase of supressed moisture availability from 43 – 37 ka onwards, with conditions persisting until the Holocene (Chapter 2; Lewis et al., 2020; Chapter 3; Lewis et al., 2021). The disappearance of megafauna from the tropical region was established to have occurred sometime after 40.1 ± 1.7 ka (Chapter 4), with evidence suggesting this demise was associated with an overall decrease in fluvial activity. The compilation of additional chronological datasets from South Walker Creek sites and the use of Bayesian modelling enabled further refinement of local megafauna disappearance to 41.7 – 35.8 ka (95 % C.I.) (Chapter 5). Comparisons of the South Walker Creek fluvial records with those already published for other catchments (Chapter 5) supports the conclusion that, prior to extinction, Australian megafauna were subjected to widespread habitat change in response to hydroclimate deterioration. The nature, timing and extent of local human interactions with megafauna during this period of increased aridity is less certain. However, as analytical techniques improve and new palaeontological and archaeological site are discovered, it is hoped that the deeper understanding of environmental change gleaned from this thesis will enable us to make better-informed decisions in relation to safe-guarding Australia's environmental future.

References

Andrae, J. W., Mcinerney, F. A. & Sniderman, J. M. K. 2020. Carbon isotope systematics of leaf wax n-alkanes in a temperate lacustrine depositional environment. Organic Geochemistry, 150, 104121.

Bird, M. I., Hutley, L. B., Lawes, M. J., Lloyd, J., Luly, J. G., Ridd, P. V., Roberts, R. G., Ulm, S. & Wurster, C. M. 2013. Humans, megafauna and environmental change in tropical Australia. Journal of Quaternary Science, 28, 439-452.

Chiavari, C., Martini, M., Sibilia, E. & Vandini, M. 2001. Thermoluminescence (TL) characterisation and dating feasibility of ancient glass mosaic. Quaternary Science Reviews, 20, 967-972.

Clarkson, C., Jacobs, Z., Marwick, B., Fullagar, R., Wallis, L., Smith, M., Roberts, R. G., Hayes, E., Lowe, K. & Carah, X. 2017. Human occupation of northern Australia by 65,000 years ago. Nature, 547, 306-310.

Cooper, A., Turney, C. S., Palmer, J., Hogg, A., Mcglone, M., Wilmshurst, J., Lorrey, A. M., Heaton, T. J., Russell, J. M. & Mccracken, K. 2021. A global environmental crisis 42,000 years ago. Science, 371, 811-818.

Croke, J., Jansen, J. D., Amos, K. & Pietsch, T. J. 2011. A 100 ka record of fluvial activity in the Fitzroy River Basin, tropical northeastern Australia. Quaternary Science Reviews, 30, 1681-1695.

David, B., Arnold, L. J., Delannoy, J.-J., Fresløv, J., Urwin, C., Petchey, F., Mcdowell, M. C., Mullett, R., Land, G. & Mialanes, J. 2021. Late survival of megafauna refuted for Cloggs Cave, SE Australia: Implications for the Australian Late Pleistocene megafauna extinction debate. Quaternary Science Reviews, 253, 106781.

De Deckker, P., Arnold, L. J., Van Der Kaars, S., Bayon, G., Stuut, J.-B. W., Perner, K., Dos Santos, R. L., Uemura, R. & Demuro, M. 2019. Marine Isotope Stage 4 in Australasia: a full glacial culminating 65,000 years ago–global connections and implications for human dispersal. Quaternary Science Reviews, 204, 187-207.

Del Río, I., Sawakuchi, A. O., Góes, A. M., Helena, M., Hollanda, B. M., Furukawa, L. Y., Porat, N., Jain, M., Mineli, T. D. & De Assis Negri, F. 2021. Luminescence signals of quartz and feldspar as new methods for stratigraphic discrimination and provenance analysis of siliciclastic successions: the case of the Parnaíba Basin (Brazil) of West Gondwana. Basin Research, n/a.

Demuro, M., Arnold, L. J., Duval, M., Méndez-Quintas, E., Santonja, M. & Pérez-González, A. 2020. Refining the chronology of Acheulean deposits at Porto Maior in the River Miño basin (Galicia, Spain) using a comparative luminescence and ESR dating approach. Quaternary International, 556, 96-112.

Diefendorf, A. F. & Freimuth, E. J. 2017. Extracting the most from terrestrial plant-derived n-alkyl lipids and their carbon isotopes from the sedimentary record: A review. Organic Geochemistry, 103, 1-21.

Field, J., Wroe, S., Trueman, C. N., Garvey, J. & Wyatt-Spratt, S. 2013. Looking for the archaeological signature in Australian megafaunal extinctions. Quaternary International, 285, 76-88.

Flannery, T. 1994. The future eaters: an ecological history of the Australasian lands and people, Port Melbourne, Port Melbourne : Reed Books.

Fu, X., Cohen, T. J. & Arnold, L. J. 2017. Extending the record of lacustrine phases beyond the last interglacial for Lake Eyre in central Australia using luminescence dating. Quaternary Science Reviews, 162, 88-110.

Gehrels, M. J., Newnham, R. M., Lowe, D. J., Wynne, S., Hazell, Z. J. & Caseldine, C. 2008. Towards rapid assay of cryptotephra in peat cores: Review and evaluation of various methods. Quaternary International, 178, 68-84.

Genade, G. 2020. Planning Report, Material change of use for special industry and environmentally relevant activity (chemical manufacturing) [Online]. Rockhampton Regional Council. Available: https://www.rockhamptonregion.qld.gov.au/files/assets/public/communities/planning-building-plumbing/development/public-notification/d69-2020-public-notification.pdf [Accessed 2021].

Gladstone Area Water Board 2008. Gladstone-Fitzroy pipeline project: environmental impact statement. In: Department of Regional Development, M. a. W. (ed.). Gladstone, Queensland: Gladstone Area Water Board.

Hocknull, S. A., Lewis, R., Arnold, L. J., Pietsch, T., Joannes-Boyau, R., Price, G. J., Moss, P., Wood, R., Dosseto, A., Louys, J., Olley, J. & Lawrence, R. A. 2020. Extinction of eastern Sahul megafauna coincides with sustained environmental deterioration. Nature communications, 11, 1-14.
Kemp, C. W., Tibby, J., Arnold, L. J., Barr, C., Gadd, P. S., Marshall, J. C., Mcgregor, G. B. & Jacobsen, G. E. 2020. Climates of the last three interglacials in subtropical eastern Australia inferred from wetland sediment geochemistry. Palaeogeography, Palaeoclimatology, Palaeoecology, 538, 109463.
Kershaw, A. P., Van Der Kaars, S. & Moss, P. T. 2003. Late Quaternary Milankovitch-scale climatic change and variability and its impact on monsoonal Australasia. Marine Geology, 201, 81-95.
Lewis, R. J., Tibby, J., Arnold, L. J., Barr, C., Marshall, J., Mcgregor, G., Gadd, P. & Yokoyama, Y. 2020. Insights into subtropical Australian aridity from Welsby Lagoon, north Stradbroke Island, over the past 80,000 years. Quaternary Science Reviews, 234, 106262.
Lewis, R. J., Tibby, J., Arnold, L. J., Gadd, P., Jacobsen, G., Barr, C., Negus, P. M., Mariani, M., Penny, D., Chittleborough, D. & Moss, E. 2021. Patterns of aeolian deposition in subtropical Australia through the last glacial and deglacial periods. Quaternary Research, 1-23.
Lowe, D. J. 2011. Tephrochronology and its application: a review. Quaternary Geochronology, 6, 107-153.
Lu, Z.-T. & Mueller, P. 2010. Chapter 4 - Atom Trap Trace Analysis of Rare Noble Gas Isotopes. In: Berman, P., Arimondo, E. & Lin, C. (eds.) Advances In Atomic, Molecular, and Optical Physics. Academic Press.
Makou, M. C., Hughen, K. A., Xu, L., Sylva, S. P. & Eglinton, T. I. 2007. Isotopic records of tropical vegetation and climate change from terrestrial vascular plant biomarkers preserved in Cariaco Basin sediments. Organic Geochemistry, 38, 1680-1691.
Mcgowan, H. A., Petherick, L. M. & Kamber, B. S. 2008. Aeolian sedimentation and climate variability during the late Quaternary in southeast Queensland, Australia. Palaeogeography, Palaeoclimatology, Palaeoecology, 265, 171-181.
Miller, G. H., Fogel, M. L., Magee, J. W., Gagan, M. K., Clarke, S. J. & Johnson, B. J. 2005. Ecosystem collapse in Pleistocene Australia and a human role in megafaunal extinction. science, 309, 287-290.
Moss, P. T., Tibby, J., Petherick, L., Mcgowan, H. & Barr, C. 2013. Late Quaternary vegetation history of North Stradbroke Island, Queensland, eastern Australia. Quaternary Science Reviews, 74, 257-272.
Nepal, S., Flügel, W.-A. & Shrestha, A. B. 2014. Upstream-downstream linkages of hydrological processes in the Himalayan region. Ecological Processes, 3, 19.
O'connell, J. F. & Allen, J. 2004. Dating the colonization of Sahul (Pleistocene Australia–New Guinea): a review of recent research. Journal of Archaeological Science, 31, 835-853.
Peters, K. J., Saltré, F., Friedrich, T., Jacobs, Z., Wood, R., Mcdowell, M., Ulm, S. & Bradshaw, C. J. A. 2019. FosSahul 2.0, an updated database for the Late Quaternary fossil records of Sahul. Scientific data, 6, 1-7.
Petherick, L., Bostock, H., Cohen, T. J., Fitzsimmons, K., Tibby, J., Fletcher, M.-S., Moss, P., Reeves, J., Mooney, S. & Barrows, T. 2013. Climatic records over the past 30 ka from temperate Australia–a synthesis from the Oz-INTIMATE workgroup. Quaternary Science Reviews, 74, 58-77.
Petherick, L. M., Mcgowan, H. A. & Kamber, B. S. 2009. Reconstructing transport pathways for late Quaternary dust from eastern Australia using the composition of trace elements of long travelled dusts. Geomorphology, 105, 67-79.
Prescott, J. R. & Fox, P. J. 1993. Three-dimensional thermoluminescence spectra of feldspars. Journal of Physics D: Applied Physics, 26, 2245-2254.
Price, G. J., Fitzsimmons, K. E., Nguyen, A. D., Zhao, J.-X., Feng, Y.-X., Sobbe, I. H., Godthelp, H., Archer, M. & Hand, S. J. 2021. New ages of the world's largest-ever marsupial: Diprotodon optatum from Pleistocene Australia. Quaternary International.
Reeves, J. M., Barrows, T. T., Cohen, T. J., Kiem, A. S., Bostock, H. C., Fitzsimmons, K. E., Jansen, J. D., Kemp, J., Krause, C. & Petherick, L. 2013. Climate variability over the last 35,000 years recorded in marine and terrestrial archives in the Australian region: an OZ-INTIMATE compilation. Quaternary Science Reviews, 74, 21-34.

Reichel, T., Kersting, A., Ritterbusch, F., Ebser, S., Bender, K., Purtschert, R., Oberthaler, M. & Aeschbach-Hertig, W. First dating of groundwater with Atom Trap Trace Analysis of 39Ar-application. EGU General Assembly Conference Abstracts, 2013. EGU2013-10901.
Rodríguez-Rey, M., Herrando-Pérez, S., Gillespie, R., Jacobs, Z., Saltré, F., Brook, B. W., Prideaux, G. J., Roberts, R. G., Cooper, A. & Alroy, J. 2015. Criteria for assessing the quality of Middle Pleistocene to Holocene vertebrate fossil ages. Quaternary Geochronology, 30, 69-79.
Saltré, F., Rodríguez-Rey, M., Brook, B. W., Johnson, C. N., Turney, C. S. M., Alroy, J., Cooper, A., Beeton, N., Bird, M. I. & Fordham, D. A. 2016. Climate change not to blame for late Quaternary megafauna extinctions in Australia. Nature communications, 7, 1-7.
Stout, J., Goh, K. & Rafter, T. 2021. Resistant organic compounds in soil. Soil Biochemistry, 1.
Tibby, J., Barr, C., Marshall, J. C., Mcgregor, G. B., Moss, P. T., Arnold, L. J., Page, T. J., Questiaux, D., Olley, J. & Kemp, J. 2017. Persistence of wetlands on North Stradbroke Island (south-east Queensland, Australia) during the last glacial cycle: implications for Quaternary science and biogeography. Journal of Quaternary Science, 32, 770-781.
Turney, C. S. M., Flannery, T. F., Roberts, R. G., Reid, C., Fifield, L. K., Higham, T. F. G., Jacobs, Z., Kemp, N., Colhoun, E. A., Kalin, R. M. & Ogle, N. 2008. Late-surviving megafauna in Tasmania, Australia, implicate human involvement in their extinction. Proceedings of the National Academy of Sciences, 105, 12150-12153.
Vodyanitskii, Y. & Minkina, T. 2020. Changing the properties of samples after extraction from wet soil: a short review. Geochemistry: Exploration, Environment, Analysis, 20, 399-407.
Zappala, J. C. 2017. Atom trap trace analysis: Developments & applications, The University of Chicago.

Appendix A. Supplementary Information for Chapter 2

This Appendix contains supplementary information that accompanies Chapter 2, which has been published in *Quaternary Science Reviews* as:

Lewis, R. J., Tibby, J., Arnold, L. J., Barr, C., Marshall, J., McGregor, G., Gadd, P. & Yokoyama, Y., 2020, Insights into subtropical Australian aridity from Welsby Lagoon, North Stradbroke Island, over the past 80,000 years. Quaternary Science Reviews, 234, 106262.

A1. OSL dating methodology

A1.1. Sample preparation

Quartz fractions for OSL dating were extracted from WEL15-1 and WEL15-2 and prepared under controlled lighting conditions (subdued red lighting) to prevent depletion of the naturally accumulated burial dose signals.

The extracted samples were treated with 10 % sodium hydroxide to disperse clay aggregates prior to wet sieving using a nest of 355, 250, 212, 180, 125, 90, 63 μm sieves. Size fractions smaller than 63 μm were retained for grain size analysis and allowed a minimum of 1 hour to settle out of suspension before excess water was decanted. Fractions > 60 μm were then treated with hydrochloric acid (30 %) and hydrogen peroxide (30 %) to dissolve remaining carbonates and organic material, respectively, following the procedure of Aitken (1998). Heavy liquid density separation was utilised to isolate quartz from other minerals (e.g., feldspars, zircons and clays) using LST prepared to densities of 2.72 g/cm^3 and 2.62 g/cm^3. Coarse grains (180–250 μm or 212–250 μm for the silicate-rich basal dune layer) were then treated with hydrofluoric acid (48 %) for 40 mins to etch away the alpha-irradiated quartz margin and retreated with hydrochloric acid (30 %) to dissolve any fluoride precipitates.

A1.2. OSL instrumentation

OSL measurements were made using a Risø TL-DA-20 reader equipped with blue LEDs, an array of infrared LEDs, and a 10 mW Nd:YVO_4 single-grain laser attachment emitting at 532 nm. Ultraviolet OSL signals were detected using an EMI9235QA photomultiplier tube, fitted with 7.5 mm thick Hoya U-340 filters. Samples were irradiated with a $^{90}Sr/^{90}Y$ β source that had been calibrated for individual grain-hole positions to account for spatial variations in beta dose rate across each disc.

A1.3. Single-grain OSL D_e results

Prior to applying the SAR procedure for single-grain equivalent dose (D_e) determination, we tested the suitability of the chosen measurement conditions through a dose-recovery test on sample WEL15-2(1). Four replicate multi-grain discs, containing approximately 100 grains, were administered a known laboratory dose of 25 Gy following optical bleaching of their natural signal (two cycles of blue LED exposure for 1,000 s, separated by 10,000 s pause). A multi-grain version of the SAR procedure was then applied to the discs (replacing single-grain laser stimulations in steps 4 and 7 of Table A1 with blue LED OSL stimulations performed at 125 °C for 60 s), using variable preheat conditions prior to each OSL measurement (Figure A1). This assessment of D_e determination conditions showed that a preheat of 260 °C for 10 s prior to the natural (L_n) or regenerative dose (L_x) measurement, and a preheat of 220 °C for 10 s prior to the test-dose (T_n or T_x) measurement provided accurate dose recovery ratios (Table A1). The suitability of these preheat conditions was validated at the single-grain level using a repeated dose recovery performed on 300-600 grains of samples WEL15-2(1), WEL15-2(12) and WEL15-2(11) under the same bleaching and dosing parameters (Figure A2). The weighted mean single-grain measured/given dose ratios ranged from 0.99 ± 0.02 to 1.01 ± 0.01, with all three samples exhibiting low overdispersion values (3–5 % (Figure A2b).

The OSL signal from each individual grain was assessed and vetted against a series of quality assurance criteria (Arnold et al., 2016; Arnold et al., 2013; Arnold & Roberts, 2011) as part of our D_e determination procedure. Individual grains were required to pass the following tests before being accepted in the final age determination (Table A2): (1) the net intensity of the natural test-dose signal,

(T_n), was more than three times the standard deviation of the late-light background signal, (2) the ratios of sensitivity-corrected luminescence response (L_x/T_x) for two identical regenerative doses were consistent with unity at 2σ, (3) the ratio of the L_x/T_x values obtained from two identical regenerative doses measured with and without prior IR stimulation (OSL IR depletion ratio; (Duller, 2003)) was not less than unity at 2σ, (4) the sensitivity-corrected luminescence response of the 0 Gy regenerative-dose point amounted to less than 5 % of the sensitivity-corrected natural signal response (L_n/T_n) at 2σ, (5) the L_n/T_n values were less than, the I-max saturation limit of the dose-response curve at 2σ, (6) the dose response curve did not display anomalous behaviour such as a zero or negative response with increasing dose, or very scattered L_x/T_x values (i.e., the dose response curve could be successfully fitted with the Monte Carlo procedure and, hence, did yielded finite D_e values and uncertainty ranges). Statistics were retained during the quality assurance vetting to allow comparisons between sample grain populations (Table A2). An example of a single-grain OSL response that passed all quality checks is presented in Figure A3.

Individual D_e values were derived from the first 0.2 s of the OSL signal, minus a background integrated over the last 0.25 s of stimulation. Dose response curves were fitted using a single saturating exponential or saturating exponential plus linear function, depending on the option that yielded optimum fitting uncertainties. The single-grain D_e uncertainties incorporate an empirically determined instrument reproducibility uncertainty of 2.5 % for each single-grain OSL measurement (calculated for the Risø reader used in this study, following the approach outlined in Jacobs et al. (2006), and a dose response curve fitting uncertainty determined from 1000 iterations of the Monte Carlo method outlined in Duller (2007).

A1.4. Dose rate

The lithogenic radionuclide activity of the sedimentary matrix was ascertained for each OSL sample using ~30 g (dry weight) of bulk material removed during the sample preparation process. Individual sample geochemistry, in particular the concentrations of U, Th, K, were measured using a combination of inductively coupled plasma mass spectrometry (ICP-MS) and inductively coupled plasma optical emission spectrometry (ICP-OES), following preparation with lithium borate fusion. Elemental concentrations were nearing detecting limits (0.01 % for K and 0.05 ppm for U and Th), however they were in sufficient abundance for finite calculations of beta and gamma dose rates using the published conversion factors of Guérin et al. (2011). Given the low dose rate of these samples, we have undertaken a site-specific evaluation of internal dose rate contribution on a representative sample, WEL15-2(1). For this purpose, U and Th concentrations of fully prepared, isolated and etched quartz from WEL15-2(1) were analysed using ICP-OES (Table A3). The measured internal U and Th concentrations of this sample were 0.05 ± 0.01 ppm and 0.47 ± 0.02 ppm, respectively, which yield an internal dose rate of 0.02 ± 0.01 Gy/ka when using an alpha efficiency factor (a-value) of 0.04 ± 0.01 (Rees-Jones & Tite, 1997; Rees-Jones, 1995). The final dose rate calculations include allowances for beta-dose attenuation and sample moisture content (Mejdahl, 1979) (Table A4). The cosmic ray contribution to the total environmental dose rate has been determined using the approach of Prescott & Hutton (1994), assuming steady post-depositional overburden accumulation and a constant lake depth (equivalent to present-day conditions).

Sediment water content has been evaluated through the entire core profile to ascertain the potential for temporal dewatering and compaction with subsequent overburden accumulation. Bulk sediment

samples were extracted from the WEL15-2 core in ~1 cm^3 sections at 10 cm intervals. The wet weight of these samples was initially measured, and the samples were then dried at 100 °C for 24 hours, followed by reweighing. The (wet) water content measurements (Figure A7) ranged between 21 and 93 %. Between core depths of 10 and 500 cm, the water content shows no correlation with depth and exhibits localised, non-monotonic variations. Between 500 and 1180 cm, the water content shows a weak linear trend with a mean value of 86 % (1σ = 0.1 %). At depths greater than 1180 cm, the water content gradually decreases to 54 % prior to a sharper decline towards the basal value of 21 %. Notably, the changes in the water content appear to be proportional to the changes in terrigenous material (silicate sands) and organic material (Figure A7), indicating dominant lithological controls rather than simple depth-dewatering trends. As lithology appears to be strongly dictating water content values down-core, it was not considered suitable to apply a dewatering compaction correction to the long-term moisture attenuation calculations of individual OSL samples. Therefore, the empirical values have been used to determine the long-term water contents for beta / gamma / cosmic-ray dose rate attenuation, expressed as % of dry mass of mineral fraction, with an assigned relative uncertainty of ±5 % (Table A3). The final beta dose rates have been adjusted for moisture attenuation using the measured water contents determined from the midpoint of each OSL sample depth. The final gamma dose rates have been adjusted using the average water content measured from each OSL sample midpoint, as well as from 1 cm^3 bulk sediment samples collected from the overlying and underlying 10 cm of each OSL sample position. The final cosmic-ray dose rates have been adjusted using the average water content measured from 1 cm^3 bulk sediment samples collected at 10 cm intervals throughout the overlying core sequence. The samples collected from the high porosity, silicate rich, basal aeolian sands (in the lowermost core drive) are considered to have been affected by dewatering during the sample process, as their measured water content are unreliably low. Given that these basal sands would have resided within the localised perched water table zone for the duration of the burial period, we have calculated the long-term beta, gamma and cosmic dose rate water corrections using the empirically derived saturated moisture contents (values shown for samples WEL15-2(2), WEL15-1(6), WEL15-1(7), WEL15-2(1) in Table 2.1 and Table A4).

An additional organic content attenuation factor has not been incorporated into our dose rate calculation (e.g., Lian et al., 1995; because all dosimetric evaluations have been made on non-ashed samples; hence the measured specific activities and elemental concentrations approximate present-day organic-attenuated conditions. In adopting this approach, we assume that the present-day organic contents of the Welsby Lagoon sediments are broadly representative of the long-term organic conditions prevailing throughout the burial period. This assumption is supported by the preservation of identifiable plant macro-fossils, plant remains and charcoal (e.g., ^{14}C samples in Table A5), and the absence of any systematic post-depositional mixing signatures in the single-grain D_e datasets (Figure 2.3 & Figure A4); both of which suggest minimal physical degradation of organic remains following burial.

High-resolution gamma spectrometry (HRGS) was additionally performed on a sub-set of six OSL samples to evaluate the state of secular equilibrium in the ^{238}U and ^{232}Th decay series for both the organic-rich and inorganic sediments of the Welsby Lagoon sequence (Table A7). Daughter-parent isotopic ratios for ^{238}U, ^{226}Ra, ^{210}Pb, ^{228}Ra and ^{228}Th are consistent with unity at either 1σ or 2σ for five of the six samples (WEL15-2(6), WEL15-2(7), WEL15-2(9), WEL15-2(12), WEL15-2(1)), confirming that the ^{238}U and ^{232}Th chains are in present-day secular equilibrium the majority of the

Welsby Lagoon deposits. The remaining sample (WEL15-2(2)) shows statistically significant disequilibrium in the ^{238}U decay chain, as the ^{226}Ra:^{238}U and ^{210}Pb:^{226}Ra ratios do not overlap with unity at 2σ (0.73 ± 0.07 and 1.59 ± 0.13, respectively). This disequilibrium may reflect the uptake of unsupported ^{238}U and ^{210}Pb following burial, or the loss of radon (^{222}Rn) gas to the atmosphere (since we have used the post-radon daughter emissions of ^{214}Pb and ^{214}Bi to derive ^{226}Ra activities).

The ^{238}U series disequilibrium for sample WEL15-2(2) is not considered to have a significant effect on the final dose rate estimate, as borne out by the stratigraphic consistency of the single-grain OSL ages for the WL15-1 and WL15-2 cores (see Table 2.1 and Figure 2.4). Dosimetry modelling studies undertaken elsewhere have also shown that isotopic disequilibria of similar magnitudes are only likely to give rise to minor deviations (<5 %) in long-term dose rate estimates (e.g., Preusser & Degering, 2007; Olley et al., 1997; Olley et al., 1996). Such systematic biases would be significantly less than the existing uncertainty ranges on our final dose rate estimates. The effects of ^{238}U disequilibrium will be further diminished for sample WEL15-2(2) because the ^{238}U decay series only contributes <28 % (excluding the base sand WEL15-1(7)) to the total quartz dose rate (calculated using the high-resolution gamma spectrometry results).

Table A2.7 shows the final environmental dose rates obtained using the HRGS results, which have been calculated after taking into consideration the fractional beta and gamma dose rate contributions of different isotopes in the ^{238}U decay series (Guérin et al., 2011; Stokes et al., 2003). For all six samples, the final dose rates derived using HRGS are in agreement, at either 1 or 2σ, with those obtained using a combination of ICP-MA and ICP-OES (Table A4); including for sample WEL15-2(2), which exhibits signs of ^{238}U series disequilibrium. The consistency of results obtained using these different dosimetric evaluations further supports the suitability of the final dose rate estimates obtained for the Welsby Lagoon sample dataset.

A2. WD-XRF sample preparation

WD-XRF measurements were quantified on a PANalytical Axios Advanced WD-XRF system on fused glass disks at the CSIRO Land and Water laboratories in Urrbrae, South Australia. Fused disks were prepared using the following approach: approximately 1 g of each oven-dried sample (105 °C) was weighed with 4 g of 12:22 lithium borate flux into a Pt/Au crucible and thoroughly mixed. Mixtures were slowly heated to 700 °C in a furnace to fully oxidise the organic material. After cooling samples were heated to 1050 °C in the same Pt/Au crucible for 20 minutes to dissolve the sample, then poured into a 32 mm Pt/Au mould heated to a similar temperature. The melt was cooled rapidly over a compressed air stream forming the glass disks.

Table A 1 Single-aliquot regenerative-dose (SAR) procedure used for single-grain D_e determination. The SAR measurement cycle shown here was repeated for the natural dose, five different-sized regenerative doses and a 0 Gy regenerative dose (to measure OSL signal recuperation). Both the smallest and largest non-zero Gy regenerative dose cycles were repeated at the end of the SAR procedure to assess the suitability of the test dose sensitivity correction. The smallest regenerative dose cycle was then repeated a second time with the inclusion of step 2 to check for the presence of feldspar contaminants using the OSL IR depletion ratio of Duller (2003). L_x = regenerative dose signal response; L_n = natural dose signal response; T_x = test dose signal response for a laboratory dose cycle T_n = test dose signal response for the natural dose cycle.

Step	Treatment	Symbol
1	Dose (natural or laboratory)	N or D
2[a]	IRSL stimulation (50 C for 60 s)	
3	Preheat 1 (260 C for 10 s)	PH1
4	Single-grain OSL stimulation (125 C for 2 s)	L_n or L_x
5	Test dose (10 Gy)	T_d
6	Preheat 2 (220 C for 10 s)	PH2
7	Single-grain OSL stimulation (125 C for 2 s)	T_n or T_x
8	Repeat measurement cycle for different sized regenerative doses	

[a] Step 2 is only included in the single-grain OSL SAR procedure when measuring the OSL IR depletion ratio (Duller, 2003)

Table A 2 Single-grain OSL grain classification statistics, showing proportion of rejected and accepted grains after applying the SAR quality assurance criteria. Data are also shown for the single-grain OSL dose recovery test (DRT) measurements made on samples WEL15-2(12), WEL15-2(11), WEL15-2(1) (in the first three rows).

			Rejected grains (%)						
Sample	**Depth (cm)**	**Grains measured (n)**	**Tn <3σ BG**	**Poor dose recycling ratio**	**IR depletion ratio**	**Recupera-tion >5%**	**Saturated**	**Anomalous dose response curve**	**Accepted grains (%)**
WEL15-2(12) (DRT)	815	300	54	5	6	0	1	17	17
WEL15-2(11) (DRT)	775	500	46	9	6	0	1	19	20
WEL15-2(1) (DRT)	1270	600	37	15	4	0	1	15	28
WEL15-2(3)	380	500	60	7	3	1	0	13	16
WEL15-2(6)	510	500	45	15	5	0	0	13	23
WEL15-1(2)	543	700	54	8	7	0	0	13	17
WEL15-2(7)	580	1200	59	14	4	0	0	8	15
WEL15-2(8)	610	700	50	9	5	0	0	13	22
WEL15-2(9)	680	800	58	8	5	0	1	10	19
WEL15-2(10)	710	900	47	8	5	0	0	12	25
WEL15-2(11)	775	900	48	10	3	0	1	12	27
WEL15-2(12)	815	800	48	11	4	0	1	11	25
WEL15-2(13)	880	200	53	20	7	0	1	7	14
WEL15-1(5)	892	600	43	12	6	0	1	16	24
WEL15-2(15)	980	200	57	18	7	0	0	7	12
WEL15-1(21)	1047	400	47	19	7	0	2	12	14
WEL15-1(22)	1119	400	50	18	4	0	2	8	19
WEL15-2(19)	1180	500	48	20	7	0	4	3	18
WEL15-2(20)	1210	600	50	16	6	0	2	10	16
WEL15-1(23)	1213	400	50	20	6	0	2	9	14
WEL15-2(2)	1259	900	41	14	4	0	2	12	27
WEL15-1(6)	1261	700	44	11	4	0	1	15	25
WEL15-1(7)	1263	800	48	10	4	0	4	13	22
WEL15-2(1)	1270	900	39	10	7	1	2	14	28

Table A 3 Elemental concentrations for OSL dating samples, as measured on dry sediment using ICP-OES (K) and ICP-MS (U and Th).

Sample	Depth (cm)	K(%)	Th (ppm)	U (ppm)
WEL15-2(3)	380	0.01 ± 0.001	0.38 ± 0.028	0.26 ± 0.014
WEL15-2(6)	510	0.19 ± 0.006	4.52 ± 0.147	0.90 ± 0.032
WEL15-1(2)	543	0.22 ± 0.007	8.41 ± 0.260	1.97 ± 0.063
WEL15-2(7)	580	0.20 ± 0.006	7.55 ± 0.235	1.65 ± 0.054
WEL15-2(8)	610	0.23 ± 0.007	7.10 ± 0.222	1.64 ± 0.054
WEL15-2(9)	680	0.22 ± 0.007	6.66 ± 0.209	1.52 ± 0.050
WEL15-2(10)	710	0.23 ± 0.007	7.02 ± 0.219	1.64 ± 0.054
WEL15-2(11)	775	0.29 ± 0.009	8.07 ± 0.250	1.58 ± 0.052
WEL15-2(12)	815	0.35 ± 0.011	8.45 ± 0.261	1.71 ± 0.056
WEL15-2(13)	880	0.28 ± 0.008	7.40 ± 0.230	1.70 ± 0.055
WEL15-1(5)	892	0.32 ± 0.010	8.15 ± 0.252	1.70 ± 0.055
WEL15-2(15)	980	0.26 ± 0.008	5.80 ± 0.184	1.20 ± 0.041
WEL15-1(21)	1047	0.27 ± 0.008	7.00 ± 0.219	1.40 ± 0.047
WEL15-1(22)	1119	0.30 ± 0.009	9.60 ± 0.294	1.70 ± 0.055
WEL15-2(19)	1180	0.09 ± 0.003	12.00 ± 0 363	2.00 ± 0.064
WEL15-2(20)	1210	0.09 ± 0.003	7.30 ± 0.227	1.90 ± 0.061
WEL15-1(23)	1213	0.10 ± 0.003	10.30 ± 0 314	1.80 ± 0.058
WEL15-2(2)	1259	0.04 ± 0.001	3.37 ± 0.114	0.87 ± 0.032
WEL15-1(6)	1261	0.06 ± 0.002	3.86 ± 0.128	1.42 ± 0.047
WEL15-1(7)	1263	0.02 ± 0.001	2.28 ± 0.082	0.50 ± 0.021
WEL15-2(1)	1270	0.02 ± 0.001	1.15 ± 0.050	0.36 ± 0.017

Table A 4 Environmental dose rates for the Welsby Lagoon quartz OSL samples.

			Water Content (% $_{Dry}$) [a]			Environmental dose rate (Gy/ka) [b,c,d,e,f,g]				
Sample ID	Depth (cm)	Grain size (μm)	Beta	Gamma	Cosmic	Beta	Gamma	Internal	Cosmic	Total
WEL15-2(3)	380	180 – 250	505	630	923	0.01 ± 0.001	0.01 ± 0.001	0.02 ± 0.007	0.02 ± 0.002	0.05 ± 0.008
WEL15-2(6)	510	180 – 250	575	620	945	0.04 ± 0.010	0.05 ± 0.001	0.02 ± 0.007	0.01 ± 0.001	0.12 ± 0.014
WEL15-1(2)	543	180 – 250	484	573	918	0.08 ± 0.018	0.09 ± 0.002	0.02 ± 0.007	0.01 ± 0.001	0.21 ± 0.022
WEL15-2(7)	580	180 – 250	586	611	902	0.06 ± 0.015	0.07 ± 0.002	0.02 ± 0.007	0.01 ± 0.001	0.17 ± 0.020
WEL15-2(8)	610	180 – 250	500	555	881	0.07 ± 0.016	0.08 ± 0.002	0.02 ± 0.007	0.01 ± 0.001	0.19 ± 0.020
WEL15-2(9)	680	180 – 250	468	474	841	0.07 ± 0.015	0.08 ± 0.002	0.02 ± 0.007	0.01 ± 0.001	0.19 ± 0.020
WEL15-2(10)	710	180 – 250	505	489	824	0.07 ± 0.016	0.09 ± 0.002	0.02 ± 0.007	0.01 ± 0.001	0.20 ± 0.020
WEL15-2(11)	775	180 – 250	489	476	800	0.08 ± 0.018	0.10 ± 0.002	0.02 ± 0.007	0.01 ± 0.001	0.22 ± 0.023
WEL15-2(12)	815	180 – 250	450	442	785	0.10 ± 0.019	0.11 ± 0.002	0.02 ± 0.007	0.01 ± 0.001	0.25 ± 0.025
WEL15-2(13)	880	180 – 250	463	465	761	0.08 ± 0.017	0.10 ± 0.002	0.02 ± 0.007	0.02 ± 0.002	0.22 ± 0.022
WEL15-1(5)	892	180 – 250	442	457	774	0.10 ± 0.019	0.11 ± 0.002	0.02 ± 0.007	0.02 ± 0.002	0.24 ± 0.024
WEL15-2(15)	980	180 – 250	454	473	731	0.07 ± 0.014	0.07 ± 0.002	0.02 ± 0.007	0.02 ± 0.002	0.18 ± 0.018
WEL15-1(21)	1047	180 – 250	435	469	741	0.08 ± 0.016	0.09 ± 0.002	0.02 ± 0.007	0.02 ± 0.002	0.21 ± 0.021
WEL15-1(22)	1119	180 – 250	403	412	715	0.11 ± 0.019	0.13 ± 0.003	0.02 ± 0.007	0.02 ± 0.002	0.27 ± 0.025
WEL15-2(19)	1180	180 – 250	274	276	679	0.13 ± 0.017	0.20 ± 0.005	0.02 ± 0.007	0.02 ± 0.002	0.36 ± 0.027
WEL15-2(20)	1210	212 – 250	231	258	664	0.12 ± 0.014	0.15 ± 0.003	0.02 ± 0.007	0.02 ± 0.002	0.30 ± 0.021
WEL15-1(23)	1213	180 – 250	450	432	690	0.08 ± 0.016	0.12 ± 0.003	0.02 ± 0.007	0.02 ± 0.002	0.24 ± 0.022
WEL15-2(2)	1259	212 – 250	209	191	655	0.09 ± 0.009	0.09 ± 0.002	0.02 ± 0.007	0.02 ± 0.002	0.22 ± 0.015
WEL15-1(6)	1261	212 – 250	195	244	655	0.06 ± 0.006	0.08 ± 0.002	0.02 ± 0.007	0.02 ± 0.002	0.18 ± 0.012
WEL15-1(7)	1263	212 – 250	89	78	643	0.06 ± 0.004	0.09 ± 0.002	0.02 ± 0.007	0.02 ± 0.002	0.19 ± 0.011
WEL15-2(1)	1270	212 – 250	78	73	643	0.04 ± 0.003	0.05 ± 0.002	0.02 ± 0.007	0.02 ± 0.002	0.13 ± 0.009

[a] Long-term water contents used for beta / gamma / cosmic-ray dose rate attenuation, expressed as % of dry mass of mineral fraction, with an assigned relative uncertainty of ±5%. The final beta dose rates have been adjusted for moisture attenuation using the measured water contents determined from the midpoint of each OSL sample depth. The final gamma dose rates have been adjusted using the average water content measured from each OSL sample midpoint, as well as from 1 cm^3 bulk sediment samples collected from the overlying and underlying 10 cm depth. The final cosmic-ray dose rates have been adjusted using the average water content measured from 1 cm^3 bulk sediment samples collected at 10 cm intervals throughout the overlying core sequence.
[b] Beta, gamma and internal dose rates have been calculated on dried and powdered sediment samples using ICP-MS and ICP-OES.
[c] Radionuclide concentrations have been converted to alpha, beta and gamma dose rates using the published conversion factors of Guérin et al. (2011), allowing for beta-dose attenuation (Mejdahl, 1979, Brennan, 2003) and long-term water content correction (Aitken, 1985).
[d] An internal dose rate of 0.02±0.01 Gy / ka has been included in the final dose rate calculations, based on ICP-MS U and Th measurements made on etched quartz grains from sample WEL15-2(1) and an alpha efficiency factor (a value) of 0.04±0.01 (Rees-Jones, 1995, Rees-Jones and Tite, 1997).
[e] Cosmic-ray dose rates were calculated using the approach of Prescott and Hutton (1994), and assigned a relative uncertainty of ±10%.
[f] Mean ± total uncertainty (68% confidence interval), calculated as the quadratic sum of the random and systematic uncertainties.
[g] Total uncertainty includes a systematic component of ±2% associated with laboratory beta-source calibration.

Table A 5 Radiocarbon (^{14}C) ages for the samples extracted from WEL15-2 in this study. Measured ages have been calibrated using SHCal13 within the OxCal program (Bronk Ramsey & Lee, 2013; Hogg et al., 2013; Bronk Ramsey, 2009). All samples were treated using acid-base-acid (ABA) pre-treatments. The calibrated age range shown is the 95.4 % probability range (combining two or more potential calibration ranges, where they exist).

Lab Code	Depth (cm)	Material	$\delta^{13}C$	Conventional ^{14}C age (^{14}C yr BP)	Error (1σ)	Calibrated age range (cal yr BP)
*YAUT-022706**	*80*	*Plant residual*	*-21.13*	*1392*	*34*	*1426 – 1358*
YAUT-023321	80	Leaf fragments		1260	64	1324 – 1196
*YAUT-023004**	*100*	*Plant remains*		*940*	*21*	*961 – 919*
*YAUT-023323**	*100*	*Charcoal*		*2259*	*63*	*2322 – 2196*
*YAUT-023324**	*230*	*Bark/plant remains*		*6456*	*70*	*6526 – 6386*
*YAUT-022707**	*260*	*Plant residual*	*-33.92*	*1197*	*37*	*1234 – 1160*
*YAUT-023325**	*310*	*Charcoal*		*9653*	*64*	*9717 – 9589*
YAUT-022709	360	Bark	-23.57	9602	54	9656 – 9548
YAUT-023326	360	Seeds		9553	64	9617 – 9489
YAUT-023523	430	Seeds		16887	78	16965 – 16809
YAUT-022711	440	Bark	-20.82	17646	91	17737 – 17555
YAUT-023327	460	Bark		17538	55	17593 – 17483
*YAUT-023332**	*460*	*Plant remains*		*17359*	*69*	*17428 – 17290*
*YAUT-022712**	*480*	*Plant residual*	*-23.52*	*16089*	*82*	*16171 – 16007*
YAUT-023333	480	Wood		17453	67	17520 – 17386
*YAUT-023334**	*480*	*Charcoal*		*9003*	*50*	*9053 – 8953*
*YAUT-022713**	*490*	*Plant residual*	*-18.65*	*15581*	*80*	*15661 – 15501*
*YAUT-023524**	*490*	*Charcoal*		*17308*	*67*	*17375 – 17241*
*YAUT-022714**	*530*	*Plant residual*	*-25.9*	*13025*	*69*	*13094 – 12956*
*YAUT-023336**	*540*	*Plant remains*		*13828*	*53*	*13881 – 13775*

* excluded from final deposition model for Welsby Lagoon on the grounds of sample material type; see main text for details.

Table A 6 Correlation matrix of elements of interest shown as R^2 values. Si has been selected to represent local sourcing while K has been selected to represent distal sourcing. This decision was based on the abundance of host minerals (i.e. high silica, low feldspar) of the sand dunes (Thompson, 1992). Values in bold highlight good a relationship between the respective elements.

	Si - Local	K - Distal
Si	-	0.26
Ti	**0.92**	0.09
Fe	0.34	**0.78**
K	0.26	-

Table A 7 High-resolution gamma spectrometry results for a representative sub-set of the Welsby Lagoon OSL samples. The dose rates shown in the final column have been calculated using the long-term water content corrections, beta attenuation factors, dose rate conversation factors, internal dose rate values and cosmic dose rate values detailed for each sample in Table A4.

Sample	Sample depth (cm)	Radionuclide specific activities (Bq/kg) [a, b]						Daughter: parent isotopic ratio			Total environmental dose rate (Gy/ka) [b]
		^{238}U	^{226}Ra	^{210}Pb	^{228}Ra	^{228}Th	^{40}K	^{226}Ra:^{238}U	^{210}Pb:^{226}Ra	^{228}Th:^{228}Ra	
WEL15-2(6)	510	13.9 ± 1.5	11.9 ± 0.3	14.8 ± 1.5	17.6 ± 0.7	18.1 ± 0 5	55.1 ± 2.7	0.86 ± 0.10	1.25 ± 0.13	1.03 ± 0.05	0.13 ± 0.02
WEL15-2(7)	580	22.0 ± 2.1	19.9 ± 0.5	23.0 ± 2.6	29.7 ± 1.1	32.8 ± 0 9	60.0 ± 4.2	0.90 ± 0.09	1.15 ± 0.13	1.10 ± 0.05	0.18 ± 0.02
WEL15-2(9)	680	18.9 ± 1.7	17.6 ± 0.4	20.3 ± 2.3	25.2 ± 1.0	27.2 ± 0.7	63.8 ± 3.8	0.93 ± 0.09	1.15 ± 0.13	1.08 ± 0.05	0.19 ± 0.02
WEL15-2(12)	815	20.9 ± 2.9	24.4 ± 0.7	29.8 ± 3.7	36.9 ± 1.6	36.9 ± 1 2	100.6 ± 6.4	1.16 ± 0.17	1.22 ± 0.16	1.00 ± 0.05	0.27 ± 0.03
WEL15-2(2)	1259	10.3 ± 0.9	7.5 ± 0.2	11.9 ± 0.9	13.7 ± 0.5	14.1 ± 0.4	8.5 ± 1.5	0.73 ± 0.07	1.59 ± 0.13	1.03 ± 0.05	0.18 ± 0.01
WEL15-2(1)	1270	4.8 ± 0.5	4.1 ± 0.1	4.6 ± 0.6	4.7 ± 0.3	4.7 ± 0.2	2.9 ± 0.8	0.86 ± 0.10	1.13 ± 0.16	1.01 ± 0.07	0.13 ± 0.01

[a] Measurements made on dried and powdered samples. The specific activities of ^{238}U (determined from ^{235}U emissions after correcting for ^{226}Ra interference, and ^{234}Th emissions after correcting for ^{228}Ra interference), ^{226}Ra (derived from ^{214}Pb and ^{214}Bi emissions), ^{210}Pb, ^{228}Ra (derived from ^{228}Ac emissions), ^{228}Th (derived from ^{212}Pb and ^{208}Tl emissions) and ^{40}K were measured for each sediment sample, and used to derive the daughter-to-parent isotope ratios for ^{226}Ra:^{238}U, ^{210}Pb:^{226}Ra and ^{228}Th:^{228}Ra.

[b] Mean ± total uncertainty (68% confidence interval), calculated as the quadratic sum of the random and systematic uncertainties.

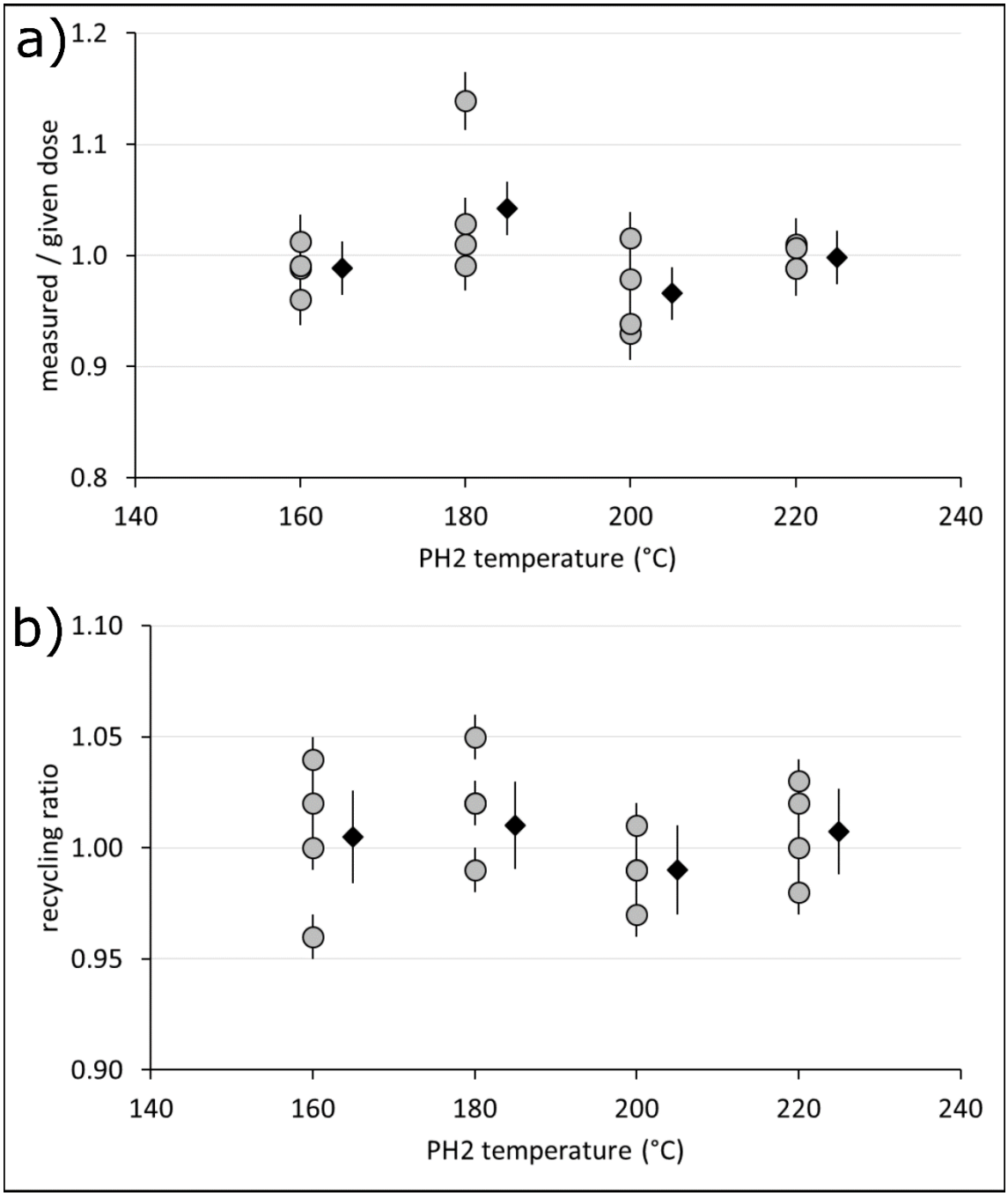

Figure A 1 Multi-grain dose recovery test results obtained for sample WEL15-2(1) after administering a dose of 50 Gy (uncertainties are shown at 1σ). For each test, a fixed natural and regenerative dose preheat (PH1) of 260 °C for 10 s was applied, and the test dose preheat (PH2) temperature was varied, as indicated in the plots (in all cases a PH2 duration of 10 s was used). Plots show (**a**) the recovered dose ratio, (**b**) the recycling ratios obtained for different preheat conditions. D_e measurements were made with a modified version of SAR protocol (replacing single-grain laser stimulations in steps 4 and 7 of Table A1 with blue LED OSL stimulations performed at 125 °C for 60 s) using various test dose preheat (PH2) conditions. D_e measurements were made on multi-grain aliquots containing ~1000 quartz grains.

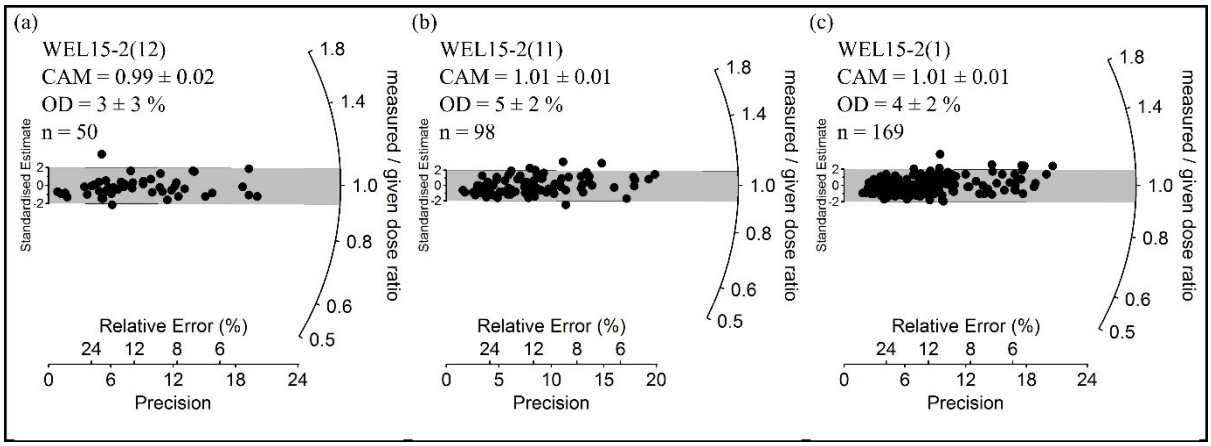

Figure A 2 Radial plots showing single-grain OSL dose recovery test results obtained for 212 – 250 μm quartz grains of samples. (a) WEL15-2(12); (b) WEL15-2(11); (c) WEL15-2(1); using the SAR protocol in Table A1 (D_e uncertainties are shown at 1σ). Grains were bleached within the Risø reader chamber using blue LEDs prior to administering a dose of 100 Gy. The central age model (CAM) measured-to-given dose ratio and the overdispersion (OD) is labelled next to each sample.

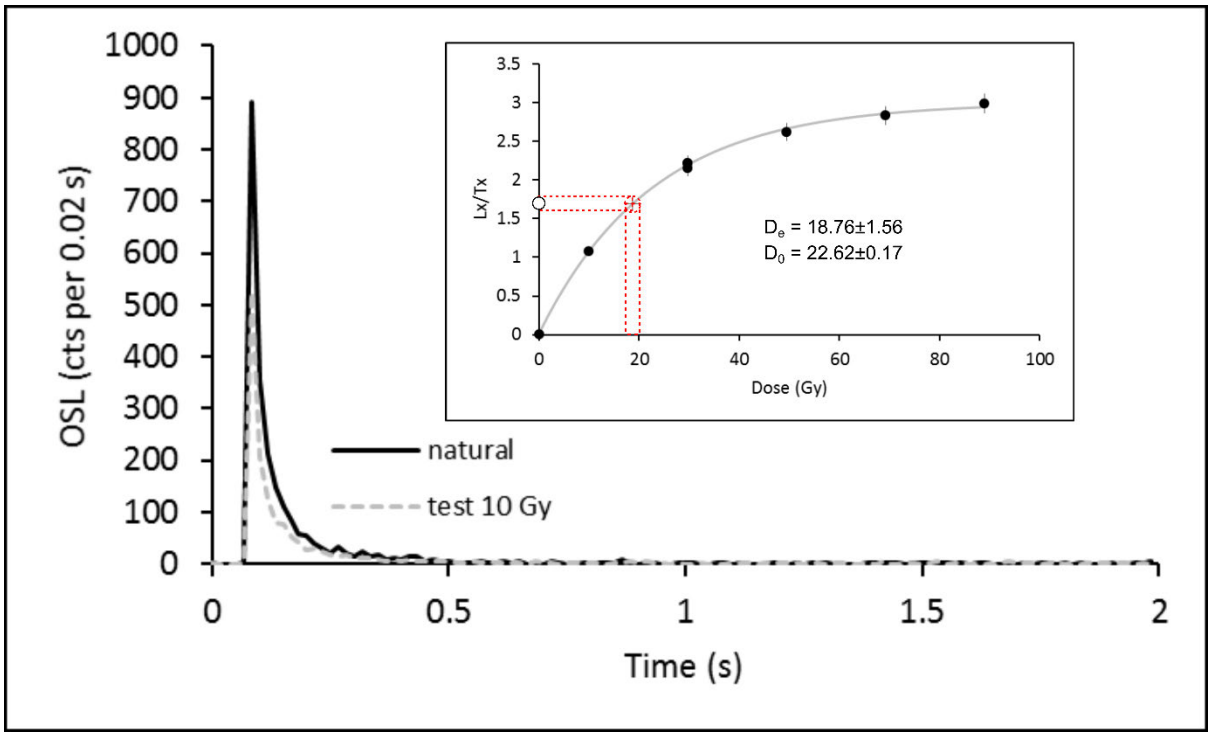

Figure A 3 Example of suitable single-grain OSL decay and dose response curve for an accepted quartz grain from WL15-2(3). The inset shows the sensitivity-corrected OSL signal through the regenerative cycles (black filled circles) and the sensitivity-corrected natural signal (open circle) from which the D_e value was derived. The D_0 value characterises the rate of signal saturation with respect to administered dose and equates to the dose value for which the saturating exponential dose-response curve slope is 1/e (or ~ 0.37) of its initial value. The D_0 value has been calculated for this grain using a single-saturating exponential dose response curve fit.

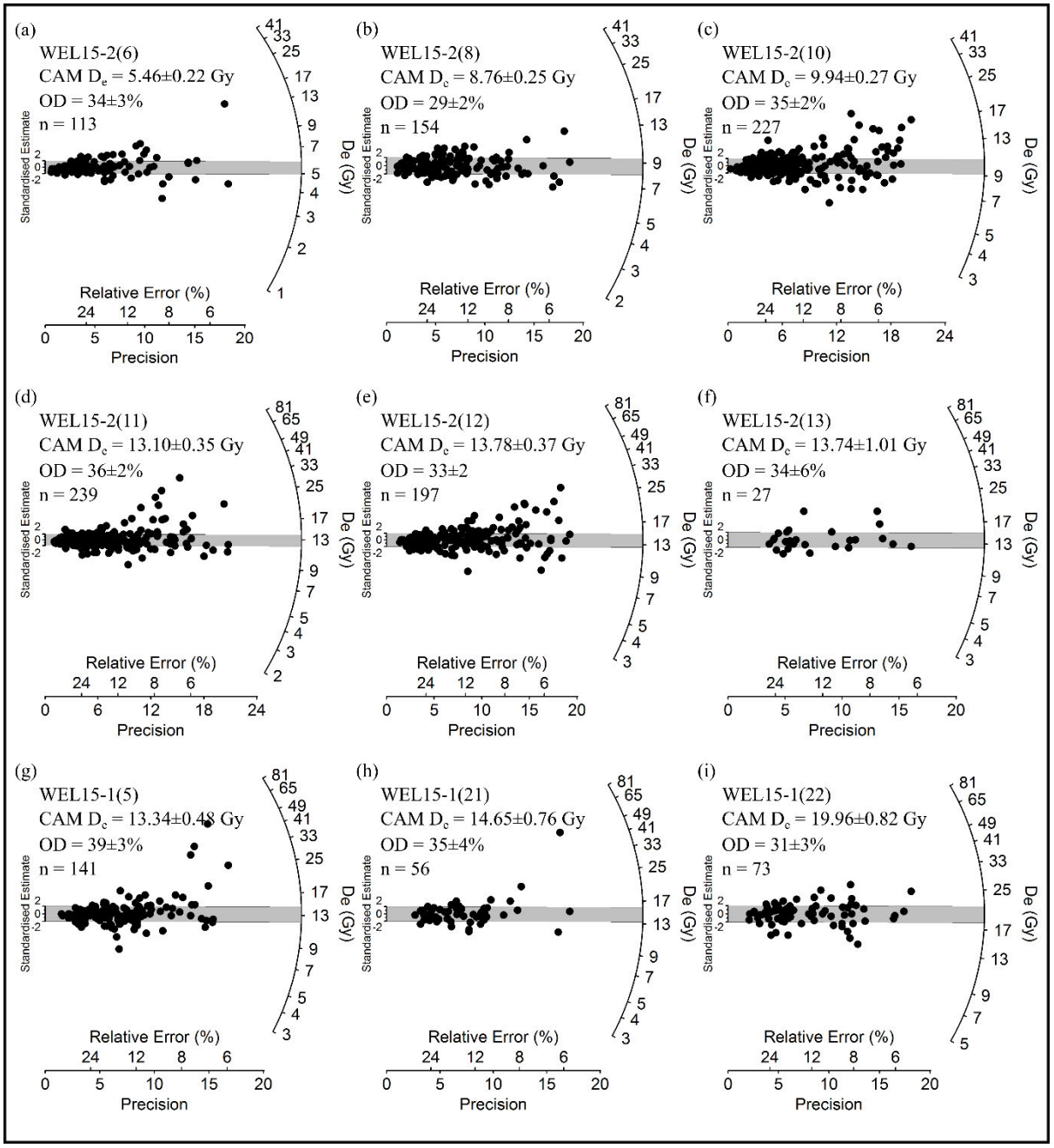

Figure A 4 Radial plots showing the single-grain OSL D_e distributions obtained for the OSL samples from core WEL15-1 and WEL15-2. The plots have been ordered from highest to lowest core position (a-o) relative to WEL15-2. The grey shaded band on each plot is centred on the D_e value (in Gy) used for the final age calculation. The D_e values were calculated using the central age model (CAM) of Galbraith et al. (1999).

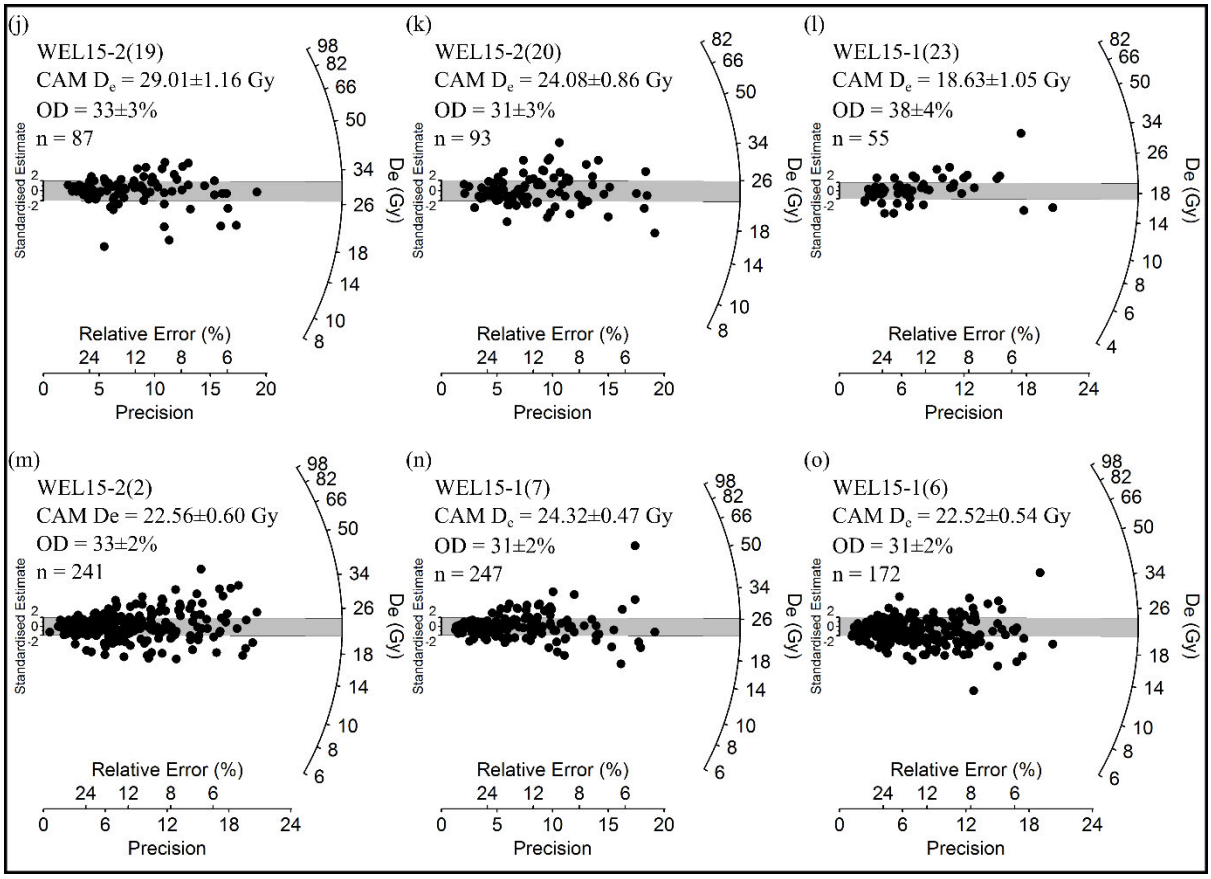

Figure 4 A continued…

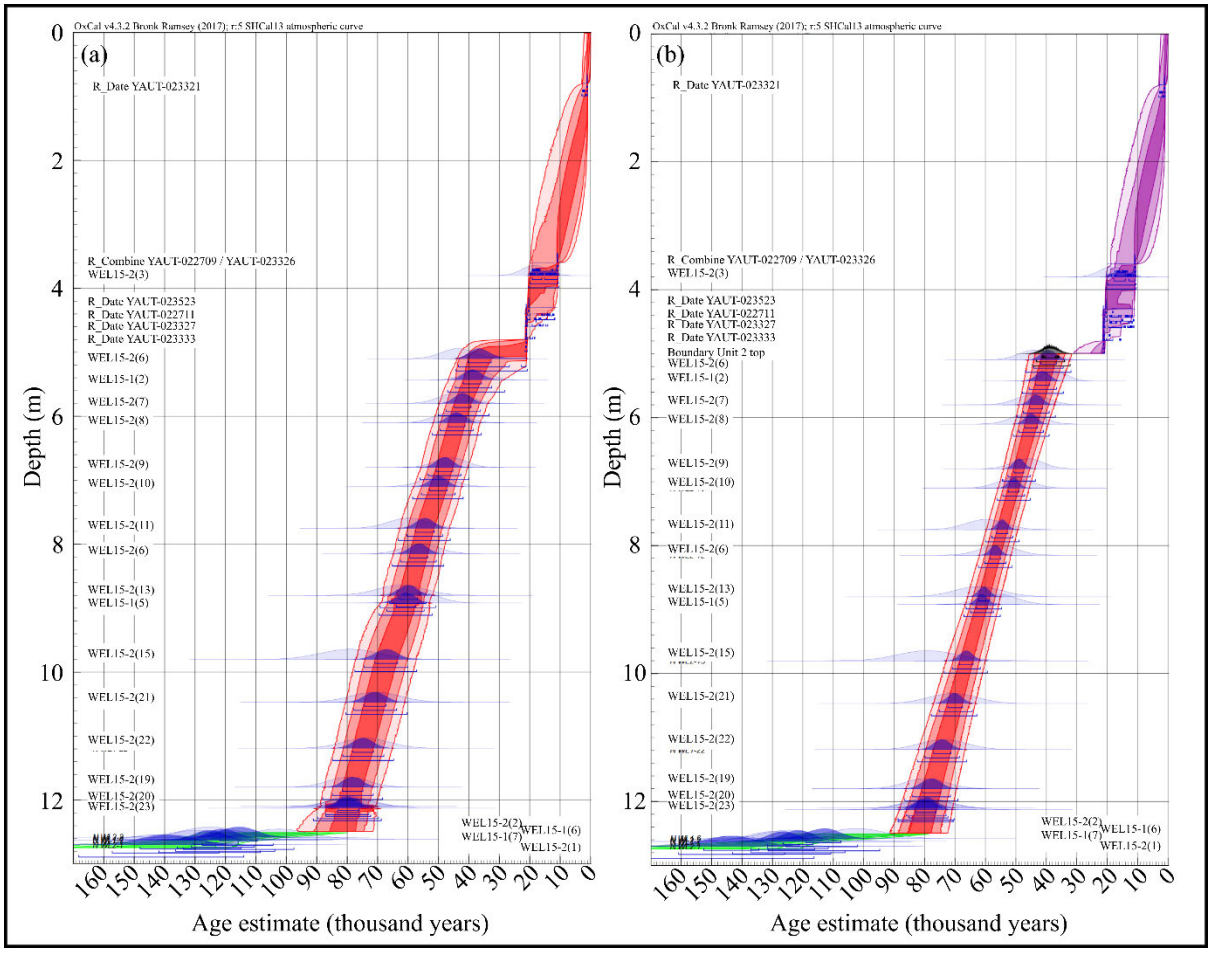

Figure A 5 Alternative Bayesian age-depth modelling results for the Welsby Lagoon sequence when applying different stratigraphic prior assumptions and boundary schemes. The original dating likelihood probabilities (prior to modelling) and posterior (mathematically modelled) distributions are shown using pale and dark shading, respectively. The different sedimentological units defined within the model(s) are represented by different colours, (green, red and magenta), with darker shades representing the 68 %, 95 % and 99 % confidence intervals of the modelled age ranges for a given depth. (a) Modelling output obtained when assuming a single, uninterrupted lacustrine sedimentation phase following establishment of the wetland basin (i.e., no boundary is included at a depth of 500 cm). (b) Modelling output for a scenario that does not presume continuous wetland deposition and is able to accommodate potential hiatuses and/or erosional discontinuities between the various sedimentary units (i.e., the three depositional phases are represented by separate *P_Sequences*, each with delineating start and end boundaries, nested within a master *Sequence*).

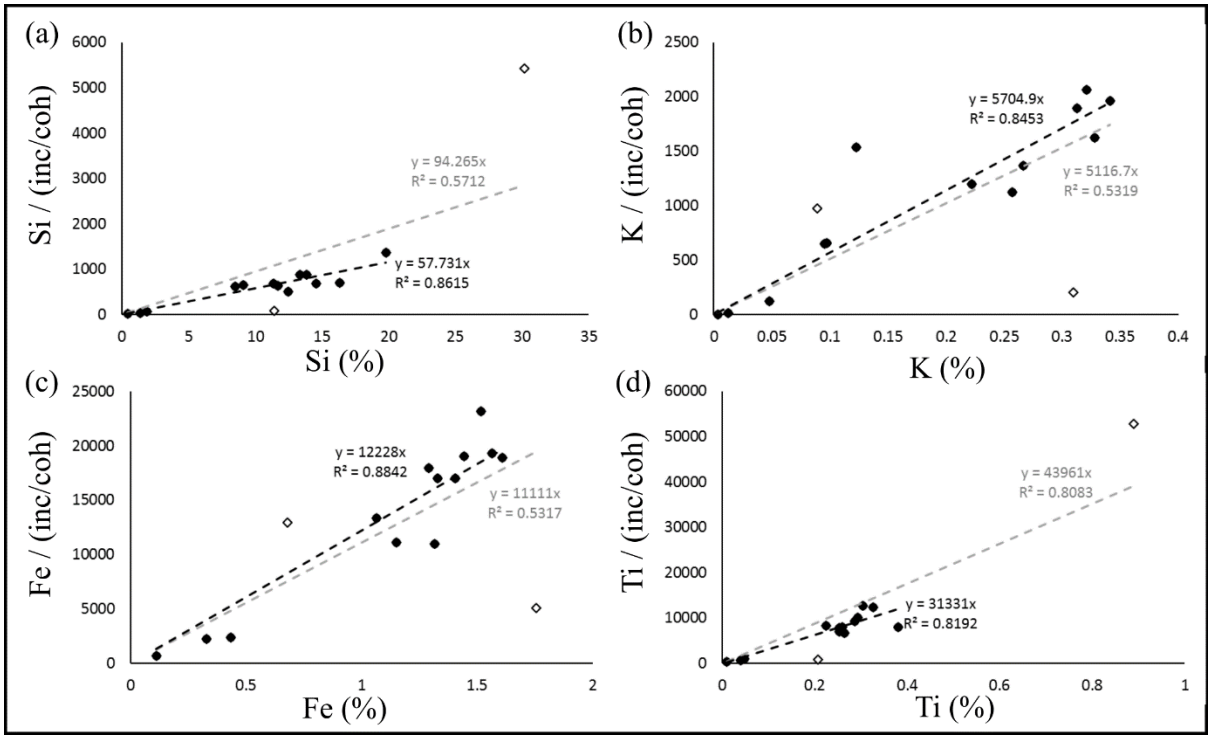

Figure A 6 Calibration of Itrax micro-XRF core scanner element intensities (normalised to ratio of incoherent (inc) and coherent (coh) scatter) using element concentration calculated from WD-XRF measurements for the WEL sequence. The elemental count calibration for (a) Si, (b) K, (c) Fe and (d) Ti are shown as linear trends that intercept the origin. Data used in the calibration are represented by filled diamonds and plotted with a dark-dashed line. Data excluded from the final calibration are shown as open diamonds with the corresponding calibration line plotted as a light-dashed line.

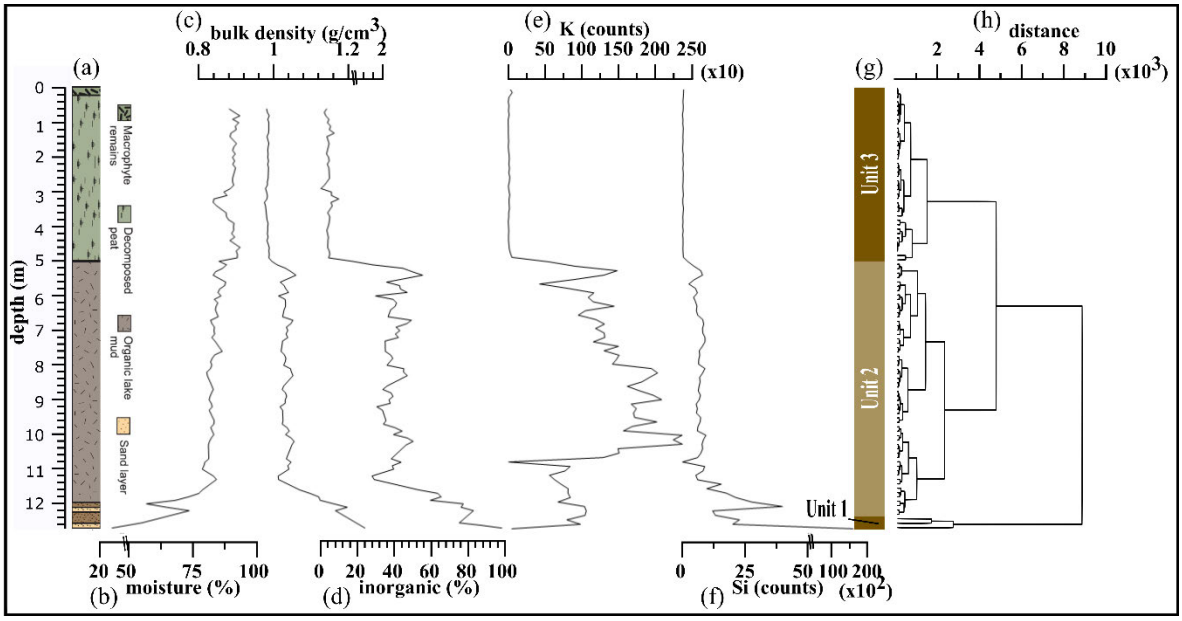

Figure A 7 Identification of sedimentological units within the WEL sequence using geochemical data in combination with a hierarchical cluster analysis. Left to right: (a) sediment lithology presented by Cadd et al., 2018; (b) moisture content expressed as % wet weight; (c) bulk density; (d) inorganic content % dry weight (e) variation in the accumulation of far-travelled material (K counts); (f) variation in the accumulation of local material (Si counts); (g) sedimentary Units 1 – 3 adjacent to the (h) Cluster Dendrogram produced following depth-constrained hierarchical clustering analysis to determine the respective boundaries.

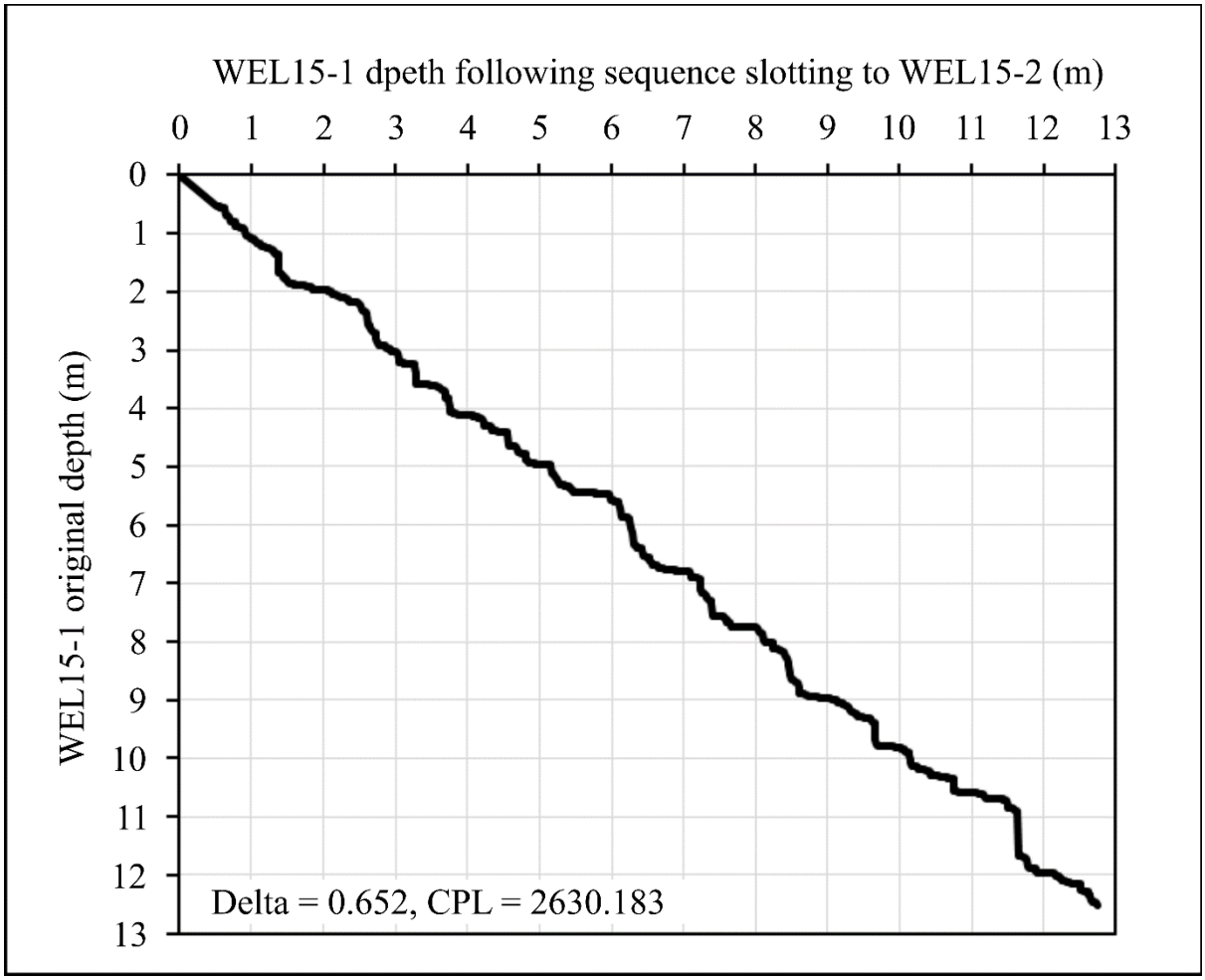

Figure A 8 WEL15-1 correlation plot output following sequence slotting of WEL15-1 to WEL15-2 in CPL Slotter using Si, K, Ti and Fe as input variables. The plot shows the depth change for WEL15-1 that results in the best correlation of variables to WEL15-2 when using the following user-defined constraints: (i) the basal sand layer of WEL15-2 that underlies the peat, a feature not observed in WEL15-1, must be the lowest part of the sequence; (ii) above the basal sand layer and to 0.5 m below the sediment surface WEL15-1 and WEL15-2 must overlap; (iii) between the surface to 0.5 m below, WEL15-1 depths remain unchanged. Delta is the quality of match statistic as discussed in Thompson & Clark (1989).

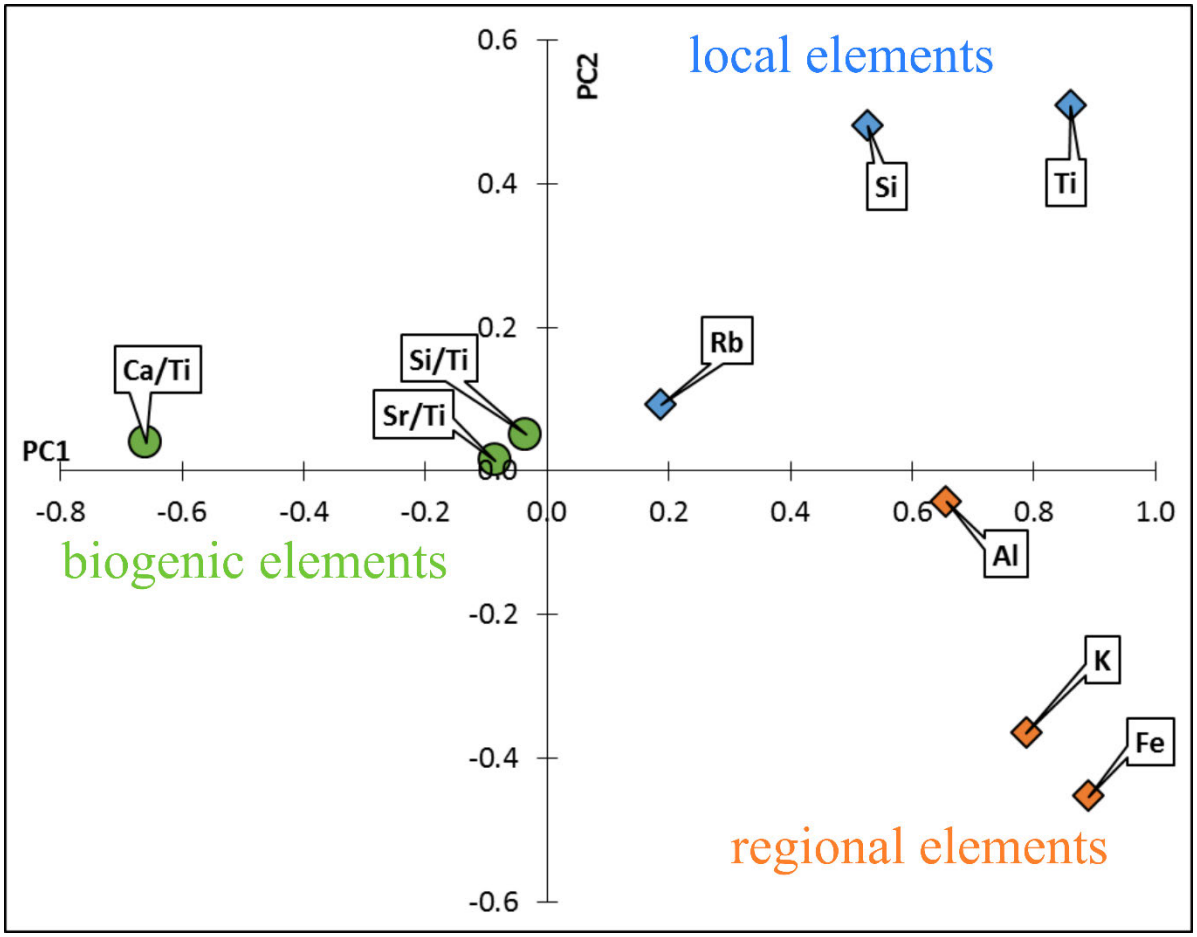

Figure A 9 Ordination diagram showing the first and second principal components (x-axis = PC1; y-axis = PC2) for data acquired using scanning XRF. Elements with high loadings on the PC1 axis are associated with terrigenous origins and shown as diamonds while biogenic sediments are circles. Elements with high loadings on PC2 are shown in blue and represent a proximal source, while orange is far-travelled dust.

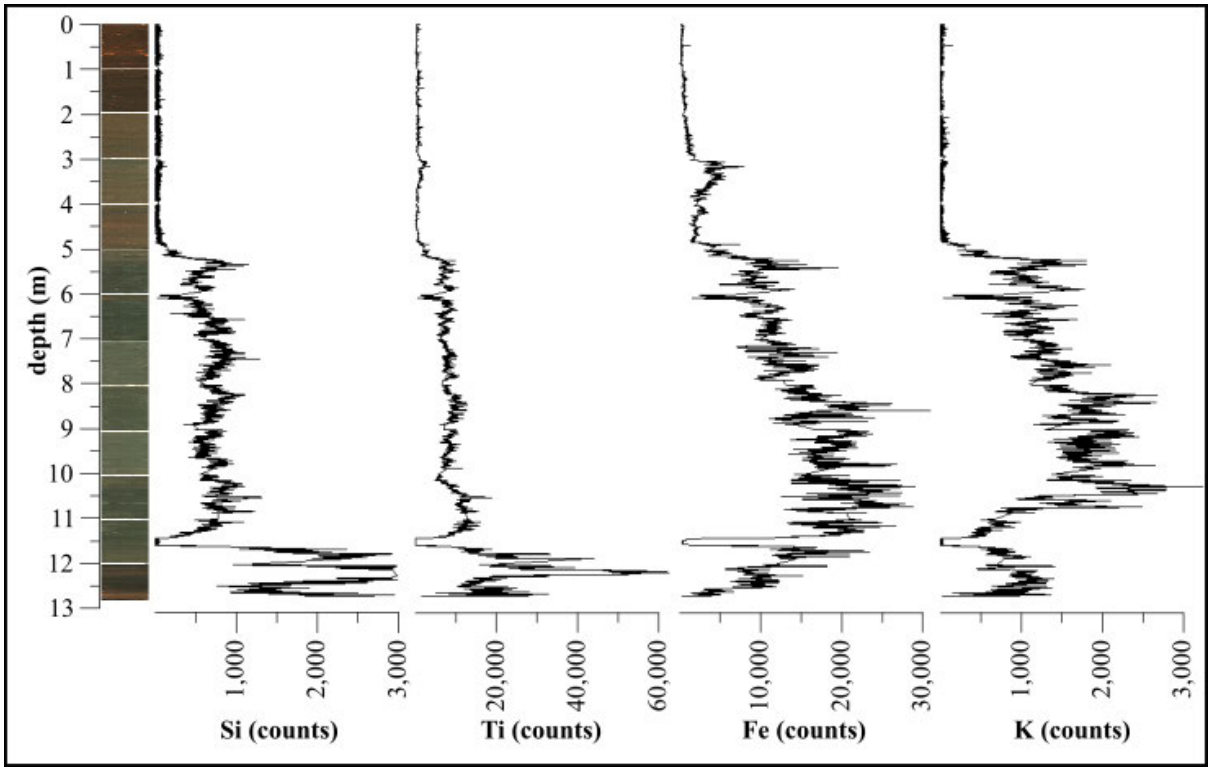

Figure A 10 Bulk sediment geochemical profile of WEL15-1 showing optical images and elemental data measured as counts from Itrax core scanning.

A3. References

Aitken, M. J. 1985. Thermoluminescence dating: Past progress and future trends. Nuclear Tracks and Radiation Measurements (1982), 10, 3-6.

Aitken, M. J. 1998. An introduction to optical dating: the dating of Quaternary sediments by the use of photon-stimulated luminescence, Oxford, Oxford University Press.

Arnold, L. J., Demuro, M., Navazo, M., Benito-Calvo, A. & Pérez-González, A. 2013. OSL dating of the Middle Palaeolithic Hotel California site, Sierra de Atapuerca, north-central Spain. Boreas, 42, 285-305.

Arnold, L. J., Duval, M., Demuro, M., Spooner, N. A., Santonja, M. & Pérez-González, A. 2016. OSL dating of individual quartz 'supergrains' from the Ancient Middle Palaeolithic site of Cuesta de la Bajada, Spain. Quaternary Geochronology, 36, 78-101.

Arnold, L. J. & Roberts, R. G. 2011. Paper I – Optically stimulated luminescence (OSL) dating of perennially frozen deposits in north-central Siberia: OSL characteristics of quartz grains and methodological considerations regarding their suitability for dating. Boreas, 40, 389-416.

Brennan, B. J. 2003. Beta doses to spherical grains. Radiation Measurements, 37, 299-303.

Bronk Ramsey, C. 2009. Dealing with outliers and offsets in radiocarbon dating. Radiocarbon, 51, 1023-1045.

Bronk Ramsey, C. & Lee, S. 2013. Recent and planned developments of the program OxCal. Radiocarbon, 55, 720-730.

Cadd, H. R., Tibby, J., Barr, C., Tyler, J., Unger, L., Leng, M. J., Marshall, J. C., Mcgregor, G., Lewis, R. & Arnold, L. J. 2018. Development of a Southern Hemisphere subtropical wetland (Welsby Lagoon, south-east Queensland, Australia) through the last glacial cycle. Quaternary Science Reviews, 202, 53-65.

Duller, G. a. T. 2003. Distinguishing quartz and feldspar in single grain luminescence measurements. Radiation measurements, 37, 161-165.

Duller, G. a. T. 2007. Luminescence Analyst. 3.24 ed. University of Wales, Aberystwyth: Aberystwyth Luminescence Research Laboratory.

Galbraith, R. F., Roberts, R. G., Laslett, G. M., Yoshida, H. & Olley, J. M. 1999. Optical dating of single and multiple grains of quartz from Jinmium rock shelter, northern Australia: Part I, experimental design and statistical models. Archaeometry, 41, 339-364.

Guérin, G., Mercier, N. & Adamiec, G. 2011. Dose-rate conversion factors: update. Ancient TL, 29, 5-8.

Hogg, A. G., Hua, Q., Blackwell, P. G., Niu, M., Buck, C. E., Guilderson, T. P., Heaton, T. J., Palmer, J. G., Reimer, P. J. & Reimer, R. W. 2013. SHCal13 Southern Hemisphere calibration, 0–50,000 years cal BP. Radiocarbon, 55, 1889-1903.

Jacobs, Z., Duller, G. A., Wintle, A. G. & Henshilwood, C. S. 2006. Extending the chronology of deposits at Blombos Cave, South Africa, back to 140 ka using optical dating of single and multiple grains of quartz. Journal of Human Evolution, 51, 255-273.

Lian, O. B., Hu, J., Huntley, D. & Hicock, S. R. 1995. Optical dating studies of Quaternary organic-rich sediments from southwestern British Columbia and northwestern Washington State. Canadian Journal of Earth Sciences, 32, 1194-1207.

Mejdahl, V. 1979. Thermoluminescence dating: Beta-dose attenuation in quartz grains. Archaeometry, 21, 61-72.

Olley, J. M., Murray, A. & Roberts, R. G. 1996. The effects of disequilibria in the uranium and thorium decay chains on burial dose rates in fluvial sediments. Quaternary Science Reviews, 15, 751-760.

Olley, J. M., Roberts, R. G. & Murray, A. S. 1997. Disequilibria in the uranium decay series in sedimentary deposits at Allen's Cave, Nullarbor Plain, Australia: implications for dose rate determinations. Radiation Measurements, 27, 433-443.

Prescott, J. R. & Hutton, J. T. 1994. Cosmic ray contributions to dose rates for luminescence and ESR dating: large depths and long-term time variations. Radiation measurements, 23, 497-500.

Preusser, F. & Degering, D. 2007. Luminescence dating of the Niederweningen mammoth site, Switzerland. Quaternary International, 164-165, 106-112.

Rees-Jones, J. 1995. Optical dating of young sediments using fine-grain quartz. Ancient TL, 13, 9-14.

Rees-Jones, J. & Tite, M. S. 1997. Optical dating results for British archaeological sediments. Archaeometry, 39, 177-187.
Stokes, S., Ingram, S., Aitken, M. J., Sirocko, F., Anderson, R. & Leuschner, D. 2003. Alternative chronologies for Late Quaternary (Last Interglacial–Holocene) deep sea sediments via optical dating of silt-sized quartz. Quaternary Science Reviews, 22, 925-941.
Thompson, C. H. 1992. Genesis of Podzols on Coastal Dunes in Southern Queensland. I. Field Relationships and Profile Morpholog. Australian Journal of Soil Research, 30, 593-613.
Thompson, R. & Clark, R. 1989. Sequence slotting for stratigraphic correlation between cores: theory and practice. Paleolimnology, 2, 173-184.

Appendix B. Supplementary Information for Chapter 3

This Appendix contains supplementary information that accompanies Chapter 3, which has been published in *Quaternary Research* as:

Lewis, R. J., Tibby, J., Arnold, L. J., Gadd, P., Jacobsen, G., Barr, C., Negus, P. M., Mariani, M., Penny, D., Chittleborough, D. & Moss, E. 2021. Patterns of aeolian deposition in subtropical Australia through the last glacial and deglacial periods. Quaternary Research, 1-23.

B1. OSL dating

B1.1. Preparation

Purified quartz fractions were extracted from the wetland (BL18) and dune (NSI18) cores under "safe light conditions" (subdued red lighting), to prevent any bleaching of the natural burial dose signal. The organic-rich BL18 sample was treated with 10 % NaOH to disperse particles before being wet sieved to isolate the material with Ø 180-212 μm. Meanwhile, the NSI18 samples were mechanically sieved to obtain mineral fractions of Ø 212-250 μm. The mineral fractions were then treated with 30 % HCl and 30 % H_2O_2, including a rinse cycle between each treatment, to dissolve carbonates and organic material, respectively (Aitken, 1998). Quartz was isolated from other minerals through heavy liquid separation, using LST prepared at densities 2.72 g/cm^3 and 2.62 g/cm^3. The alpha-irradiated outer rind of the isolated quartz grains was then etched using 48 % HF for 40 mins, followed up by a treatment with 30 % HCl to dissolve any fluoride precipitates.

B1.2. Instrumentation

A Risø TL-DA-20 reader equipped with blue LEDs, an array of infrared LEDs, and a 10 mW Nd:YVO_4 single-grain laser attachment emitting at 532 nm was used to measure the OSL signals. Ultraviolet OSL signals were detected using an EMI9235QA photomultiplier tube, fitted with 7.5 mm thick Hoya U-340 filters. Samples were irradiated with a $^{90}Sr/^{90}Y$ β source that had been calibrated for individual grain-hole positions to account for spatial variations in beta dose rate across each disk.

B1.3. D_e measurement conditions

Individual D_e values were determined using the single-aliquot regenerative-dose (SAR) procedure shown in Table B2. The suitability of the chosen SAR measurement conditions was evaluated using a dose-recovery test on samples NSI18-4. For this purpose, the natural signals of four multigrain disks (each containing ~1,000 quartz grains) were bleached using two cycles of 1,000 s blue LED exposure, separated by a 10,000 s pause. The disks were then administered a dose of 65 Gy before a multi-grain version of the SAR procedure was undertaken (replacing single-grain laser stimulations in steps 4 and 7 of Table B2 with blue LED stimulations) using different test dose preheat (PH2) conditions (Figure B4). A preheat of 260 °C for 10 s prior to measurement of the natural (L_n) or regenerative dose (L_x), and a preheat of 220 °C for 10 s prior to the test-dose (T_n or T_x) provided accurate dose recovery ratios (Figure B4). These conditions were then validated by subsequent single-grain dose recovery measurements repeated on samples NSI18-4, NSI18-7, and BL18-A; yielding measured to given dose recovery ratios of 0.98 ± 0.02, 1.02 ± 0.02 and 0.99 ± 0.01, respectively (Figure B5). These single-grain dose recoveries produced low overdispersion values ranging from 5 ± 2% to 8 ± 2%.

OSL signals from individual grains were assessed against a series of quality assurance criteria (Arnold et al., 2016; Demuro et al., 2019) prior to inclusion in the final age calculation. Grains were considered inappropriate and excluded from D_e analysis if: (i) their net T_n signals were <3σ above the late-light background; (ii) recycling ratios (sensitivity-corrected luminescence responses (L_x/T_x) for two identical regenerative doses) were not consistent with unity at 2σ. For the single-grain OSL measurements, the recycling ratio test was performed using both a low-dose and high-dose regenerative dose cycle; (iii) the OSL-IR depletion ratio (Duller, 2003) was less than unity at 2σ; (iv) the recuperation ratio, calculated as the ratio of the sensitivity-corrected 0 Gy dose point (L_0/T_x) to the sensitivity-corrected natural (L_n/T_n), was >5 %; (v) the L_n/T_n value intercepted the saturated part of the dose-response curve (L_n/T_n values were equal to Imax saturation limit of the dose-response curve

at 2σ); (vi) the dose-response curve displayed anomalous properties (i.e., zero or negative response with increasing dose) or very scattered L_x/T_x values that could not be successfully fitted with the Monte Carlo procedure; (vii) the sensitivity-corrected natural signal (L_n/T_n) did not intercept the sensitivity-corrected dose-response curve; (viii) the net D_e uncertainty was >50 %. The rejection statistics from the evaluation of single-grain OSL responses are presented in Table B3, with an example of an accepted grain's dose response and OSL characteristics presented in Figure B6.

D_e values for individual grains were derived from the integration of the first 0.2 s of emission counts, minus a background count from the last 0.25 s of stimulation. Dose response curves were fitted using a single saturating exponential function, with curve fitting uncertainty determined from 1,000 iteration of the Monte Carlo method (Duller, 2007). Single-grain D_e uncertainties additionally incorporate an empirically determined instrument reproducibility uncertainty of 2.5 % for each OSL measurement (calculated for the Risø reader used in this study, following the approach outlined in Jacobs et al. (2006)).

B1.4. Dose rate determination

Tables B1, B7 and B8 summarise the environmental dose rate results for the OSL samples. The high-resolution gamma spectrometry results confirm that the dune sediments dated in this study are in present-day secular equilibrium (daughter-parent isotopic ratios for ^{238}U and ^{232}Th series are consistent with unity at either 1σ or 2σ; Table B8). For all six samples, the final beta dose rates derived using high-resolution gamma spectrometry are in agreement at either 1 or 2σ with those obtained using beta counting (Table B1), supporting the suitability of the dose rate evaluation procedures. Figure B11 confirms that the dune OSL ages are relatively insensitive to our choice of long-term water content. Use of the present-day (as measured) water content, our preferred long-term estimate (7 ± 3 % dry weight), and the measured saturated water content of these samples all produce final ages that are in agreement at 1σ (Figure B11).

B2. Radiocarbon (^{14}C) dating

The samples were dried, milled into powder and prepared using standard ABA treatments (Brock et al., 2010). This included repeating the steps (for up to 8 cycles) of reacting with 5 % HCl to remove contaminant carbonates, a hot ultrasonic wash and dissolution of fulvic acids using up to 2M of NaOH. After pre-treatment, the samples were dried, combusted and loaded into a Pyrex tube with suitable amounts of copper granules and silver. The tubes were then placed under vacuumed, sealed and placed in a furnace overnight at a temperature of 580 °C. The released CO_2, following combustion of the samples, was transferred through vacuum lines into an additional Pyrex tube prior to graphitization. Measurements were then undertaken at the respective AMS facilities.

B3. Lake sequence age modelling

B3.1. Method

The preliminary version of the BL18 age-depth model was produced, incorporating the replicate OZX94a and OZX94b ^{14}C ages. However, the modelled likelihood estimates failed to converge, with these two samples identified as statistical outliers (79 %) owing to their incompatibility with the surrounding OSL (BL18-A) and ^{14}C ages (OZX793 and OXZ792). As such, these two major outliers were not included in the final Bayesian age-depth model for BL18 (Figure 3.6).

Differences in bottom lake sediment topography through time, inferred from modern bathymetry (Figure 3.2), were considered when developing the age models for the two cores and rather than assuming uniform sediment deposition, individual age models were produced for the separate cores. The sequences were modelled using a Poisson depositional framework (*P_Sequence*) with the base rigidity perimeter (k_0) set to a single event per 1 cm of sedimentation and allowed to vary between 0.01 to 100 events per cm to account for randomly variable deposition rates (Bronk Ramsey, 2008, 2009; Bronk Ramsey & Lee, 2013). Posterior dated events have been interpolated at 1 cm intervals throughout the sequence. A general outlier function has been included in the model, with an assigned prior outlier probability of 5 % used to identify potentially significant statistical outliers (Bronk Ramsey, 2009). Likelihood estimates that yielded posterior outlier probabilities >5 % were not excluded from the final model but were proportionally downweighed in the iterative Monte Carlo runs.

Each depositional unit is represented by a separate *P_Sequence* with delineating start and end boundaries, nested within a master *Sequence* according to stratigraphic priors. This type of modelling framework is considered advantageous for lacustrine sequences that exhibit notable sedimentological changes, as it does not presume continuous wetland deposition over time and is able to accommodate potential hiatuses or erosional discontinuities (or both) between the various sedimentary units (e.g., Fu et al., 2017).

B3.2. Results

The models selected to best represent the BL18 and BL09 sediment records include three units (represented by separate nested *P_Sequences*), each of which includes a starting and ending boundary to account for intervening depositional hiatuses or erosion events. In the BL18 model, the starting and ending *P_Sequence* unit boundaries were specified at depths of 3.57 – 2.29 m (Unit 1), 2.29 – 1.65 m (Unit 2) and 1.65 – 0.00 m (Unit 3) (Figure 3.2). These modelling priors were chosen based on the sedimentology results, as well as preliminary palynology analyses of the cores; in particular, that of BL18 where the white sand of sub-unit 2.1 overlies highly organic lake muds of sub-unit 1.2 (Figure 3.3) and fossil pollen assemblages vary abruptly. A first qualitative assessment of the pollen samples at 230 cm shows a sudden shift from an Araucaria- to a Eucalyptus/Allocasuarina-dominated assemblage. The overlying sedimentary section, sub-unit 2.2 (which grades from light brown into dark brown organic rich lake muds) is interpreted as forming during fluctuating lake levels. This is supported by what is inferred to be coatings of clay minerals and iron oxyhydroxides, perhaps ferrihydrite, which, if so, would indicate fluctuation of the water table and provide a means to provenance aeolian material. As noted earlier, the sedimentological units from BL09 can be linked to those defined in the BL18 core, allowing direct comparison of the age model results for the two cores, and consideration of a conceptual theory of sediment deposition across the basin through time (Figure 3.7).

According to the OxCal *Difference* query, the Bayesian model does not support a statistically significant depositional hiatus in BL18 (or BL09) between Unit 2 (Unit B) and Unit 1 (Unit A). However, this interpretation may simply reflect the low dating resolution of BL18 Unit 2, which contains only one likelihood, and the absence of direct age constraint for BL09 Unit B, which likely limits the precision of the model at this boundary contact. The youngest units in both cores (BL09 – Unit C; BL18 – Unit 3) began to develop at 8.5 ± 1.8 ka and 8.0 ± 0.2 ka, with accumulation

continuing up to the present. While there is no evidence of a statistically significant break in deposition between the upper two units of the BL09 model, the OxCal *Difference* query does identify a statistically significant hiatus in the BL18 model between Unit 3 and Unit 2 spanning ~2.0 – 12.2 ka (95 % confidence interval). This disparity between the two records may be a result of heterogeneous accumulation or erosion of sediment across the basin, or the lower dating resolution of the BL09 core between the Unit 2 boundaries (Figure 6).

B4. µXRF core scanning

An Itrax µXRF was used to measure the elemental abundance down the sediment profile of the overlapping and vertically offset BL18-3 and BL18-4 cores, in addition to the single BL09 core. Prior to measurement, the surface of the sediment to be scanned was prepared to minimise the effect of changes in surface topography. Photon emissions were measured every millimetre following stimulation with a molybdenum (Mo) tube (30 kV, 55 mA and dwell time of 10 s), with 35 elements used during the integration of the total count signal (Al, Si, P, S, Cl, Ar, K, Ca, Ti, V, Cr, Mn, Fe, Ni, Cu, Zn, Br, Rb, Sr, Y, Zr, Sn, Sb, Cs, Ba, La, Nd, Eu, Gd, Tb, Dy, Tm, Hf, Pb, Bi).

Table B 1 Environmental dose rates for the Brown Lake and North Stradbroke Island dune samples.

			Water Content (% dry mass) [a]			Environmental dose rate (Gy/ka) [b, c, d, e, f, g]				
Sample ID	**Depth (cm)**	**Grain size (µm)**	**Beta**	**Gamma**	**Cosmic**	**Beta**	**Gamma**	**Internal**	**Cosmic**	**Total**
BL18-A	351	180 – 212	253 ± 13	242 ± 12	340 ± 17	0.22 ± 0.028	0.39 ± 0.009	0.02 ± 0.007	0.04 ± 0.004	0.67 ± 0.04
NSI18-1	160	212 – 250	7 ± 3	7 ± 3	7 ± 3	0.06 ± 0.005	0.08 ± 0.004	0.02 ± 0.007	0.16 ± 0.016	0.33 ± 0.02
NSI18-2	150	212 – 250	7 ± 3	7 ± 3	7 ± 3	0.10 ± 0.007	0.12 ± 0.006	0.02 ± 0.007	0.17 ± 0.017	0.41 ± 0.03
NSI18-3	183	212 – 250	7 ± 3	7 ± 3	7 ± 3	0.19 ± 0.016	0.21 ± 0.009	0.02 ± 0.007	0.16 ± 0.016	0.58 ± 0.04
NSI18-4	170	212 – 250	7 ± 3	7 ± 3	7 ± 3	0.05 ± 0.005	0.06 ± 0.003	0.02 ± 0.007	0.16 ± 0.015	0.30 ± 0.02
NSI18-5	70	212 – 250	7 ± 3	7 ± 3	7 ± 3	0.35 ± 0.019	0.71 ± 0.029	0.02 ± 0.007	0.18 ± 0.018	1.26 ± 0.07
NSI18-6	170	212 – 250	7 ± 3	7 ± 3	7 ± 3	0.08 ± 0.006	0.08 ± 0.004	0.02 ± 0.007	0.16 ± 0.016	0.35 ± 0.02
NSI18-7	130	212 – 250	7 ± 3	7 ± 3	7 ± 3	0.12 ± 0.008	0.09 ± 0.004	0.02 ± 0.007	0.17 ± 0.017	0.40 ± 0.03

[a] Long-term water contents used for beta / gamma / cosmic-ray dose rate attenuation, respectively, expressed as % of dry mass of mineral fraction, with an assigned relative uncertainty of ±5%. For sample BL18-A, the final beta dose rate has been adjusted for moisture attenuation using the measured water contents determined from the midpoint of the OSL sample depth. The final gamma dose rate has been adjusted using the average water content measured from the OSL sample midpoint, as well as from 1 cm^3 bulk sediment samples collected for the overlying and underlying 10 cm depth. The final cosmic-ray dose rate has been adjusted using the average water content measured from 1 cm^3 bulk sediment samples collected at 1 cm intervals throughout the overlying core sequence. For the NSI18 samples, beta, gamma and cosmic dose rates have been corrected using a fixed long-term water content of 7 ± 3 %, following approaches used in comparable OSL dating studies of dune deposits in the region (e.g., Ellerton et al., 2020).

[b] Beta dose rates were calculated on dried, powdered sediment samples using a combination of ICP-MS and ICP-OES (sample BL18-A) or a Risø GM-25-5 low level beta counting (all other samples), after making allowance for beta dose attenuation due to grain-size effects and HF etching (Brennan, 2003; Mejdahl, 1979).

[c] Dose rate value represent mean ± total uncertainty (68% confidence interval), calculated as the quadratic sum of the random and systematic uncertainties.

[d] Gamma dose rates were calculated using a combination of ICP-MS and ICP-OES measurements performed on dried, powdered sediment samples (sample BL18-A) or from *in situ* gamma-ray spectrometry measurements made at each sample position with a NaI:Tl detector, using the 'energy windows' approach (Arnold et al., 2012) (all other samples).

[e] Specific activities and radionuclide concentrations have been converted to dose rates using the conversion factors given in Guérin et al. (2011).

[f] An internal dose rate of 0.02 ± 0.01 Gy / ka has been included in the final dose rate calculations, based on measurements made on etched quartz grains from North Stradbroke Island (Lewis et al., 2020).

[g] Cosmic-ray dose rates were calculated using the approach of Prescott & Hutton (1994), and assigned a relative uncertainty of ±10%.

Table B 2 Single-aliquot regenerative-dose (SAR) procedure used for single-grain D_e determination. The SAR measurement cycle shown here was repeated for the natural dose, different-sized regenerative doses - including a 0 Gy regenerative dose (to measure OSL signal recuperation). Both the smallest and largest non-zero Gy regenerative dose cycles were repeated at the end of the SAR procedure to assess the suitability of the test dose sensitivity correction. The smallest regenerative dose cycle was then repeated a second time with the inclusion of step 2 to check for the presence of feldspar contaminants using the OSL IR depletion ratio of Duller (2003). L_x = regenerative dose signal response; L_n = natural dose signal response; T_x = test dose signal response for a laboratory dose cycle T_n = test dose signal response for the natural dose cycle.

Step	Treatment	Symbol
1	Dose (natural or laboratory)	N or D
2 [a]	IRSL stimulation (50 C for 60 s)	
3	Preheat 1 (260 C for 10 s)	PH1
4	Single-grain OSL stimulation (125 C for 2 s)	L_n or L_x
5	Test dose (10 Gy)	T_d
6	Preheat 2 (220 C for 10 s)	PH2
7	Single-grain OSL stimulation (125 C for 2 s)	T_n or T_x
8	Repeat measurement cycle for different sized regenerative doses	

[a] Step 2 is only included in the single-grain OSL SAR procedure when measuring the OSL IR depletion ratio (Duller, 2003).

Table B 3 Single-grain OSL grain classification statistics, showing proportion of rejected and accepted grains after applying the SAR quality assurance criteria. Data are also shown for the single-grain OSL dose recovery test (DRT) measurements made on samples BL18-A, NSI18-4 and NSI18-7.

			Rejected grains (%)									
				Poor recycling ratio								
Sample	Depth (cm)	Grains measured (n)	T_n <3σ BG	low	high	IR depletion ratio	Recuperation >5%	Saturated	Anomalous DRC	L_n/T_n not intersecting DRC	Relative error of D_e >50%	Accepted grains (%)
BL18-A (DRT)	353	600	41	18	0	12	6	1	1	8	0	13
NSI18-4 (DRT)	170	1100	60	16	1	6	3	2	5	1	0	7
NSI18-7 (DRT)	130	900	52	20	0	8	5	0	6	0	0	9
BL18-A	353	600	45	22	11	7	1	1	2	5	0	8
NSI18-1	160	900	63	17	3	6	3	0	4	0	0	3
NSI18-2	150	900	58	17	5	9	2	1	5	0	0	4
NSI18-3	183	900	63	14	3	7	3	1	5	0	0	4
NSI18-4	170	1100	61	15	5	6	2	2	5	1	0	3
NSI18-5	70	1600	58	17	4	7	2	5	5	1	0	2
NSI18-6	170	600	54	18	4	6	4	1	7	1	0	6
NSI18-7	130	1100	53	17	5	8	6	0	5	0	0	5

Table B 4 Finite mixture model fitting results for sample NSI18-4, which exhibits a D_e distribution with multiple dose components. The FMM was fitted by varying the common overdispersion (OD) parameter between 20 % and 30 % (to adequately cover the range of overdispersion observed in 'ideal' (well-bleached and unmixed) sedimentary samples from this study (BL18-A, NSI18-1, NSI18-2, NSI18-3 and NSI18-6) and from global overdispersion datasets (Arnold and Roberts, 2009)) and incrementally increasing the specified number of dose components until the FMM fits would no longer converge. The Bayes Information Criteria (BIC) and log-likelihood (llik) scores are shown for each of the different FMM parameterisation scenarios tested with sample NSI18-4. The BIC score has been used to assess the suitability of the FMM fits, with the lowest BIC score taken to represent the optimum parameterisation of the FMM (shown in bold).

NSI18-4									
OD	**# comps**	**llik**	**BIC**	**comp 1 (Gy)**	**proportion of grains**	**comp 2 (Gy)**	**proportion of grains**	**comp 3 (Gy)**	**proportion of grains**
20	1	-45.10	93.67	49.40					
20	2	-26.82	64.03	32.33 ± 3.04	0.39 ± 0.11	67.17 ± 4.89	0.61 ± 0.11		
20	3	-21.51	60.35	13.38 ± 3.36	0.03 ± 0.03	43.29 ± 2.51	0.72 ± 0.1	95.83 ± 13.34	0.25 ± 0.10
25	1	-34.33	72.13	50.01					
25	2	-24.59	59.57	34.05 ± 5.18	0.43 ± 0.18	68.30 ± 8.18	0.57 ± 0.18		
25	3	-21.15	59.64	13.47 ± 4.07	0.03 ± 0.03	43.72 ± 3.34	0.71 ± 0.12	92.08 ± 17.02	0.25 ± 0.12
30	1	-28.25	59.97	50.37					
30	**2**	**-23.48**	**57.36**	**37.00 ± 9.26**	**0.51 ± 0.38**	**70.54 ± 19.01**	**0.49 ± 0.38**		
30	3	-21.58	60.49	13.70 ± 5.08	0.03 ± 0.03	44.45 ± 4.60	0.71 ± 0.17	86.99 ± 21.26	0.26 ± 0.17

Table B 5 Finite mixture model fitting results for sample NSI18-5, which exhibits a D_e distribution with multiple dose components. The FMM was fitted by varying the common overdispersion (OD) parameter between 20 % and 30 % (to adequately cover the range of overdispersion observed in 'ideal' (well-bleached and unmixed) sedimentary samples from this study (BL18-A, NSI18-1, NSI18-2, NSI18-3 and NSI18-6) and from global overdispersion datasets (Arnold and Roberts, 2009)) and incrementally increasing the specified number of dose components until the FMM fits would no longer converge. The Bayes Information Criteria (BIC) and log-likelihood (llik) scores are shown for each of the different FMM parameterisation scenarios tested with sample NSI18-5. The BIC score has been used to assess the suitability of the FMM fits, with the lowest BIC score taken to represent the optimum parameterisation of the FMM (shown in bold).

NSI18-5									
OD	**# comps**	**llik**	**BIC**	**comp 1 (Gy)**	**proportion of grains**	**comp 2 (Gy)**	**proportion of grains**	**comp 3 (Gy)**	**proportion of grains**
20	1	-35.35	74.16	117 2					
20	**2**	**-19.20**	**48.80**	**77.4 ± 7.7**	**0.49 ± 0.12**	**166.6 ± 14.5**	**0.51 ± 0.12**		
20	3	FAIL	-	-	-	-	-	-	-
25	1	-27.99	59.44	116 5					
25	2	-19.42	49.23	79.0 ± 9.5	0.49 ± 0.14	163.7 ± 17.8	0.51 ± 0.14		
25	3	FAIL	-	-	-	-	-	-	-
30	1	-23.81	51.09	116.0					
30	2	-19.94	50.28	81.7 ± 12.5	0.49 ± 0.19	158.6 ± 22.4	0.51 ± 0.19		
30	3	FAIL	-	-	-	-	-	-	-

Table B 6 Finite mixture model fitting results for sample NSI18-7, which exhibits a D_e distribution with multiple dose components. The FMM was fitted by varying the common overdispersion (OD) parameter between 20 % and 30 % (to adequately cover the range of overdispersion observed in 'ideal' (well-bleached and unmixed) sedimentary samples from this study (BL18-A, NSI18-1, NSI18-2, NSI18-3 and NSI18-6) and from global overdispersion datasets (Arnold and Roberts, 2009)) and incrementally increasing the specified number of dose components until the FMM fits would no longer converge. The Bayes Information Criteria (BIC) and log-likelihood (llik) scores are shown for each of the different FMM parameterisation scenarios tested with sample NSI18-7. The BIC score has been used to assess the suitability of the FMM fits, with the lowest BIC score taken to represent the optimum parameterisation of the FMM (shown in bold).

NSI18-7									
OD	**# comps**	**llik**	**BIC**	**comp 1 (Gy)**	**proportion of grains**	**comp 2 (Gy)**	**proportion of grains**	**comp 3 (Gy)**	**proportion of grains**
20	1	-216.88	437.78	10.0					
20	2	-69.32	150.66	5.3 ± 0.3	0.51 ± 0.07	20.4 ± 1.4	0.49 ± 0.07		
20	**3**	**-55.39**	**130.82**	**4.5 ± 0.3**	**0.36 ± 0.07**	**10.8 ± 1.0**	**0.29 ± 0.08**	**24.2 ± 1.8**	**0.35 ± 0.07**
25	1	-161.13	326.27	10.0					
25	2	-62.66	137.34	5.3 ± 0.4	0.50 ± 0.08	20.2 ± 1.6	0.50 ± 0.08		
25	3	-56.25	132.53	4.5 ± 0.4	0.37 ± 0.08	10.8 ± 1.4	0.27 ± 0.09	23.8 ± 2.2	0.36 ± 0.08
30	1	-126.34	256.70	10.1					
30	2	-59.67	131.35	5.3 ± 0.4	0.50 ± 0.08	19.9 ± 1.8	0.50 ± 0.08		
30	3	-57.38	134.80	4.7 ± 0.5	0.39 ± 0.09	10.8 ± 2.3	0.24 ± 0.11	23.0 ± 2.7	0.37 ± 0.10

Table B 7 Elemental concentrations for OSL dating samples, measured on dry sediment subsamples using ICP-OES and ICP-MS (BL18-A), or using *in situ* FGS and the energy windows approach detailed in Arnold et al. (2012) (all other samples). The as measured (i.e., *in situ* moisture-attenuated) FGS concentrations have been converted to dry equivalent values (0 % water content) for direct comparisons with the ICP-MS/ICP-OES data for BL18-A.

Sample	Method	Depth (cm)	K(%)	Th (ppm)	U (ppm)
BL18-A	ICP-MS/ICP-OES	353	0.08 ± 0.002	23.8 ± 0.7	2.72 ± 0.08
NSI18-1	FGS (dry calc)	160	0.01 ± 0.003	0.88 ± 0.06	0.37 ± 0.03
NSI18-2	FGS(dry calc)	150	0.01 ± 0.003	1.04 ± 0.07	0.73 ± 0.05
NSI18-3	FGS(dry calc)	183	0.03 ± 0.004	2.81 ± 0.16	0.69 ± 0.05
NSI18-4	FGS(dry calc)	170	0.02 ± 0.002	0.62 ± 0.05	0.31 ± 0.03
NSI18-5	FGS(dry calc)	70	0.05 ± 0.007	8.08 ± 0.43	1.38 ± 0.09
NSI18-6	FGS(dry calc)	170	0.01 ± 0.003	0.65 ± 0.05	0.50 ± 0.03
NSI18-7	FGS(dry calc)	130	0.02 ± 0.003	0.71 ± 0.05	0.49 ± 0.03

Table B 8 High-resolution gamma spectrometry results for the NSI18 dune sand samples. The beta dose rates shown in the final column have been calculated using the long-term water content corrections, beta attenuation factors and dose rate conversation factors detailed for each sample in Table B1.

		Radionuclide specific activities (Bq/kg) [a, b]						Daughter: parent isotopic ratio			
Sample	**depth (cm)**	**^{238}U**	**^{226}Ra**	**^{210}Pb**	**^{228}Ra**	**^{228}Th**	**^{40}K**	**^{226}Ra:^{238}U**	**^{210}Pb:^{226}Ra**	**^{228}Th:^{228}Ra**	**HRGS beta dose rate (Gy/ka) [b]**
NSI18-1	160	5.3 ± 1.2	4.3 ± 0.2	4.5 ± 1.4	2.7 ± 0.4	2.5 ± 0.3	0.4 ± 1.7	0.98 ± 0.53	1.05 ± 0.33	0.92 ± 0 17	0.05 ± 0.012
NSI18-2	183	10.2 ± 1 3	9.3 ± 0.3	9.6 ± 1.5	6.6 ± 0.5	6.1 ± 0.4	1.0 ± 2.0	0.91 ± 0.12	1.04 ± 0.16	0.93 ± 0.09	0.13 ± 0.013
NSI18-3	150	8.1 ± 1.5	7.0 ± 0.3	6.3 ± 2.2	12.3 ± 0.6	13.8 ± 0.5	11.0 ± 2.7	0.87 ± 0.17	0.90 ± 0.32	1.12 ± 0.07	0.12 ± 0.013
NSI18-4	170	3.4 ± 1.0	4.1 ± 0.3	3.9 ± 1.2	2.7 ± 0.7	3.2 ± 0.3	0.7 ± 2.1	1.21 ± 0.36	0.95 ± 0.30	1.17 ± 0 30	0.05 ± 0.011
NSI18-5	70	15.9 ± 1 9	15.6 ± 0.4	15.7 ± 2.6	23.1 ± 0.8	20.5 ± 0.6	15.5 ± 2.6	0.99 ± 0.12	1.00 ± 0.17	0.89 ± 0.04	0.27 ± 0.023
NSI18-6	170	6.4 ± 1.4	6.6 ± 0.3	5.7 ± 1.3	2.6 ± 0.6	2.8 ± 0.4	0.1 ± 2.5	1.03 ± 0.22	0.86 ± 0.20	1.06 ± 0 29	0.06 ± 0.013
NSI18-7	130	9.0 ± 0.8	8.5 ± 0.2	9.8 ± 1.4	3.7 ± 0.4	3.1 ± 0.3	2.2 ± 2.1	1.02 ± 0.22	1.15 ± 0.17	0.84 ± 0 12	0.10 ± 0.012

[a] Measurements made on dried and powdered samples. The specific activities of ^{238}U (determined from ^{235}U emissions after correcting for ^{226}Ra interference, and ^{234}Th emissions after correcting for ^{228}Ra interference), ^{226}Ra (derived from ^{214}Pb and ^{214}Bi emissions), ^{210}Pb, ^{228}Ra (derived from ^{228}Ac emissions), ^{228}Th (derived from ^{212}Pb and ^{208}Tl emissions) and ^{40}K were measured for each sediment sample, and used to derive the daughter-to-parent isotope ratios for ^{226}Ra:^{238}U, ^{210}Pb:^{226}Ra and ^{228}Th:^{228}Ra.

[b] Mean ± total uncertainty (68% confidence interval), calculated as the quadratic sum of the random and systematic uncertainties.

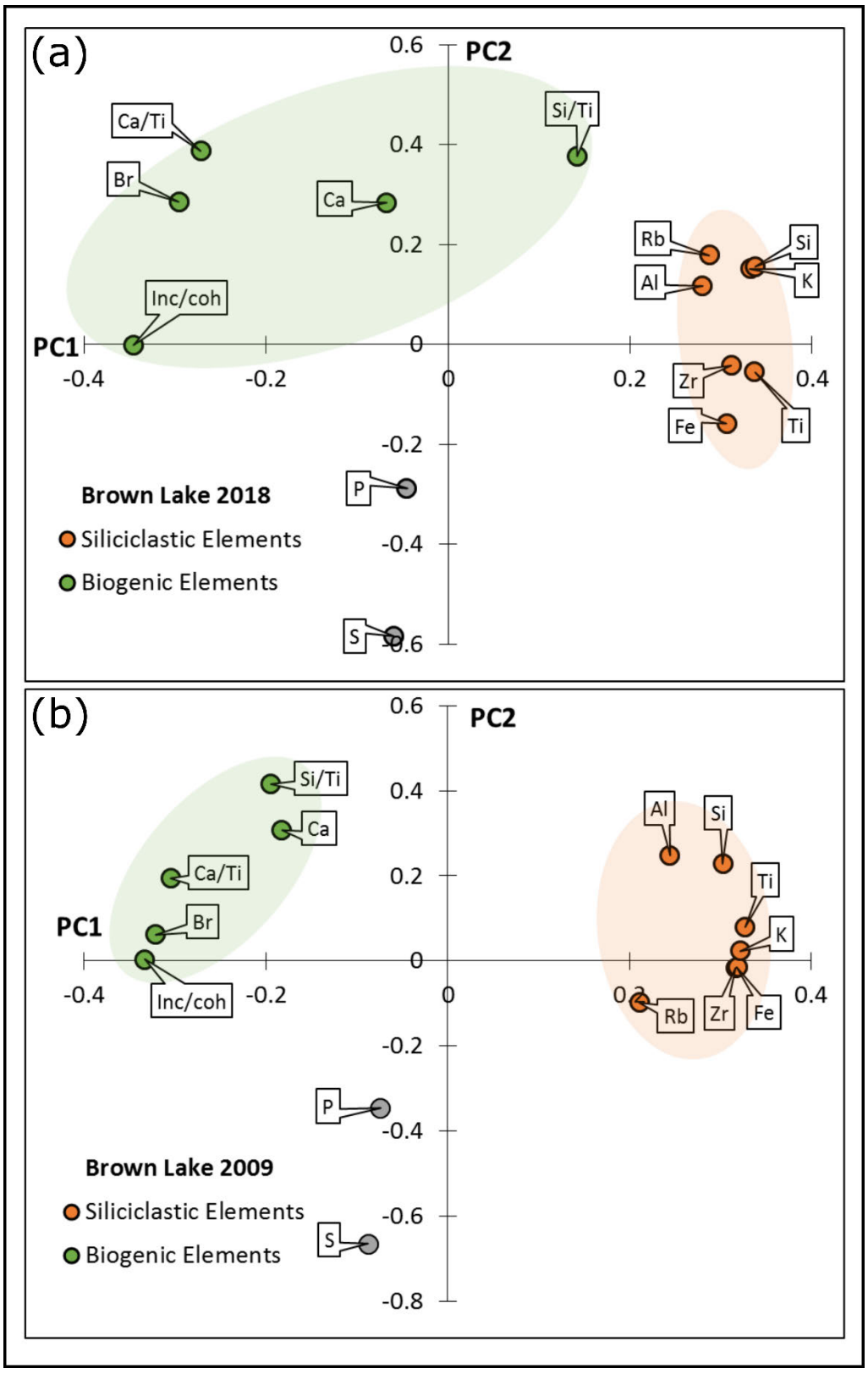

Figure B 1 Ordination diagram of the first two principal components of the scanning XRF data for (a) BL18-3 and BL18-4 composite core and, (b) the BL09 core. Elements associated with siliciclastic sediments and high loadings for PC1 are displayed as orange circles, while elemental ratios associated with biogenic sediments and high loadings for PC2 are displayed as green circles.

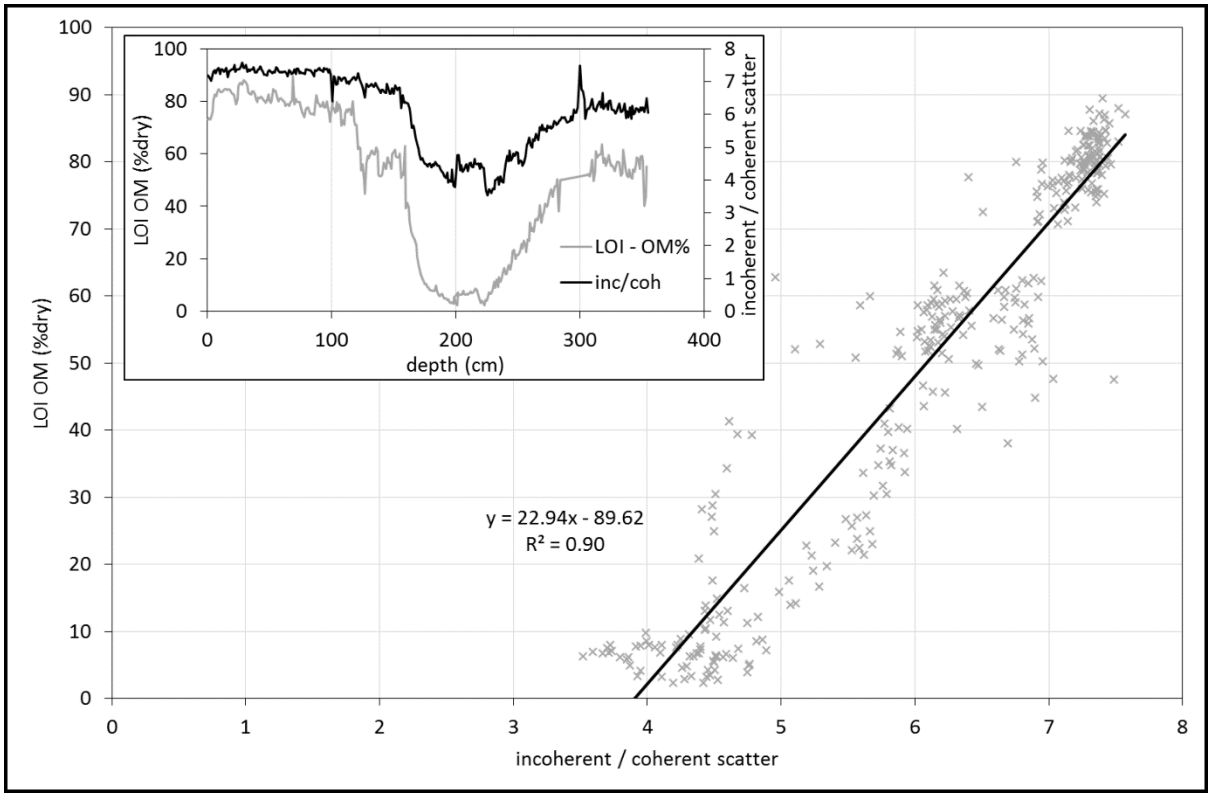

Figure B 2 Calibration of organic matter (OM) from Itrax data (incoherent scatter / coherent scatter) plotted against empirically derived OM content from LOI analysis for core BL18-3.

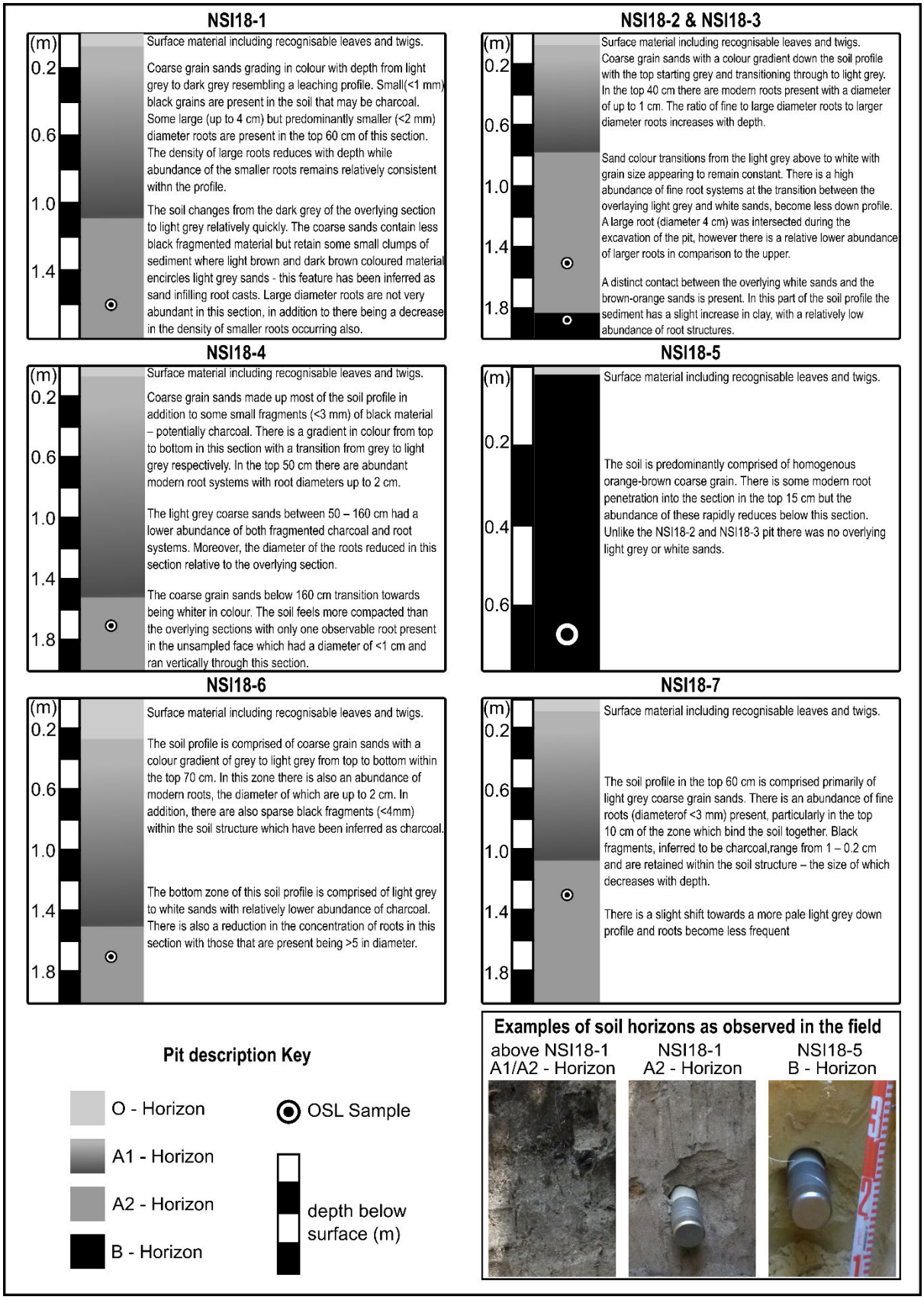

Figure B 3 Pit photos and descriptions for the NSI18 OSL dune core samples reported in this paper. The black and white circles represent the position of the OSL core(s) extracted from a given pit. Note the change in scale between individual photos.

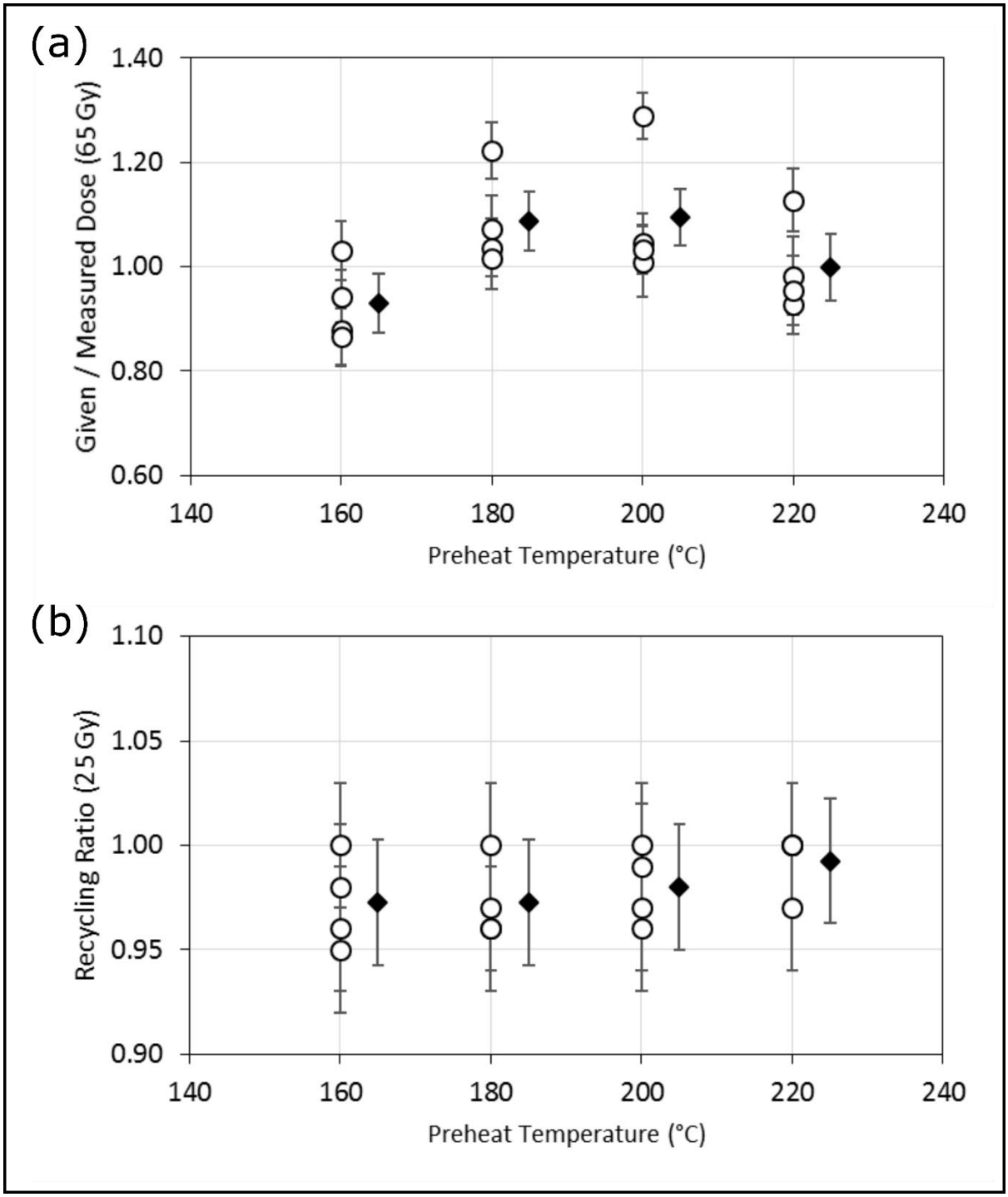

Figure B 4 Multi-grain dose recovery test results obtained for sample NSI18-4 after administering a dose of 65 Gy (uncertainties are shown at 1σ). For each test, a fixed natural and regenerative dose preheat (PH1) of 260 °C for 10 s was applied, and the test dose preheat (PH2) temperature was varied, as indicated in the plots (in all cases a PH2 duration of 10 s was used). (a) the recovered doses (open circles = individual aliquot D_e values; black diamonds = weighted mean D_e values). (b) the recycling ratios obtained for different preheat conditions. D_e measurements were made with a modified version of SAR protocol (replacing single-grain laser stimulations in steps 4 and 7 of Table B2, with blue LED OSL stimulations performed at 125 °C for 60 s) using various test dose preheat (PH2) conditions. D_e measurements were made on multi-grain aliquots containing ~1000 quartz grains.

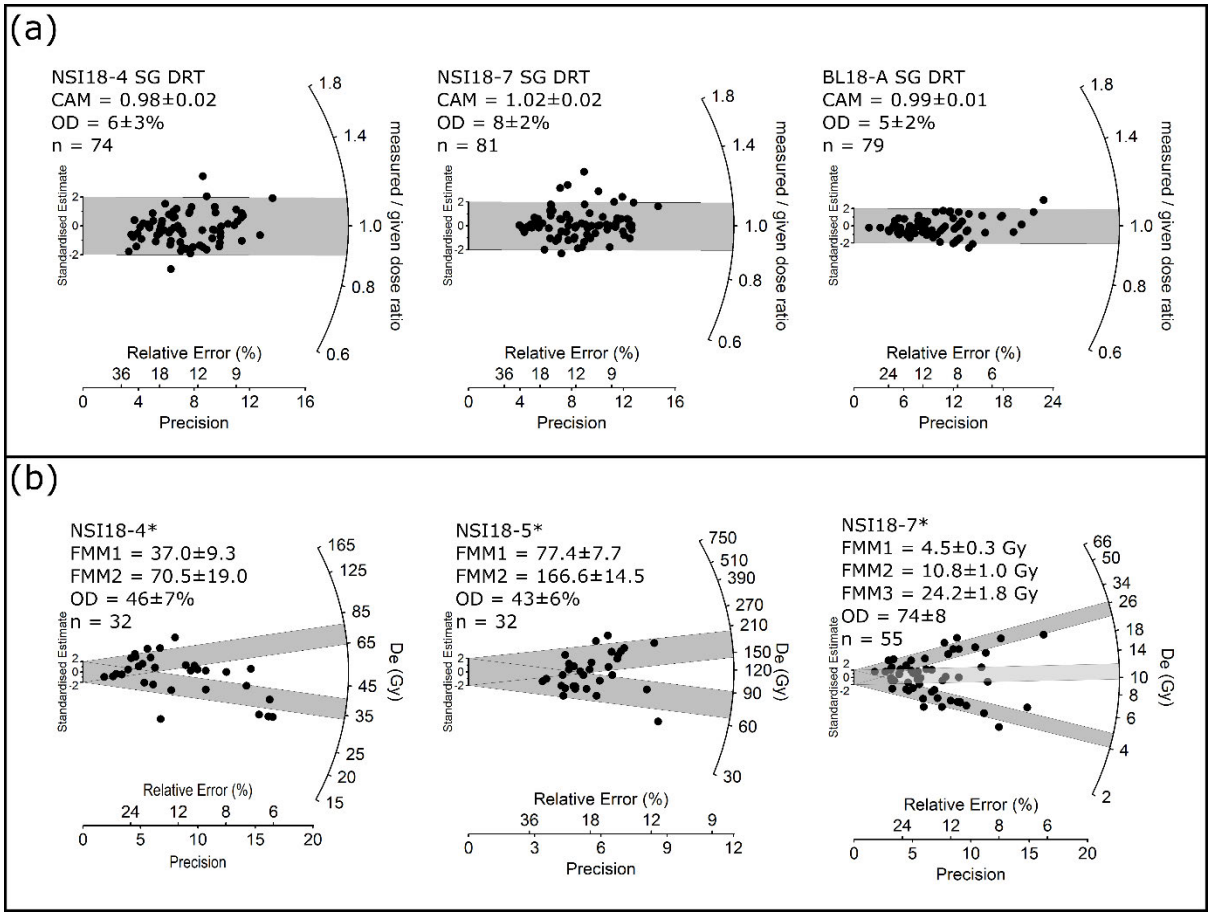

Figure B 5 Radial plots showing single-grain OSL dose recovery test results and alternate age model fits obtained for 212-250 µm quartz grains. (a) Dose recovery test results from samples NSI18-4, NSI18-7 and BL18-A respectively, using the SAR protocol in Table B2 (D_e uncertainties are shown at 1σ). Grains were bleached within the Risø reader chamber using blue LEDs prior to administering a dose of 65 Gy. The central age model (CAM) measured-to-given dose ratio and the overdispersion (OD) is shown next to each sample. (b) alternate age model fits for samples identified with (*) in Figure 3.5 with final D_e values calculated using the finite mixture model (FMM; Galbraith and Green, 1990) for comparative purposes.

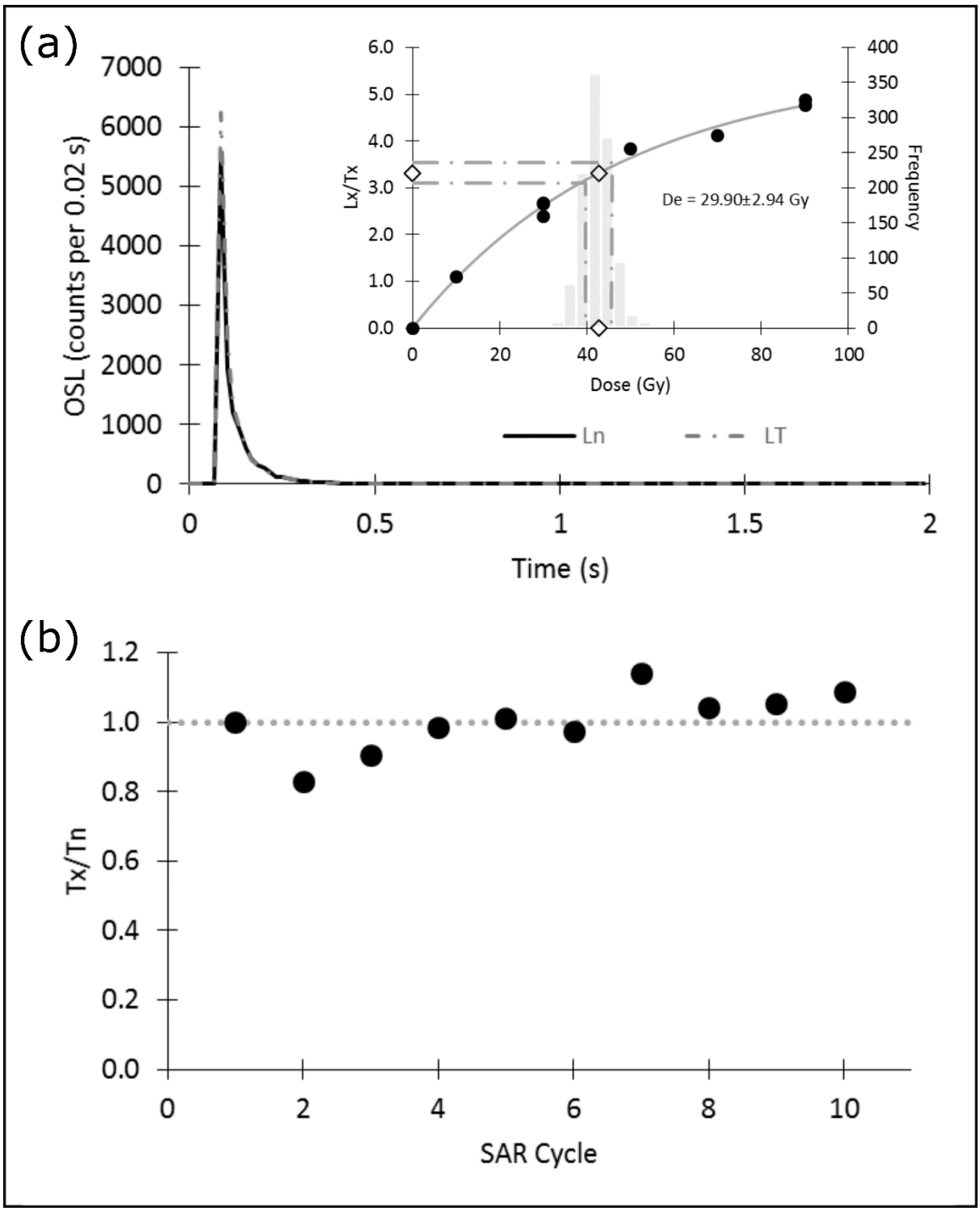

Figure B 6 Example of the OSL and dose-response characteristics of an accepted grain from sample BL18-A. (a) OSL decay curve showing the OSL counts measured for the natural signal (L_n; black line) and 10 Gy test-dose signal (T_n; grey dashed line). The inset of (a) shows the sensitivity-corrected OSL dose response curve solid grey line) reconstructed using different regenerative dose cycles (black filled circles). The grey columns represent the frequency of intercepts following 1,000 Monte Carlo repeats; open diamonds and dashed grey line represent the calculation of D_e and associated error. (b) The normalised test dose sensitivity (T_x/T_n) response through the SAR measurement cycles.

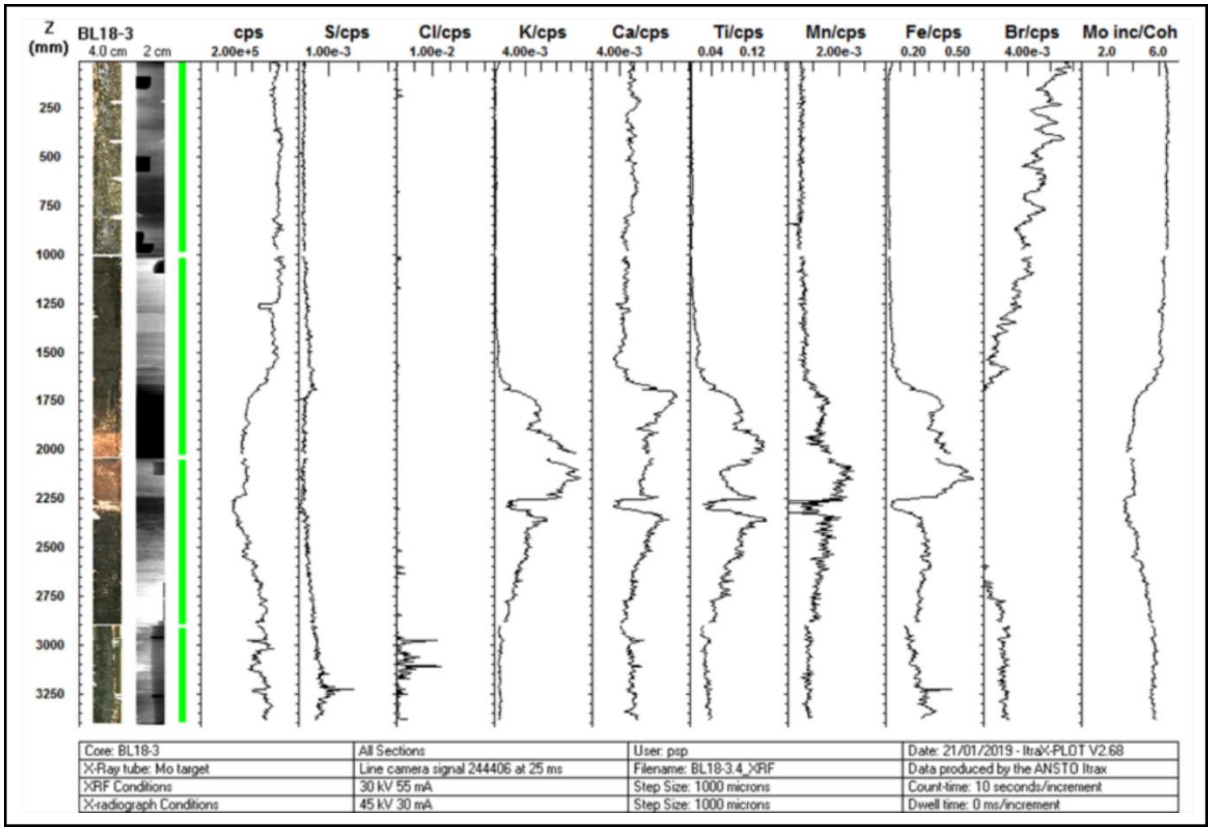

Figure B 7 Scanning XRF output data for core BL18-3. (Left to right) Cumulative scan length relative to top of core, optical image capture of scanned sediment surface, radiographic image, element, elemental ratio and scattering counts.

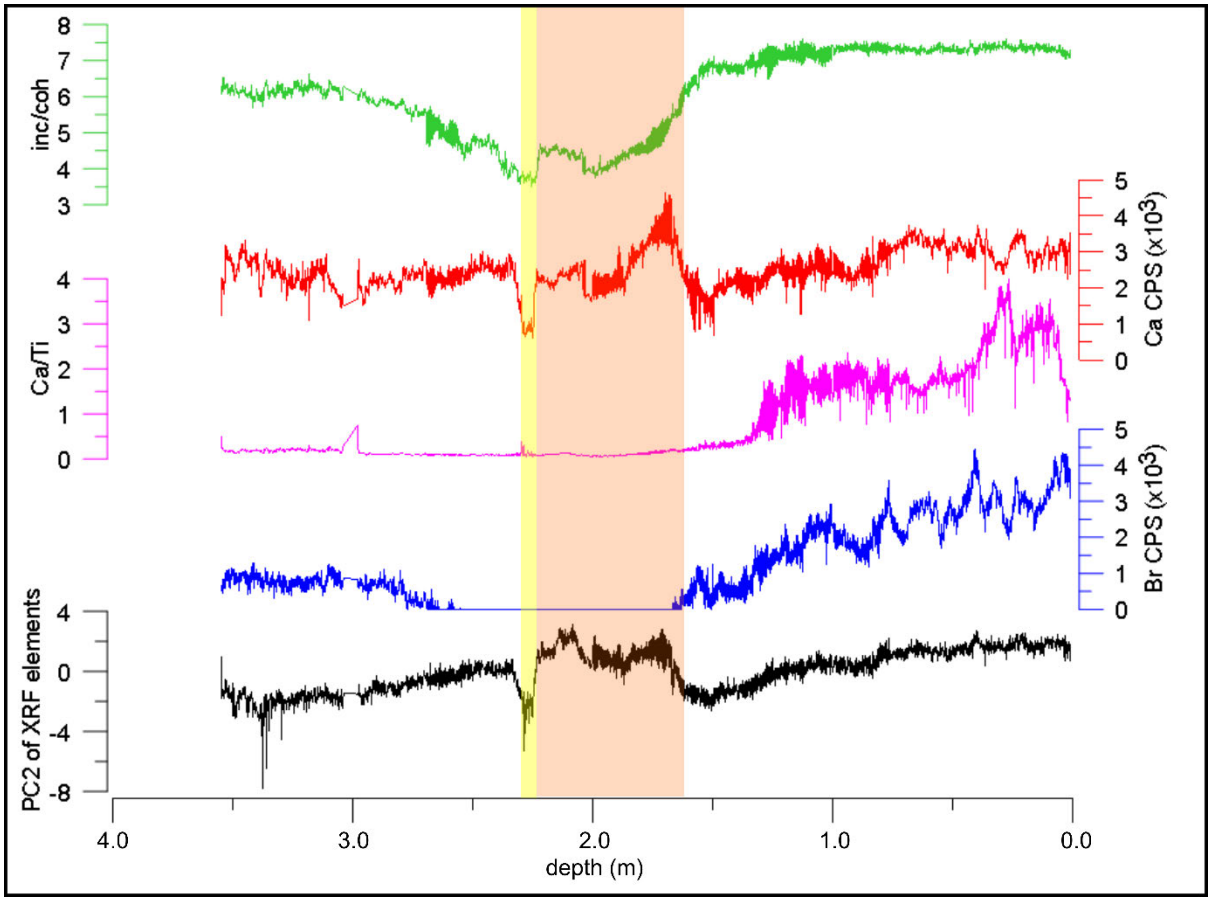

Figure B 8 XRF elemental counts per second (CPS) of selected biogenic elements (as identified using Principal Component Analysis). Yellow and orange shading represent, the sand (sub-unit 2.2) and transitional (sub-unit 2.1) layers observed in the sedimentary sequence. For terrigenous element correlations the reader is directed to Figure 3.4.

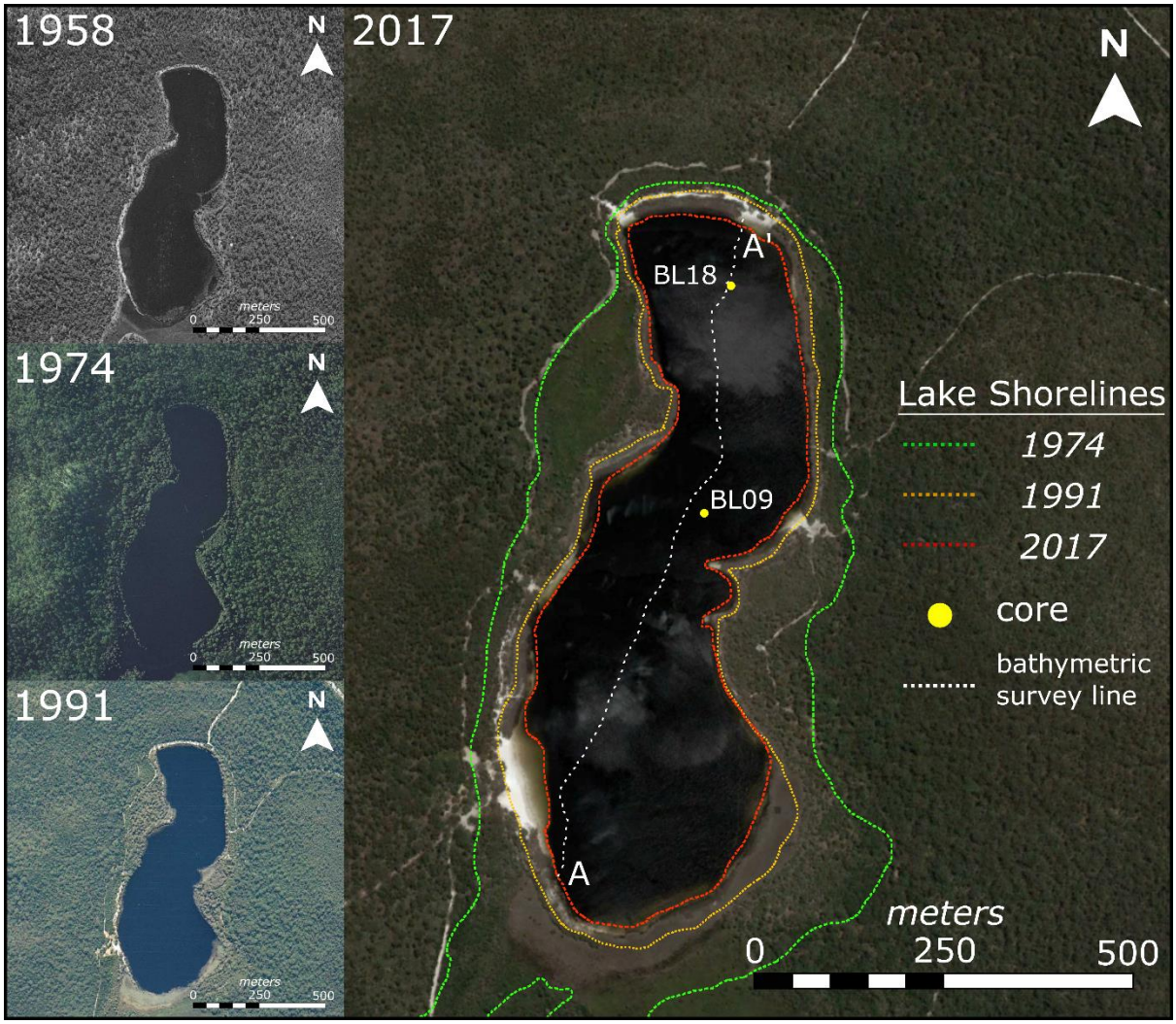

Figure B 9 Aerial images of Brown Lake showing water level variation from 1958 to 2017. The imbedded 1958 (QAP768139), 1974 (QAP768139) and 1991 (QAP4951) historic aerial photographs were downloaded from the Queensland Government, QImagery web-database (State of Queensland; 2007). The large 2017 image is a satellite capture that shows fluctuations in lake level relative to 2017 shorelines, in addition to data collection locations in this study.

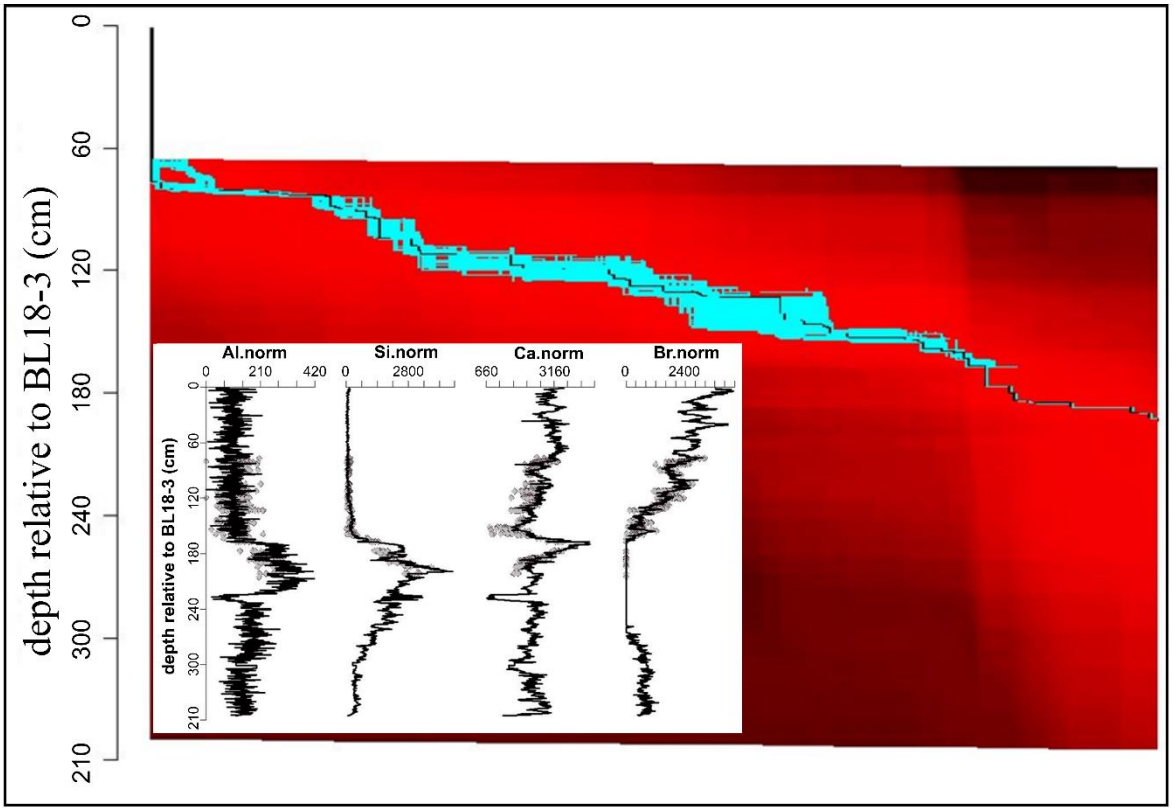

Figure B 10 Core correlation H-matrix and data plot (inset) following sequence slotting in CPLSlot (Hounslow and Clark, 2016). The possible slotting positions are shown on the H-matrix as a gradient from blue (more likely), to red (less likely) when BL18-4 is fitted to BL18-3. The inset plot shows the mean slotting positions of BL18-4 (grey diamonds) against BL18-3 (black line) for the selected elements.

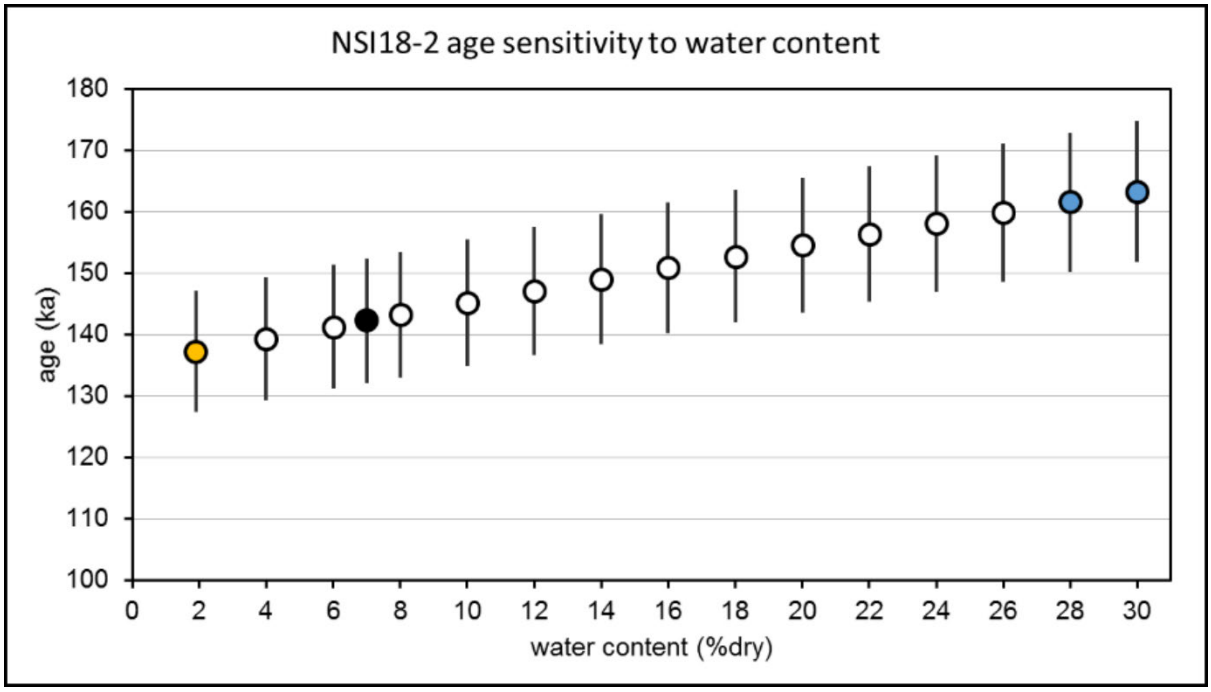

Figure B 11 Influence of changing water content on OSL age for NSI18-2. Orange, blue and black points indicate ages associated with present-day (as measured) water content, the measured saturated water content and the long-term assumed value adopted in this study, respectively.

B5. References

Aitken, M. J. 1998. Introduction to optical dating: the dating of Quaternary sediments by the use of photon-stimulated luminescence, Oxford, Oxford University Press.

Arnold, L. & Roberts, R. 2009. Stochastic modelling of multi-grain equivalent dose (De) distributions: Implications for OSL dating of sediment mixtures. Quaternary Geochronology, 4, 204-230.

Arnold, L. J., Duval, M., Demuro, M., Spooner, N. A., Santonja, M. & Pérez-González, A. 2016. OSL dating of individual quartz 'supergrains' from the Ancient Middle Palaeolithic site of Cuesta de la Bajada, Spain. Quaternary Geochronology, 36, 78-101.

Arnold, L. J., Duval, M., Falguères, C., Bahain, J. J. & Demuro, M. 2012. Portable gamma spectrometry with cerium-doped lanthanum bromide scintillators: Suitability assessments for luminescence and electron spin resonance dating applications. Radiation Measurements, 47, 6-18.

Brennan, B. J. 2003. Beta doses to spherical grains. Radiation Measurements, 37, 299-303.

Brock, F., Higham, T., Ditchfield, P. & Ramsey, C. B. 2010. Current pretreatment methods for AMS radiocarbon dating at the Oxford Radiocarbon Accelerator Unit (ORAU). Radiocarbon, 52, 103-112.

Bronk Ramsey, C. 2008. Deposition models for chronological records. Quaternary Science Reviews, 27, 42-60.

Bronk Ramsey, C. 2009. Dealing with outliers and offsets in radiocarbon dating. Radiocarbon, 51, 1023-1045.

Bronk Ramsey, C. & Lee, S. 2013. Recent and planned developments of the program OxCal. Radiocarbon, 55, 720-730.

Demuro, M., Arnold, L. J., Aranburu, A., Sala, N. & Arsuaga, J.-L. 2019. New bracketing luminescence ages constrain the Sima de los Huesos hominin fossils (Atapuerca, Spain) to MIS 12. Journal of Human Evolution, 131, 76-95.

Duller, G. a. T. 2003. Distinguishing quartz and feldspar in single grain luminescence measurements. Radiation measurements, 37, 161-165.

Duller, G. a. T. 2007. Luminescence Analyst. 3.24 ed. University of Wales, Aberystwyth: Aberystwyth Luminescence Research Laboratory.

Ellerton, D., Rittenour, T., Shulmeister, J., Gontz, A., Welsh, K. J. & Patton, N. 2020. An 800 kyr record of dune emplacement in relationship to high sea level forcing, Cooloola Sand Mass, Queensland, Australia. Geomorphology, 354, 106999.

Fu, X., Cohen, T. J. & Arnold, L. J. 2017. Extending the record of lacustrine phases beyond the last interglacial for Lake Eyre in central Australia using luminescence dating. Quaternary Science Reviews, 162, 88-110.

Galbraith, R. & Green, P. 1990. Estimating the component ages in a finite mixture. International Journal of Radiation Applications and Instrumentation. Part D. Nuclear Tracks and Radiation Measurements, 17, 197-206.

Guérin, G., Mercier, N. & Adamiec, G. 2011. Dose-rate conversion factors: update. Ancient TL, 29, 5-8.

Hounslow, M. W. & Clark, R. M. 2016. CPLSlot a program for objective correlation between successions using sequence slotting.

Jacobs, Z., Duller, G. A., Wintle, A. G. & Henshilwood, C. S. 2006. Extending the chronology of deposits at Blombos Cave, South Africa, back to 140 ka using optical dating of single and multiple grains of quartz. Journal of Human Evolution, 51, 255-273.

Lewis, R. J., Tibby, J., Arnold, L. J., Barr, C., Marshall, J., Mcgregor, G., Gadd, P. & Yokoyama, Y. 2020. Insights into subtropical Australian aridity from Welsby Lagoon, north Stradbroke Island, over the past 80,000 years. Quaternary Science Reviews, 234, 106262.

Mejdahl, V. 1979. Thermoluminescence dating: Beta-dose attenuation in quartz grains. Archaeometry, 21, 61-72.

Prescott, J. R. & Hutton, J. T. 1994. Cosmic ray contributions to dose rates for luminescence and ESR dating: large depths and long-term time variations. Radiation measurements, 23, 497-500.

Appendix C. Supplementary information for Chapter 4

This Appendix contains supplementary information that accompanies Chapter 4, which has been published in *Nature Communications* as:

Hocknull, S. A., Lewis, R., Arnold, L. J., Pietsch, T., Joannes-Boyau, R., Price, G. J., Moss, P., Wood, R., Dosseto, A., Louys, J., Olley, J. & Lawrence, R. A. 2020. Extinction of eastern Sahul megafauna coincides with sustained environmental deterioration. Nature communications, 11, 1-14.

C1. Systematic identification of megafauna remains

Scott A. Hocknull & Rochelle A. Lawrence

Taxonomic assignment of megafauna fossils recovered from the SWC sites and nearby Kemmis Creek and Homevale Station are justified here. This work was undertaken to develop a base taxonomic list of megafauna species recovered from each site discussed in the main text and listed in Table 4.2. The taxonomic identifications were also used to assist in determining associations of cranial and postcranial material within fossil deposits.

Identifications were made using published characteristics for known species, direct morphological and morphometric comparisons with securely identified megafauna from the Queensland Museum Geosciences collection, and via correspondence with institutions holding material valuable for identification. Taxonomic identifications of megafauna were complicated due to very poor characterisation of most Pleistocene species. Where possible, specimens were compared directly with taxonomic type material.

Other non-megafauna fossil remains such as small aquatic vertebrates and invertebrates, terrestrial insects and flora have also been found at these sites and help justify the depositional settings. Examples of these are figured in Figure C1 (a-z) & C2 (u). Detailed taxonomic appraisals of these remains will form part of a full systematic treatment elsewhere.

Figure C 1 Plants, bivalves, crustaceans, insects and fish remains from QML1470 (SW9) and QML1470 (SW3). Acacia sp. (a–e) partial leaves showing thick parallel venation, dried leaf split (arrow) in (c) and dried leaf curl in (e); (a) QMF59891, (b) QMF59892, (c) QMF59893, (d) QMF60003, (e) QMF59900. Melaleuca sp. (f) partial leaf showing fine reticulate venation (arrow) QMF59899. ?Eucalyptus sp. (g) partial leaf showing mid-leaf dry breakage pattern (arrow) QMF59906. ?Lomandra sp. (h) strap leaf showing fine parallel venation and soft leaf deformation QMF59903. Goodeniaceae (i) seed showing soft anatomy QMF59895. ?Allocasuarina sp. (j) seed showing internal anatomy QMF59896. Unidentified seeds (k) QMF59898 and (l) QMF59905. Bivalves, Velesunio wilsoni (m–q) articulated and isolated valves; (m) QMF59904, (n–p) QMF59890, (q) QMF59902. Corbiculidae (r) indeterminate species isolated valve QMF59889. Crustacean gastroliths ('yabby buttons') (s–t); (s) QMF59894 and (t) QMF59901. Teleostei (u-x); (u–v) vertebra QMF59908; (w) operculum QMF59907; (x) scale. Insecta, ?Curculionidae (y–z) articulated weevil elytron QMF59897. Scale bars equal 5 mm (a–h & m–t) and 1 mm (i–l & u–z).

C1.1. Reptilia

Crocodylia (Owen, 1842)

Crocodylidae (Cuvier, 1807)

Isolated teeth (both shed and broken), osteoderms, fragmentary skull elements, a partial edentulous posterior dentary and isolated coprolites represent crocodilian remains recovered from QML1470 (SW9, SW3, SWCC & SWJ). Three or possibly four distinctive crocodilian tooth morphologies are present in addition to two different osteoderm morphologies. Comparisons have been made with large collections of isolated teeth and osteoderms from Queensland Paleogene and Neogene fossil sites; these include associated teeth and osteoderms from described cranial and postcranial remains in addition to a large comparative collection of teeth and osteoderms from extant species of crocodilians (Molnar, 1979, 1981, 1982b; Willis & Molnar, 1991, 1997a, b). A preliminary identification of tooth morphotype and osteoderms to known taxa is provided here (Table C1). A more thorough assessment of crocodilian tooth and osteoderm morphological diversity from Australian Neogene fossil sites is underway (Chiotakis, 2018) to further test and refine the identification traits established previously for teeth Chiotakis, 2018; Willis & Molnar, 1997a) whilst combining this with morphological diversity in osteoderms.

Table C 1 Crocodilian tooth and osteoderm characteristics used to identify isolated remains at South Walker Creek sites.

		Tooth Morphology				Osteoderm Morphology	
Morphotype	**Taxon**	**Profile & base shape**	**Serrations**	**Denticles**	**Fluting**	**Osteoderm base**	**Osteoderm keel and surface pitting**
1	*Crocodylus porosus*	Gracile conical, circular	Faint	Absent	Strong	Shape – Circular to ovoid with thick bone base. Bone texture – irregular. ragged edge.	Tall, curved surface with irregular pitting.
2	*Pallimnarchus gracilis*	Robust conical, circular	Fine	Absent	Faint	Shape – oblong to rectangular with thick bone base. Bone texture – smooth, regular edge.	Low, straight surface with regular large pits.
3	*Pallimnarchus pollens*	Robust conical, circular	Thick	Absent	Absent	Shape – oblong to rectangular with thick bone base. Bone texture – smooth, regular edge.	Low, straight surface with regular large pits.
4	'*Quinkana*' sp. ziphodont crocodilian	Tapered asymmetrical, labio-lingually compressed	Thick	Present	Absent		

Crocodylus (Laurenti, 1768)

Crocodylus* sp. cf. *C. porosus (Schneider, 1801)

Figure C2 (a-h)

Referred material: QML1470. Osteoderm QMF57048; teeth QMF57085, QMF59863, QMF59867, QMF57058, QMF57076, QMF57077, QMF59864.

The presence of crocodilian morphotype 1 suggests the presence of *C. porosus* at several sites (QML1470 SW9, SW3, SWCC). Isolated teeth and a single osteoderm very closely match the morphology of extant and extinct species of *Crocodylus porosus*. In particular, the shape of the osteoderm compares very favourably with that observed in *C. porosus* (Table C1) and to that in other observed species of *Crocodylus* (i.e. *C. niloticus*, *C. novaeguineae*, C. *johnstoni*). The presence of a species of *Crocodylus* likely that of *C. porosus* is not surprising because *C. porosus* is presently located in the lower reaches of the Fitzroy River, into which Walker Creek drains. However, the site occurs near the head waters of the Fitzroy River catchment, which suggests a major range contraction downstream over the Upper Pleistocene and evidently continued into the Holocene. In addition, *C. porosus* has been identified from Pliocene (Molnar, 1979) sites found in the Burdekin River catchment, which is adjacent to the Fitzroy River catchment to the North; therefore, this taxon has a well-established longevity in the region.

Pallimnarchus (de Vis, 1886)

Pallimnarchus gracilis (Willis & Molnar, 1997b)

Pallimnarchus pollens (de Vis, 1886)

Figure C2 (i-p, t)

Referred material: QML1470. Osteoderm QMF57094; teeth QMF59868, QMF57095, QMF59861, QMF57051, QMF59866, QMF59865; right dentary (partial) QMF57092.

Crocodilian Morphotype 2 + 3. As with the first morphotype, osteoderms representing a species of *Pallimnarchus* species are rare. However, they are distinctively broad, rectangular-ovoid in shape, flat with a low keel, a thick smooth base with large regular surface pitting, which differs substantially from those osteoderms of *C. porosus* (Table C1). Osteoderms found in association with the partial skull and postcranial remains of QMF1752 from Lansdowne, near Tambo, ~440 kms southwest of South Walker Creek, provide the only known associated cranial specimen with osteoderms and dentition. Willis & Molnar (1997b) identify QMF1752 as *Pallimnarchus gracilis*, therefore, the associated osteoderms and teeth can be used to help differentiate this species from the type species, *P. pollens*. Based on comparisons with large numbers of isolated teeth from the Queensland Museum collection there are two different morphotypes for teeth pertaining to *Pallimnarchus*: *P. pollens* are conical with no fluting and thick serrations, whilst the teeth associated with *P. gracilis* specimens are conical with faint fluting and fine serrations. Both morphotypes occur at South Walker Creek sites (QML1470 SW9 and SW3) suggesting the presence of both species but we will treat these initial

differences with caution pending thorough analysis. In the current study we tentatively consider these two separate morphotypes as a singular taxonomic grouping.

A near complete skull, without teeth, of *Pallimnarchus gracilis* was recovered from a nearby creek at Homevale Station (Willis & Molnar, 1997b), therefore, the presence of *P. gracilis* from South Walker Creek is not surprising. The presence of the more robust, typically southern distributed species (Willis & Molnar, 1997b), *P. pollens*, is new and may represent the northern limit of the species' geographic. This is plausible considering the catchment that abuts the southern perimeter of the Fitzroy River catchment is the upper reaches of the Condamine River (Murray-Darling Basin), which includes the type locality for *P. pollens* and the majority of its recorded occurrences. Directly adjacent to the western margin of Fitzroy River catchment is the west-draining Lake Eyre basin, which also records the presence of *P. pollens* (Willis & Molnar, 1997b). The southern-most record of *P. gracilis* occurs along the catchment abutment between these two basins at Landsdowne, indicating that these species could cross over major drainage divides.

'Quinkana' sp.

Figure C2 (q-s)

Referred material: QML1470. Teeth QMF59862, QMF59870 & QMF57062.

Crocodilian Morphotype 4 (Table C1). Isolated, labio-lingually compressed denticulate teeth represent a fourth morphotype of tooth found at South Walker Creek. These teeth are easily distinguished by the presence of clearly denticulate carinae. The only other tooth morphotype commonly encountered in Australian Pleistocene sites with denticulate carinae are those of varanids, in particular the giant *Varanus priscus*. Differentiating this tooth morphotype from *V. priscus* and all other varanids is straight forward with varanid teeth being considerably more labio-lingually compressed, and possessing both greater crown curvature and plicidentine. Crocodilians with this type of ziphodont dentition are generally considered to be closest to *Quinkana*; however, direct comparison of these teeth referred to *Quinkana* (e.g. QMF10141, QMF23220, QMF51503 and QMF58607) reveals the teeth to be much larger, less labio-lingual compressed and straighter, thus not a direct match to the SWC teeth (or other denticulate teeth observed from other localities within Queensland (Chiotakis, 2018)). These teeth are less compressed and we term them 'semi-ziphodont' to differentiate them from the highly compressed or conical crocodilian dentition typically found in Australian Neogene sites (Chiotakis, 2018; Molnar, 1981, 1982a; Sobbe et al., 2013; Willis & Molnar, 1997a). The tooth morphology indicates the presence of a large crocodilian unlike that of *Crocodylus* or *Pallimnarchus* within the fauna but bearing some resemblance to specimens referred to as *Quinkana*. Direct comparison of the South Walker Creek teeth to ziphodont dentition recovered from Middle Pleistocene cave deposits at Mt. Etna (Hocknull, 2005, 2009; Hocknull et al., 2007) indicates an additional morphotype of crocodilian living in the Fitzroy River Basin during the Quaternary, bringing the total to at least four.

Figure C 2 Crocodylidae and Chelidae. *Crocodylus* sp. (a) osteoderm QMF57048; (b–h) teeth; (b) QMF57085, (c) QMF59863, (d) QMF59867, (e) QMF57058, (f) QMF57076, (g) QMF57077, (h) QMF59864. *Pallimnarchus* sp. (i) osteoderm QMF57094; (j–o) teeth; (j) QMF59868, (k) QMF57095, (l) QMF59861, (m) QMF57051, (n) QMF59866, (o) QMF59865; (p) right dentary (partial) QMF57092. '*Quinkana'* sp. (q–s); teeth (q) QMF59862, (r) QMF59870, (s) QMF57062; (t) coprolite QMF59960. Chelidae indet. (u) carapace QMF59909. Scale bars = 5 mm.

C1.2. Aves

Casuariiformes

Casuariidae (Kaup, 1847)

Dromaius (Vieillot, 1816)

Dromaius* sp. cf. *D. novaehollandiae

Figure C3 (a & b)

Referred material: QML1470. Distal tarsometatarsus QMF57167; eggshell QMF60000.

A giant bird, likely the extant emu, *Dromaius novaehollandiae* is represented by a partial distal tarsometatarsus and eggshell. The tarsometatarus is similar in size to extant *Dromaius novaehollandiae* specimens possessing gracile condylar articular ends, unlike that seen in more robust *Casuarius* and the even more robust and thickened condyles observed in the Upper Pleistocene giant bird *Genyornis*. The eggshell bears the typical rugose surface ornamentation typical of *Dromaius novaehollandiae*.

C1.3. Squamata

Veranidae (Merrem, 1820)

Varanus

Varanus priscus (Owen, 1859)

Figure C3 (d-f, i, m & n)

Referred material: QML1470. Osteoderm (and impression) QMF60001; teeth QMF59914, QMF57054, QMF59916; dorsal vertebrae QMF59991, QMF57091.

Varanus priscus is represented by isolated teeth, large osteoderms and vertebrae across several sites. The tooth, osteoderm and vertebrae are diagnostic as varanid in morphology and their very large size makes them indistinguishable from *V. priscus* (Hocknull et al., 2009). Teeth are labio-lingually compressed (ziphodont), recurved, serrate with denticles and basal plicidentine (Hocknull et al., 2009; Willis & Molnar, 1997a). The sizes of the teeth are comparable to *V. priscus*, being much larger than *V. komodoensis*. The vermiform osteoderms are also diagnostic for varanids, with most osteoderms recovered from the sites being very large >15 mm long and outside the maximum size range of extant *V. komodoensis* but within the size range of *V. priscus* from the Eastern Darling Downs (Murray Darling Basin). The two dorsal vertebrae are morphologically and morphometrically similar to the type specimen of *V. priscus* (BMNH 32908c) and additional vertebrae referred to *V. priscus* in the Queensland Museum Geosciences collection.

***Varanus* sp. (large)**

Figure C3 (c, g, h, j & k, l)

Referred material: QML1470. Osteoderm QMF60002; teeth QMF59917, QMF59915; parietal bone QMF59913; sacral vertebra QMF57053.

A second species of giant *Varanus* is indicated by the presence of isolated teeth, a sacral vertebra, small osteoderms and a partial parietal bone. All elements are considerably smaller and morphologically distinct from those known of *V. priscus* and *V. komodoensis*. However, the overall size of the elements is similar to that of *V. komodoensis*. In particular, the sacral differs by having a more circular cotyle and relatively smaller zygopophyses compared to that seen in extant *V. komodoensis*. QMF59913 is a parietal bone that has been split in half but preserves the right side, the channel for the pineal foramen, and the medial margin of the supratemporal fenestrae. It differs substantially from the parietal of *V. komodensis* and *V. priscus* with the angle between the anterior and posterior supratemporal bars being more acute than that seen in *V. komodoensis* (Hocknull et al., 2009), and lacking a central parietal ridge as seen in *V. priscus*. These differences observed suggest a morphologically distinct species of *Varanus*. The possibility of intermediate *Varanus* species between *V. komodoensis* and *V. priscus* being present in the Australian Pleistocene has been suggested previously (Hocknull et al., 2009); however, without an ontogentic series of *V. priscus* known it is difficult to exclude the possibility that these elements represent a juvenile *V. priscus* which would indicate significant morphological change through ontogeny.

Figure C 3 Casuariidae and Varanidae. *Dromaius* sp. cf. *D. novaehollandiae* (a) distal tarsometatarsal QMF57167; (b) egg shell QMF60000. *Varanus* sp. (large) (c) osteoderm QMF60002. *Varanus priscus* (d) osteoderm (and impression) QMF60001. *Varanus* teeth (e–i): (e) *V. priscus* QMF59914, (f) *V. priscus* QMF57054, (g) *Varanus* sp. (large) QMF59917, (h) *Varanus* sp. (large) QMF59915, (i) *V. priscus* QMF59916. *Varanus* sp. (large) (j-l); (j+k) parietal bone (right side) QMF59913; (l) sacral vertebra QMF57053. *V. priscus* dorsal vertebra (m) QMF59991, (n) QMF57091. Scale bars equal 5 mm.

C1.4. Mammalia

Diprotodontia (Owen, 1866)

Macropodidae (Gray, 1821)

The most abundant and taxonomically diverse herbivores recovered from South Walker Creek sites are macropodines, in particular species previously within *Macropus*. We use the diagnostic molar morphology that have been used to define subgenera of *Macropus* (Dawson & Flannery, 1985); however, to remain consistent with current taxonomy, we have elevated these subgenera to genus level (Celik et al., 2019). Four species of macropodine kangaroos are currently recognised in the fauna: a species each of *Macropus*, *Notamacropus*, *Osphranter* and *Protemnodon*, as well as a species of a small-sized sthenurine. We recognise three extinct species that are possibly new or significant variants, including a giant species of *Macropus* with affinities to *Macropus pearsoni*; a giant species of *Notamacropus* distinct from *Notamacropus agilis siva* and a species of high-crowned *Protemnodon* that is similar in size to *Protemnodon brehus*. The extant *Osphranter rufus* and a small sthenurine are the rarest components of the macropodid fauna.

Macropodinae (Gray, 1821)

Notamacropus (Dawson & Flannery, 1985)

***Notamacropus* sp. (giant)**

Figure C5 (a-i)

Referred material: QML1470. Mandible with R+L I_1- P_3-M_4 QMF59990; partial left dentary I_1-M_2 QMF59992; associated dentition and postcranial remains QMF57047 including RI^3, RM_3, left calcaneum, right and left tibiae; LM^{2-3} QMF59994; RP^3 QMF59993.

Notomacropus sp. occurs across most sites and includes a near complete mandible (SW3-P), associated dentition and postcranial remains (SW9), along with isolated dentition (SW3, SWCC and Kemmis). QMF59990 and QMF59992 are mandibles possessing features seen in species of *Notomacropus*, including a lanceolate I_1 and vertical hypolophids that lack a vertical groove or notch (Dawson & Flannery, 1985). Isolated lower molars also lack the vertical groove or notch or very tall hypolophids. These remains are comparable to the largest individuals assigned to *Notomacropus agilis siva* (Bartholomai, 1975); however, it is clearly different in P_3 morphology when compared to specimens from the Darling Downs (e.g. QMF4492). Of the largest species of *Notomacropus* QMF59994 is comparable to *N. agilis siva* due to it lacking a distinctive fore-link which is present in *N. thor* and not in *N. agilis siva*. QMF59993 is a RP^3 and possesses distinctive morphological features that cannot be firmly placed with a known taxon. Superficially the premolar is similar in morphology to *M. dryas* (De Vis, 1895) and the exposed P^3 in *N. agilis siva* (QMF4541). Based on its size and in comparison to the P_3 available in QMF59990, it is likely that this P^3 (QMF59993) represents the same taxon. This premolar has been compared to extant and extinct species and does not match the morphology seen in species of *Protemnodon*, *Osphranter*, *Macropus*, *Troposodon*, *Wallabia*, *Petrogale*, *Thylogale*, *Dendrolagus*, *Dorcopsis*, *Dorcopsulus* or any species of sthenurine. On comparison with the lectotype of *Macropus dryas* (QMF3582), it shares a similar antero-posterior central crest with one large and three small cuspules each with an accessory buccal vertical crest

running to the base of the tooth, and presence of a posterolingual pocket and two large well-developed lingual margin cuspules. It differs by being larger; possessing distinct lingual cuspules and missing an antero-lingual cuspule; and a more tapered anterior margin and smaller postero-lingual basin. Together, this suite of specimens likely represents a species of giant *Notomacropus* at the larger size range of the genus and is as yet an unnamed taxon.

Osphranter

Osphranter sp. cf. *O. rufus* (Desmarest, 1822)

Figure C5 (j)

Referred material: QML1470. RM_4 QMF59929; posterior half of $RM^{2 \text{ or } 3}$ QMF59918.

A lower molar and partial upper molar represent a large species of *Osphranter* with very close morphology to that observed in the extant Red Kangaroo, *Osphranter rufus*. In molar dimensions the lower molar is just within the largest available specimens for comparison, which were all from male specimens. The molar bears distinctively high crowns with thick and unkinked fore and mid-links. The shallow lingual to buccal angle made by these straightened fore and mid-links, as seen in *O. rufus*, are not found in other similarly-sized species of *Macropus* bearing a posterior hypolophid groove, such as *M. titan* and *M. ferragus*. The shallower hypolophid groove in QMF59929 also differentiates the fossil from most specimens examined of these later extinct species. The fossil also falls within the lower size limit of these later extinct species. On inspection of the macropodid collections at Queensland Museum, three fossil dentary fragments (QMF9405, QMF9407 and QMF9408) from the same locality on the Eastern Darling Downs, bear near identical morphology to QMF59929. These combined records are the first identifications of Pleistocene records for the Red Kangaroo (*O. rufus*) in Queensland (Molnar & Kurz, 1997). The presence of *O. rufus* at South Walker Creek is not surprising because it has modern collection records from approximately 150 kms to the west.

Macropus (Shaw, 1790)

Macropus sp. (giant)

Figure C5 (l-aa)

Referred material: QML1470. LI_1 QM59921; LI_1 QMF59992; LI^3 QMF57163; $LM_{2\text{-}3}$ QMF59928; associated hind limb elements, calcaneum, astragali, metatarsal IV, associated phalanges IV.I, II & III, tibiae and associated distal epiphyses QMF57039; IV.III (ungual) QMF57161; left femora QMF57086, QMF57038; right humerus QMF57036; associated tibiae, epiphyses and astragali QM59997; articulated metatarsals V and VI QMF59911.

Two isolated distal tips from left lower incisors, an isolated left I^3 , and two longitudinally split molars (M_{2+3}) represent a very large species of macropodine referrable to *Macropus* based on: 1) the presence of enamel covering the ventro- and lingual faces of the lower incisors, extending up to well above halfway up the lingual face; and 2) posterior surface of the hypolophid rounded and possessing a vertical groove emanating from just below the hypoconid crest (Bartholomai, 1975; Dawson & Flannery, 1985; Flannery & Archer, 1982). On comparison to similarly-sized species of *Macropus* the

fossils resemble *M. pearsoni*, such as the very thick ventro-lingual enamel covering, development of the hypolophid groove into a steep, deep groove with a sharp lingual (buccal) margin and a tall anterior cingulum on lower molars (Dawson & Flannery, 1985; Flannery & Archer, 1982). In addition to these features, the fossils also share with *M. pearsoni* and *M. pan* a near-vertical and sharp post-protocristid that runs down the protolophid to the anterior termination of a very high and kinked cristid obliqua. This feature is developed to an extreme in *M. pan* and *M. pearsoni*. As the dental remains are fragmentary this leaves doubt that a definitive identification to previously described taxa is possible.

Postcranial elements representing a very large macropodine may represent the same taxon. At least ten tibiae representing a giant macropodine are among the most common macropodid element recovered from the South Walker Creek sites. The tibiae are very long and gracile elements with a straight diaphysis in lateral aspect. The condylar surface of the proximal epiphysis is flat, near horizontal and possesses a distinct intracondylar eminence. The anterior tibial crest is antero-posteriorly narrow, gently convex in profile, and extends distally, tapering into the diaphysis proximal to the mid-shaft. The articular surface of the distal epiphysis is near perpendicular to the antero-posterior plane of the anterior tibial crest. Based on characteristics of the tibiae established for macropodids (Murray, 1995) these tibiae share features with both macropodines and sthenurines, however, the predominance of macropodine characters over sthenurine characters favours a macropodine placement. In particular a macropodine placement is supported by the combination of a near straight diaphysis, and the near horizontal proximal and perpendicular distal epiphyseal articular surfaces. The distally elongate and smoothly convex anterior tibial crest is a feature present in sthenurines (Murray, 1995; Wells & Tedford, 1995), although this feature has been observed in *Macropus rufus* (Murray, 1995). On comparison to available very large macropodines with associated postcranial remains (including *Macropus giganteus*, *M. rufus*, *M. giganteus titan*, *M. ferragus*, *Protemnodon anak* and *P. snewini*) these tibia differ most clearly on their overall smaller size (Figures C4 & C5), stockier proportion and presence of an abrupt end to the distal margin of the anterior tibial crest. A single morphologically very similar, but proximo-distally shorter and more robust, tibia occurs within the Pliocene Chinchilla Sands Local Fauna (WC5928). WC5928 is the only known example of this tibia morphotype found outside of the South Walker Creek sites. WC = Wilkinson Collection within the Queensland Museum collection.

Fibulae, calcaneum, astragali, metatarsal IVs, digit IV phalanges and two digit IV unguals represent the giant *Macropus* from the South Walker Creek fauna. All exhibit typical macropodine characteristics (Murray, 1995). The digit IV ungual (QMF57039 & QMF57161) deserves further consideration due to its unique morphology. It is straight, triangular in both longitudinal and cross-sectional, and has a sharp tapered distal point. The dorso-lateral sides of the main body are straight with the distal claw tip curved slightly dorsally, creating a unique recurvirostral-like shape. Morphologically similar unguals are exceptionally rare in the literature, having only been published from the Quanbun fauna (Flannery, 1984) and figured twice in comparison to other macropodid taxa (Flannery, 1980, 1984). These unguals have been tenuously assigned to *Macropus pan* on the basis that unguals of this morphology represent the largest species of *Macropus* from their respective faunas (Quanbun and Chinchilla) and that the largest *Macropus* known from dentition at these same sites is *M. pan* (Flannery, 1984). Inspection of the Chinchilla Sands Local Fauna collections at Queensland Museum confirm that this ungual morphotype is present, albeit uncommon, and does

represent the largest macropodine ungual recorded. Therefore, assignment of this ungual to *M. pan* at Chinchilla does seem warranted even though no direct associations are available. The tibia mentioned above, from the Chinchilla Sands Fauna, also represents the largest macropodine tibia recovered so far from Chinchilla. This tibia shares closest morphological features with the taxon from South Walker Creek, albeit a smaller, more robust and considerably geologically older taxon.

Macropus pearsoni, a large Pleistocene species, shares similar, but further specialised, dental characteristics with *M. pan* (Dawson & Flannery, 1985; Flannery & Archer, 1982). Both species have been previously considered members of a separate genus or subgenus *Fissuridon* (Bartholomai, 1973a; Flannery & Archer, 1982). Based on the close dental morphological similarities seen between *M. pan* and *M. pearsoni*, it seems likely that if the postcranial elements referred to *M. pan* are indeed correctly assigned, the postcranial morphology of *M. pearsoni* would bear closest resemblance to that of *M. pan*. However, no post-cranial remains (partial or otherwise) with similar morphology and size to those found at SWC are known from any other Pleistocene site or localities from which *M. pearsoni* is presently known. Post-cranial remains of macropodines from these other Queensland Pleistocene localities are much smaller.

As the fragmentary dental remains found at South Walker Creek are similar in features to *M. pearsoni*, and that the postcranial remains bear closest morphological resemblance to postcranial material assigned to *M. pan*, we regard the most likely candidate for the giant macropodine both in dentition and postcranial remains at South Walker Creek to be closely related to *M. pearsoni* and *M. pan*. However, we refrain from formally allocating these remains to either taxon due to the reasons mentioned above and because we cannot rule out an as yet undescribed species.

Protemnodon (Owen, 1874)

***Protemnodon* sp. nov?**

Figure C5 (ab-an)

Referred material: QML1470. Isolated metatarsal IV QMF57037; an associated juvenile with RI_1, LP^2-M^2, LP^2, LP^3, thoracic vertebrae, left femur, left fibula, left and right tibiae, tibial epiphyses, metatarsal IV-IV.III, mtV-V.I and III.I QMF57165; associated adult with LI_1, RI^3, LP^3, a left mandible with P_3-M_4, left pelvis, left proximal femur QMF57035; left proximal femur QMF57127; P3 QMF59933.

The best preserved macropodid dentition so far recovered from South Walker Creek includes teeth from two individuals, an adult and a sub-adult, from QML1470 (SW9). These two individuals also possess associated postcranial remains that are either semi-articulated or closely associated in the site. We assign these adult and sub-adult dental remains to their respective post-cranial associations. On comparison with species of *Protemnodon* (Bartholomai, 1966, 1973b, 1978a; Dawson, 2004; Flannery & Archer, 1983; Flannery, 1992; Piper, 2016; Plane, 1965), this taxon is larger than *P. snewni*, *P. anak*, *P. chinchillaensis*, *P. devisi*, *P. otibanda* and *P. nombe*. It is smaller than *P. roechus*, leaving *P. hopei* and *P. brehus* for comparison. The lower dentition is higher crowned than *P. hopei* but shares closest morphological features with *P. brehus*. The South Walker Creek taxon differs in upper molar morphology to *P. brehus* by possessing less developed central and buccal crests and better developed anterior cingulum on P^2. dP^3 is lower crowned with a distinct mid-link and buccal protoloph-hypoloph

link, and broader posterior cingulum. P^3 is higher crowned with anterior cingulum present and a deep posterior fosset. Upper molars are distinctly higher crowned than referred specimens of *P. brehus* from the eastern Darling Downs (e.g. QMF4954, QMF4947 and QMF12505). Posterior unworn crown heights of M^2 (11.24 mm) and M^3 (13.03 mm) in QMF57165 are taller than measured unworn molars of the Darling Downs *P. brehus* specimens (e.g. QMF4954, M^2 (7.66 mm) and M^3 (9.04 mm) and QMF4947 M^3 (8.84 mm)). M^{1-3} possesses prominent buccal links between protoloph and hypoloph with a narrower anterior cingulum. Overall, the SWC *Protemnodon* is either a new taxon or a higher crowned northern variant of *P. brehus*.

Sthenurinae (Glauert, 1926)

Sthenurine indeterminate

Figure C5 (k)

Referred material: QML1470. Partial RM^{1or2} QMF59999.

A fragment of an anterior upper right molar represents the only definitive evidence of the Sthenurinae within the Pleistocene South Walker Creek fauna. It is the second record of sthenurines within the Fitzroy River Catchment, the only other evidence being an unpublished partial molar from a Middle Pleistocene cave deposit at Mt. Etna (Hocknull, 2009) in the lower reaches of the Fitzroy River Basin. QMF59999 preserves the antero-buccal corner of the upper molar, including the paracone, protoloph and anterior cingulum. The combination of features of this molar that identify it as a species of sthenurine include; a low crowned protoloph with the anterior slope possessing crenulations (3, possibly 4 crenulations); a broad, low anterior cingulum; and a distinct indentation and groove located at the junction of the preparacrista and the anterior cingulum. On comparison with sthenurines (Prideaux, 2004) this taxon is a very small species, similar in size to *Simosthenurus andersoni* and *Procoptodon gilli*. There are no additional features that assist with identifying QMF59999 further than a species of small-sized sthenurine.

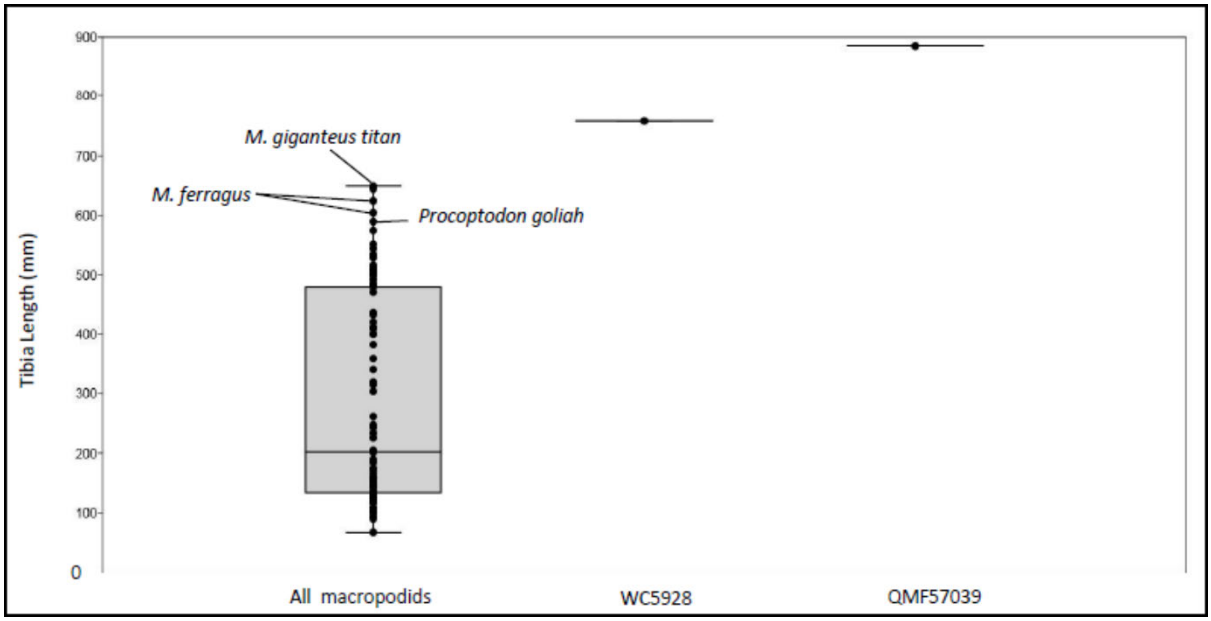

Figure C 4 Box plots of tibia lengths (mm) for macropodids from published records of museum specimens (Tedford, 1967; Janis et al., 2014) (left), *Macropus ?pan* WC 5928 (centre) and the South Walker Creek *Macropus* sp. (giant) QMF57039 (right).

Figure C 5 Macropodidae. *Notamacropus* sp. (a–i); (a) left dentary showing P_3-M_4 of mandible QMF59990; (b) partial left dentary I_1-M_2 QMF59992; (c–g) associated dentition and postcranial remains of QMF57047; (c) RI^3, (d–e) RM_3, (f) left calcaneum, (g) right tibia; (h) $LM_{2\text{-}3}$ QMF59994; (i) RP^3 QMF59993. *Osphranter* sp. cf. *O. rufus* (j) RM_4 extant *O. rufus* QMJ4452 (left) and RM_4 fossil QMF59929 (right). Sthenurinae (k) Sthenurine indeterminate RM^{1or2} QMF59999. *Macropus* sp. (l) LI_1 QM57039; (m) LI_1 QMF59921; (n) LI^3 QMF57163; (o) $LM_{2\text{-}3}$ QMF59928; (p–q) associated hind limb elements IV.III (ungual) in lateral and ventral views, (t) calcaneum, (u) metatarsal IV, (v) associated phalanges IV.I, II & III; (r-s) IV.III (ungual) in dorsal and ventral views QMF57161; (w) left femur QMF57086; (x) left femur QMF57038; (y) right humerus QMF57036; (z) 3-D models generated through CT scans, aligned together of macropodids for comparison to the giant *Macropus* sp. Left – Right; *Protemnodon* sp. QMF57165; *Protemnodon snewini* QMF9075; *Macropus ferragus* MVP28290; *Protemnodon* sp. QMF14.624, *Macropus titan* QMF12262; *Macropus titan* QMF3298; *Macropus giganteus* (modern); *Macropus ?pan* (Chinchilla) WC5928; *Macropus* sp. QM59997, QMF57039 (right and left tibia); *Sthenurus stirlingi* MVP150275. *Macropus* sp. (giant) (aa) articulated metatarsal V and VI QMF59911. *Protemnodon* sp. (ab) isolated metatarsal IV QMF57037; an associated juvenile (ac) RI_1 , (ad) LP^2-M^2, (ae) LP^2, (af) LP^3, (ag) femur, fibula, tibia, metatarsal IV-IV.III, mtV-V.I and III.I QMF57165; associated adult (ah) LI_1, (ai) RI^3, (aj) LP^3, (ak+al) left mandible with P_3-M_4, (am) left pelvis, (an) left femur QMF57035. Scale bars equal 5 mm (a–y, aa–an); 500 mm (z).

C1.5. Vombatiformes

Palorchestidae (Owen, 1874)

Palorchestes (Owen, 1874)

***Palorchestes* sp. nov?**

Figure C6 (a-c)

Referred material: QML1470. Left I^3 and M^2 QMF57059.

Two teeth referrable to *Palorchestes* were found together within QML1470 (SW9), both similarly worn and coming from the left upper dentition, we therefore regard them as associated. The LI^3 is heavily worn and difficult to directly compare with species of *Palorchestes* due to few I^3s being known for described *Palorchestes* species (Bartholomai, 1978b). The I^3 is larger than the I^3 preserved in *P. parvus* (QMF789) but is morphologically similar. It differs by possessing thicker enamel on the antero-buccal surface. The tooth is split medially but would have been antero-posteriorly broader than QMF789. The I^3 of *P. azael* is unknown so it was not possible to be directly compared; however, the illustrated rostrum (Bartholomai, 1978b) of *P. azael* (QMF3837) indicates an I^3 alveolus that would have received an incisor that was proportionately broader than that seen in *P. parvus* or *P. painei*. However, *P. azael* is much larger than *P. parvus*, and the I^3 of QMF57059 would have therefore been much smaller than that expected in *P. azael*. Similarly, the LM^2 is worn and is much smaller than the Upper Pleistocene *P. azael* specimens (e.g. QMF772 & QMF33510). It is, however, more morphologically similar to *P. azael* than it is to *Palorchestes* closer in size to QMF57059 such as *P. parvus* (Banks et al., 1976; Bartholomai, 1978b; Black, 1997; Davis & Archer, 1997; Mackness, 1995; Piper, 2006; Pledge, 1991; Price & Hocknull, 2005; Trusler & Sharp, 2016). Even though QMF57059 is missing the lingual third of the molar and is heavily worn, there are a number of features that differentiate it from all other species of described *Palorchestes*. The projected unworn tooth crown height along with a steeper tooth wear gradient across the lophs is greater than that seen in smaller species of *Palorchestes* but similar to the much larger *P. azael*. An accessory buccal anterior link on the anterior cingulum, buccal interloph cuspule, faint protoloph crenulations and posterobuccal vertical groove of the hypoloph provides a combination of features not seen in species so far described. Due to the poor representation of this taxon a firm species-level allocation cannot be made; however, it is likely that it represents either a new species or a significantly small-sized variant of *P. azael*.

Thylacoleonidae (Gill, 1872)

Thylacoleo (Owen, 1859)

***Thylacoleo* sp.**

Figure C6 (d-i)

Referred material: QML1470. Associated *Thylacoleo* postcranial remains including a left fibula, left metacarpal III, phalanx, ?left V.I phalanx QM59910; isolated phalanx QMF59912.

Although the distinctive dentition of *Thylacoleo* has yet to be recovered from Quaternary sites within the South Walker Creek system this taxon is represented at QML1470 (SW9) by several associated postcranial elements and rare, but distinctive bite-marked bones. The elements recovered from this individual include a left fibula and left manual elements. On comparison with described skeletal elements of *Thylacoleo carnifex* (Finch & Freedman, 1988; Wells, 1977; Wells & Camens, 2018; Wells et al., 2009), and additional comparison with photographs of the fibula, pes and manual elements of *T. carnifex* specimens (kindly provided by Aaron Camens, Liz Reed and Steve Bourne, respectively), it is clear that these elements are referrable to *Thylacoleo*. The fibula is a thin, elongate limb, with expanded proximal epiphysis that possesses a bevelled proximal articular end with flattened femoral and tibial facets as illustrated here (Finch & Freedman, 1988). The metacarpals and phalanges are gracile and elongate elements, easily distinguished from macropodid, vombatid and diprotodontid pedal and manual elements. They possess narrow mid-shafts that bend dorsally with flared proximal and distal articular ends. The fossils are directly comparable to those illustrated here (Wells, 1977; Wells et al., 2009). Based on their similar size and the Upper Pleistocene age of the South Walker Creek deposits, it is likely that the species is *Thylacoleo carnifex*. However, without dental remains to confirm this identification, we will refer these fossils to *Thylacoleo* sp.

Vombatidae (Burnett, 1830)

Sedophascolomys (Louys, 2015)

Sedophascolomys* sp. cf. *S. medius (Owen, 1872)

Figure C6 (j-o)

Referred material: QML1470. RM^{3-4} QMF59934; associated right and left I_1s QMF57069.

The lower right and left incisors, along with isolated pedal phalanges, so far represent a single large vombatid individual, smaller in size than the largest known vombatid species *Phascolonus gigas*. The specimens are both larger and morphologically different to members of the extant genera, *Lasiorhinus* and *Vombatus*. Following the traits set out by Dawson (1981) for the lower incisors of extant and extinct wombat taxa, these fossils share traits with *Phascolomys medius*, now established within its own genus, *Sedophascolomys* (Louys, 2015). In crosssectional shape the incisors are ovoid with the height of the incisor slightly taller than wide. Enamel is distributed around the ventral half of the tooth with fine longitudinal striations evident. Both incisors preserve partial wear facets from the upper incisors. These facets indicate an elongate wear area, similar to that seen in specimens assigned to *S. medius*. The tooth shafts are straight, lacking any dorso-ventral curvature along their length. This is a unique trait and unlike any of the incisors observed in well-preserved specimens.

On closer inspection of comparative specimens available for this study and through X-ray computed tomographic scanning of several specimens (Figure C6, p-r), the incisors of *S. medius* show limited or no bending along their antero-posterior length. This traits is here considered to be an autapomorphy of *Sedophascolomys*, although it will require further investigation with other fossil vombatid taxa where lower incisors are known but not entirely visible due to preservation. Based on the above features, along with the very close size to comparative specimens at the Queensland Museum collection from the Darling Downs and Chinchilla sites of Queensland, it is most likely that this wombat represents the youngest fossil occurrence for *Sedophascolomys* and a Pleistocene range extension into northern

Australia. Since the genus is monotypic we tentatively allocate these specimens to the PlioPleistocene species, *S. medius*, until further material is available.

Phascolonus (Owen, 1872)

Phascolonus gigas (Owen, 1858)

Figure C6 (p-v)

Referred material: QML1470. An associated specimen including right and left femora, pelvis and articulated sacral and caudal vertebrae, and associated teeth including RI^1, RI_1 fragment, $RM^{3 \text{ or } 4}$, RM_4, LM_2, LM_3 and LM_4 QMF57065.

Phascolonus gigas is represented at QML1470 (SW9) by a single partial skeleton including dentition, hind appendicular elements along with a large pelvis with articulated caudal vertebrae. Isolated ribs and pedal elements likely belong to this same individual, but comparative material of *P. gigas* was difficult to attain for this preliminary identification. *P. gigas* has been identified on the basis of the autapomorphic dorso-ventrally compressed and medio-laterally broad upper incisors (Dawson, 1981); large hypselodont molars and morphologically similar postcranial elements as seen in specimens recovered from Lake Callabonna (Stirling, 1913) and via photography provided to us by A. Camens (*pers comm*., 2014) of cast specimens lodged within the South Australian Museum.

Figure C 6 Palorchestidae, Thylacoleonidae and Vombatidae. Associated *Palorchestes* sp. teeth (a–b) LM^2, (c) LI^3 QMF57059. *Thylacoleo* sp. associated postcranial remains; (d) left fibula, (e–f) left metacarpal III, (g) phalanx, (h) ?left V.I phalanx QM59910; (i) phalanx QMF59912. *Sedophascolomys* sp. cf. *S. medius* (j–k) RM^{3-4} QMF59934; (l–n) associated right and left I_1s showing drill position for uranium-series samples QMF57069 (o); LM_4 QMF59920. *Sedophascolomys medius* mandible CT scans (p-r) showing the straight lower incisor with ventral enamel and dorso-ventrally oblong circular cross-section, QMF12493. *Phascolonus gigas* associated remains (s-y) including (s) right and (t) left femora, (u) pelvis with articulated sacral and caudal vertebrae, (v-w) RI^1, (x) RM^{3or4} and (y) RM_4 QMF57065. Scale bars equal 5 mm (a–r, v–y) and 10 mm (s, t + u).

Diprotodontidae (Owen, 1838)

Diprotodon (Owen, 1838)

Diprotodon optatum (Owen, 1838)

Figure C7 (a-g) & Table C2

Referred material: QML1470. An associated small-sized sub-adult with skull, mandible, pelvis, tibia shard and pedal elements QMF54689; an associated small-sized old individual with right dentary, skull, cervical vertebra, scapula and femur QMF59996; an isolated large skull QMF57172; astragulus QMF57066.

The cranial, incisor, premolar and molar morphology along with postcranial elements are indistinguishable from specimens referred to as *D. optatum* (Huxley, 1862; Pledge et al., 2002; Price, 2008; Price & Piper, 2009; Price & Sobbe, 2011) and those compared directly; therefore we refer all of these specimens to *D. optatum*. However, the specimens from QML1470 (SW9) are worthy of further description. Two individuals are presently recognised within the prepared portion of fossil collection, a smallsized sub-adult large form and a small-sized, small form old individual. Both individuals are very small in overall size being at the minimum size range for *D. optatum* dentaries as described by Price (2008). The dentary depth to width of QMF54689 is 59.5 mm / 45.2 mm and of QMF59996 is 72 mm / 48 mm which is within the smallest range figured here (Price, 2008). However, on the basis of molar size QMF54689, the sub-adult, plots within the largest of the large form of Price (2008) whilst QMF59996 plots within the small form size range (Table C2). The sub-adult individual exhibits a large degree of wear on M_{1-2}, whilst the old individual has a fully erupted dental arcade that exhibits extreme levels of wear on all teeth. QMF54689 represents a sub-adult large morph individual (e.g. a male) and QMF59996 represents a very old small morph (e.g. a female), yet both individuals are at the minimum overall size for *Diprotodon optatum* defined by Price (2008). We conjecture that these specimens represent a population of *Diprotodon* that has undergone some degree of body-size reduction (dwarfing), or is a population exhibiting a small body-size variant not usual for Upper Pleistocene populations typical of southern Australia (Price & Piper, 2009).

Table C 2 Dental measurements of *Diprotodon optatum* from South Walker Creek and inferred size form based on comparison to measurements in Price (2008).

	M_1	**M_2**	**M_3**	**M_4**	**M^1**	**M^2**	**M^3**	**M^4**	**Size**
	L x PW (Area)	L x PW (Area)	L x PW (Area)	L x PW (Area)	L x PW (Area)	L x PW (Area)	L x PW (Area))	L x PW (Area)	Large or Small Form
QMF 54689	37.88 x 25.9 mm (981 mm^2)	45.99 x 31.8 mm (1463 mm^2)	56.96 x 40.09 mm (2283 mm^2)	erupting					Large
QMF 59996	missing	heavily worn	48.5x ?mm (??? mm^2)	54.72 x 33.76mm (1849 mm^2)	32 x 34mm (1088 mm^2)	40.4 x ? mm (??? mm^2)	45.2 x ? mm (??? mm^2)	42.3 x ? mm (??? mm^2)	Small
QMF 57172					32.97 x 31.48mm (1037mm^2)	42.33 x 38.3mm (1621mm^2)	50.82 x 41.27mm (2097mm^2)	48.82 x 44.78mm (2186mm^2)	Small

Zygomaturus (Owen, 1858)

Zygomaturus trilobus (Macleay, 1857)

Referred material: Homevale Station. Mandible QMF11136.

A near complete mandible preserving the right and left dentition from I_1-M_4 represents *Zygomaturus trilobus*. This specimen possesses the typical morphological traits of *Z. trilobus* including molars that are broad and square in occlusal outline, crescentic lophids with wide u-shaped median valleys, a small triangular P_3 and parallel short incisors.

Figure C 7 Diprotodontidae. *Diprotodon optatum* (a–d) an associated skull and mandible; (a) skull in lateral and (b) oblique ventral views; (c–d) mandible showing (c) prepared right dentary and (d) unprepared left dentary QMF54689; (e) associated right dentary and (f) skull QMF59996; (g) skull in occlusal view QMF57172. *Zygomaturus trilobus* (Homevale Station) (h) mandible QMF11136. Scale bars equal 10 mm.

C2. Faunal associations

Scott A. Hocknull & Rochelle A. Lawrence

Articulated and semi-articulated remains were recorded during excavations and preparation. Association of remains was determined through a process using: 1) identical taxonomic identification, 2) observations of relationship within the excavation, 3) assessment of element duplication, 4) establishing the minimum number of individuals, 5) determining the proximity of any element to another sequential element within a body part, and 5) determining re-articulation fit for sequential associated elements.

Table C 3 Faunal Associations observed per site and per taxon. Numbering indicates the minimum number of individuals (MNI) recorded from each site. > = many isolated specimens (MNI not known). Abbreviations: Art = Articulated; Sem = Semi-articulated; Ass = Associated; Iso = Isolated; Trace = trace fossil; bm = bone modification (bite/cut marks); c = coprolite.

QML1470 (SW9) Taxon	Art	Sem	Ass	Iso	Trace
Crocodile					bm
Pallimnarchus sp.				>	
Crocodylus sp. cf. *C. porosus*				>	
Varanus priscus				1	
Varanus sp. (large)				1	
Thylacoleo sp.			1		bm
Phascolonus gigas	1				
Sedophascolomys sp. cf. *S. medius*			1		
Protemnodon sp. nov?		2			
Macropus sp. (giant)		1	2	1	
Notamacropus sp. (giant)			1		
Palorchestes sp. nov?			1		
Diprotodon optatum			2		
Dromaius sp. cf. *D. novaehollandiae*					shell
Velesunio wilsoni	2	1		>	
corbiculidae				2	
Arthropoda			>	>	

Table C 3b Faunal Associations observed for QML1470 (SW3) and per taxon. Numbering indicates the minimum number of individuals (MNI) recorded from each site. > = many isolated specimens (MNI not known). Abbreviations: Art = Articulated; Sem = Semi-articulated; Ass = Associated; Iso = Isolated; Trace = trace fossil; bm = bone modification (bite/cut marks); c = coprolite.

QML1470 (SW3) Taxon	Art	Sem	Ass	Iso*	Trace
Crocodile					bm/c
Pallimnarchus sp.				>	
Crocodylus sp. cf. *C. porosus*				>	
'Quinkana' sp.				1	
Varanus sp. (large)				1	
Varanus priscus				1	
Sedophascolomys sp. cf. *S. medius*				1	
Protemnodon sp. nov?			1	2	
Macropus sp. (giant)	1		1	1	
Notamacropus sp. (giant)	1			1	
Osphranter sp. cf. *O. rufus*				2	
Diprotodon optatum				2	
Dromaius sp. cf. *D. novaehollandiae*				1	

Table C 3c Faunal Associations observed for QML1470 (SWJ) and per taxon. Numbering indicates the minimum number of individuals (MNI) recorded from each site. > = many isolated specimens (MNI not known). Abbreviations: Art = Articulated; Sem = Semi-articulated; Ass = Associated; Iso = Isolated; Trace = trace fossil; bm = bone modification (bite/cut marks); c = coprolite.

QML1470 (SWJ) Taxon	Art	Sem	Ass	Iso*	Trace
Pallimnarchus sp.				1	
Quinkana' sp.				1	
Varanus priscus				1	
Notamacropus sp. (giant)				1?	
Macropus sp. (giant)				1	

Table C 3d Faunal Associations observed for QML1470 (SWCC) and per taxon. Numbering indicates the minimum number of individuals (MNI) recorded from each site. > = many isolated specimens (MNI not known). Abbreviations: Art = Articulated; Sem = Semi-articulated; Ass = Associated; Iso = Isolated; Trace = trace fossil; bm = bone modification (bite/cut marks); c = coprolite.

QML1470 (SWCC) Taxon	Art	Sem	Ass	Iso*	Trace
Pallimnarchus sp.				>	
Crocodylus sp. cf. *C. porosus*				1	
Quinkana' sp.				1	
Varanus priscus				1	
Protemnodon sp. nov?				1	
Macropus sp. (giant)			1		
Notamacropus sp. (giant)				1	
sthenurine				1	

C3. Body mass estimation for *Macropus* sp. (giant)

Scott A. Hocknull

Macropus sp. (giant) left femur (QMF57038) mid-shaft circumference = 160 mm

Mass estimate of *Macropus* sp. from Equation 2 of Helgen et al. (2006)

$$M_{est} = 1.0146*10^{[2\ 5932\ \log10(c) - 3\ 2842]}$$

$$M_{est} = 274.0431\ kg$$

C4. Stratigraphic and sedimentological description of QML1470 sites

Scott A. Hocknull & Rochelle A. Lawrence

The fossil sites described herein are located along the eroded gully and rill systems of Walker Creek, nearby the South Walker Creek Mine (Latitude -21.708883°; Longitude 148.349112°). Walker Creek is a headwater tributary of the Isaac River system that drains the northern section of the Fitzroy River catchment. The sites are located approximately 30 km downstream of Lake Elphinstone. Several tributaries run in a north to southeast and southwest direction draining a northern headwater catchment created between the western Carborough Range, northern Pisgah (and Connors) Range and eastern Balaclava and Blue Mountains. Quaternary vertebrate fossils have been collected from the intervening valley system, derived from three separate areas along Walker Creek, Kemmis Creek and Homevale National Park. This system drains into the Bee Creek and Funnel Creek systems that enter the Isaac River. Funnel Creek formed a component of a previous Fitzroy River catchment-wide assessment of Quaternary alluvial sedimentation (Croke et al., 2011). The fossil deposits presented here are derived entirely from the South Walker Creek sites; however, discussion of faunal remains will include those other sites in this headwater catchment, including fauna from Kemmis Creek and Homevale National Park.

Based on the current extent of surveys undertaken along Walker Creek the fossil sites are localised to short stretches of two meanders presently eroding Quaternary-aged alluvial deposits. The meanders are bedrock-controlled, with the basement of the creek system and alluvial deposits wedged upon the downward slope of a locally dipping Permo-Triassic Rangal and Fort Cooper Coal Measures and Triassic Rewan Group.

Sediments preserving the Quaternary fossils range from singular matrix-supported muddy cobble beds (~50 cm thick) through fine-grained sandy muds (~1-1.5 m thick) to confined coarse-grained gravel beds (~20-40 cm thick). These types of fossil deposits occur within a more broadly horizontally distributed, fine-grained, and internally unstructured, alluvial overbank fines. Notably, only one site (QML1420 SWCC) records fossils from a depositional environment not typically flood plain. Most of the numerous, better structured, and well-sorted channel, point bar or crevasse splay deposits associated with the floodplain deposits are not fossiliferous. The fossil deposits occur in localised areas of the alluvial floodplain where they sit above the bedrock, with indications of some form of scouring prior to deposition, either directly scouring the bedrock or scouring into older floodplain sediments.

The fossil deposits are laterally discontinuous over scales of tens to hundreds of metres with limited opportunity directly correlate each site stratigraphically; however, within sites the relative positions of the fossils can be determined and thus relative stratigraphic height attained. SW9, SWJ and SWCC are locally confined deposits with lateral extents less than 50 m^2 (SWCC) to approximately 70 m^2 (SW9). SW3 is the only laterally extensive site, with fossil concentrations found in an area covering approximately 6000 m^2. Isolated remains have been recovered from a few additional sites, but these deposits are neither laterally extensive, nor fossiliferous. However, each site so far recorded has been sampled for dating and this will form part of a larger work.

C4.1. QML1470 (SW9) (Figure C11 & Table C4)

The stratigraphy at QML1470 (SW9) is divided into three depositional units above Rewan Group bedrock. Unit A comprises cemented slightly gravelly sandy mud to muddy gravel (see Figure C8 for sedimentological definitions) that is poorly sorted, poorly structured and containing angular medium gravel-sized clasts comprised only of Rewan Group. The unit is not fossiliferous and contacts the basement Rewan Group as an unconformity along its eastern margin. Unit B comprises slightly gravelly sandy mud to sandy mud, which is poorly sorted with limited sedimentary structure and includes sporadic lenses of angular fine to medium-sized gravel clasts of Rewan Group and reworked cemented sediment. The unit is not fossiliferous and contacts Unit A as a scoured surface forming an unconformity at the junction of both units, thickening to the west and southwest. Unit C is divided into three subunits (C1-C3). Unit C1 comprises a single bed of poorly sorted, poorly structured sediment ranging from mud to gravelly mud which forms a matrix supporting coarse pebble to small cobble-sized clasts. Gravel to pebble-sized clay-rich clasts that are likely rip-up clasts preserve some macro-floral remains, including macro-charcoal; however, there is limited sedimentological structure to define these structures. The lithified siliceous and bedrock clasts are dispersed throughout the bed, are concentrated toward its base, and are usually associated with large bones. These larger clasts include lithified angular to rounded pieces of petrified wood, silcrete, sandstone and siltstone that are derived from bedrock sources. Unique to all units within this sequence, unit C1 is fossiliferous preserving abundant vertebrate, invertebrate and plant remains throughout. Unit C1 contacts Unit B and the bedrock at an irregular scoured surface, which is identifiable as a slightly more gravelly muddy iron-oxide stained lens on which the lowermost fossils, pebbles and cobbles rest. This scoured surface forms a shallow northeast-southwest oriented basin into which unit C1 has accumulated. Fossils and the non-Rewan Group clasts are not found in unit B, or above the C1 bed in C2-C3. Unit C1 transitions into unit C2 with no definable contact between the two. The within-unit transition retains the massive slightly gravelly sandy mud matrix, but lacks the pebble to cobble clasts and fossils that define C1. Unit C3 is a slightly gravelly sandy mud lens with well-sorted sand that transitions from the poorly sorted, structureless unit C2. This transitional zone is not horizontal and thickens slightly to the southwest, but is not laterally extensive. The transition between units C2 and C3 is marked by a greater concentration of iron-oxide staining of the sediment. Unit C1 to C3 combined shows a general fining upwards trend with basal matrix-supported fossiliferous gravel to pebble and cobble bed that transitions into a well-sorted fine sandy mud with the absence of larger clasts and fossils. A shallow, clay-rich soil profile caps the site, and comprises fine carbonate nodules.

Fossil remains recovered from the site include flora and fauna representing both aquatic and terrestrial taxa. Floral preservation has only been observed at this site and is dominated by oxidised organic remains and impressions of leaves and seeds. Very small pieces/flecks of reworked charcoal of similar size to the clasts entraining them are sporadically recovered exhibiting significant weathering and are mostly oxidised. Leaves and seeds preserve limited structure; however, those leaves with thick sclerophyllous cuticle and rigid venation create good impressions when the matrix surrounding them is almost entirely fine clay. Similarly, seeds are found as both oxidised organic remains or moulds and casts. Oxidised leaves and seeds are found throughout unit C1 being well preserved in clay-rich matrix but poorly preserved when included in more sandier or gravelly matrix. No plant remains have been recovered from units C2 or C3 overlying this. The distribution and orientation of plant fossil remains is haphazard, with leaves and seeds showing pre-burial fragmentation, splitting, curling and

orthogonal breakage, indicating that the leaves were dry prior to deposition (Figure C1, c, e & g). However, other plant remains show labile deformation within the sediment and entire portions preserved indicating soft plant tissue that had not completely dried out prior to deposition (Figure C1, f, h–l). A small ~50 cm x 50 cm patch of dominantly clay matrix has produced the best preserved plant remains and has also returned low but present pollen counts (Figure C31 and Table C22). Tiny seeds, preserving very fine organs, are found preserved in relatively coarse sediment, indicating rapid burial with limited transport (Figure C1, i–l). In particular, a seed from the Goodeniaceae (Figure C1, i) family represents a member of a small-sized short-lived herbaceous taxon suggesting that this deposit was formed rapidly when seeds were available, perhaps within a season. These types of seeds do not survive intact and will germinate if sown; therefore, it would be expected that the time between seeding of this particular seed being deposited was very short, perhaps within weeks.

Aquatic and terrestrial invertebrate fossils are preserved in unit C1 as oxidised moulds and casts. Terrestrial insects are only preserved at QML1470 (SW9), represented by three-dimensionally preserved abdomens with oxidised elytra and suspected (but indeterminate) wing and limb impressions. The elytra compare closely to members of the weevil family, Curculionidae (Figure C1, y–z), a diverse terrestrial insect group. Aquatic invertebrates include two freshwater bivalve taxa from the hyriidae and corbiculidae, both preserved as either moulds or casts with impressions of the commarginal ornament and dentition. These bivalves are small-sized (10 mm – 60 mm shell length) and are found either as isolated or articulated valves not in life position, indicating that they have been displaced from their life habitat and transported pre-burial. No original shell material remains, nor has it been replaced. Oxidisation has occurred at the interface between where the internal or external organic bivalve has contacted the surrounding matrix. Freshwater crustaceans are represented by very rare oxidised gastroliths.

Sieving and sorting of approximately 500 kgs of sediment from unit C1 recovered rare and poorly preserved vertebrate microfossils. Partial fish vertebrae, scales and broken spines are the most common remains, whilst the rarest fossils include a heavily rounded dasyurid molar, a fragment of scincid maxilla, few isolated murid teeth and a calcaneum. Of the sites preserving small vertebrates, QML1470 (SW9) is the least well preserved. In comparison, the larger vertebrate remains are the best preserved remains of all sites so far excavated and include both aquatic and terrestrial taxa, with the terrestrial fauna most abundant. Within the C1 bed, crocodilians are known from isolated teeth representing hatchling to large adult size. A single carapace piece is the only known freshwater chelid turtle fossil within the bed (Figure C2, u). No large-sized teleost remains (e.g. vertebrae >5 – 10 mm in length) are present (Figure C2, u-x).

Terrestrial taxa are predominantly represented by appendicular postcranial remains; however, Voorhies groups IIII including associated cranial, articulated and semi-articulated appendicular and associated axial remains of differing sizes are observed at similar proportions (Figure C9). Breakage patterns and surface weathering features indicate a similar proportion of dry to wet fractures with little to no long-term surface exposure. Skeletal associations are observed for nine species (Table C3) with clear articulation present in the pelvis of the only *Phascolonus gigas* individual (QMF57065) (Figure C6) and semiarticulation of a hind limb of a small *Protemnodon* individual (QMF57165) (Figure C5). Low minimum number of individual (MNI) counts for each taxon is supported by the element associations and supports rapid burial with limited time averaging of the deposit. Predatory

modification of bone is observed and include puncture, gouge and cut marks made by crocodilians along with one macropodid rib preserving sequential cut and bone peel marks likely made by *Thylacoleo* (Figure C10).

Bone long-axis orientations do not show a well-defined directional mode and bone orientations are not statistically significant (Figure C11); however, there is a tendency for the longest bones (e.g. tibiae, femora and humeri) to be oriented in a northeast-southwest, or orthogonal to this, direction. This, albeit weak, tendency does reflect the overall shape and orientation of the shallow basin that has been infilled, indicating some influence of flow direction on the largest elements during deposition. This general direction of flow is reflected in the proximity of associated elements to one another, for example, the associated hind-limb of *Protemnodon* sp. (QMF57165) (Figure C5, ag) has disassociated along a southwest to north east trajectory with the proximal pelvic element in the southwest with subsequently more distal elements dispersed in a general northeast direction from this point. This relationship is also seen in the associated *Phascolonus gigas* pelvis and hind limbs elements (QMF57065) (Figure C6). Similar dislocation of elements, but in an orthogonal direction to this, is observed with the associated subadult *Diprotodon* skull, and isolated left and right dentaries (QMF54689), with each element distributed along a near east-west trajectory. These differing trajectories implicate a relatively turbid and changing flow regime during rapid deposition, possibly part of a localised hyperconcentrated flow.

Post-depositional modifications of bones and teeth within the deposit have been observed at different levels of frequency. In decreasing frequency modifications include: 1) cortical surface bone splitting due to clay contraction and swelling within matrix surrounding and internal to the bone (common); 2) medullary cavity collapse due to loss of internal integrity (collagen loss and lithostatic pressure) (common); 3) slight lateral and vertical dislocation of once competent bone elements due to a combination of clay sediment slippage (e.g. showing microslickensides) and opening of cracks due to long-term drying (rare); and 4) termite damage (very rare, a single observation). Some elements collected during the early period of excavation and preparation have experienced modifications due to human-induced accidental damage and preparation.

Table C 4 QML1470 (SW9) Sedimentological and Taphonomic Summary and Interpretation.

Site	Sedimentology	Sedimentary Structure	Fossil Preservation	Fossil Modification	Interpretation
SW9	Multimodal, mud-dominant matrix-supported poorly-sorted gravel to cobble bed transitions to well-sorted mud-dominated fine sand cap. Iron-oxide precipitation.	Basal scour unconformity. Unstructured. Localised post depositional surface cracking.	Well preserved, articulated and associated terrestrial and aquatic invertebrate, vertebrate and plant taxa. Fine preservation of plants and insects. No coprolites. Single definable fossiliferous bed 0.3-0.5m thick.	Crocodile, marsupial carnivore (thylacoleo) bone modification. Pre-depositional dry and wet bone fracturing. Post-depositional lithostatic compression and swelling clay bone-splitting and dislocation. Dry leaf splitting preservation.	Flood event on floodplain. Short-lived high energy deposition (localised hyperconcentrated flow), rapid burial of proximal faunal and floral remains within a scoured floodplain. Transition into suspended load and fine sorting (~1-1.2m thick deposit), then vertical accretion.

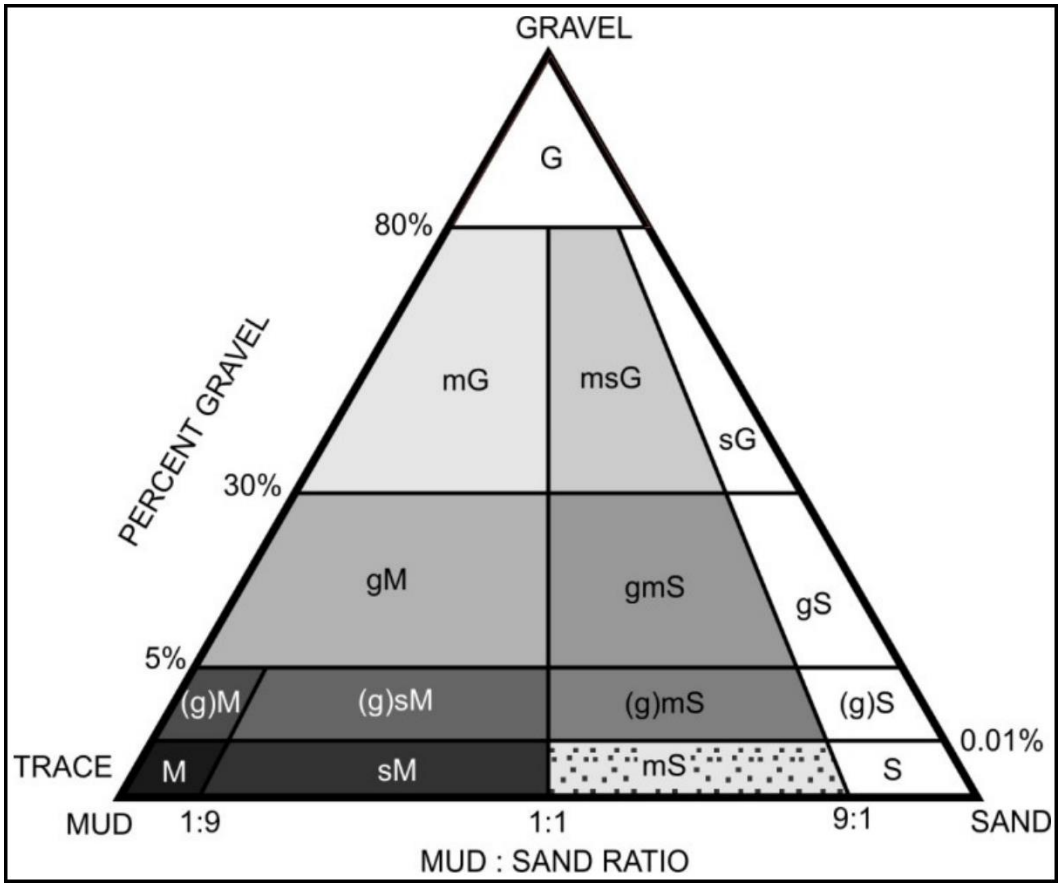

Figure C 8 Sediment classification and composition following Folk (1954). G – gravel; M – Mud; S – Sand; g – gravelly; m – muddy; s – sandy; (g) slightly gravelly.

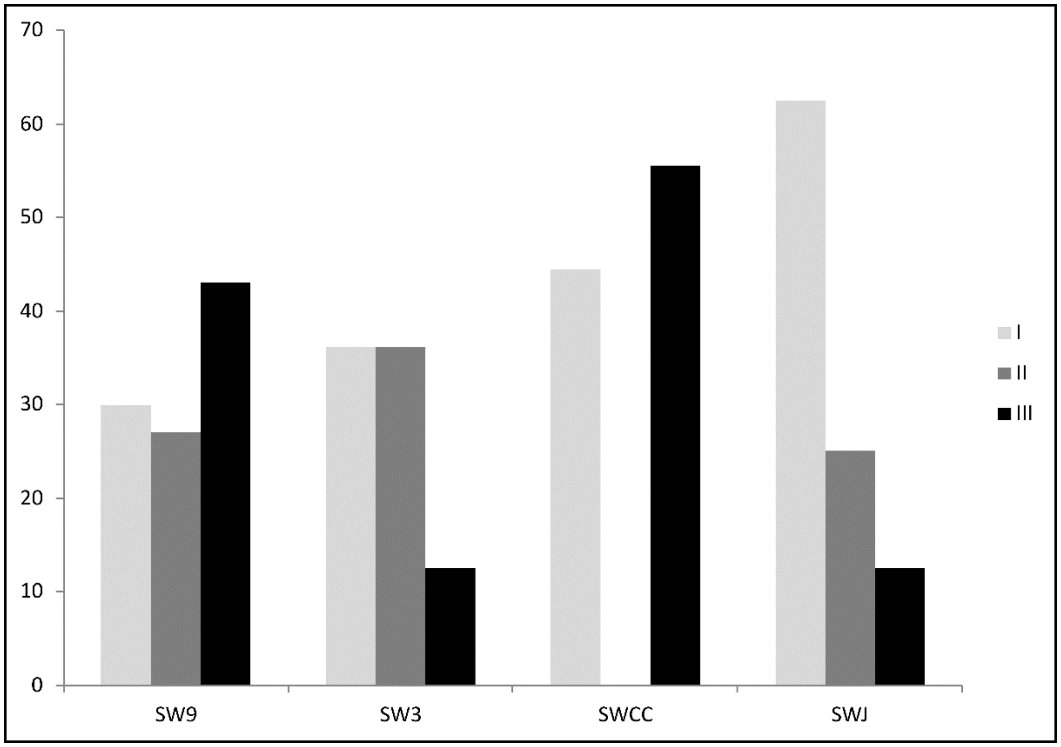

Figure C 9 Percentage of bone elements represented by Voorhies Group per site.

Figure C 10 Taphonomic examples. Puncture and cut marks (arrows) in (a-d); (a) distal macropodid fibula with crocodile puncture mark and dry fracture QMF59989; (b–c) right *Macropus* sp. humerus with crocodile puncture and cut marks, and unfused epiphyses QMF57036; (d) rib shaft showing consecutive cut and bone peeling along rib surface by *Thylacoleo* QMF59995. (e) piece of tibial shaft illustrating wet (left margin) and dry (right margin) fracture patterns QMF59988. (f-j) post-depositional subsurface deformation of fossils with direction indicated by arrows; (f+g) movement through drying and crack filling with silt; (f) *Pallimnarchus* sp. tooth QMF57051; (g) macropodid tibial shaft QMF59952; (h–i) subsurface deformation of fossilised long bones; (h) *Macropus* sp. (giant) fibula QMF57039; (i) *Protemnodon* sp. tibia QMF57165; (j) *Macropus* sp. (giant) tibia QMF57039. Scale bars equal 10 mm (a, b, c, e, g, h, i, j) and 5 mm (d, f).

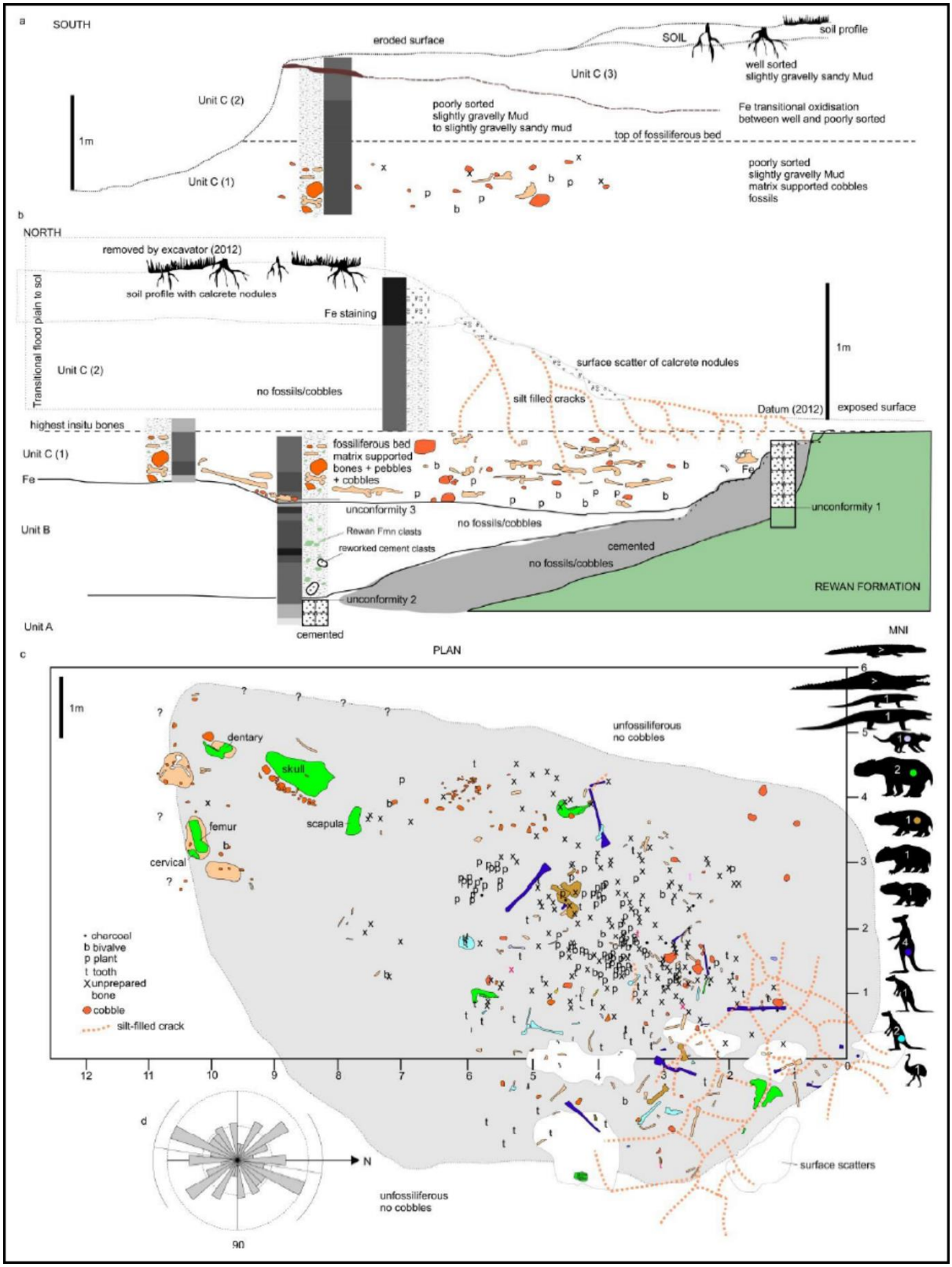

Figure C 11 Stratigraphic map of QML1470 (SW9) in South Section (a), North Section (b) and Plan view (c). In situ bone orientations indicated in rose diagram (d). Minimum number of individuals (MNI) of megafauna indicated within the silhouette. Sediment classification and composition key provided in Ternary diagram of Figure C8.

C4.2. QML1470 (SW3) (Figure C12 & Table C5)

The fossiliferous bed at QML1470 (SW3) is the most laterally extensive of the sites. Fossil vertebrate remains are found throughout the entire unit with the highest concentration at the north-northeastern margin of the exposed deposit. The unit contacts the basement bedrock as a sharp contact with and immediately transitioning into poorly sorted, poorly structured, slightly gravelly sandy mud. Occasional small lenses of angular to rounded Rewan Group gravels are present within the lower metre of the unit; however, these are localised and are not directly associated with bone accumulations. The unit is composed of relatively uniform sandy mud with the only definable component of change within the unit being the increasing concentrations of fossil bone up sequence and to the North. A soil profile is evident at the top of this unit.

Both aquatic and terrestrial vertebrate fauna have been found. No plant or terrestrial invertebrates are known and crustacean gastroliths are present, but rare. Terrestrial vertebrate faunal postcranial remains are the predominant vertebrate fossil recovered; however, aquatic vertebrate fauna are better represented at QML1470 (SW3) compared to QML1470 (SW9). Aquatic fauna are also represented by coprolites. Faunal remains predominantly represent large terrestrial taxa, only a single maxilla from a species of dasyurid has been found that represents small fauna. No fish remains have been recovered. Large portions of carapace and plastron represent chelid turtles, whilst isolated teeth, osteoderms, skull fragments, coprolites, postcranial remains and a partial dentary represent crocodilian remains. Appendicular elements are the most abundant component of terrestrial fauna; however, axial remains are better represented at SW3 than at other sites. Skeletal associations are recognised for three species found at the site (Table C3).

Pre-depositional modification of bone is difficult to ascertain due to the heavy carbonate encrustation and surface corrosion of bone; however, bone modification through predator action includes puncture, gouge and cut marks on bones from crocodilians (Figure C10, b & c). Pre-depositional fracture patterns are hard to discern due to the exposed weathering of this site prior to excavation. Excavated remains include almost complete elements suggesting that limited fracturing occurred prior to burial. Post-depositional modification includes surface cortical bone splitting through clay swelling; organic acid corrosion of bone surfaces and deposition of thick penetrating carbonate encrustation (caliche). This encrustation adheres very tightly to the bone and is difficult to remove to reveal original bone surface. However, when removal of the carbonate is possible, bone modifications are revealed, including evidence of wet bone fractures and predator modification.

Table C 5 QML1470 (SW3) Sedimentological and Taphonomic Summary and Interpretation.

Site	Sedimentology	Sedimentary Structure	Fossil Preservation	Fossil Modification	Interpretation
SW3	Mud-dominated, poorly-sorted matrix. No cobbles or pebbles. Carbonate precipitation.	Basal contact with bedrock. Unstructured / massive.	Caliche-encrusted terrestrial and aquatic vertebrate fauna, invertebrates minor, no plants. Coprolites common. Concentration of fossil bones up profile ~2.5m thick.	Crocodile bone modification. Pre-depositional dry and wet bone fractures. Swelling clay surface bone splitting. Organic acid / root surface corrosion of surface bone.	Vertical accretion on floodplain. Low energy accretion on flood plain (muddier than SWJ). Dispersed fossil beds within a 2.5-3m thick depositional sequence.

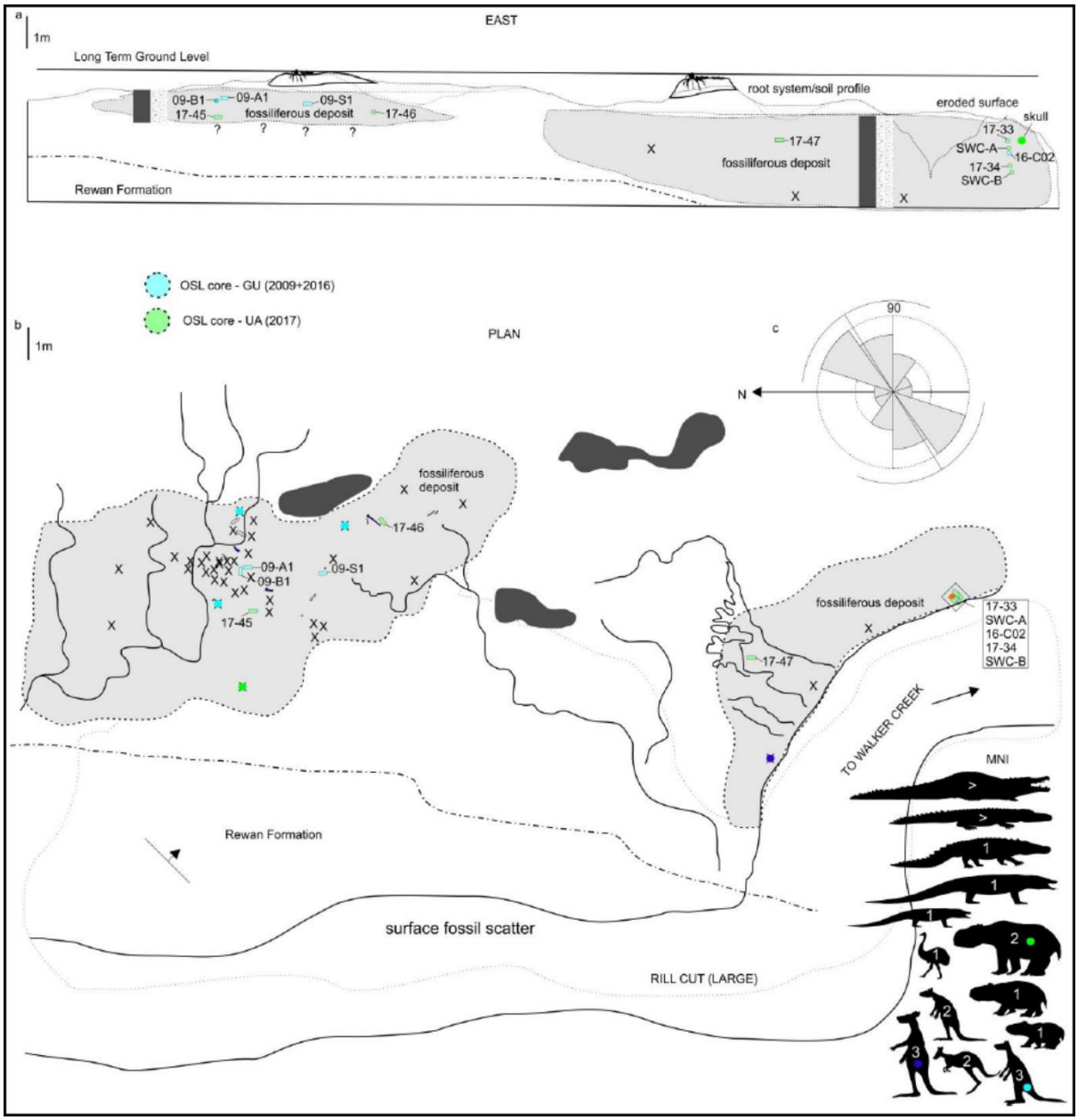

Figure C 12 Stratigraphic map of QML1470 (SW3) in East Section (a) and Plan view (b). *In situ* bone orientations indicated in rose diagram (c). MNI of megafauna indicated within the silhouette. Sediment classification and composition key provided in Ternary diagram of Figure C8.

C4.3. QML147 (SWJ) (Figure C13 & Table C6)

The QML1470 (SWJ) fossils are exposed at the top of an eroded slope above a thick exposure of Rewan Group bedrock. Above this bedrock a series of exposed cemented beds form a basal unit (unit A) consisting of a coarsely to finely-graded sandy gravel with cemented calcrete rhizoliths. Contact between unit A and the unit above (unit B) is not observable, but the lowest observable point of unit B is un-cemented indicating a transition from cemented to un-cemented sediments between units A and B. Unit B is comprised of slightly gravelly muddy sand to muddy gravel, which is poorly sorted with limited structure. Unit C consists of two subunits C1 and C2; C1 is approximately 15 cm thick and contacts the top of unit B which is a scoured surface unconformity. It consists of sandy gravel comprising angular coarse pebbles of Rewan Group. C1 transitions into the C2 bed which is the fossiliferous section and is comprised of well sorted gravelly muddy sand. A soil profile exists above unit C.

Only vertebrate fossils are known from SWJ. All vertebrate remains are rare and poorly preserved, including a ziphodont tooth, a piece of chelid carapace, mammalian vertebrae and appendicular elements. An exception to this overall poor preservation is a single, well-preserved, dorsal vertebra from *Varanus priscus*. With the exception of a small number of bones, no primary bone pre-depositional modifications are visible due to the extensive removal of most surface bone through post-depositional corrosive processes. Surface corrosion reveals internal trabeculae on most elements except the varanid vertebra. It is likely that bone in this deposit has undergone a significant degree of post-depositional alteration through the actions of organic acids, more so than the corrosive features observed on bones from SW3.

Table C 6 QML1470 (SWJ) Sedimentological and Taphonomic Summary and Interpretation.

Site	Sedimentology	Sedimentary Structure	Fossil Preservation	Fossil Modification	Interpretation
SWJ	Fine sand-dominated, well-sorted matrix.	Fining upwards from gravelly base, otherwise unstructured.	Very poorly preserved terrestrial and aquatic vertebrate taxa.	Surface bone corrosion, minor exceptions.	Vertical accretion on floodplain. Higher energy deposition compared to SW3 and SW9, however, lower energy deposition compared to SWCC. Dispersed fossil bed at the top of a 2.5-3m thick non-fossiliferous sequence.

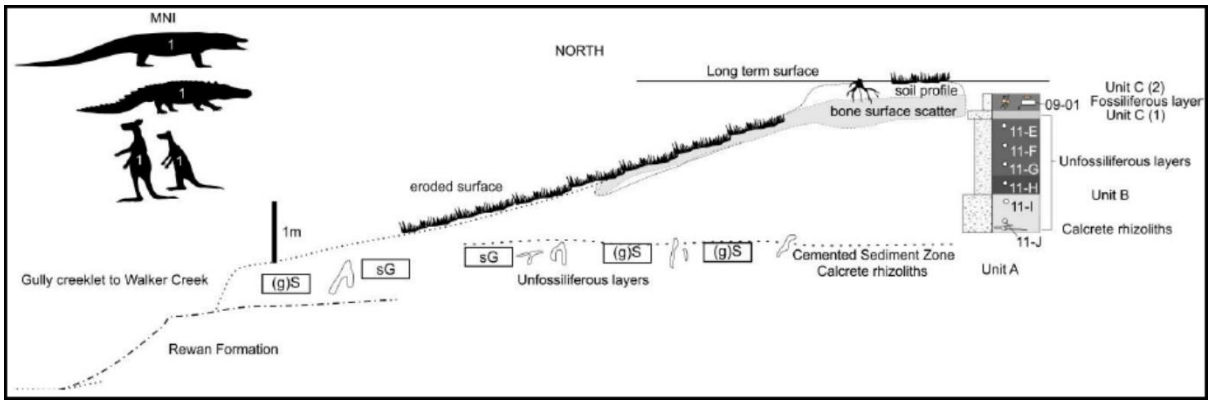

Figure C 13 . Stratigraphic map of QML1470 (SWJ) in North Section (a). MNI of megafauna indicated within the silhouette. Sediment classification and composition key provided in Ternary diagram of Figure C8.

C4.4. SWCC (Figure C14 & Table C7)

QML1470 (SWCC) is the most sedimentologically complex deposit of the localities investigated, made up of five units A-E, with the basal unit contacting Rewan Group bedrock. Fossils have been recovered from units A-D, with the better preserved material derived from unit B. Unit A consists of a course-grained sandy to pebble-cobble matrix comprising angular to rounded Rewan Group gravel and small siliceous cobbles that fines to the northeast. Unit B contacts unit A at a sharp-based scour unconformity and consists of poorly structured gravelly muddy sand that fines upwards and toward the west, capped by an irregular mud drape. Unit C is a lens of coarse-grained sandy gravels to pebbles consisting of angular and rounded clasts that cut into unit B as a scour deposit and fines to the West. Unit D replicates unit B as a poorly structured gravelly muddy sand unit that fines upwards and to the East with a capping mud drape. It sharply contacts and bounds the top surface of both unit B and C laterally. Unit E is a poorly sorted, unstructured sandy mud unit that sharply contacts Unit D forming a scour unconformity. A soil profile is present above unit D.

Aquatic and terrestrial fauna are preserved within these deposits. Crustacean gastroliths and small corbiculid bivalve valves represent the aquatic invertebrate fauna. Aquatic vertebrates include small to large fish remains, crocodilian teeth and cranial remains and large numbers of turtle carapace and plastron pieces. Terrestrial vertebrate remains are rare, but include a diverse range of isolated mammalian and reptilian teeth, fragmented postcranial remains, and an isolated and well-preserved dorsal vertebra from *Varanus priscus*. The large vertebrate remains are fragmented into small pieces, close to the size of the largest entraining clasts within the matrix. The bone fragments show limited signs of rounding indicating limited transport time, but due to the coarseness of the matrix breakages are abundant. Smaller vertebrate remains are fragmented; however, they are generally better preserved also showing limited time of transportation. Dental association is recognised for one species (Table C3).

Table C 7 QML1470 (SWCC) Sedimentological and Taphonomic Summary and Interpretation.

Site	Sedimentology	Sedimentary Structure	Fossil Preservation	Fossil Modification	Interpretation
SWCC	Variable grain-size between units, poorly sorted matrix.	Multi-directional sediment grading, with sharp basal scours and muddy drapes above unit.	Well-preserved but fragmented terrestrial and aquatic vertebrate taxa. Very well preserved micro fossils.	Variable – complete to fragmented, unmodified to rounded teeth and bones.	Small inter / chute channel flash flood events. Short-lived, high energy, multiple events proximal to a main channel (possibly a chute channel). Rapid burial with coarse sediment and post event mud drape.

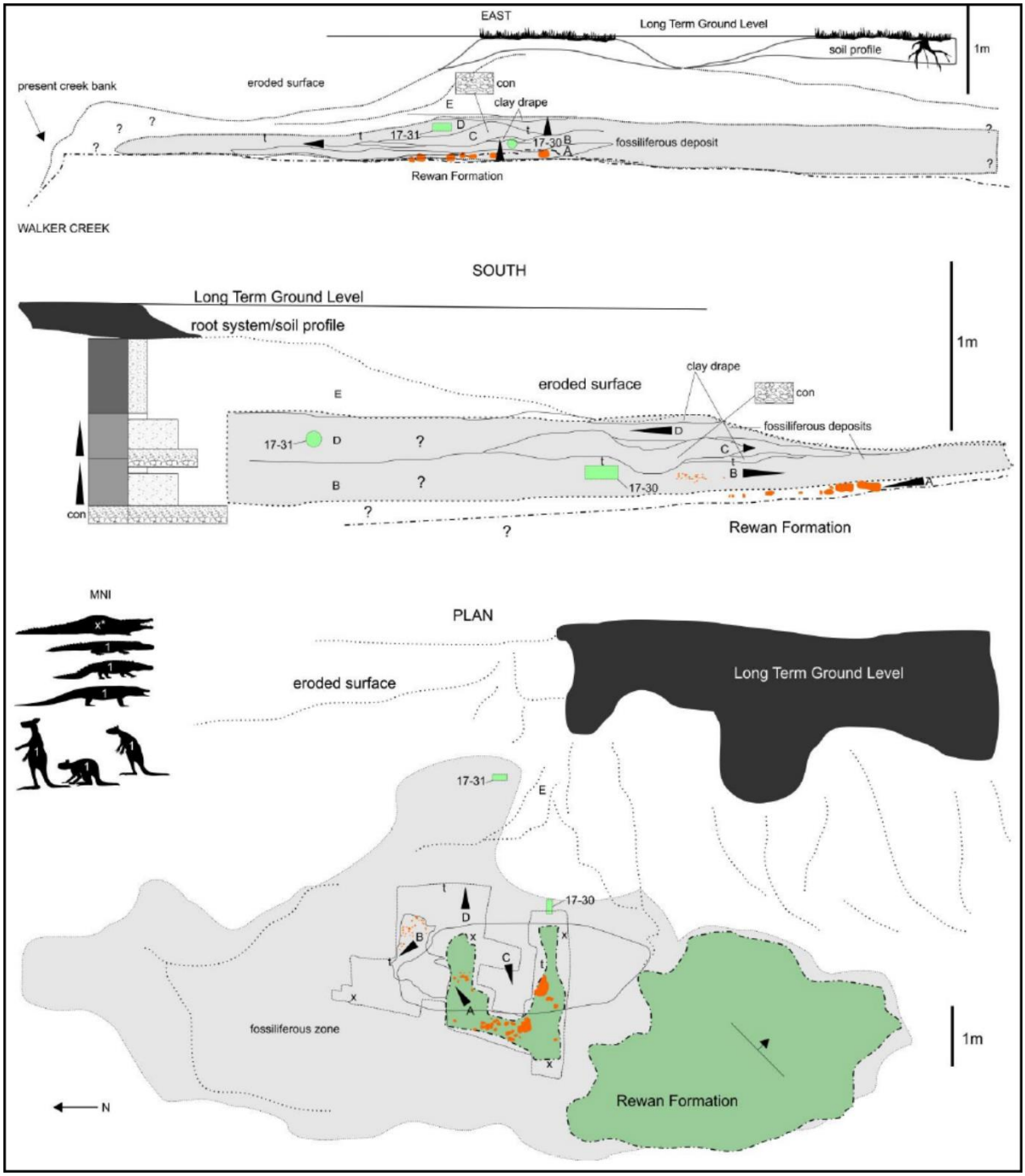

Figure C 14 Stratigraphic map of QML1470 (SWCC) in East Section (a), South Section (b) and Plan view (c). MNI of megafauna indicated within the silhouette. Sediment classification and composition key provided in Ternary diagram of Figure C8. Arrows and letters indicate direction of grading and unit.

C5. Geochronology of South Walker Creek (QML1470) sites

Richard Lewis, Lee J. Arnold, Tim Pietsch, Scott A. Hocknull, Jon Olley, Rochelle A. Lawrence & Julien Louys.

C5.1. Sample collection

C5.1.1. QML1470 (SW9)

QML1470 (SW9) has been most intensively sampled for dating. Twenty-two OSL samples have been taken vertically and horizontally in an effort to capture as much of the depositional age of the target fossil bed of Unit C as possible. OSL cores were taken in vertical section within Unit C from C3 down to C1, along with two cores recovered in vertical sequence from the lower Unit B. One core sampled Unit C3 (OSL 11-01), five cores sampled Unit C2, twelve cores sampled Unit C1 (fossil bed), two cores sampled Unit B (SW9-16-C1 and SW9-16-C2) and two additional cores sampled deposits extralimital to the main site. Nine ^{14}C dating samples were derived from Unit C1. An additional six samples from Unit C1 were used for U-series and/ or ESR dating. Sample locations are provided in Figure C15.

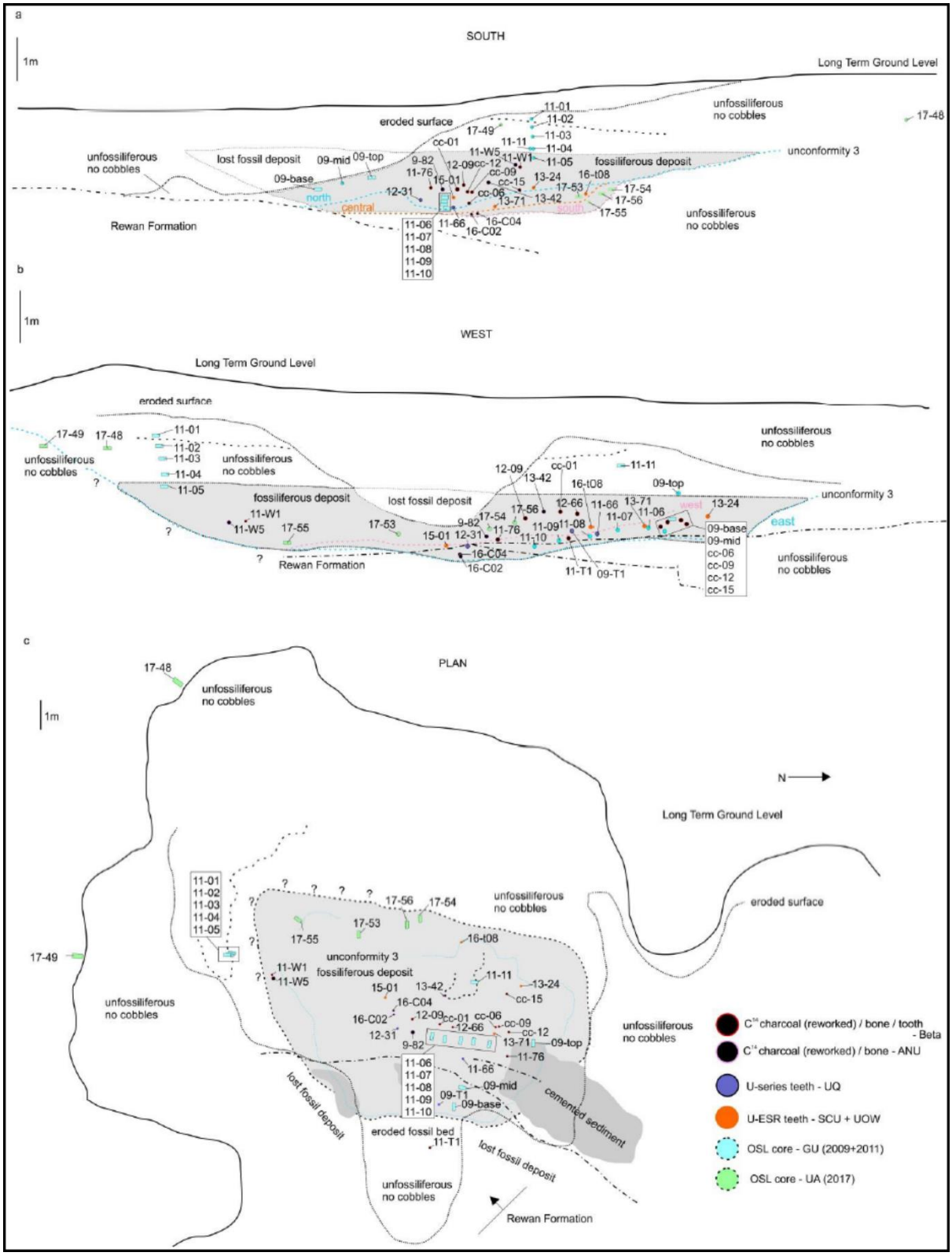

Figure C 15 QML1420 (SW9), dating sample locations within the SW9 site in southern (a), western (b) and plan (c) views.

C5.1.2. QML1470 (SW3)

OSL and U-series / ESR samples were taken from this locality in 2009, 2016 and 2017. Only the OSL samples have been successfully processed. Eleven OSL cores were sampled vertically and

horizontally across the entire site, focusing on two fossiliferous areas. The highest samples come from the northern section of the site (OSL-09 A1, and S1); however, these did not yield viable OSL ages (see below). The lowest sample (OSL-17-34) was collected toward the southern margin, at the base of a vertical series of samples taken at and below the level of a large *Diprotodon* skull. Sample locations are provided in Figure C12.

C5.1.3. QML1470 (SWJ)

OSL samples were collected from this locality in 2009 and 2011 along a vertical sequence crossing Units B and C (C1 and C2). Unit B and C1 are unfossiliferous, with the OSL sample from C2 representing the stratigraphically closest approximation of fossil depositional age. Sample locations are provided in Figure C13.

C5.1.4. QML1470 (SWCC)

Two OSL samples were collected in 2017 from Units B and D of this locality. Sample locations are provided in Figure C14.

C5.2. Optically stimulated luminescence

Richard Lewis, Lee J. Arnold, Tim Pietsch and Jon Olley.

C5.2.1. Sample acquisition and preparation

OSL samples were collected from four sites within the SWC fossil deposit area QML1470 (SW9, SW3, SWJ, SWCC). The sampled sediments are considered to represent a combination of flood and channel deposits. The preserved sediments at SW3 and SWJ are thought to have been deposited quickly when channel banks were breached and flooding occurred. OSL samples at these sites have been taken in stratigraphic succession to ascertain whether there is evidence to support several generations of flooding events. Fossil-bearing units at SW9 and SWCC occur within sediments that are incised into underlying units and down to the bedrock as a result of fluvial activity. The fossil-bearing sedimentary layer at SW9 is unique in exhibiting vertical sand lenses that intrude into the fossiliferous sandy clays. These features are interpreted as a younger generation of sand infill deposited after desiccation and cracking of the clay sediment. Standalone sampling was therefore conducted on these sand layers to deduce whether they might yield complex burial dose characteristics and to evaluate whether they could bias the OSL age interpretations. For this purpose, a series of comparative samples were collected from the sand intrusion (SWC17-52), the clay layer (control; SWC17-56) and a combination of the two layers (SWC17-54).

OSL samples collected in 2011, 2015 and 2017 are considered to be the most informative and stratigraphically reliable for undertaking chronological evaluations of the four SWC sites. The following methodological descriptions and dating assessments therefore focus on these three groups of OSL samples. The preliminary group of OSL samples collected ad hoc by the excavation team in 2009 (Griffith University Batch 1) all showed clear evidence of contamination with younger material (e.g., Figure C16). This contamination was attributed to sub-optimal sampling conditions and/ or sediment mixing via modern bovine trampling. These samples were subsequently not deemed suitable for OSL dating and a new study was undertaken in 2011 with a series of replacement samples collected from carefully excavated exposures at SW9 (SW9 1-11) and SWJ (SWJ EJ). An additional five OSL dating cores were collected from SW3 (SW3 A, SW3-15-C2 and SW3 B) and SW9 (SW9-16-C1 and SW9-16-C2 – both from Unit B) in 2015 and 2016 respectively. However, these samples yielded very low grain recovery ratios (i.e. number of grains accepted as a proportion of grains analysed). The low accepted grain yields (7-11 single-grain D_e values per sample), which may be partly related to variations in sediment sourcing (and hence luminescence properties) between different units, are considered insufficient to characterise the true D_e scatter affecting these five samples and to derive meaningful burial dose estimates, hence they have not been considered further in our site chronological evaluations.

Finally, in 2017 additional cores were recovered from SW9, SW3 and SWCC that included in situ dosimetry measurements to provide corroboration of previous samples and to broaden the range of sites assessed.

The 2017 (SWC17) and 2015 (SWC) OSL samples were extracted from their coring tubes and prepared under controlled lighting conditions (subdued red lighting) at the Prescott Environmental Luminescence Laboratory (The University of Adelaide; AU). The 2011 OSL samples (SW9-(X)) were extracted and prepared under similar safelight conditions at the Environmental Forensics Laboratory (Griffith University; GU). Purified coarse-grain quartz fractions (SWC17 & SWC = 212-

250 µm; SW9-X = 180-212 µm) were prepared using standard procedures (Aitken, 1998). This process included wet sieving of sediments, chemical treatment with HCl and H_2O_2 to remove carbonates, organic material and clay, and isolation of quartz fractions through heavy liquid density separation. Isolated quartz grains were etched with concentrated HF (48 %) for 40 mins (a double etch was used for the GU 2011 samples) to remove the alpha-irradiated outer layer of the quartz grains, and subsequently washed with HCl to dissolve any fluoride precipitates. The etched quartz grains were re-sieved using a smaller mesh size to ensure any remaining partially etched feldspars and smaller disaggregated quartz grains were removed prior to OSL measurement.

C5.2.2. Instrumentation and equivalent dose (D_e) measurement

The 2011 (GU), 2015 (AU) and 2017 (AU) samples were measured using Risø TL-DA-20 readers equipped with 10 mW Nd:YV04 (532 nm) single-grain laser attachments, EMI 9235QA photomultiplier tubes fitted with 7.5 mm thick Hoya U-340 filters, and calibrated $^{90}Sr/^{90}Y$ β sources. D_e measurements were made using standard single-grain aluminium discs drilled with an array of 300 µm x 300 µm holes, the positions of which had been individually calibrated to account for spatial variations in the beta dose rate across the disc plain. Single-grain OSL D_e measurements were conducted using single-aliquot regenerative-dose (SAR) protocols (Murray & Wintle, 2000) that had been modified to allow measurement of individual grains (Demuro et al., 2019) (Table C8). D_e measurements were calculated by interpolation of the sensitivity-corrected natural signal onto a single saturating exponential fit of the sensitivity corrected dose response curve (Figure C17). For the 2015 and 2017 samples (AU), the sensitivity corrected dose response cures were generated by subtracting the background signal (last 0.25 s of stimulation) from the integrated signal measured over first 0.10 s – 0.18 s of laser stimulation (adjusted to avoid integrating the non-decaying part of the signal, and to obtain dose-response curve fits with the smallest possible curve-fitting errors). The dose response curves of the 2011 (GU) samples were determined from the initial 0.1 s of each OSL decay curve, using the final 0.2 s to estimate the background count rate.

OSL dose recovery tests were undertaken on representative samples from various locations (SWC17-53/SW9, SWC17-B/SW3, SWC17-G/SWJ) to assess the suitability of the SAR preheating conditions used in this study. Multi-grain OSL dose recovery tests were first performed on sample SWC17-B to determine optimum preheating conditions (using blue LED OSL stimulation instead of green laser stimulation in steps 4 and 7 of the AU SAR sequence shown in Table C8). A known laboratory dose of 100 Gy was applied to groups of aliquots after optically bleaching their natural OSL signals using two 1,000 s blue LED stimulations separated by a 10,000 s pause (to ensure complete decay of any phototransferred charge in the 110 °C TL trap). Regenerative dose preheat treatments (PH1) of either 220 °C for 10 s or 240 °C for 10 s, and a test dose preheat treatment of 160 °C for 10 s, were found to yield reliable weighted mean measured-to-given dose ratios and recycling ratios at 2σ (Figure C18). The suitability of one of these preheat combinations (PH1 = 240 °C for 10 s; PH2 = 160 °C for 10 s) was examined in greater detail at the single-grain scale of analysis. Single-grain OSL dose recovery tests were made on three samples following bleaching of their natural signals (using the same conditions as with the multi-grain dose recovery tests) and administering a known dose of 100 Gy. Weighted mean measured-to-given dose ratios for this suite of samples ranged from 0.95 ± 0.05 to 0.96 ± 0.02, and overdispersion values varied between 2 – 11 % (Figure C19, Table C9). Notably, these dose recovery ratios are within 2σ of unity, and therefore support the general suitability of the single-grain D_e measurement conditions used in this study.

For the 2015 and 2017 AU samples, single-grain OSL D_e estimates were not considered suitable for final age calculation if they exhibited any of the following properties (Arnold et al., 2016; Demuro et al., 2019): (i) their net T_n signals were <3σ above the late-light background; (ii) recycling ratios (sensitivity-corrected luminescence responses (L_x/T_x) for two identical regenerative doses) were not consistent with unity at 2σ. For the single-grain OSL measurements, the recycling ratio test was performed using both a low-dose and high-dose regenerative dose cycle; (iii) the OSL-IR depletion ratio (Duller, 2003) was less than unity at 2σ; (iv) the recuperation ratio, calculated as the ratio of the sensitivity-corrected 0 Gy dose point (L_0/T_x) to the sensitivity-corrected natural (L_n/T_n), was >5 %; (v) the L_n/T_n value intercepted the saturated part of the dose-response curve (L_n/T_n values were equal to $2D_0$ saturation limit of the dose-response curve at 2σ); (vi) the dose-response curve displayed anomalous properties (i.e., zero or negative response with increasing dose) or very scattered L_x/T_x values that could not be successfully fitted with the Monte Carlo procedure; (vii) the sensitivity-corrected natural signal (L_n/T_n) did not intercept the sensitivity-corrected dose-response curve; (viii) the net D_e uncertainty is >50 %. The single-grain OSL rejection statistics for the 2015 and 2017 AU samples are shown in Table C10.

The single-grain quality assurance criteria used for the 2009 GU samples are based on those of Pietsch (2009) and Pietsch et al. (2013). Single-grain OSL D_e estimates were not considered suitable for final age calculation if they: (i) failed to produce a measurable (i.e. >3 standard deviations above background) OSL signal in response to the natural test dose; (ii) had OSL decay curves that did not reach background after 1 s of laser stimulation; (iii) produced natural OSL signals that did not intercept the regenerated dose-response curves; (iv) had unacceptable sensitivity changes throughout the measurement cycle, i.e. they were rejected if either of the second or third test dose signals varied in sensitivity from the natural test dose by more than 20 %; (v) had dose response curves with observable recuperation, as indicated by 0 Gy dose points with a sensitivity-corrected OSL response beyond zero at 1σ, and (vi) exhibited recycling ratios that were not consistent with unity at 1σ.

The accepted single-grain D_e distributions for the 2011, 2015 and 2017 OSL samples are presented as radial plots in Figures C20 – C25. Table C11 provides a summary of the D_e statistics and age model preferences for the various samples from SW9, SW3, SWJ and SWC-CC. The single-grain D_e distributions are generally characterised by moderate D_e scatter and overdispersion values ranging between 25 – 35 %, though there are some noteworthy exceptions. Samples SWC17-53 and SW9-2 exhibit the lowest overdispersion values (22 ± 3 % and 22 ± 4 %, respectively) and the most homogenous D_e distribution of the thirty-two AU and GU samples (Figures C23 & C25). These D_e characteristics are consistent with those typically reported for ideal (well-bleached and unmixed) single-grain D_e datasets at 2σ (e.g., the global average overdispersion of 20 ± 1 %; Arnold & Roberts, 2009). These two samples have therefore been used to derive a site-specific, baseline assessment of the overdispersion expected for well-bleached and unmixed sediments in the SWC basin.

Twenty-eight of the remaining thirty OSL samples exhibit moderate D_e scatter and slightly higher overdispersion values of 26 ± 4 % to 40 ± 6 %, (Table C11). However, the overdispersion values of these twenty-eight samples are all consistent at 2σ with the overdispersion value of our site-specific 'best-case scenario' samples (SWC17-53 and SW9-2), suggesting limited influences of additional extrinsic D_e scatter. Most of these D_e datasets are characterised by largely unstructured and broadly symmetric D_e scatter, with a limited number of outlying D_e values found either side of the weighted

mean shaded bands on the radial plots (e.g., SWC-E, SWC-B, SWC17-33). Some of these samples show more asymmetric D_e scatter, including possible leading-edges of low D_e values or elongated tails of higher D_e values (e.g., SWC17-55, SW9-9, SW9-3), which might be indicative of heterogeneously bleached single-grain populations (Arnold et al., 2007; Arnold et al., 2008). However, the limited number of accepted D_e values obtained for some of these samples (i.e., n <50) makes it difficult to fully resolve their underlying D_e characteristics.

The remaining two samples from the combined SWC dataset (SWC17-49 and SW9-11) exhibit complex D_e distributions characterised by very high overdispersion values (97 – 116 %) and multiple discrete dose populations (see details of finite mixture model (FMM) fitting below) (Figures C23 & C25). These multimodal D_e datasets are consistent with those commonly reported for samples that have been affected by locally intruded, young grain populations (e.g., Arnold et al., 2013; Arnold & Roberts, 2009) or certain sources of beta dose heterogeneity (Arnold et al., 2014; Jankowski et al., 2016; Mayya et al., 2006).

We have considered a range of statistical age models to characterise each single-grain D_e distribution and to derive representative burial dose estimates for the AU and GU OSL samples, namely: the central age model (CAM), which would be considered suitable for well-bleached and undisturbed sediments (e.g., Galbraith et al., 1999), the three-parameter minimum age model (MAM-3) and the four-parameter minimum age model (MAM-4), which are generally considered useful for isolating the most suitably bleached dose components in otherwise heterogeneously bleached samples (Arnold et al., 2007; Arnold et al., 2008; Bailey & Arnold, 2006), and the FMM, which can be used to identify discrete dose components in samples affected by post-depositional mixing (Arnold et al., 2013; Arnold & Roberts, 2009; Galbraith & Green, 1990). The choice of age model for final burial dose estimation has been made on a sample-by-sample basis according to the maximum log likelihood (llik or L_{max}) criterion of Arnold et al. (2009) (i.e., using the age model that provides the most statistically suitable fit for each empirical dataset after taking into consideration model parameterisation complexity), in conjunction with consideration of the depositional contexts of the SWC samples.

Full details of the llik criterion and age model fitting results are provided in Table C12. According to the llik criterion, the CAM is deemed the most statistically suitable age model for burial dose estimation for twenty nine of the thirty-two GU and AU OSL samples. The MAM-3 is marginally favoured over the CAM for one of the three remaining samples (SWC H) according to the llik criterion (Table C12). However, the llik scores for this sample seem to be unduly influenced by the presence of a single, precise high D_e value (Table C13), as indicated by sensitivity tests performed on the same D_e dataset after elimination of this outlying grain (Table C12). Given the limited number of individual D_e values obtained for sample SWC H (n = 39) and the disproportionate influence of this single outlying grain on the llik scores, we have opted to derive the final burial dose using the CAM to ensure consistency with the other OSL samples from site SWJ.

Samples SWC17-49 and SW9-11, which display complex D_e distributions and overdispersion values of 97 – 116 % (Figures C24 & C25), are not adequately represented by the CAM according to the llik criterion (Table C12). Given the multimodal D_e scatter apparent for these two samples, we have applied the FMM to formally identify any discrete dose components that may be present. As detailed in Tables C13 and C14, the optimum FMM fits identify three discrete dose components for each sample. Assuming that the multiple discrete dose components of samples SWC17-49 and SW9-11 can

be explained by localised post-depositional mixing or beta dose rate heterogeneity (which, along with possible contamination during sampling, seem the most feasible explanations in this sedimentary context), it follows that the bulk (sample-average) dose rate of these two samples may not be entirely representative of that experienced by the dominant dose components during burial. Owing to the impracticalities of retrospectively deriving a component-specific dose rate for the identified FMM components, these two samples are not deemed suitable for dating and have not been considered further in out chronological evaluations of SW9.

C5.2.3. Dose rate evaluation and age calculation

Environmental dose rates (Table C11) have been calculated using a combination of *in situ* field gamma spectrometry (FGS) and low-level beta counting (2017 AU samples), and high-resolution gamma spectrometry (HRGS) (2015 AU samples and 2011 GU samples) (Tables C11, C15 & C16). Gamma dose rates were determined from in situ gamma spectrometry measurements made with a 3 inch Canberra NaI:Tl detector, following the 'energy windows' method (Arnold et al., 2012). External beta dose rates for the 2017 AU samples were determined from measurements made using a Risø GM-25-5 beta counter (Bøtter-Jensen et al., 2000; Bøtter-Jensen & Mejdahl, 1988) on dried and homogenised, bulk sediments collected directly from the OSL sampling positions. Background-subtracted count rates were measured for three aliquots of each sample and compared with net count rates obtained simultaneously for a loess sediment standard with known U, Th and K concentrations (Potts et al., 2003). HRGS measurements were performed at the University of Adelaide and the Forensic and Scientific Services department of Queensland Health, and used to derive the external gamma and beta dose rates of the 2015 AU and 2011 GU samples, respectively. Additional HRGS measurements were also conducted on the 2017 AU samples to evaluate the state of secular equilibrium in their ^{238}U, ^{235}U and ^{232}Th decay series. To calculate representative dose rates from the HRGS radionuclide concentrations, we have considered the proportional beta and gamma dose rate contributions from different parent or daughter isotopes measured in the ^{238}U and ^{232}Th decay series, and we have assumed that the present-day state of (dis)equilibrium observed in the ^{238}U and ^{232}Th decay chains has prevailed throughout the burial period. Cosmic-ray dose rates have been calculated using the approach described in Prescott & Hutton (1994) after taking into consideration site altitude, geomagnetic latitude, density, thickness and geometry of sediment overburden. A small, assumed internal (alpha plus beta) dose rate of 0.03 ± 0.01 Gy / ka has been included in the final dose rate calculations, based on published ^{238}U and ^{232}Th measurements for etched quartz grains from a range of locations (Bowler et al., 2003; Jacobs et al., 2006; Mejdahl, 1987; Pawley et al., 2008) and an alpha efficiency factor (a-value) of 0.04 ± 0.01 (Rees-Jones, 1995; Rees-Jones & Tite, 1997).

Radionuclide concentrations and specific activities have been converted to dose rates using the conversion factors given in Guérin et al. (2011) and Stokes et al. (2003), making adjustments for beta dose attenuation and long-term sediment moisture contents (Aitken, 1985; Brennan, 2003; Mejdahl, 1979). The present-day sediment water contents of the SWC samples are not considered to be entirely representative of those prevailing throughout the sample burial periods because (i) the excavation pits and sediment exposures had partially dried out prior to sampling, (ii) OSL samples were collected during dry-season months, and (iii) local hydrological conditions are known to have been significantly wetter at various times in the past (see Appendix C4 for stratigraphic and sedimentological descriptions). To determine more suitable long-term sediment moisture contents, we examined the range of present-day 'proportional saturated water content' values (i.e., present-day water contents /

saturated water contents x 100) obtained for the 2015 and 2017 OSL samples. The highest proportional saturated water content for the SWC samples (31 % of saturated water content; obtained from a freshly dug sampling exposure at SW3) was used to establish a more reliable estimate of present-day water content (as a proportion of sediment saturation capacity) in the absence of any prior sediment exposure bias. Based on these results and factoring in the potential for intermittently wetter climatic conditions and significant flooding of SWC basin in the past (based on the preserved sedimentology and faunal remains), we have adopted conservative long-term sediment moisture contents of 40 % (instead of 31 %) present-day saturated water contents for each OSL sample. The long-term sediment moisture contents for the 2015 and 2017 samples range between 10 – 38 % of dry sediment weight (Tables C11 & 15) and have been assigned a 1σ relative uncertainty of 20 % (40 % at 2σ) to accommodate any variations in hydrologic conditions during burial. Whilst 40 % of the saturated water content is our best estimate of long-term water content, the effect of assuming a value closer to the measured present-day water content would be modest. For example, the incorporation of 30 % saturated water content for SW9 samples would produce a weighted average burial age of 40.5 ± 1.6 ka (within error of the weighted mean age reported in Table C17 which uses 40 %). As saturated water content data was not originally recorded for the 2011 GU samples, we have used the average long-term water content calculated for the 2015 and 2017 AU samples (22 ± 4 % of dry sediment weight) to derive surrogate long-term estimates for dose rate determination (Tables C11 & C15).

The HRGS radionuclide activities obtained for each OSL sample are summarised in Table C16. The daughter-parent isotopic ratios for ^{238}U, ^{226}Ra, ^{210}Pb, ^{228}Ra and ^{228}Th are consistent with unity at either 1σ or 2σ for all samples, confirming that the ^{238}U and ^{232}Th chains are in present-day secular equilibrium. There is evidence of minor disequilibrium in the ^{238}U series for five samples (albeit not statistically significant at 2σ), with samples SW9-2 and SW9-11 exhibiting ^{226}Ra:^{238}U activity ratios of 0.6, and samples SW9-5, SW9-6 and SW9-7 exhibiting ^{226}Ra:^{238}U activity ratios of 0.7 (Table C16). These results imply the uptake of unsupported ^{238}U following burial or the loss of radon (^{222}Rn) gas (since we have used the post-radon daughter emissions of ^{214}Pb and ^{214}Bi to derive ^{226}Ra activities). The minor secular disequilibrium observed for these samples is not sufficient to change our calculated ages beyond those that would result from assuming equilibrium conditions have persisted throughout the burial period. Dosimetry modelling studies undertaken elsewhere have demonstrated that isotopic disequilibria of similar magnitudes are only likely to give rise to minor deviations (<5 %) in long-term dose rate estimates (Olley et al., 1996; Olley et al., 1997; Preusser & Degering, 2007). Such systematic biases would be significantly less than the existing uncertainty ranges on our final dose rate estimates.

Table C11 summarises the final ages for the 2011, 2015 and 2017 OSL samples from sites SW9, SWC-CC, SW3 and SWJ. Tables C17 & C18 summarise the weighted mean OSL ages calculated for the main fossil unit of each site. To derive these weighted mean estimates, individual OSL ages have been combined from the fossiliferous and non-fossiliferous sub-layers of the main fossil unit(s) at each site (e.g., Unit C1-C3 at SW9, Units B and D at SWC-CC), since these sub-units are not separated by any major unconformities and likely represent related phases of a broader depositional sequence. Samples from underlying non-fossiliferous unit that are separated from the main fossil unit(s) by an erosional unconformity (e.g., Unit B at SWJ) are not included in the weighted mean OSL age calculations shown in Table C17. The weighted mean GU and AU OSL ages obtained for the main fossil unit (Unit C) at SW9 are statistically indistinguishable from each other, confirming the

validity of our inter-laboratory comparison results. The comparative OSL samples collected from the sand intrusion and clay layers at SW9 also yielded consistent ages (e.g., SWC17-52, SWC17-54, SWC17-56; Table C11), suggesting that they represent broadly coeval deposits (relative to the size of our OSL dating uncertainties). The fossil deposits preserved at the SWC sites exhibit weighted mean OSL ages ranging from 41.3 ± 1.9 ka (SW9) to 58.2 ± 6.1 ka (SWJ) (Table C17). All of the final OSL ages for SWJ have been derived from Unit B, which underlies the main fossil unit (Unit C). As such, the weighted mean OSL age for this site (65.6 ± 2.2 ka) represents a maximum age estimate for the formation of the overlying megafaunal deposit.

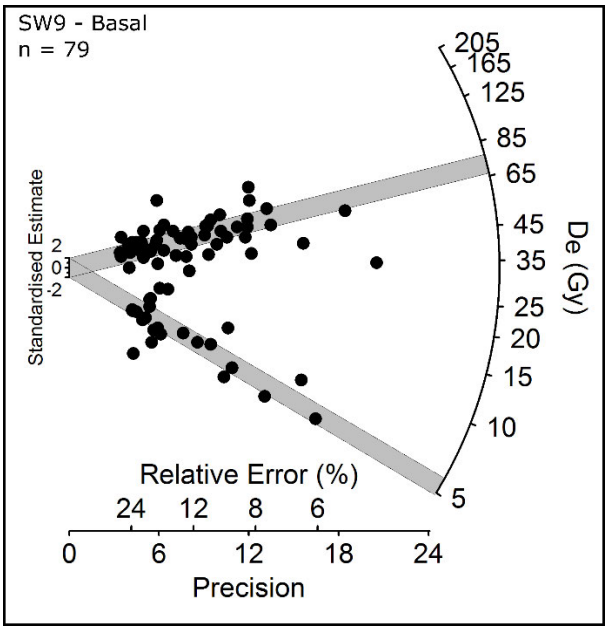

Figure C 16 Example of a contaminated single-grain D_e distribution from the preliminary group of OSL samples collected in 2009 (sample SW9-Basal). The grey shaded bands correspond to discrete dose component identified by the optimum finite mixture model (FMM) fit (see Tables C13-C14 for FMM fitting details).

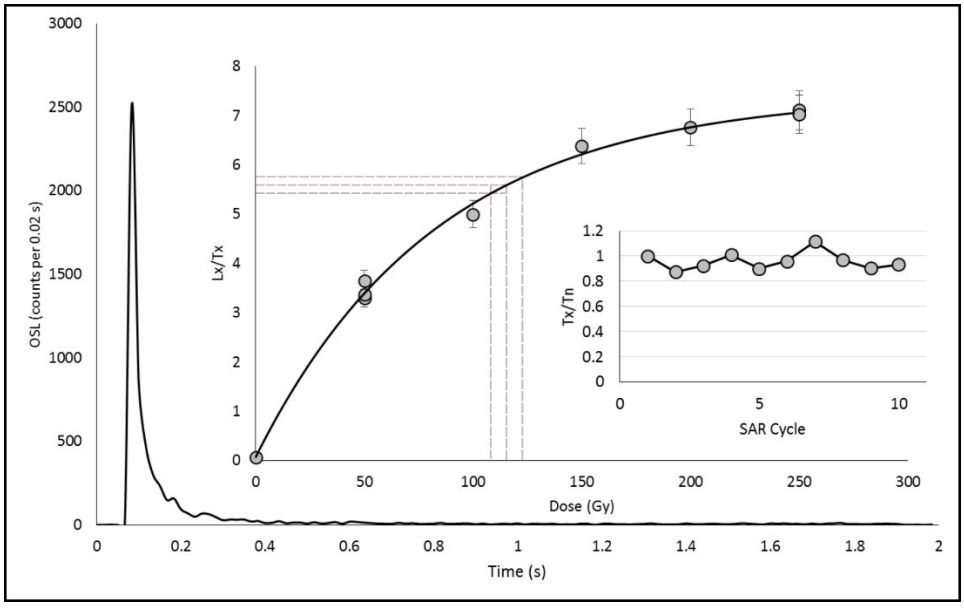

Figure C 17 Examples of a single-grain OSL decay and dose response. The main plot shows the natural OSL signal decay curve for a grain from sample SWC17-31. The secondary and tertiary inset graphs (left to right) show the dose-response curve for this grain and its normalised test dose sensitivity (T_x/T_n) response through the SAR measurement cycles, respectively.

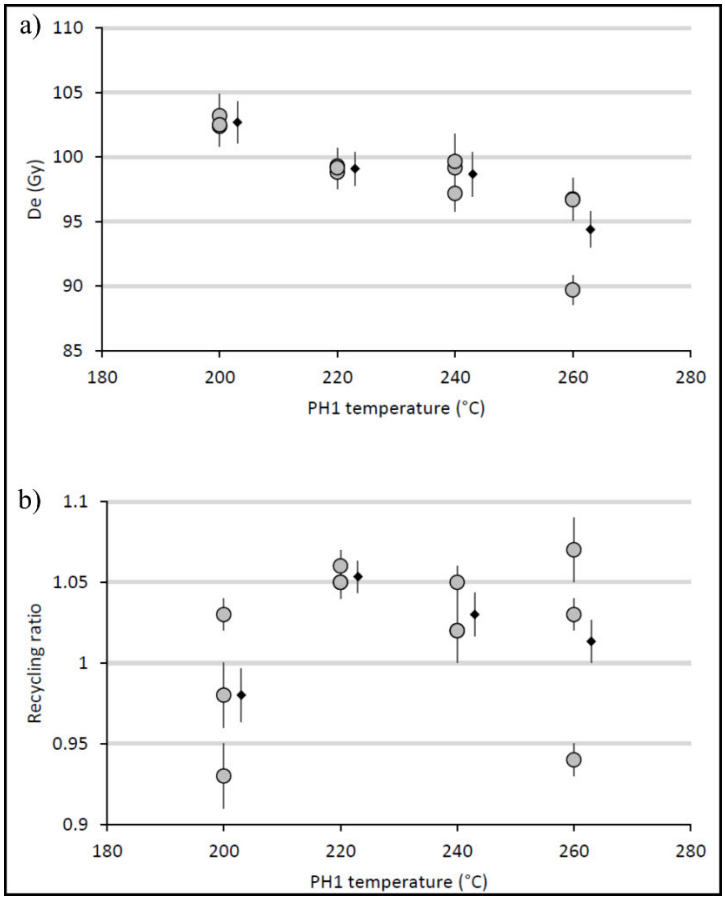

Figure C 18 Multi-grain dose recovery test results obtained for sample SWC-B after administering a dose of 100 Gy (uncertainties are shown at 1σ). Plots show (a) the recovered doses (grey circles = individual aliquot D_e values; black circles = weighted mean D_e values) and (b) the recycling ratios obtained for different preheat conditions. D_e measurements were made with a multi-grain version of the AU SAR protocol (replacing single-grain laser stimulations in steps 4 and 7 with blue LED OSL stimulations performed at 125 °C for 10 s) using various regenerative-dose preheat (PH1) and maintaining a test-dose preheat (PH2) of 160 °C for 10 s. D_e measurements were made on multi-grain aliquots containing ~600 quartz grains.

C5.2.4. Dose recovery test

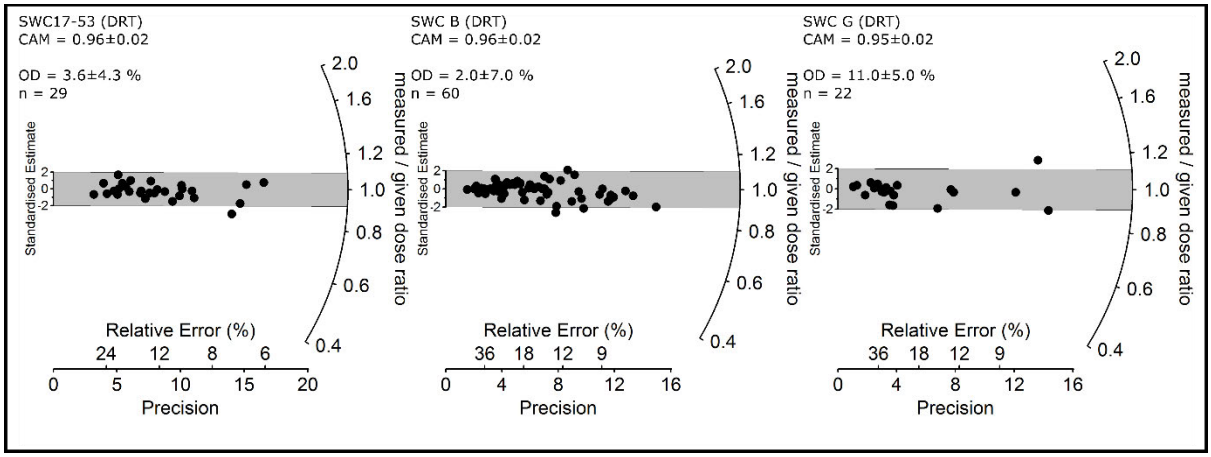

Figure C 19 Radial plots showing single-grain OSL dose recovery test results obtained for samples SWC17-53, SWC-B and SWC-G using the AU SAR protocol shown in Table C1 (D_e errors are shown at 1σ). Grains were bleached within the Risø reader chamber using blue LEDs prior to administering a dose of 100 Gy. The central age model (CAM) measured-to-given dose ratio and the overdispersion (OD) value is shown for each sample.

C5.2.5. SWC-CC

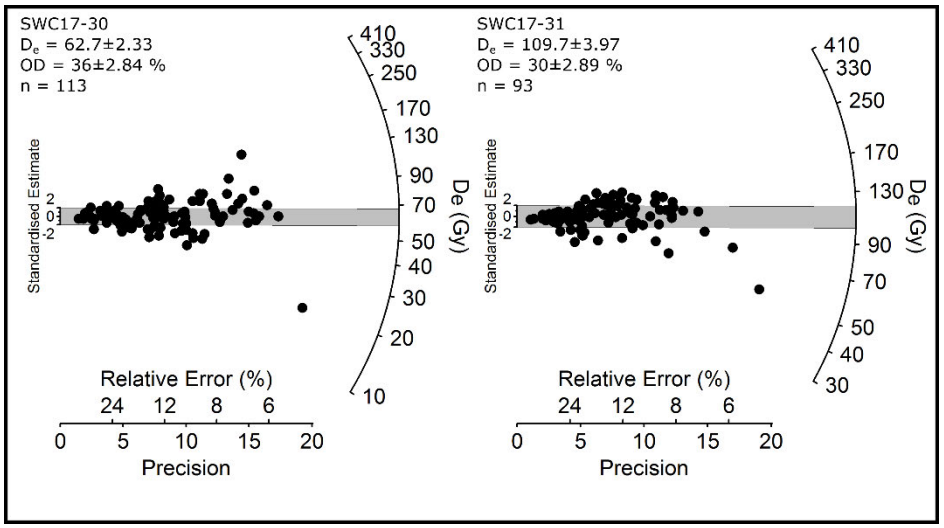

Figure C 20 Radial plots showing the single-grain OSL D_e distributions obtained for the South Walker Creek, SWC-CC samples (D_e errors are shown at 1σ). The dark grey bands are centred on the weighted mean D_e values, which have been calculated using the CAM.

C5.2.6. SWJ

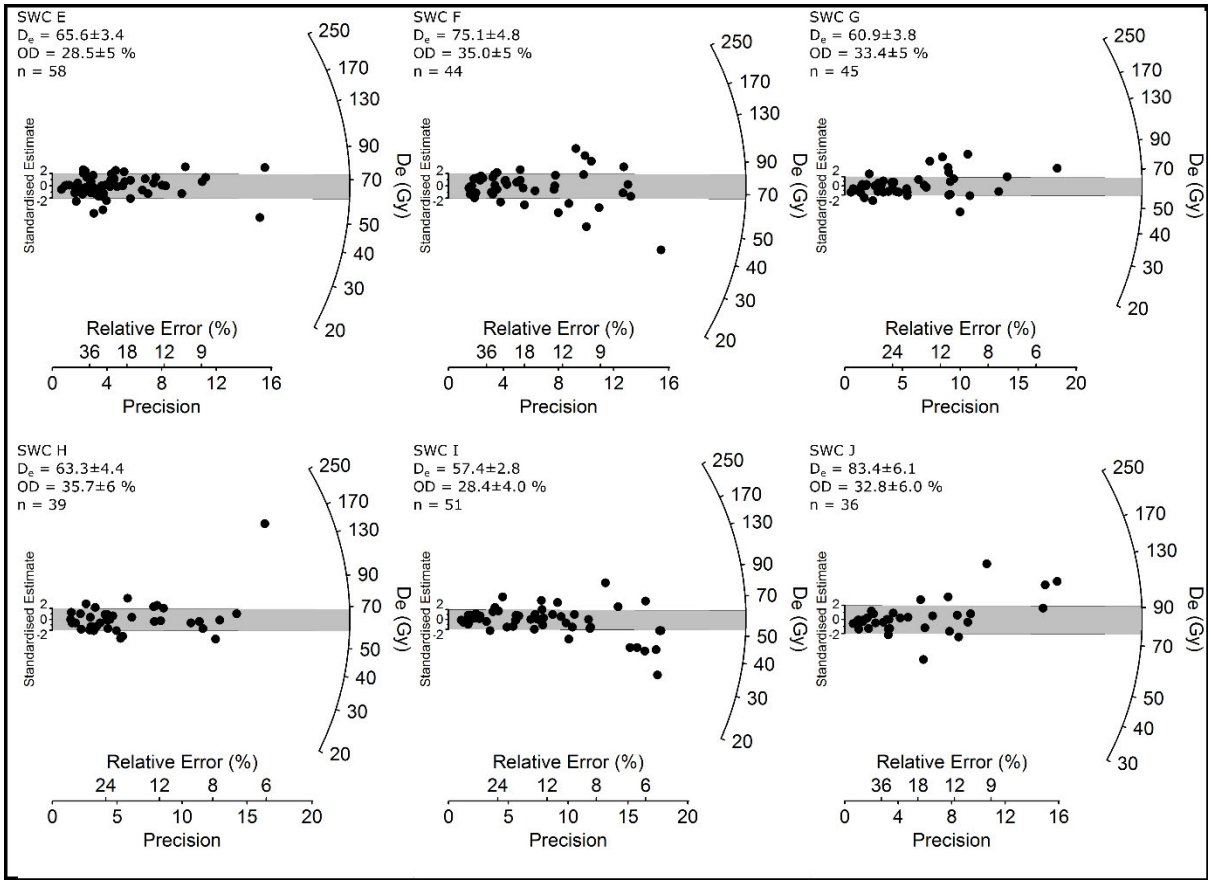

Figure C 21 Radial plots showing the single-grain OSL D_e distributions obtained for the South Walker Creek, SWJ samples (D_e errors are shown at 1σ). The dark grey bands are centred on the weighted mean D_e values, which have been calculated using the CAM.

C5.2.7. SW3

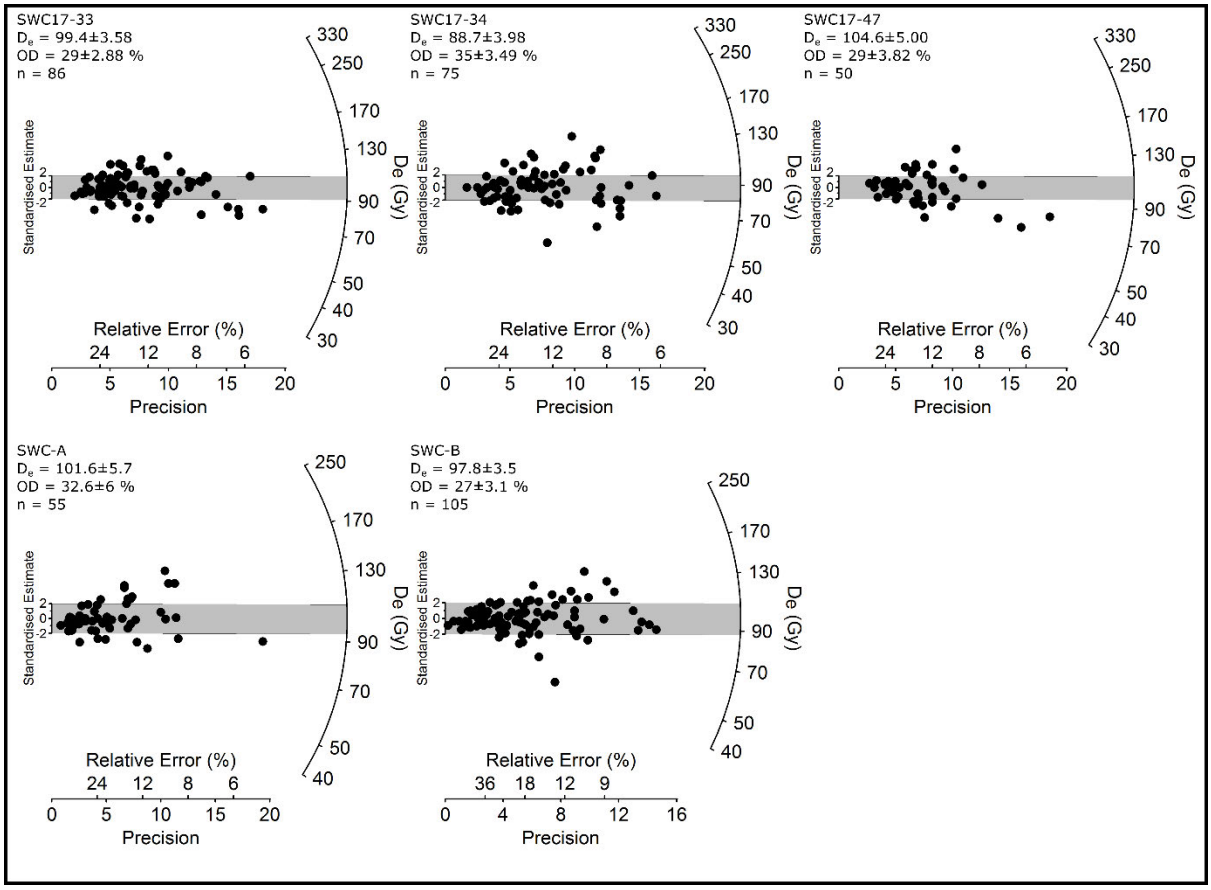

Figure C 22 Radial plots showing the single-grain OSL D_e distributions obtained for the South Walker Creek, SW3 samples (D_e errors are shown at 1σ). The dark grey bands are centred on the weighted mean D_e values, which have been calculated using the CAM.

C5.2.8. SW9 – AU (Unit C – main fossil unit)

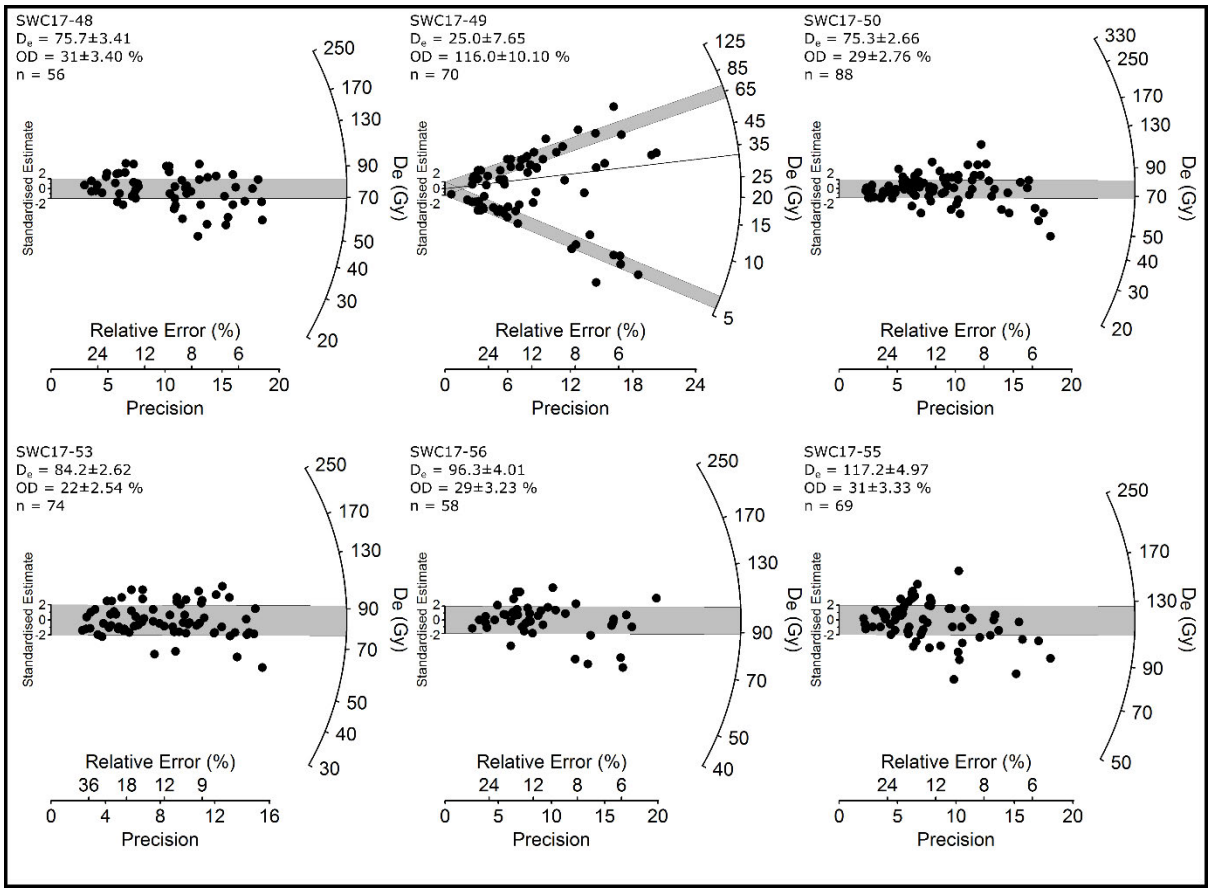

Figure C 23 Radial plots showing the single-grain OSL D_e distributions obtained for the South Walker Creek, SW9 samples (D_e errors are shown at 1σ) that were taken from the main fossil unit (Unit C; including both sediments in association with fossil remains and those surrounding fossil remains). The dark grey bands are centred on the weighted mean D_e values, calculated using the CAM, or the discrete dose populations identified by the FMM (SWC17-49).

C5.2.9. SW9 – AU (sand lens samples)

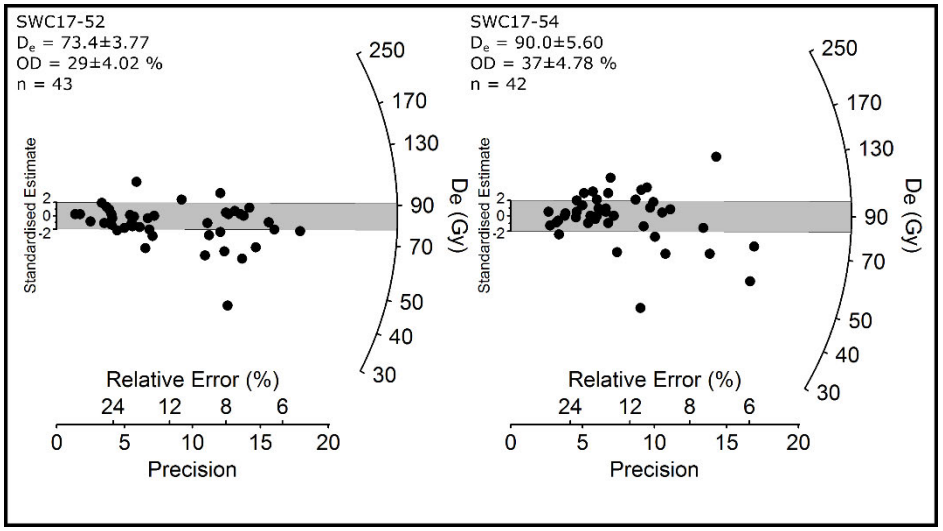

Figure C 24 Radial plots showing the single-grain OSL D_e distributions obtained for the South Walker Creek, SW9 samples (D_e errors are shown at 1σ) that were extracted from sand intrusions. The dark grey bands are centred on the weighted mean D_e values, which have been calculated using the CAM.

C5.2.10. SW9 – GU (Unit C – main fossil unit)

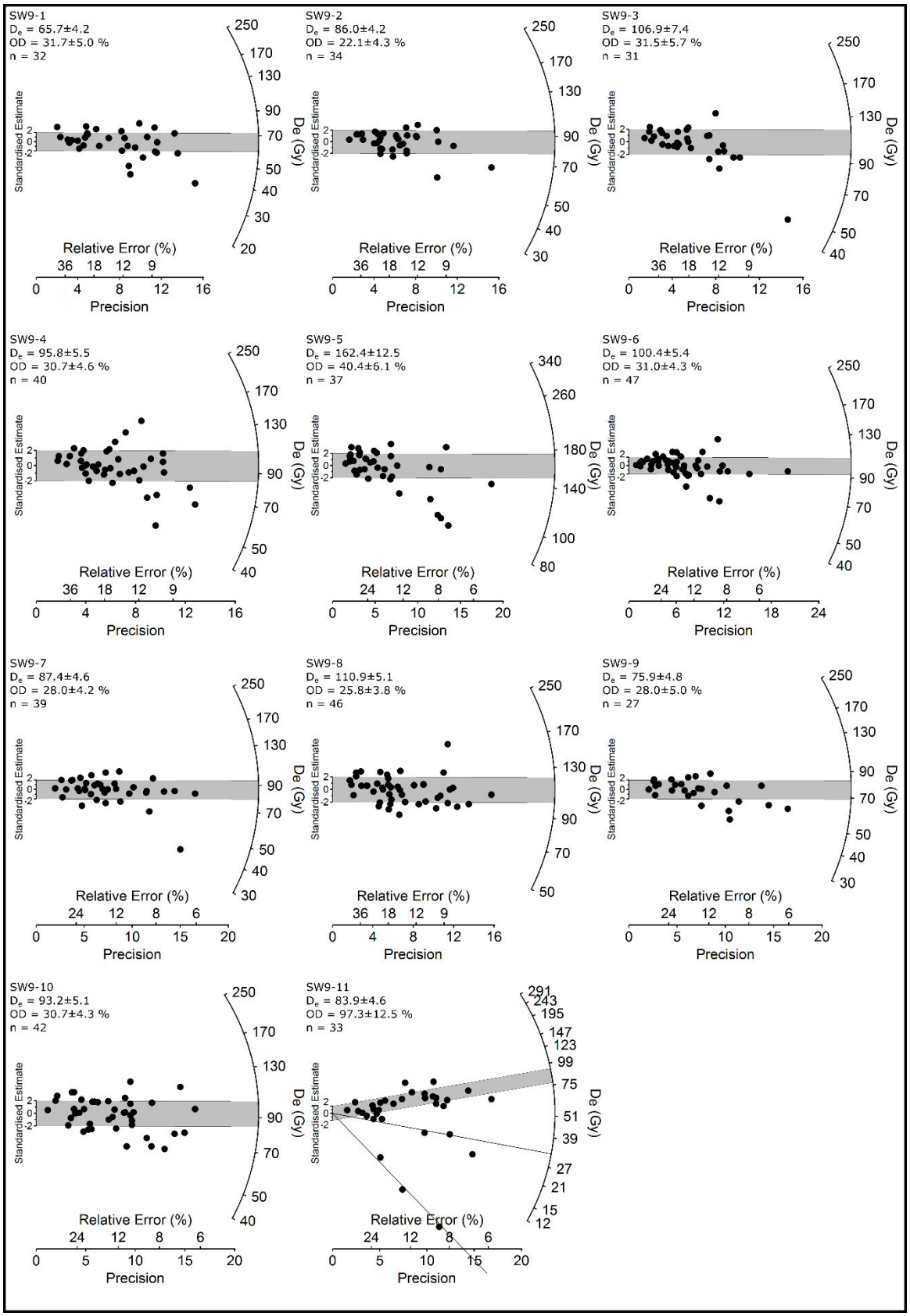

Figure C 25 Radial plots showing the single-grain OSL D_e distributions obtained for the South Walker Creek, SW9 (GU) samples (D_e errors are shown at 1σ) constraining the vertical and horizontal age distribution of the main fossil unit (Unit C). The dark grey bands are centred on the weighted mean D_e values, calculated using the CAM, or the discrete dose populations identified by the FMM (SW9-11).

Table C 8 SAR protocols used by the Adelaide University (AU) and Griffith University (GU) laboratories in this study to obtain single-grain OSL ages. L_n and L_x refer to the natural and regenerative-dose signal measurements, respectively. T_n and T_x refer to the test dose signals measured after the L_n and L_x signals, respectively.

Step	AU single-grain OSL SAR	Notation	Step	GU single-grain OSL SAR	Notation
1[a]	Give dose		1	Give dose	
2[b]	Stimulate with infrared diodes at 50 C for 40 s (90 % power)		2[c]	Stimulate with infrared diodes at 125 C for 40 s (90 % power)	
3	Preheat at 240 C for 10 s		3	Preheat at 240 C for 10 s	
4	Stimulate with green laser at 125 C for 2 s (90% power)	L_n or L_x	4	Stimulate with green laser at 125 C for 1 s (90 % power)	L_n or L_x
5	Give test dose (5 Gy)		5	Give test dose (5 Gy)	
6	Preheat to 160 C for 10 s		6c	Stimulate with infrared diodes at 125 C for 40 s (90 % power)	
7	Stimulate with green laser at 125 C for 2 s (90 % power)	T_n or T_x	7	Preheat to 160 C for 10 s	
8	Return to 1		8	Stimulate with green laser at 125 C for 1 s (90% power)	T_n or T_x
			9	Return to 1	

[a] Step omitted when measuring the natural signal (L_n).
[b] Step added only when measuring the OSL-IR depletion ratio described in Duller (2003).
[c] Each single-grain disc was stimulated with infrared diodes prior to OSL signal measurement to bleach any IR-sensitive signal.

Table C 9 Single-grain dose recovery results obtained for 212-250 μm quartz grains of samples SWC17-53, SWC-B and SWCG using the AU SAR protocol shown in Table C8. n = number of accepted D_e values; OD = overdispersion value.

ID	n	measured-to-given ratio	OD (%)
SWC17-53 (DRT)	29	0.96 ± 0.02	3.6 ± 4.3
SWC B (DRT)	60	0.96 ± 0.02	2.0 ± 6.6
SWC G (DRT)	22	0.95 ± 0.05	10.7 ± 5.4

Table C 10 Single-grain OSL statistics showing proportion of rejected and accepted grains after applying the SAR rejection criteria to the 2015 and 2017 samples. Data are also shown for the single-grain OSL dose recovery test (DRT) measurements made on samples SWC17-53, SWC-B, SWC-G, (in the first three rows).

Sample	Total Grains (n)	Rejected grains (%)									Accepted grains (%)
		T_n <3σ BG	Poor low dose recycling ratio	Poor high dose recycling ratio	IR depletion ratio	Recuperation >5%	Saturated	Anomalous dose response curve	L_n/T_n not intersect DRC	Relative error of D_e >50%	
SWC17-53 (DRT)	500	62	14	6	4	2	0	6	0	0	6
SWC17-B (DRT)	1000	58	10	5	5	6	1	8	2	0	5
SWC17-G (DRT)	300	26	33	12	8	7	1	3	4	0	7
SWC17-30	1400	67	9	6	4	3	0	2	0	0	8
SWC17-31	2100	67	15	5	4	3	0	2	0	0	4
SWC17-47	600	64	16	3	4	2	0	1	1	0	8
SWC17-33	1800	62	17	5	5	3	0	3	1	0	5
SWC17-34	1800	59	20	5	5	3	0	3	0	0	4
SWC17-A	600	33	26	11	6	7	1	3	4	0	9
SWC17-B	1200	52	14	7	5	6	2	4	3	0	9
SWC17-53	1600	68	12	4	5	3	0	3	1	1	5
SWC17-55	800	65	6	5	5	5	0	4	2	1	9
SWC17-56	600	66	11	4	5	2	0	1	2	0	10
SWC17-52	1300	69	15	4	3	2	0	2	0	0	3
SWC17-54	700	64	16	4	5	2	0	1	0	0	6
SWC17-50	900	62	11	5	3	5	0	3	1	1	10
SWC17-48	800	68	8	4	4	6	0	2	1	1	7
SWC17-49	1400	67	14	5	4	4	0	2	0	0	5
SWC17-E	800	60	15	6	4	4	1	2	1	0	7
SWC17-F	500	42	24	10	5	5	0	3	2	0	9
SWC17-G	500	49	17	9	6	5	1	3	1	0	9
SWC17-H	500	52	19	9	5	4	0	2	1	0	8
SWC17-I	1300	68	15	3	5	3	0	2	0	0	4
SWC17-J	700	70	10	4	4	4	0	2	1	0	5

Table C 11 Dose rate data, single-grain equivalent doses (D_e) and quartz OSL ages for the 2009, 2015 and 2017 SWC samples.

			Environmental dose rate data		Equivalent dose (D_e) data				
LOC	ID	Grain Size (μm)	Water Content ($\%_{Dry}$) [a]	Total Dose Rate (Gy/kyr) [b,c]	n [d]	OD (%) [e]	Age Model [f]	D_e (Gy) [c]	Final Age (ka) [g]
SWCC	SWC17-30	212 – 250	12 ± 2.4	1.25 ± 0.1	113	36 ± 2.8	CAM	62.7 ± 2.3	50.2 ± 3.1
SWCC	SWC17-31	212 – 250	12 ± 2.4	1.62 ± 0.1	93	30 ± 2.9	CAM	109.7 ± 4.0	67.5 ± 4.2
SW3	SWC17-47	212 – 250	23 ± 4.7	2.18 ± 0.1	50	29 ± 3.8	CAM	104.6 ± 5.0	48.0 ± 3.8
SW3	SWC17-33	212 – 250	20 ± 4.0	2.22 ± 0.1	86	29 ± 2.9	CAM	99.4 ± 3.6	44.8 ± 3.1
SW3	SWC17-34	212 – 250	20 ± 4.0	2.04 ± 0.1	75	35 ± 3.5	CAM	88.7 ± 4.0	43.5 ± 3.2
SW3	SWC-A	212 – 250	16 ± 3.3	2.03 ± 0.1	55	33 ± 4.6	CAM	101.6 ± 5.7	50.1 ± 3.9
SW3	SWC-B	212 – 250	31 ± 6.3	1.59 ± 0.1	105	27 ± 3.1	CAM	97.8 ± 3.5	61.5 ± 5.0
SW9	SWC17-53	212 – 250	26 ± 5.1	2.22 ± 0.1	74	22 ± 2.5	CAM	84.2 ± 2.6	37.9 ± 2.7
SW9	SWC17-55	212 – 250	24 ± 4.7	2.54 ± 0.1	69	31 ± 3.3	CAM	117.2 ± 5.0	46.1 ± 3.4
SW9	SWC17-56	212 – 250	19 ± 3.8	2.30 ± 0.1	58	29 ± 3.2	CAM	96.3 ± 4.0	42.0 ± 2.9
SW9	SWC17-52	212 – 250	19 ± 3.8	1.80 ± 0.1	43	29 ± 4.0	CAM	73.4 ± 3.8	40.7 ± 3.1
SW9	SWC17-54	212 – 250	21 ± 4.1	1.89 ± 0.1	42	37 ± 4.8	CAM	90.0 ± 5.6	47.5 ± 4.1
SW9	SWC17-50	212 – 250	10 ± 2.0	1.76 ± 0.1	88	29 ± 2.8	CAM	75.3 ± 2.7	42.8 ± 2.6
SW9	SWC17-48	212 – 250	12 ± 2.4	1.40 ± 0.1	56	31 ± 3.4	CAM	75.7 ± 3.4	54.2 ± 3.7
SW9	SWC17-49	212 – 250	20 ± 4.0	1.57 ± 0.1	70	116 ± 10.1	FMM	65.1 ± 6.0	41.6 ± 5.1
SW9	SW9-1	180 – 212	22 ± 4.0	1.65 ± 0.1	32	32 ± 5.0	CAM	65.7 ± 4.2	39.7 ± 4.3
SW9	SW9-2	180 – 212	22 ± 4.0	2.02 ± 0.2	34	22 ± 4.3	CAM	86.0 ± 4.2	42.6 ± 4.3
SW9	SW9-3	180 – 212	22 ± 4.0	2.43 ± 0.2	31	31 ± 5.7	CAM	106.9 ± 7.4	43.9 ± 4.7
SW9	SW9-4	180 – 212	22 ± 4.0	2.52 ± 0.2	40	31 ± 4.6	CAM	95.8 ± 5.5	38.0 ± 4.2
SW9	SW9-5	180 – 212	22 ± 4.0	2.37 ± 0.2	37	40 ± 6.1	CAM	162.4 ± 12.5	68.6 ± 8.4
SW9	SW9-6	180 – 212	22 ± 4.0	2.15 ± 0.2	47	31 ± 4.3	CAM	100.4 ± 5.4	46.6 ± 5.0
SW9	SW9-7	180 – 212	22 ± 4.0	2.66 ± 0.2	39	28 ± 4.2	CAM	87.4 ± 4.6	32.9 ± 3.4
SW9	SW9-8	180 – 212	22 ± 4.0	2.62 ± 0.2	46	26 ± 3.8	CAM	110.9 ± 5.1	42.3 ± 4.1
SW9	SW9-9	180 – 212	22 ± 4.0	2.56 ± 0.2	27	28 ± 5.0	CAM	75.9 ± 4.8	29.7 ± 3.1
SW9	SW9-10	180 – 212	22 ± 4.0	2.47 ± 0.2	42	31 ± 4.3	CAM	93.2 ± 5.1	37.7 ± 3.6
SW9	SW9-11	180 – 212	22 ± 4.0	1.85 ± 0.2	33	97 ± 12.5	FMM	83.9 ± 4.6	45.3 ± 5.5
SWJ	SWC-E	212 – 250	31 ± 6.3	0.99 ± 0.1	58	29 ± 4.6	CAM	65.6 ± 3.4	66.6 ± 6.2
SWJ	SWC-F	212 – 250	28 ± 5.6	1.24 ± 0.1	44	35 ± 5.2	CAM	75.1 ± 4.8	60.5 ± 5.8
SWJ	SWC-G	212 – 250	26 ± 5.1	0.91 ± 0.1	45	33 ± 5.2	CAM	60.9 ± 3.8	66.6 ± 6.5
SWJ	SWC-H	212 – 250	30 ± 6.0	0.97 ± 0.1	39	36 ± 5.6	CAM	63.3 ± 4.4	65.6 ± 6.7
SWJ	SWC-I	212 – 250	22 ± 4.4	0.77 ± 0.1	51	28 ± 3.8	CAM	57.4 ± 2.8	74.7 ± 6.3
SWJ	SWC-J	212 – 250	38 ± 7.6	1.39 ± 0.1	36	33 ± 6.1	CAM	83.4 ± 6.1	60.1 ± 6.5

[a] Long-term water content, expressed as % of dry mass of mineral fraction, with an assigned relative uncertainty of ±20%.
[b] Total dose rate components (i.e., gamma, beta, internal and cosmic contributions); the breakdown of individual dose rate components is outlined in Table C15.
[c] Mean ± total uncertainty (68% confidence interval), calculated in quadrature as the sum of the random and systematic uncertainties. The FMM D_e values for SWC17-49 and SW9-11 have been calculated using the dominant dose components (those containing the largest proportion of accepted grains), as identified from the optimum FMM fits for these samples (the fit with the lowest BIC score; Arnold and Roberts, 2009) (see Tables C12 – 14).
[d] Number of D_e measurements that passed the SAR rejection criteria and were used for D_e determination.
[e] OD = overdispersion; the relative spread in the D_e dataset beyond that associated with the measurement uncertainties of individual D_e values, and calculated using the central age model (CAM) of Galbraith et al. (1999).
[f] Age model used to calculate the sample-averaged D_e value for each sample. CAM = central age model (Galbraith et al., 1999); FMM = finite mixture model (Galbraith & Green, 1990). The FMM D_e values and ages shown for samples SWC17-49 and SW9-11 are included for indicative purposes only and have not been included in our final age evaluations for SW9.
[g] Total uncertainty includes a systematic component of ±2% associated with laboratory beta-source calibration.

Table C 12 . Log likelihood (llik) statistics (Roberts et al., 2000; Galbraith & Roberts, 2012) associated with the of D_e populations of the South Walker Creek samples. The minimum age model was calculated using an assumed overdispersion of 20% based on sample SW9-2, considered 'ideal' for representing expected beta dose heterogeneity within local sediments (Arnold & Roberts, 2009). The llik values shown in bold indicate the most statistically suitable age model fit for each D_e dataset.

LOC	ID	CAM llik [c]	MAM-3 llik [c, d]	MAM-4 [c, d]
SWCC	SWC17-30	**-55.4**	-59.2	-56.1
SWCC	SWC17-31	**-35.2**	-38.2	-31.5
SW3	SWC17-47	**-15.8**	-15.6	-15.0
SW3	SWC17-33	**-30.3**	-30.6	-30.3
SW3	SWC17-34	**-35.9**	-37.9	-35.2
SW3	SWC A	**-32.0**	-32.0	-30.8
SW3	SWC B	**-48.5**	-49.9	-46.4
SW9	SWC17-53	**-11.5**	-11.3	-11.2
SW9	SWC17-55	**-25.6**	-26.1	-25.4
SW9	SWC17-56	**-7.7**	-7.9	-7.3
SW9	SWC17-52	**-14.7**	-15.6	-13.5
SW9	SWC17-54	**-20.8**	-25.3	-18.8
SW9	SWC17-50	**-28.8**	-29.0	-28.7
SW9	SWC17-48	**-19.0**	-19.3	-18.9
SW9	SWC17-49 [a]	-114.9	-107.4	-714.5
SW9	SW9-1	**-14.5**	-15.3	-14.1
SW9	SW9-2	**-6.3**	-6.4	-6.2
SW9	SW9-3	**-15.3**	-16.1	-14.8
SW9	SW9-4	**-16.1**	-16.2	-16.1
SW9	SW9-5	**-26.5**	-26.3	-25.7
SW9	SW9-6	**-20.9**	-21.9	-20.0
SW9	SW9-7	**-12.6**	-13.7	-10.8
SW9	SW9-8	**-17.1**	-16.6	-16.1
SW9	SW9-9	**-9.6**	-9.6	-9.2
SW9	SW9-10	**-20.1**	-19.8	-19.7
SW9	SW9-11 [a]	-180.3	-62.0	-161.7
SWJ	SWC E	**-37.6**	-38.4	-35.7
SWJ	SWC F	**-26.3**	-27.4	-25.3
SWJ	SWC G	**-31.1**	-30.9	-30.8
SWJ	SWC H	-23.7	**-21.6**	-21.1
	SWC H [b]	**-18.3**	-18.2	-18.2
SWJ	SWC I	**-19.4**	-19.1	-19.1
SWJ	SWC J	**-22.9**	-23.8	-22.1

[a] Designates samples exhibiting complex D_e distributions with very high overdispersion values of ~100%, and which were subsequently fitted using the finite mixture model (FMM).

[b] Comparative age model llik scores calculated for sample SWC H after elimination of a single, precise, high outlier D_e value of 182 ± 11 Gy (refer to Table C11).

[c] Llik represents the maximum log likelihood score of the CAM, MAM-3 or MAM-4 fit. For a given sample, the llik score of the MAM-3 is expected to be substantially higher (i.e., at least 1.92 greater) than that of the CAM when the addition of the extra model parameter improves the fit to the data. Likewise, the llik score of the MAM-4 is expected to be significantly greater than that of the MAM-3 (by at least 1.92 when compared with the 95% C.I. of a χ^2 distribution) when the addition of the extra model parameter improves the fit to the data. If the extra parameter of the MAM-3 (or MAM-4) is not supported by the data, then its llik score will be similar to (i.e., within 1.92 of) the CAM (or MAM-3) llik score, indicating that the simpler age model explains the data equally well (Arnold et al., 2009).

[d] MAM-3 and MAM-4 D_e estimates were calculated after adding, in quadrature, a relative error of 20% to each individual D_e measurement error to approximate the underlying dose overdispersion observed in an 'ideal' (well-bleached and unmixed) sedimentary sample from SWC (SWC17-53 and SW9-2), which is consistent with global overdispersion datasets (Arnold & Roberts, 2009).

Table C 13 Finite mixture model fitting results for sample SW9-11, which exhibits a complex D_e distribution with multiple dose components. The FMM was fitted by varying the common overdispersion (OD) parameter between 10 and 30% and incrementally increasing the specified number of dose components until the FMM fits would no longer converge. The Bayes Information Criteria (BIC) and log-likelihood (llik) scores are shown for each of the different FMM parameterisation scenarios tested with sample SW9-11. The BIC score has been used to assess the suitability of the FMM fits, with the lowest BIC score taken to represent the optimum parameterisation of the FMM (shown in bold). The grey text identifies FMM parameterisation scenarios that are deemed empirically unsupported, since the specified common overdispersion value is smaller than that observed for 'ideal' (well-bleached and unmixed) sedimentary sample from SWC (SWC17-53 and SW9-2).

SW9-11									
OD	**# comps**	**llik**	**BIC**	**comp 1 (Gy)**	**proportion of grains**	**comp 2 (Gy)**	**proportion of grains**	**comp 3 (Gy)**	**proportion of grains**
10	1	-570.22	1143.93	50.78					
10	2	-109.87	230.24	3.23 ± 0.31	0.09 ± 0.05	67.59 ± 2.05	0.91 ± 0.05		
10	3	-31.21	79.91	3.23 ± 0.31	0.09 ± 0.05	30.53 ± 2.14	0.18 ± 0.07	83.68 ± 2.94	0.73 ± 0.08
15	1	-367.80	739.10	50.9					
15	2	-69.17	148.84	3.28 ± 0.38	0.09 ± 0.05	68.47 ± 2.61	0.91 ± 0.05		
15	3	-26.99	71.47	3.28 ± 0.38	0.09 ± 0.05	31.44 ± 2.83	0.18 ± 0.07	84.09 ± 3.76	0.72 ± 0.08
20	1	-250.36	504.21	51.15					
20	2	-49.17	108.82	3.31 ± 0.46	0.09 ± 0.05	68.89 ± 3.19	0.91 ± 0.05		
20	**3**	**-26.04**	**69.57**	**3.31 ± 0.46**	**0.09 ± 0.05**	**32.08 ± 3.62**	**0.18 ± 0.08**	**83.91 ± 4.62**	**0.73 ± 0.08**
25	1	-180.32	364.14	51.35					
25	2	-39.11	88.72	3.34 ± 0.55	0.09 ± 0.05	69.12 ± 0.05	0.91 ± 0.05		
25	3	-26.61	70.69	3.34 ± 0.55	0.09 ± 0.05	32.58 ± 6.63	0.17 ± 0.08	83.26 ± 5.54	0.74 ± 0.09
30	1	-136.70	276.90	51.56					
30	2	-34.08	78.65	3.36 ± 0.64	0.09 ± 0.05	69.28 ± 4.36	0.91 ± 0.05		
30	3	-27.75	72.98	3.36 ± 0.64	0.09 ± 0.05	33.16 ± 6.08	0.16 ± 0.08	82.10 ± 6.52	0.75 ± 0.09

Table C 14 Finite mixture model fitting results for sample SWC17-49, which exhibits a complex D_e distribution with multiple dose components. The FMM was fitted by varying the common overdispersion (OD) parameter between 10 and 30 % and incrementally increasing the specified number of dose components until the FMM fits would no longer converge. The Bayes Information Criteria (BIC) and log-likelihood (llik) scores are shown for each of the different FMM parameterisation scenarios tested with sample SWC17-49. The BIC score has been used to assess the suitability of the FMM fits, with the lowest BIC score taken to represent the optimum parameterisation of the FMM (shown in bold). The grey text identifies FMM parameterisation scenarios that are deemed empirically unsupported, since the specified common overdispersion value is smaller than that observed for 'ideal' (well-bleached and unmixed) sedimentary sample from SWC (SWC17-53 and SW9-2).

SWC17-49									
OD	**# comps**	**llik**	**BIC**	**comp 1 (Gy)**	**proportion of grains**	**comp 2 (Gy)**	**proportion of grains**	**comp 3 (Gy)**	**proportion of grains**
10	1	-1519.07	3042.40	22.57					
10	2	-212.50	437.75	6.07 ± 0.19	0.44 ± 0.06	51.20 ± 0.56	0.60 ± 0.06		
10	3	-118.45	258.14	6.08 ± 0.20	0.44 ± 0.06	32.88 ± 1.36	0.22 ± 0.05	72.00 ± 2.58	0.34 ± 0.06
15	1	-961.65	1927.54						
15	2	-145.60	303.94	6.10 ± 0.25	0.44 ± 0.06	51.87 ± 1.67	0.56 ± 0.06		
15	3	-96.71	214.65	6.09 ± 0.25	0.44 ± 0.06	32.76 ± 1.95	0.21 ± 0.05	71.35 ± 3.40	0.35 ± 0.06
20	1	-662.74	1329.73	22.17					
20	2	-113.44	239.62	6.09 ± 0.30	0.44 ± 0.06	52.35 ± 2.08	0.56 ± 0.06		
20	3	-87.91	197.06	6.06 ± 0.30	0.44 ± 0.06	32.66 ± 2.73	0.21 ± 0.06	70.41 ± 0.06	4.32 ± 0.06
25	1	-486.53	977.32	21.87					
25	2	-97.75	208.25	6.08 ± 0.36	0.44 ± 0.06	52.77 ± 2.52	0.56 ± 0.06		
25	3	-84.96	191.16	6.02 ± 0.35	0.44 ± 0.06	32.51 ± 3.88	0.19 ± 0.07	68.62 ± 5.52	0.37 ± 0.07
30	1	-375.07	754.38	21.63					
30	2	-90.36	193.46	6.08 ± 0.42	0.44 ± 0.06	53.16 ± 2.98	0.56 ± 0.06		
30	**3**	**-84.56**	**190.36**	**5.98 ± 0.40**	**0.44 ± 0.06**	**31.69 ± 6.30**	**0.16 ± 0.09**	**65.16 ± 7.12**	**0.40 ± 0.10**

Table C 15 Environmental dose rate values calculated for the quartz fractions of the 2011, 2015 and 2017 OSL samples.

			Environmental dose rate (Gy/ka)					
LOC	**ID [d]**	**Depth (cm)**	**W_c ($\%_{Dry}$)[a]**	**Beta [b, c]**	**Gamma [c, d]**	**Internal [c, e]**	**Cosmic [c, f]**	**Total [c]**
SWCC	SWC17-30	92	12 ± 2.4	0.54 ± 0.03 $^{\beta}$	0.50 ± 0.02 ^{FGS}	0.03 ± 0.01	0 17 ± 0.02	1.25 ± 0.06
SWCC	SWC17-31	78	12 ± 2.4	0.73 ± 0.04 $^{\beta}$	0.69 ± 0.02 ^{FGS}	0.03 ± 0.01	0 17 ± 0.02	1.62 ± 0.07
SW3	SWC17-47	194	23 ± 4.7	1.21 ± 0.06 $^{\beta}$	0.80 ± 0.03 ^{FGS}	0.03 ± 0.01	0 13 ± 0.01	2.18 ± 0.13
SW3	SWC17-33	194	20 ± 4.0	1.22 ± 0.06 $^{\beta}$	0.83 ± 0.03 ^{FGS}	0.03 ± 0.01	0 14 ± 0.01	2.22 ± 0.12
SW3	SWC17-34	263	20 ± 4.0	1.15 ± 0.06 $^{\beta}$	0.72 ± 0.02 ^{FGS}	0.03 ± 0.01	0 13 ± 0.01	2.04 ± 0.11
SW3	SWC A	95	16 ± 3.3	1.02 ± 0.04 ^{HRGS}	0.81 ± 0.03^{HRGS}	0.03 ± 0.01	0 16 ± 0.02	2.03 ± 0.10
SW3	SWC B	155	31 ± 6.3	0.80 ± 0.04 ^{HRGS}	0.62 ± 0.03 ^{HRGS}	0.03 ± 0.01	0 13 ± 0.01	1.59 ± 0.13
SW9	SWC17-53	252	26 ± 5.1	1.13 ± 0.06 $^{\beta}$	0.93 ± 0.02 ^{FGS}	0.03 ± 0.01	0 12 ± 0.01	2.22 ± 0.13
SW9	SWC17-55	260	24 ± 4.7	1.30 ± 0.07 $^{\beta}$	1.08 ± 0.03 ^{FGS}	0.03 ± 0.01	0 12 ± 0.01	2.54 ± 0.14
SW9	SWC17-56	245	19 ± 3.8	1.18 ± 0.06 $^{\beta}$	0.95 ± 0.02 ^{FGS}	0.03 ± 0.01	0 13 ± 0.01	2.30 ± 0.12
SW9	SWC17-52	230	19 ± 3.8	0.86 ± 0.04 $^{\beta}$	0.77 ± 0.02 ^{FGS}	0.03 ± 0.01	0 13 ± 0.01	1.80 ± 0.10
SW9	SWC17-54	230	21 ± 4.1	1.00 ± 0.05 $^{\beta}$	0.73 ± 0.02 ^{FGS}	0.03 ± 0.01	0 13 ± 0.01	1.89 ± 0.11
SW9	SWC17-50	30	10 ± 2.0	0.85 ± 0.04 $^{\beta}$	0.68 ± 0.02 ^{FGS}	0.03 ± 0.01	0 19 ± 0.02	1.76 ± 0.08
SW9	SWC17-48	100	12 ± 2.4	0.67 ± 0.03 $^{\beta}$	0.52 ± 0.02 ^{FGS}	0.03 ± 0.01	0 17 ± 0.02	1.40 ± 0.07
SW9	SWC17-49	64	20 ± 4.0	0.72 ± 0.04 $^{\beta}$	0.65 ± 0.02^{FGS}	0.03 ± 0.01	0 16 ± 0.02	1.57 ± 0.09
SW9	SW9-1	120	22 ± 4.0	0.87 ± 0.08 ^{HRGS}	0.62 ± 0.05 ^{HRGS}	0.03 ± 0.01	0 13 ± 0.01	1.65 ± 0.14
SW9	SW9-2	140	22 ± 4.0	1.12 ± 0.01 ^{HRGS}	0.74 ± 0.06 ^{HRGS}	0.03 ± 0.01	0 13 ± 0.01	2.02 ± 0.17
SW9	SW9-3	160	22 ± 4.0	1.36 ± 0.11 ^{HRGS}	0.91 ± 0.06 ^{HRGS}	0.03 ± 0.01	0 13 ± 0.01	2.43 ± 0.19
SW9	SW9-4	180	22 ± 4.0	1.40 ± 0.13 ^{HRGS}	0.96 ± 0.08 ^{HRGS}	0.03 ± 0.01	0 13 ± 0.01	2.52 ± 0.24
SW9	SW9-5	200	22 ± 4.0	1.34 ± 0.13 ^{HRGS}	0.87 ± 0.07 ^{HRGS}	0.03 ± 0.01	0 13 ± 0.01	2.37 ± 0.22
SW9	SW9-6	200	22 ± 4.0	1.20 ± 0.11 ^{HRGS}	0.79 ± 0.07 ^{HRGS}	0.03 ± 0.01	0 13 ± 0.01	2.15 ± 0.20
SW9	SW9-7	200	22 ± 4.0	1.50 ± 0.13 ^{HRGS}	1.00 ± 0.08 ^{HRGS}	0.03 ± 0.01	0 13 ± 0.01	2.66 ± 0.23
SW9	SW9-8	200	22 ± 4.0	1.49 ± 0.12 ^{HRGS}	0.97 ± 0.07 ^{HRGS}	0.03 ± 0.01	0 13 ± 0.01	2.62 ± 0.22
SW9	SW9-9	200	22 ± 4.0	1.46 ± 0.12 ^{HRGS}	0.94 ± 0.06 ^{HRGS}	0.03 ± 0.01	0 13 ± 0.01	2.56 ± 0.20
SW9	SW9-10	200	22 ± 4.0	1.38 ± 0.10 ^{HRGS}	0.93 ± 0.06 ^{HRGS}	0.03 ± 0.01	0 13 ± 0.01	2.47 ± 0.19
SW9	SW9-11	150	22 ± 4.0	1.03 ± 0.11 ^{HRGS}	0.66 ± 0.07 ^{HRGS}	0.03 ± 0.01	0 13 ± 0.01	1.85 ± 0.20
SWJ	SWC E	20	31 ± 6.3	0.44 ± 0.02 ^{HRGS}	0.36±0.02 ^{HRGS}	0.03 ± 0.01	0 15 ± 0.02	0.99 ± 0.08
SWJ	SWC F	50	28 ± 5.6	0.60 ± 0.03 ^{HRGS}	0.46±0.03 ^{HRGS}	0.03 ± 0.01	0 15 ± 0.02	1.24 ± 0.10
SWJ	SWC G	80	26 ± 5.1	0.40 ± 0.02 ^{HRGS}	0.33±0.02 ^{HRGS}	0.03 ± 0.01	0 15 ± 0.02	0.91 ± 0.07
SWJ	SWC H	120	30 ± 6.0	0.45 ± 0.02 ^{HRGS}	0.35±0.02 ^{HRGS}	0.03 ± 0.01	0 14 ± 0.01	0.97 ± 0.08
SWJ	SWC I	150	22 ± 4.4	0.32 ± 0.02 ^{HRGS}	0.27±0.02 ^{HRGS}	0.03 ± 0.01	0 14 ± 0.01	0.77 ± 0.06
SWJ	SWC J	180	38 ± 7.6	0.77 ± 0.04 ^{HRGS}	0.46±0.02 ^{HRGS}	0.03 ± 0.01	0 12 ± 0.01	1.39 ± 0.11

[a] Long-term water content, expressed as % of dry mass of mineral fraction, with an assigned relative uncertainty of ±20%.
[b] Beta dose rates were calculated on dried, powdered sediment samples using a Risø GM-25-5 low level beta counting (β) or, high resolution gamma spectroscopy (HRGS) after making allowance for beta dose attenuation due to grain-size effects and HF etching (Brennan, 2003; Mejdahl, 1979).
[c] Mean ± total uncertainty (68% confidence interval), calculated as the quadratic sum of the random and systematic uncertainties.
[d] Gamma dose rates were calculated from *in situ* gamma-ray spectrometry measurements made at each sample position with a NaI:Tl detector, using the 'energy windows' approach (i.e., Arnold et al., 2012) (FGS) where possible and; high resolution gamma spectroscopy on dried powdered sediment (HRGS) using published conversion factors (Stokes et al., 2003; Guérin et al., 2011).
[e] An assumed internal dose rate of 0.03 Gy / ka, with an assigned relative uncertainty of ±30% (±0.01 Gy/ka) is included for each sample, based on published intrinsic ^{238}U and ^{232}Th contents (Bowler et al., 2003; Jacobs et al., 2006; Mejdahl, 1987; Pawley et al., 2008) and an alpha efficiency factor (a-value) of 0.04 ± 0.01 (Rees-Jones, 1995; Rees-Jones & Tite, 1997).
[f] Cosmic-ray dose rates were calculated using the approach of Prescott & Hutton (1994) and assigned a relative uncertainty of ±10%.

Table C 16 High-resolution gamma spectrometry (HRGS) results for the OSL samples from South Walker Creek. The specific activities of ^{238}U, ^{226}Ra, ^{210}Pb, ^{228}Ra, ^{228}Th and ^{40}K were measured for each sediment sample, and used to calculate daughter-to-parent isotope ratios for ^{226}Ra:^{238}U, ^{210}Pb:^{226}Ra and ^{228}Th:^{228}Ra. Radionuclide specific activities and daughter-to-parent isotopic ratios are shown with their associated 1σ uncertainty ranges.

Sample	Radionuclide specific activities (Bq / kg)						Daughter-to-parent isotopic ratios		
	^{238}U	^{226}Ra	^{210}Pb	^{228}Ra	^{228}Th	^{40}K	^{226}Ra:^{238}U	^{210}Pb:^{226}Ra	^{228}Th:^{228}Ra
SWC17-30	13 ± 1.3	13 ± 0.3	13 ± 1.4	19 ± 0.7	19 ± 0.5	146 ± 5	1.0 ± 0.1	0.9 ± 0.1	1.0 ± 0.05
SWC17-31	18 ± 2.2	21 ± 0.5	19 ± 2.7	25 ±1.0	25 ± 0.7	211 ± 7	1.1 ± 0.1	0.9 ± 0.1	1.0 ± 0.05
SWC17-47	30 ± 1.6	31 ± 0.5	29 ± 2.0	40 ± 0 9	40 ± 0.8	412 ± 10	1.0 ± 0.1	0.9 ± 0.1	1.0 ± 0.03
SWC17-33	23 ± 1.7	23 ± 0.4	22 ± 2.0	41 ± 1 2	40 ± 0.9	405 ± 11	1.0 ± 0.1	1.0 ± 0.1	1.0 ± 0.04
SWC17-34	25 ± 2.7	24 ± 0.5	24 ± 3.3	38 ± 1 3	40 ± 1.0	385 ± 11	1.0 ± 0.1	1.0 ± 0.1	1.0 ± 0.04
SWC-A	24 ± 1.5	22 ± 0.5	24 ± 2.0	35 ± 1.0	36 ± 0.8	352 ± 10	0.9 ± 0.1	1.1 ± 0.1	1.0 ± 0.04
SWC-B	25 ± 1.9	27 ± 0.5	26 ± 2.3	34 ± 0 9	34 ± 0.8	298 ± 8	1.1 ± 0.1	1.0 ± 0.1	1.0 ± 0.03
SWC17-53	25 ± 2.7	27 ± 0.6	25 ± 3.8	38 ± 1 3	39 ± 1.0	382 ± 11	1.1 ± 0.1	0.9 ± 0.1	1.0 ± 0.04
SWC17-55	20 ± 2.8	22 ± 0.5	21 ± 2.7	43 ± 1 5	43 ± 1.1	481 ± 14	1.1 ± 0.2	1.0 ± 0.1	1.0 ± 0.04
SWC17-56	20 ± 1.5	19 ± 0.4	20 ± 2.2	44 ± 1 1	44 ± 1.0	418 ± 10	1.0 ± 0.1	1.1 ± 0.1	1.0 ± 0.03
SWC17-52	20 ± 1.4	21 ± 0.4	21 ± 2.4	31 ± 0 9	30 ± 0.7	248 ± 7	1.1 ± 0.1	1.0 ± 0.1	1.0 ± 0.04
SWC17-54	24 ± 1.6	24 ± 0.5	24 ± 2.6	32 ± 0 9	31 ± 0.8	313 ± 9	1.0 ± 0.1	1.0 ± 0.1	1.0 ± 0.04
SWC17-50	25 ± 1.9	24 ± 0.5	24 ± 2.8	31 ± 1.0	32 ± 0.8	225 ± 7	1.0 ± 0.1	1.0 ± 0.1	1.0 ± 0.04
SWC17-48	13 ± 1.5	15 ± 0.3	13 ± 1.4	21 ± 0.7	20 ± 0.5	197 ± 6	1.1 ± 0.1	0.9 ± 0.1	1.0 ± 0.04
SWC17-49	20 ± 1.6	19 ± 0.4	19 ± 1.9	31 ± 1.0	31 ± 0.8	190 ± 6	0.9 ± 0.1	1.0 ± 0.1	1.0 ± 0.04
SW9-1	19 ± 6.0	25 ± 2.0	26 ± 6.0	26 ± 2.0	-	320 ± 30	1.3 ± 0.4	1.0 ± 0.2	-
SW9-2	27 ± 7.0	17 ± 1.0	15 ± 6.0	38 ± 3.0	-	440 ± 40	0.6 ± 0.2	1.1 ± 0.5	-
SW9-3	27 ± 1.0	23 ± 2.0	23 ± 1.0	44 ± 5.0	-	540 ± 50	0.9 ± 0.1	1.0 ± 0.1	-
SW9-4	30 ± 10.0	23 ± 2.0	30 ± 10.0	44 ± 4.0	-	540 ± 50	0.8 ± 0.3	0.8 ± 0.3	-
SW9-5	30 ± 10.0	22 ± 2.0	22 ± 8.0	41 ± 4.0	-	530 ± 50	0.7 ± 0.3	1.0 ± 0.4	-
SW9-6	32 ± 9.0	22 ± 2.0	18 ± 8.0	39 ± 4.0	-	470 ± 40	0.7 ± 0.2	1.2 ± 0.6	-
SW9-7	40 ± 10.0	26 ± 2.0	29 ± 9.0	47 ± 4.0	-	570 ± 50	0.7 ± 0.2	0.9 ± 0.3	-
SW9-8	33 ± 8.0	28 ± 2.0	21 ± 7.0	47 ± 4.0	-	600 ± 50	0.8 ± 0.2	1.3 ± 0.5	-
SW9-9	31 ± 7.0	24 ± 2.0	22 ± 6.0	44 ± 3.0	-	590 ± 50	0.8 ± 0.2	1.1 ± 0.3	-
SW9-10	37 ± 7.0	41 ± 2.0	29 ± 6.0	43 ± 3.0	-	520 ± 40	1.1 ± 0.2	1.4 ± 0.3	-
SW9-11	30 ± 10.0	18 ± 2.0	17 ± 9.0	31 ± 3.0	-	400 ± 40	0.6 ± 0.2	1.1 ± 0.6	-
SWC-E	15 ± 1.5	13 ± 0.4	13 ± 1.9	21 ± 0 9	20 ± 0.6	163 ± 6	0.8 ± 0.1	1.0 ± 0.2	1.1 ± 0.05
SWC-F	19 ± 1.8	19 ± 0.4	17 ± 2.3	27 ± 0 9	28 ± 0.7	214 ± 7	1.0 ± 0.1	0.9 ± 0.1	1.0 ± 0.04
SWC-G	11 ± 1.5	11 ± 0.3	11 ± 1.9	16 ± 0.8	18 ± 0.6	143 ± 5	1.0 ± 0.1	1.0 ± 0.2	0.9 ± 0.05
SWC-H	12 ± 1.3	13 ± 0.3	15 ± 1.7	18 ± 0.7	20 ± 0.5	162 ± 5	1.1 ± 0.1	1.2 ± 0.1	0.9 ± 0.05
SWC-I	11 ± 1.5	10 ± 0.3	10 ± 1.3	11 ± 0 5	12 ± 0.4	109 ± 4	0.9 ± 0.1	1.1 ± 0.1	1.0 ± 0.06
SWC-J	22 ± 1.4	22 ± 0.4	22 ± 2.0	30 ± 0 9	29 ± 0.7	335 ± 9	1.0 ± 0.1	1.0 ± 0.1	1.0 ± 0.01

Table C 17 Weighted mean ages for OSL samples collected from the fossil-bearing and associated non-fossiliferous sediment of each site.

LOC	Samples (n =)	Age (ka)
SWC-CC	2	58.2 ± 6.1
SW3	5	47.7 ± 3.2
SWJ [a]	-	-
SW9 [b]	19	41.3 ± 1.9
SW9 (AU)	8	43.3 ± 1.8
SW9 (GU)	11	38.9 ± 3.0

[a] The six OSL ages for SWJ have all been derived from Unit B, which underlies the main fossil unit. It is therefore not possible to calculate a weighted mean OSL age for the main fossil unit at SWJ, though the underlying unit yields a weighted mean OSL age of 65.6 ± 2.2 ka (n = 6).
[b] Combined results from SW9 (AU) and SW9 (GU) samples.

Table C 18 Details of the OSL samples used to calculate the weighted mean ages for the fossil units at each site, as shown in Table C17.

LOC	Sample(s)
SWC-CC	SWC17-30, SWC17-31
SW3	SWC17-47, SWC17-33, SWC17-34, SWC-A, SWC-B
SWJ	Main fossil unit = none
	Underlying unit = SWC-E, SWC-F, SWC-G, SWC-H, SWC-I, SWC-J
SW9 (AU)	SWC17-53, SWC17-55, SWC17-56, SWC17-52, SWC17-54, SWC17-50, SWC17-48, SWC17-49.
SW9 (GU)	SW9-1, SW9-2, SW9-3, SW9-4, SW9-5, SW9-6, SW9-7, SW9-8, SW9-9, SW9-10, SW9-11

C5.3. Radiocarbon dating

Rachel Wood & Scott A. Hocknull

Bones and teeth from the megafauna were submitted to the Australian National University (ANU) and Beta-analytic radiocarbon facilities. At the ANU, the %N was measured in two bones from SW9 using EA-IRMS (following Brock et al. (2012)). The majority of nitrogen within a bone is contained in the protein extracted for dating called collagen. Theoretically, 0.2 %N is required to recover the 1 % collagen required for radiocarbon dating, although in practice 0.5 – 0.7 %N is often required (Brock et al., 2012). Therefore, values of 0.1 %N in SW9-W5 (*Diprotodon optatum* femur) and 0.0 %N in SW9-82 (*Macropus* sp. (giant) tibia) suggest that insufficient collagen is preserved for radiocarbon dating. This result was supported by unsuccessful attempts to recover collagen at the Beta-analytic radiocarbon facility.

Bone, teeth and charcoal were submitted to Beta Analytic for radiocarbon dating and pre-treated using their standard physical and chemical methods for retrieving collagen from bones and teeth and carbon from charcoal or organic sediments (https://www.radiocarbon.com/pretreatment-carbon-dating.htm). No collagen or dateable charcoal was recovered from any sample similar to the ANU result. Organic sediment was then attempted. The bulk organic fraction was collected by sieving to <180 microns to remove roots and macrofossils, and acid washing to remove carbonates. This fraction of sediment contains carbon from a large variety of sources. Each may have a different ^{14}C age. For example, microcharcoal or coal/lignin from sediment eroded into the river may be older than deposition of the sediment, whilst alkali soluble and mobile humic acids derived from degraded plant material may be younger (Fowler et al., 1986; McGeehin et al., 2001; Wakeham & Canuel, 2016). As a result, age estimates on the bulk organic (Table C19) fraction rarely date the deposition of the sediment so we have excluded these results from subsequent age interpretation.

Given the exceptionally young age of the bulk organic fraction of the sediment and doubts regarding its reliability for age control, S.H. searched for macro-charcoal from within and below the fossil bone bed and any macro-charcoal associated with bone remains. All samples were collected using methods to limit contamination. When sampled in the field, samples were placed into clean foil with surrounding sediment. In the laboratory, spatulas or tweezers were used to remove pieces and place directly into a plastic bag. Although many samples were recovered over the course of excavations, few proved suitable for dating, or survived pre-treatments. All macro-charcoal remains were tiny in size, being similar in size to the clasts surrounding them. The largest pieces were recovered from clay-rich pieces of matrix that likely derived as rip up clasts from older sediment. Unfortunately, clear sedimentary structures are not easily defined in the matrix of the SW9 bone-bed; therefore, we cannot be conclusive about the primary nature of the macro-charcoal. It is suspected that these macro-charcoal remains are reworked from older fluvial sediments.

Figure C15 indicates the location of samples that returned a date. SW9-13-42 was recovered from directly within the bone-bed close to the main concentration of fossils, whilst SW9-16-C02 and SW9-16-C04 were recovered from within the base of the bone bed below any vertebrate remains, just above an unconformity.

Six samples of charcoal were submitted for dating at the Australian National University. One sample contained enough material to attempt ABOx-SC (Bird et al., 1999; Wood et al., 2016), but the sample

completely dissolved during pre-treatment. After removing visible contaminants (only sediment) with a scalpel where possible, all remaining samples were gently crushed and pre-treated with an ABA protocol involving 1 M HCl (30 min, 70 °C), 1 M NaOH (1 h, 70 °C, replaced until colourless) and 1 M HCl (30 min, 70 °C). After each treatment the sample was rinsed in ultrapure water, and after NaOH treatment was rinsed in ultrapure water until the solution remained colourless. Cleaned material was combusted in an evacuated sealed quartz tube with CuO wire and Ag foil. The CO_2 generated was cryogenically collected and purified prior to graphitisation over an Fe catalyst with H_2. %C was measured volumetrically during CO_2 collection. Samples were dated on a NEC single stage AMS (Fallon et al., 2010), and dates calculated using a $\delta^{13}C$ measured by AMS and according to Stuiver & Polach (1977). Dates were calibrated against SHCal13 (Hogg et al., 2013) in OxCal (Bronk Ramsey, 2009).

Three of five charcoal samples survived the ABA pre-treatment. Only one sample is a single entity. The other two consist of multiple small pieces of charcoal. Sample SW9-13-42a (S-ANU40224) had a low % yield, suggesting poor preservation and/ or low firing temperature. It was also <50 %C after pre-treatment, suggesting that sediment grains were present in the dated sample. All samples, and particularly SW9-13-42a (S-ANU40224), must be considered a minimum age as the ABA pre-treatment does not always remove sufficient contaminants to produce an accurate age estimate. Given the extreme sensitivity of samples beyond 40 ka to young contamination, if inaccurate, they are most likely erroneously young. Radiocarbon dates on charcoal from fluvial sediments must be older than the deposition of the sediment, and this effect may be up to several thousand years (Blong & Gillespie, 1978; Frueh & Lancaster, 2014; Martin et al., 2019).

Taken together, the macro-charcoal at SW9 is older than 40 cal kBP. However, it is most likely that it dates to beyond the limit of radiocarbon dating. This is rather uninformative, implying that the sediment was deposited after 40 cal kBP, and quite possibly after > 50 cal kBP. Reworking of the macro-charcoal within rip up clasts could explain this greater age in comparison with other methods.

Table C 19 Radiocarbon Dates. Calibration is against SHCal13 (Hogg et al., 2013) in OxCal (Bronk Ramsey, 2009). * Date may extend beyond calibration curve.

Laboratory Code	Sample Name	Number of charcoal pieces	$F^{14}C$	%C	% yield	IRMS $\delta^{13}C$	^{14}C age (BP)	Calibrated age (95% probability)
Sediment								
Beta-359939	CC15	1 (not recovered)	0 1420 ± 0.0012			-20.8	15680 ± 70	19060 - 18720
Beta-359938	CC12	1 (not recovered)	0 1095 ± 0.0010			-19.1	17770 ± 70	21760 - 21170
Beta-359937	CC09	1 (not recovered)	0.0953 ± 0.0008			-24.8	18880 ± 70	22930 - 22470
Beta-359936	CC06	1 (not recovered)	0 1072 ± 0.0009			-22.1	17940 ± 70	21910 - 21440
Beta-359935	CC01	1 (not recovered)	0.0691 ± 0.0009			-23.1	21460 ± 100	25950 - 25520
Charcoal								
S-ANU 52436	SW9-16-CO2	4	0.0041 ± 0.0006	60	23.2		44115 ± 1224	49880 – 45590*
S-ANU 52437	SW9-16-04	Multiple	0.0075 ± 0.0006	59	12.6		39266 ± 674	44340 - 42170
S-ANU 40224	SW9-13-42a	1	0.51 ± 0.05	33	1.68		42350 ± 900	47840 - 44140

C5.4. U-series direct dating of South Walker Creek megafauna fossils

Gilbert J. Price

Fossil teeth are open systems for U. Living tissues contain little to no U, thus for such fossil materials to be dateable with U-series methods, U must be taken up from the burial environment postdeposition. U subsequently decays via alpha and beta emissions via a series of intermediate, short-lived isotopes, principally ^{234}U, ^{234}Th, ^{230}Th, and ^{231}Pa. The U-Th age is then calculated by determining the amount of ^{230}Th in relation to the original ^{238}U (via ^{234}U). This U-Th age will typically be a minimum, or 'fossilisation', age in the most ideal circumstances. The degree to which a given specimen will approximate a 'true' age can, in part, be determined by using other independent geochronological methods. In some situations, U, which is highly soluble in water, may be leached from a tooth at various times during or after radioactive decay, thus resulting in age overestimation (in contrast, Th is typically insoluble in water). Such U leaching, and thus the reliability of a given fossil tooth to produce meaningful geochronological information, can be determined by constructing ^{230}Th age and U profiles through a given tooth.

In this study, we dated several fossil teeth with U-Th methods using two sampling approaches: micro-profiling (described in this section) and laser ablation (see below). For micro-profiling, we followed the approach described in Price et al. (2013), whereby samples of dentine were collected from transects through a given tooth using 1 mm diameter stainless steel drill bits (Figures C26 – C29). In most cases, the dentine was already exposed as a result of mastication-related tooth wear or post-mortem breakages of the respective teeth. One specimen, QMF54689 (molar from a *Diprotodon optatum* lower jaw), was sampled by drilling a single hole into the occlusal surface of the dentine, with powders collected at approximate intervals of 1 mm for the entire depth of the hole (ca. 10 mm). Although laser ablation profiling requires substantially less material for dating (see below), this approach is less destructive in that the fossil did not need to be cut and slabbed, thus remains largely intact, barring the small drill hole (Figure C25).

24 independent ages were generated from transects through four teeth (Figures C26 – C29; Table C20). In each tooth, U concentration varied somewhat, but we believe that this is more a consequence of challenges in accurately weighing very small masses (i.e., individual dentine samples weighed, on average, 2 mg.). In contrast, the ^{230}Th age profiles through the respective teeth are remarkably consistent resulting in 'plateau' age profiles in each dated specimen. Thus, we find no evidence of post-burial / post-fossilisation loss of U from the teeth, strongly indicating that the teeth have provided reliable minimum ^{230}Th ages (Table C20). In fact, it appears that the teeth, although open systems for U, may have acted as closed-systems following recrystallisation of the phosphates.

The minimum ^{230}Th ages of the four micro-profiled teeth of *Pallimnarchus* sp. (QMF59869), *D. optatum* (QMF54689), *Sedophascolomys* sp. cf. *S. medius* (QMF57069), and *Phascolonus gigas* (QMF57065) are ca. 20 ka, 15 ka, 23 ka, and 23 ka, respectively (Table C20).

Table C 20 U-series results for micro-profiled teeth and measured in the Radiogenic Isotope Facility at The University of Queensland.

Taxon QMF	Sample name	U (ppm)	^{232}Th (ppb)	(^{230}Th/ ^{232}Th)	(^{230}Th/^{238}U)	(^{234}U/ ^{238}U)	Uncorr. Age (ka)	corr. Age (ka)	corr. Initial (^{234}U/ ^{238}U)
Pallimnarchus sp. QMF59869	SW-1A	166.12 ± 0.11	20.1 ± 0.2	5958	0.238 ± 0.001	1.425 ± 0.001	19.8 ± 0.1	19.8 ± 0.1	1.449 ± 0.001
	SW-1B	70.46± 0.03	2.9 ± 0.1	15347	0.210 ± 0.002	1.389 ± 0.002	17.8 ± 0.1	17.8 ± 0.1	1.409 ± 0.002
	SW-1C	147.54 ± 0.09	19.5 ± 0.2	5740	0.250 ± 0.001	1.420 ± 0.001	21.0 ± 0.1	21.0 ± 0.1	1.446 ± 0.001
	SW-1D	131.81 ± 0.08	11.8 ± 0.1	7949	0.234 ± 0.001	1.419 ± 0.001	19.5 ± 0.1	19.5 ± 0.1	1.443 ± 0.001
	SW-1E	79.12 ± 0.04	17.7 ± 0.1	3382	0.249 ± 0.001	1.418 ± 0.001	20.9 ± 0.1	20.9 ± 0.1	1.443 ± 0.002
Diprotodon optatum QMF54689	SW9-31-A	131.56 ± 0.07	25.9 ± 0.3	3284	0.213 ± 0.001	1.462 ± 0.001	17.1 ± 0.1	17.1 ± 0.1	1.485 ± 0.001
	SW9-31-B	104.55 ± 0.04	69.3 ± 0.2	1030	0.225 ± 0.001	1.467 ± 0.001	18.0 ± 0.1	18.0 ± 0.1	1.491 ± 0.001
	SW9-31-C	112.57 ± 0.07	22.5 ± 0.2	3070	0.202 ± 0.001	1.464 ± 0.001	16.1 ± 0.1	16.1 ± 0.1	1.486 ± 0.001
	SW9-31-D	100.68 ± 0.05	23.2 ± 0.2	2586	0.196 ± 0.001	1.463 ± 0.001	15.6 ± 0.1	15.6 ± 0.1	1.484 ± 0.001
	SW9-31-E	121.38 ± 0.06	17.5 ± 0.2	4016	0.190 ± 0.001	1.460 ± 0.001	15.1 ± 0.1	15.1 ± 0.1	1.480 ± 0.001
	SW9-31-F	117.47 ± 0.07	8.7 ± 0.2	7931	0.194 ± 0.001	1.459 ± 0.002	15.5 ± 0.1	15.5 ± 0.1	1.480 ± 0.002
	SW9-31-G	118.24 ± 0.06	19.7 ± 0.3	3612	0.199 ± 0.001	1.459 ± 0.001	15.9 ± 0.1	15.9 ± 0.1	1.480 ± 0.001
	SW9-31-H	105.92 ± 0.07	41.4 ± 0.3	1562	0.201 ± 0.001	1.460 ± 0.001	16.1 ± 0.1	16.1 ± 0.1	1.481 ± 0.001
	SW9-31-I	96.44 ± 0.04	15.8 ± 0.2	3724	0.202 ± 0.002	1.460 ± 0.001	16.1 ± 0.1	16.1 ± 0.1	1.481 ± 0.001
	SW9-31-J	107.46 ± 0.07	4.4 ± 0.1	14853	0.201 ± 0.001	1.461 ± 0.001	16.1 ± 0.1	16.1 ± 0.1	1.483 ± 0.001
Sedophascolomys sp. cf. *S. medius* QMF57069	SW9-66-A	149.80 ± 0.08	35.4 ± 0.2	3598	0.281 ± 0.001	1.457 ± 0.001	23.1 ± 0.1	23.1 ± 0.1	1.488 ± 0.002
	SW9-66-B	185.13 ± 0.10	9.8 ± 0.4	15816	0.276 ± 0.001	1.453 ± 0.002	22.7 ± 0.1	22.7 ± 0.1	1.484 ± 0.002
	SW9-66-C	195.43 ± 0.10	10.8 ± 0.3	15384	0.280 ± 0.001	1.455 ± 0.002	23.1 ± 0.1	23.1 ± 0.1	1.486 ± 0.002
	SW9-66-D	182.95 ± 0.07	81.2 ± 0.8	1886	0.276 ± 0.002	1.464 ± 0.002	22.6 ± 0.1	22.6 ± 0.1	1.494 ± 0.002
	SW9-66-E	182.05 ± 0.09	457.8 ± 1.8	331	0.274 ± 0.001	1.468 ± 0.001	22.3 ± 0.1	22.3 ± 0.1	1.498 ± 0.001
Phascolonus gigas QMF57065	SW9-13-A	197.25 ± 0.08	929.3 ± 232.0	183	0.284 ± 0.001	1.449 ± 0.001	23.6 ± 0.1	23.5 ± 0.1	1.481 ± 0.002
	SW9-13-B	174.23 ± 0.08	241.8 ± 8.6	612	0.280 ± 0.001	1.452 ± 0.002	23.1 ± 0.1	23.1 ± 0.1	1.482 ± 0.002
	SW9-13-C	210.60 ± 0.12	269.6 ± 94.6	700	0.296 ± 0.001	1.453 ± 0.001	24.5 ± 0.1	24.5 ± 0.1	1.486 ± 0.001
	SW9-13-D	158.86 ± 0.09	109.6 ± 44.0	1233	0.280 ± 0.001	1.454 ± 0.001	23.1 ± 0.1	23.1 ± 0.1	1.485 ± 0.001

Note: Ratios in parentheses are activity ratios calculated from the atomic ratios, but normalised to measured values of secular-equilibrium HU-1 standard following the method of Ludwig et al. (1992)**.** Errors are at 2σ level. ^{230}Th ages are calculated using Isoplot EX 3.0 (Ludwig, 2003) with decay constants $\lambda_{238} = 1.551 \times 10^{-10}$ yr^{-1} (for ^{238}U), $\lambda_{234} = 2.826 \times 10^{-6}$ yr^{-1}(for ^{234}U) and $\lambda_{230} = 9.158 \times 10^{-6}$ yr^{-1} (for ^{230}Th), respectively (after Cheng et al. (2000)). 2σ errors in the uncorrected (uncorr.) ages were propagated directly from the uncertainties in the (^{230}Th/^{238}U) and (^{234}U/^{238}U). The corrected (corr.) ^{230}Th age was calculated using the assumed bulk Earth or upper crust value equivalent to the detrital ^{230}Th/^{232}Th activity ratio of 0.83.

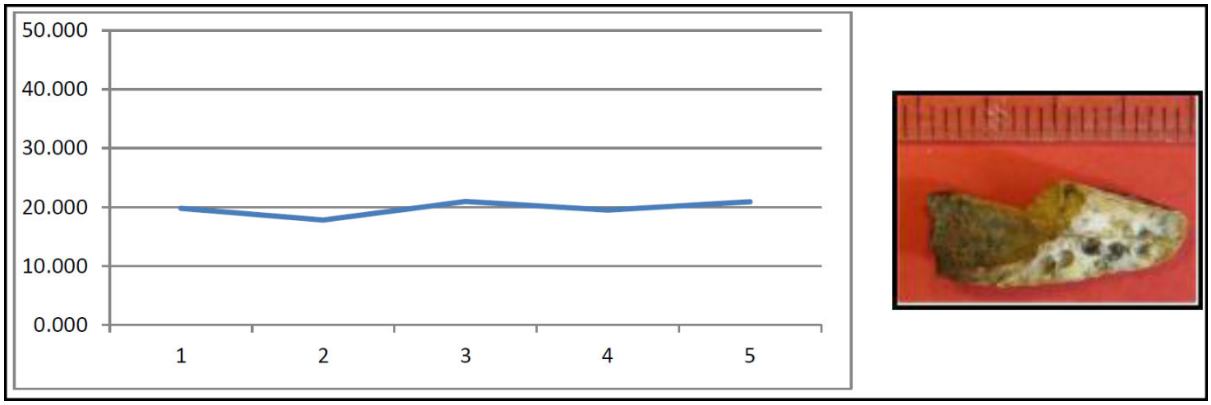

Figure C 26 SW-1A-E *Pallimnarchus* sp. tooth QMF59869, QML1470 (SW9).

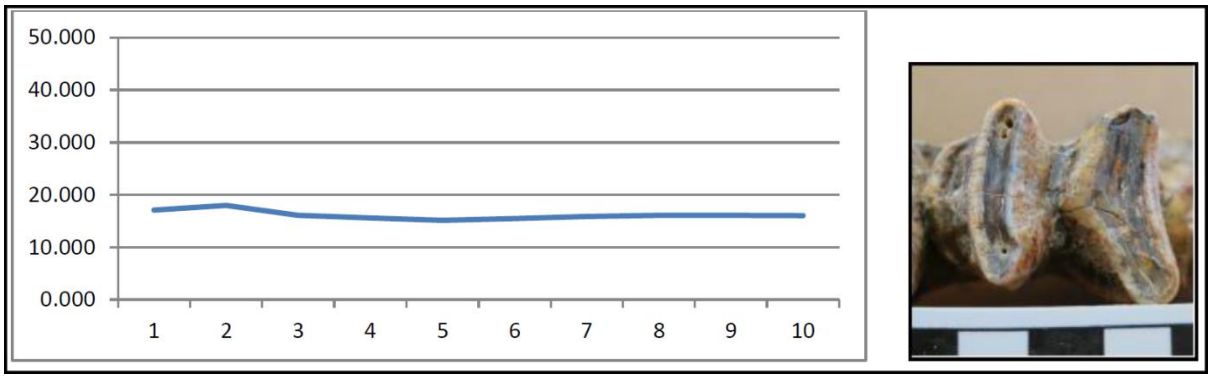

Figure C 27 SW9-31- *Diprotodon optatum* QMF54689 M_4 (associated mandible), QML1470 (SW9).

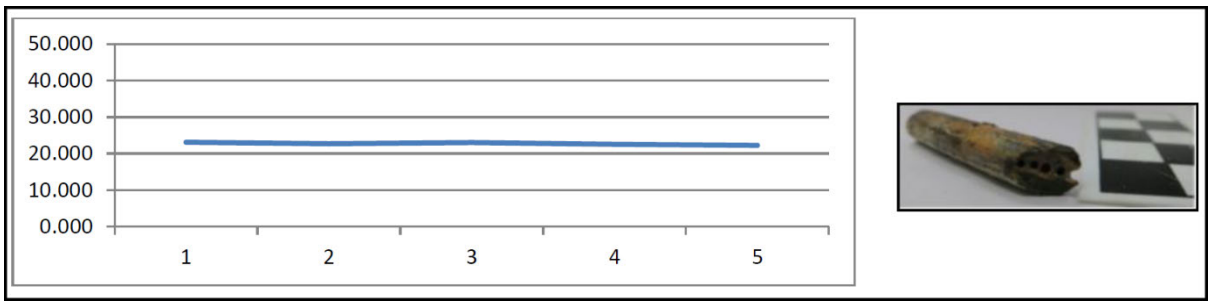

Figure C 28 SW9-66 *Sedophascolomys* sp. cf. *S. medius* (associated incisors) QMF57069, QML1470 (SW9).

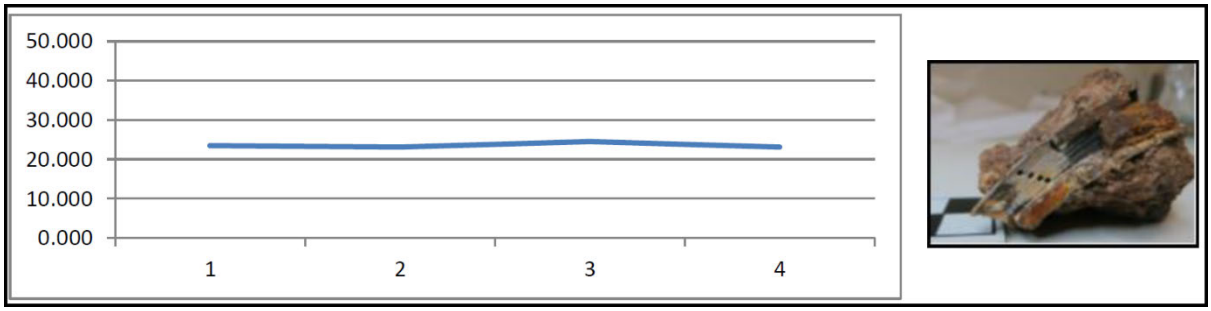

Figure C 29 SW13 – *Phascolonus gigas* molar (associated remains) QMF57065, QML1470 (SW9).

C5.5. U-series laser ablation and ESR direct dating of south Walker Creek megafauna fossils

Renaud Joannes-Boyau & Anthony Dosseto

C5.5.1. Sample description and methods

Samples used for the dating showed signs of some level of diagenetic patterns, with superficial discoloration of the enamel and traces of sediment introduction in the dentine. The sample set consisted of (i) (SW9-MSCUA and SW9-MSCUB) a *Phascolonus gigas* molar tooth fragment removed from a complete molar of associated skeletal remains of individual QMF57065. US-ESR and U-Th dating (UQ) was applied to this specimen. The molar was still embedded in matrix; (ii) (SW9-PSCU01) a complete *Protemnodon* sp. nov? (QMF57035) right P^3 from an associated adult individual with shinny enamel and white dentine; (iii) (SW3-SCU-01) a *Diprotodon optatum* molar tooth fragment from skull (QMF57172) with several discoloration and sediment introductions; and (iv) (SW9-ISCU02) a near complete *Macropus* sp. (large) incisor, slight discoloration of the enamel and sediment introduction into the dentine (QMF57039). (i) The SW9-MSCUA and SW9-MSCUB are two fragments from the same *Phascolonus gigas* molar. The tooth was sectioned in half exposing dentine and parts of enamel. Directly next to the Uranium micro-drilling, a fragment of 8 mm length was cut from the tooth containing both dentine and enamel. Two enamel fragments A and B were extracted from the fossil.

SW9-PSCU-01 was sectioned at one of the extremity of the tooth, and a small piece of enamel including dentine was removed. The fragment was profiled by LA-ICPMS for DAD U-series modelling and a wide fragment directly in contact was removed, divided in two (A&B), and cleaned for ESR experiments. (see detailed protocol below). SW3-SCU-01 was sectioned and preliminary measurements showed that the tooth was not suitable for US-ESR dating. SW9-ISCU-02 was sectioned at the base along the growth axis. A small fragment was removed and analysed DAD U-series modelling, an enamel fragment directly attached was removed and cleaned for ESR experiments (see detailed protocol below). Two enamel fragments (A&B) were extracted for US-ESR dating. Unfortunately, one fragment (A) broke during experiments and could not give an ESR age.

C5.5.2. *In situ* U-series analysis

Open-system uranium-series series dating of the teeth was undertaken by laser ablation multi-collector ICP-MS at the Wollongong Isotope Geochronology Laboratory, University of Wollongong.

Laser ablation was performed with a New Wave Research 193 nm ArF excimer laser, equipped with a TV2 cell. Thorium (^{230}Th, ^{232}Th) and uranium (^{234}U, ^{235}U, ^{238}U) isotopes were measured on a Thermo Neptune Plus multi-collector ICP-MS mounted with jet sample and x-skimmer cones. All five isotopes were collected in static mode, with ^{230}Th and ^{234}U collected in ion counters. Helium flow rate and ICP-MS parameters were tuned with NIST612 element standard to derive a ^{232}Th/^{238}U ratio for this standard greater than 0.8 and thus minimise differences in fractionation between Th and U (Bernal et al., 2005). For tuning, a fluence of 2.3 J/cm^2, pulse rate of 20 Hz, spot size of 100 μm and scan speed of 5 μm/s was used. This yielded 0.35 V of ^{238}U and 0.32 V of ^{232}Th. Uranium-238 tail on ^{234}U, and ^{232}Th tail on ^{230}Th (although negligible for phosphates and carbonates) were measured using a coral and glass standard NIST612, respectively. A fluence of 0.9 J/cm^2, pulse rate of 10 Hz, spot size of 150 μm and scan speed of 5 μm/s was used. The cut teeth were ablated using rasters instead of

spots. Trials performed on a MIS5 coral (unpublished. data) show that while calculated ages were within error of each other between raster and spot analyses, counting statistics was better using raster analyses (because ablation duration was ~120 sec, versus 60 sec for spot analysis). Each raster was ~620 μm long. A fluence of 0.9 J/cm^2, pulse rate of 10 Hz, spot size of 150 μm and scan speed of 5 μm/s was used. A trial was done using spot analyses instead (same pulse rate, fluence and spot size; ablation duration = 60 sec). A longer ablation duration for spot analysis is not recommended since in this case downhole fractionation becomes significant. Helium was used as a carrier gas at a flow rate of 0.9 L/min. Before and after each sample, three rasters were done on NIST612, MK10 (a MIS7 coral used as primary standard; Woodroffe et al., 1991); and MK16 (a MIS5 coral used as secondary standard; Woodroffe et al., 1991). Measured $^{234}U/^{238}U$ and $^{230}Th/^{238}U$ isotopic ratios were corrected for elemental fractionation and Faraday cup/SEM yield by comparison with MK10 coral (see above) for which ratios were previously characterised internally by solution analysis. Concentrations of U and Th were determined using NIST612 glass as calibration standard. Background subtraction, concentration quantification and ratio corrections were performed using Iolite™ software. The corrected ($^{234}U/^{238}U$) and ($^{230}Th/^{238}U$) isotope ratios for the secondary standard (MK16 coral; 1.106 ± 0.003 and 0.759 ± 0.06, respectively; 2σ, n = 15) were within error of the values determined by solution analysis (1.110 ± 0.002 and 0.764± 0.007). The calculated closed-system ^{230}Th-U age for MK16 was 123 ± 2 ka (2σ, n=15), within error of the value determined by solution analysis (124 ± 2 ka).

C5.5.3. Modelling of open-system U-series age

In-situ U-series analyses were used to calculate an open-system age for each tooth. On QML1470 incisor I-SCU-02, 10 rasters were produced, parallel to the surface (Figure C29). On QML1470 SW9-2015 P-SCU01, 20 rasters were produced, parallel to the surface (Figure C30). The Diffusion-Adsorption-Decay model of Sambridge et al. (2012), was used to derive an open-system U-series age from each transect of analyses. This was undertaken using UThwigl R package (Dosseto & Marwick, 2019) which is available upon request from A.D. The uranium diffusion coefficient was allowed to take values between 10^{-11} and 10^{-14} cm^2/s.

C5.5.4. U-series for ESR model

For the dentine directly in contact with the enamel fragments used for ESR dating, several rasters were measured and averaged to obtain the U-series values. For the ESR fragments SW9-ISCU-02B, SW9-PSCU-01A and SW9-PSCU-01B the concentration was obtained using LA-ICPMS quadrupole Agilent 7700 (large cell 20 Hz, ablation raster of 100 μm spot size, 1 min ablation length, 5 μm ablation depth, translation speed 20 μm/s, NIST 612 correction for drift and tooth standard with known concentration for matrix effect), while the remaining enamel attached to the dentine was used to obtained the U-series values. All age calculations were carried out with the USESR program (Shao et al., 2014), which utilizes the dose rate conversion factors (Guérin et al., 2011).

C5.5.5. ESR protocol

ESR dating was performed on a Freiberg MS5000 X-band at 1G modulation amplitude, 2 mW power, 100G sweep, 100 KHz modulation frequency. X-ray irradiation was performed at SCU on a Freiberg Xray irradiation chamber which contains a Varian VF50, with irradiation parameters: 40 kV voltage and 0.5 mA current with dose rate calibrating depending on the output value of the X-ray gun. Each ESR fragment was irradiated with an incremental dose step at 90 s, 380 s, 900 s, 1800 s, 3600 s, 7200

s, 14400 s, with an average dose rate of 0.25 Gy/s. For each irradiation step, the energy output of the X-ray gun is recorded at the beginning and end and averaged, which allows us to correct for the dose rate received by the sample. For each irradiation step the fragment was measured over 180° in x, y and z-configurations with a 20° step (Joannes-Boyau, 2013; Joannes-Boyau & Grün, 2011). ESR intensities were extracted from T1-B2 peak-to-peak amplitudes on the merged ESR signal. Isotropic and baseline corrections were applied uniformly across the measured spectra (Joannes-Boyau & Grün, 2009). The amount of NOCORs was estimated using the protocol described by Joannes-Boyau (2013). The sample was mounted onto a Teflon sample holder, which expose directly the fragment to the x-ray source with no shielding (apart from a 200-micron aluminium foil). Dose response curve (DRC) and equivalent dose (D_e) were calculated using the MCDoseE 2.0 program (Joannes-Boyau et al., 2018). The program uses a Bayesian framework, where the solution is a full probability distribution on the dose equivalent (for more information see Joannes-Boyau et al. (2018) and Metropolis et al. (1953)). DRC was estimated using SSE the maximum irradiation dose (Dmax) adjusted to meet the criteria defined (Duval & Grün, 2016) (Figure C32). The external dose was calculated using the values obtained by the gamma spectrometer measurement in the field. The U, Th and K concentration in the sediment surrounding the tooth was obtain from *in situ* measurements. Cosmic dose rate was estimated from Prescott & Hutton (1994).

C5.5.6. Open-system U-series ages

For QML1470 incisor I-SCU-02 (Figure C29), the calculated age is 25.5 ± 0.1 ka. The calculated initial ($^{234}U/^{238}U$) ratio at x = -1 is 1.46 and the diffusion coefficient is 9.09 x 10^{-12} cm^2/s. For QML1470 SW9-2015 P-SCU01 (Figure C30), only the 11 rasters in the dentine were used, considering the very low U concentrations in the enamel. The calculated age is 22.6 +0.6/-0.5 ka. The calculated initial ($^{234}U/^{238}U$) ratio at x = -1 is 1.40 and the diffusion coefficient is 5.98 x 10^{-12} cm^2/s.

Table C 21 Uranium-series isotope data for the teeth and the coral standard (MK16) produced at University of Wollongong. Errors shown at 2σ.

Raster ID	Position relative to the centre	Th (ppm)	U (ppm)	(^{234}U / ^{238}U)	(^{230}Th / ^{238}U)	(^{232}Th / ^{238}U)
I_SLU_02_0	-0.49	0.0172 ± 0.0048	351 ± 5.1	1.4641 ± 0.0015	0.2928 ± 0.0018	1.79E-05 ± 5.2E-06
I_SLU_02_1	-0.34	0.011 ± 0.0047	245.9 ± 6.4	1.4675 ± 0.0021	0.294 ± 0.0023	1.42E-05 ± 0.000006
I_SLU_02_2	-0.18	0.0092 ± 0.0039	239 ± 6.5	1.4656 ± 0.0015	0.3004 ± 0.0026	1.26E-05 ± 5.5E-06
I_SLU_02_3	-0.03	0.0139 ± 0.0099	240.3 ± 3.7	1.4671 ± 0.0019	0.3026 ± 0.0022	0.000019 ± 0.000014
I_SLU_02_4	0.12	0.0184 ± 0.009	241.7 ± 6.7	1.4633 ± 0.0017	0.3053 ± 0.0019	0.000027 ± 0.000014
I_SLU_02_5	0.28	0.035 ± 0.03	239.4 ± 5.3	1.4623 ± 0.0018	0.3053 ± 0.0022	0.000052 ± 0.000049
I_SLU_02_6	0.43	0.005 ± 0.0017	250.4 ± 6.5	1.4597 ± 0.0024	0.3094 ± 0.0024	6.5E-06 ± 2.2E-06
I_SLU_02_7	0.58	0.00095 ± 0.00027	264.2 ± 3.2	1.4577 ± 0.0025	0.3151 ± 0.0022	1.18E-06 ± 3.3E-07
I_SLU_02_8	0.74	0.00084 ± 0.00021	262.9 ± 2.7	1.4571 ± 0.0023	0.3154 ± 0.002	1.04E-06 ± 2.5E-07
I_SLU_02_9	0.89	0.00113 ± 0.00054	231 ± 5.2	1.4578 ± 0.0023	0.3169 ± 0.0024	1.65E-06 ± 8.4E-07
P_SLU_01_0		*0.0009 ± 0.0013*	*0.33 ± 0.25*	*1.343 ± 0.064*	*0.49 ± 0.17*	*0.00025 ± 0.00094*
P_SLU_01_1		*0.0002 ± 0.00027*	*0.25 ± 0.14*	*1.45 ± 0.1*	*0.5 ± 0.24*	*0.00015 ± 0.00077*
P_SLU_01_2		*0.002 ± 0.0034*	*0.199 ± 0.046*	*2.5 ± 1.1*	*3.7 ± 3.2*	*0.0007 ± 0.0011*
P_SLU_01_3		*Below LOD*	*0.313 ± 0.044*	*1.424 ± 0.062*	*0.256 ± 0.052*	*-0.00003 ± 0.00019*
P_SLU_01_4		*Below LOD*	*3.19 ± 0.62*	*1.389 ± 0.02*	*0.21 ± 0.014*	*-1.5E-05 ± 0.00002*
P_SLU_01_5		*0.00037 ± 0.00077*	*4.63 ± 0.56*	*1.392 ± 0.01*	*0.2255 ± 0.0074*	*0.000049 ± 0.000097*
P_SLU_01_6		*0.00006 ± 0.00013*	*3.54 ± 0.27*	*1.411 ± 0.019*	*0.262 ± 0.015*	*0.000004 ± 0.000013*
P_SLU_01_7		*0.00033 ± 0.0005*	*4.14 ± 0.12*	*1.41 ± 0.014*	*0.252 ± 0.01*	*0.000025 ± 0.00004*
P_SLU_01_8		*0.00009 ± 0.00014*	*189.6 ± 8.3*	*1.3995 ± 0.0022*	*0.2365 ± 0.002*	*1.7E-07 ± 2.4E-07*
P_SLU_01_9	-0.91	0.00016 ± 0.00015	258.3 ± 9.3	1.4021 ± 0.0019	0.2671 ± 0.0023	1.8E-07 ± 1.9E-07
P_SLU_01_10	-0.73	0.0002 ± 0.00022	253.1 ± 9.8	1.4006 ± 0.0024	0.2605 ± 0.002	2.5E-07 ± 2.7E-07
P_SLU_01_11	-0.55	0.00027 ± 0.00029	252 ± 13	1.3992 ± 0.0026	0.2522 ± 0.0026	3.2E-07 ± 4.1E-07
P_SLU_01_12	-0.37	0.00004 ± 0.00022	180 ± 34	1.4003 ± 0.0044	0.255 ± 0.003	-2E-07 ± 5.7E-07
P_SLU_01_13	-0.19	Below LOD	109 ± 35	1.4051 ± 0.0054	0.274 ± 0.0063	-2E-06 ± 1.5E-06
P_SLU_01_14	-0.01	Below LOD	58 ± 21	1.411 ± 0.0079	0.283 ± 0.02	-3.7E-06 ± 2.5E-06
MK16 (n = 15)		0.00021 ± 0.00006	3.3 ± 0.1	1.106 ± 0.003	0.759 ± 0.006	2.3E-05 ± 7E-06

Activity ratios are corrected values, using a MIS7 coral as standard (for which isotopic ratios were characterised by solution analysis). Parentheses denote activity ratios. Italicised rows are data not used for open-system model age calculation, because of large errors on either activity ratio. Position relative to the centre = -1 or 1 for either surface of the sample, 0 for the centre of the transect.

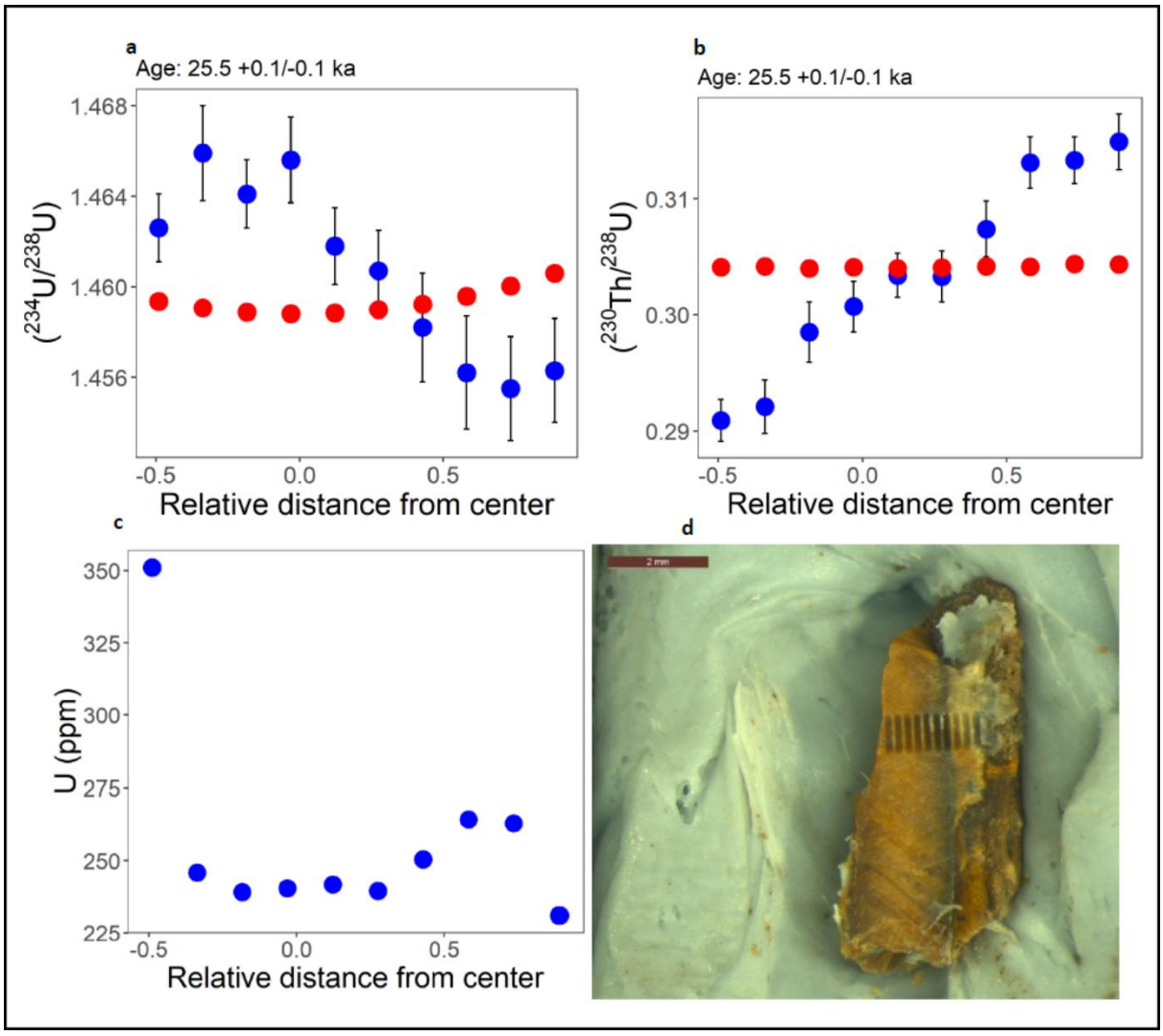

Figure C 30 Measured (a) ($^{234}U/^{238}U$) and (b) ($^{230}Th/^{238}U$) activity ratios (blue dots) and modelled ratios (red dots) for QML1470 incisor I-SCU-02. (c) Measured uranium concentrations. The x-axis represents dimensionless positions, where x=-1 and 1 are surfaces on either side of the sample. Decreasing the diffusion coefficient would result in a higher curvature in the modelled compositions, however it does not significantly affect the calculated age. (d) Picture of the sample (QMF57039) after ablation.

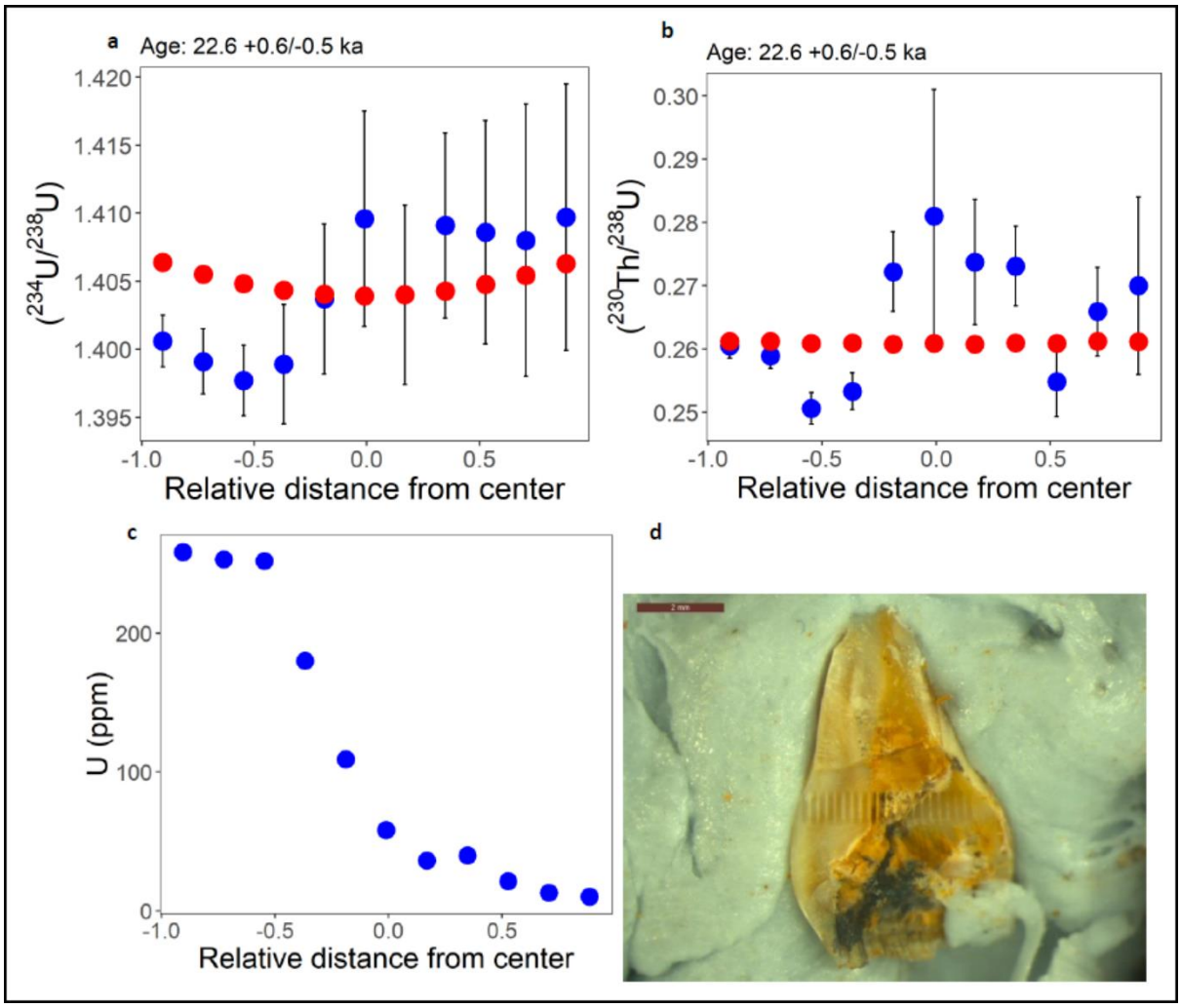

Figure C 31 Measured (a) ($^{234}U/^{238}U$) and (b) ($^{230}Th/^{238}U$) activity ratios (blue dots) and modelled ratios (red dots) for QML1470 SW9-2015 P-SCU01 dentine. (c) Measured uranium concentrations. The x-axis represents dimensionless positions, where x=-1 is the boundary between the enamel and the dentine, and x=1 is the base of the dentine. (d) Picture of the sample (QMF57035) after ablation. Note the nine tracks on the left (in the enamel) were not used for open-system age modelling as the errors on activity ratios were too large.

C5.5.7. US-ESR age modelling

The detailed calculation, values and aliquots ages of South Walker Creek fossil teeth for SW9-MSCU, SW9-PSCU-01 and SW9-ISCU-02 are summarized in Table C22, with ages of 35 ± 11 ka, 41 ± 11 ka and 30 ± 7 ka respectively. Two teeth were dated using two aliquots. SW9-MSCU A and B and PSCU A and B yield ages consistent with each other and statistically indistinguishable from each other respectively. Unexpectedly, the large concentration of uranium within the enamel of MSCU A and B does not seem to be detrimental to the age calculation. Perhaps, the destruction of radical by alpha particles has not been sufficient to impact the DRC yet. It has to be noted that the DRC of SW9-PSCU-01B presented outsider points that influenced the accuracy of the fitting, hence the large error on the equivalent dose. The minor offset in age between the SW9-PSCU-01B and SW9-PSCU-01A replicates could be attributed to the potential U-series differences within each enamel fragment, for

which the values were not measured. However, the replicate results remain within error of each other, and are therefore both considered in the final age evaluation of SW9.

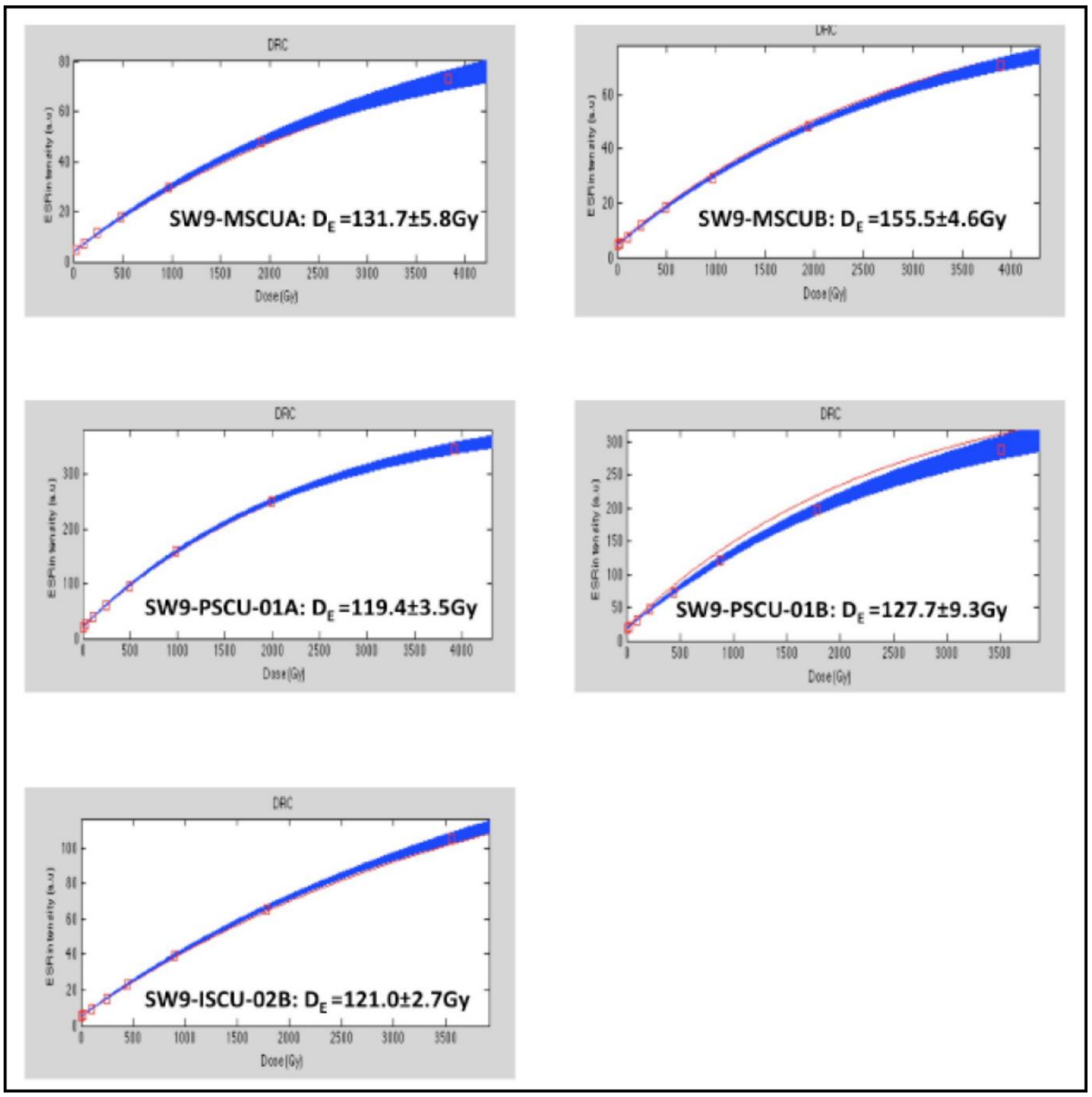

Figure C 32 Dose Response curve (DRC) were calculated using MCDoseE 2.0, with 250k iterations and Burning of 125k and a Double Saturated Exponential (DSE) function (Joannes-Boyau et al., 2018). D_E values are express at 2-sigma error. D_E were used to calculate the US-ESR age reported in Table C22.

Table C 22 US-ESR dating data for SW9 teeth.

Sample SW9	MSCU-1(A)	MSCU-1(B)	PSCU-01A	PSCU-01B	ISCU-02B
			Enamel		
Dose (Gy) [a]	131.7 ± 5.8	155.5 ± 4.6	119.4 ± 3.5	127.7 ± 9.3	121.0 ± 2.7
U (ppm)	10.65 ± 0.94	17.2 ± 1.3	6.78 ± 0.38		7.01 ± 0.8
^{234}U / ^{238}U	1.4150 ± 0.028	1.4035 ± 0.074	1.3990 ± 0.0160		1.4550 ± 0.0223
^{230}Th / ^{234}U	0.1910 ± 0.031	0.1904 ± 0.046	0.1680 ± 0.0181		0.1981 ± 0.077
Thickness (m)	862 ± 172	805 ± 161	743 ± 149	758 ± 152	881 ± 106
Water (%)			3 ± 1		
			Dentine		
U (ppm) [b]	187.8 ± 5.1	207.5 ± 5.4	220.8 ± 14.5		250.4 ± 5
^{234}U / ^{238}U	1.4831 ± 0.060		1.3988 ± 0.0027		1.4607 ± 0.0021
^{230}Th / ^{234}U	0.1890 ± 0.0149		0.1806 ± 0.0096		0.2080 ± 0.0136
Water (%)			5 ± 3		
			Sediment		
U (ppm)			2.01 ± 0.12		
Th (ppm)			10.03 ± 0.48		
K (%)			1.30 ± 0.06		
Water (%)			22 ± 4		
			External dose rate sediment		
Beta Dose (μGy a^{-1})	162 ± 26	173 ± 27	186 ± 28	182 ± 27	158 ± 17
G&C Dose (μGy a^{-1})			983 ± 79		
			Combine US-ESR age		
Internal dose rate (μGy a^{-1})	1220 ± 548	2225 ± 891	637 ± 285	568 ± 301	1007 ± 444
Beta Dose rate dentine (μGy a^{-1})	1104 ± 498	1478 ± 592	1336 ± 598	1169 ± 619	1885 ± 830
P enamel	-0.39 ± 0 32	-0.62 ± 0.28	-0.15 ± 0.37	0.13 ± 0.46	-0.76 ± 0.27
P dentine	-0.37 ± 0 32	-0.61 ± 0.28	-0.29 ± 0.34	-0.03 ± 0.43	-0.82 ± 0.25
Total Dose rate (μGy a^{-1})	3466 ± 745	4859 ± 1073	3142 ± 668	2902 ± 693	4033 ± 945
Age (ka)	**38 ± 8**	**32 ± 7**	**38 ± 8**	**44 ± 10**	**30 ± 7**

[a] Dose equivalent (D_e) obtained using McDoseE 2.0, with DSE (Joannes-Boyau et al., 2018).

C6. Palynological assessment of QML1470 (SW9)

Patrick Moss

Relatively low pollen yields (96 grains and spores) were recovered from the QML1470 (SW9) sub-samples, which have been combined into a single pollen and charcoal record (Figure C32 and Table C23). This may reflect an environment that underwent a high level of oxidation, as pollen preservation requires an anaerobic environment and may reflect climate variability, i.e. increased aridity at the time of deposition (Moss, 2013). However, enough pollen is preserved to suggest that the regional environment was mainly a sclerophyll forest dominated by eucalypts and she oak (Casuarinaceae) canopy with a heath understorey. The streams would have been fringed by paperbark (*Melaleuca*) trees/shrubs and this landscape is typical of the region during Marine Isotope Stage 3 based on existing records from southeast Queensland (Moss et al., 2013) and northeast Queensland (Moss et al., 2017). Fire was also an environmental component of the site based on the presence of charcoal particles in the sediment and *Sporormiella* was also found suggesting the presence of herbivourous grazers (Rule et al., 2012).

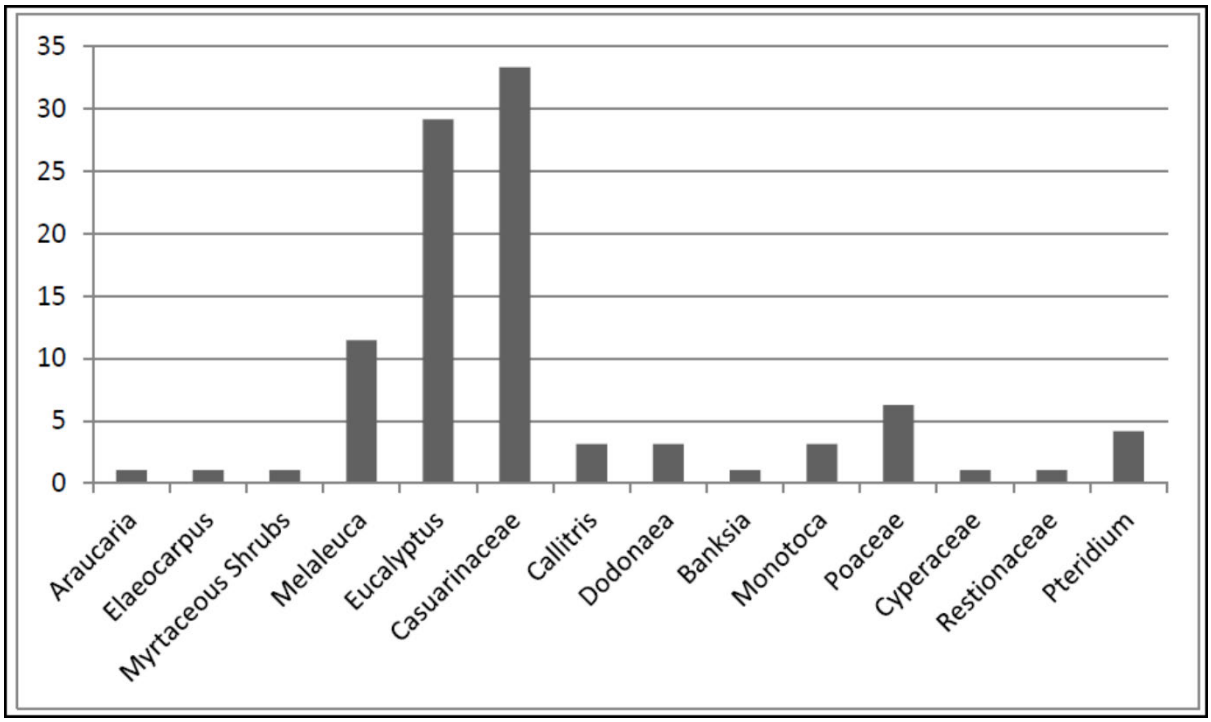

Figure C 33 Identified pollen counts from QML1470 (SW9).

Table C 23 Pollen, habitat interpretation, *Sporomiella* (dung fungus) and Charcoal counts for ten subsamples (SW1-SW10) from QML1470 (SW9).

	Habitat	**SW 1**	**SW 2**	**SW 3**	**SW 4**	**SW 5**	**SW 6**	**SW 7**	**SW 8**	**SW 9**	**SW 10**	**Total**
Araucaria	Emergent Rainforest	0	0	1	0	0	0	0	0	0	0	1
Elaeocarpus	Canopy Rainforest	1	0	0	0	0	0	0	0	0	0	1
Myrtaceous Shrubs	Sclerophyll and Heath	0	0	1	0	0	0	0	0	0	0	1
Melaleuca	Wetland Canopy	0	0	1	0	4	4	0	1	0	1	11
Eucalyptus	Sclerophyll canopy	7	0	6	3	1	9	0	1	0	1	28
Casuarinaceae	Sclerophyll canopy	7	0	9	2	4	7	3	0	0	0	32
Callitris	Sclerophyll canopy	1	0	0	0	1	0	1	0	0	0	3
Dodonaea	Sclerophyll shrub (hopbush)	0	0	1	0	1	1	0	0	0	0	3
Banksia	Heath and Sclerophyll shrubs	0	0	0	0	0	0	1	0	0	0	1
Monotoca	Heath Shrub	1	0	2	0	0	0	0	0	0	0	3
Poaceae	Dryland and Aquatic Herb (grass)	3	0	2	0	0	0	0	0	0	1	6
Cyperaceae	Aquatic Herb (sedge)	0	0	0	0	0	1	0	0	0	0	1
Restionaceae	Aquatic Herb (rush)	0	0	0	0	0	1	0	0	0	0	1
Pteridium	Bracken	2	1	0	1	0	0	0	0	0	0	4
Total		22	1	23	6	11	23	5	2	0	3	96
Sporormiella concentration (grains / cm^3)		28.8	0	3.6	38.4	12.2	40.3	79.6	46.1	51.2	59.8	
Charcoal concentration (particles per cm^3)		4971	0	355	3585	5136	1428	7526	6514	695	515	

C7. References

Aitken, M. J. 1985. Thermoluminescence dating: Past progress and future trends. Nuclear Tracks and Radiation Measurements (1982), 10, 3-6. .

Aitken, M. J. 1998. Introduction to optical dating: the dating of Quaternary sediments by the use of photon-stimulated luminescence, Oxford, Oxford University Press.

Arnold, L. J., Bailey, R. M. & Tucker, G. E. 2007. Statistical treatment of fluvial dose distributions from southern Colorado arroyo deposits. Quaternary Geochronology, 2, 162-167.

Arnold, L. J., Demuro, M., Navazo, M., Benito-Calvo, A. & Pérez-González, A. 2013. OSL dating of the Middle Palaeolithic Hotel California site, Sierra de Atapuerca, north-central Spain. Boreas, 42, 285-305.

Arnold, L. J., Demuro, M., Pares, J. M., Arsuaga, J. L., Aranburu, A., De Castro, J. M. B. & Carbonell, E. 2014. Luminescence dating and palaeomagnetic age constraint on hominins from Sima de los Huesos, Atapuerca, Spain. Journal of human evolution, 67, 85-107.

Arnold, L. J., Duval, M., Demuro, M., Spooner, N. A., Santonja, M. & Pérez-González, A. 2016. OSL dating of individual quartz 'supergrains' from the Ancient Middle Palaeolithic site of Cuesta de la Bajada, Spain. Quaternary Geochronology, 36, 78-101.

Arnold, L. J., Duval, M., Falguères, C., Bahain, J.-J. & Demuro, M. 2012. Portable gamma spectrometry with cerium-doped lanthanum bromide scintillators: Suitability assessments for luminescence and electron spin resonance dating applications. Radiation Measurements, 47, 6-18.

Arnold, L. J. & Roberts, R. G. 2009. Stochastic modelling of multi-grain equivalent dose (De) distributions: Implications for OSL dating of sediment mixtures. Quaternary Geochronology, 4, 204-230.

Arnold, L. J., Roberts, R. G., Galbraith, R. F. & Delong, S. B. 2009. A revised burial dose estimation procedure for optical dating of young and modern-age sediments. Quaternary Geochronology, 4, 306-325.

Arnold, L. J., Roberts, R. G., Macphee, R. D. E., Willerslev, E., Tikhonov, A. N. & Brock, F. 2008. Optical dating of perennially frozen deposits associated with preserved ancient plant and animal DNA in north-central Siberia. Quaternary Geochronology, 3, 114-136.

Bailey, R. M. & Arnold, L. J. 2006. Statistical modelling of single grain quartz De distributions and an assessment of procedures for estimating burial dose. Quaternary Science Reviews, 25, 2475-2502.

Banks, M. R., Colhoun, E. A. & Van De Geer, G. 1976. Late Quaternary Palorchestes azael (Mammalia, Diprotodontidae) from northwestern Tasmania. Alcheringa, 1, 159-166.

Bartholomai, A. 1966. The type specimens of some of de Vis' species of fossil Macropodidae. Memoirs of the Queensland Museum, 14, 115-126.

Bartholomai, A. 1973a. Fissuridon pearsoni, a new fossil macropodid (Marsupialia) from Queensland. Memoirs of the Queensland Museum, 16, 365-368.

Bartholomai, A. 1973b. The genus Protemnodon Owen (Marsupialia: Macropodidae) in the upper Cainozoic deposits of Queensland. Memoirs of the Queensland Museum, 16, 309-363.

Bartholomai, A. 1975. The genus Macropus Shaw (Marsupialia: Macropodidae) in the Upper Cainozoic deposits of Queensland.

Bartholomai, A. 1978a. The Macropodidae (Marsupialia) from the Allingham formation, northern Queensland. Results of the Ray E. Lemley Expeditions, part II.

Bartholomai, A. 1978b. The rostrum in Palorchestes Owen (Marsupialia: Diprotodontidae). Results of the Ray E. Lemley Expeditions, part 3.

Bernal, J.-P., Eggins, S. M. & Mcculloch, M. T. 2005. Accurate in situ 238 U–234 U–232 Th–230 Th analysis of silicate glasses and iron oxides by laser-ablation MC-ICP-MS. Journal of Analytical Atomic Spectrometry, 20, 1240-1249.

Bird, M. I., Ayliffe, L., Fifield, L., Turney, C. S., Cresswell, R., Barrows, T. & David, B. 1999. Radiocarbon dating of "old" charcoal using a wet oxidation, stepped-combustion procedure. Radiocarbon, 41, 127-140.

Black, K. 1997. A new species of Palorchestidae (Marsupialia) from the late middle to early late Miocene Encore Local Fauna, Riversleigh, northwestern Queensland. Memoirs-Queensland Museum, 41, 181-186.

Blong, R. & Gillespie, R. 1978. Fluvially transported charcoal gives erroneous 14 C ages for recent deposits. Nature, 271, 739-741.
Bøtter-Jensen, L., Bulur, E., Duller, G. & Murray, A. 2000. Advances in luminescence instrument systems. Radiation Measurements, 32, 523-528.
Bøtter-Jensen, L. & Mejdahl, V. 1988. Assessment of beta dose-rate using a GM multicounter system. International Journal of Radiation Applications and Instrumentation. Part D. Nuclear Tracks and Radiation Measurements, 14, 187-191.
Bowler, J. M., Johnston, H., Olley, J. M., Prescott, J. R., Roberts, R. G., Shawcross, W. & Spooner, N. A. 2003. New ages for human occupation and climatic change at Lake Mungo, Australia. Nature, 421, 837-840.
Brennan, B. J. 2003. Beta doses to spherical grains. Radiation Measurements, 37, 299-303.
Brock, F., Wood, R., Higham, T. F., Ditchfield, P., Bayliss, A. & Ramsey, C. B. 2012. Reliability of nitrogen content (% N) and carbon: nitrogen atomic ratios (C: N) as indicators of collagen preservation suitable for radiocarbon dating. Radiocarbon, 54, 879-886.
Bronk Ramsey, C. 2009. Bayesian Analysis of Radiocarbon Dates. Radiocarbon, 51, 337-360.
Celik, M., Cascini, M., Haouchar, D., Van Der Burg, C., Dodt, W., Evans, A. R., Prentis, P., Bunce, M., Fruciano, C. & Phillips, M. J. 2019. A molecular and morphometric assessment of the systematics of the Macropus complex clarifies the tempo and mode of kangaroo evolution. Zoological Journal of the Linnean Society, 186, 793-812.
Cheng, H., Edwards, R. L., Hoff, J., Gallup, C. D., Richards, D. & Asmerom, Y. 2000. The half-lives of uranium-234 and thorium-230. Chemical Geology, 169, 17-33.
Chiotakis, C. 2018. Pliocene crocodilians of Chinchilla: identification using dental morphometrics. Queensland University of Technology.
Croke, J., Jansen, J. D., Amos, K. & Pietsch, T. J. 2011. A 100 ka record of fluvial activity in the Fitzroy River Basin, tropical northeastern Australia. Quaternary Science Reviews, 30, 1681-1695.
Cuvier, F. 1807. Sur les diffèrentes espèces de Crocodiles vivans et Sur leurs caractères distinctiss.
Davis, A. & Archer, M. 1997. Palorchestes azael (Mammalia, Palorchestidae) from the late Pleistocene Terrace Site Local Fauna, Riversleigh, northwestern Queensland. Memoirs-Queensland Museum, 41, 315-320.
Dawson, L. 1981. The status of the taxa of extinct giant wombats (Vombatidae: Marsupialia), and a consideration of vombatid phylogeny. Australian Mammalogy, 4, 65-79.
Dawson, L. 2004. A new fossil genus of forest wallaby (Marsupialia, Macropodinae) and a review of Protemnodon from eastern Australia and New Guinea. Alcheringa, 28, 275-290.
Dawson, L. & Flannery, T. 1985. Taxonomic and phylogenetic status of living and fossil kangaroos and wallabies of the genus Macropus Shaw (Macropodidae: Marsupialia), with a new subgeneric name for the larger wallabies. Australian Journal of Zoology, 33, 473-498.
De Vis, C. W. A review of the fossil jaws of the Macropodidae in the Queensland Museum. Proceedings of the Linnean Society of New South Wales, 1895. 75-133.
Demuro, M., Arnold, L. J., Aranburu, A., Gomez-Olivencia, A. & Arsuaga, J.-L. 2019. Single-grain OSL dating of the Middle Palaeolithic site of Galería de las Estatuas, Atapuerca (Burgos, Spain). Quaternary Geochronology, 49, 254-261.
Dosseto, A. & Marwick, B. 2019. UThwigl—An R Package for Closed- and Opensystem Uranium-thorium Dating.
Duller, G. 2003. Distinguishing quartz and feldspar in single grain luminescence measurements. Radiation measurements, 37, 161-165.
Duval, M. & Grün, R. 2016. Are published ESR dose assessments on fossil tooth enamel reliable? Quaternary Geochronology, 31, 19-27.
Fallon, S., Fifield, L. K. & Chappell, J. 2010. The next chapter in radiocarbon dating at the Australian National University: status report on the single stage AMS. Nuclear Instruments and Methods in Physics Research Section B: Beam Interactions with Materials and Atoms, 268, 898-901.
Finch, M. & Freedman, L. 1988. Functional-Morphology of the Limbs of Thylacoleo-Carnifex Owen (Thylacoleonidae, Marsupialia). Australian Journal of Zoology, 36, 251-272.
Flannery, T. & Archer, M. 1982. The taxonomy and distribution of Macropus (Fissuridon) pearsoni (Marsupialia: Macropodidae). Australian Mammalogy, 5, 261-265.

Flannery, T. & Archer, M. 1983. Revision of the genus Troposodon Bartholomai (Macropodidae: Marsupialia). Alcheringa, 7, 263-279.
Flannery, T. F. 1980. Macropus mundjabus, a new kangaroo (Marsupialia: Macropodidae) of uncertain age from Victoria, Australia. Australian Mammalogy, 3, 35-51.
Flannery, T. F. 1984. Re-examination of the Quanbun Local Fauna, a late Cenozoic vertebrate fauna from Western Australia. Records of the Western Australian Museum, 11, 119-128.
Flannery, T. F. 1992. New Pleistocene marsupials (Macropodidae, Diprotodontidae) from subalpine habitats in Irian Jaya, Indonesia. Alcheringa, 16, 321-331.
Folk, R. L. 1954. The distinction between grain size and mineral composition in sedimentary-rock nomenclature. The Journal of Geology, 62, 344-359.
Fowler, A. J., Gillespie, R. & Hedges, R. E. 1986. Radiocarbon dating of sediments. Radiocarbon, 28, 441-450.
Frueh, W. T. & Lancaster, S. T. 2014. Correction of deposit ages for inherited ages of charcoal: implications for sediment dynamics inferred from random sampling of deposits on headwater valley floors. Quaternary Science Reviews, 88, 110-124.
Galbraith, R. F. & Green, P. F. 1990. Estimating the component ages in a finite mixture. International Journal of Radiation Applications and Instrumentation. Part D. Nuclear Tracks and Radiation Measurements, 17, 197-206.
Galbraith, R. F. & Roberts, R. G. 2012. Statistical aspects of equivalent dose and error calculation and display in OSL dating: an overview and some recommendations. Quaternary Geochronology, 11, 1-27.
Galbraith, R. F., Roberts, R. G., Laslett, G. M., Yoshida, H. & Olley, J. M. 1999. Optical dating of single and multiple grains of quartz from Jinmium rock shelter, northern Australia: Part I, experimental design and statistical models. Archaeometry, 41, 339-364.
Guérin, G., Mercier, N. & Adamiec, G. 2011. Dose-rate conversion factors: update. Ancient TL, 29, 5-8.
Helgen, K. M., Wells, R. T., Kear, B. P., Gerdtz, W. R. & Flannery, T. F. 2006. Ecological and evolutionary significance of sizes of giant extinct kangaroos. Australian Journal of Zoology, 54, 293-303.
Hocknull, S. A. 2005. Ecological succession during the late Cainozoic of central eastern Queensland: extinction of a diverse rainforest community. Memoirs of the Queensland Museum, 51, 39-122.
Hocknull, S. A. 2009. Late Cainozoic rainforest vertebrates from Australopapua: evolution, biogeography and extinction.
Hocknull, S. A., Piper, P. J., Van Den Bergh, G. D., Due, R. A., Morwood, M. J. & Kurniawan, I. 2009. Dragon's paradise lost: palaeobiogeography, evolution and extinction of the largest-ever terrestrial lizards (Varanidae). PloS one, 4, e7241.
Hocknull, S. A., Zhao, J.-X., Feng, Y.-X. & Webb, G. E. 2007. Responses of Quaternary rainforest vertebrates to climate change in Australia. Earth and Planetary Science Letters, 264, 317-331.
Hogg, A. G., Hua, Q., Blackwell, P. G., Niu, M., Buck, C. E., Guilderson, T. P., Heaton, T. J., Palmer, J. G., Reimer, P. J. & Reimer, R. W. 2013. SHCal13 Southern Hemisphere calibration, 0–50,000 years cal BP. Radiocarbon, 55, 1889-1903.
Huxley, T. H. 1862. On the premolar teeth of Diprotodon, and on a new species of that genus. Quarterly Journal of the Geological Society, 18, 422-427.
Jacobs, Z., Duller, G. A., Wintle, A. G. & Henshilwood, C. S. 2006. Extending the chronology of deposits at Blombos Cave, South Africa, back to 140 ka using optical dating of single and multiple grains of quartz. Journal of Human Evolution, 51, 255-273.
Janis, C. M., Buttrill, K. & Figueirido, B. 2014. Locomotion in extinct giant kangaroos: were sthenurines hop-less monsters? PloS one, 9, e109888.
Jankowski, N. R., Gully, G. A., Jacobs, Z., Roberts, R. G. & Prideaux, G. J. 2016. A late Quaternary vertebrate deposit in Kudjal Yolgah Cave, south-western Australia: refining regional late Pleistocene extinctions. Journal of Quaternary Science, 31, 538-550.
Joannes-Boyau, R. 2013. Detailed protocol for an accurate non-destructive direct dating of tooth enamel fragment using Electron Spin Resonance. Geochronometria, 40, 322-333.

Joannes-Boyau, R., Duval, M. & Bodin, T. 2018. MCDoseE 2.0 A new Markov Chain Monte Carlo program for ESR dose response curve fitting and dose evaluation. Quaternary Geochronology, 44, 13-22.
Joannes-Boyau, R. & Grün, R. 2009. Thermal behaviour of orientated and non-orientated CO_2^- radicals in tooth enamel. Radiation Measurements, 44, 505-511.
Joannes-Boyau, R. & Grün, R. 2011. A comprehensive model for CO_2^- radicals in fossil tooth enamel: implications for ESR dating. Quaternary Geochronology, 6, 82-97.
Laurenti, J.-N. 1768. Specimen medicum, exhibens synopin reptilium emendatam cum experimentis circa venena et antidota reptilium Austriacorum, Trattner.
Louys, J. 2015. Wombats (Vombatidae: Marsupialia) from the Pliocene Chinchilla Sand, southeast Queensland, Australia. Alcheringa: An Australasian Journal of Palaeontology, 39, 394-406.
Ludwig, K. R. 2003. User's manual for isoplot 3.00, a geochronlogical toolkit for microsoft excel. Berkeley Geochronl. Cent. Spec. Publ., 4, 25-32.
Ludwig, K. R., Simmons, K. R., Szabo, B. J., Winograd, I. J., Landwehr, J. M., Riggs, A. C. & Hoffman, R. J. 1992. Mass-spectrometric 230Th-234U-238U dating of the Devils Hole calcite vein. Science, 258, 284-287.
Mackness, B. 1995. Palorchestes selestiae, a new species of palorchestid marsupial from the early Pliocene Bluff Downs Local Fauna, northeastern Queensland. Memoirs-Queensland Museum, 38, 603-610.
Martin, L., Goff, J., Jacobsen, G. & Mooney, S. 2019. The radiocarbon ages of different organic components in the Mires of Eastern Australia. Radiocarbon, 61, 173-184.
Mayya, Y., Morthekai, P., Murari, M. K. & Singhvi, A. 2006. Towards quantifying beta microdosimetric effects in single-grain quartz dose distribution. Radiation Measurements, 41, 1032-1039.
Mcgeehin, J., Burr, G. S., Jull, A. T., Reines, D., Gosse, J., Davis, P., Muhs, D. & Southon, J. R. 2001. Stepped-combustion 14C dating of sediment: a comparison with established techniques. Radiocarbon, 43, 255-261.
Mejdahl, V. 1979. Thermoluminescence dating: beta-dose attenuation in quartz grains. Archaeometry, 21, 61-72.
Mejdahl, V. 1987. Internal radioactivity in quartz and feldspar grains. Ancient TL, 5, 10-17.
Metropolis, N., Rosenbluth, A. W., Rosenbluth, M. N., Teller, A. H. & Teller, E. 1953. Equation of state calculations by fast computing machines. The journal of chemical physics, 21, 1087-1092.
Molnar, R. 1979. Crocodylus porosus from the Pliocene Allingham formation of North Queensland. Results of the Ray E. Lemley expeditions, part 5. Memoirs of the Queensland Museum, 19, 357-365.
Molnar, R. 1981. Pleistocene ziphodont crocodilians of Queensland. Records of the Australian Museum, 33, 803-834.
Molnar, R. 1982a. Cenozoic fossil reptiles in Australia. The Fossil Vertebrate Record of Australia. Clayton: Monash University Offset Printing Unit, 228-233.
Molnar, R. 1982b. Pallimnarchus and other Cenozoic crocodiles in Queensland. Memoirs of the Queensland Museum, 20, 657-673.
Molnar, R. & Kurz, C. The distribution of Pleistocene vertebrates on the eastern Darling Downs, based on the Queensland Museum collections. Proceedings-Linnean Society of New South Wales, 1997. Linnean Society of New South Wales, 107-134.
Moss, P. T. 2013. Palynology and its Application to Geomorphology. In: Shroder, J. F. (ed.) Treatise on Geomorphology. San Diego: Academic Press.
Moss, P. T., Dunbar, G. B., Thomas, Z., Turney, C., Kershaw, A. P. & Jacobsen, G. E. 2017. A 60 000-year record of environmental change for the Wet Tropics of north-eastern Australia based on the ODP 820 marine core. Journal of Quaternary Science, 32, 704-716.
Moss, P. T., Tibby, J., Petherick, L., Mcgowan, H. & Barr, C. 2013. Late Quaternary vegetation history of North Stradbroke Island, Queensland, eastern Australia. Quaternary Science Reviews, 74, 257-272.
Murray, A. S. & Wintle, A. G. 2000. Luminescence dating of quartz using an improved single-aliquot regenerative-dose protocol. Radiation measurements, 32, 57-73.

Murray, P. F. 1995. The postcranial skeleton of the Miocene kangaroo, Hadronomas puckridgi Woodburne (Marsupialia, Macropodidae). Alcheringa: An Australasian journal of palaeontology, 19, 119-170.
Olley, J. M., Murray, A. & Roberts, R. G. 1996. The effects of disequilibria in the uranium and thorium decay chains on burial dose rates in fluvial sediments. Quaternary Science Reviews, 15, 751-760.
Olley, J. M., Roberts, R. G. & Murray, A. S. 1997. Disequilibria in the uranium decay series in sedimentary deposits at Allen's Cave, Nullarbor Plain, Australia: implications for dose rate determinations. Radiation Measurements, 27, 433-443.
Owen, R. 1842. Report on British Fossil Reptiles. Part II. Report of the eleventh meeting of the british association for the advancement of science; held at Plymouth in July 1841. London (Murray).
Pawley, S. M., Bailey, R. M., Rose, J., Moorlock, B. S., Hamblin, R. J., Booth, S. J. & Lee, J. R. 2008. Age limits on Middle Pleistocene glacial sediments from OSL dating, north Norfolk, UK. Quaternary Science Reviews, 27, 1363-1377.
Pietsch, T. J. 2009. Optically stimulated luminescence dating of young (< 500 years old) sediments: Testing estimates of burial dose. Quaternary Geochronology, 4, 406-422.
Pietsch, T. J., Nanson, G. C. & Olley, J. M. 2013. Late Quaternary changes in flow-regime on the Gwydir distributive fluvial system, southeastern Australia. Quaternary Science Reviews, 69, 168-180.
Piper, K. J. 2006. A new species of Palorchestidae (Marsupialia) from the Pliocene and early Pleistocene of Victoria. Alcheringa: An Australasian Journal of Palaeontology, 30, 281-294.
Piper, K. J. 2016. The Macropodidae (Marsupialia) of the early Pleistocene Nelson Bay Local Fauna, Victoria, Australia. Memoirs of Museum Victoria, 74, 233-253.
Plane, M. D. 1965. The stratigraphy and vertebrate fauna of the Otibanda Formation, New Guinea, University of California.
Pledge, N., Prescott, J. & Hutton, J. 2002. A late Pleistocene occurrence of Diprotodon at Hallett Cove, South Australia. Transactions of the Royal Society of South Australia, 126, 39-44.
Pledge, N. S. 1991. Occurrences of Palorchestes species (Marsupialia: Palorchestidae) in South Australia. Records of the South Australian Museum, 25, 161-74.
Potts, P. J., Thompson, M., Chenery, S. R., Webb, P. C. & Kasper, H. U. 2003. GeoPT13-An international proficiency test for analytical geochemistry laboratories-report on round 13/July 2003 (Köln Loess). International Association of Geoanalysts.
Prescott, J. R. & Hutton, J. T. 1994. Cosmic ray contributions to dose rates for luminescence and ESR dating: large depths and long-term time variations. Radiation measurements, 23, 497-500.
Preusser, F. & Degering, D. 2007. Luminescence dating of the Niederweningen mammoth site, Switzerland. Quaternary International, 164, 106-112.
Price, G. J. 2008. Taxonomy and palaeobiology of the largest-ever marsupial, Diprotodon (Diprotodontidae, Marsupialia). Zoological Journal of the Linnean Society, 153, 369-397.
Price, G. J., Feng, Y.-X., Zhao, J.-X. & Webb, G. E. 2013. Direct U–Th dating of vertebrate fossils with minimum sampling destruction and application to museum specimens. Quaternary Geochronology, 18, 1-8.
Price, G. J. & Hocknull, S. 2005. A small adult Palorchestes (Marsupialia, Palorchestidae) from the Pleistocene of the Darling Downs, southeast Queensland. Memoirs of the Queensland Museum, 51, 202-202.
Price, G. J. & Piper, K. J. 2009. Gigantism of the Australian Diprotodon Owen 1838 (Marsupialia, Diprotodontoidea) through the Pleistocene. Journal of Quaternary Science: Published for the Quaternary Research Association, 24, 1029-1038.
Price, G. J. & Sobbe, I. H. 2011. Morphological variation within an individual Pleistocene Diprotodon optatum Owen, 1838 (Diprotodontinae; Marsupialia): implications for taxonomy within diprotodontoids. Alcheringa, 35, 21-29.
Prideaux, G. 2004. Systematics and evolution of the sthenurine kangaroos, Univ of California Press.
Rees-Jones, J. 1995. Optical dating of young sediments using fine-grain quartz. Ancient TL, 13, 9-14.
Rees-Jones, J. & Tite, M. S. 1997. Optical dating results for British archaeological sediments. Archaeometry, 39, 177-187.

Roberts, R. G., Galbraith, R., Yoshida, H., Laslett, G. & Olley, J. M. 2000. Distinguishing dose populations in sediment mixtures: a test of single-grain optical dating procedures using mixtures of laboratory-dosed quartz. Radiation Measurements, 32, 459-465.
Rule, S., Brook, B. W., Haberle, S. G., Turney, C. S., Kershaw, A. P. & Johnson, C. N. 2012. The aftermath of megafaunal extinction: ecosystem transformation in Pleistocene Australia. Science, 335, 1483-1486.
Sambridge, M., Grün, R. & Eggins, S. 2012. U-series dating of bone in an open system: the diffusion-adsorption-decay model. Quaternary Geochronology, 9, 42-53.
Shao, Q., Bahain, J.-J., Dolo, J.-M. & Falguères, C. 2014. Monte Carlo approach to calculate US-ESR age and age uncertainty for tooth enamel. Quaternary Geochronology, 22, 99-106.
Sobbe, I. H., Price, G. J. & Knezour, R. A. 2013. A ziphodont crocodile from the late Pleistocene King Creek catchment, Darling Downs, Queensland. Memoirs of the Queensland Museum-Nature, 56, 601-606.
Stirling, E. 1913. On the identity of Phascolomys (Phascolonus) gigas, Owen, and Sceparnodon ramsayi, Owen, with a description with some parts of its skeleton. Memoirs of the Royal Society of South Australia, 1, 127-178.
Stokes, S., Ingram, S., Aitken, M., Sirocko, F., Anderson, R. & Leuschner, D. 2003. Alternative chronologies for Late Quaternary (Last Interglacial–Holocene) deep sea sediments via optical dating of silt-sized quartz. Quaternary Science Reviews, 22, 925-941.
Stuiver, M. & Polach, H. A. 1977. Discussion reporting of 14C data. Radiocarbon, 19, 355-363.
Tedford, R. H. 1967. fossil Macropodidae from Lake Menindee, New South Wales.
Trusler, P. W. & Sharp, A. C. 2016. Description of new cranial material of Propalorchestes (Marsupialia: Palorchestidae) from the middle Miocene camfield beds, Northern Territory, Australia. Memoirs of Museum Victoria, 74, 291-324.
Wakeham, S. & Canuel, E. A. 2016. The nature of organic carbon in density-fractionated sediments in the Sacramento-San Joaquin River Delta (California). Biogeosciences, 13, 567-582.
Wells, R. 1977. On the manus and pes of Thylacoleo carnifex Owen (Marsupialia).
Wells, R. T. & Camens, A. B. 2018. New skeletal material sheds light on the palaeobiology of the Pleistocene marsupial carnivore, Thylacoleo carnifex. Plos one, 13, e0208020.
Wells, R. T., Murray, P. F. & Bourne, S. J. 2009. Pedal morphology of the marsupial lion Thylacoleo carnifex (Diprotodontia: Thylacoleonidae) from the Pleistocene of Australia. Journal of Vertebrate Paleontology, 29, 1335-1340.
Wells, R. T. & Tedford, R. H. 1995. Sthenurus (Macropodidae, Marsupialia) from the Pleistocene of Lake Callabonna, South Australia. Bulletin of the AMNH; no. 225.
Willis, P. & Molnar, R. 1991. A new middle Tertiary crocodile from Lake Palankarinna, South Australia. Records of the South Australian Museum, 25, 39-55.
Willis, P. & Molnar, R. Identification of large reptilian teeth from the Plio-Pleistocene deposits of Australia. Journal and Proceedings of the Royal Society of New South Wales, 1997a. 79-92.
Willis, P. & Molnar, R. A review of the Plio-Pleistocene crocodilian genus Pallimnarchus. PROCEEDINGS-LINNEAN SOCIETY OF NEW SOUTH WALES, 1997b. LINNEAN SOCIETY OF NEW SOUTH WALES, 223-242.
Wood, R., Jacobs, Z., Vannieuwenhuyse, D., Balme, J., O'connor, S. & Whitau, R. 2016. Towards an accurate and precise chronology for the colonization of Australia: The example of Riwi, Kimberley, Western Australia. PloS one, 11, e0160123.
Woodroffe, C. D., Short, S. A., Stoddart, D. R., Spencer, T. & Harmon, R. S. 1991. Stratigraphy and chronology of late Pleistocene reefs in the southern Cook Islands, south Pacific. Quaternary Research, 35, 246-263.

Appendix D. Supplementary Information for Chapter 5

This Appendix contains supplementary information that accompanies Chapter 5, written in the format of an article and intended for submission as:

Lewis, R. J., Arnold, L. J.; Hocknull, S. A.; Tibby, J.; Demuro, M.; Lawrence, R. A., The hydroclimatic and chronological context of late Pleistocene megafauna extinction in north-eastern Australia

---

D1. OSL dating methodology

D1.1. Sample extraction and preparation

OSL core tube samples were extracted from four sites (SWP, SWS, SWJS and SWC-US) within the South Walker Creek fossil deposit area, targeting deposits of hydrological significance, fossiliferous beds and bracketing sedimentary layers. Samples were carefully extracted from the core tubes under safe light conditions (subdued red lighting) at the Prescott Environmental Luminescence Laboratory, University of Adelaide.

Bulk minerals with a diameter of 212 – 250 μm were separated via wet sieving, and treated with 30% HCl and 30% H_2O_2 to dissolve remaining carbonates and organic material, respectively (Aitken, 1998). Quartz grains were then isolated using heavy liquid separation prepared to densities of 2.72 g/cm^3 and 2.62 g/cm^3. The alpha-irradiated rinds of the prepared quartz grains were etched using 48% HF for 40 mins, which was followed by treatment with 30% HCl to dissolve any fluoride precipitates.

D1.2. Equivalent dose (D_e) determination procedures and instrumentation

All of the samples were measured using a Risø TL/OSL DA-20 reader equipped with an EMI9235QA photomultiplier tube, a mounted $^{90}Sr/^{90}Y$ β source and, a 10mW Nd:YVO_4 single-grain (523 nm) laser attachment. Single-grain equivalent dose (D_e) measurements were conducted by loading individual quartz grains onto standard single-grain aluminium discs with a drilled array of 300 μm x 300 μm holes, each of which had been individually calibrated to account for beta dose heterogeneity across the surface of the disc. Single-grain OSL D_e measurements were conducted using a modified version of the single-aliquot regenerative-dose (SAR) protocol (Murray & Wintle, 2000) to allow the measurement of individual grains (Table D2). Individual D_e measurements were calculated by fitting a single-saturating exponential function to the sensitivity-corrected dose response curve for each grain (Figure D1). The sensitivity-corrected dose response curve points and sensitivity-corrected natural OSL signal were determined by integrating the first 0.08 s – 0.14 s of the OSL signal following laser stimulation and subtracting a background calculated from the last 0.25 s of stimulation (Figure D1).

Optimum SAR preheating conditions for samples from the SWC area have been previously determined by Hocknull et al. (2020) using both multi-grain aliquot and single-grain dose recovery tests (DRTs). To ensure that these previously determined SAR conditions (Table D2) are appropriate for the new sites detailed in this study, additional single-grain OSL DRTs were conducted on one sample from each site (Table D3) using the optimum preheat combination adopted by Hocknull et al. (2020) (natural and regenerative dose preheat = 240°C for 10 s, test dose preheat = 160°C for 10 s). Single-grain DRTs were performed on samples SWC-C, SWC-K, SWC-R and SWC-P following bleaching of their natural signals using two 1,000 s blue LED stimulations separated by a 10,000 s pause (to ensure complete decay of any phototransferred charge in the 110°C TL trap) and then administering a known dose of 100 Gy. The weighted mean measured-to-given dose ratios for this suite of samples were found to overlap with unity at 2σ (ranging from 0.95 ± 0.03 to 0.97 ± 0.02; Table D3), with overdispersion values that varied between 4 – 9% (Figure D2). These results support the general suitability of the single-grain D_e measurement conditions used in this study.

Prior to inclusion in the final age calculation, individual single-grain D_e measurements were screened against a series of routine quality assurance criteria (Demuro et al., 2019; Arnold et al., 2016). The OSL D_e estimates were not considered suitable for age calculation if: (1) the net T_n signals were <3σ

above the background; (2) two identical sensitivity-corrected (L_x/T_x) high- or low-regenerative dose ratios were not consistent with unity at 2σ (recycling ratio); (3) the OSL-IR depletion ratio (Duller, 2003) was less than unity at 2σ; (4) the sensitivity-corrected 0 Gy regenerative dose (L_0/T_x) was >5% of the natural signal (L_n/T_n); (5) the L_n/T_n were equal to the Imax saturation limit of the dose-response curve at 2σ; (6) the dose-response curve displayed anomalous properties (i.e., zero or negative response with increasing dose) or very scattered L_x/T_x values that could not be successfully fitted with the Monte Carlo procedure; (7) the L_n/T_n did not intercept the dose-response curve; (8) the net D_e uncertainty was >50%. The single-grain classification and rejection statistics obtained after applying these quality assurance criteria are presented in Table D4, with an example of an accepted grain's dose response and OSL characteristics presented in Figure D1.

In this study, we have considered a range of statistical age models to characterise each single-grain D_e distribution and derive representative burial dose estimates. The weighted mean D_e value (calculated using the central age model; CAM (Galbraith et al., 1999)) has been used to derive the final burial dose estimates for samples considered to be well-bleached and undisturbed following deposition. Samples exhibiting D_e distribution characteristics consistent with heterogeneous bleaching prior to deposition (e.g., Arnold et al., 2008; Arnold et al., 2007; Bailey & Arnold, 2006) have been analysed using the three-parameter minimum age model (MAM3) and four-parameter minimum age model (MAM4). The final choice of age model for burial dose determination has been made on a sample-by-sample basis in accordance with the maximum log likelihood (llik) criterion of Arnold & Roberts (2009) (see Table D5 for further details), as well as the amount of observed D_e overdispersion, and consideration of the depositional context and sedimentary characteristics of each site. The results of applying the llik statistical test to each sample are presented in Table D5. According to the llik criterion, the CAM provides the most suitable statistical fit for thirteen of the twenty samples considered in this study. The other seven samples, all of which were collected from the SWC-US site, yielded llik scores that favoured application of MAM3 over the MAM4 or CAM (Table D5).

D1.3. Dose rate

Environmental dose rates were calculated using in situ field gamma spectrometry (FGS), high resolution gamma spectrometry (HRGS) and low-level beta counting (Table 5.2, Table D6, Table D7). Gamma dose rates were determined from in situ gamma spectrometry measurements made with a 3 inch Canberra NaI:Tl detector, applying the 'energy windows' approach (Arnold et al., 2012). External beta dose rates of samples were determined from measurements made using a Risø GM-25-5 beta counter (Bøtter-Jensen et al., 2000), with experiments conducted on dried and homogenised, bulk sediments collected directly from the OSL sampling positions. Background-subtracted count rates were measured for three aliquots of each sample and compared with net count rates obtained simultaneously for a loess sediment standard (with known U, Th and K concentrations (Potts et al., 2003)). HRGS measurements were conducted at the University of Adelaide following the procedures outlined in Leslie (2009) and were used to derive external gamma and beta dose rates for the 2015 samples. This approach was necessary as it was not possible to conduct in situ FGS measurements during the 2015 excavations (see details in Hocknull et al., 2020). Representative dose rates have been calculated from the HRGS radionuclide concentrations after considering the proportional beta and gamma dose rate contributions from different parent or daughter isotopes measured in the ^{238}U and ^{232}Th decay series. As part of this analysis, the present-day state of (dis)equilibrium observed in the ^{238}U and ^{232}Th decay chains are assumed to have prevailed throughout the burial period. Additional

HRGS measurements were also conducted on the samples collected in 2017 to evaluate the state of secular equilibrium in their ^{238}U, ^{235}U and ^{232}Th decay series. HRGS radionuclide activities obtained for each of the 2015 and 2017 OSL samples are summarised in Table D7. The ^{238}U and ^{232}Th decay chains of all samples are in present-day secular equilibrium, i.e., the daughter-parent isotopic ratios for ^{238}U, ^{226}Ra, ^{210}Pb, ^{228}Ra and ^{228}Th are consistent with unity at 1σ.

The cosmic ray contribution to the environmental dose rate was calculated following Prescott & Hutton (1994), taking into consideration post-depositional overburden (i.e., sediment thickness and density), altitude and geomagnetic latitude. An assumed internal dose rate of 0.03 ± 0.01 Gy/ka was applied to the final dose rate calculation based on published values for etched quartz grains from a suite of locations (Pawley et al., 2008; Jacobs et al., 2006; Bowler et al., 2003; Mejdahl, 1987) and an alpha efficiency factor (a-value) of 0.04 ± 0.01 (Rees-Jones & Tite, 1997; Rees-Jones, 1995), as adopted in the previous OSL dating study of the SWC area (Hocknull et al., 2020).

Radionuclide concentrations and specific activities have been converted to dose rates using the conversion factors of Guérin et al., 2011; Stokes et al., 2003), making adjustments for beta dose attenuation and long-term sediment moisture contents (Brennan, 2003; Aitken, 1985; Mejdahl, 1979). As outlined in Hocknull et al. (2020), the present-day sediment water contents of the SWC samples are not considered to be entirely representative of those prevailing throughout the sample burial periods because: (i) the excavation pits and sediment exposures had partially dried out prior to sampling; (ii) OSL samples were collected during dry-season months; and (iii) local hydrological conditions are known to have been significantly wetter at various times in the past. To determine more suitable long-term sediment moisture contents, we have used 40% of their present-day saturated water contents based on the proportional saturation water content assessments undertaken by Hocknull et al. (2020), which factor in the potential for wetter climatic conditions and intermittent flooding of SWC area in the past, and include a 1σ relative uncertainty of 20% to accommodate any post-depositional variations in hydrological conditions. Sensitivity analysis performed on the South Walker Creek OSL samples reveals that the choice of long-term water content has a relatively minor effect on the final OSL age calculation; the final ages obtained for all reasonable possible water content scenarios between the lower long-term limit (measured present-day water content) and upper long-term limit (measured saturated water content) are statistically indistinguishable at 1σ (Figure D4).

Table D 1 List of all chronometric data available for the eight South Walker Creek sites (Hocknull et al., 2020 and the current study), including details of the sedimentary units sampled.

Site	Unit	ID	Final Age (ka)(±1σ)	Institute [a]	Technique
SWC-US	7	SWC P	3.1 ± 2.6	AU	SG-OSL
	7	SWC17-38	4.0 ± 3.3	AU	SG-OSL
	6	SWC17-43	10.5 ± 2.1	AU	SG-OSL
	5	SWC17-41	12.8 ± 2.5	AU	SG-OSL
	4	SWC17-44	16.1 ± 2.4	AU	SG-OSL
	3	SWC17-42	14.3 ± 2.8	AU	SG-OSL
	3	SWC17-39	10.0 ± 1.5	AU	SG-OSL
	2	SWC O	45.8 ± 4.0	AU	SG-OSL
	2	SWC17-40	45.9 ± 3.1	AU	SG-OSL
	1	SWC N	48.4 ± 4.2	AU	SG-OSL
SW3	1	SWC17-34	43.5 ± 3.2	AU	SG-OSL [b]
	1	SWC17-33	44.8 ± 3.1	AU	SG-OSL [b]
	1	SWC17-47	48.0 ± 3.8	AU	SG-OSL [b]
	1	QMF57172 / SW3-SCU-01	-	UOW	US-ESR [b]
	1	SWC17-46	48.8 ± 3.1	AU	SG-OSL [b]
	1	SWC A	50.1 ± 3.9	AU	SG-OSL [b]
	1	SWC17-45	51.0 ± 4.2	AU	SG-OSL [b]
	1	SWC B	61.5 ± 5.0	AU	SG-OSL [b]
SW9	1	QMF54689	16.1 ± 0.1	UQ	U-series [b]
	1	QMF59869	19.8 ± 0.3	UQ	U-series [b]
	1	QMF57069	22.8 ± 0.0	UQ	U-series [b]
	1	QMF57065	23.5 ± 0.1	UQ	U-series [b]
	1	SW9-9	29.7 ± 3.1	GU	SG-OSL [b]
	1	QMF57039 / I-SCU-02	25.5 ± 0.1	UOW	U-series [b]
	1	*QMF57035* / P-SCU01	22.6 ± 0.3	UOW	U-series [b]
	1	QMF57039 / SW9-ISCU-02B	30.0 ± 3.5	UOW	US-ESR [b]
	1	QMF57065 / SW9-MSCU-1(B)	32.0 ± 3.5	UOW	US-ESR [b]
	1	SW9-7	32.9 ± 3.4	GU	SG-OSL [b]
	1	SW9-10	37.7 ± 3.6	GU	SG-OSL [b]
	1	SWC17-53	37.9 ± 2.7	AU	SG-OSL [b]
	1	QMF57065 / SW9-MSCU-1(A)	38.0 ± 4.0	UOW	US-ESR [b]
	1	SWC17-52	40.7 ± 3.1	AU	SG-OSL [b]
	1	SWC17-56	42.0 ± 2.9	AU	SG-OSL [b]
	1	SW9-8	42.3 ± 4.1	GU	SG-OSL [b]
	1	*QMF57035* / SW9-PSCU-01A	38.0 ± 4.0	UOW	US-ESR [b]
	1	*QMF57035* / SW9-PSCU-01B	44.0 ± 5.0	UOW	US-ESR [b]
	1	SWC17-55	46.1 ± 3.4	AU	SG-OSL [b]
	1	SW9-6	46.6 ± 5.0	GU	SG-OSL [b]
	1	SWC17-54	47.5 ± 4.1	AU	SG-OSL [b]
	1	SW9-4	38.0 ± 4.2	GU	SG-OSL [b]
	1	SW9-1	39.7 ± 4.3	GU	SG-OSL [b]
	1	SWC17-49	41.6 ± 5.1	AU	SG-OSL [b]
	1	SW9-2	42.6 ± 4.3	GU	SG-OSL [b]
	1	SWC17-50	42.8 ± 2.6	AU	SG-OSL [b]
	1	SW9-11	45.3 ± 5.5	GU	SG-OSL [b]
	1	SW9-3	43.9 ± 4.7	GU	SG-OSL [b]
	1	SWC17-48	54.2 ± 3.7	AU	SG-OSL [b]
	1	SW9-5	68.6 ± 8.4	GU	SG-OSL [b]
SWCC	1	SWC17-31	67.5 ± 4.2	AU	SG-OSL [b]
	1	SWC17-30	50.2 ± 3.1	AU	SG-OSL [b]
SWJS	2	SWC Q	38.8 ± 3.0	AU	SG-OSL
	2	SWC R	45.2 ± 2.8	AU	SG-OSL
	1	SWC S	42.7 ± 4.0	AU	SG-OSL
	1	SWC T	42.3 ± 3.5	AU	SG-OSL
SWP	1	SWC C	58.9 ± 5.0	AU	SG-OSL
	1	SWC D	56.5 ± 4.5	AU	SG-OSL
SWS	1	SWC K	53.1 ± 6.2	AU	SG-OSL
	1	SWC L	49.5 ± 3.7	AU	SG-OSL
	1	SWC17-36	46.0 ± 3.7	AU	SG-OSL
	1	SWC M	54.7 ± 4.1	AU	SG-OSL
SWJ	1	SWC E	66.6 ± 6.2	AU	SG-OSL [b]
	1	SWC F	60.5 ± 5.8	AU	SG-OSL [b]
	1	SWC G	66.6 ± 6.5	AU	SG-OSL [b]
	1	SWC H	65.6 ± 6.7	AU	SG-OSL [b]
	1	SWC I	74.7 ± 6.3	AU	SG-OSL [b]
	1	SWC J	60.1 ± 6.5	AU	SG-OSL [b]

[a] AU=Adelaide University; GU=Griffith University; UOW=University of Wollongong; UQ=University of Queensland.

[b] SG-OSL=single-grain optically stimulated luminescence; U-series=uranium series; US-ESR=U-series electron spin resonance.

Table D 2 SAR protocol used in this study to obtain single-grain OSL ages. L_n and L_x refer to the natural and regenerative-dose signal measurements, respectively. T_n and T_x refer to the test dose signals measured after the L_n and L_x signals, respectively.

Step	Single-grain OSL SAR	Notation
1[a]	Give dose	
2[b]	Stimulate with infrared diodes at 50 C for 40 s (90% power)	
3	Preheat at 240 C for 10 s	
4 [c]	Stimulate with green laser at 125 C for 2 s (90% power)	L_n or L_x
5	Give test dose (5 Gy)	
6	Preheat to 160 C for 10 s	
7	Stimulate with green laser at 125 C for 2 s (90% power)	T_n or T_x
8	Return to 1	

[a] Step omitted when measuring the natural signal (L_n).
[b] Step added only when measuring the OSL-IR depletion ratio (Duller, 2003).

Table D 3 Single-grain dose recovery test results obtained for 212 – 250 μm quartz grains using the SAR protocol shown in Table D2.

Site	Sample ID	Grain Size (μm)	n[a]	measured-to-given ratio	OD (%)[b]
SWP	SWC C (DRT)	212 – 250	79 / 1000	0.97 ± 0.02	4.7 ± 2.7
SWS	SWC K (DRT)	212 – 250	51 / 600	0.95 ± 0.03	9.0 ± 3.1
SWJS	SWC R (DRT)	212 – 250	79 / 800	0.95 ± 0.02	3.7 ± 3.7
SWC-US	SWC P (DRT)	212 – 250	77 / 800	0.96 ± 0.02	6.8 ± 2.4

[a] n = number of accepted D_e values/number of measured D_e values.
[b] OD = overdispersion value.

Table D 4 Single-grain OSL statistics showing grain classification following application of the SAR rejection criteria. The first four samples, above the dashed line, show the samples included in the single-grain dose recovery test (DRT).

			Rejected grains (%)									
				Poor recycling dose ratio								
Site	Sample ID	Grains measured	T_n <3σ BG	Low dose	High dose	IR depletion ratio	Recuperation >5%	Saturated	Anomalous dose response curve	L_n/T_n not intersecting DRC	Relative error of D_e >50%	Accepted grains (%)
SWP	SWC17-C	1000	44	22	7	8	5	1	5	1	0	7
SWS	SWC17-K	600	44	23	8	7	6	1	3	3	0	7
SWJS	SWC17-R	800	63	9	8	3	5	1	2	1	0	8
SWC-US	SWC17-P	800	60	10	7	5	4	1	3	2	0	9
SWP	SWC17-C	800	68	9	4	3	3	1	2	2	0	8
SWP	SWC17-D	800	68	8	4	2	5	1	3	2	0	7
SWS	SWC17-K	500	41	24	11	6	4	1	3	3	0	8
SWS	SWC17-L	1000	70	10	4	5	2	0	3	1	0	5
SWS	SWC17-M	800	64	11	4	4	3	1	5	2	0	6
SWS	SWC17-36	1400	69	16	6	3	2	0	2	0	0	3
SWJS	SWC17-Q	1100	69	12	3	6	4	0	2	0	0	4
SWJS	SWC17-R	800	63	7	5	3	3	1	7	1	0	9
SWJS	SWC17-S	800	59	11	5	8	6	1	6	1	0	4
SWJS	SWC17-T	1200	65	14	4	9	3	0	2	0	0	3
SWC-US	SWC17-N	800	70	10	4	4	2	1	3	1	0	6
SWC-US	SWC17-O	400	67	10	4	3	3	0	2	2	0	9
SWC-US	SWC17-P	700	79	5	3	0	3	0	1	0	0	8
SWC-US	SWC17-38	1200	67	17	5	3	4	0	2	0	0	2
SWC-US	SWC17-39	1400	57	13	6	6	4	0	4	0	0	9
SWC-US	SWC17-40	1400	65	17	5	3	3	0	2	0	0	5
SWC-US	SWC17-41	600	59	15	6	5	4	0	3	1	1	8
SWC-US	SWC17-42	1100	60	16	7	5	3	0	3	0	0	6
SWC-US	SWC17-43	800	51	18	7	9	4	0	4	1	0	7
SWC-US	SWC17-44	1900	63	15	5	5	3	0	5	1	0	4

Table D 5 Maximum log likelihood (llik) statistics (Galbraith & Roberts, 2012; Roberts et al., 2000) for the South Walker Creek single-grain D_e populations obtained in this study. The llik values shown in bold indicate the most statistically suitable age model fit for each D_e dataset.

Site	Sample ID	CAM llik [a]	MAM3 llik [a, b]	MAM4 [a, b]
SWP	SWC C	**-37.0**	-37.5	-36.7
SWP	SWC D	**-19.4**	-19.4	-19.4
SWS	SWC K	**-32.7**	-36.4	-30.6
SWS	SWC L	**-21.8**	-23.0	-20.7
SWS	SWC M	**-12.0**	-12.0	-12.0
SWS	SWC17-36	**-6.9**	-7.0	-6.7
SWJS	SWC Q	**-55.0**	-82.7	-112.5
SWJS	SWC R	**-13.0**	-13.1	-13.1
SWJS	SWC S	**-16.6**	-16.9	-14.6
SWJS	SWC T	**-19.0**	-20.4	-16.4
SWC-US	SWC N	**-30.9**	-31.9	-30.3
SWC-US	SWC O	**-16.5**	-16.5	-15.8
SWC-US	SWC P	-93.4	**-43.7**	-777.6
SWC-US	SWC17-38	-33.5	**-26.6**	-232.9
SWC-US	SWC17-39	-131.8	**-79.0**	-632.3
SWC-US	SWC17-40	**-20.2**	-20.0	-19.8
SWC-US	SWC17-41	-60.7	**-57.3**	-207.0
SWC-US	SWC17-42	-83.0	**-75.5**	-315.6
SWC-US	SWC17-43	-66.7	**-55.7**	-277.2
SWC-US	SWC17-44	-92.6	**-90.2**	-194.1

[a] Llik represents the maximum log likelihood score of the CAM, MAM3 or MAM4 fit. For a given sample, the llik score must improve by at least 1.92 (i.e., become more positive) when successively applying the CAM, MAM3, and MAM4 to warrant the addition of the extra model parameters. If the extra parameter of the MAM3 (or MAM4) is not supported by the data, then its llik score will be similar to (i.e., within 1.92) of the CAM (or MAM3) llik score, indicating that the simpler age model explains the data equally well (Arnold & Roberts, 2009; Roberts et al , 2000).

[b] MAM3 and MAM4 D_e estimates were calculated after adding, in quadrature, a relative error of 20% to each individual D_e error to approximate the underlying dose overdispersion observed in 'ideal' (well-bleached and unmixed) sedimentary samples from SWC (e.g., samples SWC-D, SWC-M, SWC-R, plus samples SWC17-53 and SW9-2 from Hocknull et al., 2020); consistent with global overdispersion datasets (Arnold & Roberts, 2009).

Table D 6 Environmental dose rate values calculated for the quartz fractions of the South Walker Creek OSL samples.

		Environmental dose rate (Gy/ka)						
Site	**Sample ID**	**Depth (cm)**	**WC ($\%_{Dry}$) [a]**	**Beta [b, c]**	**Gamma [c, d]**	**Internal [d, e]**	**Cosmic [c]**	**Total [c]**
SWP	SWC-C	110	25 ± 5	0.97 ± 0.05^{HRGS}	0.75 ± 0.04^{HRGS}	0.03 ± 0.01	0 15 ± 0.01	1.90 ± 0.12
SWP	SWC-D	155	25 ± 5	0.97 ± 0.05^{HRGS}	0.74 ± 0.04^{HRGS}	0.03 ± 0.01	0 14 ± 0.01	1.88 ± 0.12
SWS	SWC-K	120	31 ± 6	0.99 ± 0.05^{HRGS}	0.75 ± 0.04^{HRGS}	0.03 ± 0.01	0 14 ± 0.01	1.91 ± 0.14
SWS	SWC-L	160	10 ± 2	1.21 ± 0.05^{HRGS}	0.89 ± 0.04^{HRGS}	0.03 ± 0.01	0 16 ± 0.02	2.29 ± 0.11
SWS	SWC-M	180	19 ± 4	0.94 ± 0.04^{HRGS}	0.73 ± 0.04^{HRGS}	0.03 ± 0.01	0 14 ± 0.01	1.84 ± 0.11
SWS	SWC17-36	217	27 ± 5	1.06 ± 0.05$^{\beta}$	0.79 ± 0.03^{FGS}	0.03 ± 0.01	0 13 ± 0.01	2.01 ± 0.13
SWJS	SWC-Q	30	7 ± 1	1.44 ± 0.06^{HRGS}	0.95 ± 0.05^{HRGS}	0.03 ± 0.01	0 19 ± 0.02	2.62 ± 0.12
SWJS	SWC-R	30	10 ± 2	0.98 ± 0.04^{HRGS}	0.75 ± 0.04^{HRGS}	0.03 ± 0.01	0 19 ± 0.02	1.95 ± 0.09
SWJS	SWC-S	47	9 ± 2	1.17 ± 0.05^{HRGS}	0.83 ± 0.05^{HRGS}	0.03 ± 0.01	0 19 ± 0.02	2.22 ± 0.11
SWJS	SWC-T	86	5 ± 1	1.23 ± 0.05^{HRGS}	0.89 ± 0.05^{HRGS}	0.03 ± 0.01	0 19 ± 0.02	2.34 ± 0.11
SWC-US	SWC-N	350	7 ± 1	0.83 ± 0.04^{HRGS}	0.68 ± 0.04^{HRGS}	0.03 ± 0.01	0 13 ± 0.01	1.67 ± 0.08
SWC-US	SWC-O	260	7 ± 1	0.92 ± 0.04^{HRGS}	0.74 ± 0.03^{HRGS}	0.03 ± 0.01	0 15 ± 0.01	1.83 ± 0.08
SWC-US	SWC-P	180	6 ± 1	0.80 ± 0.03^{HRGS}	0.62 ± 0.03^{HRGS}	0.03 ± 0.01	0 16 ± 0.02	1.61 ± 0.07
SWC-US	SWC17-38	182	17 ± 3	0.90 ± 0.05 $^{\beta}$	0.65 ± 0.02^{FGS}	0.03 ± 0.01	0 15 ± 0.01	1.73 ± 0.09
SWC-US	SWC17-39	169	19 ± 4	0.75 ± 0.04 $^{\beta}$	0.57 ± 0.02 ^{FGS}	0.03 ± 0.01	0 15 ± 0.01	1.50 ± 0.08
SWC-US	SWC17-40	149	17 ± 3	0.65 ± 0.03 $^{\beta}$	0.48 ± 0.02 ^{FGS}	0.03 ± 0.01	0 15 ± 0.02	1.32 ± 0.07
SWC-US	SWC17-41	136	12 ± 2	0.83 ± 0.04 $^{\beta}$	0.55 ± 0.02 ^{FGS}	0.03 ± 0.01	0 16 ± 0.02	1.57 ± 0.07
SWC-US	SWC17-42	179	12 ± 2	0.64 ± 0.03 $^{\beta}$	0.57 ± 0.02 ^{FGS}	0.03 ± 0.01	0 16 ± 0.02	1.40 ± 0.06
SWC-US	SWC17-43	88	12 ± 2	0.70 ± 0.04 $^{\beta}$	0.53 ± 0.02 ^{FGS}	0.03 ± 0.01	0 17 ± 0.02	1.43 ± 0.07
SWC-US	SWC17-44	95	11 ± 2	0.74 ± 0.04 $^{\beta}$	0.61 ± 0.02 ^{FGS}	0.03 ± 0.01	0 17 ± 0.02	1.55 ± 0.07

[a] Long-term water content (WC), expressed as % of dry mass of mineral fraction, with an assigned relative uncertainty of ±20%.
[b] Beta dose rates were calculated on dried, powdered sediment samples using a Risø GM-25-5 low level beta counting (β) or high resolution gamma spectroscopy (HRGS), after making allowance for beta dose attenuation due to grain-size effects and HF etching (Brennan, 2003; Mejdahl, 1979).
[c] Mean ± total uncertainty (68% confidence interval), calculated as the quadratic sum of the random and systematic uncertainties.
[d] Gamma dose rates were calculated from in situ gamma-ray spectrometry measurements made at each sample position with a NaI:Tl detector, using the 'energy windows' approach (e.g. Arnold et al., 2012) (FGS) where possible, or high resolution gamma spectroscopy on dried powdered sediment (HRGS) using the conversion factors given in Stokes et al. (2003) and Guérin et al. (2011).
[e] An assumed internal dose rate of 0.03 Gy / ka, with an assigned relative uncertainty of ±30% (±0.01 Gy/ka) is included for each sample, based on published intrinsic ^{238}U and ^{232}Th contents (Pawley et al., 2008; Jacobs et al., 2006; Bowler et al., 2003; Mejdahl, 1979; Lewis et al., 2020) and an alpha efficiency factor (a-value) of 0.04 ± 0.01 (Rees-Jones & Tite, 1997; Rees-Jones, 1995).
[f] Cosmic-ray dose rates were calculated using the approach of Prescott & Hutton (1994) and assigned a relative uncertainty of ±10%.

Table D 7 Detailed high-resolution gamma spectrometry (HRGS) results for the OSL samples from South Walker Creek. The specific activities of ^{238}U, ^{226}Ra, ^{210}Pb, ^{228}Ra, ^{228}Th and ^{40}K were measured for each sediment sample and used to calculate daughter-to-parent isotope ratios for ^{226}Ra:^{238}U, ^{210}Pb:^{226}Ra and ^{228}Th:^{228}Ra. Radionuclide specific activities and daughter-to-parent isotopic ratios are shown with their associated 1σ uncertainty ranges.

Site	Sample ID	^{238}U	^{226}Ra	^{210}Pb	^{228}Ra	^{228}Th	^{40}K	^{226}Ra:^{238}U	^{210}Pb:^{226}Ra	^{228}Th:^{228}Ra
SWP	SWC-C	32 ± 2.3	32 ± 0.6	30 ± 3.3	42 ± 1.1	42 ± 1.0	387 ± 10	1.0 ± 0.1	0.9 ± 0.1	1.0 ± 0.03
SWP	SWC-D	26 ± 2.2	26 ± 0 5	25 ± 3.7	33 ± 1.0	34 ± 0.8	326 ± 9	1.0 ± 0.1	1.0 ± 0.1	1.0 ± 0.04
SWS	SWC-K	31 ± 2.0	30 ± 0.6	33 ± 3.8	44 ± 1.3	43 ± 1.0	405 ± 11	1.0 ± 0.1	1.1 ± 0.1	1.0 ± 0.04
SWS	SWC-L	26 ± 2.1	25 ± 0 5	24 ± 2.6	40 ± 1.3	39 ± 0 9	384 ± 11	1.0 ± 0.1	1.0 ± 0.1	1.0 ± 0.04
SWS	SWC-M	26 ± 2.2	25 ± 0 5	26 ± 2.6	40 ± 1.2	42 ± 1.0	378 ± 10	1.0 ± 0.1	1.0 ± 0.1	1.0 ± 0.04
SWS	SWC17-36	28 ± 2.3	28 ± 0 5	30 ± 2.6	40 ± 1.1	44 ± 1.0	379 ± 10	1.0 ± 0.1	1.1 ± 0.1	1.1 ± 0.04
SWJS	SWC-Q	26 ± 2.1	26 ± 0 5	24 ± 3.7	34 ± 1.0	35 ± 0.8	399 ± 10	1.0 ± 0.1	0.9 ± 0.1	1.0 ± 0.04
SWJS	SWC-R	27 ± 2.2	28 ± 0 5	25 ± 3.2	36 ± 1.1	36 ± 0 9	375 ± 10	1.0 ± 0.1	0.9 ± 0.1	1.0 ± 0.04
SWJS	SWC-S	26 ± 1.9	27 ± 0 5	28 ± 3.7	40 ± 1.1	41 ± 0 9	380 ± 10	1.0 ± 0.1	1.0 ± 0.1	1.0 ± 0.04
SWJS	SWC-T	31 ± 2.3	30 ± 0.6	27 ± 2.7	42 ± 1.3	42 ± 1.0	402 ± 11	1.0 ± 0.1	0.9 ± 0.1	1.0 ± 0.04
SWC-US	SWC-N	27 ± 2.6	27 ± 0 5	30 ± 2.7	31 ± 0.9	30 ± 0.7	267 ± 8	1.0 ± 0.1	1.1 ± 0.1	1.0 ± 0.04
SWC-US	SWC-O	22 ± 2.1	23 ± 0 5	22 ± 2.4	33 ± 1.2	33 ± 0.8	249 ± 8	1.1 ± 0.1	1.0 ± 0.1	1.0 ± 0.04
SWC-US	SWC-P	22 ± 2.0	23 ± 0.4	22 ± 2.4	32 ± 1.0	33 ± 0.8	222 ± 7	1.0 ± 0.1	1.0 ± 0.1	1.0 ± 0.04
SWC-US	SWC17-38	24 ± 1.9	25 ± 0 5	24 ± 2.5	35 ± 1.0	36 ± 0.8	268 ± 7	1.0 ± 0.1	1.0 ± 0.1	1.0 ± 0.04
SWC-US	SWC17-39	19 ± 1.9	16 ± 0.4	17 ± 2.3	25 ± 0.9	25 ± 0.7	253 ± 8	0.9 ± 0.1	1.0 ± 0.1	1.0 ± 0.05
SWC-US	SWC17-40	14 ± 1.5	14 ± 0.4	14 ± 1.8	17 ± 0.8	18 ± 0.6	192 ± 7	1.0 ± 0.1	1.0 ± 0.1	1.1 ± 0.06
SWC-US	SWC17-41	20 ± 2.3	21 ± 0 5	22 ± 2.4	28 ± 1.1	29 ± 0.8	233 ± 8	1.1 ± 0.1	1.0 ± 0.1	1.0 ± 0.05
SWC-US	SWC17-42	14 ± 1.9	14 ± 0 3	14 ± 1.6	22 ± 0.9	23 ± 0.6	182 ± 6	1.0 ± 0.1	1.1 ± 0.1	1.0 ± 0.05
SWC-US	SWC17-43	14 ± 1.4	15 ± 0.4	15 ± 1.7	22 ± 0.9	22 ± 0.7	193 ± 7	1.1 ± 0.1	1.0 ± 0.1	1.0 ± 0.05
SWC-US	SWC17-44	19 ± 1.9	19 ± 0.4	18 ± 1.6	25 ± 0.9	25 ± 0.7	204 ± 6	1.0 ± 0.1	0.9 ± 0.1	1.0 ± 0.05

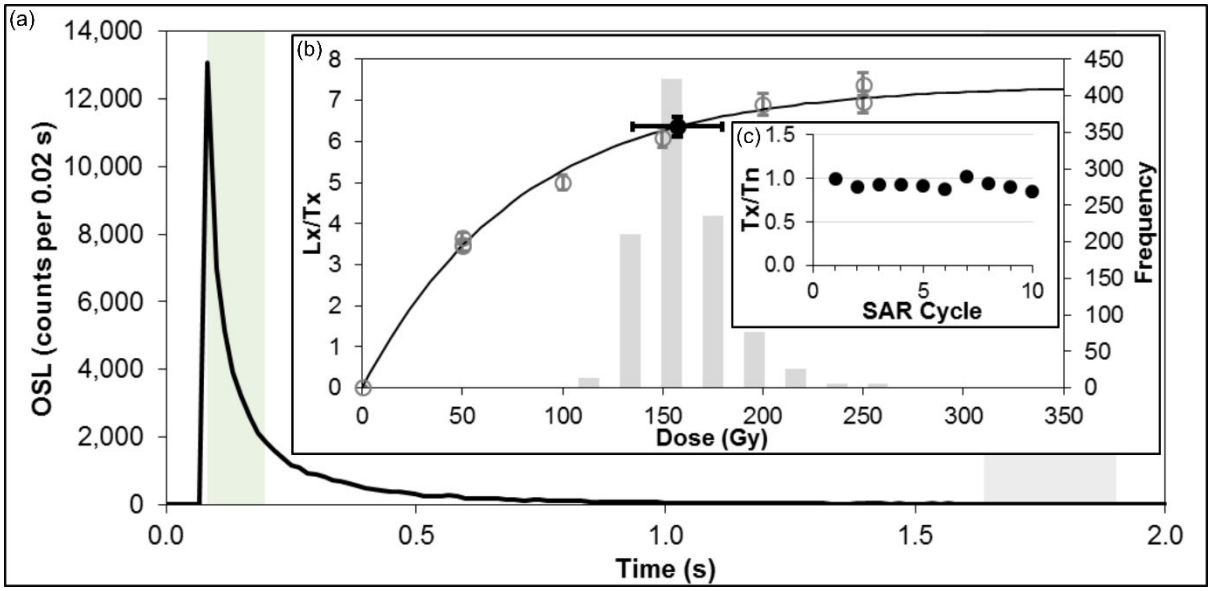

Figure D 1 Example of a representative single-grain OSL decay and dose response for the South Walker Creek OSL samples. The main plot shows the natural OSL signal decay curve for a grain from sample SWC-L, with green shading showing the integration region for the L_n, L_x, T_n, and T_x signals, and grey shading denoting the late-light background integral. The secondary and tertiary inset graphs (left to right) show the dose-response curve for this grain and its normalised test dose sensitivity (T_x/T_n) response through the SAR measurement cycles, respectively.

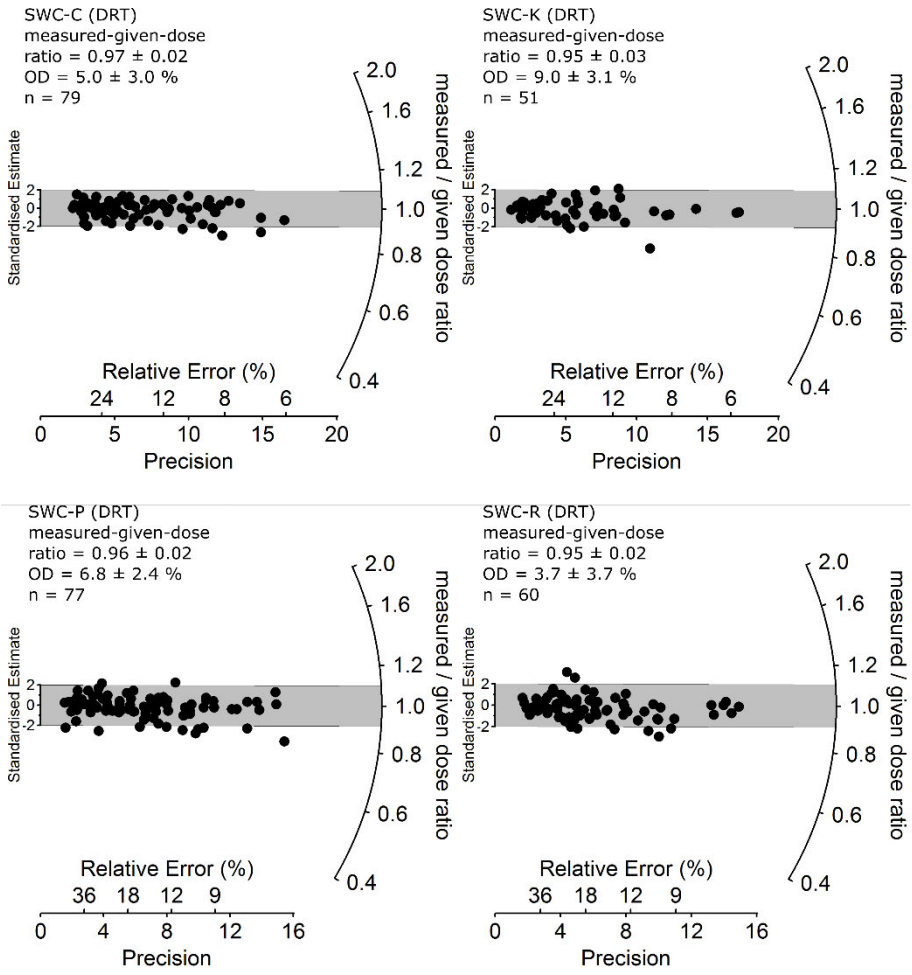

Figure D 2 Radial plots showing single-grain OSL dose recovery test results for samples SWC-C, SWC-K SWC-R and SWC-P using the SAR protocol shown in Table D2 (D_e errors are shown at 1σ). Grains were bleached within the Risø reader chamber using blue LEDs prior to administering a dose of 100 Gy. The central age model (CAM) measured-to-given dose ratio and the overdispersion (OD) value is shown for each sample.

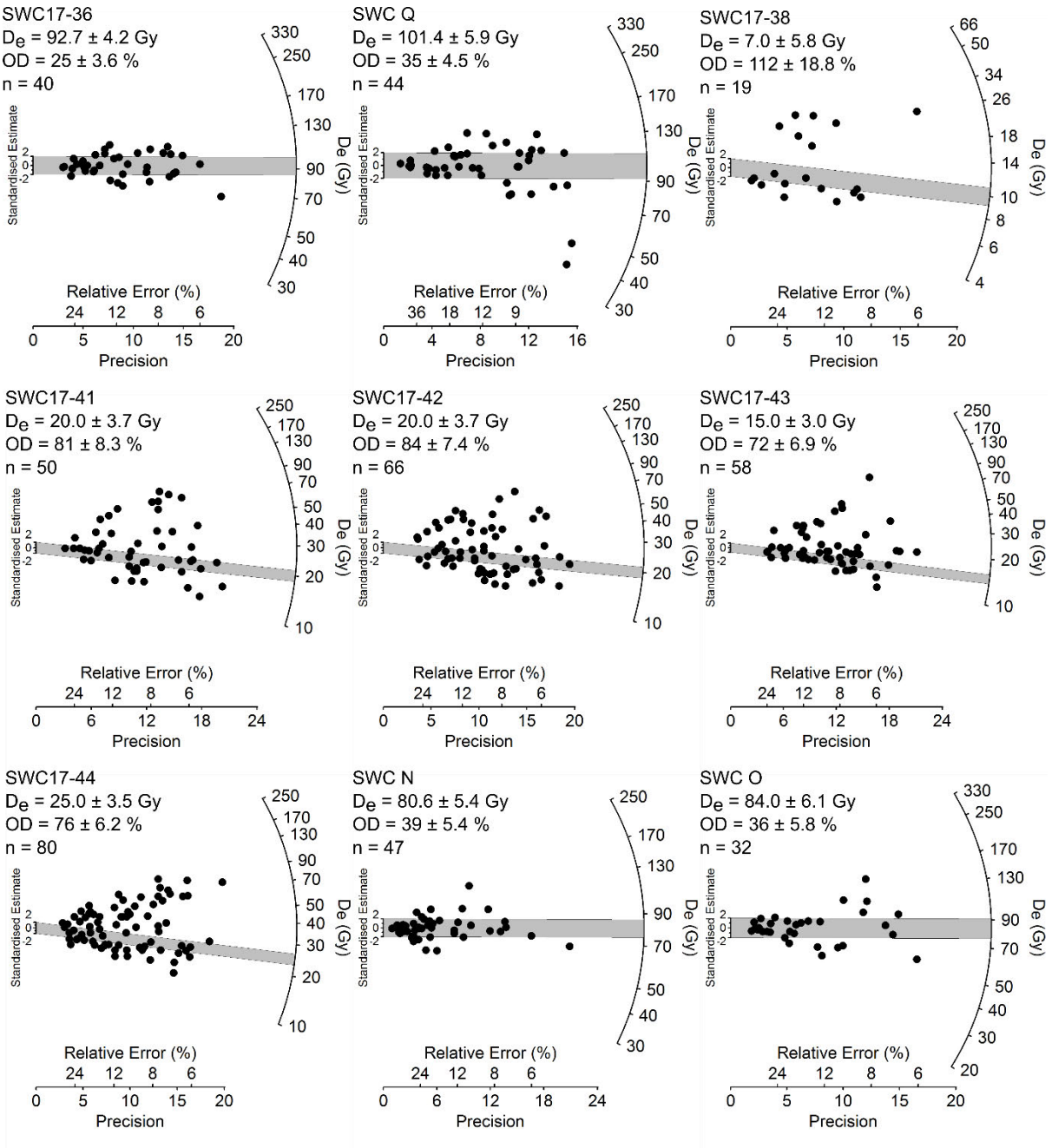

Figure D 3 Radial plots showing the single-grain OSL D_e distributions obtained for the South Walker Creek OSL samples not shown in Figure 5.4. The dark grey bands identify the subpopulation of well-bleached grains, which are centred on either the CAM D_e value (SWC17-36, SWC-Q, SWC-N and SWC-O) or MAM3 D_e value (all other samples).

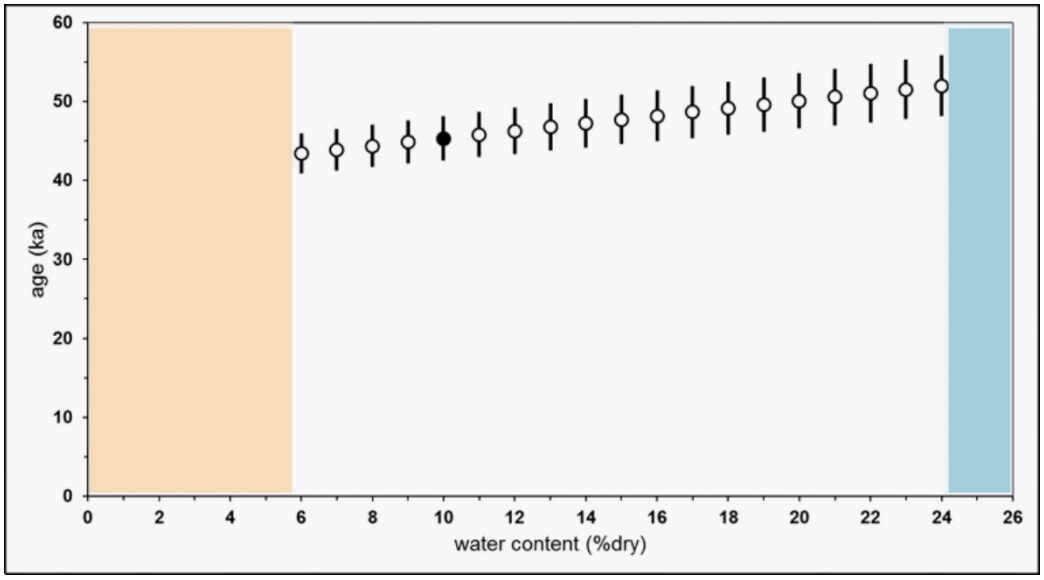

Figure D 4 The effect of varying the long-term average water content of sample SWC-R on the final OSL age estimate. The filled circle represents the long-term water content value selected for this particular sample (i.e., 40% of saturated water content) based on the proportional saturation assessments reported in Hocknull et al. (2020). The red shading represents the minimum end-member limit for long-term water content, which is approximated by the present-day water content of SWC-R. The blue shading represents the maximum end-member limit for long-term water content, which is equivalent to the saturated water content of SWC-R. The OSL age calculated using the preferred long-term water content (filled circle) is statistically indistinguishable (at 1σ) from those corresponding to all reasonable possible water content scenarios for this sample.

D2. Bayesian modelling results summaries

D2.1. Model 1 summary figure and table

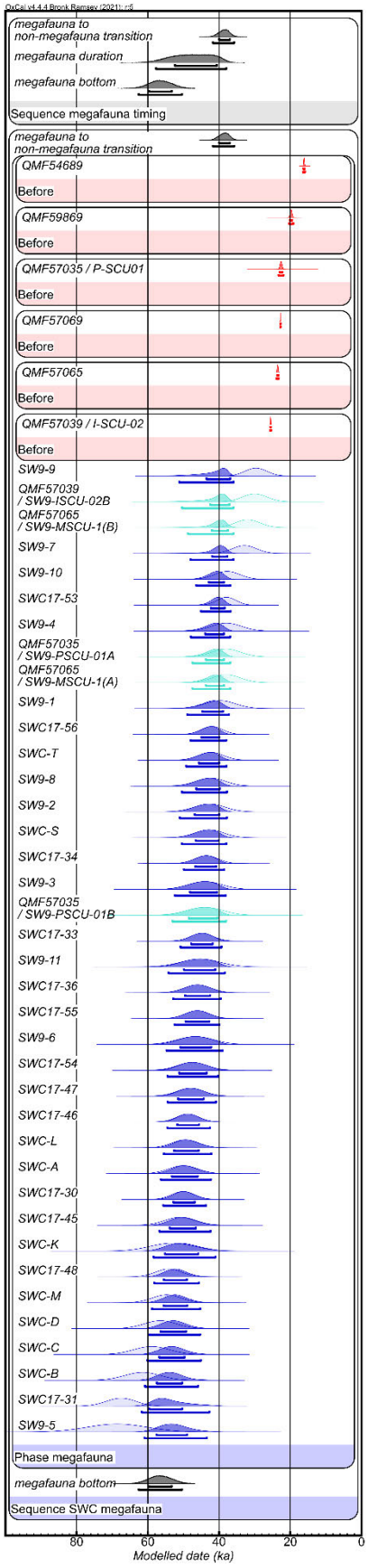

Figure D 5 Bayesian modelling results used to constrain the combined age range of the megafauna at the various South Walker Creek palaeontological sites. OSL (blue), US-ESR (aqua) and U-series (red) ages obtained in direct association with megafauna remains have been combined in a single *Phase* model, with delineating start and end boundaries. U-series ages have been modelled as minimum ages using the OxCal *Before()* command. The unmodelled age distributions for the dating samples (likelihoods) are shown in light shading, and are displayed in chronological order, as presented in Table D1. The modelled posterior distributions for the dating samples are shown in dark shading. The modelled posterior distributions for the *Phase* boundaries are shown in grey. The 68.2% and 95.4% ranges of the highest posterior probabilities are indicated by the horizontal bars underneath the probability density functions. The duration of the megafauna phase (top part of the plot) has been calculated from the modelled posterior probabilities of the upper and lower boundaries using the *Date()* query function.

Table D 8 Summary of the OxCal Bayesian modelling results for samples directly associated with megafauna fossil material within the South Walker Creek area (Model 1). The likelihood (unmodelled) and posterior (modelled) age ranges are presented for each of the numerical dating samples. Posterior (modelled) age ranges are also shown for the *Boundaries* of the *Phase* model, as well as for the duration of the *Phase* model (calculated using the *Date()* command). Posterior ages are presented as the 68.2% and 95.4% highest probability density ranges.

	Unmodelled (BP)				Modelled (BP)				outlier data		
	68%		95%		68%		95%		prior	post-erior	conver-gence
	from	to	from	to	from	to	from	to			
megafauna to non-megafauna transition					39942	36966	41711	35781			98.9
megafauna duration					**52412**	**40550**	**57705**	**37942**			**99.8**
QMF54689 [a]	16267	16019	16387	15899	16270	16003	16399	15887	5	2	99.7
QMF59869 [a]	20039	19493	20296	19236	20041	19492	20348	19182	5	3	99.9
QMF57035 / P-SCU01 [a]	22909	22291	23200	22000	22915	22285	23296	21910	5	4	99.9
QMF57069 [a]	22766	22752	22773	22745	22766	22752	22773	22744	5	1	99.8
QMF57065 [a]	23689	23399	23828	23260	23693	23396	23835	23250	5	2	100
QMF57039 / I-SCU-02 [a]	25552	25449	25600	25400	25551	25450	25600	25400	5	1	99.9
SW9-9	32812	26494	35787	23519	43499	36874	51166	35923	5	60	99.8
QMF57039 / SW9-ISCU-02B	33605	26395	37000	23000	42485	37095	50395	35940	5	44	99.8
QMF57065 / SW9-MSCU-1(B)	35605	28395	39000	25000	41995	37515	48750	35940	5	26	99.9
SW9-7	36361	29409	39701	26069	41908	37682	48008	35978	5	21	99.9
SW9-10	41362	34082	44860	30584	42855	38644	46389	36859	5	6	99.9
SWC17-53	40670	35178	43256	32592	42319	38426	45065	36747	5	6	99.9
SW9-4	42333	33623	46434	29522	43885	38600	47902	36909	5	5	100
QMF57035 / SW9-PSCU-01A	42120	33880	46000	30000	43680	38600	47440	36880	5	5	100
QMF57065 / SW9-MSCU-1(A)	42120	33880	46000	30000	43680	38600	47440	36880	5	5	100
SW9-1	44130	35294	48374	31050	44711	38907	48912	37218	5	4	99.9
SWC17-56	44946	38977	47813	36109	44975	39943	47960	38011	5	4	100
SWC T	45776	38730	49161	35345	45661	39962	49219	37924	5	4	100
SW9-8	46541	38115	50508	34148	46400	39815	50449	37770	5	4	100
SW9-2	47062	38214	51228	34048	46804	39932	51013	37827	5	4	100
SWC S	46824	38602	50695	34731	46539	40073	50450	37958	5	4	100
SWC17-34	46828	40232	49996	37064	46644	40825	49877	38562	5	4	100
SW9-3	48725	39119	53248	34596	48139	40538	52382	38160	5	4	100
QMF57035 / SW9-PSCU-01B	49150	38850	54000	34000	48500	40450	53050	38050	5	4	100
SWC17-33	47942	41622	50978	38586	47825	41814	50830	39336	5	4	100
SW9-11	50895	39657	56186	34366	49856	41074	54220	38346	5	4	100
SWC17-36	49844	42242	53423	38663	49559	42511	52880	39559	5	4	100
SWC17-55	49595	42603	52887	39311	49415	42728	52503	39911	5	4	100
SW9-6	51837	41449	56729	36557	50852	42228	54735	39001	5	4	100
SWC17-54	51694	43383	55686	39390	51189	43448	54489	40189	5	4	100
SWC17-47	51888	44172	55594	40466	51483	44297	54471	40818	5	4	100
SWC17-46	51989	45636	54980	42644	51699	45623	54505	42539	5	4	100
SWC L	53275	45759	56885	42149	52611	45759	55485	42149	5	4	100
SWC A	54196	46098	58009	42285	53214	46020	56320	42286	5	4	100
SWC17-30	53394	46926	56440	43880	52808	46842	55634	43671	5	4	100
SWC17-45	55335	46707	59479	42563	53859	46501	56735	42356	5	4	100
SWC K	59509	46687	65546	40650	55189	45853	58425	40998	5	4	100
SWC17-48	57913	50418	61513	46817	55535	49069	58217	45652	5	5	99.9
SWC M	58859	50579	62837	46601	55574	48917	58821	45305	5	5	99.9
SWC D	61109	51859	65552	47416	56398	49280	59527	45335	5	5	99.9
SWC C	64043	53825	68952	48916	56803	49690	60109	45132	5	7	99.9
SWC B	66627	56290	71494	51422	57459	50334	60821	45868	5	10	99.9
SWC17-31	71799	63219	75839	59179	59576	50330	61742	42708	5	48	99.9
SW9-5	77152	60092	85348	51896	57567	48954	60913	43434	5	9	99.9
megafauna bottom					59687	53312	62548	50439			99.5

[a] modelled as minimum ages using the OxCal *Before()* command.

D2.2. Model 2 and Model 3 summary figures and tables

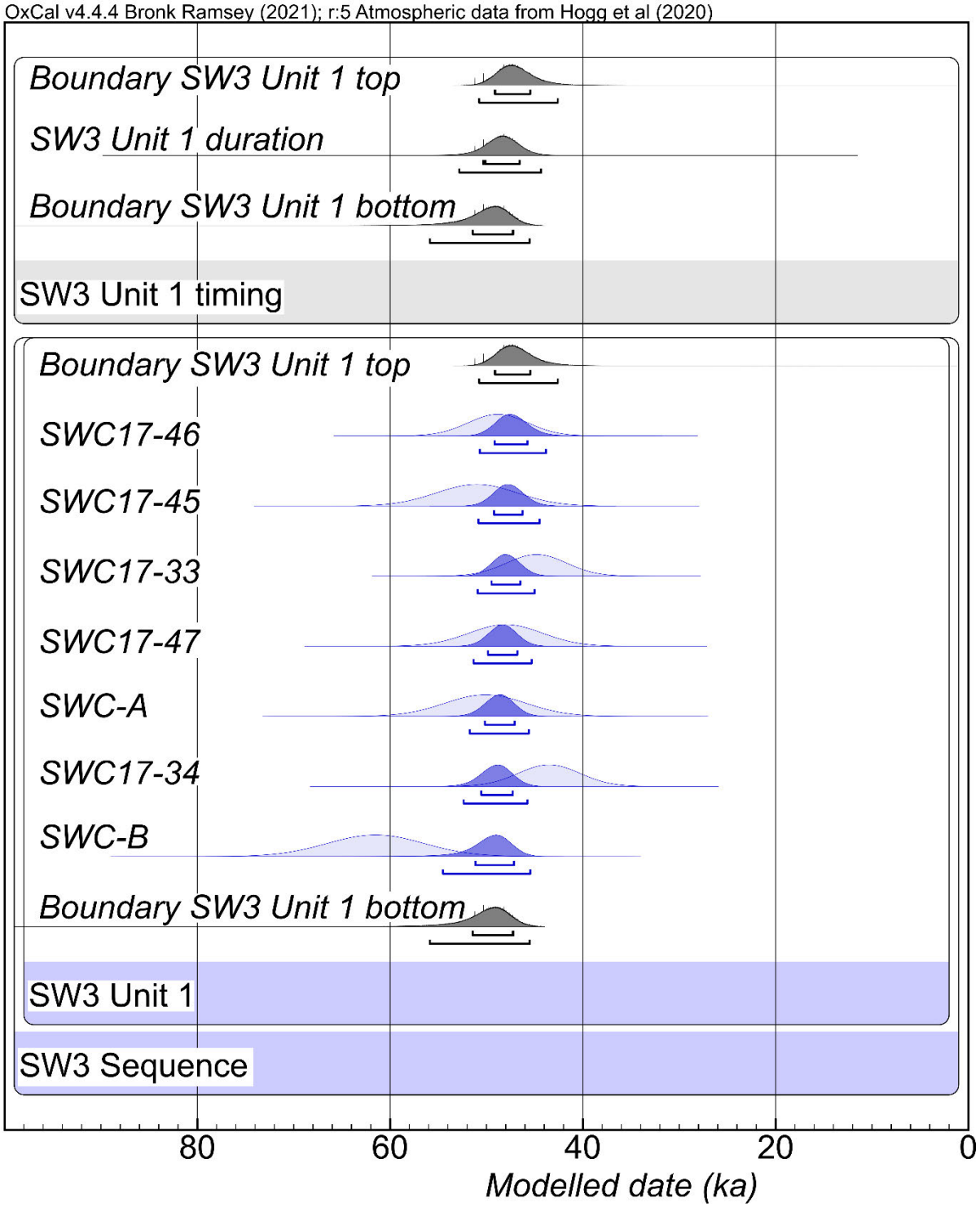

Figure D 6 Bayesian modelling results for the South Walker Creek SW3 (QML1470) stratigraphic sequence (Model 2). The unmodelled age distributions for the OSL dating samples (likelihoods) are shown as light blue probability density functions (PDFs). The modelled posterior distributions for the dating samples and stratigraphic unit boundaries are shown as dark blue and grey PDFs, respectively. The 68.2% and 95.4% ranges of the highest posterior probabilities are indicated by the horizontal bars underneath the PDFs. The duration of the SW3 Unit 1 Sequence (top part of the plot) has been calculated from the modelled posterior probabilities of the upper and lower boundaries using the *Date()* query function. Numerical modelling results are presented in Table D9.

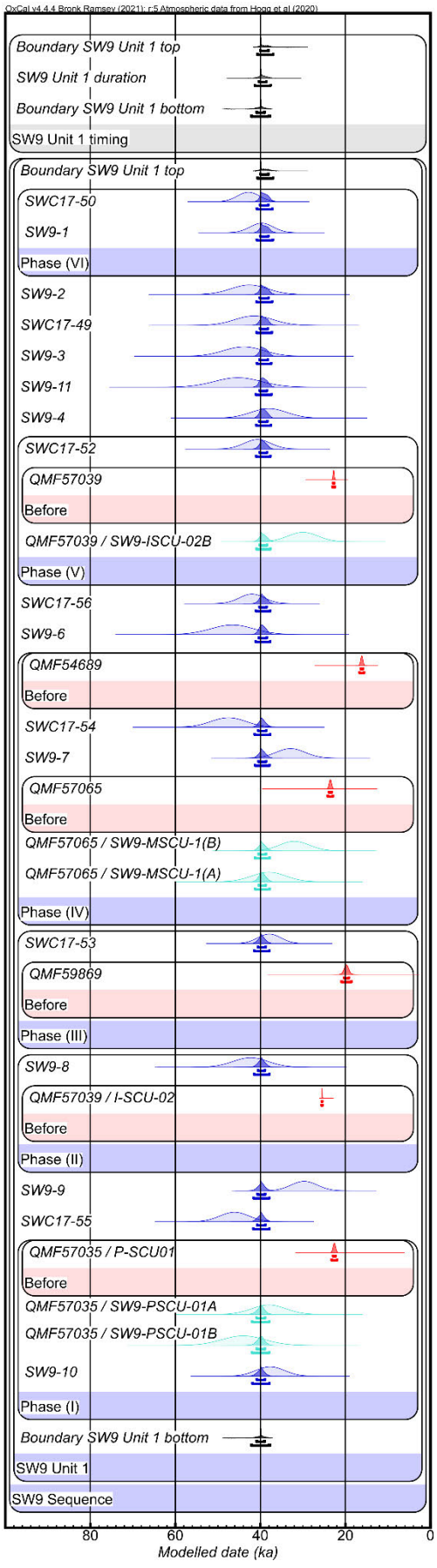

Figure D 7 Bayesian modelling results for the South Walker Creek SW9 (QML1470) stratigraphic sequence (Model 2). The unmodelled age distributions for the OSL (blue), US-ESR (aqua) and U-series (red) dating samples (likelihoods) are shown as light shading probability density functions (PDFs). U-series ages (red) have been modelled as minimum ages using the OxCal *Before()* command. The modelled posterior distributions for the OSL dating samples and stratigraphic unit boundaries are shown as dark blue and grey PDFs, respectively. OSL samples SW9-5 and SC17-48 were excluded from the model after being identified as significant outliers. The 68.2% and 95.4% ranges of the highest posterior probabilities are indicated by the horizontal bars underneath the PDFs. The durations of the SW9 Unit 1 and Unit 2 Sequences (top parts of the plot) have been calculated from the modelled posterior probabilities of the upper and lower boundaries for each Unit using the *Date()* query function. Numerical modelling results are presented in Table D9.

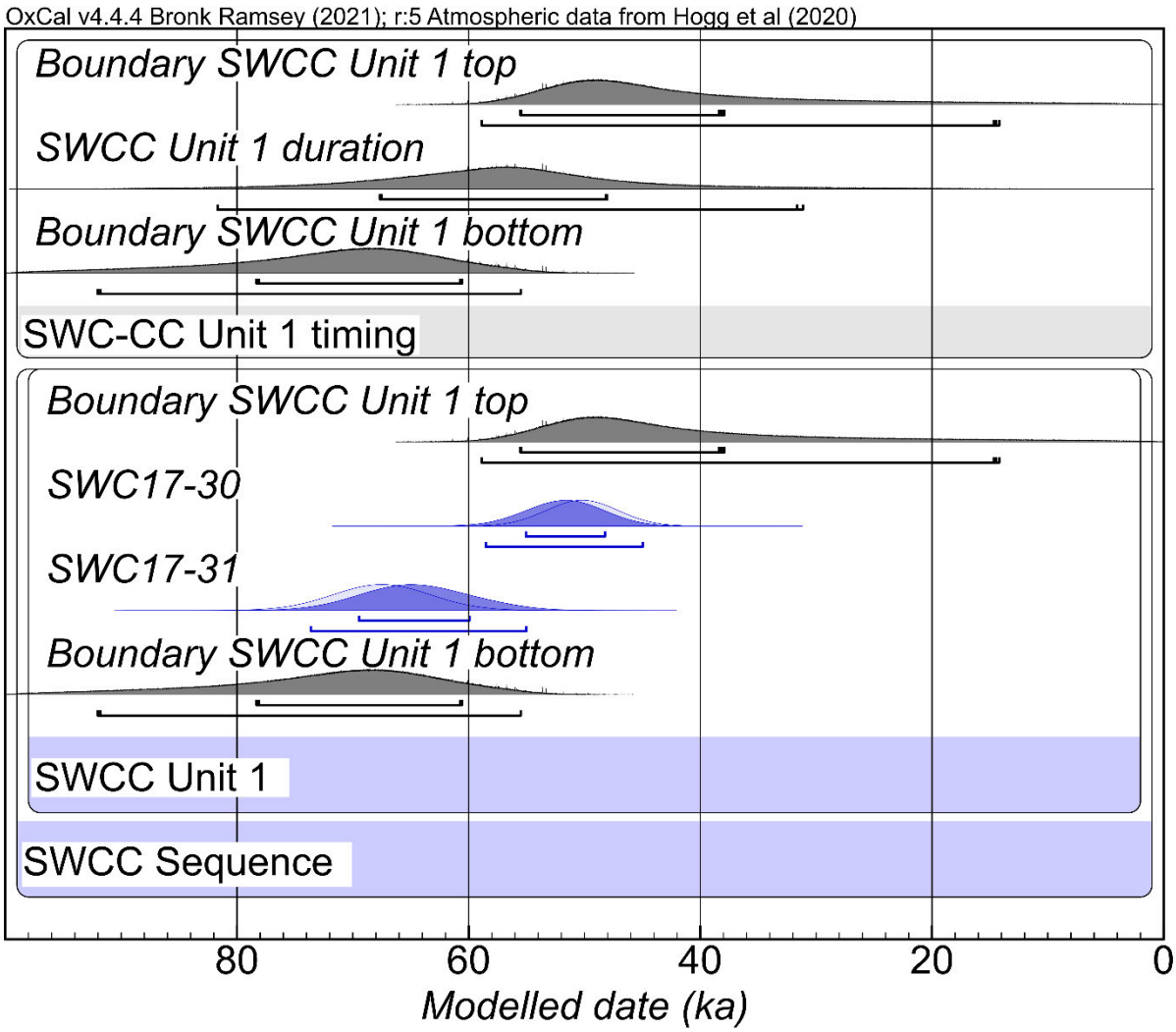

Figure D 8 Bayesian modelling results for the South Walker Creek SWCC (QML1470) stratigraphic sequence (Model 2). The unmodelled age distributions for the OSL dating samples (likelihoods) are shown as light blue probability density functions (PDFs). The modelled posterior distributions for the dating samples and stratigraphic unit boundaries are shown as dark blue and grey PDFs, respectively. The 68.2% and 95.4% ranges of the highest posterior probabilities are indicated by the horizontal bars underneath the PDFs. The durations of the SWCC Unit 1 and Unit 2 Sequences (top parts of the plot) have been calculated from the modelled posterior probabilities of the upper and lower boundaries for each Unit using the *Date()* query function. Numerical modelling results are presented in Table D9.

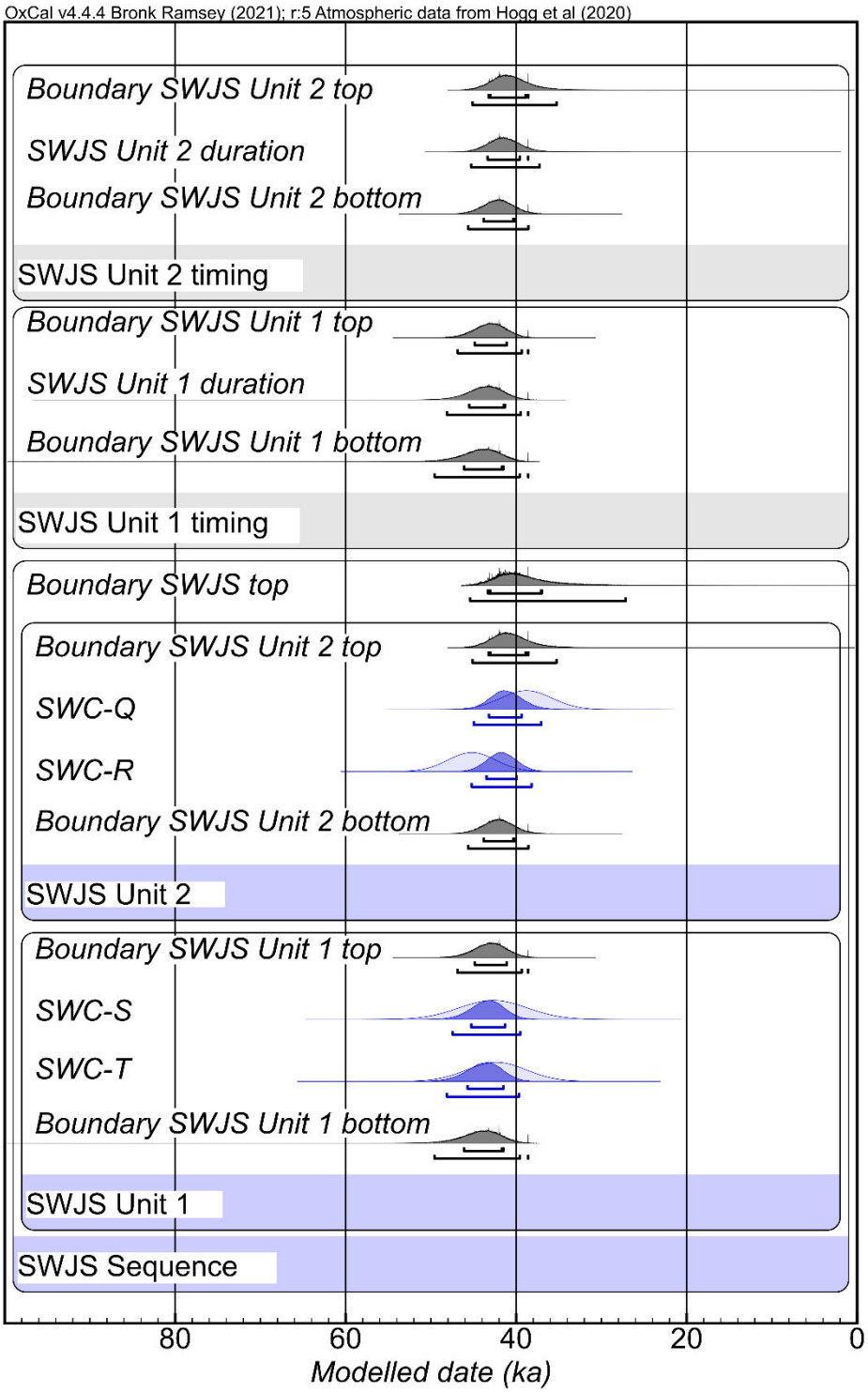

Figure D 9 Bayesian modelling results for the South Walker Creek, SWJS (QML1470) stratigraphic sequence (Model 2). The unmodelled age distributions for the OSL dating samples (likelihoods) are shown as light blue probability density functions (PDFs). The modelled posterior distributions for the dating samples and stratigraphic unit boundaries are shown as dark blue and grey PDFs, respectively. The 68.2% and 95.4% ranges of the highest posterior probabilities are indicated by the horizontal bars underneath the PDFs. The durations of the SWJS Unit 1 and Unit 2 Sequences (top parts of the plot) have been calculated from the modelled posterior probabilities of the upper and lower boundaries for each Unit using the *Date()* query function. Numerical modelling results are presented in Table D9.

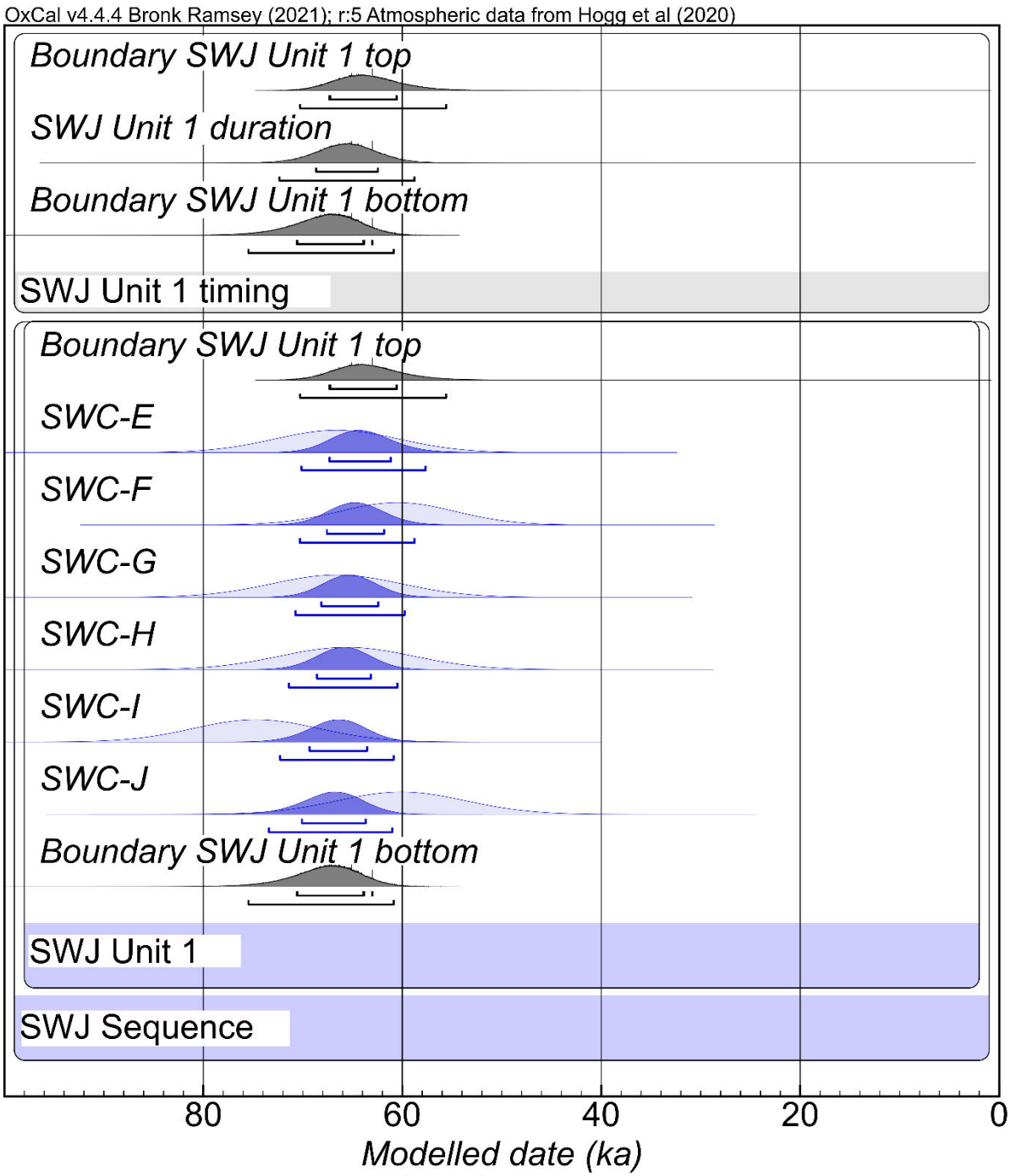

Figure D 10 Bayesian modelling results for the South Walker Creek, SWJ (QML1470) stratigraphic sequence (Model 2). The unmodelled age distributions for the OSL dating samples (likelihoods) are shown as light blue probability density functions (PDFs). The modelled posterior distributions for the dating samples and stratigraphic unit boundaries are shown as dark blue and grey PDFs, respectively. The 68.2% and 95.4% ranges of the highest posterior probabilities are indicated by the horizontal bars underneath the PDFs. The duration of the SWJ Unit 1 Sequence (top part of the plot) has been calculated from the modelled posterior probabilities of the upper and lower boundaries using the *Date()* query function. Numerical modelling results are presented in Table D9.

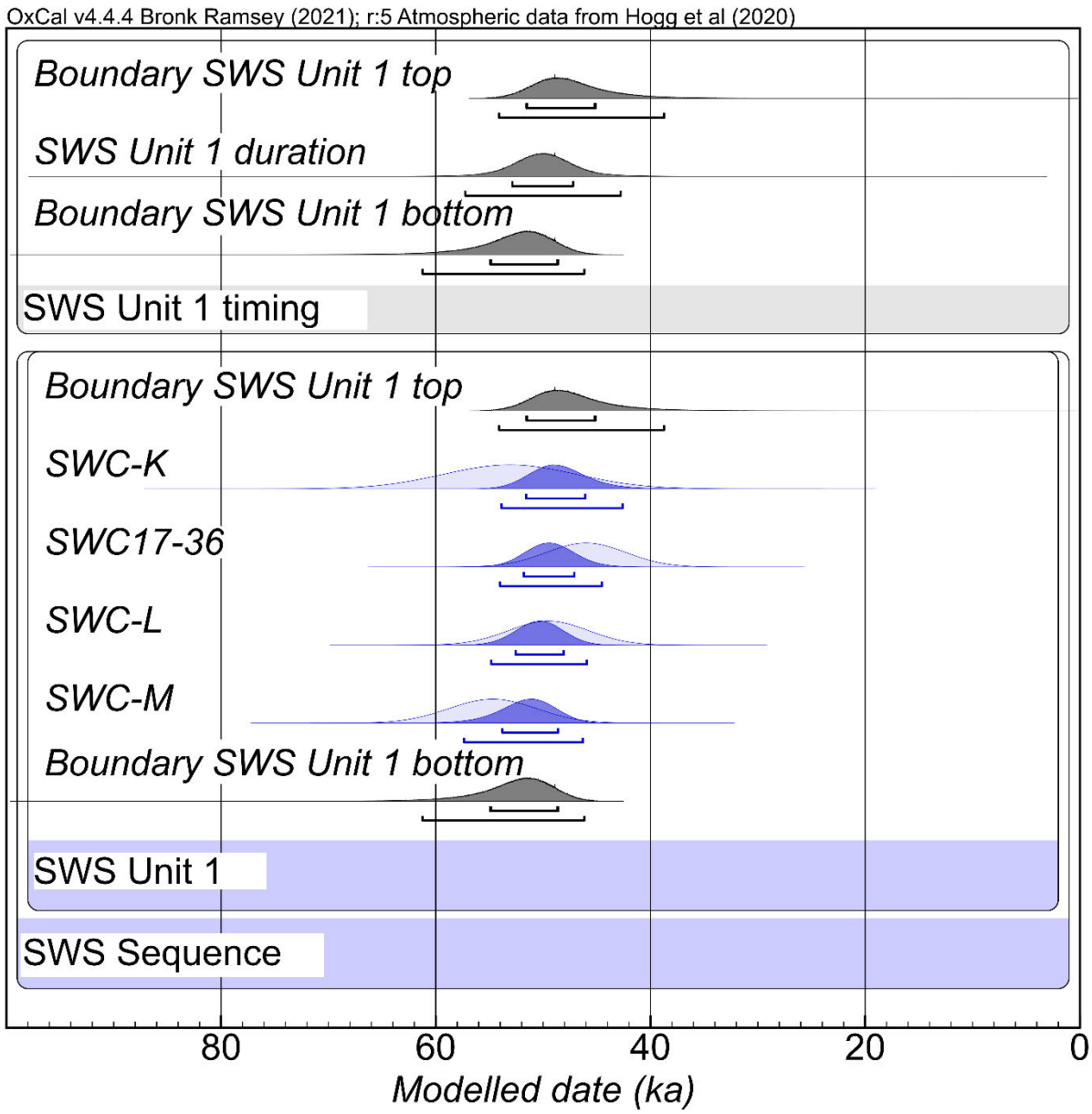

Figure D 11 Bayesian modelling results for the South Walker Creek, SWS (QML140) stratigraphic sequence (Model 2). The unmodelled age distributions for the OSL dating samples (likelihoods) are shown as light blue probability density functions (PDFs). The modelled posterior distributions for the dating samples and stratigraphic unit boundaries are shown as dark blue and grey PDFs, respectively. The 68.2% and 95.4% ranges of the highest posterior probabilities are indicated by the horizontal bars underneath the PDFs. The duration of the SWS Unit 1 Sequence (top part of the plot) has been calculated from the modelled posterior probabilities of the upper and lower boundaries using the *Date()* query function. Numerical modelling results are presented in Table D9.

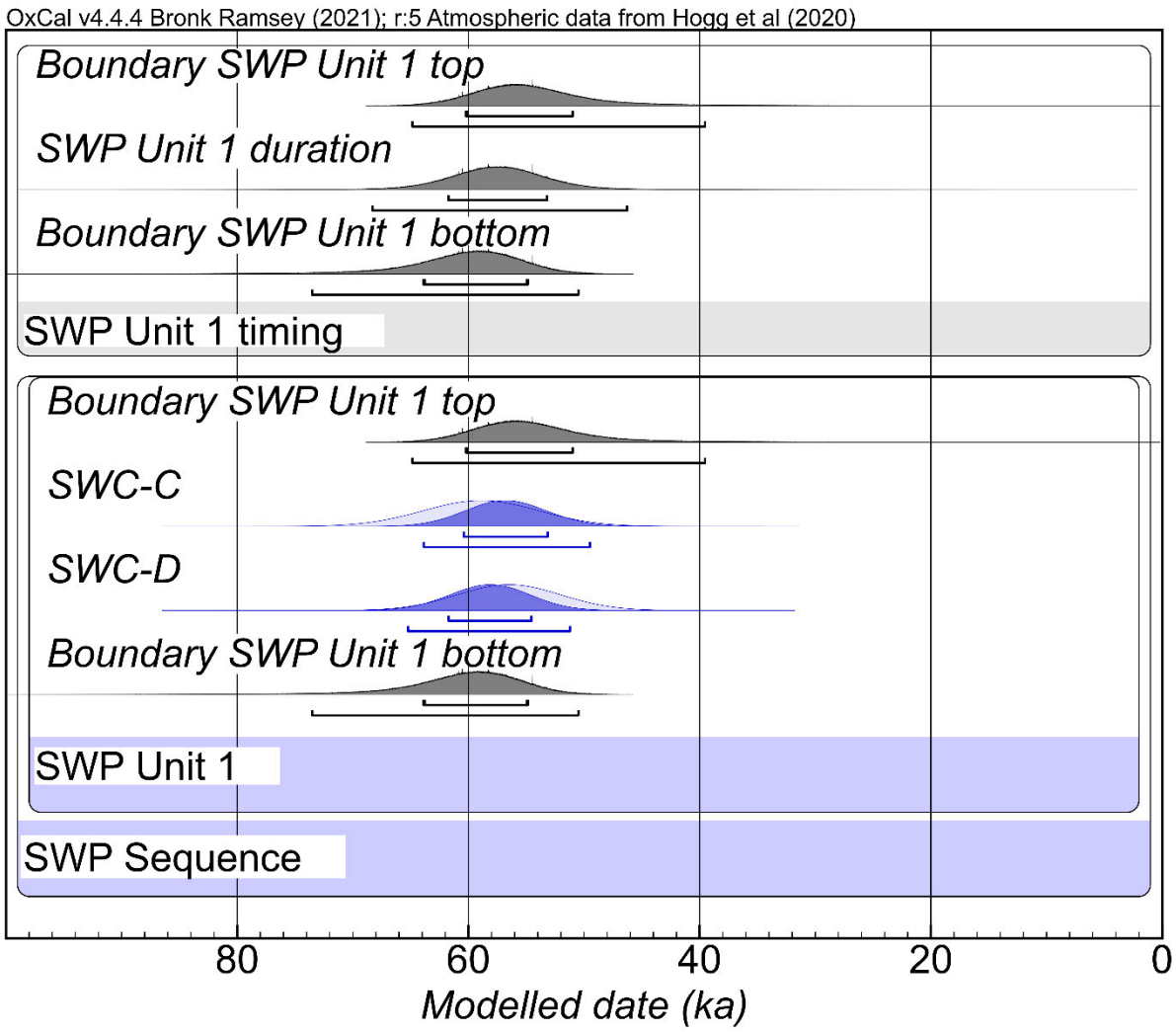

Figure D 12 Bayesian modelling results for the South Walker Creek, SWP (QML1470) stratigraphic sequence (Model 2). The unmodelled age distributions for the OSL dating samples (likelihoods) are shown as light blue probability density functions (PDFs). The modelled posterior distributions for the dating samples and stratigraphic unit boundaries are shown as dark blue and grey PDFs, respectively. The 68.2% and 95.4% ranges of the highest posterior probabilities are indicated by the horizontal bars underneath the PDFs. The duration of the SWP Unit 1 Sequence (top part of the plot) has been calculated from the modelled posterior probabilities of the upper and lower boundaries using the *Date()* query function. Numerical modelling results are presented in Table D9.

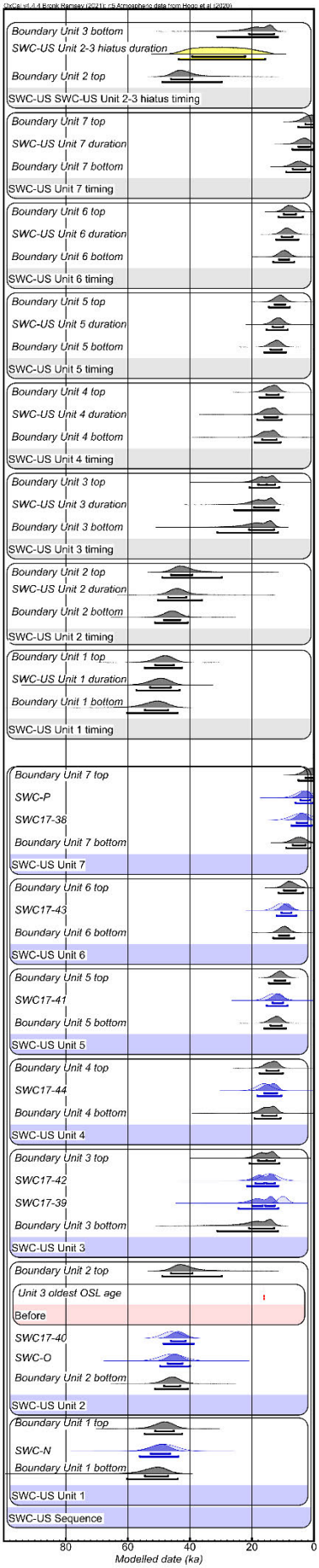

Figure D 13 Bayesian modelling results for the South Walker Creek, SWC-US (QML1470) stratigraphic sequence (Model 2). The unmodelled age distributions for the OSL dating samples (likelihoods) are shown as light blue probability density functions (PDFs). The modelled posterior distributions for the dating samples and stratigraphic unit boundaries are shown as dark blue and grey PDFs, respectively. The 68.2% and 95.4% ranges of the highest posterior probabilities are indicated by the horizontal bars underneath the PDFs. The durations of the various SWC-US Unit Sequences (top parts of the plot) have been calculated from the modelled posterior probabilities of the upper and lower boundaries for each Unit using the *Date()* query function. Note - An initial version of SWC-US Model 2, set up as described in the Methods section, yielded a model that was inadequate in resolving the prolonged temporal gap between Units 2 and 3, due to uncertainties. This issue resulted in high frequency noise in the lowermost 95% C.I. for the "Unit 2 top Boundary" posterior distribution. An additional *Before()* constraint has therefore been included in the final version of the SWC-US model, specifying that the Unit 2 likelihoods (SWC17-40 and SWC-O) precede the oldest likelihood obtained for the significantly younger overlying units. This minor, additional modelling constraint successfully removed the high frequency noise from the "Unit 2 top Boundary" marginal distribution, for the final version of SWC-US Model 2. Numerical modelling results are presented in Table D9.

Table D 9 Summary of the OxCal Bayesian modelling results for the timing of fluvial deposition at individual South Walker Creek sites dated in the present study and Chapter 4 (Model 2). The likelihood (unmodelled) and posterior (modelled) age ranges are presented for each of the numerical dating samples. Posterior (modelled) age ranges are also shown for the boundaries of each stratigraphic unit, as well as for the duration of each unit (calculated using the *Date()* command). Posterior ages are presented as the 68 % and 95 % highest probability density ranges.

SW9	Unmodelled (BP)				Modelled (BP)				Outlier data		
	68%		95%		68%		95%		prior	posterior	convergence
	from	to	from	to	from	to	from	to			
Boundary SW9 Unit 1 top					40017	38042	40723	36983			8.3
SW9 Unit 1 duration					**40367**	**38569**	**41311**	**37581**			**17.5**
SWC17-50 [a, (i)]	45478	40122	48000	37600	40096	38146	40824	37132	5	5	58.5
SW9-1 [a, (i)]	42481	36919	45100	34300	40060	38116	40843	37063	5	4	43.8
SW9-2 [a,]	47029	38171	51200	34000	40144	38080	40918	37220	5	5	55.2
SWC17-49 [a,]	46135	36865	50500	32500	40105	38215	40915	37270	5	4	58.2
SW9-3 [a,]	48741	39059	53300	34500	40216	38242	40827	37443	5	5	58.4
SW9-11 [a,]	50965	39635	56300	34300	40215	38455	41095	37355	5	5	70.5
SW9-4 [a,]	42326	33674	46400	29600	40276	38344	40990	37504	5	4	60.9
SWC17-52 [a, (ii)]	43893	37507	46900	34500	40201	38434	41007	37628	5	4	54.7
QMF57039 [a, b, (ii)]	22899	22619	23033	22485	22902	22617	23061	22457	5	4	99.9
QMF57039 / SW9-ISCU-02B [a, (ii)]	33605	26395	37000	23000	40185	38435	40955	37630	5	14	52.3
SWC17-56 [a,]	44987	39013	47800	36200	40260	38520	41072	37650	5	4	63.3
SW9-6 [a,]	51750	41450	56600	36600	40400	38500	41150	37700	5	5	70.5
QMF54689 [a, b, (iii)]	16392	15894	16631	15655	16396	15869	16681	15603	5	5	99.9
SWC17-54 [a, (iii)]	51723	43277	55700	39300	40509	38623	41370	37680	5	6	60.3
SW9-7 [a, (iii)]	36402	29398	39700	26100	40466	38664	41248	37814	5	7	52.9
QMF57065 [a, b, (iii)]	23836	23253	24110	22978	23836	23248	24165	22925	5	5	99.9
QMF57065 / SW9-MSCU-1(B) [a, (iii)]	35605	28395	39000	25000	40430	38680	41235	37805	5	8	53.3
QMF57065 / SW9-MSCU-1(A) [a, (iii)]	42120	33880	46000	30000	40400	38720	41240	37800	5	4	70.7
SWC17-53 [a, (iv)]	40681	35119	43300	32500	40600	38737	41437	37900	5	4	50.9
QMF59869 [a, b, (iv)]	20306	19226	20824	18708	20317	19169	20930	18598	5	5	99.9
N SW9-8 [a, (v)]	46523	38077	50500	34100	40550	38910	41493	37885	5	4	61.5
QMF57039 / I-SCU-02 [a, b, (v)]	25552	25449	25600	25400	25552	25449	25610	25390	5	4	99.8
SW9-9 [a,]	32893	26507	35900	23500	40666	38868	41627	37876	5	25	54.8
SWC17-55 [a,]	49602	42598	52900	39300	40772	38834	41690	37882	5	6	51.5
QMF57035 / P-SCU01 [a, b (vi)]	22909	22291	23200	22000	22909	22291	23263	21940	5	5	99.9
QMF57035 / SW9-PSCU-01A [a, (vi)]	42120	33880	46000	30000	40880	38880	41960	37920	5	4	70.9
QMF57035 / SW9-PSCU-01B [a, (vi)]	49150	38850	54000	34000	40850	38900	42000	37900	5	5	74.9
SW9-10 [a, (vi)]	41202	34198	44500	30900	40840	38902	41894	37916	5	4	49.9
Boundary SW9 Unit 1 bottom					40943	38987	42132	37696			10.8

SW3	Unmodelled (BP)				Modelled (BP)				Outlier data		
	68%		95%		68%		95%		prior	posterior	convergence
	from	to	from	to	from	to	from	to			
Boundary SW3 Unit 1 top					49121	45432	50752	42602			95.3
SW3 Unit 1 duration					**50324**	**46557**	**52799**	**44346**			**96.1**
SWC17-46	51993	45607	55000	42600	49160	45750	50679	43828	5	5	99.8
SWC17-45	55326	46674	59400	42600	49222	46240	50818	44476	5	5	99.9
SWC17-33 [a]	47993	41607	51000	38600	49470	46494	50927	45006	5	5	99.9
SWC17-47 [a]	51914	44086	55600	40400	49840	46800	51322	45318	5	5	99.9
SWC-A [a]	54426	45774	58500	41700	50146	47080	51742	45610	5	5	99.9
SWC17-34 [a]	46796	40204	49900	37100	50528	47264	52352	45760	5	6	99.9
SWC-B [a]	66650	56350	71500	51500	51150	47150	54500	45450	5	7	99.9
Boundary SW3 Unit 1 bottom					51431	47195	55877	45501			95.3

SWCC	Unmodelled (BP)				Modelled (BP)				Outlier data		
	68%		95%		68%		95%		prior	posterior	convergence
	from	to	from	to	from	to	from	to			
Boundary SWCC Unit 1 top					55539	37913	58881	14195			98.6
SWCC Unit 1 duration					**67652**	**48032**	**81678**	**31141**			**98.8**
SWC17-30 [a,]	53393	47007	56400	44000	55050	48230	58522	44975	5	5	100
SWC17-31 [a,]	71826	63174	75900	59100	69466	59932	73624	55018	5	5	99.9
Boundary SWCC Unit 1 bottom					78312	60584	92017	55498			98.6

SWJ	Unmodelled (BP)				Modelled (BP)				Outlier data		
	68%		95%		68%		95%		prior	posterior	convergence
	from	to	from	to	from	to	from	to			
Boundary SWJ Unit 1 top					67314	60563	70265	55611			98.4
SWJ Unit 1 duration					**68646**	**62456**	**72342**	**58768**			**98.9**
SWC-E [a,]	73006	60182	79044	54144	67319	61156	70120	57670	5	5	99.9
SWC-F [a,]	66474	54526	72100	48900	67578	61836	70304	58762	5	5	99.9
SWC-G [a,]	73295	59905	79600	53600	68150	62430	70750	59765	5	5	99.9
SWC-H [a,]	72501	58699	79000	52200	68577	63150	71391	60470	5	5	99.9
SWC-I [a,]	81189	68211	87300	62100	69319	63523	72280	60877	5	5	99.9
SWC-J [a,]	66795	53405	73100	47100	70100	63665	73415	61000	5	5	99.9
Boundary SWJ Unit 1 bottom					70588	63017	75457	60873			98.2

SWJS	Unmodelled (BP)				Modelled (BP)				Outlier data		
	68%		95%		68%		95%		prior	posterior	convergence
	from	to	from	to	from	to	from	to			
Boundary SWJS Unit 2 top					43211	38567	45108	35277			88.6
SWJS Unit 2 duration					**43358**	**38576**	**45284**	**37240**			**90.2**
SWC-Q	41890	35710	44800	32800	43180	39340	44980	37060	5	5	99.1
SWC-R	48084	42316	50800	39600	43468	39940	45204	38176	5	5	99.1
Boundary SWJS Unit 2 bottom					43813	40222	45597	38555			91.2
SWJS Unit 1-2 Transition											
Boundary SWJS Unit 1 top					44832	41108	46875	38573			91.2
SWJS Unit 1 duration					**45486**	**41320**	**48095**	**38575**			**90.2**
SWC-S	46820	38580	50700	34700	45280	41280	47440	39520	5	5	99.3
SWC-T	45905	38695	49300	35300	45680	41515	48130	39660	5	5	99
Boundary SWJS Unit 1 bottom					46107	41480	49559	38575			88

SWP	Unmodelled (BP)				Modelled (BP)				Outlier data		
	68%		95%		68%		95%		prior	posterior	convergence
	from	to	from	to	from	to	from	to			
Boundary SWP Unit 1 top					60199	50980	64840	39533			97.9
SWP Unit 1 duration					**61729**	**53191**	**68303**	**46280**			**98.1**
SWC-C	64050	53750	68900	48900	60400	53150	63850	49500	5	5	99.9
SWC-D	61135	51865	65500	47500	61705	54550	65215	51220	5	5	99.9
Boundary SWP Unit 1 bottom					63887	54866	73519	50487			97.6

SWS	Unmodelled (BP)				Modelled (BP)				Outlier data		
	68%		95%		68%		95%		prior	posterior	convergence
	from	to	from	to	from	to	from	to			
Boundary SWS Unit 1 top					51557	45104	54108	38719			98.8
SWS Unit 1 duration					**52872**	**47207**	**57257**	**42776**			**99.1**
SWC-K	59486	46714	65500	40700	51578	46060	53872	42588	5	5	100
SWC17-36	49811	42189	53400	38600	51789	47090	54009	44537	5	5	99.9
SWC-L	53311	45689	56900	42100	52566	48089	54823	45943	5	5	99.9
SWC-M	58923	50477	62900	46500	53793	48627	57360	46290	5	5	99.9
Boundary SWS Unit 1 bottom					54942	48590	61231	46172			98.7

SWC-US	Unmodelled (BP)				Modelled (BP)				Outlier data		
	68%		95%		68%		95%		prior	posterior	convergence
	from	to	from	to	from	to	from	to			
Boundary SWC-US Unit 7 top					2791	-2	5057	-2			98
SWC-US Unit 7 duration					**5056**	**1463**	**6986**	**349**			**97.7**
SWC-P	5778	422	8300	-2	4372	1278	5958	316	5	3	100
SWC17-38	7399	601	10600	-2	5620	2089	7303	769	5	4	100
Boundary SWC-US Unit 7 bottom					6877	2727	8958	1157			97.2
SWC-US Unit 6-7 Transition											
Boundary SWC-US Unit 6 top					9748	-2	11417	3579			97.6
SWC-US Unit 6 duration					**10446**	**-2**	**12199**	**5045**			**98**
SWC17-43	12663	8337	14700	6300	10498	7264	12052	5710	5	4	100
Boundary SWC-US Unit 6 bottom					11332	7977	13121	6337			98
SWC-US Unit 5-6 Transition											
Boundary SWC-US Unit 5 top					12698	-2	14567	7759			97.9
SWC-US Unit 5 duration					**13315**	**-2**	**15276**	**8454**			**98**
SWC17-41	15375	10225	17800	7800	13350	9975	15250	8550	5	3	99.9
Boundary SWC-US Unit 5 bottom					14037	-2	16078	9015			97.8
SWC-US Unit 4-5 Transition											
Boundary SWC-US Unit 4 top					15406	11351	17574	10040			99.4
SWC-US Unit 4 duration					**15999**	**11727**	**18295**	**10428**			**99.5**
SWC17-44	18572	13628	20900	11300	16048	11848	18256	10504	5	4	99.6
Boundary SWC-US Unit 4 bottom					16694	12082	19150	10777			99.3
SWC-US Unit 3-4 Transition											
Boundary SWC-US Unit 3 top					18058	12514	20814	11239			99.3
SWC-US Unit 3 duration					**19387**	**12705**	**25689**	**11307**			**99.2**
SWC17-42	17184	11416	19900	8700	18884	12612	21600	11492	5	7	99.5
SWC17-39	11545	8455	13000	7000	19945	12640	24340	11500	5	64	99.4
Boundary SWC-US Unit 3 bottom					20923	12864	31161	11575			97.4
SWC-US Unit 2-3 hiatus duration [c]					***39288***	***22118***	***43595***	***15753***			***99.7***
Boundary SWC-US Unit 2 top					46104	39172	48904	29717			97.8
SWC-US Unit 2 duration					**47018**	**41174**	**50283**	**36112**			**99.1**
SWC17-40	49093	42707	52100	39700	46122	41379	48509	38744	5	5	99.8
SWC-O	49920	41680	53800	37800	47200	42400	49600	40000	5	4	99.9
Boundary SWC-US Unit 2 bottom					48378	43114	51290	40636			99
SWC-US Unit 1-2 Transition											
Boundary SWC-US Unit 1 top					51163	45155	54610	42507			99.5
SWC-US Unit 1 duration					**52815**	**46155**	**57265**	**43316**			**99.7**
SWC-N	52726	44074	56800	40000	52624	46366	56194	43678	5	4	100
Boundary SWC-US Unit 1 bottom					54513	46964	60269	43941			99.2

[a] ages sourced from Supplementary Table 11 of Hocknull et al. (2020).
[b] modelled as minimum ages using the OxCal *Before()* command.
[c] modelled age represents the duration of time missing between adjacent units (expressed as a temporal range in years, rather than a numerical age in years ago). This modelled duration has been calculated using the *Interval*() query function, and provides the temporal range between the posterior probability density distributions of successive stratigraphic boundaries.
[(i)–(vi)] ages from equivalent depths, or replicate samples, modelled using individual *Phase()* commands.

D2.3. Model 4 summary figures and tables

The likelihood datasets included in the basin-specific models below (Model 4) are sourced from published materials, as detailed in the main text. Individual ages have been modelled as reported in the original publications, and take into account any relevant interpretations or complications noted by the authors (e.g., ages reported as non-finite estimates or indirect ages derived from bracketing deposits have been represented in the model using the *Before()* and *After()* commands). The modelled temporal distribution of hydrological activity for each basin-specific *Phase* model has been calculated using the *KDE_Plot* and *Sum* functions.

The Cohen et al. (2015) dataset includes a first-order power-law correction for potential time-dependent preservation biases that could affect frequency distributions of preserved sedimentary events over protracted geological timescales (the so-called Sadler Effect; Sadler (1981); Schumer and Jerolmack, 2009). Unfortunately, the necessary elevation or comparative baseline datasets needed to perform these preservation corrections are not available for the other records included in our comparison (including the SWC datasets). As such, we exert caution when comparing the amplitudes of KDE peaks over different time periods or across different basins; though we expect the overall temporal distribution of probability peaks within/between basins to be minimally affected by the Sadler effect given the relatively limited timescale under consideration (at least by geological standards) and the similar depositional dynamics (fluvial or alluvial) experienced by the various river and wetland sites.

D2.3.1. Gilbert River

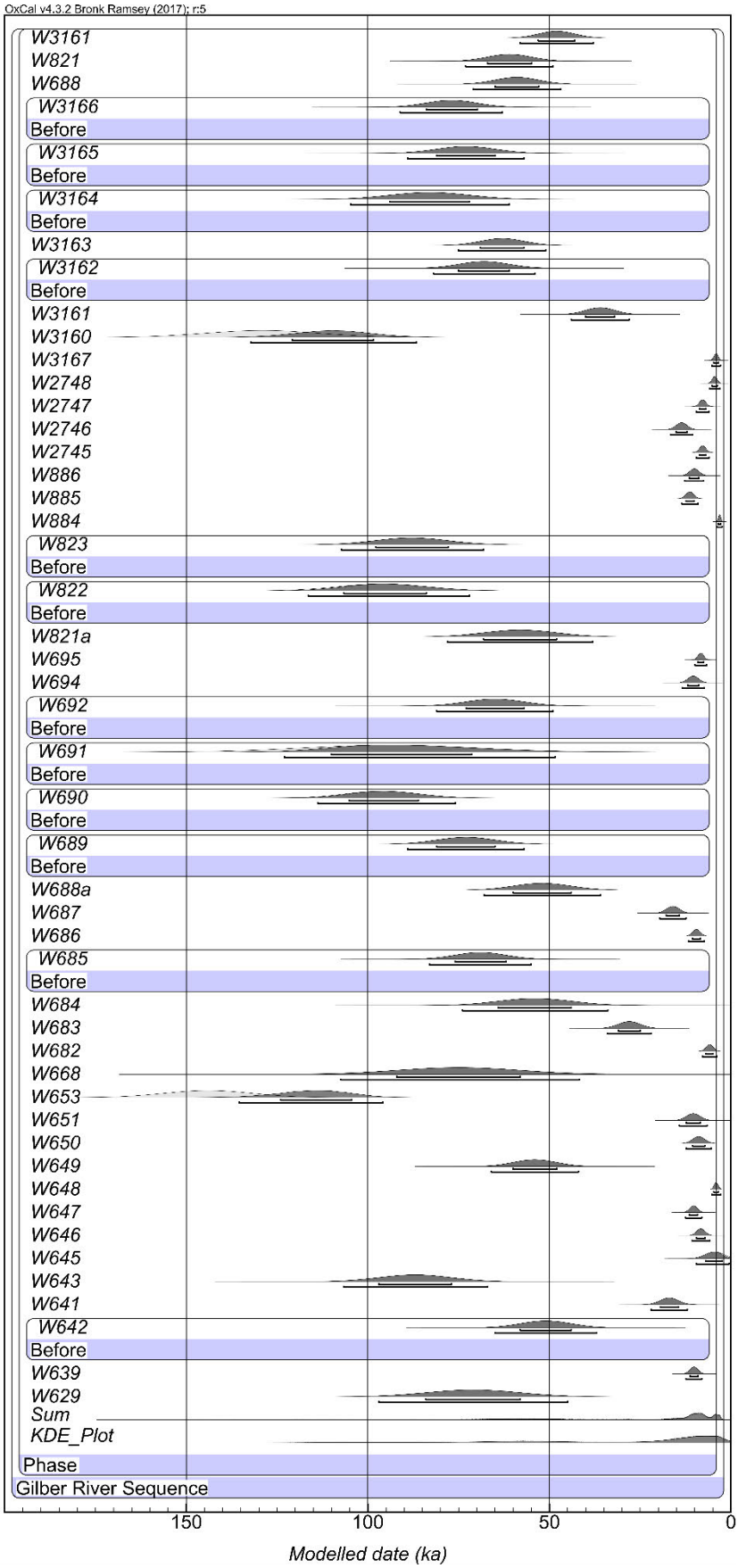

Figure D 14 Bayesian modelling results used to constrain the temporal distribution of hydrological activity within the Gilbert River catchment (Model 4) (Nanson et al., 2005). All likelihoods obtained on sedimentary units representing episodes of fluvial deposition have been combined in a single *Phase* model. Likelihoods that were originally interpreted as minimum ages by (Nanson et al., 2005) have been modelled as such using the OxCal *Before()* command. The unmodelled age distributions for the dating samples (likelihoods) are shown in light shading, and are presented in Table D10. The modelled posterior distributions for the dating samples are shown in dark shading. The 68.2% and 95.4% ranges of the highest posterior probabilities are indicated by the horizontal bars underneath the probability density functions. The temporal distributions of hydrological activity (bottom part of the plot) has been calculated from the modelled posterior probabilities using the *KDE_Plot* and *Sum()* query functions.

Table D 10 Summary of the OxCal Bayesian modelling results for hydrological activity in the Gilbert River catchment (Figure D14), as inferred from modelled fluvial sediment deposition across the sites described in (Nanson et al., 2005). The likelihood (unmodelled) and posterior (modelled) age ranges are presented for each of the numerical dating samples. Posterior (modelled) age ranges are also shown for the *Boundaries* of the *Phase* model. Posterior ages are presented as the 68.2% and 95.4% highest probability density ranges.

	Unmodelled (BP)				Modelled (BP)				
	68%		95%		68%		95%		Conver -gence
	from	to	from	to	from	to	from	to	
Boundary End 1					3303	-3167	3472	-6433	31.4
W3161	53100	42900	58000	38000	53100	43000	58000	37950	99.7
W821	67120	54880	73000	49000	67000	54940	73060	49000	99.7
W688	65120	52880	71000	47000	65000	52940	70940	46940	99.7
W3166 [a]	84140	69860	91000	63000	83930	69790	91070	63000	99.7
W3165 [a]	81160	64840	89000	57000	81080	65000	89000	57000	99.7
W3164 [a]	94220	71780	105001	61000	94000	72000	104671	61110	99.8
W3163	69120	56880	75000	51000	69060	57000	75060	51060	99.7
W3162 [a]	75140	60860	82000	54000	75000	61000	81930	53930	99.7
W3161	40080	31920	44000	28000	40040	32040	44000	28000	99.7
W3160	145321	112681	161001	97000	120841	98440	132201	86600	99.3
W3167	4712	3488	5300	2900	4706	3506	5306	2918	99.8
W2748	5214	3786	5900	3100	5200	3793	5900	3107	99.7
W2747	8718	6882	9600	6000	8700	6891	9600	6000	99.8
W2746	15130	12070	16600	10600	15100	12085	16600	10570	99.8
W2745	8718	6882	9600	6000	8691	6882	9591	5982	99.8
W886	11426	8774	12700	7500	11413	8800	12700	7500	99.6
W885	12422	10178	13500	9100	12411	10200	13511	9100	99.7
W884	3467	2773	3800	2440	3487	2804	3820	2471	99.7
W823 [a]	98200	77800	108001	68000	97800	77800	107201	68100	99.8
W822 [a]	108241	83760	120001	72000	106561	83880	116401	72000	99.8
W821a	68200	47800	78000	38000	68100	48000	78100	38100	99.7
W695	9116	7484	9900	6700	9092	7492	9908	6700	99.7
W694	11930	8870	13400	7400	11900	8885	13430	7415	99.7
W692 [a]	73160	56840	81000	49000	72920	56920	81000	49000	99.7
W691 [a]	117461	70540	140001	48000	110101	71460	122981	48460	99.8
W690 [a]	106201	85800	116001	76000	105201	86100	113801	75900	99.8
W689 [a]	81160	64840	89000	57000	81080	65000	89000	56920	99.7
W688	60160	43840	68000	36000	60000	44000	68000	36000	99.8
W687	17836	14164	19600	12400	17800	14200	19600	12400	99.7
W686	10622	8378	11700	7300	10600	8400	11700	7300	99.7
W685 [a]	76140	61860	83000	55000	76000	62000	83070	55070	99.7
W684	64200	43800	74000	34000	64100	44000	73900	33900	99.7
W683	31060	24940	34000	22000	30970	24940	34000	21970	99.8
W682	6920	4880	7900	3900	6910	4910	7890	3890	99.8
W668	92340	57660	109001	41000	92000	58000	107471	41680	99.8
W653	156241	131761	168001	120001	123961	104401	135481	95880	98.5
W651	12338	8462	14200	6600	12319	8500	14219	6600	99.7
W650	10634	7166	12300	5500	10583	7166	12317	5500	99.8
W649	60120	47880	66000	42000	60000	48000	66000	42000	99.7
W648	4712	3488	5300	2900	4706	3506	5306	2912	99.8
W647	11422	9178	12500	8100	11400	9189	12489	8089	99.7
W646	9524	7076	10700	5900	9500	7100	10700	5900	99.8
W645	7050	1950	9500	-500	7000	2500	9600	550	99.8
W643	97200	76800	107001	67000	97000	77000	106701	67000	99.8
W641	19550	14450	22000	12000	19500	14500	22000	12000	99.8
W642 [a]	58140	43860	65000	37000	58000	44000	65000	37000	99.7
W639	11322	9078	12400	8000	11300	9089	12411	8000	99.7
W629	84260	57740	97000	45000	84000	58000	97000	45000	99.7
Boundary Start 1					131888	103260	135806	101846	7 3

[a] modelled as minimum ages using the OxCal *Before()* command.

D2.3.2. Fitzroy River Basin

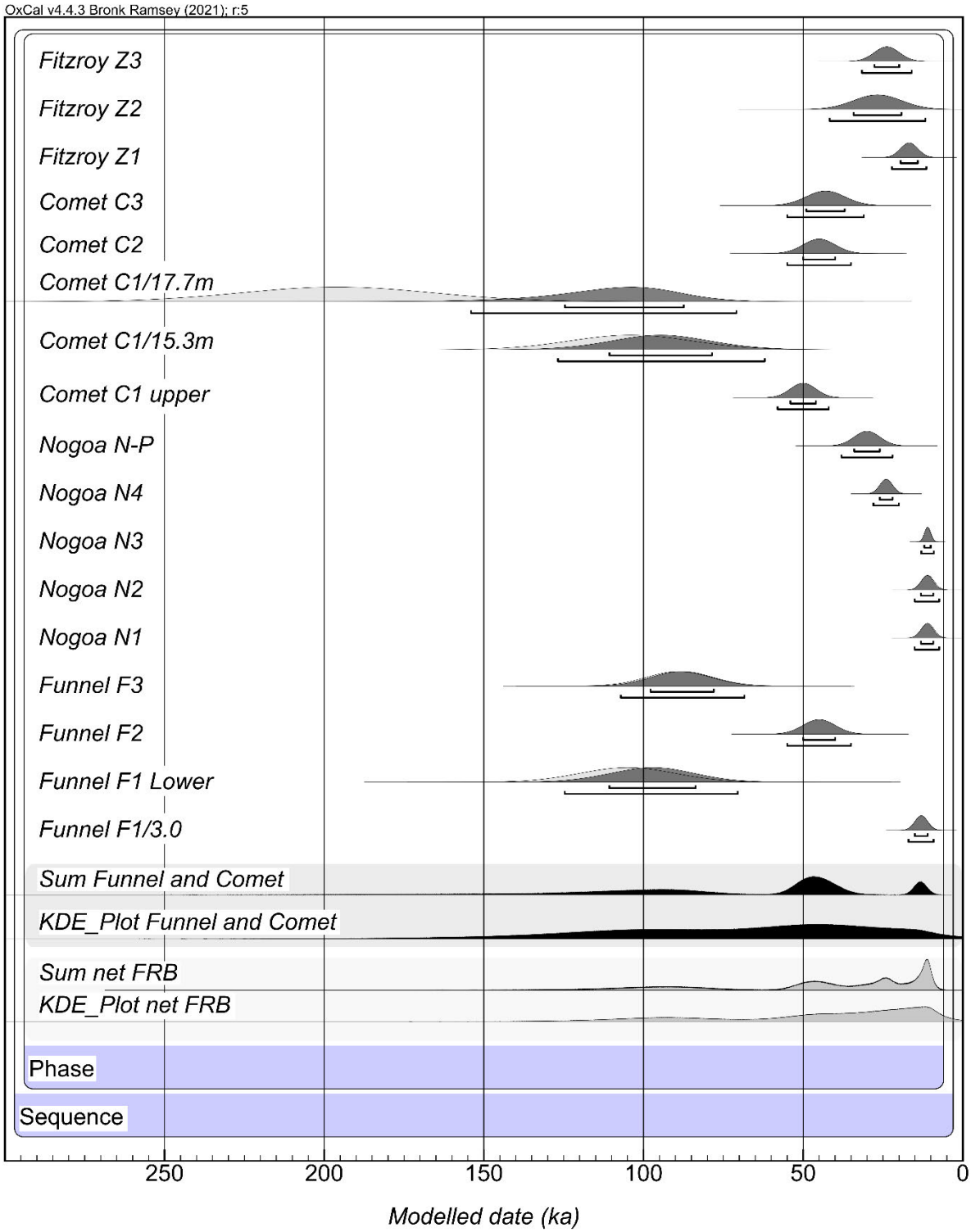

Figure D 15 Bayesian modelling results used to constrain the temporal distribution of hydrological activity within the Fitzroy River Basin (Model 4) (Croke et al., 2011). All likelihoods obtained on sedimentary units representing episodes of fluvial deposition have been combined in a single *Phase* model. The unmodelled age distributions for the dating samples (likelihoods) are shown in light shading, and are presented in Table D11. The modelled posterior distributions for the dating samples are shown in dark shading. The 68.2% and 95.4% ranges of the highest posterior probabilities are indicated by the horizontal bars underneath the probability density functions. The temporal distributions of hydrological activity (bottom part of the plot) has been calculated from the modelled posterior probabilities using the *KDE_Plot* and *Sum()* query functions.

Table D 11 Summary of the OxCal Bayesian modelling results for hydrological activity in the Fitzroy River basin (Figure D15), as inferred from modelled fluvial sediment deposition across the sites described in (Croke et al., 2011). The likelihood (unmodelled) and posterior (modelled) age ranges are presented for each of the numerical dating samples. Posterior (modelled) age ranges are also shown for the *Boundaries* of the *Phase* model. Posterior ages are presented as the 68.2% and 95.4% highest probability density ranges.

	Unmodelled (BP)				Modelled (BP)				
	68%		95%		68%		95%		Conver-gence
	from	to	from	to	from	to	from	to	
Boundary End 1					10589	-816	11332	-10222	26.6
Fitzroy Z3	27778	19822	31600	16000	27700	19861	31600	16000	99.8
Fitzroy Z2	34350	19050	41700	11700	34200	19200	41550	11775	99.8
Fitzroy Z1	19554	14046	22200	11400	19473	14073	22227	11427	99.8
Comet C3	49120	36880	55000	31000	49000	37000	55000	31000	99.8
Comet C2	50100	39900	55000	35000	50000	39950	55050	35000	99.8
Comet C1/17.7m	226601	165401	256001	136001	127901	88900	155801	73000	98.8
Comet C1/15.3m	123381	84620	142001	66000	111791	79490	128131	62200	99.6
Comet C1 upper	54080	45920	58000	42000	54000	46000	58000	42000	99.8
Nogoa N-P/	34080	25920	38000	22000	34000	25960	38000	21960	99.8
Nogoa N4	26040	21960	28000	20000	26000	21980	27980	19960	99.7
Nogoa N3	12020	9980	13000	9000	12040	10030	13000	9100	99.8
Nogoa N2	13040	8960	15000	7000	13120	9260	15040	7400	99.8
Nogoa N1	13040	8960	15000	7000	13120	9260	15080	7400	99.8
Funnel F3	99200	78800	109001	69000	98000	78300	107201	68800	99.8
Funnel F2	50100	39900	55000	35000	50000	39950	55000	35000	99.7
Funnel F1 Lower	120301	89700	135001	75000	111901	84600	125701	70950	99.4
Funnel F1/3.0	15040	10960	17000	9000	15020	11020	17000	9160	99.8
Boundary Start 1					140437	86780	158724	86780	7.9

D2.3.3. Coastal subtropical wetlands

OxCal age-depth models (*P_Sequence* models) have been published for several waterbodies that extend >50 ka on North Stradbroke Island, providing existing constraints on the timing of lake / wetland accumulation episodes for Brown Lake (Lewis et al., 2021), Fern Gully Lagoon (Kemp et al., 2020), and Welsby Lagoon (Lewis et al., 2020). The durations of sediment accumulation (lake full) events at each of these wetlands (summarised in Figure 5.7) have been calculated from the existing modelled posterior probabilities (or generated in OxCal from existing data and interpretations where required) of the upper and lower boundaries using the *Date()* query function. A comparable OxCal *P_Sequence* age-depth model has been generated as part of the present study for Lake Allom, Frasier Island, using the dating results and stratigraphic constraints presented by Donders et al. (2006). This ensures that direct comparisons can be made with the existing Bayesian modelling results for the Stradbroke Island wetlands.

In order to derive the *KDE_Plot* temporal distributions of sediment accumulation at these various wetland sites (shown collectively for all sites in Figure 7h), we have additionally combined the published likelihoods for individual catchments in *Phase* groupings as part of Model 4. The results of these catchment-specific *Phase* models are summarised below.

Lake Allom | Fraser Island

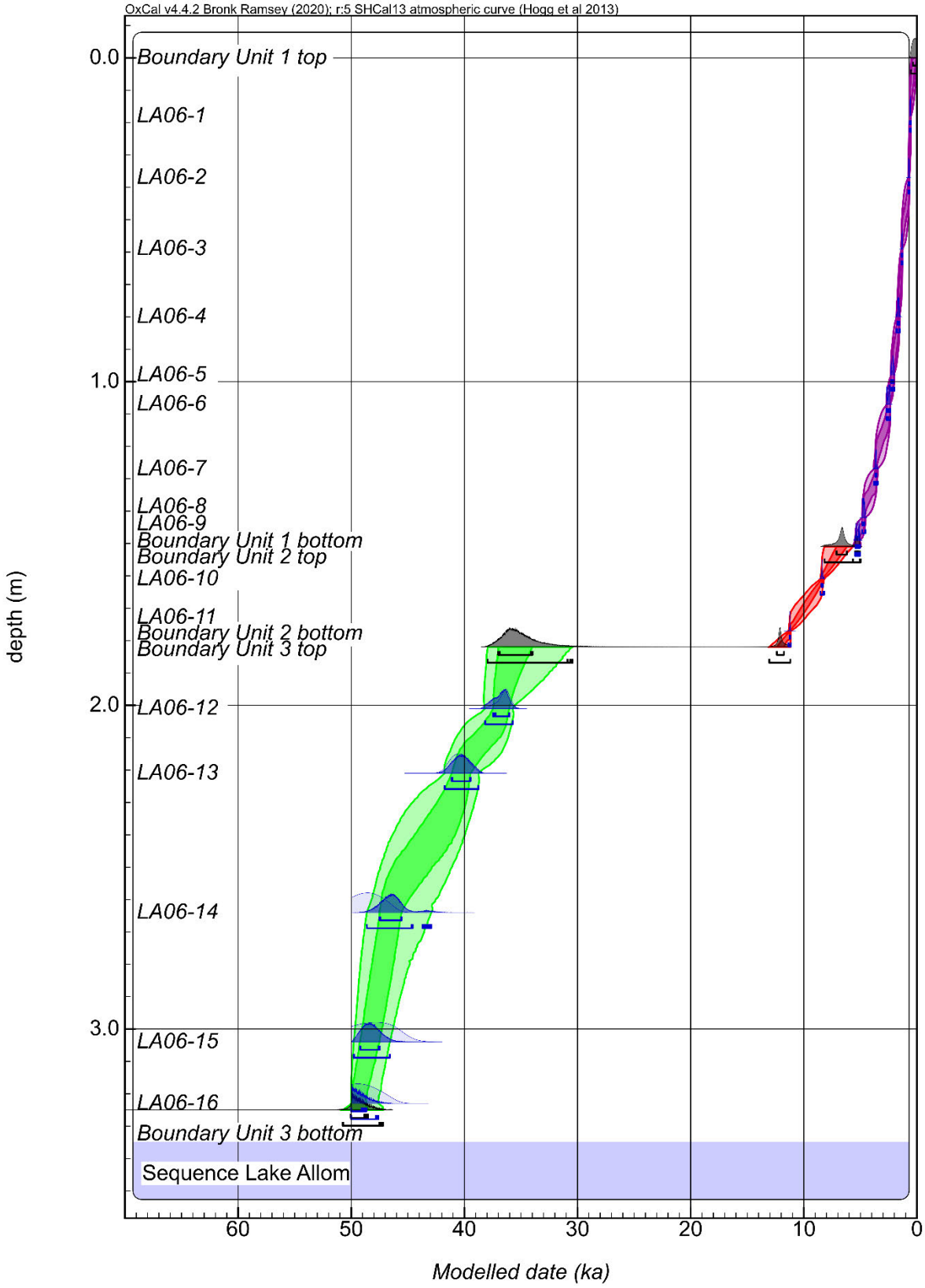

Figure D 16 Bayesian age-depth model constructed using the ^{14}C ages obtained by Donders et al. (2006) for Lake Allom. The original ^{14}C age estimates (likelihoods) are shown in light blue and the posterior modelling distributions are represented by dark blue shading. The age-depth model envelopes show the 95% and 68% highest probability density ranges for each of the three sedimentary units (green, red, and purple), as identified in Donders et al. (2006).

Table D 12 Summary of the OxCal Bayesian modelling results for Lake Allom using the dataset of Donders et al. (2006). The likelihood (unmodelled) and posterior (modelled) age ranges are presented for each of the numerical dating samples. Posterior (modelled) age ranges are also shown for the boundaries of each stratigraphic unit, as well as for the duration of each unit (calculated using the *Date()* command). Posterior ages are presented as the 68.2% and 95.4% highest probability density ranges.

Lake Allom	Unmodelled (BP)				Modelled (BP)				Outlier data		Conver-gence
	68%		95%		68%		95%				
	from	to	from	to	from	to	from	to	Prior	Post.	
Boundary Unit 1 top					356	11	523	-1			99.5
Unit 1 duration					**5073**	**549**	**5183**	**315**			**98.7**
LA06-1	630	543	644	529	627	541	641	525	5	0	99.8
LA06-2	735	684	767	675	740	686	771	675	5	0	99.8
LA06-3	1350	1301	1374	1279	1348	1301	1371	1280	5	0	99.7
LA06-4	1708	1573	1820	1521	1713	1584	1816	1533	5	0	99.7
LA06-5	2295	2050	2305	2009	2299	2060	2307	2013	5	0	99.7
LA06-6	2680	2363	2702	2355	2676	2360	2700	2354	5	0	99.7
LA06-7	3686	3573	3720	3481	3687	3573	3808	3482	5	0	99.5
LA06-8	4826	4628	4840	4569	4828	4643	4841	4571	5	0	99.6
LA06-9	5450	5076	5468	5052	5443	5055	5460	5044	5	0	95.5
Boundary Unit 1 bottom					5456	5063	5677	4988			94
Unit 2-1 hiatus duration [a]					*839*	*1859*	*248*	*2846*			*97.5*
Boundary Unit 2 top					7113	6194	8170	5666			97.8
Unit 2 duration					**11528**	**7684**	**12142**	**6609**			**98.3**
LA06-10	8434	8330	8538	8210	8436	8334	8538	8211	5	0	99.5
LA06-11	11261	11196	11346	11154	11259	11196	11347	11148	5	0	99.3
Boundary Unit 2 bottom					12380	11759	13050	11195			97.5
Unit 3-2 hiatus duration [a]					*21797*	*24911*	*18100*	*26054*			*91.1*
Boundary Unit 3 top					37010	33989	37944	30452			90.6
Unit 3 duration					**47916**	**37140**	**49640**	**34699**			**96**
LA06-12	36924	35865	37800	35515	37472	36025	38170	35721	5	0	96.2
LA06-13	41321	39710	41947	38892	41120	39451	41739	38738	5	0	96.7
LA06-14 [b]	49783	47440	...	46233	47496	45559	48619	42919	5	7	94.6
LA06-15 [b]	49602	46415	...	44937	49223	47495	49788	46586	5	0	96.6
LA06-16 [b]	...	47845	...	46303	50004	48664	50004	47601	5	0	70.2
Boundary Unit 3 bottom					50039	48529	50760	47181			63.6

[a] modelled age represents the duration of time missing between adjacent units (expressed as a temporal range in years, rather than a numerical age in years ago). This modelled duration has been calculated using the *Interval()* query function, and provides the temporal range between the posterior probability density distributions of successive stratigraphic boundaries.
[b] date may extend out of reliable radiocarbon age range – 45,200 ± 1,500 cal. BP

Welsby Lagoon | North Stradbroke Island

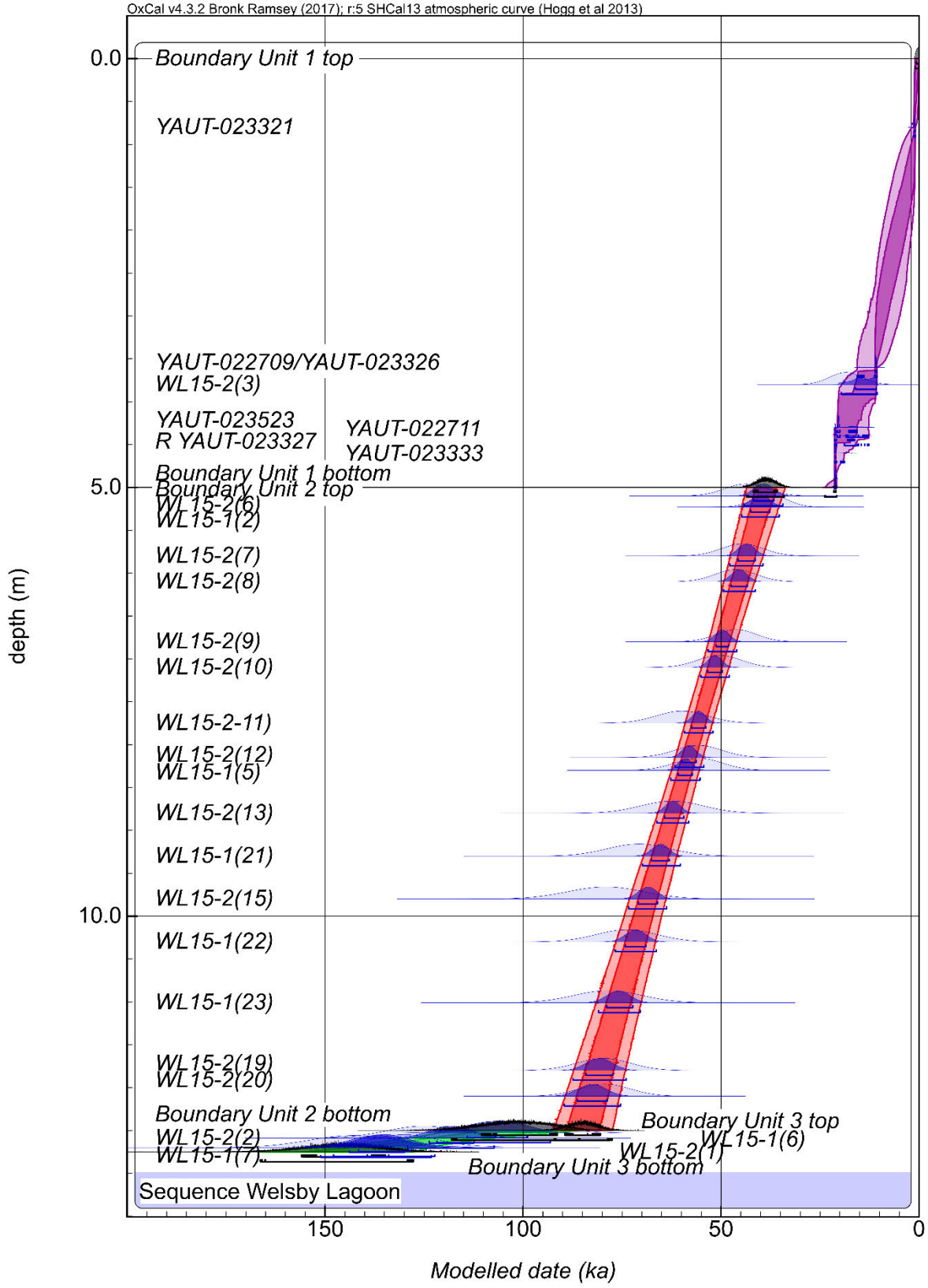

Figure D 17 Bayesian age-depth model constructed using the ^{14}C ages and OSL dates presented in Cadd et al. (2018); Lewis et al. (2020) for Welsby Lagoon. The original ^{14}C and OSL age estimates (likelihoods) are shown in light blue and the posterior modelling distributions are represented by dark blue shading. The age-depth model envelopes show the 95% and 68% highest probability density ranges for each of the three sedimentary units (green, red, and purple), as identified in Lewis et al. (2020).

Table D 13 Summary of the OxCal Bayesian modelling results for Welsby Lagoon using the datasets of Cadd et al. (2018); Lewis et al. (2020). The likelihood (unmodelled) and posterior (modelled) age ranges are presented for each of the numerical dating samples. Posterior (modelled) age ranges are also shown for the boundaries of each stratigraphic unit, as well as for the duration of each unit (calculated using the *Date()* command). Posterior ages are presented as the 68.2% and 95.4%.

Welsby Lagoon	Unmodelled (BP)				Modelled (BP)				Outlier data		Convergence
	68%		95%		68%		95%				
	from	to	from	to	from	to	from	to	Prior	Posterior	
Boundary Unit 1 top					637	2	1040	-1			98.2
Unit 1 duration					**20998**	**1009**	**21059**	**890**			**95.2**
YAUT-023321	1261	1062	1273	980	1262	1066	1301	957	5	4	93.6
YAUT-022709/ YAUT-023326	11070	10734	11090	10700	11076	10730	15600	10588	5	16	
WL15-2(3)	22637	14337	26625	10349	16074	10784	19574	10540	5	1	33.8
YAUT-023523	20450	20195	20548	20070	20608	15617	20663	12817	5	45	2.1
YAUT-022711	21440	21110	21600	20961	21290	16259	21320	12697	5	36	1.2
YAUT-023327	21252	21001	21368	20895	21198	20991	21363	18854	5	8	79
YAUT-023333	21135	20876	21287	20771	21256	21026	21360	20929	5	0	65.7
Boundary Unit 1 bottom					21498	20956	23860	20784			49
Unit 2-1 hiatus duration [a]					*14252*	*20425*	*11764*	*22292*			*63.9*
Boundary Unit 2 top					41887	35742	43510	33998			61.5
Unit 2 duration					**78772**	**42340**	**84878**	**38630**			**89.5**
WL15-2(6)	49116	38151	54383	32883	41827	36721	44139	34410	5	1	98.8
WL15-1(2)	41881	33143	46078	28946	42490	37650	44760	35337	5	0	98.6
WL15-2(7)	50076	39146	55327	33895	45754	41414	47737	39378	5	0	99.4
WL15-2(8)	51631	40989	56744	35876	47477	43356	49407	41373	5	0	99.4
WL15-2(9)	51312	40940	56294	35958	51217	48115	53250	46031	5	0	99.5
WL15-2(10)	56007	44783	61399	39391	53415	49728	55120	47913	5	0	99.5
WL15-2(11)	66493	53243	72858	46878	57424	53852	59178	52033	5	1	99.3
WL15-2(12)	61752	49726	67529	43949	59946	56291	61715	54405	5	0	99.3
WL15-1(5)	61826	49518	67738	43606	60867	57247	62676	55316	5	0	99.6
WL15-2(13)	70425	54311	78166	46570	64217	59398	66191	58134	5	0	99.6
WL15-1(21)	78925	62527	86802	54650	67538	63118	69789	60304	5	1	99.6
WL15-2(15)	88854	69312	98241	59925	70874	66084	73268	63785	5	3	99.5
WL15-1(22)	81619	65983	89131	58471	74166	68954	76695	66348	5	1	99.3
WL15-1(23)	87296	69784	95708	61372	78922	72312	80896	70424	5	1	99
WL15-2(19)	86607	72745	93266	66086	84135	77340	87397	73943	5	0	98.5
WL15-2(20)	85990	72804	92325	66469	86268	78770	89565	75344	5	0	98
Boundary Unit 2 bottom					89403	80469	92132	77487			55.9
Unit 3-2 hiatus duration [a]					*4611*	*25246*	*0*	*32086*			*76.6*
Boundary Unit 3 top					110521	91304	118021	85685			74.3
Unit 3 duration					**138737**	**108769**	**151505**	**96048**			**88.7**
WL15-1(6)	112095	92710	121407	83398	114123	98919	121725	93123	5	0	99.8
WL15-2(2)	134701	115316	144013	106005	123720	112413	129231	107281	5	2	99.8
WL15-1(7)	138355	121542	146432	113464	141537	128597	147883	122250	5	0	99.6
WL15-2(1)	154368	131259	165470	120158	143858	129925	151108	123128	5	2	99.7
Boundary Unit 3 bottom					155899	133915	166311	127703			55.7

[a] modelled age represents the duration of time missing between adjacent units (expressed as a temporal range in years, rather than a numerical age in years ago). This modelled duration has been calculated using the *Interval()* query function, and provides the temporal range between the posterior probability density distributions of successive stratigraphic boundaries.

Brown Lake | North Stradbroke Island

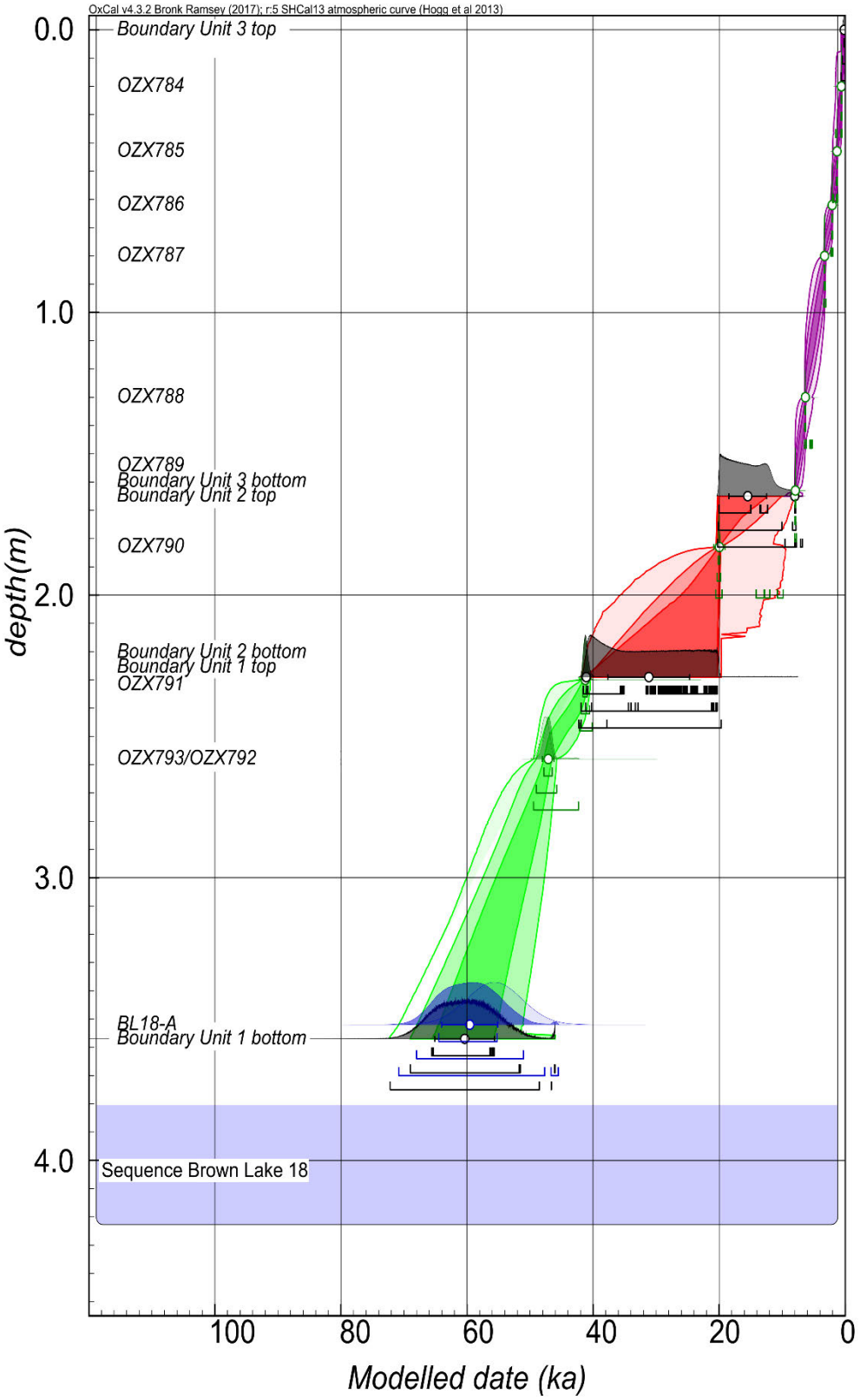

Figure D 18 Bayesian age-depth model constructed using the ^{14}C ages and OSL date presented in Lewis et al. (2021) for Brown Lake. The original ^{14}C and OSL age estimates (likelihoods) are shown in light blue and the posterior modelling distributions are represented by dark blue shading. The age-depth model envelopes show the 95% and 68% highest probability density ranges for each of the three sedimentary units (green, red, and purple), as identified in Lewis et al. (2021).

Table D 14 Summary of the OxCal Bayesian modelling results for Brown Lake using the datasets of Lewis et al. (2021). The likelihood (unmodelled) and posterior (modelled) age ranges are presented for each of the numerical dating samples. Posterior (modelled) age ranges are also shown for the boundaries of each stratigraphic unit, as well as for the duration of each unit (calculated using the *Date()* command). Posterior ages are presented as the 68.2% and 95.4%.

Brown Lake (BL18)	Unmodelled (BP)				Modelled (BP)				Outlier data		Convergence
	68%		95%		68%		95%				
	from	to	from	to	from	to	from	to	Prior	Posterior	
Boundary Unit 1 top					205	-1	446	-1			100
Unit 1 duration					**7824**	**594**	**7936**	**401**			**99.9**
OZXY784	651	566	660	559	652	568	661	559	5	0	100
OZXY785	1350	1306	1366	1299	1350	1307	1369	1298	5	0	100
OZXY786	2290	2064	2303	2018	2294	2086	2304	2020	5	0	100
OZXY787	3377	3256	3397	3230	3375	3256	3396	3229	5	0	100
OZXY788	6397	6317	6435	6295	6394	6315	6433	6294	5	0	100
OZXY789	7997	7936	8017	7869	7995	7936	8020	7867	5	1	99.9
Boundary Unit 1 bottom					8096	7934	8407	7861			99.8
Unit 2-1 hiatus duration [a]					*4231*	*12040*	*1582*	*12230*			*88.2*
Boundary Unit 2 top					20091	12260	20244	9630			88.3
Unit 2 duration					**27803**	**16965**	**36519**	**12431**			**92.9**
OZXY790	20247	20016	20376	19908	20256	20008	20525	19706	5	5	99.4
Boundary Unit 2 bottom					41212	20285	41237	20284			94.3
Unit 3-2 hiatus duration [a]					*0*	*20452*	*0*	*20560*			*94.7*
Boundary Unit 3 top					41578	40930	41887	40399			99.3
Unit 3 duration					**54284**	**41551**	**62729**	**41015**			**99.5**
OZXY791	41570	40988	41810	40627	41641	41068	41882	40718	5	0	99.6
OXZY793/OXZY792	47979	47044	48472	46633	47763	46791	48623	46148	5	8	99.4
BL18-A	60099	51199	64375	46923	64896	55429	68256	51546	5	0	95.7
Boundary Unit 3 bottom					65982	55761	69404	52110			91.9

[a] modelled age represents the duration of time missing between adjacent units (expressed as a temporal range in years, rather than a numerical age in years ago). This modelled duration has been calculated using the *Interval()* query function, and provides the temporal range between the posterior probability density distributions of successive stratigraphic boundaries.

Fern Gully Lagoon | North Stradbroke Island

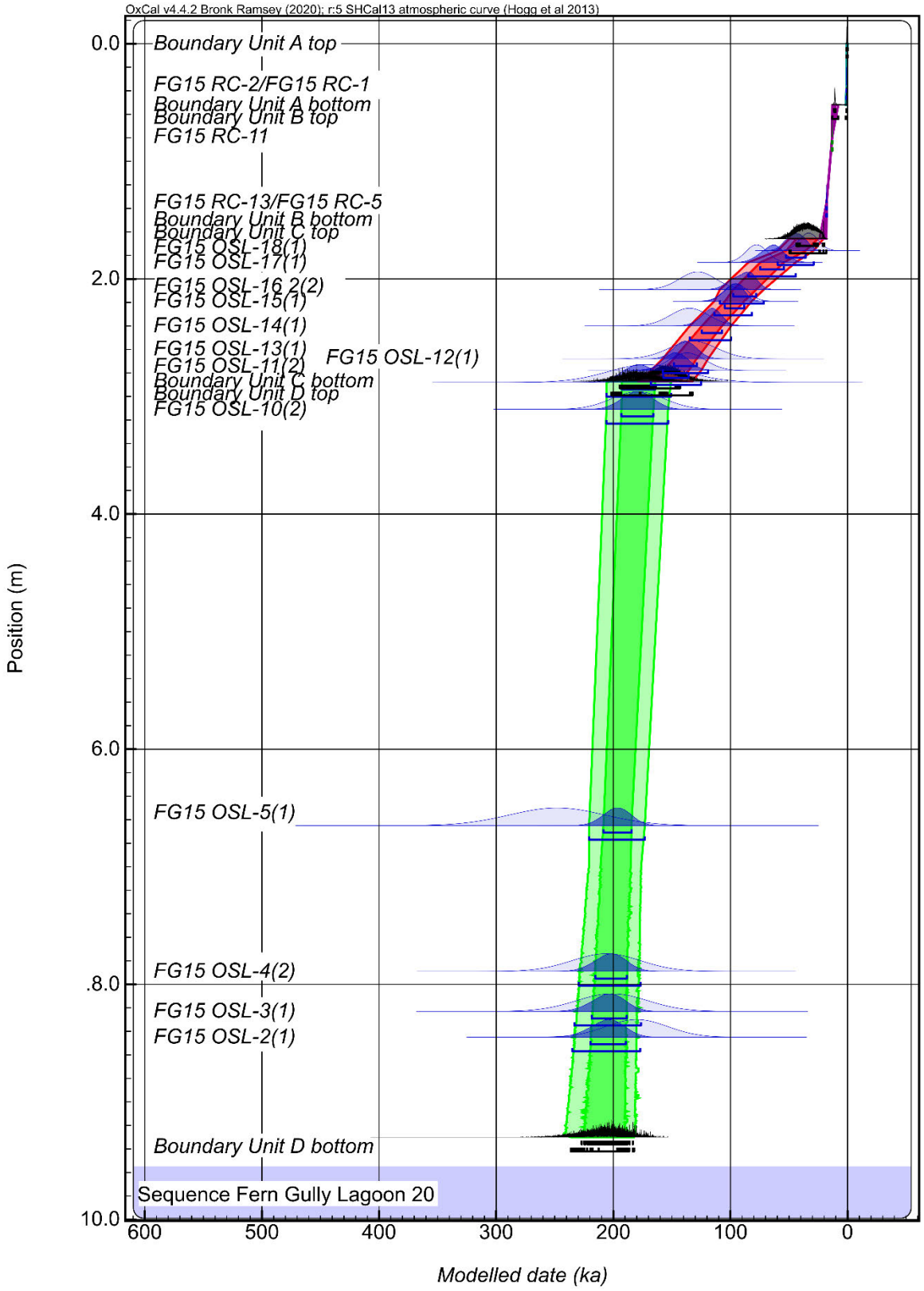

Figure D 19 Bayesian age-depth model constructed using the ^{14}C ages and OSL date presented in Kemp et al. (2020) for Fern Gully Lagoon. The original ^{14}C and OSL age estimates (likelihoods) are shown in light blue and the posterior modelling distributions are represented by dark blue shading. The age-depth model envelopes show the 95% and 68% highest probability density ranges for each of the three sedimentary units (green, red, and purple), as identified in Kemp et al. (2020).

Table D 15 Summary of the OxCal Bayesian modelling results for Fern Gully Lagoon using the datasets of Kemp et al. (2020). The likelihood (unmodelled) and posterior (modelled) age ranges are presented for each of the numerical dating samples. Posterior (modelled) age ranges are also shown for the boundaries of each stratigraphic unit, as well as for the duration of each unit (calculated using the *Date()* command). Posterior ages are presented as the 68.2% and 95.4%.

Fern Gully Lagoon	Unmodelled (BP)				Modelled (BP)				Outlier data		Convergence
	68%		95%		68%		95%				
	from	to	from	to	from	to	from	to	Prior	Posterior	
Boundary Unit A top					736	6	747	4			94.6
Unit A duration					**919**	**497**	**1164**	**100**			**95.6**
FG15 RC-2/FG15 RC-1	791	747	898	730	792	747	899	729	5	3	99.3
Boundary Unit A bottom					1088	779	1692	729			85.4
Unit A-B hiatus duration [a]					*9142*	*10530*	*6244*	*12101*			*91.9*
Boundary Unit B top					11434	10226	13090	7855			92.5
Unit B duration					**19376**	**11890**	**21053**	**10260**			**97.5**
FG15 RC-11	13200	13045	13292	12934	13202	13048	13292	12925	5	0	96.7
FG15 RC-13/FG15 RC-5	17995	17825	18063	17717	17992	17819	18067	17705	5	4	97
Boundary Unit B bottom					21188	19859	23976	17975			92.2
Unit B-C hiatus duration [a]					*3666*	*22871*	*0*	*28835*			*81.3*
Boundary Unit C top					43795	25248	49734	20631			77
Unit C duration					**137078**	**49667**	**154837**	**34740**			**75.3**
FG15 OSL-18(1)	41440	24960	49200	17200	52401	35681	59761	29041	5	0	99.5
FG15 OSL-17(1)	87176	68224	96100	59300	74549	54401	84761	44281	5	17	99.4
FG15 OSL-16 2(2)	143759	112241	158601	97400	97489	77905	108965	71479	5	51	99.5
FG15 OSL-15(1)	105522	85478	114961	76040	104684	88240	113733	81818	5	1	99.4
FG15 OSL-14(1)	151789	118211	167601	102401	124327	107213	134759	99388	5	8	99.7
FG15 OSL-13(1)	152909	111091	172601	91400	148343	128855	157885	119111	5	1	99.5
FG15 OSL-12(1)	152863	121139	167801	106201	157401	135687	168027	125061	5	1	99.3
Boundary Unit C bottom					167211	143045	177533	132409			63.8
Unit C-D hiatus duration [a]					*98*	*32530*	*0*	*48339*			*69.7*
Boundary Unit D top					194335	163642	201505	153765			26.5
Unit D duration					**207899**	**178269**	**223570**	**165487**			**87.9**
FG15 OSL-11(2)	205403	136599	237801	104201	192821	164097	205847	150737	5	3	99.2
FG15 OSL-10(2)	202073	155929	223801	134201	193073	165745	205841	153201	5	3	99.2
FG15 OSL-5(1)	289819	206183	329201	166801	208431	184477	220611	173109	5	9	99.5
FG15 OSL-4(2)	236283	175719	264801	147201	215389	188341	229501	176581	5	3	98.9
FG15 OSL-3(1)	232313	169689	261801	140201	218353	188561	233249	176401	5	3	98.8
FG15 OSL-2(1)	207193	152809	232801	127201	219529	189433	235105	177025	5	1	98.8
Boundary Unit D bottom					226980	183280	236299	182282			6.5

[a] modelled age represents the duration of time missing between adjacent units (expressed as a temporal range in years, rather than a numerical age in years ago). This modelled duration has been calculated using the *Interval()* query function, and provides the temporal range between the posterior probability density distributions of successive stratigraphic boundaries.

Duration of wetland and lake full conditions

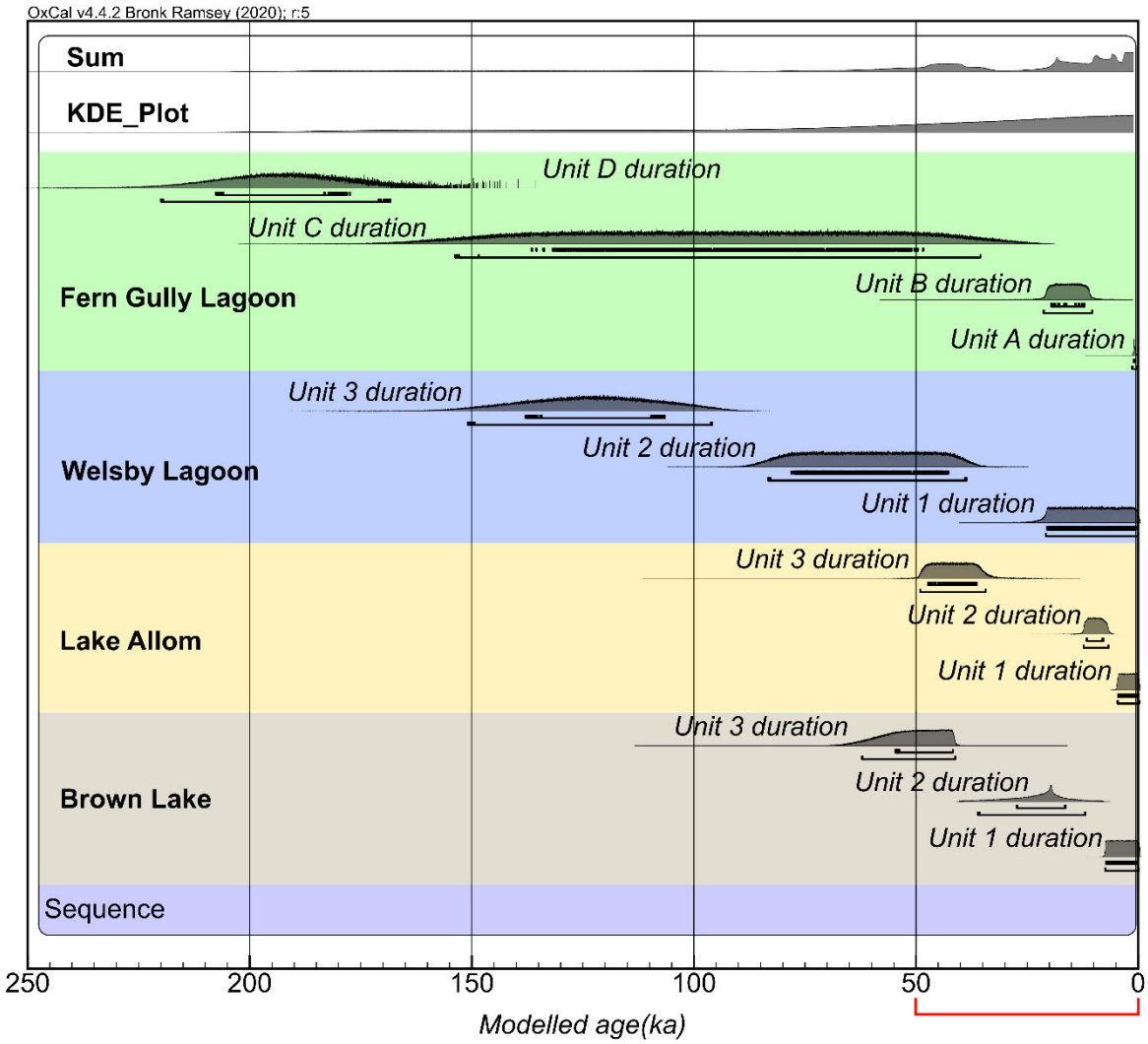

Figure D 20 Bayesian modelling results used to constrain the temporal distribution of hydrological activity within the lakes and wetlands of Fraser Island and North Stradbroke Island over the last 250 ka. All likelihoods obtained on sedimentary units representing lake accumulation episodes have been combined in a single model. The unmodelled age distributions for the dating samples (likelihoods) are shown in light shading, and are presented in Figures D16 – D19, and Tables D12 – D15. The 68.2% and 95.4% ranges of the highest posterior probabilities are indicated by the horizontal bars underneath the probability density functions. The temporal distributions of hydrological activity (top part of the plot) has been calculated from the modelled posterior probabilities using the *Sum()* and *KDE_Plot* query functions. The red bracket (spanning 50 – 0 ka) highlights the temporal range of Figure D21.

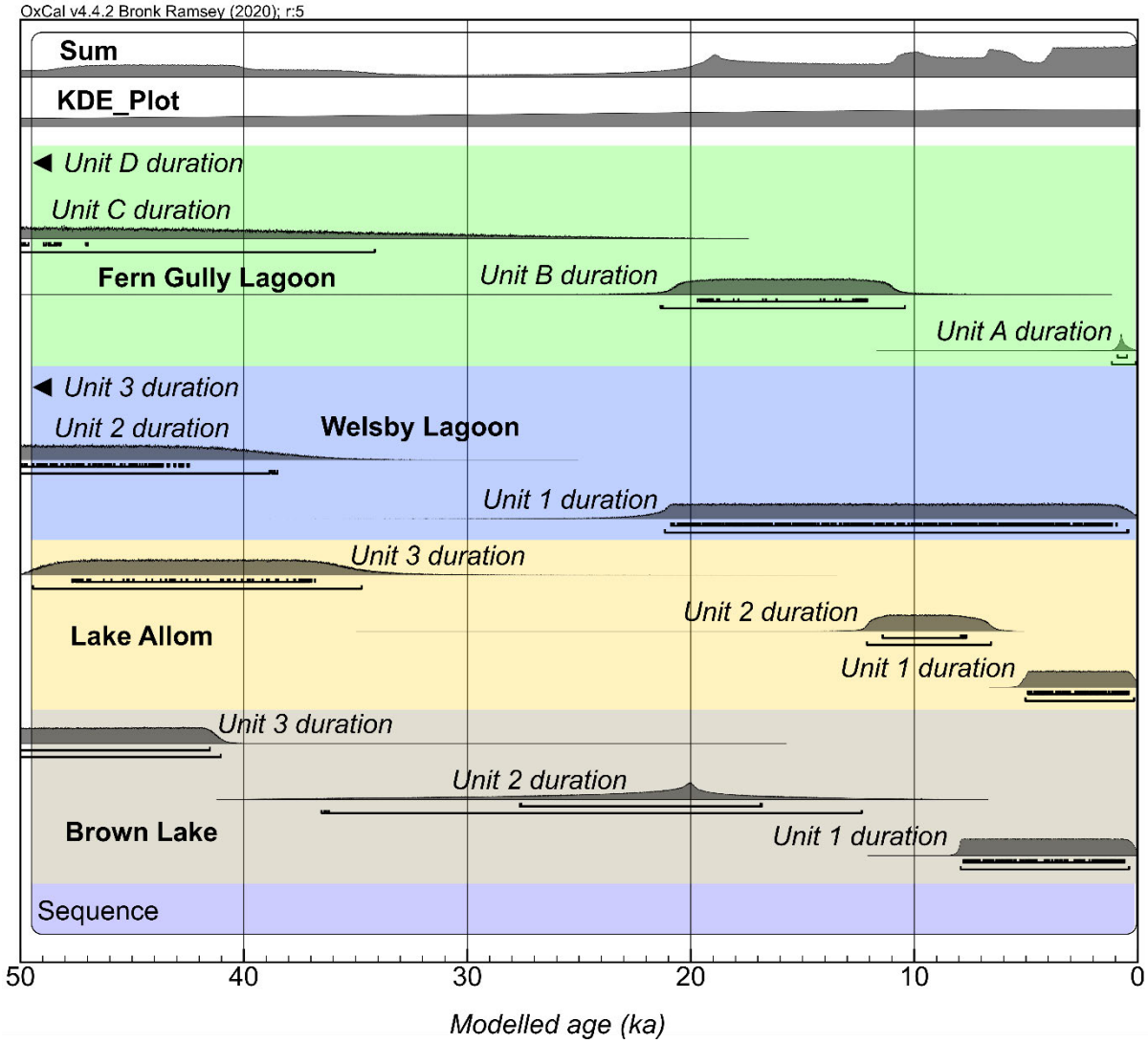

Figure D 21 Bayesian modelling results used to constrain the temporal distribution of hydrological activity within the lakes and wetlands of Fraser Island and North Stradbroke Island over the last 50 ka. All likelihoods obtained on sedimentary units representing lake accumulation episodes have been combined in a single model. The unmodelled age distributions for the dating samples (likelihoods) are shown in light shading, and are presented in Figures D16 – D19 and Tables D12 – D15. The 68.2% and 95.4% ranges of the highest posterior probabilities are indicated by the horizontal bars underneath the probability density functions. The temporal distributions of hydrological activity (top part of the plot) has been calculated from the modelled posterior probabilities using the *Sum()* and *KDE_Plot* query functions.

Lachlan River

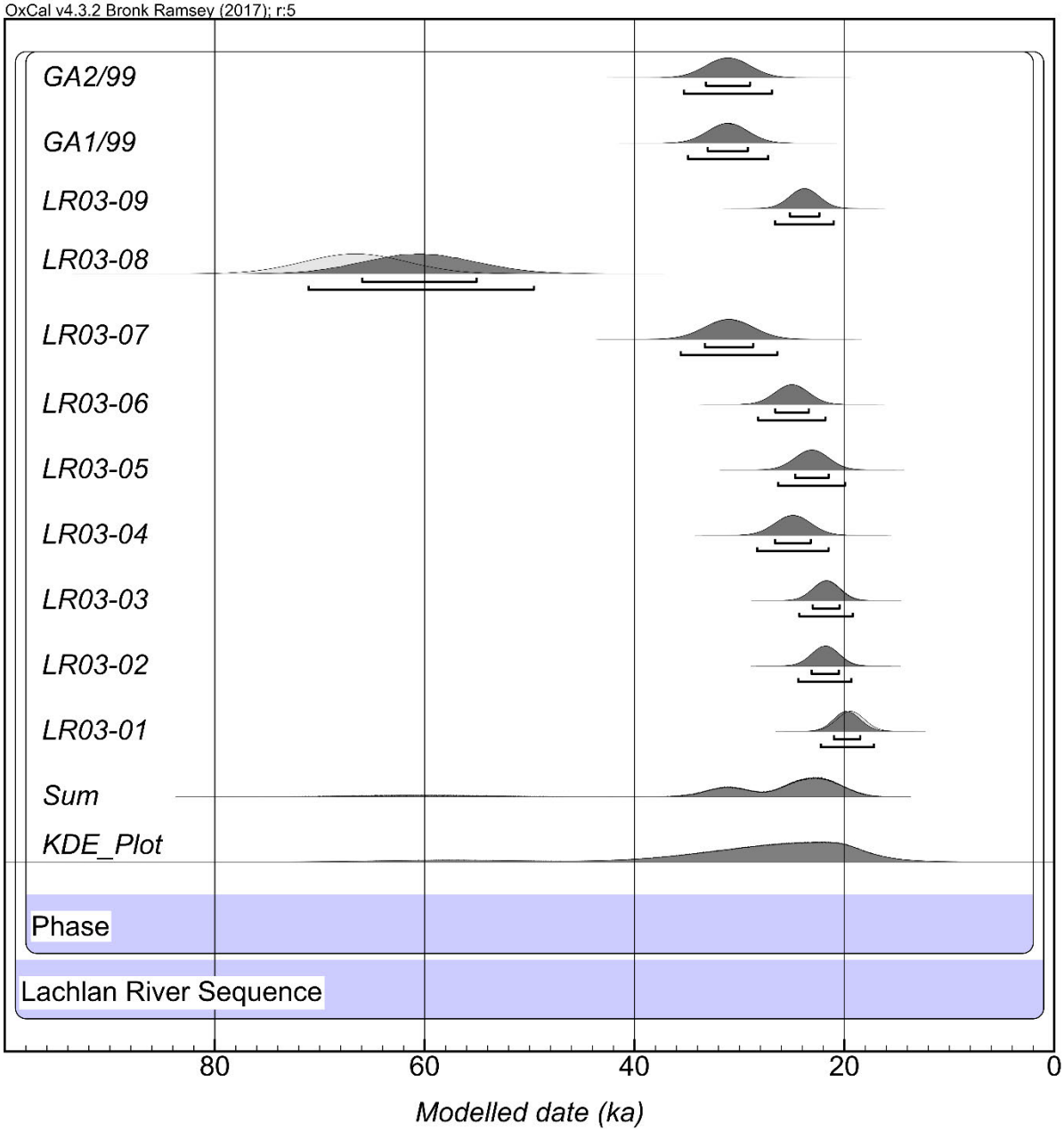

Figure D 22 Bayesian modelling results used to constrain the temporal distribution of hydrological activity within the Lachlan River catchment (Model 4) (Kemp & Rhodes, 2010). All likelihoods obtained on sedimentary units representing episodes of fluvial deposition have been combined in a single *Phase* model. The unmodelled age distributions for the dating samples (likelihoods) are shown in light shading, and are presented in Table D16. The modelled posterior distributions for the dating samples are shown in dark shading. The 68.2% and 95.4% ranges of the highest posterior probabilities are indicated by the horizontal bars underneath the probability density functions. The temporal distributions of hydrological activity (bottom part of the plot) has been calculated from the modelled posterior probabilities using the *KDE_Plot* and *Sum()* query functions.

Table D 16 Summary of the OxCal Bayesian modelling results for hydrological activity in the Lachlan River catchment (Figure D22), as inferred from modelled fluvial sediment deposition across the sites described in (Kemp & Rhodes, 2010). The likelihood (unmodelled) and posterior (modelled) age ranges are presented for each of the numerical dating samples. Posterior (modelled) age ranges are also shown for the *Boundaries* of the *Phase* model. Posterior ages are presented as the 68.2% and 95.4% highest probability density ranges.

	Unmodelled (BP)				Modelled (BP)				
	68.2%		95.4%		68.2%		95.4%		Convergence
	from	to	from	to	from	to	from	to	
Boundary End 1					20261	13789	21190	5893	61.1
GA2/99	33242	28958	35300	26900	33200	29000	35300	26900	99.8
GA1/99	33038	29162	34900	27300	33019	29200	34900	27262	99.8
LR03-09	25228	22372	26600	21000	25200	22386	26614	21014	99.9
LR03-08	71598	61602	76400	56800	65963	55036	71059	49597	99.2
LR03-07	33346	28654	35600	26400	33300	28700	35600	26400	99.8
LR03-06	26632	23368	28200	21800	26584	23384	28216	21816	99.8
LR03-05	24732	21468	26300	19900	24700	21484	26316	19948	99.8
LR03-04	26634	23166	28300	21500	26617	23200	28317	21517	99.9
LR03-03	23026	20374	24300	19100	23013	20452	24287	19204	99.8
LR03-02	23126	20474	24400	19200	23126	20526	24400	19330	99.8
LR03-01	20726	18074	22000	16800	20999	18490	22234	17177	99.8
Boundary Start 1					71289	55344	77359	51631	36.4

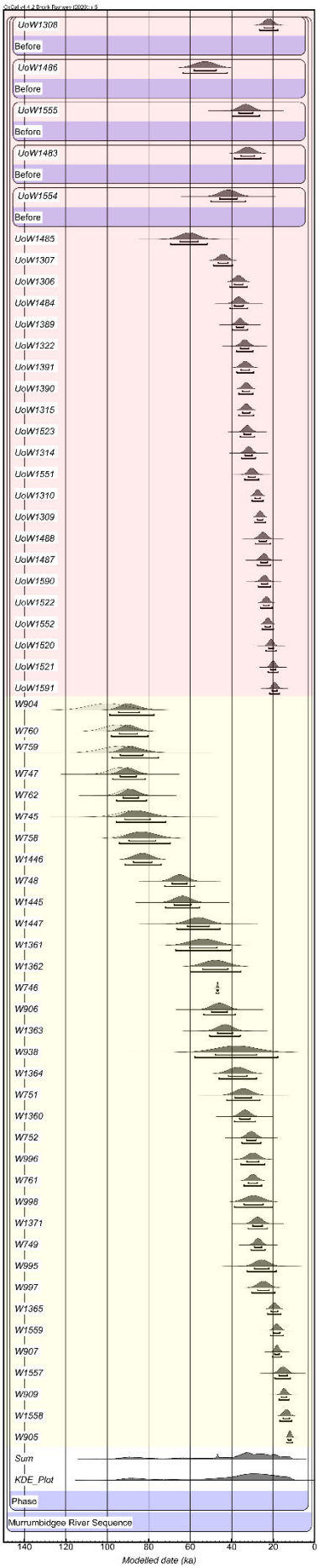

Figure D 23 Bayesian modelling results used to constrain the temporal distribution of hydrological activity within the Murrumbidgee Basin (Model 4) (Mueller et al., 2018; Page et al., 1996). All likelihoods obtained on sedimentary units representing episodes of fluvial deposition have been combined in a single *Phase* model, with ages shaded in red sourced from Mueller et al. (2018) and ages shown in yellow sourced from Page et al. (1996). Likelihoods that were originally interpreted as minimum ages by Mueller et al. (2018) have been modelled as such using the OxCal *Before()* command. The unmodelled age distributions for the dating samples (likelihoods) are shown in light shading, and are presented in Table D17. The modelled posterior distributions for the dating samples are shown in dark shading. The 68.2% and 95.4% ranges of the highest posterior probabilities are indicated by the horizontal bars underneath the probability density functions. The temporal distributions of hydrological activity (bottom part of the plot) has been calculated from the modelled posterior probabilities using the *KDE_Plot* and *Sum()* query functions.

Table D 17 Summary of the OxCal Bayesian modelling results for hydrological activity in the Murrumbidgee River catchment (Figure D23), incorporating the TL ages of Page et al. (1996) and the SG-OSL ages of Mueller et al. (2018). The unmodelled and modelled age ranges are presented for each of the numerical dating samples. Posterior age ranges are shown for the *Boundaries* of the *Phase* model as the 68.2% and 95.4% highest probability density ranges.

	Unmodelled (BP)				Modelled (BP)				
	68.2%		95.4%		68.2%		95.4%		Convergence
	from	to	from	to	from	to	from	to	
Boundary End 1					12597	9290	13076	7299	33.8
UoW1308[a]	24376	19824	26520	17680	24310	19890	26520	17680	99.7
UoW1486[a]	58349	47451	63480	42320	58137	47504	63480	42267	99.7
UoW1555[a]	36620	29780	39840	26560	36553	29880	39840	26560	99.7
UoW1483[a]	35627	28973	38760	25840	35498	29005	38760	25840	99.7
UoW1554[a]	45885	37315	49920	33280	45760	37357	49962	33280	99.7
UoW1485	65132	56068	69400	51800	65000	56200	69400	51800	99.7
UoW1307	46569	41831	48800	39600	46477	41877	48777	39577	99.7
UoW1306	38863	34537	40900	32500	38779	34579	40921	32500	99.7
UoW1484	38763	34437	40800	32400	38700	34479	40800	32400	99.7
UoW1389	37854	34146	39600	32400	37818	34200	39600	32382	99.6
UoW1322	35760	31640	37700	29700	35720	31720	37700	29700	99.7
UoW1391	35560	31440	37500	29500	35500	31480	37500	29480	99.8
UoW1390	34851	31349	36500	29700	34800	31400	36500	29700	99.7
UoW1315	34854	31146	36600	29400	34800	31200	36600	29382	99.7
UoW1523	34151	30649	35800	29000	34134	30717	35800	28983	99.7
UoW1314	33651	30149	35300	28500	33583	30183	35300	28500	99.7
UoW1551	32051	28549	33700	26900	32017	28617	33700	26900	99.7
UoW1310	28839	26161	30100	24900	28800	26200	30100	24887	99.7
UoW1309	27639	24961	28900	23700	27600	25000	28913	23700	99.8
UoW1488	26854	23146	28600	21400	26818	23218	28600	21400	99.7
UoW1487	26048	22752	27600	21200	26048	22816	27600	21200	99.6
UoW1590	25745	22655	27200	21200	25700	22700	27200	21200	99.7
UoW1522	24742	21858	26100	20500	24714	21914	26114	20514	99.7
UoW1552	23939	21261	25200	20000	23900	21287	25213	20000	99.7
UoW1520	22236	19764	23400	18600	22212	19800	23400	18600	99.7
UoW1521	21236	18764	22400	17600	21212	18800	22400	17600	99.8
UoW1591	20536	18064	21700	16900	20500	18088	21712	16900	99.8
W904	109271	90730	118001	82000	94510	84520	98830	77410	98.6
W760	101789	88811	107901	82700	94040	85472	97946	80369	99.1
W759	102955	85445	111201	77200	93775	82810	97685	75415	99.1
W747	99256	88544	104301	83500	93744	86048	97436	81680	99
W762	94529	85671	98700	81500	92293	85026	95604	81027	99.5
W745	94525	79075	101800	71800	91525	79375	95725	71725	99.6
W758	90813	76187	97700	69300	89606	76684	94150	69584	99.8
W1446	87635	78365	92000	74000	87410	78455	91415	74090	99.8
W748	68808	61392	72300	57900	68772	61536	72300	57864	99.7
W1445	67923	59477	71900	55500	67841	59600	71941	55500	99.7
W1447	61356	50644	66400	45600	61252	50800	66452	45600	99.7
W1361	60498	46902	66900	40500	60366	47100	67032	40500	99.7
W1362	54083	41517	60000	35600	54022	41761	60000	35600	99.8
W746	47109	46491	47400	46200	47100	46500	47400	46197	99.7
W906	49814	41986	53500	38300	49776	42100	53462	38224	99.7
W1363	47011	39389	50600	35800	46863	39463	50637	35837	99.8
W938	48100	27500	57800	17800	47900	27900	57700	17800	99.8
W1364	41735	32465	46100	28100	41600	32600	46145	28100	99.7
W751	38520	30280	42400	26400	38440	30400	42400	26400	99.7
W1360	36175	31025	38600	28600	36100	31100	38575	28575	99.8
W752	32869	28131	35100	25900	32823	28200	35077	25877	99.7
W996	32787	26813	35600	24000	32700	26900	35600	24000	99.8
W761	31963	27637	34000	25600	31879	27658	34000	25600	99.7
W998	34138	24662	38600	20200	34000	24800	38554	20154	99.7
W1371	29869	25131	32100	22900	29823	25200	32100	22877	99.8
W749	29051	25549	30700	23900	29000	25600	30700	23900	99.7
W995	29105	21895	32500	18500	29000	22000	32535	18500	99.8
W997	27584	21816	30300	19100	27500	21900	30356	19128	99.7
W1365	21048	17752	22600	16200	21000	17800	22632	16216	99.7
W1559	19745	16655	21200	15200	19715	16700	21200	15185	99.7
W907	19333	17067	20400	16000	19300	17100	20411	16000	99.8
W1557	17260	13140	19200	11200	17200	13220	19160	11600	99.8
W909	15936	13464	17100	12300	15924	13512	17100	12336	99.8
W1558	15248	11952	16800	10400	15200	12160	16784	10992	99.7
W905	12521	11079	13200	10400	12780	11387	13424	10722	99.6
Boundary Start 1					99109	87531	100523	87528	11.1

[a] modelled as minimum ages, following the interpretation of Mueller et al. (2018), using the OxCal *Before()* command and assuming associated 1σ ranges of 10%. The latter have been chosen as broadly equating to the average relative uncertainties reported for finite-age samples by Mueller et al. (2018).

D3. References

Aitken, M. J. 1985. Thermoluminescence dating: Past progress and future trends. Nuclear Tracks and Radiation Measurements (1982), 10, 3-6. .

Aitken, M. J. 1998. An introduction to optical dating: the dating of Quaternary sediments by the use of photon-stimulated luminescence, Oxford, Oxford University Press.

Arnold, L. & Roberts, R. 2009. Stochastic modelling of multi-grain equivalent dose (De) distributions: Implications for OSL dating of sediment mixtures. Quaternary Geochronology, 4, 204-230.

Arnold, L. J., Bailey, R. M. & Tucker, G. E. 2007. Statistical treatment of fluvial dose distributions from southern Colorado arroyo deposits. Quaternary Geochronology, 2, 162-167.

Arnold, L. J., Duval, M., Demuro, M., Spooner, N. A., Santonja, M. & Pérez-González, A. 2016. OSL dating of individual quartz 'supergrains' from the Ancient Middle Palaeolithic site of Cuesta de la Bajada, Spain. Quaternary Geochronology, 36, 78-101.

Arnold, L. J., Duval, M., Falguères, C., Bahain, J. J. & Demuro, M. 2012. Portable gamma spectrometry with cerium-doped lanthanum bromide scintillators: Suitability assessments for luminescence and electron spin resonance dating applications. Radiation Measurements, 47, 6-18.

Arnold, L. J., Roberts, R. G., Macphee, R. D. E., Willerslev, E., Tikhonov, A. N. & Brock, F. 2008. Optical dating of perennially frozen deposits associated with preserved ancient plant and animal DNA in north-central Siberia. Quaternary Geochronology, 3, 114-136.

Bailey, R. M. & Arnold, L. J. 2006. Statistical modelling of single grain quartz De distributions and an assessment of procedures for estimating burial dose. Quaternary Science Reviews, 25, 2475-2502.

Bøtter-Jensen, L., Bulur, E., Duller, G. a. T. & Murray, A. S. 2000. Advances in luminescence instrument systems. Radiation Measurements, 32, 523-528.

Bowler, J., Johnston, H., Olley, J., Prescott, J., Roberts, R., Shawcross, W. & Spooner, N. 2003. New ages for human occupation and climatic change at Lake Mungo, Australia. Nature, 421, 837.

Brennan, B. J. 2003. Beta doses to spherical grains. Radiation Measurements, 37, 299-303.

Cadd, H. R., Tibby, J., Barr, C., Tyler, J., Unger, L., Leng, M. J., Marshall, J. C., Mcgregor, G., Lewis, R. & Arnold, L. J. 2018. Development of a Southern Hemisphere subtropical wetland (Welsby Lagoon, south-east Queensland, Australia) through the last glacial cycle. Quaternary Science Reviews, 202, 53-65.

Cohen, T. J., Jansen, J. D., Gliganic, L. A., Larsen, J. R., Nanson, G. C., May, J. H., Jones, B. G. & Price, D. M. 2015. Hydrological transformation coincided with megafaunal extinction in central Australia. Geology, 43, 195-198.

Croke, J., Jansen, J. D., Amos, K. & Pietsch, T. J. 2011. A 100 ka record of fluvial activity in the Fitzroy River Basin, tropical northeastern Australia. Quaternary Science Reviews, 30, 1681-1695.

Demuro, M., Arnold, L. J., Aranburu, A., Sala, N. & Arsuaga, J.-L. 2019. New bracketing luminescence ages constrain the Sima de los Huesos hominin fossils (Atapuerca, Spain) to MIS 12. Journal of Human Evolution, 131, 76-95.

Donders, T. H., Wagner, F. & Visscher, H. 2006. Late Pleistocene and Holocene subtropical vegetation dynamics recorded in perched lake deposits on Fraser Island, Queensland, Australia. Palaeogeography, Palaeoclimatology, Palaeoecology, 241, 417-439.

Duller, G. a. T. 2003. Distinguishing quartz and feldspar in single grain luminescence measurements. Radiation measurements, 37, 161-165.

Galbraith, R. F. & Roberts, R. G. 2012. Statistical aspects of equivalent dose and error calculation and display in OSL dating: An overview and some recommendations. Quaternary Geochronology, 11, 1-27.

Galbraith, R. F., Roberts, R. G., Laslett, G. M., Yoshida, H. & Olley, J. M. 1999. Optical dating of single and multiple grains of quartz from Jinmium Rock Shelter, Northern Australia: part I, experimental design and statistical models. Archaeometry, 41, 339-364.

Guérin, G., Mercier, N. & Adamiec, G. 2011. Dose-rate conversion factors: update. Ancient TL, 29, 5-8.

Hocknull, S. A., Lewis, R., Arnold, L. J., Pietsch, T., Joannes-Boyau, R., Price, G. J., Moss, P., Wood, R., Dosseto, A., Louys, J., Olley, J. & Lawrence, R. A. 2020. Extinction of eastern Sahul megafauna coincides with sustained environmental deterioration. Nature Communications, 11, 2250.

Jacobs, Z., Duller, G. A., Wintle, A. G. & Henshilwood, C. S. 2006. Extending the chronology of deposits at Blombos Cave, South Africa, back to 140 ka using optical dating of single and multiple grains of quartz. Journal of Human Evolution, 51, 255-273.

Kemp, C. W., Tibby, J., Arnold, L. J., Barr, C., Gadd, P. S., Marshall, J. C., Mcgregor, G. B. & Jacobsen, G. E. 2020. Climates of the last three interglacials in subtropical eastern Australia inferred from wetland sediment geochemistry. Palaeogeography, Palaeoclimatology, Palaeoecology, 538, 109463.

Kemp, J. & Rhodes, E. 2010. Episodic fluvial activity of inland rivers in southeastern Australia: Palaeochannel systems and terraces of the Lachlan River. Quaternary Science Reviews, 29, 732-752.

Leslie, C. 2009. Analysing environmental radioactivity in soils and sediments using high-purity germanium gamma detectors at CSIRO Land and Water: Procedures and protocols, CSIRO Land and Water Science Report.

Lewis, R. J., Tibby, J., Arnold, L. J., Barr, C., Marshall, J., Mcgregor, G., Gadd, P. & Yokoyama, Y. 2020. Insights into subtropical Australian aridity from Welsby Lagoon, north Stradbroke Island, over the past 80,000 years. Quaternary Science Reviews, 234, 106262.

Lewis, R. J., Tibby, J., Arnold, L. J., Gadd, P., Jacobsen, G., Barr, C., Negus, P. M., Mariani, M., Penny, D., Chittleborough, D. & Moss, E. 2021. Patterns of aeolian deposition in subtropical Australia through the last glacial and deglacial periods. Quaternary Research, 1-23.

Mejdahl, V. 1979. Thermoluminescence dating: Beta-dose attenuation in quartz grains. Archaeometry, 21, 61-72.

Mejdahl, V. 1987. Internal radioactivity in quartz and feldspar grains. Ancient TL, 5, 10-17.

Mueller, D., Jacobs, Z., Cohen, T. J., Price, D. M., Reinfelds, I. V. & Shulmeister, J. 2018. Revisiting an arid LGM using fluvial archives: a luminescence chronology for palaeochannels of the Murrumbidgee River, south-eastern Australia. Journal of Quaternary Science, 33, 777-793.

Murray, A. S. & Wintle, A. G. 2000. Luminescence dating of quartz using an improved single-aliquot regenerative-dose protocol. Radiation measurements, 32, 57-73.

Nanson, G. C., Jones, B. G., Price, D. M. & Pietsch, T. J. 2005. Rivers turned to rock: Late Quaternary alluvial induration influencing the behaviour and morphology of an anabranching river in the Australian monsoon tropics. Geomorphology, 70, 398-420.

Page, K., Nanson, G. & Price, D. 1996. Chronology of Murrumbidgee river palaeochannels on the Riverine Plain, southeastern Australia. Journal of Quaternary Science: Published for the Quaternary Research Association, 11, 311-326.

Pawley, S. M., Bailey, R. M., Rose, J., Moorlock, B. S., Hamblin, R. J., Booth, S. J. & Lee, J. R. 2008. Age limits on Middle Pleistocene glacial sediments from OSL dating, north Norfolk, UK. Quaternary Science Reviews, 27, 1363-1377.

Potts, P. J., Thompson, M., Chenery, S. R., Webb, P. C. & Kasper, H. U. 2003. GeoPT13-An international proficiency test for analytical geochemistry laboratories-report on round 13/July 2003 (Köln Loess). International Association of Geoanalysts.

Prescott, J. R. & Hutton, J. T. 1994. Cosmic ray contributions to dose rates for luminescence and ESR dating: large depths and long-term time variations. Radiation measurements, 23, 497-500.

Rees-Jones, J. 1995. Optical dating of young sediments using fine-grain quartz. Ancient TL, 13, 9-14.

Rees-Jones, J. & Tite, M. S. 1997. Optical dating results for British archaeological sediments. Archaeometry, 39, 177-187.

Roberts, R. G., Galbraith, R., Yoshida, H., Laslett, G. & Olley, J. M. 2000. Distinguishing dose populations in sediment mixtures: a test of single-grain optical dating procedures using mixtures of laboratory-dosed quartz. Radiation Measurements, 32, 459-465.

Stokes, S., Ingram, S., Aitken, M. J., Sirocko, F., Anderson, R. & Leuschner, D. 2003. Alternative chronologies for Late Quaternary (Last Interglacial–Holocene) deep sea sediments via optical dating of silt-sized quartz. Quaternary Science Reviews, 22, 925-941.

Appendix E. Supplementary Information for Chapter 6

This Appendix contains supplementary information that accompanies Chapter 6

E1. North Stradbroke Island wetland data table

Table E 1 Synthesis of ^{14}C and OSL ages published for wetland sediments from North Stradbroke Island as referred to in Figure 6.2.

Site Name	Core ID	Coring method [a]	Other ID(s)	OSL / ^{14}C	Type/Material	Age [b] (yrs BP)	Error 1σ	Reference [c]
Brown Lake	BL18-3	BOL	OZX784	^{14}C	Lake Sediment	640	20	Lewis et al , 2021
Brown Lake	BL18-3	BOL	OZX785	^{14}C	Lake Sediment	1430	25	Lewis et al , 2021
Brown Lake	BL18-3	BOL	OZX786	^{14}C	Lake Sediment	2130	25	Lewis et al , 2021
Brown Lake	BL18-3	BOL	OZX787	^{14}C	Lake Sediment	3100	25	Lewis et al , 2021
Brown Lake	BL18-3	BOL	OZX788	^{14}C	Lake Sediment	5570	30	Lewis et al , 2021
Brown Lake	BL18-3	BOL	OZX789	^{14}C	Lake Sediment	7120	30	Lewis et al , 2021
Brown Lake	BL18-3	BOL	OZX790	^{14}C	Lake Sediment	16660	70	Lewis et al , 2021
Brown Lake	BL18-3	BOL	OZX794a	^{14}C	Lake Sediment	34970	220	Lewis et al , 2021
Brown Lake	BL18-3	BOL	OZX794b	^{14}C	Lake Sediment	35230	190	Lewis et al , 2021
Brown Lake	BL18-3	BOL	OZX791	^{14}C	Lake Sediment	36570	290	Lewis et al , 2021
Brown Lake	BL18-3	BOL	OZX792	^{14}C	Lake Sediment	43770	490	Lewis et al , 2021
Brown Lake	BL18-3	BOL	OZX793	^{14}C	Lake Sediment	44870	410	Lewis et al , 2021
Brown Lake	BL09	LIV	Beta-361743	^{14}C	Organic Sediment	540	30	Lewis et al , 2021
Brown Lake	BL09	LIV	Beta-361744	^{14}C	Organic Sediment	2420	30	Lewis et al , 2021
Brown Lake	BL09	LIV	Beta-361745	^{14}C	Organic Sediment	3310	40	Lewis et al , 2021
Brown Lake	BL09	LIV	Beta-361746	^{14}C	Organic Sediment	6530	110	Lewis et al , 2021
Brown Lake	BL09	LIV	Beta-361748	^{14}C	Organic Sediment	31980	230	Lewis et al , 2021
Brown Lake	BL09	LIV	Wk-33179	^{14}C	Lake sediment	36974	737	Tibby et al , 2017
Brown Lake	-	LIV	GU5 3	SG-OSL	FMM	47200	8600	Tibby et al , 2017
Welsby Lagoon	WEL15-2	BOL	YAUT-023004*	^{14}C	Plant remains	940	21	Lewis et al , 2020
Welsby Lagoon	WEL15-2	BOL	YAUT-022707*	^{14}C	Plant residual	1197	37	Lewis et al , 2020
Welsby Lagoon	WEL15-2	BOL	YAUT-023321	^{14}C	Leaf fragments	1260	64	Lewis et al , 2020
Welsby Lagoon	WEL15-2	BOL	YAUT-022706*	^{14}C	Plant residual	1392	34	Lewis et al , 2020
Welsby Lagoon	WEL15-2	BOL	YAUT-023323*	^{14}C	Charcoal	2259	63	Lewis et al , 2020
Welsby Lagoon	WEL15-2	BOL	YAUT-023324*	^{14}C	Bark/plant remains	6456	70	Lewis et al , 2020
Welsby Lagoon	WEL15-2	BOL	YAUT-023334*	^{14}C	Charcoal	9003	50	Lewis et al , 2020
Welsby Lagoon	WEL15-2	BOL	YAUT-023326	^{14}C	Seeds	9553	64	Lewis et al , 2020
Welsby Lagoon	WEL15-2	BOL	YAUT-022709	^{14}C	Bark	9602	54	Lewis et al , 2020
Welsby Lagoon	WEL15-2	BOL	YAUT-023325*	^{14}C	Charcoal	9653	64	Lewis et al , 2020
Welsby Lagoon	WEL15-2	BOL	YAUT-022714*	^{14}C	Plant residual	13025	69	Lewis et al , 2020
Welsby Lagoon	WEL15-2	BOL	YAUT-023336*	^{14}C	Plant remains	13828	53	Lewis et al , 2020
Welsby Lagoon	WEL15-2	BOL	YAUT-022713*	^{14}C	Plant residual	15581	80	Lewis et al , 2020
Welsby Lagoon	WEL15-2	BOL	YAUT-022712*	^{14}C	Plant residual	16089	82	Lewis et al , 2020
Welsby Lagoon	WEL15-2	BOL	YAUT-023523	^{14}C	Seeds	16887	78	Lewis et al , 2020
Welsby Lagoon	WEL15-2	BOL	YAUT-023524*	^{14}C	Charcoal	17308	67	Lewis et al , 2020
Welsby Lagoon	WEL15-2	BOL	YAUT-023332*	^{14}C	Plant remains	17359	69	Lewis et al , 2020
Welsby Lagoon	WEL15-2	BOL	YAUT-023333	^{14}C	Wood	17453	67	Lewis et al , 2020
Welsby Lagoon	WEL15-2	BOL	YAUT-023327	^{14}C	Bark	17538	55	Lewis et al , 2020
Welsby Lagoon	WEL15-2	BOL	YAUT-022711	^{14}C	Bark	17646	91	Lewis et al , 2020
Welsby Lagoon	WEL15-2	BOL	WEL15-2(3)	SG-OSL	MAM-4UL	18600	4100	Lewis et al , 2020
Welsby Lagoon	WEL15-1	BOL	WEL15-1(2)	SG-OSL	CAM	37600	4300	Lewis et al , 2020
Welsby Lagoon	WEL15-2	BOL	WEL15-2(6)	SG-OSL	CAM	43700	5400	Lewis et al , 2020
Welsby Lagoon	WEL15-2	BOL	WEL15-2(7)	SG-OSL	CAM	44700	5400	Lewis et al , 2020
Welsby Lagoon	WEL15-2	BOL	WEL15-2(9)	SG-OSL	MAM-3	46200	5100	Lewis et al , 2020
Welsby Lagoon	WEL15-2	BOL	WEL15-2(8)	SG-OSL	CAM	46400	5200	Lewis et al , 2020
Welsby Lagoon	WEL15-2	BOL	WEL15-2(10)	SG-OSL	CAM	50500	5500	Lewis et al , 2020
Welsby Lagoon	WEL15-1	BOL	WEL15-1(5)	SG-OSL	CAM	55700	6000	Lewis et al , 2020
Welsby Lagoon	WEL15-2	BOL	WEL15-2(12)	SG-OSL	CAM	55800	5900	Lewis et al , 2020
Welsby Lagoon	WEL15-2	BOL	WEL15-2(11)	SG-OSL	CAM	59900	6500	Lewis et al , 2020
Welsby Lagoon	WEL15-2	BOL	WEL15-2(13)	SG-OSL	CAM	62400	7900	Lewis et al , 2020
Welsby Lagoon	WEL15-1	BOL	WEL15-1(21)	SG-OSL	CAM	70700	8000	Lewis et al , 2020
Welsby Lagoon	WEL15-1	BOL	WEL15-1(22)	SG-OSL	CAM	73800	7700	Lewis et al , 2020
Welsby Lagoon	WEL15-1	BOL	WEL15-1(23)	SG-OSL	CAM	78500	8600	Lewis et al , 2020
Welsby Lagoon	WEL15-2	BOL	WEL15-2(15)	SG-OSL	CAM	79100	9600	Lewis et al , 2020
Welsby Lagoon	WEL15-2	BOL	WEL15-2(20)	SG-OSL	CAM	79500	6500	Lewis et al , 2020
Welsby Lagoon	WEL15-2	BOL	WEL15-2(19)	SG-OSL	CAM	79600	6800	Lewis et al , 2020
Welsby Lagoon	WEL15-2	BOL	WEL15-2(2)	SG-OSL	CAM	102500	7900	Lewis et al , 2020
Welsby Lagoon	WEL15-1	BOL	WEL15-1(6)	SG-OSL	CAM	125100	9500	Lewis et al , 2020
Welsby Lagoon	WEL15-1	BOL	WEL15-1(7)	SG-OSL	CAM	130000	8200	Lewis et al , 2020
Welsby Lagoon	WEL15-2	BOL	WEL15-2(1)	SG-OSL	CAM	142900	11300	Lewis et al , 2020
Welsby Lagoon	WEL 'edge core'	D	Wk-29036	^{14}C	Charcoal	1803	30	Moss et al , 2013
Welsby Lagoon	WEL 'edge core'	D	Wk-29037	^{14}C	Charcoal	4070	30	Moss et al , 2013
Welsby Lagoon	WEL 'edge core'	D	Wk-30668	^{14}C	Charcoal	5556	26	Moss et al , 2013
Welsby Lagoon	WEL 'edge core'	D	Wk-29038	^{14}C	Charcoal	8043	30	Moss et al , 2013
Welsby Lagoon	WEL 'edge core'	D	Wk-30669	^{14}C	Charcoal	9903	38	Moss et al , 2013
Welsby Lagoon	WEL 'edge core'	D	Beta - 306711	^{14}C	Pollen	14250	50	Moss et al , 2013
Welsby Lagoon	WEL 'edge core'	D	Beta - 306712	^{14}C	Pollen	16350	70	Moss et al , 2013
Welsby Lagoon	WEL 'edge core'	D	Beta - 270553	^{14}C	Peat	18320	90	Moss et al , 2013
Welsby Lagoon	WEL 'edge core'	D	Wk-29039	^{14}C	Peat	18696	88	Moss et al , 2013
Welsby Lagoon	WEL 'edge core'	D	Beta - 306713	^{14}C	Pollen	18980	80	Moss et al , 2013
Welsby Lagoon	WEL 'edge core'	D	Wk-30670	^{14}C	Charcoal	29096	250	Moss et al , 2013
Welsby Lagoon	WEL 'edge core'	D	GU5 1	SG-OSL	CAM	130000	15300	Tibby et al , 2017
Black Snake Lagoon	-	D	Beta-270549	^{14}C	Lake sediment	15480	80	Tibby et al , 2017
Blue Lake	Core 1	LIV	Wk-30238	^{14}C	lake sediment	2397	30	Barr et al , 2013
Blue Lake	Core 1	LIV	Wk-30239	^{14}C	lake sediment	3807	30	Barr et al , 2013
Blue Lake	Core 1	LIV	Wk-21707	^{14}C	lake sediment	5111	37	Barr et al , 2013
Blue Lake	Core 1	LIV	Wk-22011	^{14}C	lake sediment	5781	108	Barr et al , 2013
Blue Lake	Core 1	LIV	Wk-21708	^{14}C	lake sediment	6494	40	Barr et al , 2013
Blue Lake - outflow	-	D	Beta-270547	^{14}C	wood	6780	50	Tibby et al , 2017
Campembah swamp	-	D	Beta-270550	^{14}C	charcoal	6100	50	Tibby et al , 2017
Duck Lagoon	-	D	Wk-29033	^{14}C	charcoal	4210	30	Tibby et al , 2017
Eighteen Mile Swamp	18MS-N1	LIV	Beta-270545	^{14}C	Seed (unidentified)	320	30	Mettam et al , 2011
Eighteen Mile Swamp	18MS-N1	LIV	R32496/2	^{14}C	OM 1 5g/ml floatation	411	15	Mettam et al , 2011
Eighteen Mile Swamp	18MS-N1	LIV	R32496/1	^{14}C	>150 micron OM	4602	30	Mettam et al , 2011
Eighteen Mile Swamp	18MS-N1	LIV	R32496/2	^{14}C	OM 1 2g/ml floatation	5823	30	Mettam et al , 2011
Fern Gully Lagoon	FG15-1	BOL	OZU195	^{14}C	Reed stalk segment	165	50	Kemp et al , 2020
Fern Gully Lagoon	FG15-1	BOL	OZU190	^{14}C	Leaf fragment	790	30	Kemp et al , 2020
Fern Gully Lagoon	FG15-1	BOL	OZU189	^{14}C	Terrestrial gum nut	1040	30	Kemp et al , 2020
Fern Gully Lagoon	FG15-1	BOL	OZU795	^{14}C	Reed stalk segment	1925	30	Kemp et al , 2020
Fern Gully Lagoon	FG15-1	BOL	OZU793	^{14}C	Reed stalk segment	6225	35	Kemp et al , 2020

Fern Gully Lagoon	FG15-1	BOL	OSL-1(2)	SG-OSL	MAM-3	6690	2000	Kemp et al , 2020
Fern Gully Lagoon	FG15-1	BOL	OZU792	^{14}C	Bark fragment	11290	40	Kemp et al , 2020
Fern Gully Lagoon	FG15-1	BOL	OSL-16(1)	SG-OSL	MAM-3	13300	2000	Kemp et al , 2020
Fern Gully Lagoon	FG15-1	BOL	OZU193	^{14}C	Leaf fragment	14480	60	Kemp et al , 2020
Fern Gully Lagoon	FG15-1	BOL	OZU192	^{14}C	Terrestrial seed	15000	60	Kemp et al , 2020
Fern Gully Lagoon	FG15-1	BOL	OZU794	^{14}C	Bark fragment	16290	60	Kemp et al , 2020
Fern Gully Lagoon	FG15-1	BOL	OSL-8 2(2)	SG-OSL	MAM-4	17500	2300	Kemp et al , 2020
Fern Gully Lagoon	FG15-1	BOL	OSL-8(1)	SG-OSL	MAM-4	19900	2700	Kemp et al , 2020
Fern Gully Lagoon	FG15-1	BOL	OSL-9(1)	SG-OSL	MAM-4	20000	2800	Kemp et al , 2020
Fern Gully Lagoon	FG15-1	BOL	OSL-10(1)	SG-OSL	MAM-3	21200	2600	Kemp et al , 2020
Fern Gully Lagoon	FG15-1	BOL	OZU194	^{14}C	Charcoal	28330	120	Kemp et al , 2020
Fern Gully Lagoon	FG15-1	BOL	OZU198	^{14}C	Reed stalk segment	30420	240	Kemp et al , 2020
Fern Gully Lagoon	FG15-1	BOL	OSL-18(1)	SG-OSL	MAM-3	33200	8000	Kemp et al , 2020
Fern Gully Lagoon	FG15-1	BOL	OZU799	^{14}C	Reed stalk segment	37300	360	Kemp et al , 2020
Fern Gully Lagoon	FG15-1	BOL	OZU796	^{14}C	Bark fragment	39730	810	Kemp et al , 2020
Fern Gully Lagoon	FG15-1	BOL	OZU196	^{14}C	Charcoal	39880	330	Kemp et al , 2020
Fern Gully Lagoon	FG15-1	BOL	OZU798	^{14}C	Charcoal	44110	850	Kemp et al , 2020
Fern Gully Lagoon	FG15-1	BOL	OZU797	^{14}C	Charcoal	45400	1500	Kemp et al , 2020
Fern Gully Lagoon	FG15-1	BOL	OZU197	^{14}C	Charcoal	48200	750	Kemp et al , 2020
Fern Gully Lagoon	FG15-1	BOL	OSL-17(1)	SG-OSL	CAM	77700	9200	Kemp et al , 2020
Fern Gully Lagoon	FG15-1	BOL	OSL-15(1)	SG-OSL	CAM	95500	9730	Kemp et al , 2020
Fern Gully Lagoon	FG15-1	BOL	OSL-16 2(2)	SG-OSL	MAM-3	128000	15300	Kemp et al , 2020
Fern Gully Lagoon	FG15-1	BOL	OSL-13(1)	SG-OSL	CAM	132000	20300	Kemp et al , 2020
Fern Gully Lagoon	FG15-1	BOL	OSL-14(1)	SG-OSL	CAM	135000	16300	Kemp et al , 2020
Fern Gully Lagoon	FG15-1	BOL	OSL-12(1)	SG-OSL	CAM	137000	15400	Kemp et al , 2020
Fern Gully Lagoon	FG15-1	BOL	OSL-11(1)	SG-OSL	CAM	171000	33400	Kemp et al , 2020
Fern Gully Lagoon	FG15-1	BOL	OSL-10 2(2)	SG-OSL	CAM	179000	22400	Kemp et al , 2020
Fern Gully Lagoon	FG15-1	BOL	OSL-2(1)	SG-OSL	MAM-4	180000	26400	Kemp et al , 2020
Fern Gully Lagoon	FG15-1	BOL	OSL-3(1)	SG-OSL	CAM	201000	30400	Kemp et al , 2020
Fern Gully Lagoon	FG15-1	BOL	OSL-4(2)	SG-OSL	CAM	206000	29400	Kemp et al , 2020
Fern Gully Lagoon	FG15-1	BOL	OSL-5(1)	SG-OSL	CAM	248000	40600	Kemp et al , 2020
Fern Gully Lagoon	FG15-1	BOL	OZU191	^{14}C	Reed stalk segment	Modern		Kemp et al , 2020
Fern Gully Lagoon	-	LIV	Wk-29035	^{14}C	Lake sediment	37155	646	Tibby et al , 2017
Fern Gully Lagoon	-	LIV	Ad13069	SG-OSL	CAM	208400	32500	Tibby et al , 2017
Ibis Lagoon West	-	D	Wk-29034	^{14}C	charcoal	5384	30	Tibby et al , 2017
Kounpee Swamp	-	D	Beta-270551	^{14}C	Charcoal	17740	100	Tibby et al , 2017
Myora Springs	-	D	ANSTO	^{14}C	bulk sediment	220	40	Moss et al , 2011
Myora Springs	-	D	Wk-18471	^{14}C	bulk sediment	652	29	Moss et al , 2011
Myora Springs	-	D	ANSTO	^{14}C	bulk sediment	Modern		Moss et al , 2011
Native Companion Lagoon	NCL	D	NC-1-001	^{14}C	Peat	540	36	Petherick et al , 2008
Native Companion Lagoon	NCL	D	NC-1-028	^{14}C	Peat	1745	37	Petherick et al , 2008
Native Companion Lagoon	NCL	D	NC-1-081	^{14}C	Peat	6176	47	Petherick et al , 2008
Native Companion Lagoon	NCL	D	NC-P-009	^{14}C	Peat	6176	47	Petherick et al , 2008
Native Companion Lagoon	NCL	D	NC-1-069	^{14}C	Peat	6353	50	Petherick et al , 2008
Native Companion Lagoon	NCL	D	NC-1-149	^{14}C	Peat	9222	65	Petherick et al , 2008
Native Companion Lagoon	NCL	D	NC-1-177	^{14}C	Peat	10130	73	Petherick et al , 2008
Native Companion Lagoon	NCL	D	NC-1-207	^{14}C	Peat	11478	79	Petherick et al , 2008
Native Companion Lagoon	NCL	D	NC-1-224	^{14}C	Peat	12714	90	Petherick et al , 2008
Native Companion Lagoon	NCL	D	NC-1-256	^{14}C	Peat	13467	98	Petherick et al , 2008
Native Companion Lagoon	NCL	D	NC-1-270	^{14}C	Peat	13570	100	Petherick et al , 2008
Native Companion Lagoon	NCL	D	NC-1-279	^{14}C	Peat	13586	100	Petherick et al , 2008
Native Companion Lagoon	NCL	D	NC-1-301	^{14}C	Peat	14762	116	Petherick et al , 2008
Native Companion Lagoon	NCL	D	NC-1-335	^{14}C	Peat	15999	132	Petherick et al , 2008
Native Companion Lagoon	NCL	D	NC-1-394	^{14}C	Peat	19311	157	Petherick et al , 2008
Native Companion Lagoon	NCL	D	NC-1-528	^{14}C	Peat	28684	456	Petherick et al , 2008
Native Companion Lagoon	NCL	D	NC-1-567	^{14}C	Peat	33187	816	Petherick et al , 2008
Native Companion Lagoon	NCL	D	NC-1-677	^{14}C	Peat	35757	1147	Petherick et al , 2008
Swallow Lagoon	SLP2	LIV	OZP517	^{14}C	Melaleuca leaves	1 2589	0 0029	Tibby et al , 2017
Swallow Lagoon	SLP2	LIV	Beta-382306	^{14}C	Melaleuca leaves	300	30	Tibby et al , 2017
Swallow Lagoon	SLP2	LIV	OZP518	^{14}C	Melaleuca leaves	560	25	Tibby et al , 2017
Swallow Lagoon	SLP2	LIV	OZP519	^{14}C	Melaleuca leaves	1050	25	Tibby et al , 2017
Swallow Lagoon	SLP2	LIV	OZO275	^{14}C	Melaleuca seed pod	1220	30	Tibby et al , 2017
Swallow Lagoon	SLP2	LIV	OZP520	^{14}C	Melaleuca leaves	1280	25	Tibby et al , 2017
Swallow Lagoon	SLP2	LIV	Wk-31579	^{14}C	Melaleuca leaves	1520	25	Tibby et al , 2017
Swallow Lagoon	SLP2	LIV	OZP521	^{14}C	Melaleuca leaves	1560	25	Tibby et al , 2017
Swallow Lagoon	SLP3	LIV	OZO276	^{14}C	Leaves	1710	30	Tibby et al , 2017
Swallow Lagoon	SLP3 (SL-2)	LIV	OZO206	^{14}C	Seed pod	2385	30	Tibby et al , 2017
Swallow Lagoon	SLP3 (SL-2)	LIV	OZO207	^{14}C	Twig	3205	30	Tibby et al , 2017
Swallow Lagoon	SLP3 (SL-2)	LIV	OZO208	^{14}C	Seed	3310	30	Tibby et al , 2017
Swallow Lagoon	SLP3 (SL-2)	LIV	OZO209	^{14}C	Seed pod	3610	30	Tibby et al , 2017
Swallow Lagoon	SLP3 (SL-2)	LIV	OZO210	^{14}C	Twigs Barl	3820	30	Tibby et al , 2017
Swallow Lagoon	SLP3 (SL-2)	LIV	OZO277	^{14}C	Twigs Bark	4935	30	Tibby et al , 2017
Swallow Lagoon	SLP3 (SL-2)	LIV	OZO278	^{14}C	Leaves	5750	30	Tibby et al , 2017
Swallow Lagoon	SLP3 (SL-2)	LIV	Wk-31580	^{14}C	Melaleuca leaves	6210	30	Tibby et al , 2017
Swallow Lagoon	SLP3 (SL-2)	LIV	OZO279	^{14}C	Leaves and seeds	6920	30	Tibby et al , 2017
Tortoise Lagoon	TOR	D	Tor-D-001	^{14}C	Peat	4160	60	Moss et al , 2013
Tortoise Lagoon	TOR	D	Tor-D-002	^{14}C	Organic Muds	6350	70	Moss et al , 2013
Tortoise Lagoon	TOR	D	Tor-D-003	^{14}C	Peat	10410	80	Moss et al , 2013
Tortoise Lagoon	TOR	D	Tor-D-004	^{14}C	Peat	13360	100	Moss et al , 2013
Tortoise Lagoon	TOR	D	Tor-D-009	^{14}C	Pollen	14420	80	Moss et al , 2013
Tortoise Lagoon	TOR	D	Tor-D-011	^{14}C	Pollen	15060	100	Moss et al , 2013
Tortoise Lagoon	TOR	D	Tor-D-010	^{14}C	Pollen	15640	280	Moss et al , 2013
Tortoise Lagoon	TOR	D	Tor-D-008	^{14}C	Pollen	16090	80	Moss et al , 2013
Tortoise Lagoon	TOR	D	Tor-D-012	^{14}C	Pollen	16710	80	Moss et al , 2013
Tortoise Lagoon	TOR	D	Tor-D-007	^{14}C	Sandy Peat	16870	140	Moss et al , 2013
Tortoise Lagoon	TOR	D	Tor-D-005	^{14}C	Peat	18630	140	Moss et al , 2013
Tortoise Lagoon	TOR	D	Tor-D-006	^{14}C	Peat	23860	180	Moss et al , 2013

[a] BOL = Bolivia piston corer (modified); D = D-section corer; LIV = Livingstone corer.

[b] where BP is 1950 for ^{14}C, and date of core extraction for OSL.

[c] Reference from which age data was extracted

* not used in age modelling.

E2 References

Barr, C., Tibby, J., Marshall, J. C., Mcgregor, G. B., Moss, P. T., Halverson, G. P. & Fluin, J. 2013. Combining monitoring, models and palaeolimnology to assess ecosystem response to environmental change at monthly to millennial timescales: the stability of Blue Lake, North Stradbroke Island, Australia. Freshwater Biology, 58, 1614-1630.

Kemp, C. W., Tibby, J., Arnold, L. J., Barr, C., Gadd, P. S., Marshall, J. C., Mcgregor, G. B. & Jacobsen, G. E. 2020. Climates of the last three interglacials in subtropical eastern Australia inferred from wetland sediment geochemistry. Palaeogeography, Palaeoclimatology, Palaeoecology, 538, 109463.

Lewis, R. J., Tibby, J., Arnold, L. J., Barr, C., Marshall, J., Mcgregor, G., Gadd, P. & Yokoyama, Y. 2020. Insights into subtropical Australian aridity from Welsby Lagoon, north Stradbroke Island, over the past 80,000 years. Quaternary Science Reviews, 234, 106262.

Lewis, R. J., Tibby, J., Arnold, L. J., Gadd, P., Jacobsen, G., Barr, C., Negus, P. M., Mariani, M., Penny, D., Chittleborough, D. & Moss, E. 2021. Patterns of aeolian deposition in subtropical Australia through the last glacial and deglacial periods. Quaternary Research, 1-23.

Mettam, P., Tibby, J., Barr, C. & Marshall, J. 2011. Development of eighteen mile swamp, North Stradbroke Island: a palaeolimnological study. Proceedings of the Royal Society of Queensland, The, 117, 119-131.

Moss, E. 2013. A Dust Record from Lacustrine Sediments on North Stradbroke Island, Queensland: Evidence for Climate Variability in Central and Southeastern Australia During the Late Quaternary. [Bachelor's Thesis], The University of Sydney.

Moss, P., Petherick, L. & Neil, D. 2011. Environmental change at Myora Springs, North Stradbroke Island over the last millennium. Proceedings of the Royal Society of Queensland, The, 117, 113-140.

Petherick, L., Mcgowan, H. & Moss, P. 2008. Climate variability during the Last Glacial Maximum in eastern Australia: evidence of two stadials? Journal of Quaternary Science: Published for the Quaternary Research Association, 23, 787-802.

Tibby, J., Barr, C., Marshall, J. C., Mcgregor, G. B., Moss, P. T., Arnold, L. J., Page, T. J., Questiaux, D., Olley, J. & Kemp, J. 2017. Persistence of wetlands on North Stradbroke Island (south-east Queensland, Australia) during the last glacial cycle: implications for Quaternary science and biogeography. Journal of Quaternary Science, 32, 770-781.

Appendix F. Conference and seminar presentation abstracts

This Appendix contains abstracts that were submitted to various associations, research groups and conference organisers in the course of this research.

GSA – GESSS (SA) 2021

Geological Society of Australia (GSA), Earth Science Students Symposium (GESSS), South Australia

The hydroclimatic and chronological context of late Pleistocene megafauna extinction in north-eastern Australia

Lewis, R.J.[a *], Arnold, L. J.[a], Hocknull, S.[b, c], Tibby, J.[d], Demuro, M.[a] & Lawrence, R.[b]

[a] School of Physical Sciences, Environment Institute, and Institute for Photonics and Advanced Sensing (IPAS), University of Adelaide, North Terrace Campus, Adelaide, SA, 5005, Australia.

[b] Geosciences, Queensland Museum, 122 Gerler Rd. Hendra, Queensland, 4011, Australia.

[c] School of BioSceinces, Faculty of Science, University of Melbourne, Melbourne, Victoria, 3010, Australia.

[d] Department of Geography, Environment and Population, University of Adelaide, Adelaide, SA 5005, Australia.

The lack of well dated palaeoenvironmental archives continues to fuel the late Pleistocene megafauna extinction debate for Sahul (Australian and New Guinea). Conventionally, palaeoenvironmental reconstructions and inferences of human- verses climate-mediated causes of megafauna extinction have relied on biological proxy data. However, a wealth of environmental information can also be inferred from abiotic data, including the type and mode of sediment deposition itself. We examine the timing and palaeoenvironmental significance of fossil-bearing sediment archives from South Walker Creek, tropical Queensland, and use a Bayesian modelling approach to compare the resulting chronometric datasets with a range of other Australian catchment records. Regional spatiotemporal patterns of hydrological activity is then inferred from this chronological framework and used to consider megafauna disappearance in the context of changing environmental conditions during the late Pleistocene. Results support a link between the last appearance of megafauna at South Walker Creek around 37.9 thousand years ago (ka) and a regional trend towards a more negative moisture balance during late Marine Isotope Stage 3 (MIS3). Limited fluvial and lacustrine deposition persist across several northern and central Australian catchments through late MIS3 and early- to mid-MIS2, including the Last Glacial Maximum – coincident with an absence of preserved fluvial deposition at South Walker Creek between 43.6 and 15.8 ka – before renewed fluvial deposition is recorded across various basins from late MIS2 onwards (~16 ka). The outcome of this analysis provides important insights into regional Australian palaeoenvironmental reconstructions during the late Pleistocene; revealing differences in catchment responses related to synoptic climate conditions during MIS3–1, and adding new constraints on megafauna extinction dynamics in the underrepresented tropical zone of Sahul.

LED2021

International Luminescence and Electron Spin Resonance Dating conference (LED2021)

Suitability of luminescence dating approaches (OSL, TT-OSL, TL) in karst systems of northeast Queensland, Australia

Lewis, R.J.[a *], Arnold, L.J.[a], Hocknull, S.[b], Demuro, M.[a]

[a] School of Physical Sciences, Environment Institute, and Institute for Photonics and Advanced Sensing (IPAS), University of Adelaide, North Terrace Campus, Adelaide, SA, 5005, Australia.

[b] Geosciences, Queensland Museum, 122 Gerler Rd., Hendra, QLD, 4011, Australia & School of BioSciences, Faculty of Science, University of Melbourne, Melbourne, VIC, 3010, Australia.

Fundamental gaps remain in our knowledge of faunal responses to late and middle Pleistocene climate change across Australia owing to geographic imbalances in fossil discoveries and limited temporal coverage of existing chronological records. These limitations are particularly evident for tropical Australia and New Guinea (Sahul), where reliably dated fossil sites and palaeoenvironmental records are both significantly underrepresented. As a consequence, regional models of Pleistocene ecological turnovers for tropical Sahul, including late Pleistocene megafauna extinction, have relied on interpolation across vast landmasses that are essentially devoid of data. The fossiliferous cave deposits at Mt Etna and Capricorn Caves, central eastern Queensland, are among the few stratified, Pleistocene rainforest vertebrate fossil records known in Australia. U-series dating of speleothems bracketing the extensive fossiliferous layers at Mt Etna provides minimum and maximum ages spanning 205 – 484 ka, and constrains a major turnover from rainforest to xeric-adapted fauna sometime after 280 ka [1]. The sediment-filled chambers of the neighbouring Capricorn Caves system contain diverse fossil assemblages potentially extending into the late Pleistocene, but are currently lacking any systematic dating evaluations.

In this study we use complementary quartz and feldspar luminescence dating approaches to establish the first direct ages for fossil-bearing clastic infill at Mt Etna, and expand the chronological coverage of the region's fauna record to include two previously undated sites at Capricorn Caves (Zig Zag and Harp Cave). Single-grain quartz OSL dating is applied to the late Pleistocene deposits at Capricorn Caves, while a combination of single-grain thermally transferred optically stimulated luminescence (TT-OSL) dating of quartz and multiple-grain post-infrared infrared stimulated luminescence (pIR-IRSL) of K-feldspars is applied to the middle Pleistocene Mt Etna clastic infill sequences. Comparisons with independent age control (capping speleothem U-series ages) at Mt Etna is used to examine the suitability of different extended-range luminescence dating signals, and refine our equivalent dose (D_e) determination procedures.

The findings of this study are used to (i) provide insights into the broader applicability of extended-range luminescence dating techniques for refining the late and middle Pleistocene faunal history of tropical Sahul; (ii) refine the timing of the major faunal turnover recorded at Mt Etna during Marine Isotope Stage 8, and; (iii) enable improved correlations of sedimentary infills and fossil assemblages across the karst systems of central eastern Queensland.

[1] Hocknull, S. A., Zhao, J.-x., Feng, Y.-x. & Webb, G. E. Responses of Quaternary rainforest vertebrates to climate change in Australia. Earth and Planetary Science Letters 264, 317-331 (2007).

IPAS Award Ceremony 2021

2021 IPAS best student-led paper prize seminar (2020), Adelaide, Australia

Applying luminescence in sedimentary deposits to shine light on Australia's Pleistocene ecology

Lewis, R.J.[a *]

[a] Department of Earth Sciences, Sprigg Geobiology Centre and Institute for Photonics and Advanced Sensing (IPAS), University of Adelaide, North Terrace, South Australia, 5005, Australia.

The scarcity of well dated palaeoenvironmental archives continues to limit resolution of the late Pleistocene megafauna extinction debate for Sahul (Australian and New Guinea). Conventionally, palaeoenvironmental reconstructions and inferences of human- verses climate-mediated causes of megafauna extinction have relied on biological proxy data, particularly pollen records. However, a wealth of environmental information can also be inferred from abiotic data, including the type and mode of sediment deposition itself. In my research, I have been examining the timing and palaeoenvironmental significance of fossil-bearing sediment archives from tropical and sub-tropical Queensland, applying Bayesian modelling to enable robust comparison of chronometric datasets. This research has potential to enhance our understanding of variables influencing ecological turnover spanning millennia.

SheMAX 2019

2019 SheMAX workshop, North Stradbroke Island, Australia

A High-resolution, chronological study of a 120 ka continuous sedimentary record in subtropical Australia

Lewis, R. J. [a, b *], Tibby, J. [b, c], Arnold, L. J. [a], Barr, C. [c], Marshall, J. [d], McGregor, G. [d]

[a] Department of Earth Sciences, University of Adelaide, North Terrace, South Australia, 5005, Australia.

[b] Sprigg Geobiology Centre, University of Adelaide, North Terrace, South Australia, 5005, Australia.

[c] Department of Geography, Environment and Population, University of Adelaide, North Terrace, South Australia, 5005.

[d] Queensland Department of Environment and Science, GPO Box 5079, Brisbane, Queensland, 5078, Australia.

Few sediment records, especially in Australia, preserve temporal environmental changes that have been rigorously chronologically defined through to MIS5 (~120 – 80 ka). The lack of chronological constraints contributes to the uncertainty when differentiating between global and local forces driving proxy responses. Resolving when environmental changes occurred extending back to MIS5, especially during MIS4, MIS3 and the LGM, is particularly important for Australia as many culturally significant questions related to human arrival and megafauna extinction remain unanswered. This study presents a new highly constrained chronological model, extending back to MIS5, from sediment cores extracted in Welsby Lagoon, a freshwater wetland in subtropical eastern Australia. We utilise XRF core scanning in combination with radiocarbon (n = 6) and optically stimulated luminescence dating (n = 21) to provide a robust age-depth model against which climactic proxies can now be compared. The age model is parameterised by an upper and lower boundary (z = 1250 cm) with consideration based on sedimentological change. The instillation of this age model, in conjunction with elemental XRF core scanning data, local and regional proxy studies [1][2], highlights the significance of Welsby Lagoon with respect to addressing questions relating to the cause of environmental and taxonomic change via climate and/or anthropogenic influence. Correlation of the XRF data with the age model shows two distinct increases in deposition of terrestrially derived material during the period of 36 – 20 ka. This is supportive of earlier onset of the cold and dry conditions associated with the Southern Hemisphere LGM persisting from 30 – 18 kyr preserved in the sediment at the proximal Native Companion Lagoon [3].

[1] Cadd, H. R., Tibby, J., Barr, C., Tyler, J., Unger, L., Leng, M. J., Marshall, J. C., Mcgregor, G., Lewis, R. & Arnold, L. J. 2018. Development of a Southern Hemisphere subtropical wetland (Welsby Lagoon, south-east Queensland, Australia) through the last glacial cycle. Quaternary Science Reviews, 202, 53-65.

[2] Tibby, J., Barr, C., Marshall, J. C., Mcgregor, G. B., Moss, P. T., Arnold, L. J., Page, T. J., Questiaux, D., Olley, J. & Kemp, J. 2017. Persistence of wetlands on North Stradbroke Island (south-east Queensland, Australia) during the last glacial cycle: implications for Quaternary science and biogeography. Journal of Quaternary Science, 32, 770-781.

[3] Petherick, L., Mcgowan, H. & Moss, P. 2008. Climate variability during the Last Glacial Maximum in eastern Australia: evidence of two stadials? Journal of Quaternary Science: Published for the Quaternary Research Association, 23, 787-802.

2019 FGC (SA)

Field geology club of South Australia seminar night, Adelaide, Australia

Wetland sediment geochemistry: what can it tell us about the past?

Lewis, R. J.[a *]

[a] Department of Earth Sciences, Sprigg Geobiology Centre and Institute for Photonics and Advanced Sensing (IPAS), University of Adelaide, North Terrace, South Australia, 5005, Australia.

Deciphering the intricacies of how the Australian environment has evolved over time is fundamental in exploring various hypotheses, especially those associated with continental wide faunal extinctions. Climate events have a profound influence on environmental change forcing shifts in the moisture balance across the nation. Sediment records in terrestrial wetlands are important for understanding temporal changes as they are capable of preserving a multitude of proxies used in reconstructing the past. As core scanning technology continue to develop, it is now possible to evaluate chemical changes in sedimentary sequences at high resolution, providing an additional proxy without needing to sacrifice material. Through combining core scanning technology and rigorous age controls across 25 m of seemingly featureless peats, we unravel the history of a >85,000-year-old wetland on North Stradbroke Island, identifying links between soil chemistry and global climate drivers.

AQUA 2018

Australia Quaternary Association: Biennial Conference, Canberra, Australia

Independent Bayesian age modelling in subtropical wetlands to assess the influence of global climate drivers across Australia

Lewis R.J. [a, b *], Tibby J. [b, c], Arnold L. J. [a, b], Barr C [b, c], Marshall J [d], McGregor G [d], Gadd P [e]

[a] Department of Earth Sciences, University of Adelaide, North Terrace, South Australia, 5005, Australia.

[b] Sprigg Geobiology Centre, University of Adelaide, North Terrace, South Australia, 5005, Australia.

[c] Department of Geography, Environment and Population, University of Adelaide, North Terrace, South Australia, 5005.

[d] Queensland Department of Environment and Science, GPO Box 5079, Brisbane, Queensland, 5078, Australia.

[e] Australian Nuclear Science & Technology Organisation, Lucas Heights, Australia

Rigorously dated, continuous sedimentological records capturing multiple glacial/interglacial cycles are important for evaluating the magnitude and range of drivers influencing ecosystem change in Australia. Multi-proxy palaeoenvironmental reconstructions are commonly used to identify changes in long-term environmental conditions, particularly when exploring the climatic backdrop to Australia's large scale faunal extinctions. However, interpretations of these records may not be straightforward as local and regional climate signals are often mixed in proxy records. In order to evaluate whether improved temporal constraint can help with differentiating such convoluted signals, thereby increasing the confidence placed in the role of teleconnections across the Southern Hemisphere, we present a comprehensively dated 12.7 m (basal age ~130 ka) wetland core consisting of 21 optically stimulated luminescence and seven radiocarbon ages from North Stradbroke Island. The amalgamation of stratigraphic information and independent age constraints within a Bayesian framework, highlights the complex depositional history of Welsby Lagoon between late MIS5 and MIS2. ITRAX core scanning data reveals fluctuations in elemental abundance through time, in particular the decrease in the amount of aeolian sediment following MIS3. Variability is attributed to regional environmental regime changes controlled by global drivers, including Heinrich events, and the influence of moisture across mainland Australia. The comprehensive dating approach undertaken at Welsby Lagoon highlights the role that the terrestrial palaeoenvironmental records of North Stradbroke Island can play in assessing long-term climate drivers across continental Australia, without relying exclusively on isotopic tuning of remote (ice core or marine) records.